Research and Technology 1988

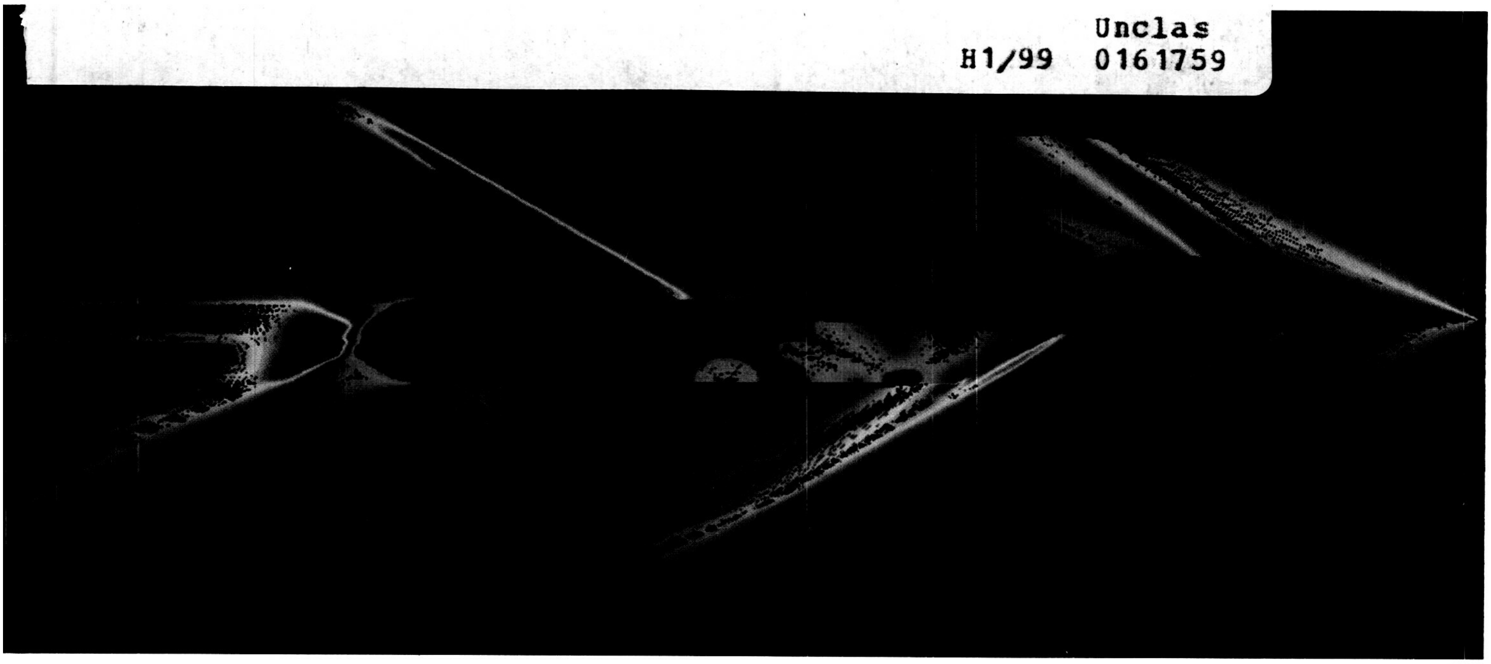

Annual Report of the Langley Research Center

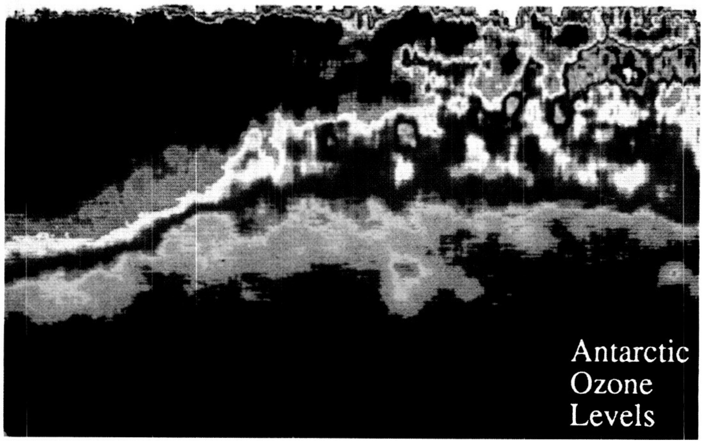

Antarctic
Ozone
Levels

ORIGINAL PAGE
COLOR PHOTOGRAPH

NASA Technical Memorandum 4078

ORIGINAL PAGE IS
OF POOR QUALITY

Research and Technology 1988

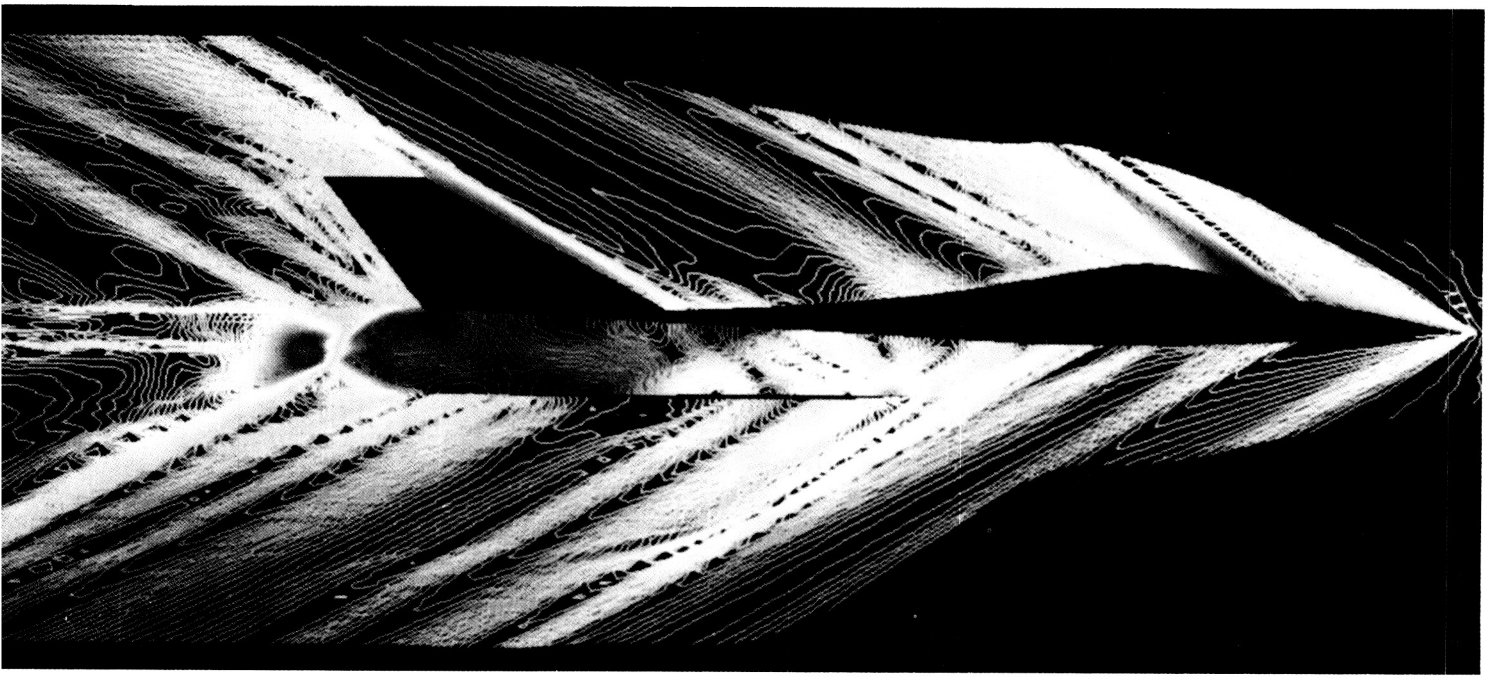

Annual Report of the Langley Research Center

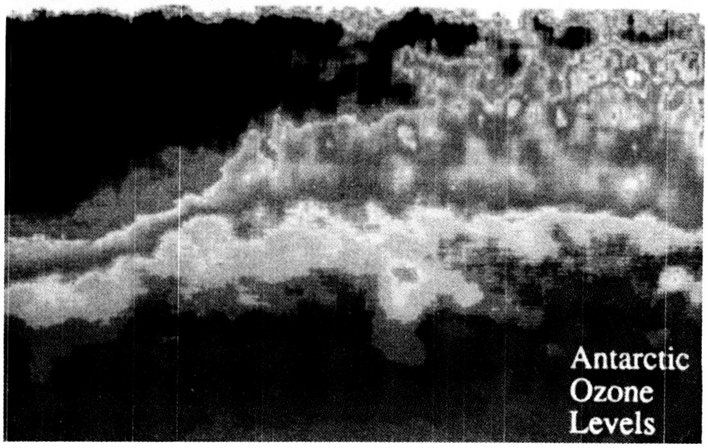

National Aeronautics and
Space Administration

Langley Research Center
Hampton, Virginia

ORIGINAL CONTAINS
COLOR ILLUSTRATIONS

NASA Technical Memorandum 4078

Foreword

The mission of the NASA Langley Research Center is to increase the knowledge and capability of the United States in a full range of aeronautics disciplines and in selected space disciplines. This mission will be accomplished by performing innovative research relevant to national needs and Agency goals, transferring technology to users in a timely manner, and providing development support to other United States Government agencies, industry, and other NASA centers. This report contains highlights of the major accomplishments and applications that have been made during the past year. The highlights illustrate both the broad range of the research and technology activities at NASA Langley Research Center and the contributions of this work toward maintaining United States leadership in aeronautics and space research. For further information about the report, contact Dr. Richard W. Barnwell, Chief Scientist, Mail Stop 105-A, NASA Langley Research Center, Hampton, Virginia 23665, (804) 864-6062.

Richard Petersen

Richard H. Petersen
Director

Availability Information

The NASA program office and the corresponding Agency-wide Research and Technology Objectives and Plans (RTOP) work breakdown structure are listed in the Contents for each research and technology accomplishment. OAST designates the Office of Aeronautics and Space Technology; OSSA designates the Office of Space Science and Applications; AA designates the Associate Administrator; OCE designates the Office of the Chief Engineer; OCP designates the Office of Commercial Programs; OSF designates the Office of Space Flight; and OSS designates the Office of the Space Station.

For additional information on any summary, contact the individual identified with the highlight. This individual is generally either a member or a leader of the research group submitting the highlight. Commercial telephone users may dial the listed extension preceded by (804) 864 (865 is anticipated to change to 864 in 1989). Telephone users with access to the Federal Telecommunications System (FTS) may dial the extension preceded by 928.

Contents

Aeronautics Directorate

Electronics Directorate

Flight Systems Directorate

Space Directorate

Structures Directorate

Systems Engineering and Operations Directorate

Technology Utilization Program

Aeronautics Directorate

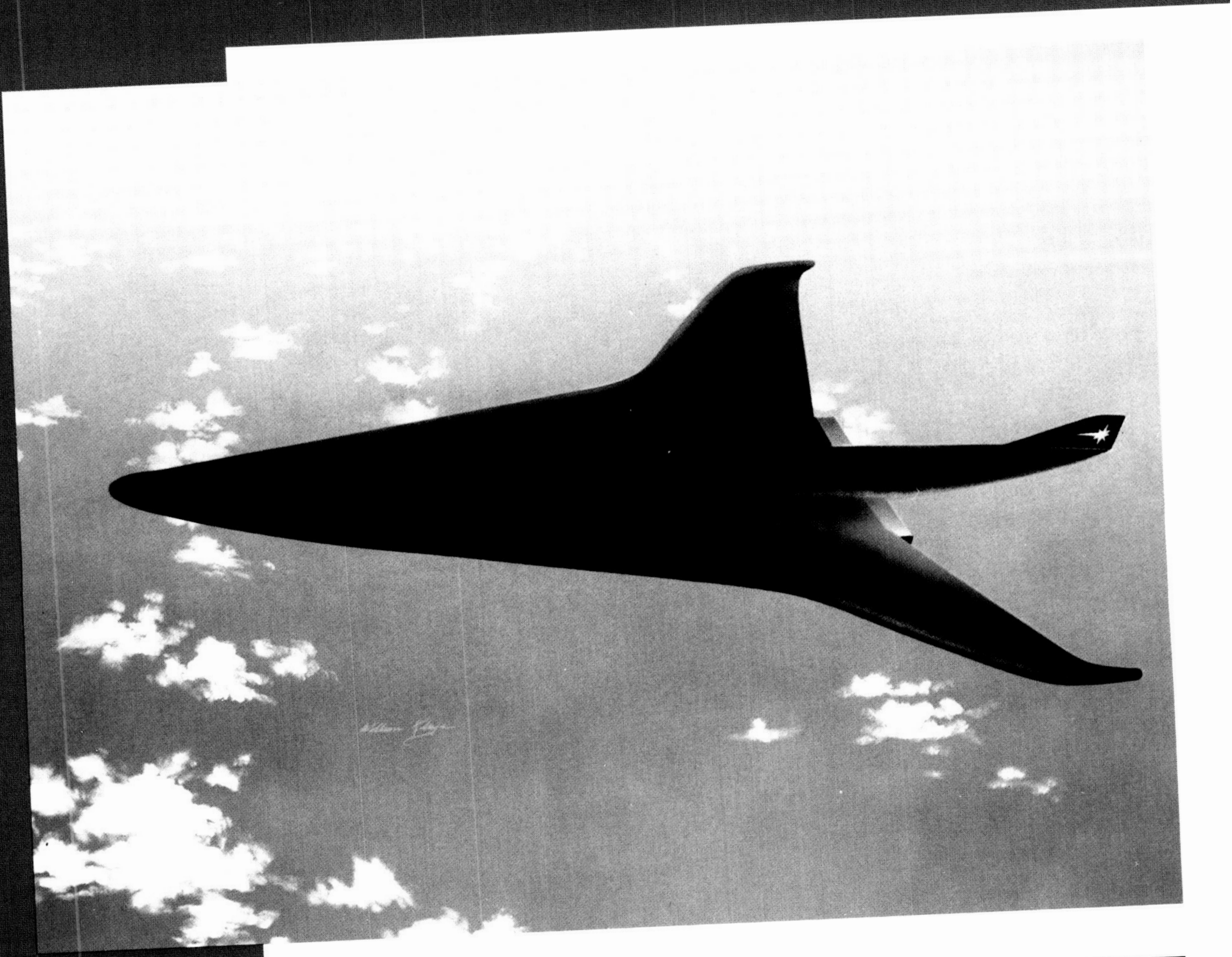

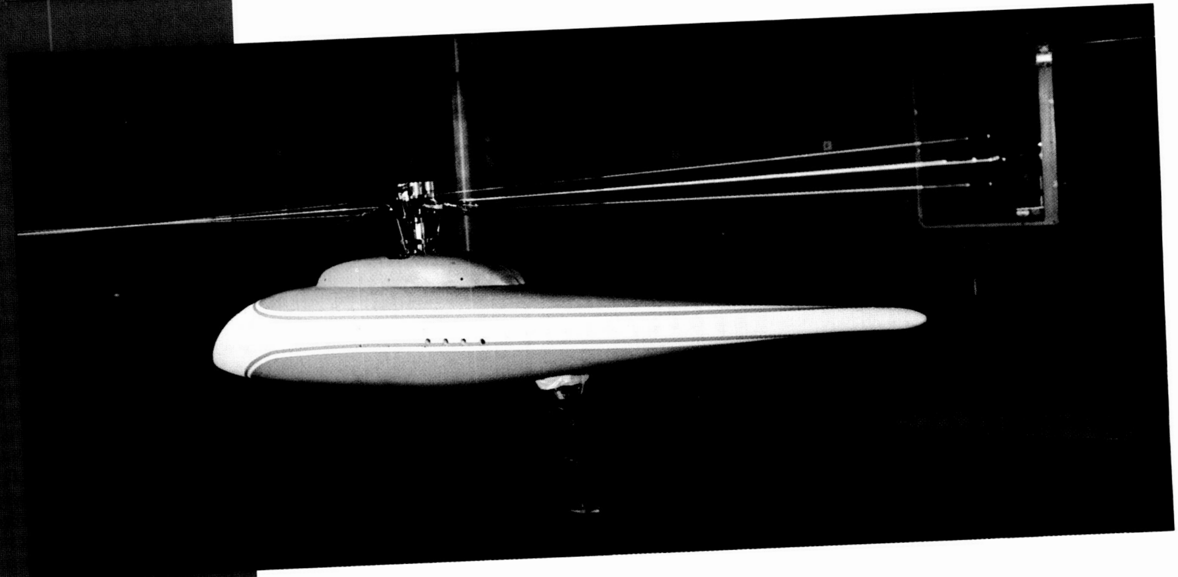

ORIGINAL PAGE
COLOR PHOTOGRAPH

The Aeronautics Directorate is composed of approximately 300 scientists and engineers engaged in basic and applied research in the various aeronautics disciplines. The directorate is organized into four research divisions and a program office, which conduct aeronautical research to advance the state of the art throughout the complete aerodynamic speed range.

The Hypersonic Technology Office coordinates broad-scope hypersonic vehicle research and technology programs including those involving the National Aero-Space Plane (NASP) and conducts design studies of various hypersonic vehicle concepts.

The Advanced Vehicles Division conducts multidisciplinary advanced aeronautical vehicle studies to assess the benefits of discipline research advances and to identify potential new research thrusts. In particular, the vehicle classes of long-haul subsonic and supersonic transports, advanced military aircraft, and general-aviation and commuter aircraft are addressed. The primary emphasis is on high-risk, far-term application of integrated research results from primary aeronautical disciplines.

The Low-Speed Aerodynamics Division conducts research in the areas of basic fluid mechanics, low-speed aerodynamics, flight dynamics and flight management, aircraft operations, aviation safety, laminar-flow control, and improved test methods. The division develops and validates theoretical aerodynamic methods for subsonic conditions and design methodology required to improve subsonic aerodynamic performance, stall/spin behavior, handling qualities, and takeoff and landing performance.

The Transonic Aerodynamics Division conducts research to advance the state of the art of transonic aircraft technology in the areas of fundamental aerodynamics, with particular emphasis on Reynolds number effects, laminar-flow concepts, stability and control, performance analysis, configuration concepts, and related aerodynamic phenomena. Particular areas of emphasis include improving the efficiency and reducing the fuel consumption of conventional jet transports, developing the technology for advanced military combat aircraft, developing theoretical and analytical methods for predicting aerodynamic characteristics in separated and transonic flows, developing advanced airfoils for low-speed and transonic aircraft and helicopters, and developing advanced experimental techniques, including advanced wall concepts, for transonic wind tunnels and cryogenic wind tunnel technology.

The High-Speed Aerodynamics Division conducts research to advance the state of the art for supersonic aircraft, hypersonic aircraft, and advanced cruise and tactical missiles, and to support the development of high-performance military aircraft, the Space Shuttle, and follow-on advanced space transportation systems. New analytical methods for design and analysis are derived and applied to advanced high-speed aircraft and missile concepts. Key experiments are conducted to validate the analytical methods, explore the potential of advanced concepts, and provide a data base for use by industry design teams.

Propulsion analysis by Langley Research Center was the distinguishing factor in the selection of the five contractor configurations for the NASP Program. The first three-dimensional Navier-Stokes calculation was performed for a complete aircraft forebody at high angle of attack. This new capability provides a significant increase in the ability to analyze complex configurations and has been used to make the first calculations of an F-18 forebody at high angle of attack. The Pilot Low-Disturbance Tunnel tests eliminated a long-standing discrepancy in the theoretical correlation with experiments for cones and flat plates. This new information has led to a redefinition of the transition criteria for NASP configurations. In-house and contracted system studies have indicated the feasibility of a viable, economic High-Speed Civil Transport for the years 2000 to 2010 and identified the high-risk/high-payoff research areas required to bring it to fruition.

Assessment of Boundary-Layer Transition Measurement Techniques

An experiment that assesses boundary-layer transition detection

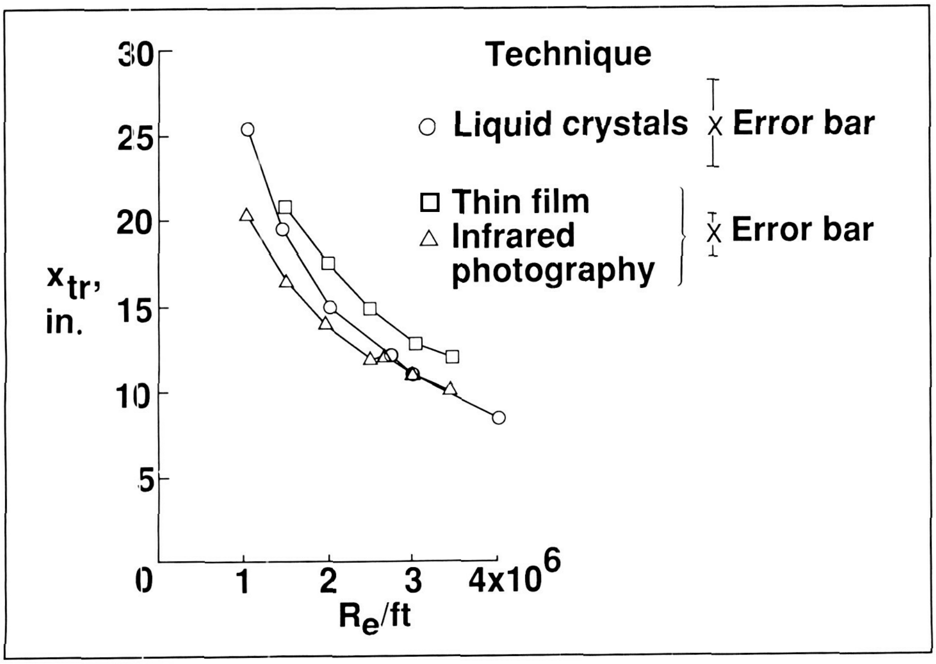

Comparison of transition measurements at $M_\infty = 2.5$.

techniques has been conducted in the Langley Unitary Plan Wind Tunnel for Mach numbers M_∞ of 1.5, 2.0, and 2.5 over a range of Reynolds numbers R_e per foot from 1.0 to 4.0 × 10^6. This assessment was to compare, for the same test model and conditions, the sensitivity and ease of use of liquid crystals, passive infrared video photography, and vapor-deposited thin films. The model used for the experiment was a flat plate at zero incidence.

Because the three measurement techniques use different flow properties to detect transition, the following criteria were established for determining the location of transition: for liquid crystals, the mid-point of the region of the fluctuating shear stress; for infrared photography, the location where the temperature of the insulated plate had increased by 0.1 K; and for the thin films, the location where the intermittency factor reached 0.5 (that is, where the flow is turbulent 50 percent of the time and laminar 50 percent of the time). Typical comparisons of the respective transition distances from the leading edge of the plate x_{tr} are illustrated in the figure for a Mach number equal to 2.5. Using the data from the thin films to locate the 50-percent intermittency point, the experiment determined that both the liquid crystals and the infrared techniques were able to detect transition near or before the 50-percent intermittency point. Choosing which technique to use for an experimental program will depend on model construction, model surface tolerances, and the Mach number range of interest.

(Robert M. Hall, 2601)

Multigrid Solution of Euler Equations on Unstructured and Adaptive Meshes

One of the major difficulties in computational fluid dynamics is the accurate representation of flow fields about complex configurations. A computer code has been developed by an ICASE (Institute for Computer Applications in Science and Engineering) researcher to solve the steady-state Euler equations about arbitrary configurations in two dimensions using the unstructured triangular meshes. Particular effort has focused on obtaining efficient and accurate solutions about multielement airfoil configurations. An adaptive meshing procedure has been incorporated in which additional mesh points are added and triangulated into the mesh locally in regions in which large flow gradients occur and extra resolution is required. This adaptive procedure is repeated several times as the flow solution converges, each time generating a newly refined mesh, until the desired level of accuracy is achieved. A multigrid technique has also been incorporated in which the previous coarse meshes, generated from the adaptive meshing strategy, are employed in the time-stepping scheme to accelerate the convergence of the solution on the finest mesh.

Solutions have been obtained for single and multiple airfoil configurations, for Mach numbers ranging from 0.125 to 2.0. The multigrid strategy has been shown to produce an order-of-magnitude increase in the speed of convergence to a steady state. The adaptive meshing strategy has been shown to produce highly accurate solutions with a relatively small number of mesh points.

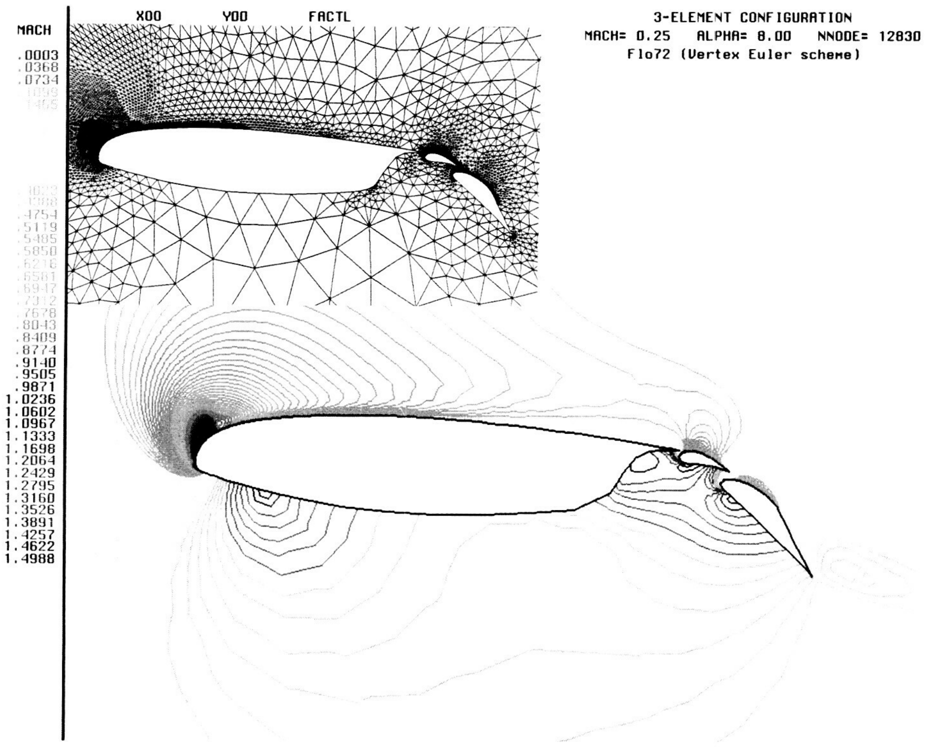

Unstructured triangular mesh and computed Mach contours in flow field for three-element airfoil configuration with Mach number = 0.25 and incidence angle = 8°.

As an example, a solution for the flow over a three-element airfoil configuration at a Mach number of 0.25 and an incidence angle of 8° was performed with 12,830 mesh points in 6 CPU (central processing unit) minutes on the CRAY-2 supercomputer. A small supersonic zone and associated shock wave at the leading edge of the main airfoil, which were not found previously, were accurately captured by the adaptive meshing strategy. **(Dimitri J. Mavriplis; Manuel D. Salas, 2627)**

Analysis of High-Speed Mixing Layers by Spectral Compressible Linear Stability Code (SPECLS)

Boundary-layer or mixing-layer transition originates in linear instability that must be understood before transition can be accurately modeled or predicted. The disturbances in this regime are small and exponentially growing, and the disturbance with the highest growth rate is assumed to cause a laminar flow to undergo transition. These disturbances can be analyzed by solving the linearized compressible Navier-Stokes equations about a specified mean flow. Discretizing this equation set results in a complex eighth-order algebraic eigenvalue problem. The solution gives the structure of the disturbance (complex eigenfunction) and its associated phase speed and growth rate (complex eigenvalue).

Spectral collocation methods have proved to be efficient discretization schemes for many aerodynamic and fluid mechanic problems. The high-order accuracy shown by these methods allows either engineering-accuracy solutions on coarse meshes or, alternatively, very accurate solutions that are essential for fluid mechanic simulations. Such a discretization has been employed in a newly developed spectral compressible linear stability code (SPECLS). A novel mesh has been employed for the pressure variable to avoid the requirement of an artificial boundary condition; and a multi-domain spectral discretization (MDSPD) is used to resolve highly irregular structures. Accuracy tests show that SPECLS requires an order of magnitude less number of points than previously used second-order methods to obtain equivalent accuracy.

SPECLS has been applied to the stability of a viscous, compressible free shear flow or mixing layer. An issue of relevance in studying the stability of free shear flows is the impact of transition on fuel/air mixing efficiency in scramjet combustors. The eventual goal is to be able to manipulate the downstream evolution of free shear flows to increase mixing efficiency. Since it is well known that turbulent mixing is several orders of magnitude stronger than laminar mixing, the ability to induce transition is a very desirable goal. It is of concern that mixing efficiency is decreased fourfold in the Mach number range of 1 to 4, since this drop encompasses the Mach number range of interest. The physical mechanism responsible for this trend is unknown. The linear stability analysis has provided a clue regarding the underlying mechanism possibly responsible for this decrease. The supersonic disturbances that predominate at high Mach numbers are shown to have very small growth rates relative to subsonic disturbances, which would

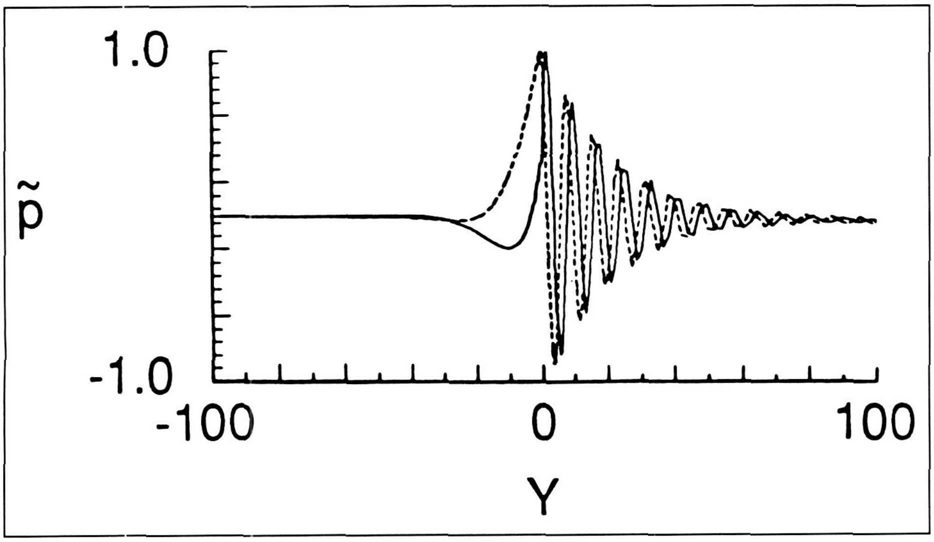

Supersonic pressure disturbance for free-stream Mach number = 4 and Reynolds number = 10,000.

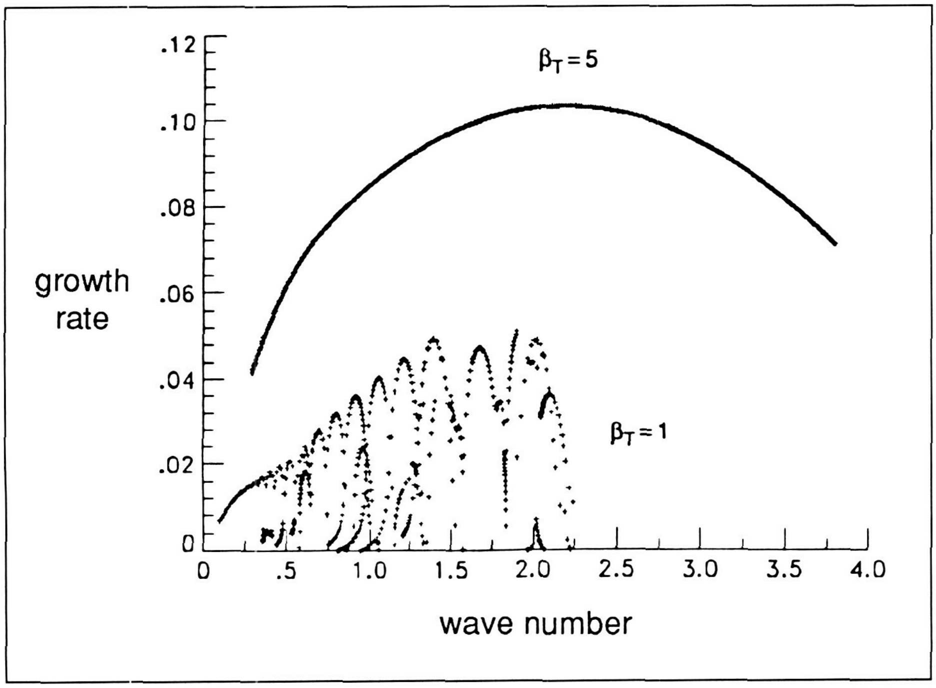

Disturbance growth rate versus streamwise wavenumber for free-stream Mach number = 3 and Reynolds number = 10,000.

have a very stabilizing influence on these flows–an undesirable effect for mixing enhancement. These disturbances have a nontrivial oscillatory structure that must be resolved for accurate studies. In the past, supersonic disturbances have not been studied in any depth and have never been adequately resolved numerically. The MDSPD incorporated in SPECLS makes an analysis of these disturbances possible. The high accuracy in the SPECLS formulation has allowed the first detailed look at the oscillatory structures of these supersonic modes that dominate the initial stages of instability for high-speed mixing layers.

The first figure is a plot of the complex pressure disturbance eigenfunction $\tilde{p}$ for a supersonic disturbance, versus the normal spatial coordinate Y. The mean flow is two parallel gases, one of which is quiescent. A sudden appearance of multiple supersonic modes is found to occur near Mach 3. Their existence has not been observed in past studies. The appearance of these modes is evident from plots of disturbance growth rate versus streamwise spatial wavenumber. Each mode is associated with an individual lobe in the growth rate curves. The second figure depicts a multiplicity of these lobes corresponding to a multiplicity of disturbances associated with a Mach 3 mixing layer and $\beta_T = T_{quies}/T_{inj} = 1$. The observation of a pronounced drop in mixing efficiency as Mach number is increased may be related to these multiple modes that have very low growth rates relative to the subsonic disturbances which predominate at low Mach numbers. It is found that by increasing the temperature of the quiescent gas relative to the injected gas in the mixing layer $\beta_T = 5$, the development of these supersonic modes is inhibited, which enhances the mixing layer instability. The study thus offers a control mechanism to induce transition so that mixing may be enhanced for high-speed free shear flows.

(Michele G. Macaraeg, 3171)

X-29A Computational Analysis

A detailed computational model of the X-29A Advanced Technology Demonstrator has been defined and analyzed in support of ground and flight experimental investigations of the configuration. The effort is part of a cooperative program with the Fluid and Flight Mechanics Branch, Ames Research Center/Dryden Flight Research Facility. The detailed computational model allows analysis of the wing/fuselage/canard configuration to investigate the complex fluid mechanics and component interactions of the unique forward-swept-wing aircraft.

Calculations on the full configuration have been performed with the CANTATA (canard/tail transonic analysis) small-disturbance analysis code developed by researchers at the Grumman Corporation-Aircraft Systems Division. Comparisons between computational predictions and both flight and wind tunnel experimental data have been made over a wide range of flight conditions. At free-stream Mach numbers less than 0.9, the comparison of pressure distributions between the computations and experiment is good on both the wing and canard. The addition of computational analysis capability complements the existing wind tunnel and flight experimental programs. For example, computational analyses allow evaluation of flight conditions outside the cleared flight envelope or estimation of the effects of configuration modifications.

(Edgar G. Waggoner, 2601)

Multielement Hot-Film Sensors in Transonic Flow

The use of multielement sensors has been extended from low to transonic speeds. Recent wind

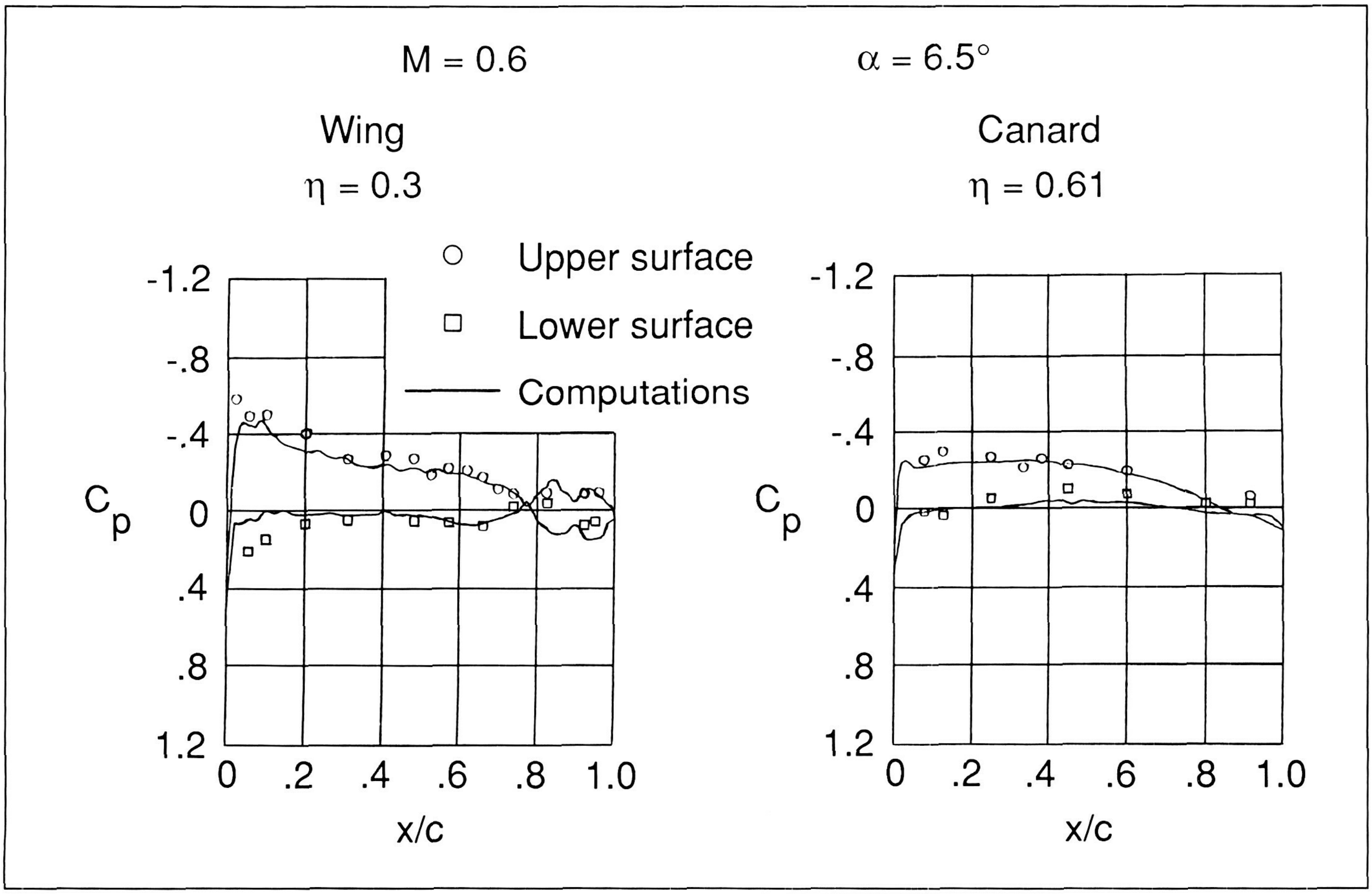

Comparison of computational results and flight test data.

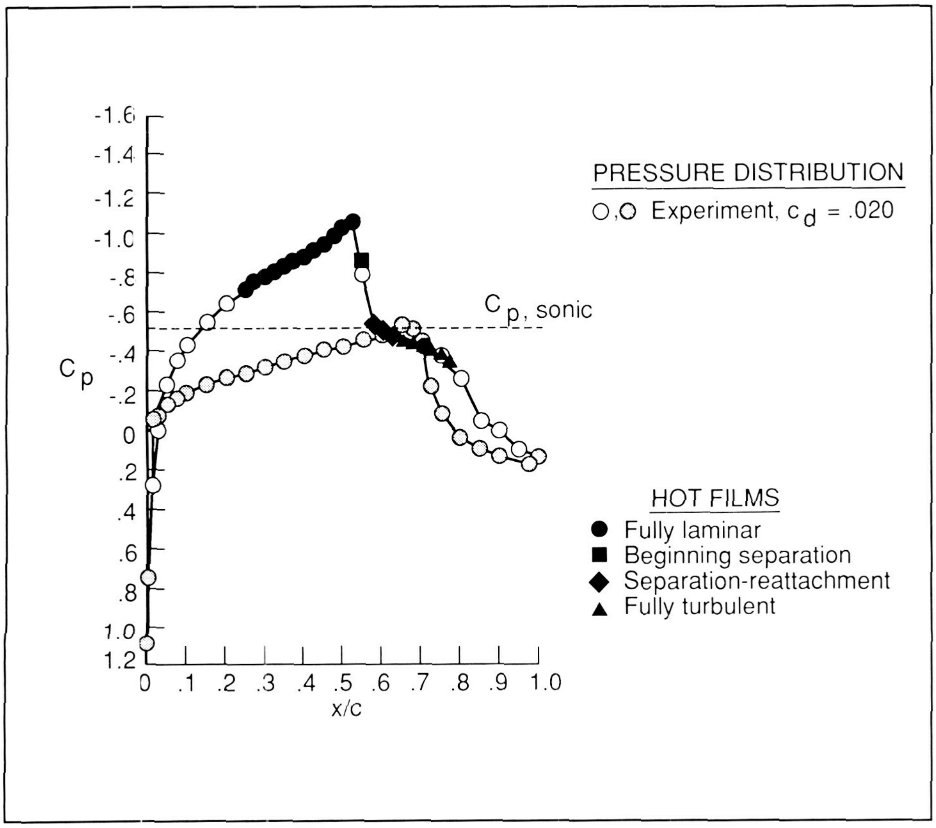

Hot-film sensor indications superimposed on pressure distribution.

tunnel tests were conducted in the Ohio State University 6- by 22-Inch Blowdown Tunnel on the HSNLF(1)-0213 airfoil model originally fabricated for chordwise pressure instrumentation. For this test, the model was also equipped with a multielement surface hot-film sensor array on a wraparound sheet of Kapton plastic. These sensors were used to detect both boundary-layer transition and separation and were extended from 28.3 percent chord to 76 percent spaced every 2.4 percent chord.

The figure presents an experimental pressure distribution at a Mach number of 0.774, chord Reynolds number of 4.3×10^6, and lift coefficient of 0.26. The hot-film sensors were located on the model upper surface, and symbols denoting the sensor indications have been superimposed on the pressure distribution in the same region.

The experimental pressure distribution indicated a strong shock wave starting at 52 percent chord on the upper surface followed by a somewhat "flattened" gradient to 70 percent chord, which commonly exists in boundary-layer separation. The positive pressure gradient from 70 percent chord to the trailing edge indicated a reattached boundary layer, thus showing that a shock-induced separation bubble had occurred.

The hot-film sensors showed a laminar boundary layer up to 52 percent chord, and the sensor at 54.5 percent chord showed intermittent "separation bursts" within the laminar boundary layer. The next sensor at 56.9 percent chord showed 180° phase shift, which indicates boundary-layer separation. Another phase shift occurred between 59.3 percent and 61.7 percent chord, indicating reattachment of the boundary layer. The remaining sensors from 61.7 percent chord to 76 percent chord showed a fully turbulent boundary layer. Again, the separation bubble appeared.
(William G. Sewall, 4516 and John P. Stack)

Relaminarization by Localized Active Surface Heating

The objective of this research is to demonstrate the phenomenon of relaminarization of a turbulent flow in air by combining passive and active surface heating. This study has been conducted with and without pressure gradients on both curved and flat surfaces. Localized active heating is achieved by a wire that is flush with the surface over a thermally insulated substrate beneath it. The stability of the flow downstream of the applied control point increases with the decreases in stream temperature along the direction of the flow. The mean and perturbation velocity profiles without control show that the flow is turbulent. With the application of control, these profiles indicate a laminar state. In the figure, u, u_τ, $u(y,t)$, and U_e are the mean, frictional, instantaneous, and free-stream velocities; ν, t, and y are kinetic viscosity, time, and distance across the boundary layer. The leading edge is elliptic with the major to minor axis ratio $a/b = 3$. In the reversion, the turbulent

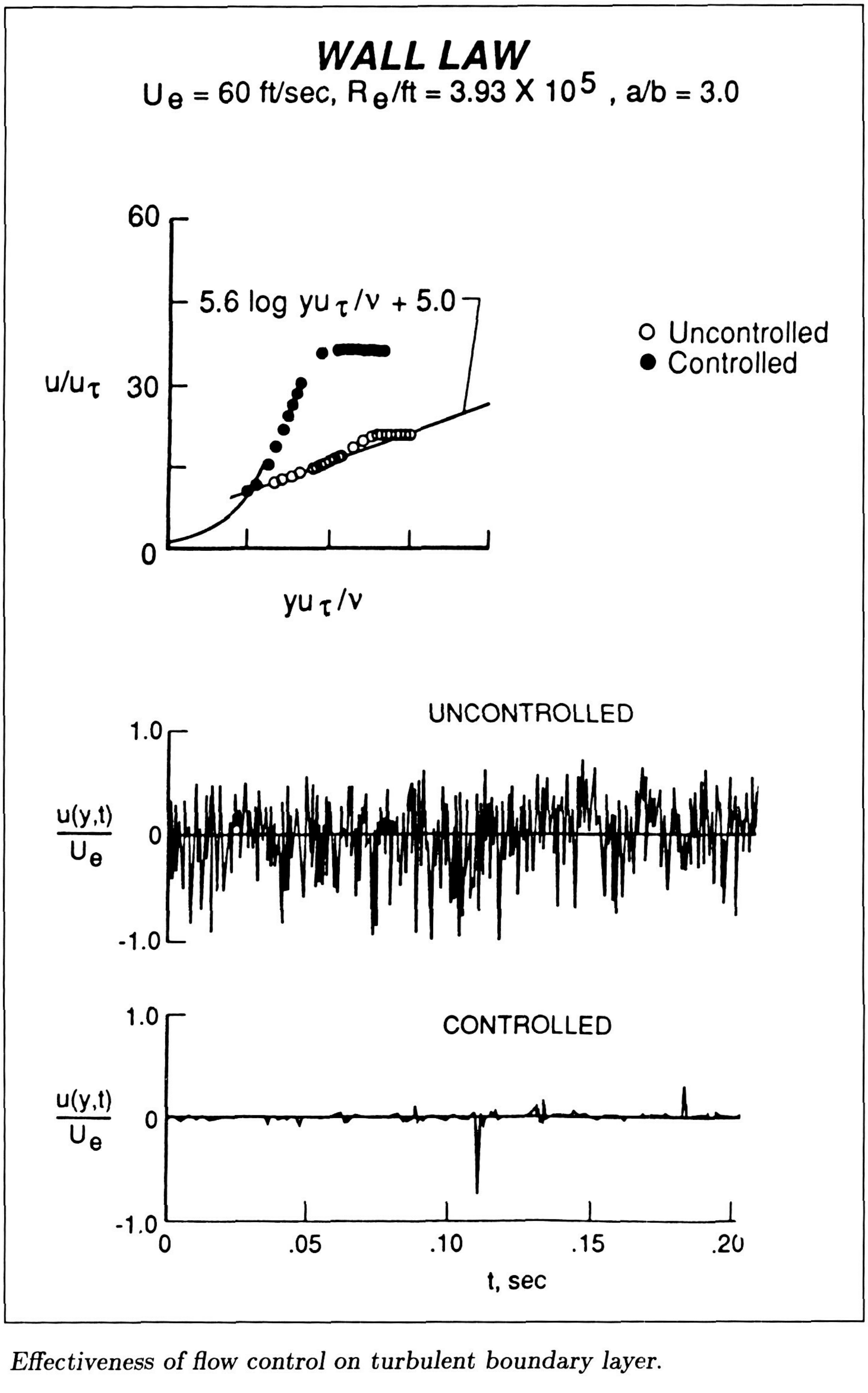

Effectiveness of flow control on turbulent boundary layer.

energy is dissipated by molecular transport due to both viscous and conductivity mechanisms. The new profile adjusts to a lower Reynolds number than that of the previous turbulent state.

These experiments show the feasibility of increasing the stability by means of localized heating. The effectiveness of this technique for relaminarization depends on free-stream conductivity, diffusivity, temperature, and Reynolds number. For an insulated flat plate with electrically heated resistance wire for control, the technique is most effective when applied in a region of pressure gradient (the leading edge of a flat plate or in the concave part of a curvature). Coupling between heat flux and the streamwise pressure gradient profoundly influences the reversion from turbulent to laminar flow. At zero-pressure gradient, the flow is poorly receptive to surface heating, and relaminarization cannot be easily obtained.
(Lucio Maestrello, 2631;
K. A. Nagabushana)

Control of Supersonic Intersection Flow Fields Through Filleting

The cruise performance of an aircraft depends on the techniques employed in controlling vortical motions at intersecting surfaces. The vortical flows originating at such junctures can seriously affect vehicle control effectiveness and drag. This research employs filleting at a simplified supersonic wing/body junction to control the juncture horseshoe vortex. A vectorized, compressible, three-dimensional Navier-Stokes code based on the MacCormack time-split, finite-volume technique has been implemented on a CYBER 205 computer for the numerical study. A modified elliptic grid-generation technique with direct control over spacing has been developed and applied for constructing the grid at a filleted wing/body junction.

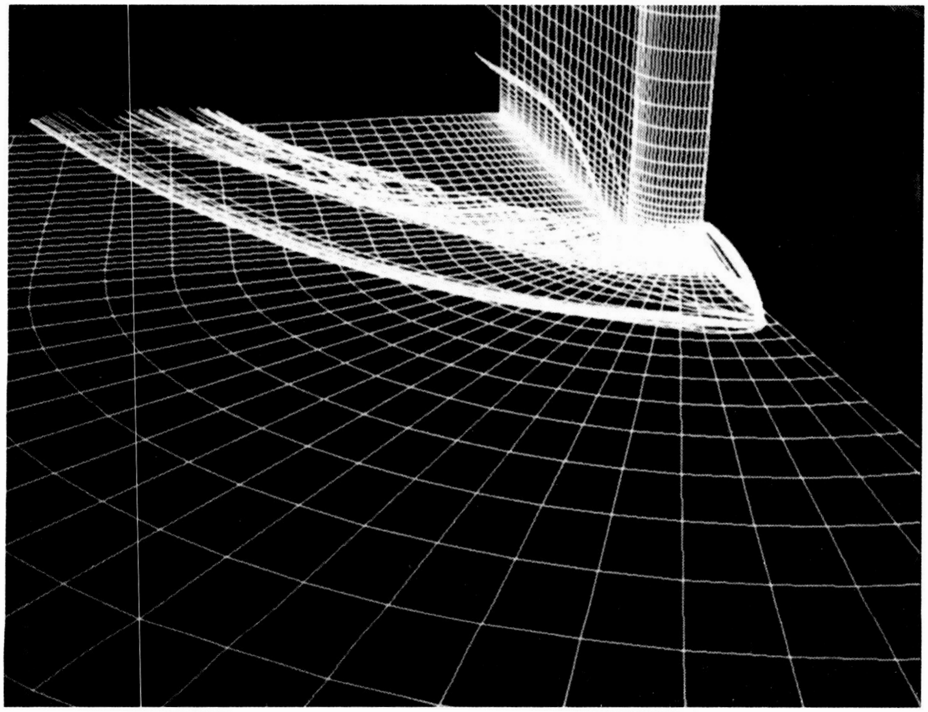

Unfilleted fin/body junction.

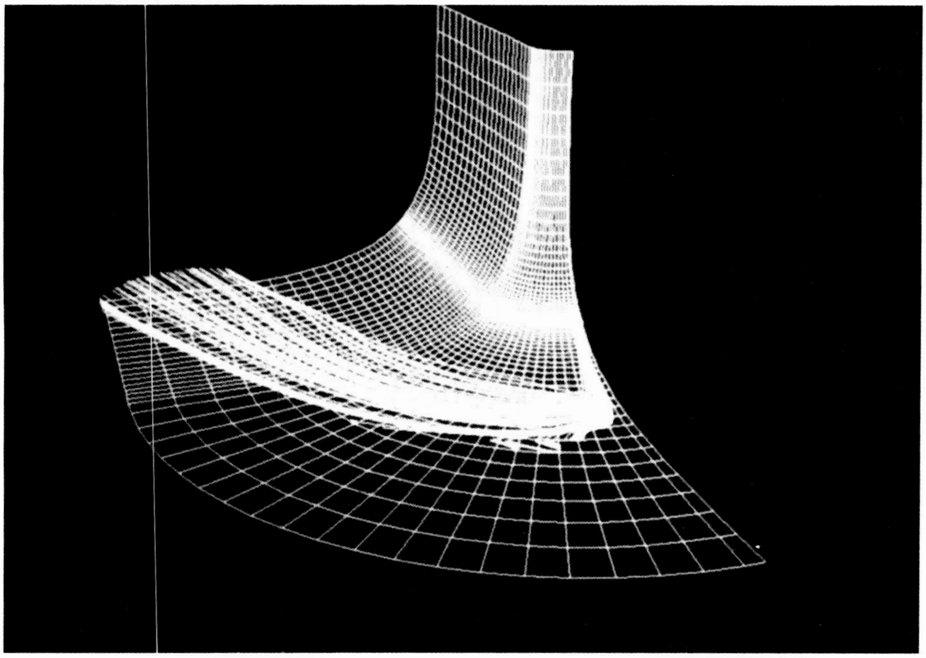

Filleted fin/body junction.

Key numerical results of the flow in unmodified and filleted junctures are presented in the figures for a Mach 3 flow. The figures show that flow streamline patterns lose much of their vortical character with proper filleting. An essential fillet radius required to weaken the horseshoe vortex has been determined from the numerical study. This numerical study predicts a factor of 3 reduction in the maximum magnitude of the vorticity in the horseshoe vortex and indicates that fillets with a radius of two times the wing leading-edge radius are required to drastically weaken the usual necklace vortex interaction. **(L. Balakrishnan; D. M. Bushnell, 4546)**

Viscous-Induced Drag

Recent experimental research on low-speed aircraft and 12-m yachts has indicated that in-plane wing sweep may significantly reduce lift-induced drag. Applying this result has been difficult since classical (flat-wake) theory predicts no drag reduction due to in-plane sweep, and more accurate but complex analytical methods provide little insight. The objective of the current research has been to develop a theory that retained the simplicity of the classical theory but did not rely on the flat-wake assumption.

This fundamentally new approach is based on the principle of minimizing entropy production due to spanwise lift variation. An approximate, closed-form solution is obtained which allows quick and easy estimation of relative induced drag levels for the in-plane sweep prob-

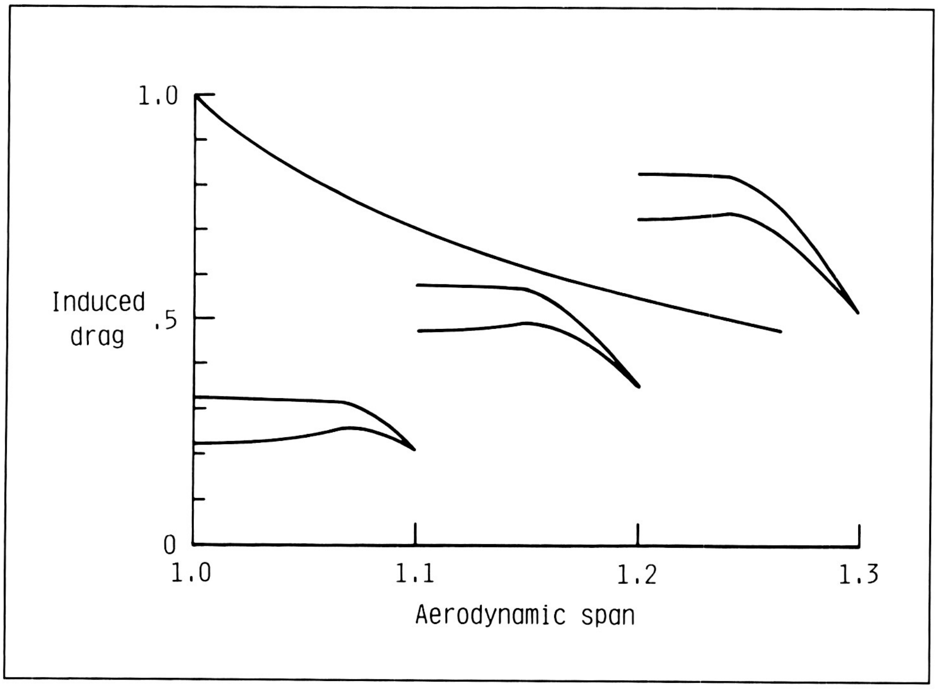

Induced drag reduction.

lem with certain constraints, such as constant lift, span, and wing-root bending moments.

The figure shows the results of optimizing a swept-back-tip wing. The ratio of the induced drag of a swept-tip wing to that of a straight wing is shown versus the aerodynamic span ratio (the aerodynamic span is measured along the lifting line, while the geometric span is measured wing tip to wing tip). The induced drag reduction is found to result from having the aerodynamic span significantly larger than the geometric span. As the aerodynamic span is increased, more sweep is required to maintain a constant geometric span.

This theory represents the first step in a fundamentally new approach to the induced drag problem (thermodynamic rather than aerodynamic). It agrees with many aspects of classical theory, but offers several new findings such as the effect of in-plane sweep and Reynolds number on the induced drag. Furthermore, this theory points out the fundamental inaccuracy of the flat-wake assumption.

(George C. Greene, 4546)

Supersonic Boundary-Layer Transition Detection Using Liquid Crystals

The location of boundary-layer transition can significantly impact aircraft performance at supersonic speeds. Generally, most transition detection techniques are impractical on standard wind tunnel models; hence, transition studies have been extremely limited. In a recent wind tunnel investigation, the liquid-crystal technique was found to be both practical and applicable in detecting natural and grit-induced transition.

Natural transition studies using liquid crystals were conducted on a flat-plate model in the Langley Unitary Plan Wind Tunnel at Mach numbers from 1.5 to 2.5. The results are comparable to flat-plate results obtained in other large tunnels using pitot and temperature-sensitive paint techniques. The frequency response of the liquid crystals was sufficient to indicate the dynamic nature of the transition front, which is represented by the band on the data.

Grit-induced transition was investigated by placing strips of various grit size near the flat-plate leading edge. The effective roughness Reynolds number $R_{k,eff}$ required for transition to occur near the grit strip is a strong function of both unit Reynolds and Mach numbers. These results illustrate the capabilities of the liquid-crystal technique for assuring that the appropriate transition grit size is employed in tests of planar aircraft surfaces. The figure is shown on the next page.

(Peter F. Covell, 3181, Clifford J. Obara, and Robert M. Hall)

- Natural Transition

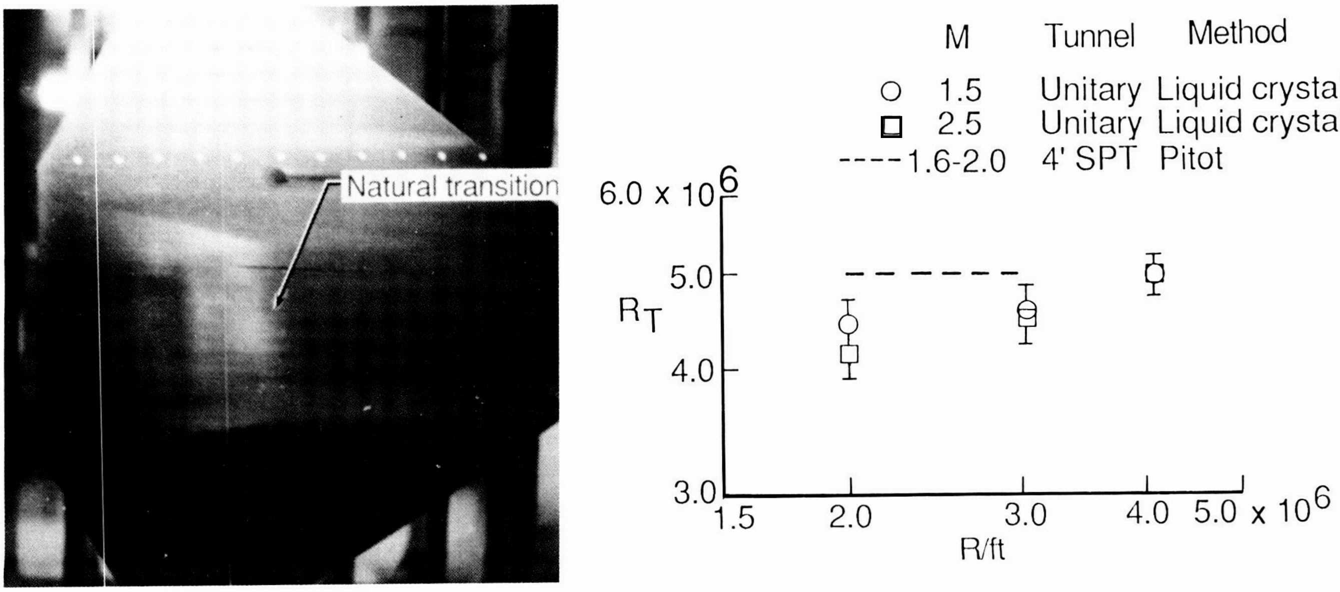

- Grit induced transition

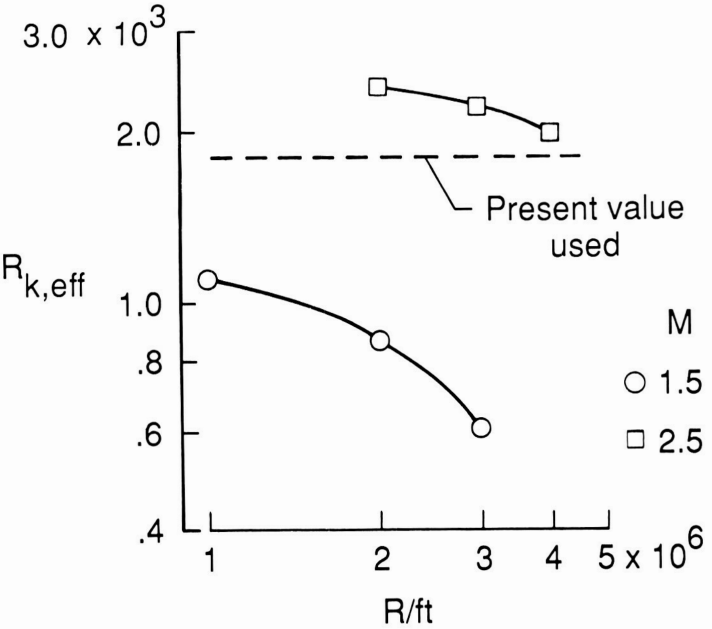

Natural and grit-induced boundary-layer transition.

Numerical Simulation of Weak Turbulence in Finite-Length Taylor-Couette Flow

Taylor-Couette flow (the flow between two concentric cylinders induced by rotating one cylinder with respect to the other) has been investigated for almost a century as a model for the instability of curved and rotating shear flows. In the case in which the concentric cylinders are very long compared to the gap between them, there is a critical rotation speed of the inner cylinder with respect to the stationary outer cylinder at which regularly sized axisymmetric annular vortices rapidly fill the entire gap. This occurrence was analyzed mathematically in 1923 by G. I. Taylor in a landmark paper on flow stability. At higher rotation speeds, these Taylor vortices lose their axial symmetry in regular azimuthal waves and eventually show contained bursts of turbulence.

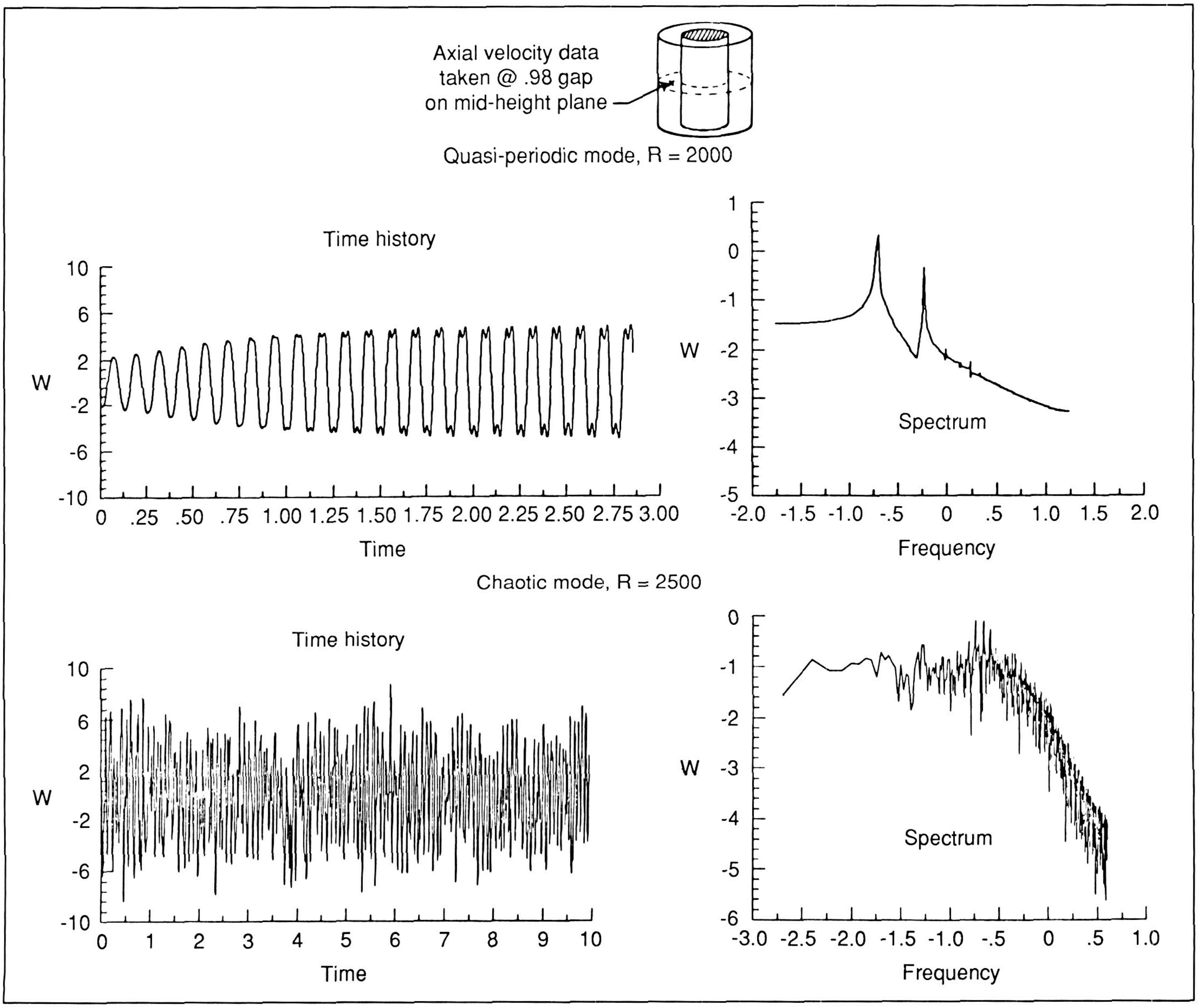

Time histories and spectra of axial velocity component for unsteady Taylor-Couette flow.

The situation in which the length of the cylinders is of the same order as the gap width, however, shows far more complicated behavior. Complex bifurcations of the axisymmetric vortex states occur with sensitive dependence on length-to-gap ratio and rotation speed. An extensive numerical study of several such bifurcations observed in experiments has been carried out, using two computer codes that solve the Navier-Stokes equations with highly accurate spectral methods. In one case, the numerical simulations were able to explain an observed discrepancy with experiments as to the appearance of a hysteresis in one set of bifurcations, by duplicating the imprecise experimental procedure.

The appearance of wavy vortices is also more complicated in the short cylinder case than for long cylinders. Experiments have shown the appearance of waves to be delayed to considerably higher rotation rates, and the structure of these wavy vortices to be less regular. Full three-dimensional time-accurate simulations have been carried out for a particular length/gap geometry to examine the progression of the wavy vortex states through transition to turbulence as the rotation rate increases. The composite figure shows one such progression. The upper left figure shows the time history of the axial velocity W measured at a specific location in the flow for a particular scaled rotation rate (Reynolds number R); the regular oscillatory nature of the signal indicates a smooth unsteady wavy vortex flow. The frequency spectrum of this oscillatory time history (upper right figure) indicates that the flow has just two dominant frequencies of oscillation at this rotation rate. At a higher rotation rate, the flow undergoes a transition to a weakly turbulent or "chaotic" state, as seen in the lower two figures. The time history is irregular and disordered, and the frequency spectrum is broadband, showing no dominant components. This type of transition to weakly turbulent flow is seen in other fluid dynamic systems such as free shear layers, but is far easier to simulate and study in the closed-system Taylor-Couette setting.

(Craig L. Streett, 2627)

Advanced Control Systems for General-Aviation Airplanes

A study of advanced control systems for general-aviation airplanes is being conducted on the General Aviation Simulator. The purpose of this research is to identify control systems that will make general-aviation airplanes easier and safer to fly, especially for the novice pilot. Additionally, experienced pilots should require less time and expertise to maintain proficiency compared to conventionally controlled airplanes.

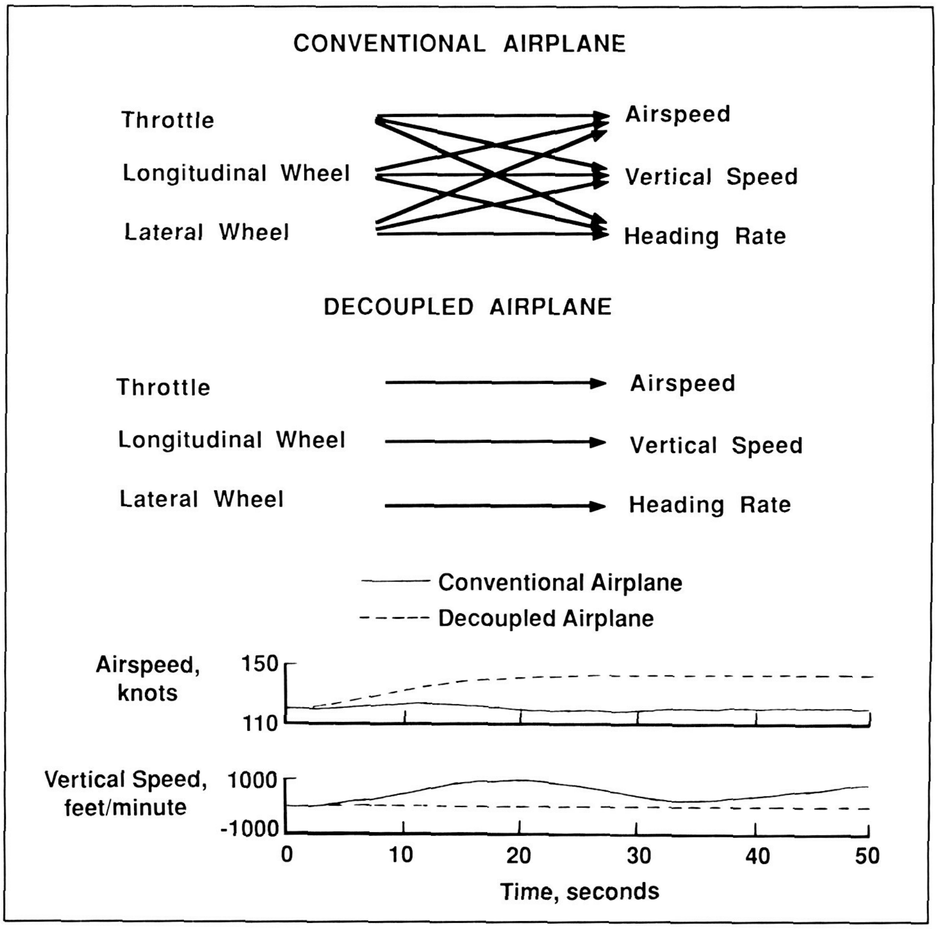

Control system studies: conceptual responses to pilot control inputs (top) and airplane response to throttle input (bottom).

Control systems that provide improved control of the pitch attitude, the airspeed, the vertical speed, or combinations of these variables are being investigated. The most desirable system appears to be one in which the throttle control commands the airspeed and the longitudinal wheel commands the vertical speed. This combination produces a strong synergistic effect because the response of the airplane to any single control input by the pilot is a change in only one primary response variable (airspeed, vertical speed, or heading rate) without any coupling to other primary variables (as shown in the figure). This "decoupling" eliminates the need for a pilot to learn to anticipate and compensate for unwanted motions in response to a control input, thus greatly reducing the pilot work load and improving the handling qualities compared to a conventional airplane. Another benefit of the system is that it automatically damps the natural oscillation of the airspeed and altitude after a pilot input is made.

The system appears to be applicable for all normal maneuvers of general-aviation airplanes from takeoff to cruise to landings. Novice pilots are able to make acceptable maneuvers with the system in a short period of time, and experienced pilots are able to reduce their work load without having to learn new piloting techniques.
(Eric C. Stewart, 3274)

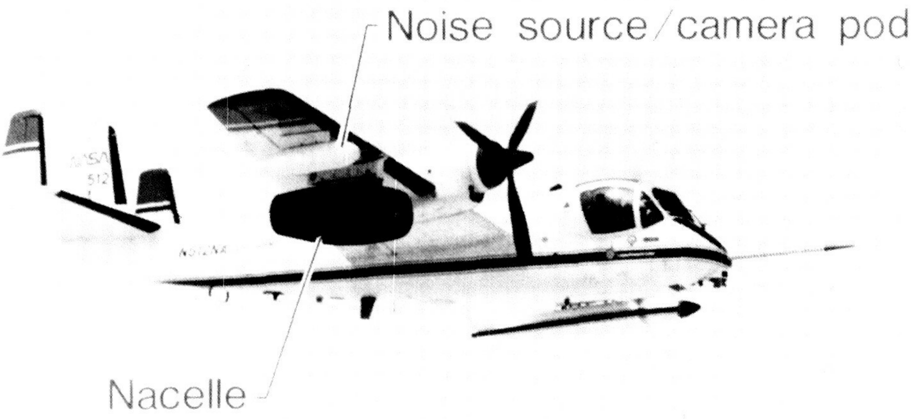

NASA/General Electric OV-1B laminar nacelle flight experiments.

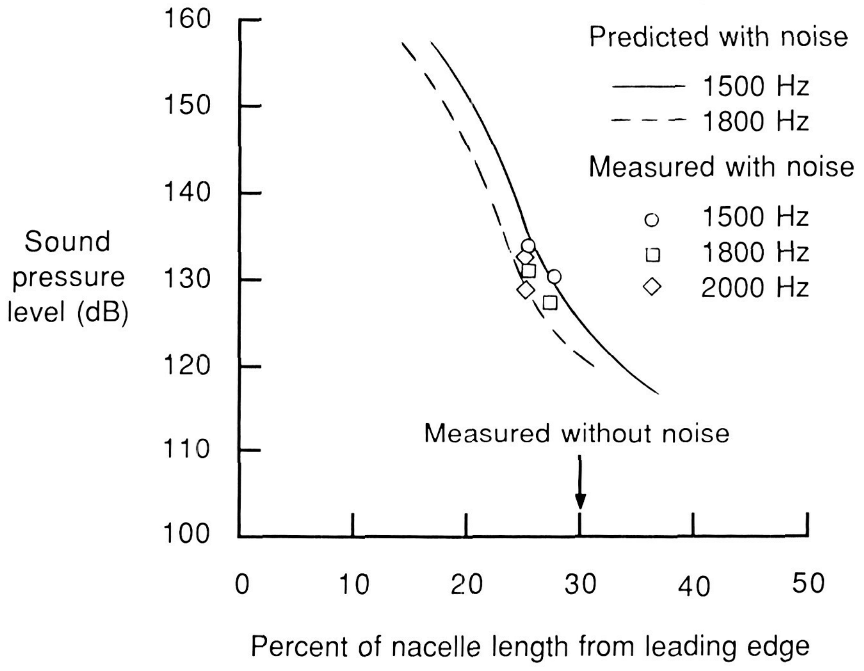

Comparison of predicted and measured location of transition from laminar to turbulent flow as affected by acoustic environment.

Natural Laminar Flow Nacelle Flight Experiments

A flight test has been conducted with a natural laminar flow (NLF) nacelle as part of a viscous drag reduction program. The objective of these experiments was to study the effect of a controlled external acoustic environment on the stability of the laminar boundary layer on the nacelle. Results of these tests are being used to validate computational methods used to design laminar-flow nacelles.

A full-scale flow-through NLF nacelle was attached to a pylon below the right wing of a Grumman Corporation OV-1B aircraft (as

shown in the first figure). The nacelle was instrumented with static and fluctuating pressure transducers. A streamlined pod containing a noise source and a small video camera was mounted on the same wing outboard of the nacelle. Liquid crystals and hot-film sensors were used on the nacelle surface to determine the boundary-layer transition location.

The flight tests showed that for a Reynolds number of 10×10^6, the transition location was approximately 30 percent of the nacelle length. The second figure shows the results of the flight tests. When the noise source was turned on at maximum power (132 dB on the nacelle surface), the transition location moved forward 3 to 5 percent as shown. The predicted effect of the noise source is also shown in the figure. For frequencies between 1500 and 2000 Hz, the predictions match closely to the experimental results for the conditions tested.
(Clifford J. Obara; Earl C. Hastings, 4870)

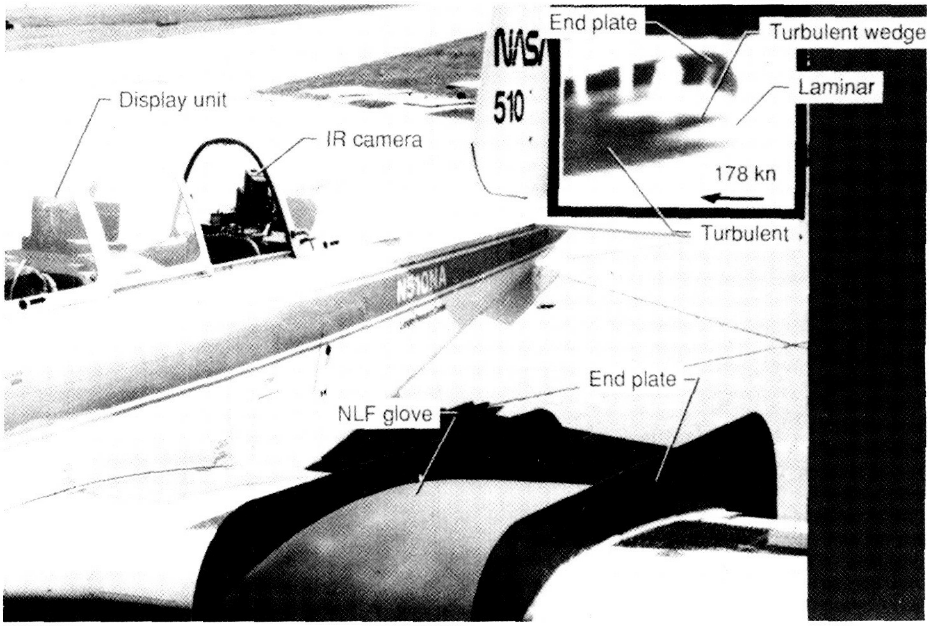

Infrared imaging for boundary-layer transition visualization.

Evaluation of Infrared Imaging for In-Flight Boundary-Layer Flow Visualization

A new method for boundary-layer flow visualization in aerodynamic testing has been developed. This technique is based on the infrared detection of heat transfer rate differences between the laminar and turbulent boundary layers. In laminar flow, the heat transfer between the fluid and the surface is low due to low rates of convection. Conversely, the turbulent boundary-layer flows exhibit higher rates of heat transfer due to increased rates of convection. This difference in heat transfer rate results in a surface temperature difference between laminar and turbulent areas.

Infrared imaging has been evaluated in flight using a single-engine turboprop T-34C airplane. For this experiment, a fiberglass-skinned, natural laminar flow glove was mounted on the left wing of the airplane as shown in the figure. The infrared camera, which was mounted behind the onboard researcher, viewed the glove section. All infrared images were recorded on a videocassette recorder. The inset data photograph shows the laminar and turbulent boundary layers at an altitude of 6,500 ft and an airspeed of 178 knots. A turbulent wedge is seen emanating from near the leading edge. Observations from infrared flow field imaging correlated with results from previous boundary-layer research in which other flow visualization techniques were utilized. A significant advantage of infrared imaging is that it does not require a coating of material to be applied to the surface being studied.

Infrared imaging is a viable nonintrusive boundary-layer flow visualization technique. It provides dynamic boundary-layer transition location capability throughout altitude and speed ranges of most subsonic aircraft flight envelopes. Infrared imaging is a new research tool that helps to further explore the limits of laminar-flow technology.
(Gregory S. Manuel and Jay M. Brandon, 3274)

Rotor Inflow Research

The third in a series of rotor inflow measurements tests was conducted in the Langley 14- by 22-Foot Subsonic Tunnel using a 2-Meter Rotor Test System and a laser velocimeter for measuring

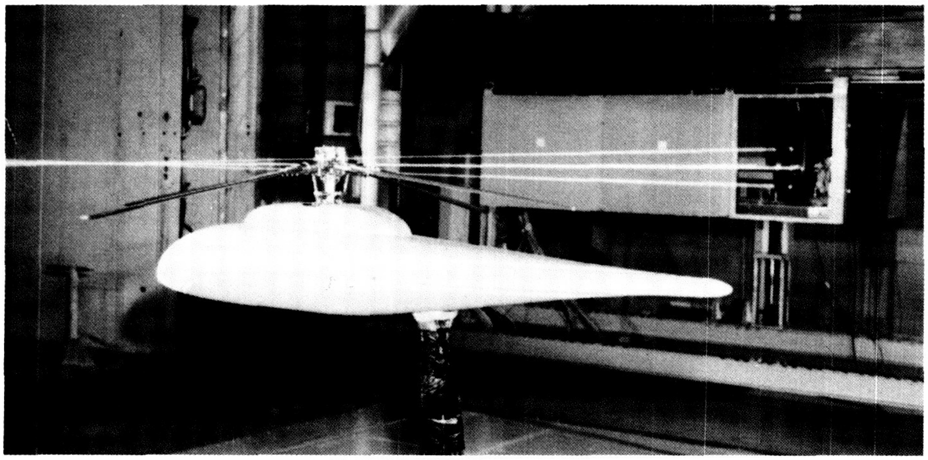

L-87-8861

Installation of 2-Meter Rotor Test System and laser velocimeter in Langley 14- by 22-Foot Subsonic Tunnel.

flow velocities. The purpose of this United States Army/NASA program is to establish an experimental data base of rotor inflow and wake velocities which can be used for the validation of computational methods that predict flow velocities near a rotor. In the most recent test, rotor inflow data were acquired for a four-bladed rotor with a generic research fuselage. The data were measured at 180 locations in a plane approximately 3 in. above the plane formed by the rotating blade tips for advance ratios (ratio of flight speed to rotor tip speed) of 0.23 and 0.30. Both average and time-dependent data were acquired for each measurement location. The predictions of various computational analyses of rotor inflow were compared to the experimental data.

The experimental data show that as wind speed is increased, the area of upflow induced by the rotor moves progressively from the far-forward region of the rotor disc to cover the complete forward half of the disc. The induced inflow characteristics at all wind speeds are asymmetric about the longitudinal axes of the rotor, with the maximum downwash concentrated in the aft portion of the rotor disk, skewed to the advancing blade side. The computational methods show significant differences from the experimental data, indicating that improvements in the methods are necessary for the proper calculation of the flow conditions affecting rotor performance.

(Susan L. Althoff, Joe W. Elliott, and Danny R. Hoad, 3611)

Static and Dynamic Stability and Control Characteristics of Generic Supersonic Cruise Fighter

Static and dynamic force tests of a generic fighter configuration designed for sustained supersonic flight have been conducted in the Langley 30- by 60-Foot Tunnel. These tests were intended to document the low-speed stability and control characteristics of several versions of the test configuration (shown mounted for roll oscillation tests).

In an effort to develop a low-speed design data base for this type of configuration, a cooperative program between Langley Research Center and the McDonnell Aircraft Company was established. This program included a supersonic wing design effort as well as a low-speed stability and control parametric study. The goal of the program was to develop a data base for the design of supersonic cruise configurations that have good low-speed flying qualities without sacrificing supersonic performance. The test configuration resulted from a series of studies in the Langley 12-Foot Low-Speed Tunnel which investigated wing, forebody, and empennage geometry variations to obtain desired static low-speed, high-angle-of-attack stability characteristics on an advanced fighter concept designed for supersonic cruise. The investigation concentrated on the effect of vertical-tail arrangement and forebody shape on high-angle-of-attack longitudinal and lateral-directional stability characteristics. Detailed static and dynamic force tests were then conducted on several of the more promising configurations in the Langley 30- by 60-Foot Tunnel. Typical results of the dynamic force tests are shown and illustrate the effect of the vertical tail on roll damping. As the data show, while the vertical tails actually reduced roll damping in the poststall region, the level of damping remains nearly constant throughout the angle-of-attack range tested. (See the two figures on the next page.) Free-flight tests to further document the dynamic characteristics are scheduled for early 1989.

(David E. Hahne, 2184)

ORIGINAL PAGE IS
OF POOR QUALITY

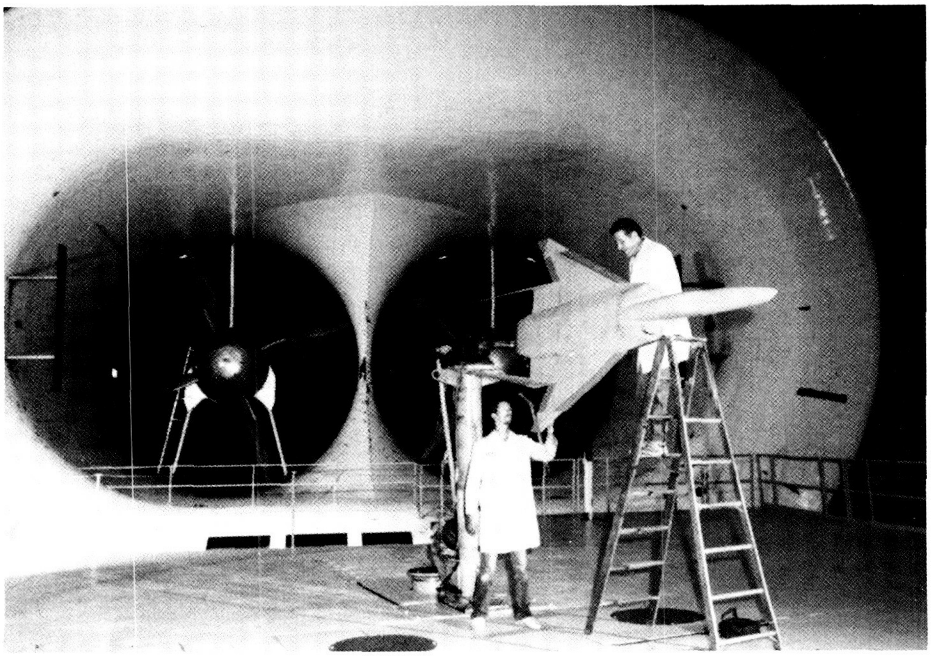

L-87-8413

Model mounted in Langley 30- by 60-Foot Tunnel for roll oscillation tests.

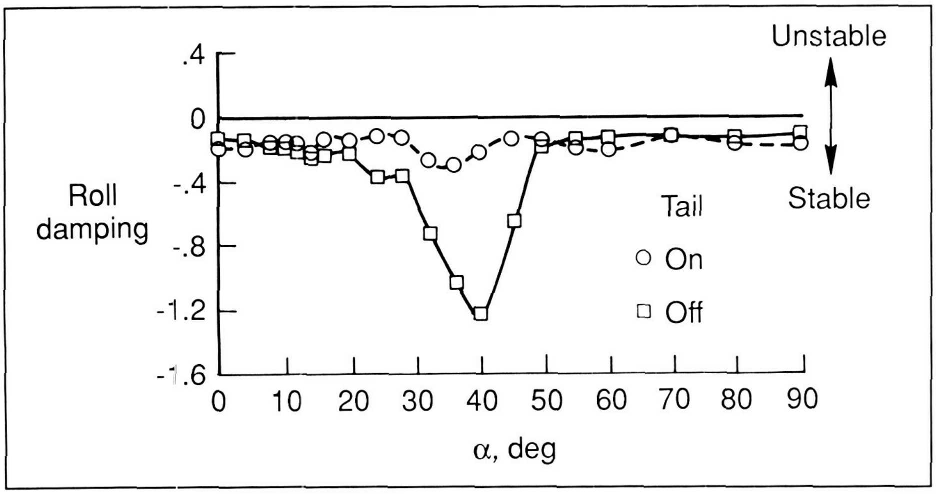

Effect of vertical tails on roll damping parameters.

Natural Flow Wing Design

A novel wing design concept has been introduced which takes advantage of the existence of conical flow that occurs at supersonic speeds. The present wing design concept is to create a near-conical wing geometry by redistributing airfoils in a spanwise direction. The standard application of airfoils to a delta wing results in a geometry that is conical about the wing tip. However, this geometry is less than optimum for wings at supersonic speeds. The conical nature of the flow at supersonic speeds over a swept wing produces large drag regions on a standard wing surface (see the upper portion of the delta wing in the lower section of the figure). The proposed near-conical wing geometry has a reduced drag region (as shown in the bottom portion of the delta wing).

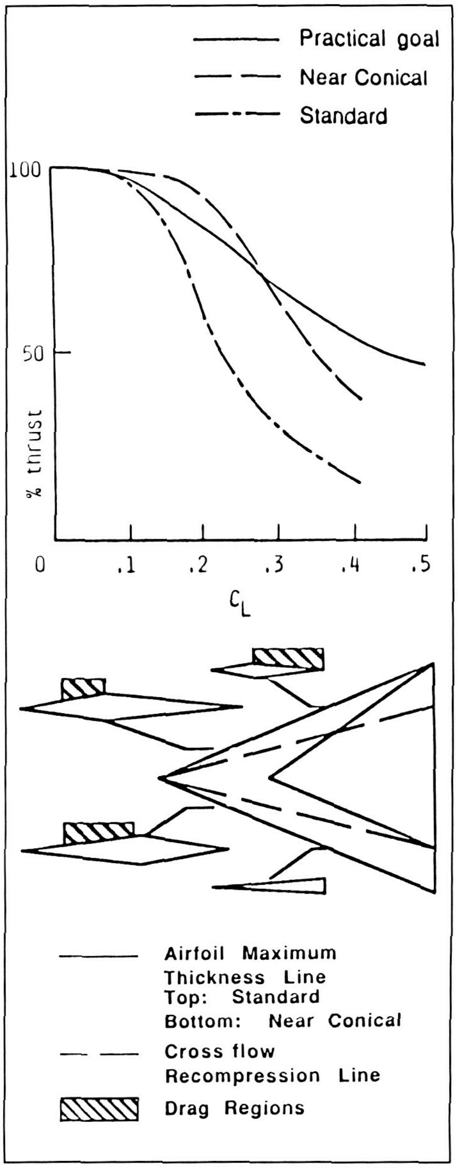

Delta wing results for standard and near-conical thickness distributions.

The design results computed using a full-potential flow code are shown in the figure. A comparison of the drag-reduction potential for a near-conical and standard 65° delta wing is presented in the top section of the figure. The data show that the near-conical wing has superior performance (larger percent thrust) compared to the standard wing and even exceeds the historical practical goal based upon experimental data. **(Richard M. Wood and Steven X. S. Bauer, 3181)**

Supersonic Flow Classification Study on Delta Wings

An experimental study has been conducted to identify and classify leeside flow characteristics that occur on uncambered delta wings at supersonic speeds. The delta wing models used in the wind tunnel study varied in leading-edge sweep from 52.5° to 75°. The leading edge of the wings was sharp, and the upper surface was flat. The tests were conducted in the Langley Unitary Plan Wind Tunnel at Mach numbers from 2.4 to 4.6. A laser vapor screen technique provided the flow visualization data used to identify the flow field characteristics.

The flow field characteristics are a function of the Mach number M_N and angle of attack α_N normal to the wing leading edge. The flow field sketches in the M_N versus α_N plot in the figure illustrate the eight basic flow types that were observed; these include (1) separation bubble, (2) classical vortex, (3) classical vortex with shock, (4) shock with no separation, (5) shock-induced separation, (6) separation bubble with shock, (7) separation bubbles that extend to the centerline, and (8) separation bubbles that bulge at centerline. Within each of these basic flow types, additional secondary-flow structures were observed. In the case shown, a string of several small vortices was observed between the primary and secondary vortex, and additional flow separation and shock structures were observed within the secondary vortex.
(Peter F. Covell and Gary F. Wesselmann, 3181)

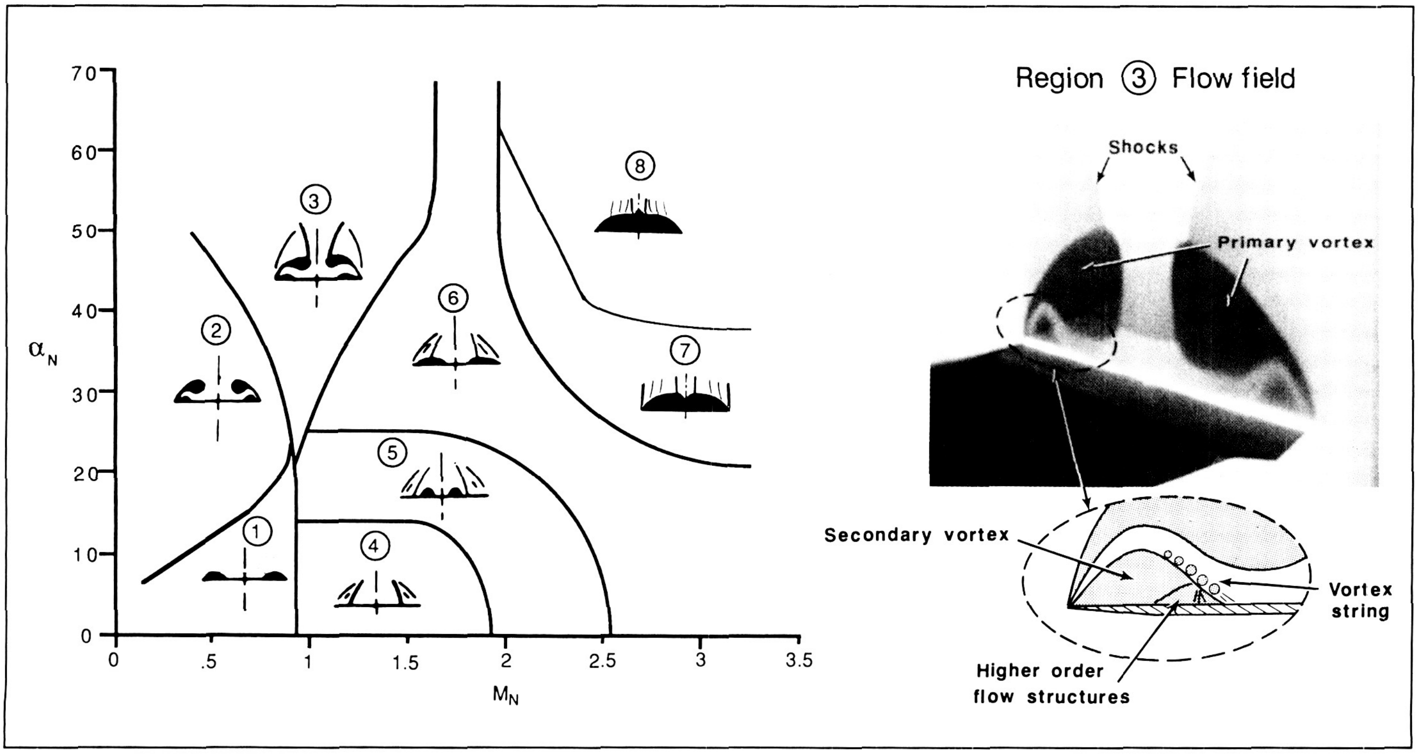

Delta wing leeside flow classification.

Euler and Navier-Stokes Solutions for Leeside Flow Over Delta Wings at Supersonic Speeds

Flow separation occurs on most aerodynamic vehicles at certain operating conditions; therefore, it is extremely important to be able to predict the effects of flow separation on vehicle performance, stability, and control. As part of an ongoing study, a computational investigation was conducted to assess the ability of an Euler and a Navier-Stokes solver to compute supersonic flow fields that contain flow separation. Highly swept, sharp leading-edge delta wings were chosen for the study to simplify geometry modeling and grid generation and to take advantage of a large, existing experimental data base.

The results shown in the figure are for a sharp leading edge, 75° leading-edge-sweep angle, delta wing at Mach 2.8, $\alpha = 8^\circ$, and a Reynolds number of 2×10^6/ft. Experimental vapor-screen data are compared with cross flow Mach number and total pressure contours as computed by the Euler and laminar Navier-Stokes solvers. Both of the flow solvers predict the occurrence of the primary leading-edge vortex for the sharp leading edge. However, the Navier-Stokes method, which includes viscosity, also predicts the secondary vortices that occur (as shown by the vapor screen data) due to boundary-layer separation under the primary vortex. The comparison of surface-pressure coefficients indicates accurate prediction of the pressure field from both methods, although the Navier-Stokes solution is more accurate.

(S. Naomi McMillin, 2945)

Prediction of Shock-Induced Separation Using Attached-Flow Methodology

At high lift conditions, two different approaches are available for wing design; these include a separated-flow approach and an attached-flow approach. At supersonic speeds and high lift conditions, cross flow shocks are a common phenomenon that can induce separation in an otherwise attached flow. A dilemma faced with the attached-flow approach to supersonic wing design is that typical attached-flow methodology cannot predict incipient cross flow shock-induced separation. Therefore, an investigation was conducted to develop a practical method of detecting incipient shock-induced separation of turbulent boundary layers at supersonic speeds. The approach was to correlate the static pres-

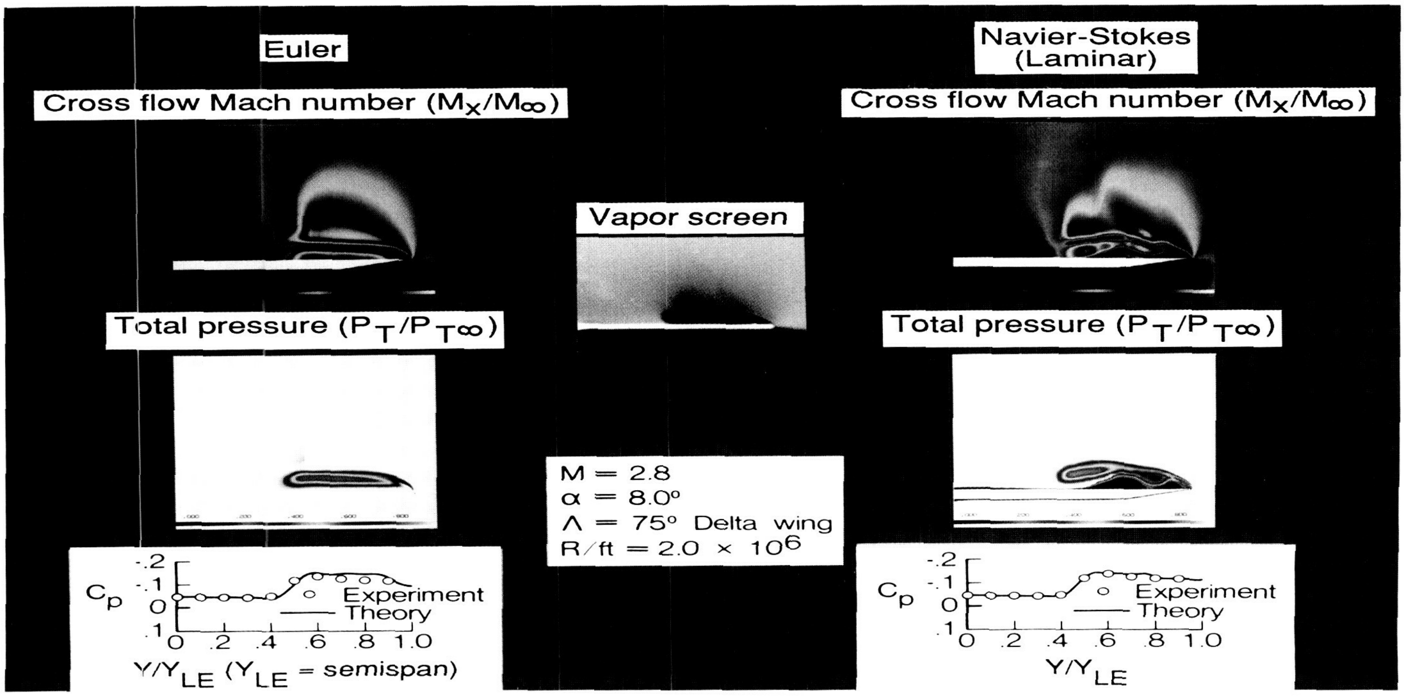

L-87-8002

Delta wing leeside flow results.

ORIGINAL PAGE
COLOR PHOTOGRAPH

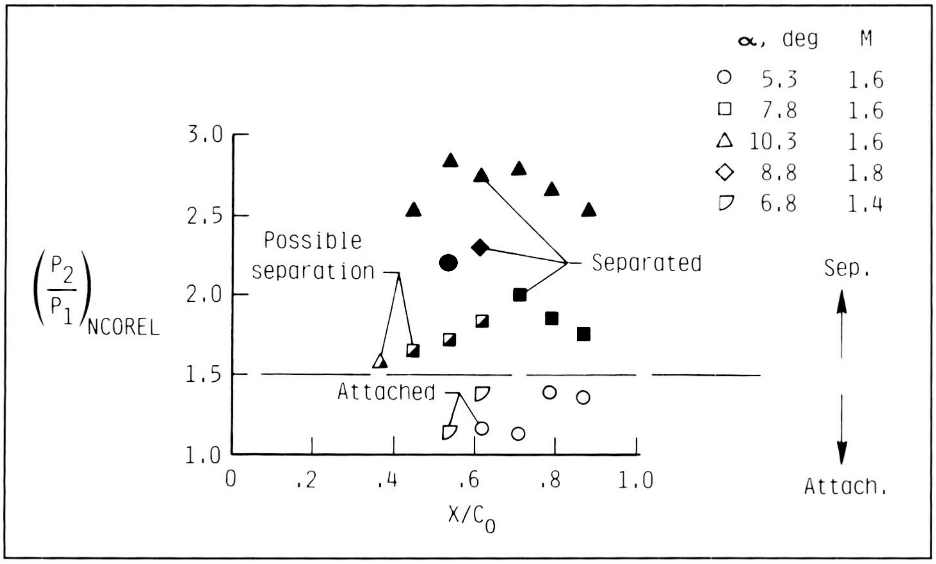

Correlation of computed cross flow shock strength with flow separation.

sure ratio P_2/P_1 across the shock, predicted by the inviscid full potential code (NCOREL), with the flow conditions (separated or attached) experimentally observed on a 60° swept delta wing. The results are shown in the figure. Predicted values of P_2/P_1 are plotted versus axial orifice position expressed as a fraction of root chord X/C_o. The open symbols represent the attached flow; the filled symbols represent the separated flow; and the half-open symbols indicate the probable separation.

This investigation shows that to avoid shock-induced separation, attached-flow wing designs should exclude cross flow shocks that have predicted pressure ratio values greater than 1.5. These data and information from other investigations imply that this criterion is valid at least in the range of free-stream Mach numbers from 1.4 to 3.5.

(O. J. Rose; J. L. Pittman, 4004)

B-1B Nozzle/Afterbody Aeroacoustics

The outer nozzle flaps of the B-1B aircraft are experiencing high wear rates resulting in unacceptable maintenance downtime and excessive replacement costs. The unacceptable structural life of the outer flaps and associated hardware is caused by high turbulence and dynamic pressure fluctuations occurring in the internozzle fairing region during flight and in ground operations of the B-1B aircraft. Other aircraft with closely spaced engines such as the F-18 and F-15 are also known to have suffered fatigue failures in the internozzle region. Recent studies at Langley Research Center have identified the phenomenon of twin supersonic jet plume resonance as a source of significantly higher internozzle dynamic pressures. An investigation has been conducted recently on a 6-percent-scale model of the B-1B aircraft to ascertain the existence of twin plume resonance and to explore some passive methods of load suppression in the outer nozzle region. This investigation has been conducted at Mach numbers

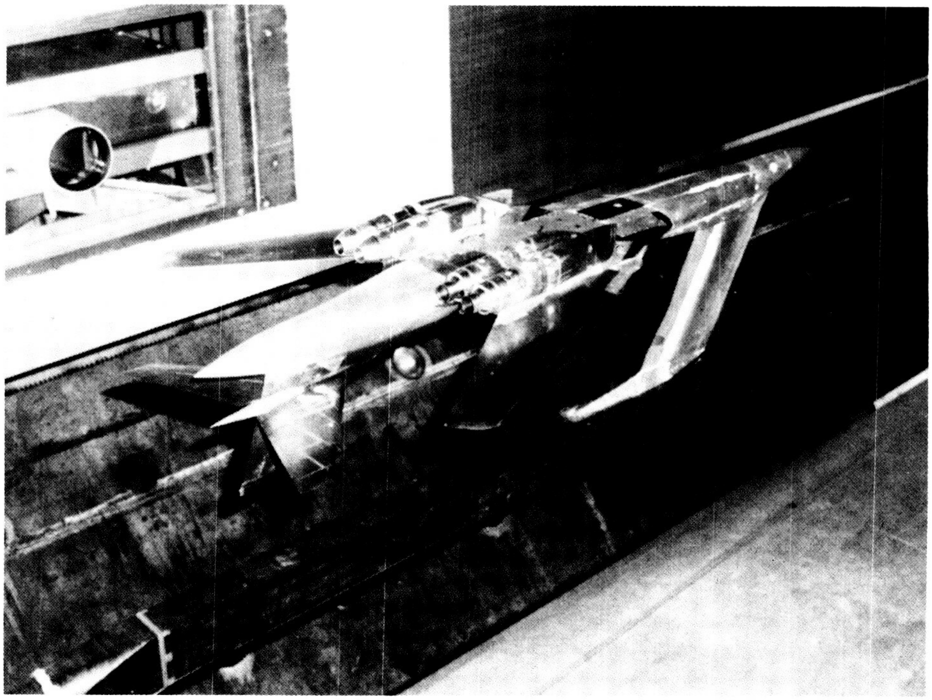

L-87-11046

B-1B model installed in Langley 16-Foot Transonic Tunnel.

from 0.2 to 0.9, angles of attack to 6°, and nozzle pressure ratios to 3.5.

The results of this investigation indicate that amplitude levels associated with this phenomenon were found to dominate the dynamic pressure fluctuations in the internozzle region at some Mach numbers. However, at other flight conditions and especially at Mach number 0.85, vortices separating from an over-the-wing fairing located between the nozzles were the major source of high dynamic loadings. Shock noise levels were reduced by utilizing an air jet injection technique.
(F. J. Capone, 2673 and J. M. Seiner)

Transonic Navier-Stokes Solutions of Three-Dimensional Afterbody Flows

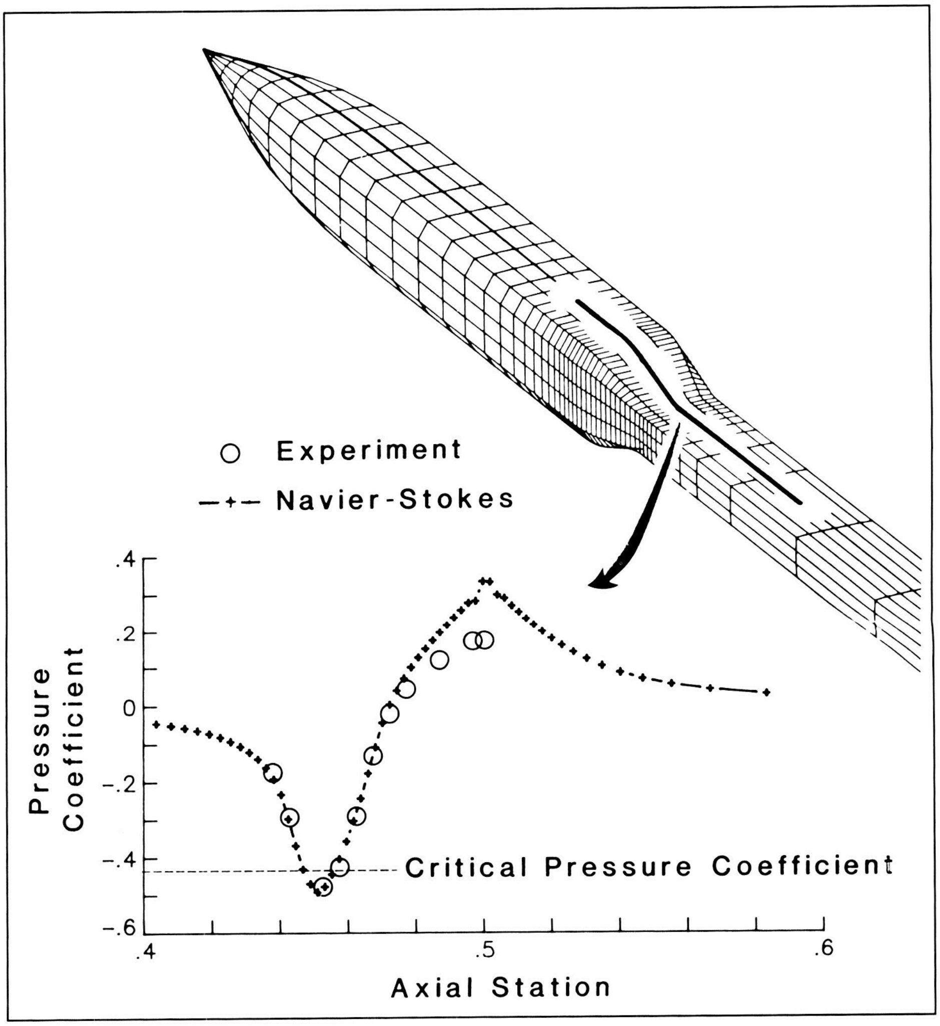

Transonic Navier-Stokes pressure coefficient predictions for a nonaxisymmetric nozzle (free-stream Mach number = 0.80, angle of attack = 0.0°, and Reynolds number = 19.5 × 10^6*).*

The performance of a three-dimensional Navier-Stokes solution technique in predicting the transonic flow past a nonaxisymmetric nozzle has been investigated. The investigation was conducted at free-stream Mach numbers ranging from 0.60 to 0.94 and at an angle of attack of 0.0°. Wind tunnel data to compare with the numerical calculations were also obtained. In the experiment, the jet exhaust was simulated by high-pressure air.

The numerical solution procedure that was evaluated employs the three-dimensional unsteady Reynolds-averaged Navier-Stokes equations written in strong conservation form. This procedure also employs a thin-layer assumption and the Baldwin-Lomax turbulence model. The equations are solved using the finite-volume principle in conjunction with an approximately factored upwind-biased numerical algorithm. For the calculations, the jet exhaust is represented by a solid sting.

The Navier-Stokes solution technique predicts well the flow over most of the afterbody when no separation is present. Under these conditions, it does a particularly good job of capturing the negative pressure peak as the flow expands around the boattail shoulder. It also successfully predicts vortices that have been experimentally shown to trail from the nonaxisymmetric nozzle. The predictions and data do not agree well at the juncture of the nozzle exit and the solid jet plume simulator. With the Baldwin-Lomax turbulence model, the procedure gives poor results when there are strong shocks and large separated areas on the nozzle.

(W. B. Compton III, 2673)

Lightning Attachment Tests on F-106B Scale Model

To further clarify the locations of the possible initial lightning leader attachment areas on the full-scale NASA Storm Hazards F-106B research airplane, scale-model lightning attachment point tests were conducted by Lightning Technologies, Incorporated, using test techniques established by the Society of Automotive Engineers.

In these tests, a 10-percent scale model of the F-106B airplane was mounted on a dielectric stand that allowed the three aircraft attitude angles to be adjusted. The model, which had been painted with a conductive coating, was positioned approximately midway between a rod electrode suspended above the model and a ground plane beneath the model. The rod electrode was used to represent the tip of a lightning leader advancing toward the aircraft, and the ground plane represented a diffuse region of opposite polarity charge.

Initial leader attachments occurred at such nonextremities on the model as the wing leading edges (shown in the figure), engine inlets, and top of the fuselage. Although attachments to such surfaces on vehicles with sharp extremities (such as the nose boom and wing tips on the F-106 airplane) were not previously expected, the model results confirm the suspected occurrence of wing leading-edge and canopy strikes to the full-scale research airplane. The lightning attachment zones determined in this program imply that new aircraft designs using delta wings or high-swept wing leading edges probably will require surface protection from lightning attachments over the complete exterior. The need for this surface protection is an especially significant design consideration for vehicles incorporating composite materials. **(Bruce D. Fisher, 3274)**

ORIGINAL PAGE IS
OF POOR QUALITY

Scale-model lightning attachment tests showing attachments to wing leading edge and engine exhaust.

Vortex Flow Interactions at Subsonic Through Supersonic Speeds

The vortex flow interactions about a slender-wing configuration were investigated at subsonic through supersonic speeds in the NASA Ames Research Center 6- by 6-Foot Transonic/Supersonic Wind Tunnel. This work was initiated in support of a cooperative program with Ames Research Center and the Air Force Wright Aeronautical Laboratories (AFWAL) to investigate methods to control the interactions of corotating vortices (vortices rotating in the same sense) on advanced aerodynamic shapes and to validate computational fluid dynamics methods. The AFWAL model featured a 65° cropped delta wing with the provision for adding a leading-edge extension (LEX) and a closely coupled canard. The testing was conducted at free-stream Mach numbers of 0.40 to 1.60, corresponding Reynolds numbers based on the wing centerline chord of 2.6×10^6 to 5.3×10^6, and angles of attack from 0° to 24°. The experimental results included off-body and surface flow visualizations using laser vapor screen and fluorescent oil methods, respectively, and model surface static pressure, force and moment, and two-component laser velocimeter measurements.

An important result of the study was that increasing the Mach number reduced the interaction of the wing-LEX and wing-canard vortical flows. For example, the coiling or wrapping around of the wing and LEX vortex cores that was typical of lower subsonic speeds did not occur at the higher subsonic, transonic, and supersonic conditions. The sensitivity of vortex positions to Mach number has important design implications regarding placement and size of other airframe components such as vertical tails. At transonic speeds, the off-body and surface flow visualizations were dominated by vortices coexisting with shock waves. The proximity of the LEX vortex to the wing surface provided a three-dimensional relief effect that reduced the severity of the

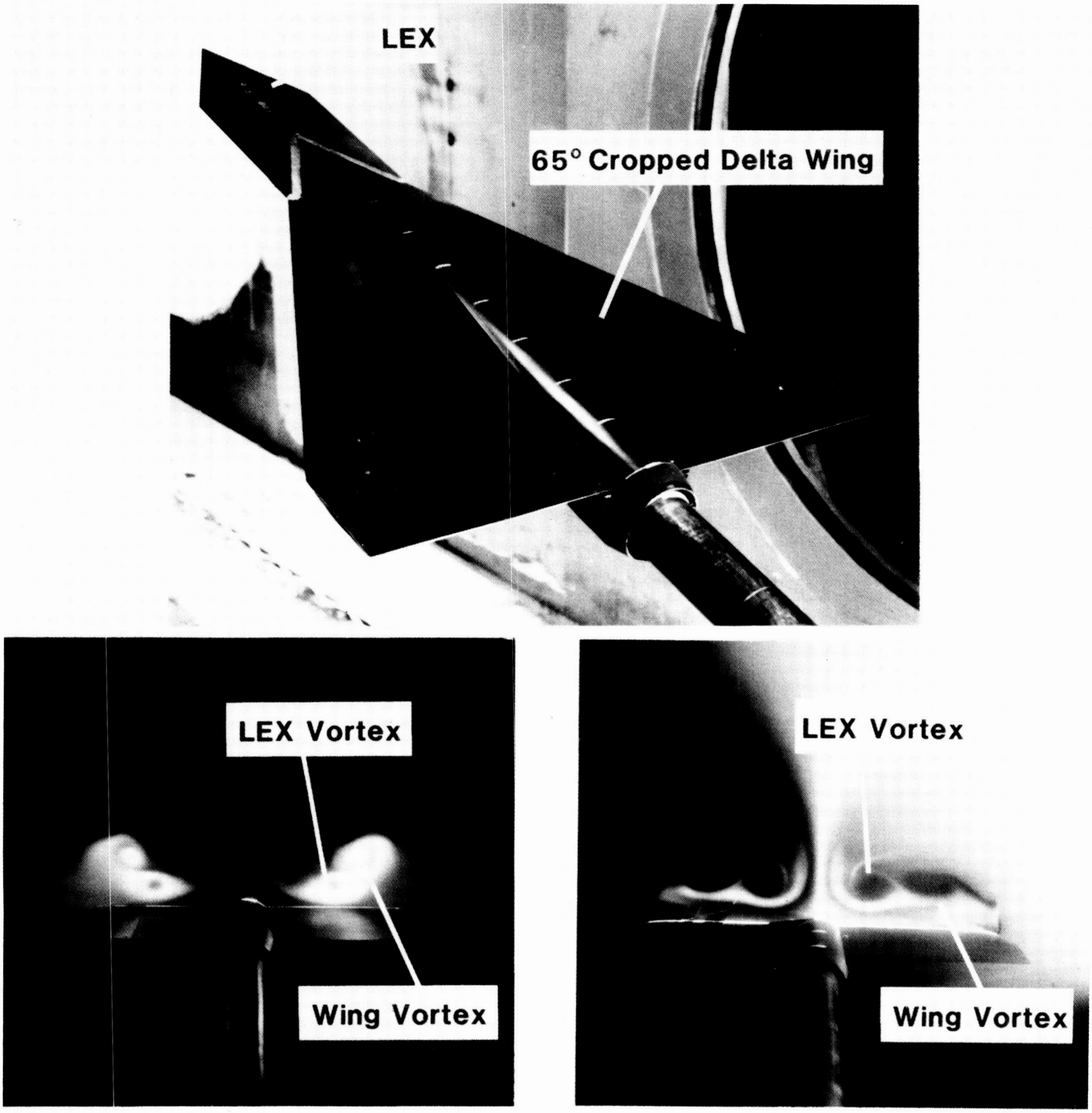

Mach =0.40

Mach =0.85

Mach number effect on 65° cropped delta wing with LEX cross flow at $\alpha = 20°$.

transonic flow mechanisms in comparison to the wing-canard arrangement.
(Gary E. Erickson, 2601)

Dynamic Stall Research

At high angles of attack, unsteady aerodynamics can have a major impact on the maneuverability of an airplane. With current emphasis on aggressive maneuvering capability at or above stall angle of attack for future airplanes, research into the effects of large-amplitude unsteady motions at high angles of attack on stability, control, and performance is critical. As part of a broad research program in the high-angle-of-attack aerodynamics area, a wind tunnel study has been conducted in the Langley 12-Foot Low-Speed Tunnel to explore the effects of large-amplitude unsteady motion on aerodynamic force and stability characteristics of a series of wings and an F-18 model. The models were oscillated sinusoidally over a range of frequency and average angle of attack.

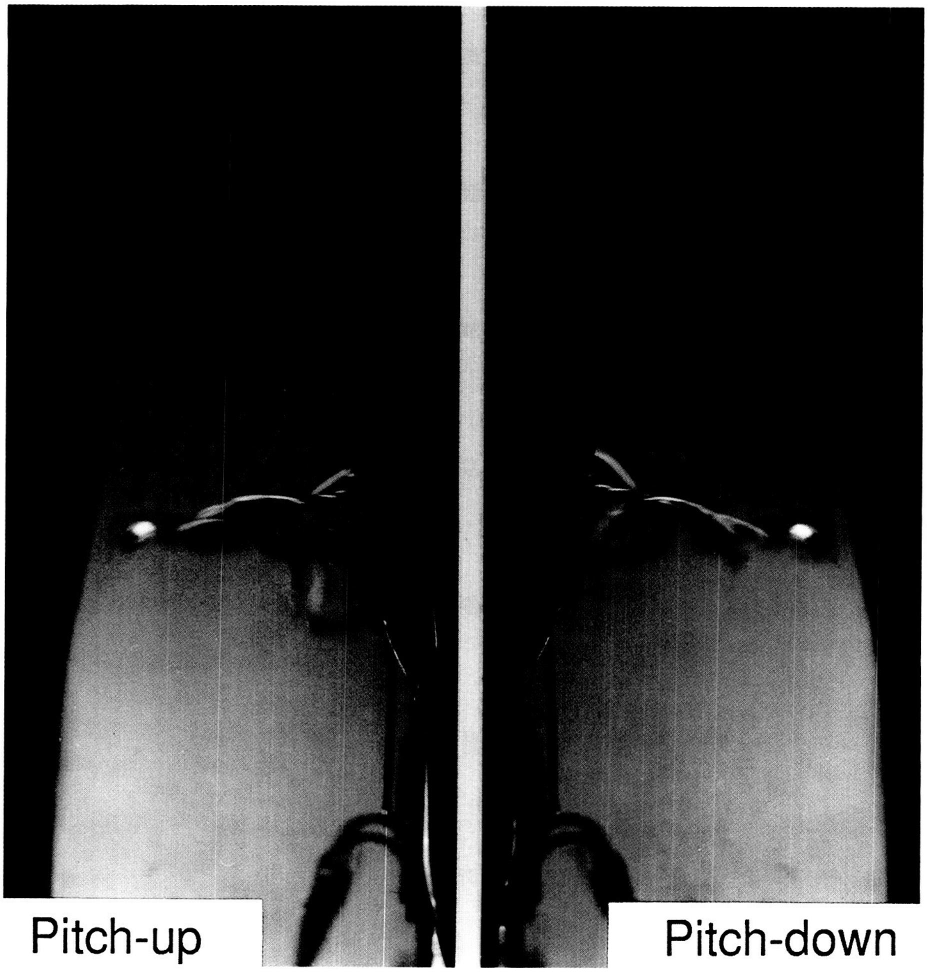

Dynamic laser light-sheet flow visualization at $\alpha = 27^\circ$.

Results of the study showed that lags in the vortex burst location and separation/reattachment of flow on the upper surface of the wing produced large overshoots and hysteresis loops in force-and-moment data. Significant dynamic effects were observed at relatively low reduced frequencies corresponding to realistic achievable pitch rates for current and future fighter configurations. The lag in the vortex flow field can be seen in laser light-sheet photographs by comparison of the vortex size during pitch-up and pitch-down motions. The figure shows a cross section of the vortex from the leading-edge extension as it passes over the wing on an F-18 model. During the pitch-up motions, the vortex size is reduced, indicating a strong, stable vortex. Conversely, during pitch-down, the vortex size is larger and near a vortex breakdown condition. The lag of the vortex system generates increased lift and drag during pitch-up. Additionally, increments to lateral stability have been observed. The magnitude of the unsteady effects is a strong function of wing planform shape, pitch rate, and angle of attack. Research is continuing to investigate unsteady aerodynamic effects on realistic configurations and to determine the impact of the observed unsteady aerodynamic effects on maneuver capability of future airplanes.
(Jay M. Brandon and Gautam H. Shah, 2184)

Navier-Stokes Solutions for F-18 Forebody-LEX

Advances in numerical solution methodology along with increased computer speed and capacity have made it feasible to seek numerical solutions to the three-dimensional

ORIGINAL PAGE
COLOR PHOTOGRAPH

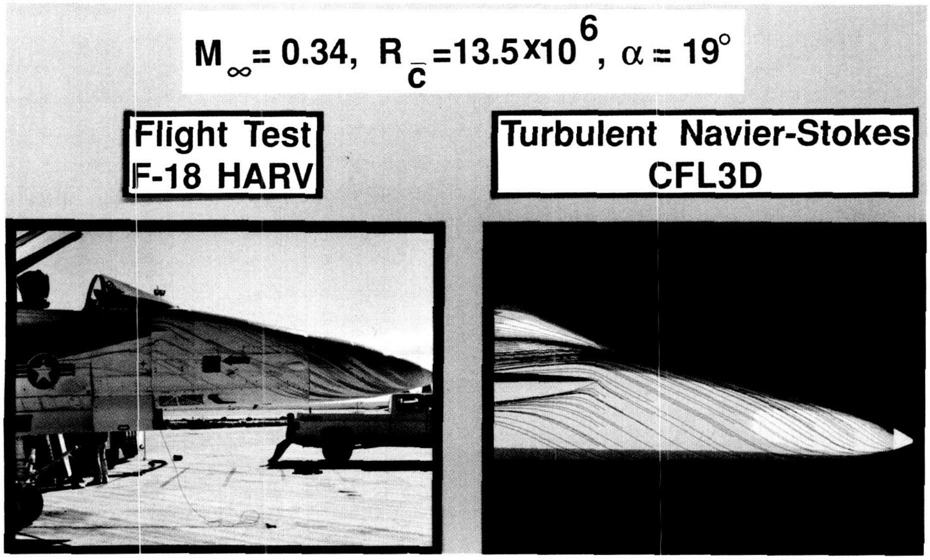

Navier-Stokes prediction of flight test.

Navier-Stokes equations at flight Reynolds numbers for relatively complicated aircraft geometries. As a step toward modeling a complete aircraft, turbulent Navier-Stokes solutions have been achieved for the forebody-LEX (leading-edge extension) portion of the F-18 High-Angle-of-Attack Research Vehicle (HARV).

The surface definition of the configuration was obtained from a detailed CAD description of a 6-percent F-18 wind tunnel model. A longitudinally blocked grid of approximately 185,000 points was generated with an H-O topology using established transfinite interpolation methodology. A solution for the flow was then obtained from a version of CFL3D that has been recently extended for longitudinally blocked grids. The CFL3D models the compressible full Navier-Stokes equations by a finite-volume technique that incorporates an upwind-biased, flux-difference-splitting approach. Turbulence effects were represented by an extended version of the Baldwin-Lomax algebraic turbulent model.

A representative turbulent solution is shown in the figure for a Mach number of 0.34, a Reynolds number of 13.5×10^6 (based upon the wing mean aerodynamic chord), and an angle of attack of 19°. These conditions correspond to recent flight tests of the NASA F-18 HARV at the Ames Research Center/Dryden Flight Research Facility. The flight tests were focused on documenting the forebody surface flow pattern; this result qualitatively compares well with the computed turbulent flow pattern as shown in the figure. The flow pattern on the aircraft was generated by emitting a fluid mixture of propylene glycol monomethyl ether (PGME) and dye from surface orifices. After flowing down the forebody, the PGME evaporates leaving the dye pattern shown. Numerical convergence corresponded to a two-to-three order-of-magnitude reduction of the residuals. This required approximately 2400 cycles corresponding to approximately 2 hours of CRAY-2 supercomputer time. Computations for other flight conditions as well as for a more complete configuration representation are under way.

(James M. Luckring, 2601 and James L. Thomas)

F-18 Vortex Flow Aerodynamics at Subsonic and Transonic Speeds

An experimental investigation was conducted in the David Taylor Research Center (DTRC) 7- by 10-Foot Transonic Wind Tunnel to improve the understanding and control of vortices from the LEX and forebody on a 6-percent-scale model of the United States Navy/McDonnell Douglas Corporation F/A-18 at subsonic through transonic speeds. Data were obtained on a baseline F-18 configuration, and modifications to the baseline included the LEX upper-surface fences, symmetric and asymmetric forebody strakes, and a flight-test nose boom. Off-body flow visualizations using a laser vapor screen technique and measurements of configuration force-and-moment and surface static pressures were obtained on each configuration. The test data were obtained at free-stream Mach numbers of 0.20 to 0.90, corresponding Reynolds numbers based on the wing mean aerodynamic chord of 1.0×10^6 to 2.7×10^6, and angles of attack and sideslip of 10° to 50° and −10° to +10°, respectively. The testing was performed in cooperation with the Naval Air Systems Command, NASA Ames Research Center, and the McDonnell Douglas Corporation. This effort was initiated in support of the full-scale flight and computational fluid dynamics re-

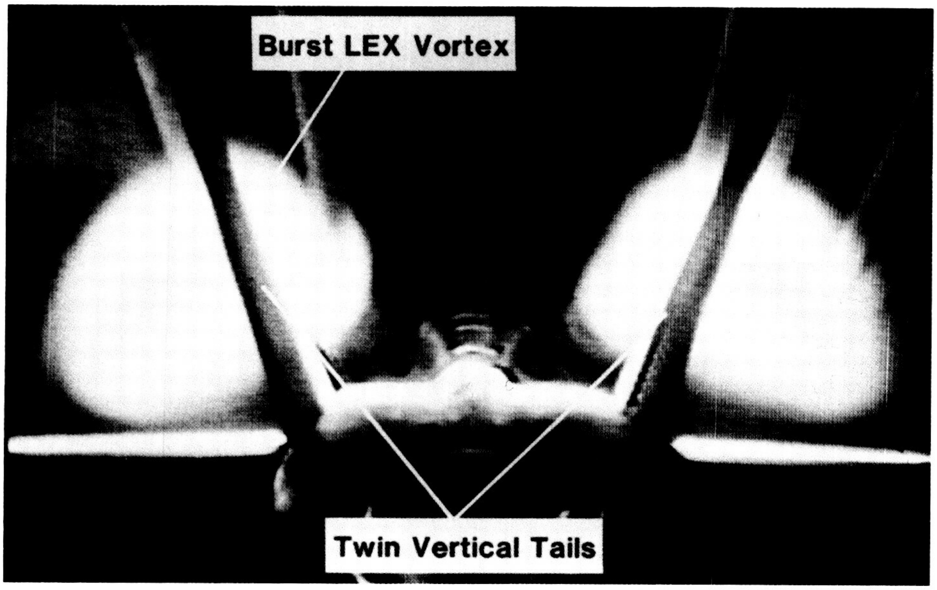

Cross flow visualization of F-18 LEX vortices at $M = 0.60$ and $\alpha = 20°$.

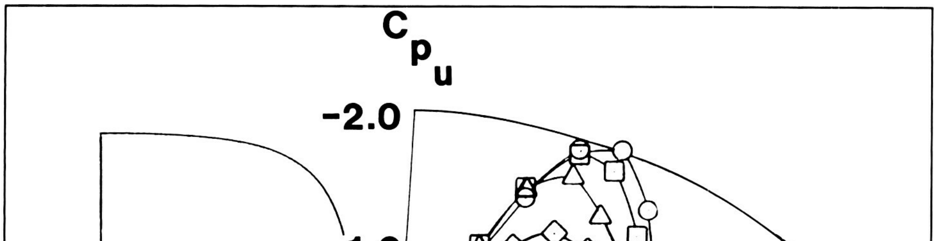

Mach number effect on LEX spanwise pressure distribution.

search activities in the NASA F-18 High Alpha Technology Program and a United States Navy flight-test program to evaluate LEX fences for improved vertical-tail buffet environment.

The laser flow visualizations provided a detailed description of the vortex cross flow structures, including the vortex size, shape, and breakdown; the interaction of the LEX and forebody vortices; and the vortex-empennage interactions. Increasing the Mach number weakened the vortical flows, and a vortex-shock interaction was apparent at transonic speeds. The LEX upper-surface fence, positioned ahead of the LEX-wing junction and below the vortex, promoted a dual, corotating vortex system instead of the single vortex on the unmodified LEX. The vertical-tail buffet was reduced as a result of weakening and repositioning the vortical flows at the tail surfaces. The vortex flow field trends agreed well with full-scale flight results. **(Gary E. Erickson, 2601)**

Transonic Cavity Flow Study

To aid in the understanding of the effects of Reynolds number and boundary-layer thickness on an internal cavity at transonic speeds, a test was conducted in the David Taylor Research Center 7- by 10-Foot Transonic Wind Tunnel. For this investigation, a 1/4-scale model (see the figure) was tested at Mach numbers from 0.3 to 1.05 and Reynolds numbers from 1.0×10^6 to 4.0×10^6/ft. The floor of the cavity could be positioned to simulate either a deep- or shallow-cavity configuration, and blocks could be

ORIGINAL PAGE IS
OF POOR QUALITY

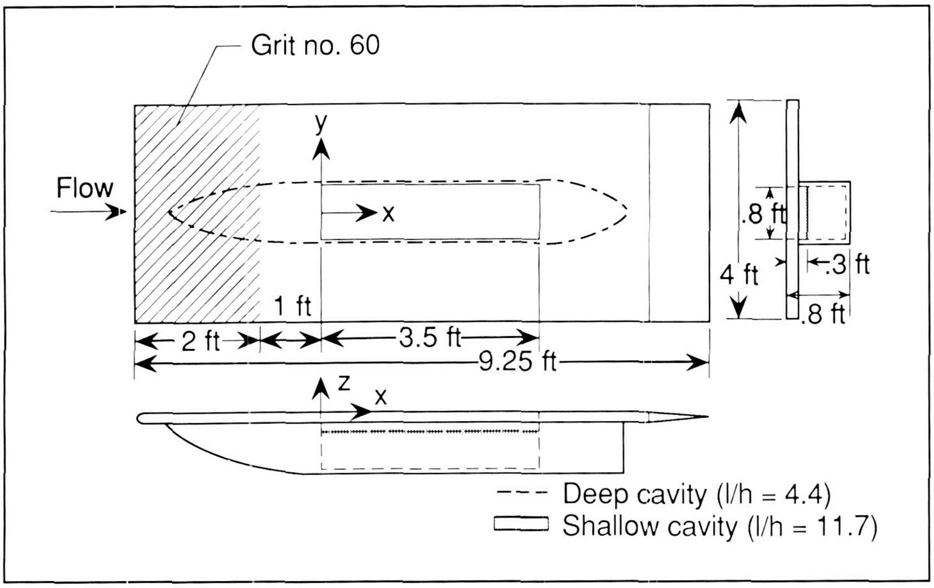

Schematic of model.

inserted to modify the shape of the forward or aft portion of the cavity. For the shallow cavity, an acoustic fence located at the forward face of the cavity was also tested. The instrumentation on the model consisted of three flush-mounted pressure transducers on the cavity floor and approximately 260 static pressure orifices on the model. The boundary-layer thickness was held nearly constant over the range of Reynolds numbers tested by artificially thickening the boundary layer with a heavy layer of grit. The effect of boundary layer was studied by replacing the heavy layer of grit with a traditional boundary-layer trip strip.

A comparison of cavity data, for either the deep or shallow configuration, showed that doubling the Reynolds number had no effect on the cavity pressure distribution; however, a decrease in boundary-layer thickness (for the shallow-cavity configuration) caused the pressure coefficient in the aft portion of the cavity to be more positive. Reynolds number was a factor in the unsteadiness of the measured static pressure, however. For the deep-cavity configuration at Reynolds numbers $>3.0 \times 10^6$/ft, the data fluctuated significantly over the 1-sec sampling period. As Reynolds number was decreased, the unsteadiness decreased. The shallow-cavity measurements showed little unsteadiness at any Reynolds number tested. Although mean static pressure distributions have been used in the past deep-cavity analysis, the unsteadiness of the data indicates that the use of averaged data may not be adequate for determining cavity loads.

(Elizabeth B. Plentovich, 2701)

Calculation of Flow Field Over Three-Dimensional Cavity

A three-dimensional, Reynolds-averaged, full Navier-Stokes computer code has been developed to define the flow field and surface conditions over a cavity. The code, which generates time-accurate solutions using the explicit MacCormack scheme, was developed by Dr. Oktay Baysal of Old Dominion University and is a result of the first phase of an ongoing program to develop a prediction method for defining the forces and moments on stores separating from three-dimensional cavities at supersonic speeds.

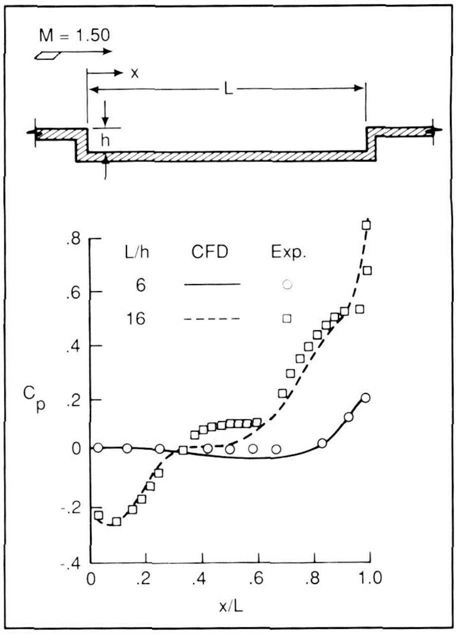

Comparison of experimental and computed cavity floor pressure distributions.

Shown in the figure is a comparison of experimental and computed pressure distributions from the present code for cavities of two length-to-depth ratios at a free-stream Mach number of 1.5. The pressure coefficients C_P are plotted versus the ratio of the downstream distance from the cavity front face x to the cavity length L. The experimental data are from NASA *Technical Publication 2683* and were obtained for a cavity embedded in a flat-plate surface. The cav-

ity was 0.5-in. deep, 2.5-in. wide, and the boundary layer approaching the cavity was turbulent and had a thickness of 0.2 in. Results are shown for the floor of the cavity and are for values of L/h that correspond to two very different types of flow fields as indicated by the pressure distributions. Good agreement is shown between experiment and computations for both values of L/h, thus confirming that the code is correctly simulating the flow fields.
(Robert L. Stallings, 4004)

High-Speed Civil Transport Studies

Contractual and in-house systems studies are being conducted to determine potential markets, economics, and technology requirements for a future High-Speed Civil Transport (HSCT) studies aircraft. The in-house system studies have been conducted for baseline Mach 3, Mach 4, and variable-sweep Mach 3 concepts. The contract studies at Boeing Commercial Airplanes and Douglas Aircraft Company have spanned the Mach number range from Mach 2 to Mach 25 with most recent emphasis on Mach 2 to Mach 5 HSCT concepts. The in-house effort was primarily aimed at determining the high-payoff technologies, including their risks and performance potential. The contract studies explored high-payoff technologies, identified and evaluated the future markets, determined economic benefits, and evaluated the impact of a future HSCT on airport infrastructure and national/international air space.

Results of the studies have shown that there is a market in the years 2000 to 2010 for a 250- to 300-passenger HSCT with a range of 6500 nmi. Although the Mach number of such a vehicle will ultimately be dictated by economic viability and environmental acceptability, the studies have shown that a cryo-fueled Mach 4 or faster HSCT could not be technically viable for the years 2000 to 2010. The studies show that a conventionally fueled (jet petroleum fuel) HSCT in the Mach number range of Mach 2 to Mach 3.2 could be viable if an aggressive national research and development program could be initiated by NASA in fiscal year 1990. The highest priority research is in the area of environmental concerns; e.g., emissions impact on ozone, sonic boom, and airport/community noise. Research has already begun, and the goal is to identify and develop technologies that will enable a future HSCT fly supersonically overland, have minimal impact on the environment, and meet current noise restrictions. Meeting these environmental goals and achieving economic viability will require that the takeoff gross weight of the HSCT be reduced 40 to 50 percent beyond that achievable with current technology. High-payoff technologies that have the potential to significantly reduce the takeoff gross weight include lightweight, thermally efficient structures, advanced variable cycle engines, supersonic through-flow fans, and supersonic laminar-flow control.
(J. N. Hefner, 2196 and S. M. Dollyhigh)

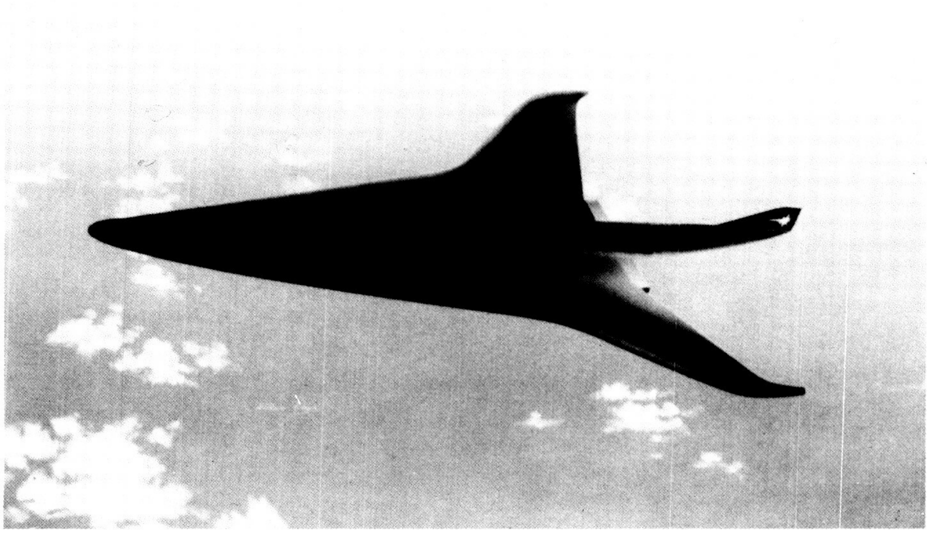

L-88-7173

Mach 3 HSCT research concept.

Transonic Reynolds Number Effects for Slender Wing-Body Configuration

A wind tunnel investigation was conducted in the National Transonic Facility (NTF) to determine the Reynolds number effects on the transonic aerodynamics of a slender wing-body configuration. The model was comprised of a cone-cylinder-frustum body with a unit-aspect-ratio delta wing and was representative of a class of vehicles capable of very-high-speed flight. The transonic data were obtained

ORIGINAL PAGE
BLACK AND WHITE PHOTOGRAPH

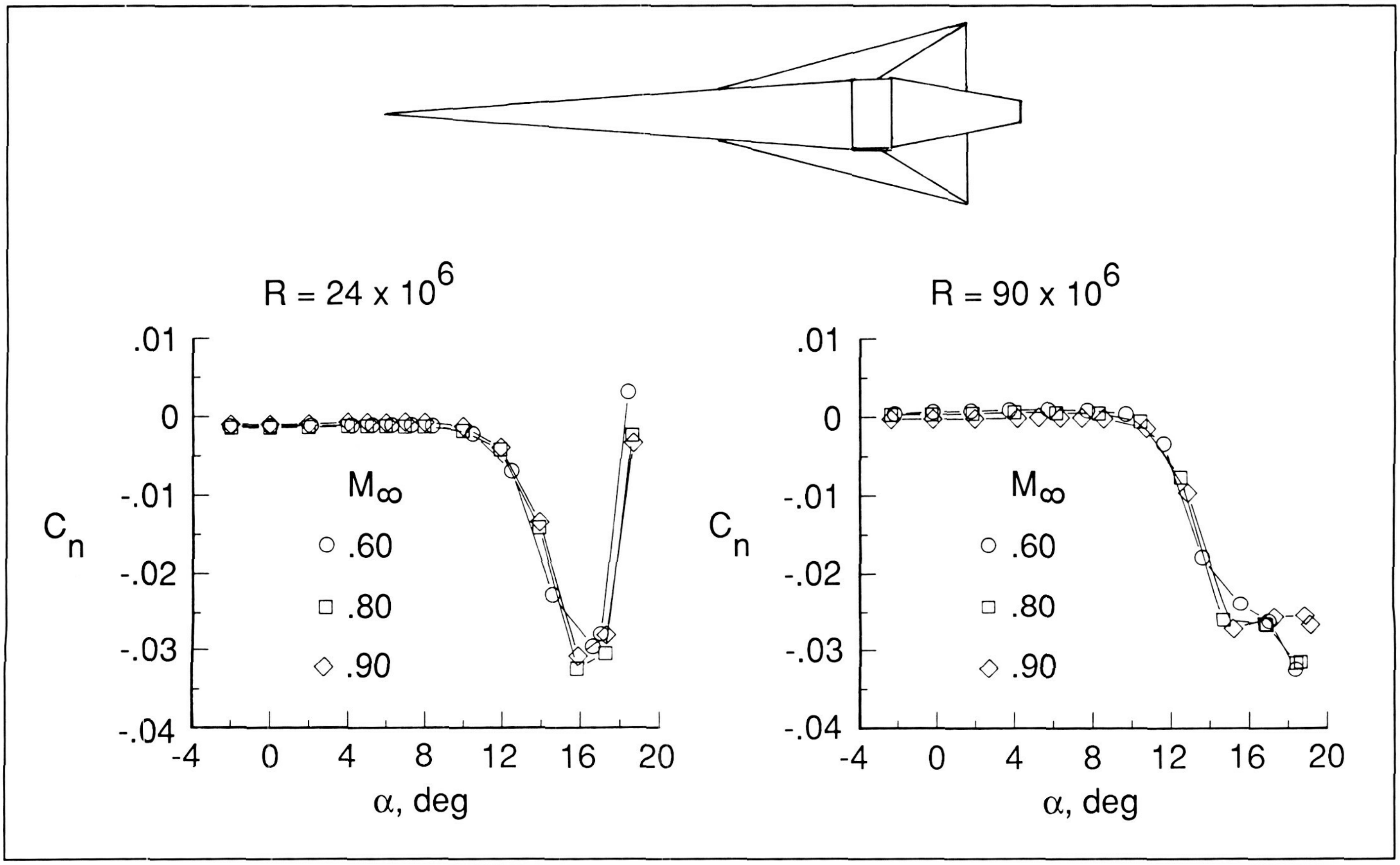

Reynolds number effect on yawing moment.

in the NTF as part of a broader experimental program for this model which included low-speed Reynolds number studies conducted in the Langley Low-Turbulence Pressure Tunnel (LTPT) as well as supersonic compressibility studies conducted in the Langley Unitary Plan Wind Tunnel (UPWT).

Tests were conducted in the NTF for Mach numbers ranging from 0.3 to 1.15 and Reynolds numbers ranging from 18×10^6 to 180×10^6 (based upon body length) such that Mach and Reynolds number effects could be isolated. Both longitudinal and lateral-directional force-and-moment data were obtained. At zero sideslip and high angles of attack, asymmetric flow separation occurred causing significant lateral-directional forces and moments. A sample result is presented in the figure for the yawing moment C_n at zero sideslip. The data demonstrate significant Reynolds number effects above an angle of attack α of approximately 14°. The low Reynolds number data show a nonlinear reversal in the yawing moment trend with angle of attack above this angle, whereas the high Reynolds number data do not evidence this effect in the angle-of-attack range investigated. The high Reynolds number data also show increased compressibility effects at the high angles of attack as compared to the low Reynolds number data.

(James M. Luckring and Charles H. Fox, Jr., 2601)

Validation of Parabolized Navier-Stokes Solver on Sharp-Nose Cone in Hypersonic Flow

Because experimental hypersonic facilities are limited in both number and capability, significant design and analysis of hypersonic vehicles must be conducted using computational fluid dynamics (CFD) methods. However, CFD methods must first undergo extensive validation with experimental data bases to

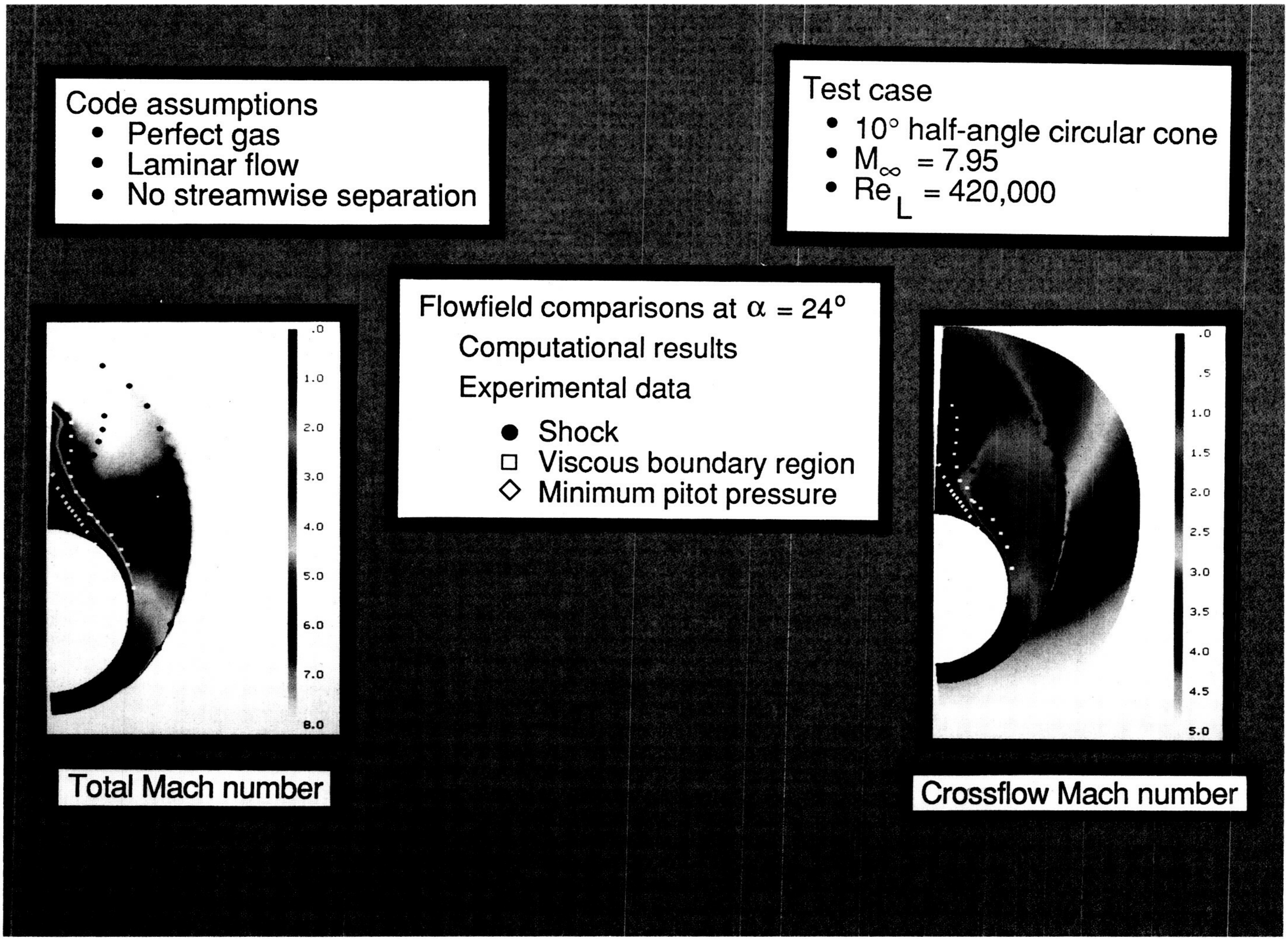

Code assumptions
- Perfect gas
- Laminar flow
- No streamwise separation

Test case
- 10° half-angle circular cone
- $M_\infty = 7.95$
- $Re_L = 420{,}000$

Flowfield comparisons at $\alpha = 24°$

Computational results

Experimental data

- ● Shock
- □ Viscous boundary region
- ◇ Minimum pitot pressure

PNS code validation results.

establish confidence in their use. A newly developed parabolized Navier-Stokes (PNS) code, based on an upwind/relaxation numerical scheme, has been validated for a 10° half-angle, sharp-nose circular cone at $M = 7.95$ and a Reynolds number of 420,000/ft. Comparisons were performed with experimental surface-pressure, heat-transfer, and flow field pitot-pressure surveys to validate the capabilities of this PNS code. In general, the code predicted the quantities accurately up through an angle of attack of 20°.

A comparison of the total and cross flow Mach number calculations with the experimental pitot-pressure survey data at $M = 7.95$ and $\alpha = 24°$ is shown in the figure. The experimental pitot-pressure data were used to define the location of the bow shock, the embedded cross flow shock, the edge of the viscous boundary region, and a line of minimum pitot pressure, which occurs inside of the viscous region on the leeward surface. The computed total Mach number data show that the PNS code accurately predicted the bow shock location, the edge of the viscous boundary region, and the line of minimum pitot pressure. Additionally, the computed cross flow Mach number data show good correlation with the location of the embedded cross flow shock. Surface pressures and heating were also well predicted.

The validation of this PNS code for the hypersonic laminar flow of a perfect gas over a simple but representative geometry gives confidence for its use in hypersonic forebody

evaluation and analysis studies under similar flow conditions.
(Lawrence D. Huebner; J. L. Pittman, 4004)

Mixing and Combustion Enhancement in Supersonic Flows

Work has been under way for a number of years at the Langley Research Center to develop a supersonic combustion ramjet (scramjet) engine that is capable of propelling a vehicle at hypersonic speeds in the atmosphere or beyond. Recent research has been directed toward the optimization of the scramjet combustor and, in particular, the efficiency of fuel-air mixing and reaction in the engine. Mixing is significantly reduced as the combustor Mach number increases with flight Mach number, and mixing enhancement is required to achieve a sufficient degree of combustion efficiency. Because of this difficulty, alternate combustor fuel injector configurations were studied to evaluate their potential for producing an improved degree of mixing and reaction.

A conventional scramjet fuel injection strut is shown schematically in the figure. Air from the scramjet inlet flows past the strut, and hydrogen fuel is injected in both a transverse and parallel direction into that air stream. A new fuel injector configuration, also shown in the figure, was considered to im-

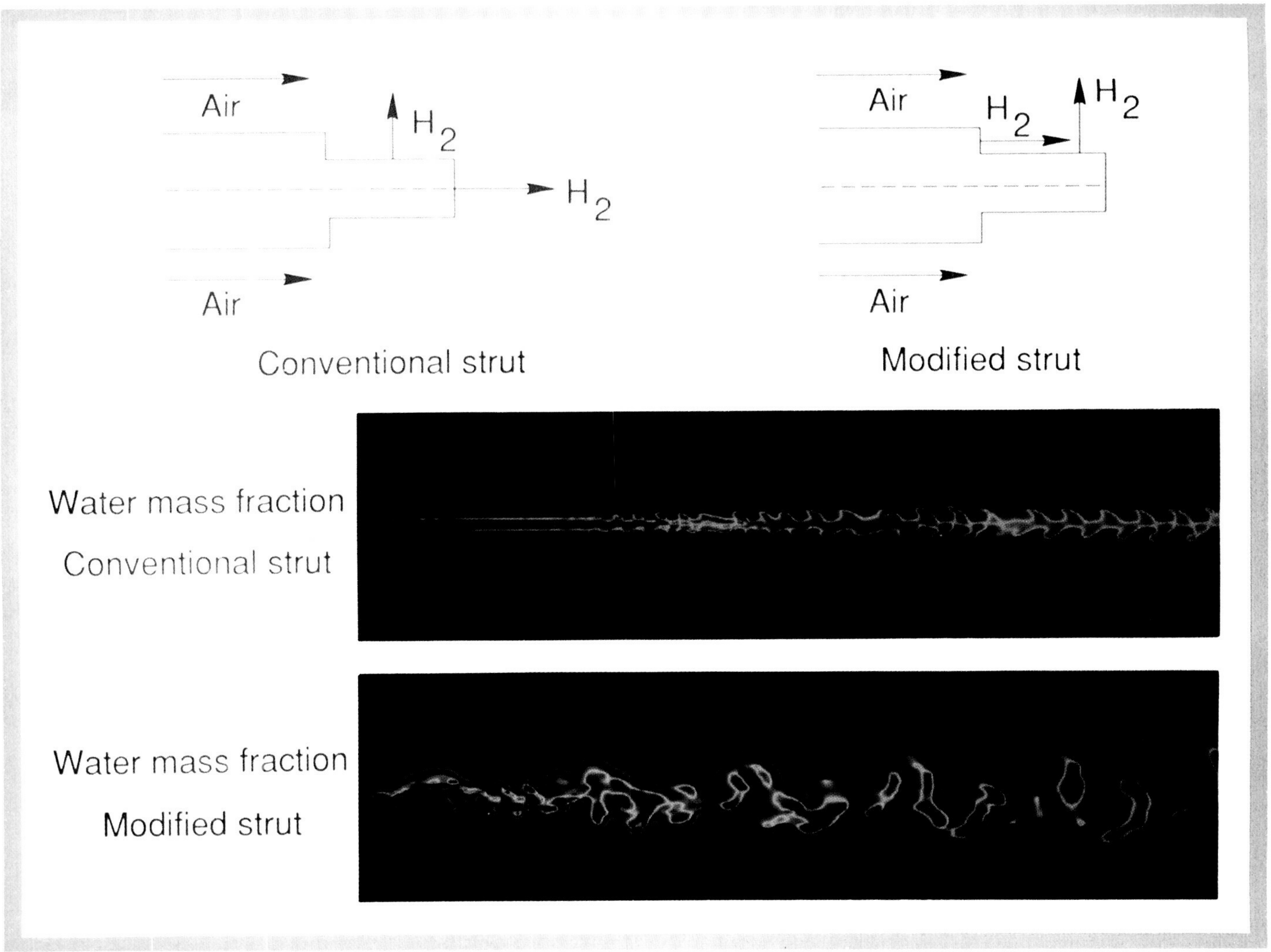

L-88-9164

Strut modification for improved combustion efficiency.

prove fuel-air mixing. In this configuration, the transverse injector causes the formation of a curved bow shock that produces vorticity and improved mixing when it interacts with the parallel injector. The new configuration was studied computationally, and a comparison was made with the old strut design. Results from the study, which show the water distribution from chemical reaction, are also given in the figure. As can be seen, the new design results in a significantly larger amount of mixing and chemical reaction that produces a marked increase in combustion efficiency. Additional research is now under way to optimize this design.
(J. P. Drummond, 3171)

Ramjet/Scramjet Engine Performance for Airframe-Integrated Engine

Engine-airframe integration for hypersonic airbreathing vehicles encompasses the use of the airframe forebody to compress the air flow before it enters the engine inlet and the airframe afterbody to expand the flow leaving the combustor. This integration concept results in minimum additional penalty in vehicle drag due to engine installation. The resulting vehicle propulsion performance is dependent on the individual performances of the forebody, inlet, combustor, internal nozzle, and external afterbody nozzle, and their performances are dependent on one another. To account for this interdependence, it is necessary to use a nose-to-tail propulsion flow path prediction technique that relates each part of the engine flow path to succeeding downstream parts. This approach makes the performance of each downstream part of the engine flow path a function of the performance of the upstream parts.

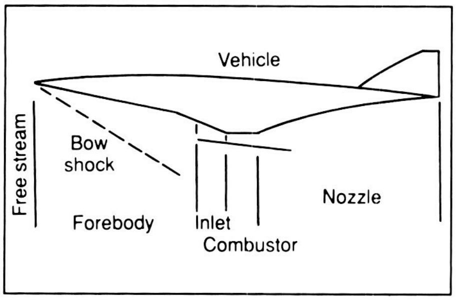

Sample vehicle having two-dimensional forebody, inlet, combustor, and nozzle.

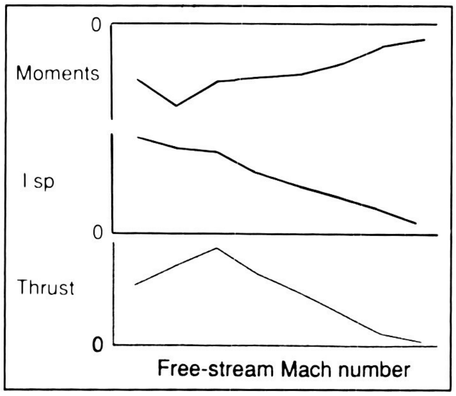

Engine performance.

A computer code has been developed which ties together the necessary analytical techniques required to predict the performance of such an integrated system. The engine performance computer code (SRGULL) combines an integral boundary-layer code (HUD), a finite-difference code for two-dimensional or axisymmetric perfect gas flows (SEAGULL), with a one-dimensional scramjet engine performance cycle code (SCRAMZ). This allows the prediction of the forebody, inlet, and nozzle flows using a finite-difference method for two-dimensional and axisymmetric perfect gas flows; the prediction of the combustor flow by the one-dimensional flow method; and the prediction of the friction and heat loss by the integral boundary-layer method. The combustor chemistry model includes a hydrogen-oxygen equilibrium chemistry model and a two-stream global finite-rate model that approximates the amount of equilibrium heat release equivalent to that of the finite rate.

The code, SRGULL, has the capability to predict both ramjet and scramjet engine performance in terms of thrust, specific impulse, and engine flow path forces and moments. Effects on engine performance can be generated for altitude, vehicle angle of attack, boundary-layer transition location, free-stream Mach number, inlet over speed, film cooling, fuel equivalence ratio, and liquid-oxygen augmentation. The vehicle forebody and aft nozzle are computed two-dimensionally or axisymmetrically, and a semi-three-dimensional modeling is included to consider side compression inlets and side expansion internal nozzles when applicable. A sample vehicle having a two-dimensional forebody, inlet, combustor, and nozzle is presented in the first figure. The second figure contains sample curves of engine thrust, specific impulse, and flow path moments as a function of free-stream Mach number.
(S. Zane Pinckney, 4711)

Electronics Directorate

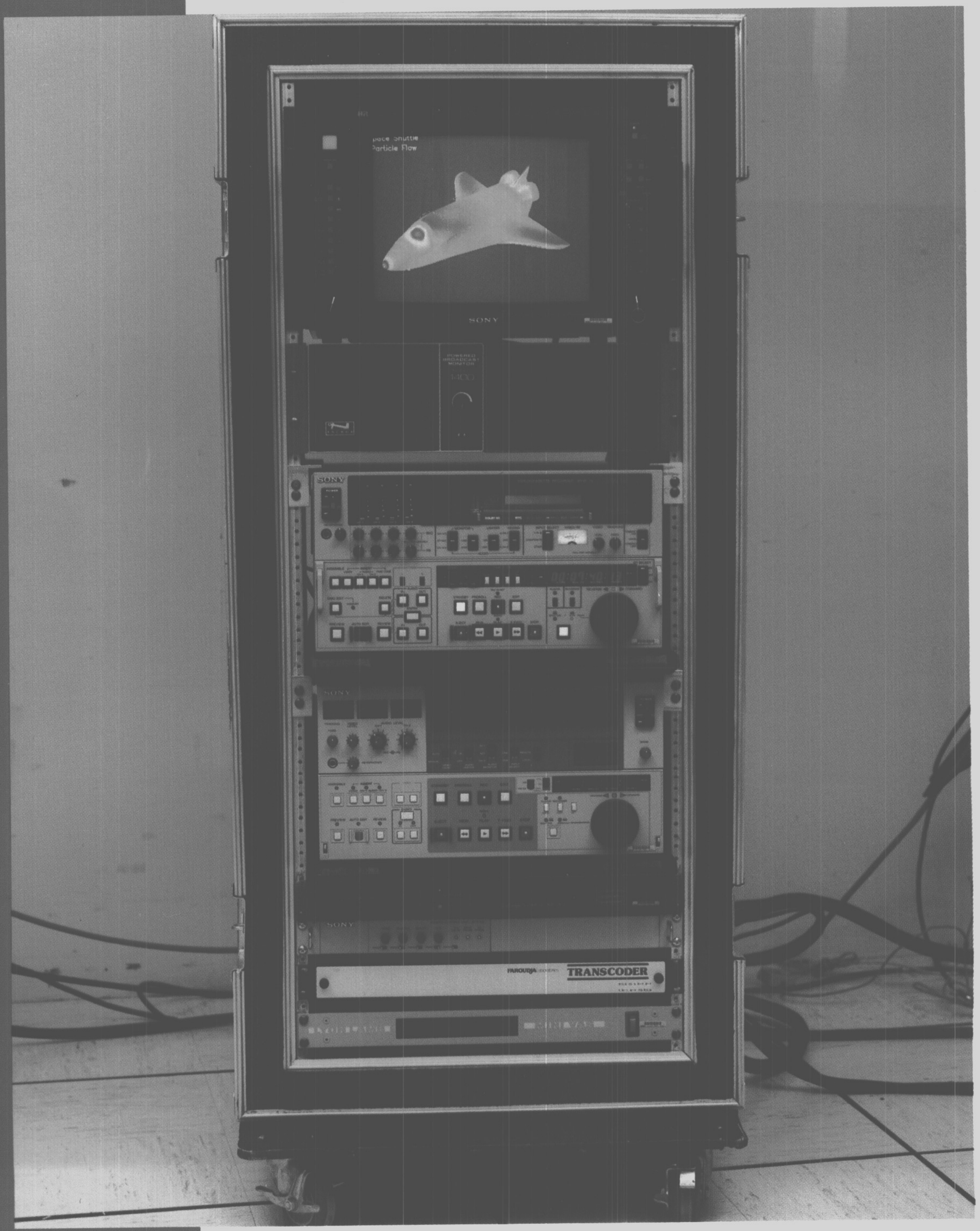

ORIGINAL PAGE
COLOR PHOTOGRAPH

The Electronics Directorate is responsible for planning, directing, and evaluating research and applications programs in the areas of measurements and computer science which will potentially benefit the Center's aerospace activities. This directorate also manages the Center's instrumentation, data acquisition, and data processing resources through the four divisions, each of which has specific support functions.

The Analysis and Computation Division is responsible for the development and application of mathematical and computer theory to the solution of computational problems arising from theoretical and experimental aerospace research activities performed at Langley Research Center. Additional responsibilities include conception, design, implementation, and management of advanced centralized data processing systems, flight software systems, and flight simulators, as well as providing consultation on Langley Research Center application of computer technology.

The Instrument Research Division provides instrumentation and measurement support for experimental aerospace research activities performed at Langley Research Center, with primary responsibility for the instrumentation of ground-based facilities. This division conducts research and development programs in instrument areas in which present measurement capabilities are deficient or nonexistent to satisfy both current and future aerospace test program requirements. Additional responsibilities include providing engineering and application expertise to support computer-based data acquisition and control requirements, developing and maintaining measurement standards, calibrating and repairing instruments, and managing an instrument pool.

The Flight Electronics Division is responsible for the development and application of electronic and electro-optical systems for aerospace flight and flight-related projects. This division conducts research and development programs in electronics, optics, lasers, and related disciplines to provide measurement, communication, and data processing systems. Additional responsibilities include design, fabrication, testing, and operation of ground and flight electronic equipment and instrumentation for approved flight projects and applications.

The Projects Division is responsible for the implementation and management of Langley Research Center's participation in major projects. Projects include those in the formative stages, such as the Hypersonic Flight and Instrumentation Research Experiment (HYFIRE) and the Earth Observing System (EOS), in addition to those in the mature stages, such as the SCOUT launch vehicle, which can place a 400-lb class payload in a low Earth orbit, and retrieval of the Long Duration Exposure Facility (LDEF), which was placed in orbit in 1983.

The accomplishments of the Electronics Directorate over the past year are as diverse as the directorate itself. Significant advances have been made in fundamental research for measurement and analysis systems. Some examples are nondestructive evaluation of the integrity of the Space Shuttle solid rocket boosters; improvements in the ability of fiber optics to transfer laser power; theoretical understanding of ion-doped solid-state lasers for application to space-based systems; new methods of electrically connecting superconducting materials to standard electronic systems; and development of computer modeling methods to more accurately represent fluid flow. In addition, the directorate, after a complete assessment of Langley Research Center's computing needs, has implemented the purchase of a world-class supercomputing system. The successful launching of five Scout-class vehicles has also been under the auspices of the Electronics Directorate.

Electrostatic Acoustic Transducer for Absolute Measurements of Ultrasonic Wave Amplitudes

The measurement of many nonlinear properties of materials depends upon accurate measurement of absolute (as opposed to relative) ultrasonic amplitudes over a wide range of frequencies. The Langley Research Center-developed Electrostatic Acoustic Transducer (ESAT) had previously been shown to have a frequency response that covered

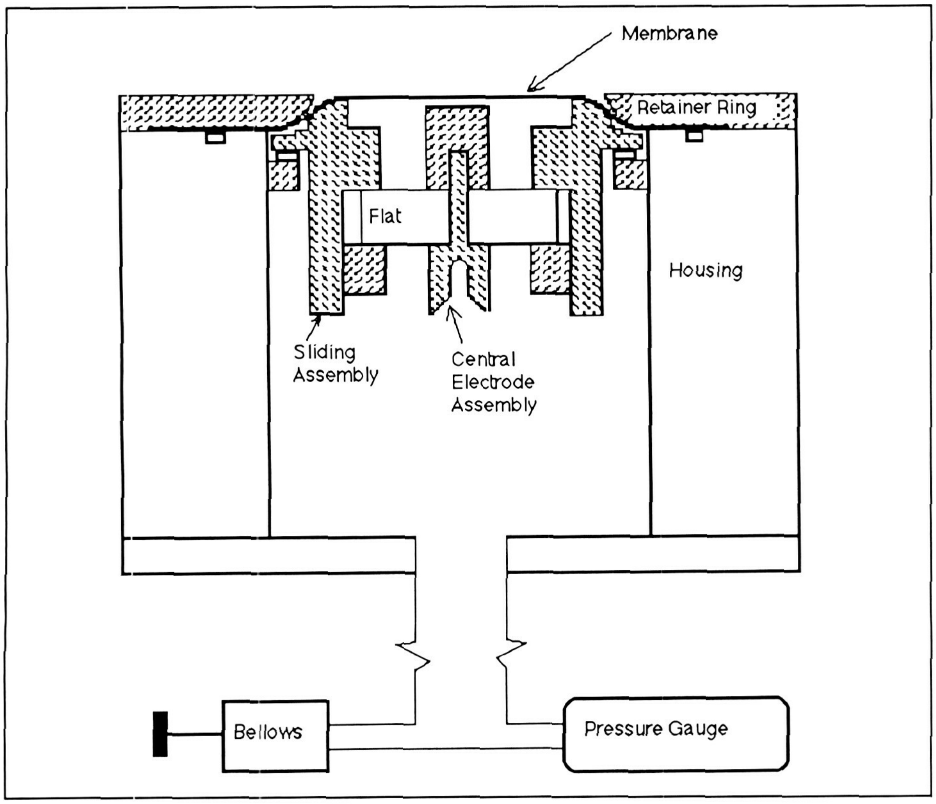

Mechanical diagram of ESAT showing pneumatic control system.

more than two decades of frequency (from approximately 100 kHz to more than 15 MHz).

Concepts and measurement techniques have been developed which permit this device to accurately measure the absolute amplitude of particle displacements associated with sound fields in liquids. These amplitudes can be in the subangstrom range and over the frequency range covered by the ESAT. The uncertainty in this technique is typically 2 percent at the lower frequencies (1 MHz or lower) and gradually rises to a maximum of no more than 4 percent at the higher frequencies.

The first figure shows a cross-sectional view of the ESAT. A thin conductive membrane is stretched over an electrically isolated cylindrical electrode that is recessed approximately 10 μm from the membrane inner surface. A pneumatic control system permits the adjustment of the membrane-central electrode spacing. The ultrasonic wave impinges on the membrane outer surface, causing it to vibrate in step with the wave. The central electrode, biased with a known dc voltage, can "sense" the small changes in spacing caused by the membrane movement.

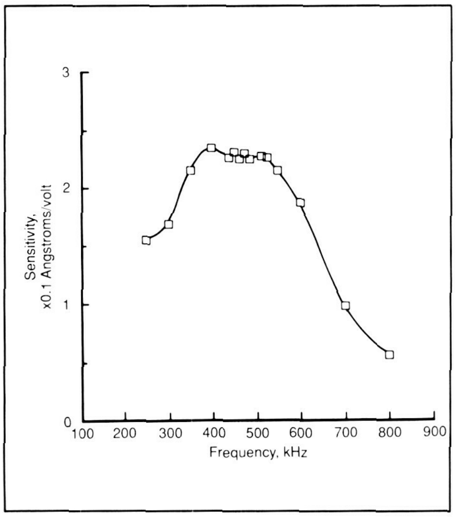

Plot of transducer sensitivity versus frequency for damped 500-kHz transducer.

The second figure shows results of using the ESAT for absolute measurement of the output of a 500-kHz damped transducer, which is a commercially available, off-the-shelf device. The abscissa shows the frequency and the ordinate shows the particle displacement amplitude/drive volt applied to the damped transducer. (The applied voltage is measured in peak-to-peak volts.) The ESAT can now be used for absolute calibration of ultrasonic transducers.

(W. T. Yost and John Cantrell, 3036)

Measurement of Gas Permeation Rates in Polymeric Materials

A mass spectrometric method of quantitative trace-gas analysis previously developed at Langley Research Center has been adapted to the measurement of gas permeation rates through polymeric membranes. This method, called the Dynamic Delta method, has recently been successfully applied to measurements of the permeation rates of oxygen, nitrogen, and carbon dioxide through small area samples of contact lens materials of varying chemical composition. A data base has been built for these contact lens materials. This data base will be used for comparison

with contact lens materials that will be made under microgravity conditions aboard the Space Shuttle as part of the Space Commercialization Project.

There is reason to believe that certain materials made under these conditions will have high and more uniform oxygen permeation rates than materials of identical chemical composition made under normal gravity conditions. As a means of comparison, the Langley Research Center data base also includes permeation rates of oxygen, nitrogen, and carbon dioxide determined using a gas chromatographic technique that does not have the inherent sensitivity of the mass spectrometric technique. Additionally, this data base contains oxygen permeation rates determined using the polarographic technique, which is the standard in the contact lens industry. The internal agreement among the three methods for oxygen is good considering that there is a gas-membrane-gas interface for the gas chromatographic and mass spectrometric measurements and a gas-membrane-liquid interface for the polarographic technique. Measurements of this type can add to the understanding of the transport mechanism of gases through these polymeric membranes.

(K. S. Burns, J. D. Van Norman, B. T. Upchurch, and G. M. Wood, 2466)

CO Oxidation Catalysts for Closed-Cycle Pulsed CO_2 Lasers

Pulsed CO_2 lasers have many remote-sensing applications from space, airborne, and ground platforms, such as the NASA Laser Atmospheric Wind Sounder (LAWS) system that will measure wind velocities from polar Earth orbit for a period of up to 3 years. Such applications require an efficient catalyst to recombine the CO and O_2 dissociation products that would otherwise degrade the laser operation. The catalyst must operate efficiently for a long period of time at low temperatures.

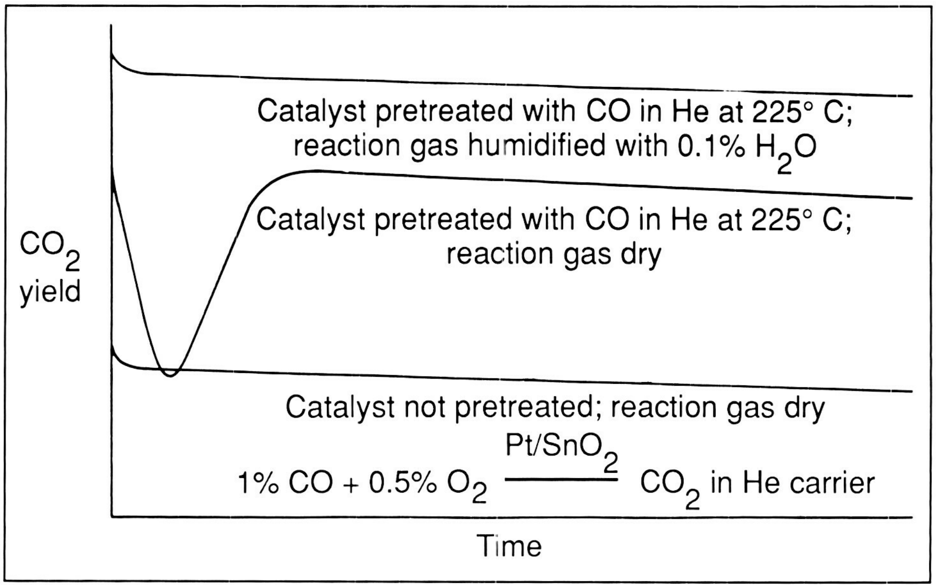

Effect of pretreatment and H_2O on activity of Pt/SnO_2 catalyst for CO oxidation.

The Pt/SnO_2 catalysts have been found to convert CO and O_2 to CO_2 with good efficiency at typical laser temperatures. However, an undesirable dip in activity is often observed before the steady-state activity of these catalysts is achieved (as shown in the first figure). It has recently been established that this initial dip in activity is caused by dehydration of the catalyst surface during catalyst pretreatment. The Pt/SnO_2 catalysts require pretreatment with a reducing gas, such as CO in He, at elevated temperature to achieve their maximum activity (see the first figure). Such pretreatment, however, can dehydrate the catalyst surface, converting highly reactive hydroxyl (OH) groups to less-reactive doubly bonded oxygen atoms. The resultant loss in catalyst activity is eventually overcome by migration of H_2O or OH from the catalyst bulk.

It has been shown that this loss-gain cycle, or dip, can be prevented by rehydrating the catalyst prior to use. The rehydration can be accomplished by exposing the catalyst to a humidified inert gas between pretreatment and exposure to the CO-O_2 reaction mixture or by humidifying the reaction mixture itself. An additional benefit is that humidification of the catalyst also enhances its activity (see the first figure).

An improved Pt/SnO_2 catalyst with a hydrous support to internally supply H_2O, and thus OH, has been developed at Langley Research Center. The catalyst is synthesized by overlaying a thin layer of tin oxide upon a hydrated silica gel support followed by deposi-

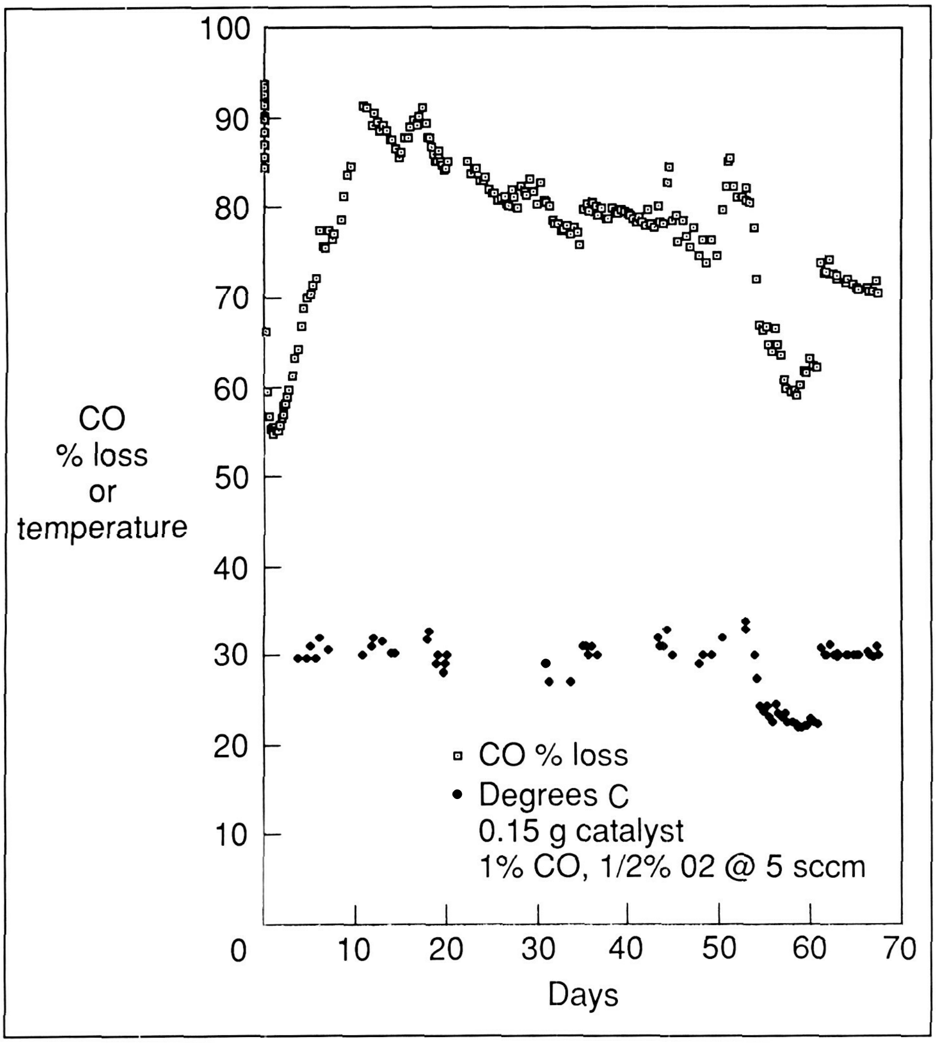

Carbon monoxide and oxygen recombination efficiency.

tion of a thin overcoat of platinum metal. The hydrous underlayer support surface enhances catalyst efficiency as it serves to provide needed moisture for the platinum-tin oxide interface without a buildup of vapor-phase H_2O concentration. After pretreating this catalyst with 5 percent CO in He at 125°C for 1 hour, the catalyst was exposed to a 5 standard cm^3/min flowing stream of test gas consisting of 1 percent CO and 0.5 percent oxygen in He to simulate the gas decomposition products in a pulsed CO_2 laser. The catalyst was tested under ambient laboratory room temperature conditions for more than 2 months, and at the time of this writing, the test was continuing with a recombination efficiency exceeding 70 percent for an 0.15 gram catalyst sample as shown in the second figure. The catalyst shows considerable promise for application in the LAWS laser, in particular, and for long-life closed-cycle CO_2 lasers, in general.

**(David R. Schryer, 2818,
B. T. Upchurch, I. M. Miller,
G. M. Wood, and D. R. Brown)**

Laser-Induced Fluorescence of O_2 at High Temperatures

Recent advances in both ultraviolet lasers and the spectroscopy of laser-induced fluorescence (LIF) of gases in the ultraviolet (UV) region indicate that LIF has the potential for nonintrusive gas diagnostics in aerodynamic and combustion test facilities. This research involves a laboratory investigation of LIF of the oxygen (O_2) molecule with the ultimate goal of developing an instrument to nonintrusively measure O_2 concentration and gas temperature in high-temperature gas flow fields, e.g., the scramjet combustor.

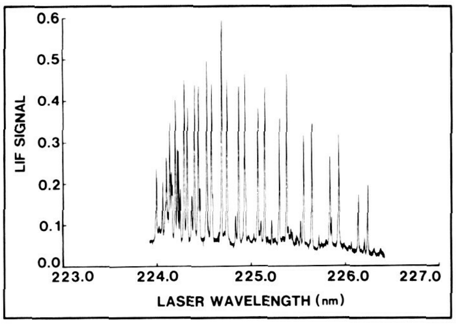

Experimental LIF O_2 spectrum.

During the past year, this research has produced both theoretical and experimental results. First, a detailed model has been developed for the LIF spectrum of molecular oxygen at flame temperatures. Molecular oxygen is significant because quenching of the fluorescence, which is difficult to quantify, is greatly reduced by predissociation; consequently, the task of quantifying quenching can be eliminated. The model identifies those transitions that can be used in this manner. The figure shows an experimental LIF spectrum of molecular oxygen; numerous transitions through the spectral region of 224

ORIGINAL PAGE
COLOR PHOTOGRAPH

to 226 nm are shown. Several line pairs that exhibit a favorable sensitivity to temperature have been identified in this region.
(Walter R. Lempert, 2791)

Nonintrusive Detection of Flow Transition With Infrared Imagers

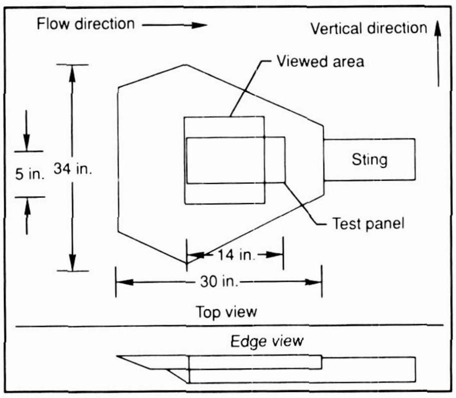

Flat model used in UPWT.

Infrared imaging techniques have been successfully tested for nonintrusive detection of boundary-layer transition in flight tests on a natural laminar flow glove on the Langley Research Center T-34 research aircraft and in wind tunnel tests of a flat plate in the Unitary Plan Wind Tunnel (UPWT). Low heat capacity, low thermal conductivity test surfaces of fiberglass or Bakelite® permitted detection of transition as a temperature jump across the transition line in both steady-state and transient conditions. The temperature jump is caused by a significant difference in the convective heat transfer coefficient between the laminar- and transition-flow regimes. Solar radiation and aerodynamic heating were the sources of heat exchange with the test surfaces for the T-34 and UPWT tests, respectively.

These tests have proved the infrared imaging technique as a viable candidate for nonintrusive boundary-layer flow visualization. The flat-plate model used in the UPWT is shown in the figure along with the infrared image of a portion of the flat plate subject to flow transition caused by tripping.
(Robert E. Wright and David W. Alderfer, 2466)

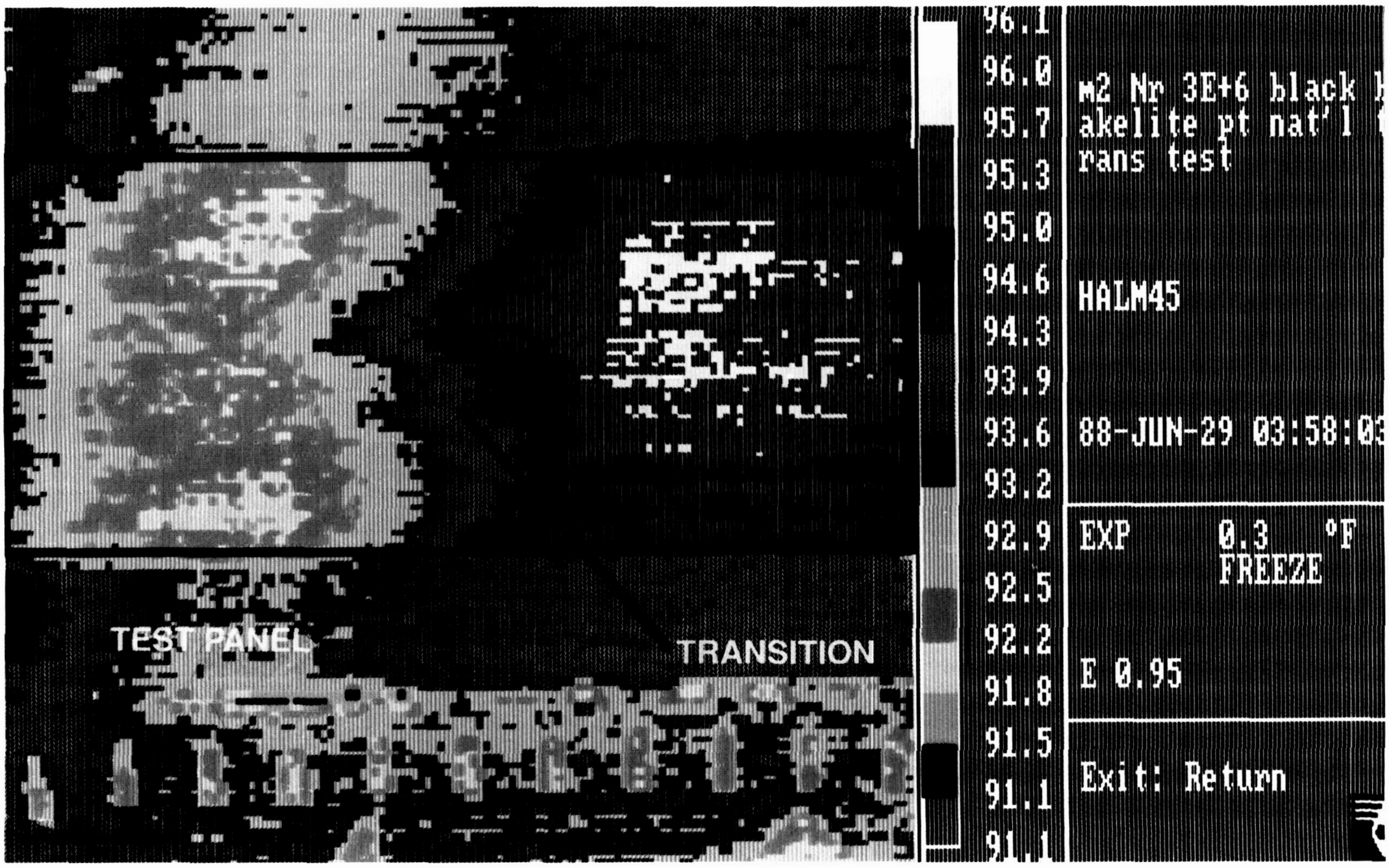

Thermal infrared image of model in UPWT showing transition line.

Rugged Low-Resistance Contacts to Superconducting Ceramics

Since the new high-temperature superconductors are ceramics, electrical contact to them presents a challenge. Silver paste and pressure contacts can be used to measure the resistive transition, but their inability to carry large currents makes them unsuitable for determining large critical currents directly or for use in high-current-carrying applications. Other authors have reported success with silver wires in silver epoxy and soldering leads onto evaporated noble metal films. Langley Research Center has observed equally low, if not lower, contact resistances with a more rugged connection to the material. Gold is melted onto the sample surface, which diffuses into the sample pores, making a strong mechanical contact in the form of a bead. It is then an easy matter to solder external leads to the beads, making good electrical contact. The figure shows a scanning electron micrograph of a gold bead contact with a soldered lead.

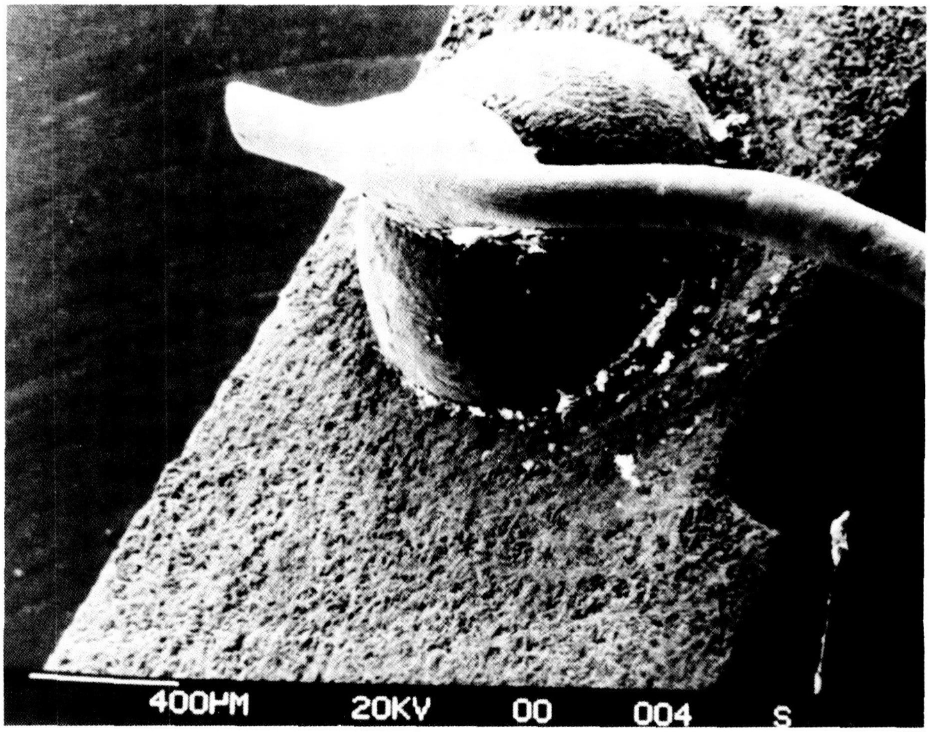

Scanning electron microscope picture of gold bead contact with soldered lead.

Samples are prepared by the standard sintering method, starting from oxide and carbonate powders. The contacts are formed by melting small squares of gold foil onto the surface of a shaped resistivity sample that has been cut from a fully oxygen-treated pellet. The sample is heated to 1065°C in air for about 1 h to melt the gold squares. The sample is then removed from the oven once it has cooled to $\approx$ 900°C. At this point the melted gold bead is slightly oxidized and firmly connected to the sample; however, the contact resistance is high (several kΩ). Some of the oxygen is lost from the sample during this process, and retreatment in oxygen is necessary. Gold bead contacts have measured contact resistances $<50\ \mu\Omega$ at 77 K. Transport critical densities of $\approx 480\ \mathrm{A/cm^2}$ were measured while passing ≈ 5 A current through the contacts without heating the sample. The shear strength of the gold bead contacts is greater than for other methods. These sturdy contacts will be of practical use in high-current-carrying applications of the novel high-temperature superconducting ceramics.

(Charles Byvik, 2818)

Improvement in Ultrasonic Detection of Disbonds at Rough Interfaces by Large Aperture, Phase-Insensitive Array Transducer

Ultrasound is frequently used when testing the bondline integrity of an interface. For example, on the Space Shuttle solid rocket motor (SRM) system, several bondline regions are interrogated by conventional pulse-echo ultrasound. Standard ultrasonic techniques fail when the surfaces are too uneven. Rough interfaces can introduce several types of artifacts on reflected ultrasonic signals. One artifact is the result of severe phase cancellation at a phase-sensitive transducer face that is typical of the transducers used in conventional ultrasonics; another artifact is the possibility of reflections of the

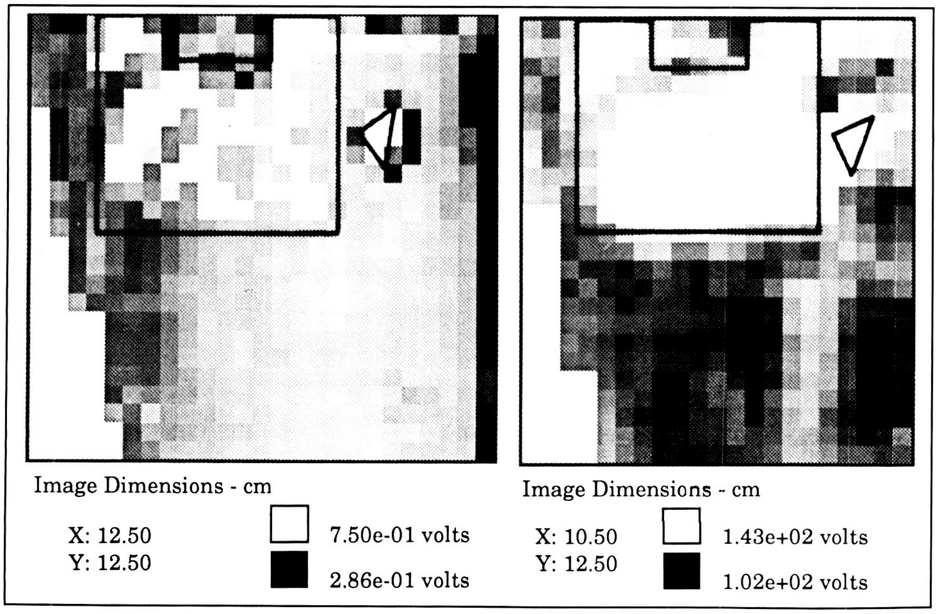

Phase-sensitive detection (left) versus phase-insensitive array detection (right).

ultrasonic beam away from the transducer. These artifacts can be detrimental to the quantitative detection of defects at interfaces because they distort waveform shapes and cause signal loss.

In this work, the practical advantages of using a large-aperture, phase-insensitive array for the detection of disbonds at rough interfaces have been demonstrated. Although elements of such an array would be constructed with standard phase-sensitive transducer materials, the small size of each array element would be less prone to phase cancellation artifacts. The signals received by all the array elements would be electronically summed in a phase-insensitive manner. The large aperture of the array would help to ensure that the ultrasonic echoes would still be detected even if they were deflected away from their initial direction. Emulating this type of system, the improvements in the detectability of disbond defects on rough interfaces were demonstrated. In one example taken from an SRM inhibitor-liner-fuel region that had a very rough boundary, the practical sensitivity to defects was increased from 42 percent for a conventional system to 79 percent for the phase-insensitive array system. The figure on the left illustrates the accuracy of conventional phase-sensitive detection, and the figure on the right illustrates the improvements resulting from the phase-insensitive array system. The bold outlined shapes are the unbond regions, and the area shown in white is the ultrasonically detected unbond region.
(Eric Madaras, 3036)

Improved Detection of Disbonds in Solid Rocket Motors Using Digital Processing of Thermographic Data

Inspection protocols are being developed for using thermography to inspect bondlines between the inhibitor, liner, and propellant in solid rocket motors used in the Space Shuttle. Based on results of earlier research, disbonds that are roughly equidimensional and several square inches in area can be detected beneath the inhibitor up to 0.5 in. in thickness. These disbonds are directly discernible, using appropriate heating protocols, in thermograms of the inspected surface. However, if the disbonds are long and thin, penetrating from an edge, they are only marginally visible and can be easily missed in an inspection of a thermogram, even though they occupy an area of several square inches. Such disbonds could be very dangerous in an operating motor because they could direct hot gases to the vicinity of the steel case. The work reported here applies numerical image analysis to the problem of detecting thin, edge-penetrating disbonds beneath the inhibitor layer.

For this inspection, heat is applied to the sample with an external heating source. The heat is then removed, and thermographic images of the cooling sample are obtained. These images are then subjected to numerical postprocessing consisting of several steps: frame-averaging, selection of the edge-parallel direction, application of the second derivative filter, and calculation of deviations from line averages, threshold choice, and display.

The figure illustrates the inspection of a laboratory sample of the Space Shuttle solid rocket motor materials; this sample had a layer of inhibitor over a layer of liner, which was over a layer of inert fuel. Two areas of damage have been created by inserting and withdrawing a screwdriver into the fuel/liner bondline and the liner/inhibitor bond-

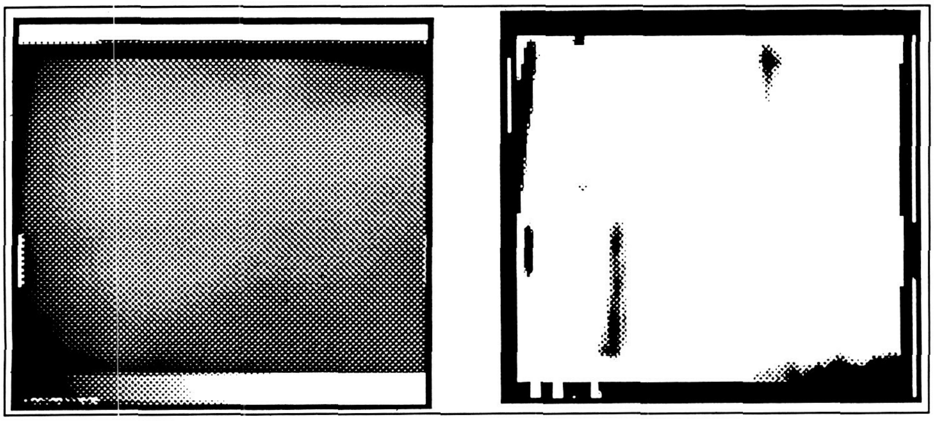

Thermogram (left) and processed image (right).

line. The left-hand figure shows the thermogram of the sample, and the right-hand figure shows the same data after the numerical processing described took place. The two black areas extending into the center of the right-hand figure correspond to the damage locations.

The results clearly show that the postprocessing developed in this effort permits a significant improvement in flaw detection over that obtained with thermography alone.
(William P. Winfree, 3036)

Electronically Scanned Pressure Transducer Capable of Operating at Cryogenic Temperature

Pressure is one of the most important parameters measured when testing models in wind tunnels. For models tested in the cryogenic environment of the National Transonic Facility, the act of mounting pressure instruments inside the models, necessary for acceptable measurement data rates, is extremely difficult because of the small internal volume of the models and the requirement to heat the pressure transducer (an electronically scanned pressure sensor) which cannot operate at the −173°C tunnel temperature.

Research on the physics of CMOS (complementary metal oxide semiconductor) electronic components and highly doped bipolar semiconductor pressure sensors at extremely cold temperatures has produced a multichannel pressure sensor design that will operate at cryogenic temperatures. Any thermally induced error obtained from this pressure sensor is a linear function of temperature. This error, therefore, lends itself to relatively easy correction using computer algorithms.

A prototype ceramic sensor substrate has been designed on which microsensors are mounted for sensing both the wind tunnel pressures and the substrate temperature to correct any thermally induced errors. A second cryogenically compatible substrate has CMOS multiplexing, amplification, and signal conditioning to control the sensors and transmit pressure data to the data acquisition computer. The

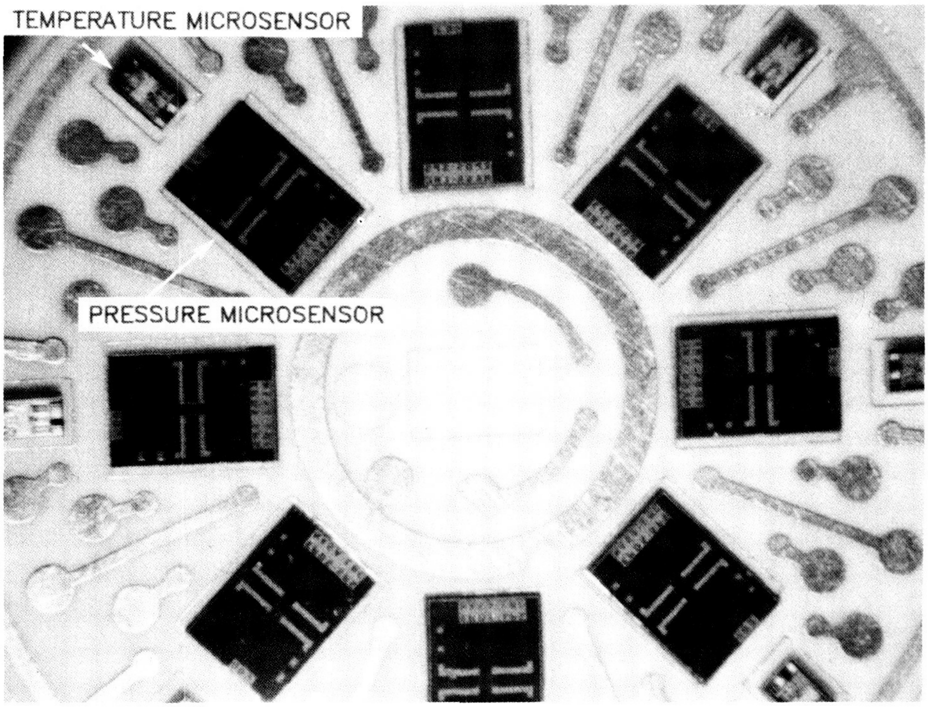

L-88-9143

Eight-channel pressure sensing substrate with temperature-compensating sensors.

prototype sensor system is being assembled for performance testing.
(John J. Chapman, 3234)

Advancements in Instrumentation for Measuring Strains at High Temperatures

An installation technique for high-temperature resistance strain gauges has been developed at Langley Research Center; this technique allows strain measurements to be made at temperatures several hundred degrees higher than can be obtained using current techniques. Additionally, this technique provides for bonding strain gauges to unconventional materials including silicone-carbide-reinforced carbon-carbon.

The technique utilizes a plasma arc flame spray concept, whereby molten aluminum oxide powder is sprayed onto the test article surface to act as an electrical insulator. The high-temperature strain gauge is then placed on the insulated area and thermally sprayed using the same plasma arc system.

The system has just recently become operational, and its limitations have not yet been defined. However, the system has been utilized for installing strain gauges on test plates for a fatigue test program at Langley where dynamic strains are measured at temperatures approaching 1200°F. Initial laboratory tests indicate strain measurements can be made at 1500°F using the plasma arc flame spray approach.
(Thomas C. Moore and Joseph G. Sikora, 3483)

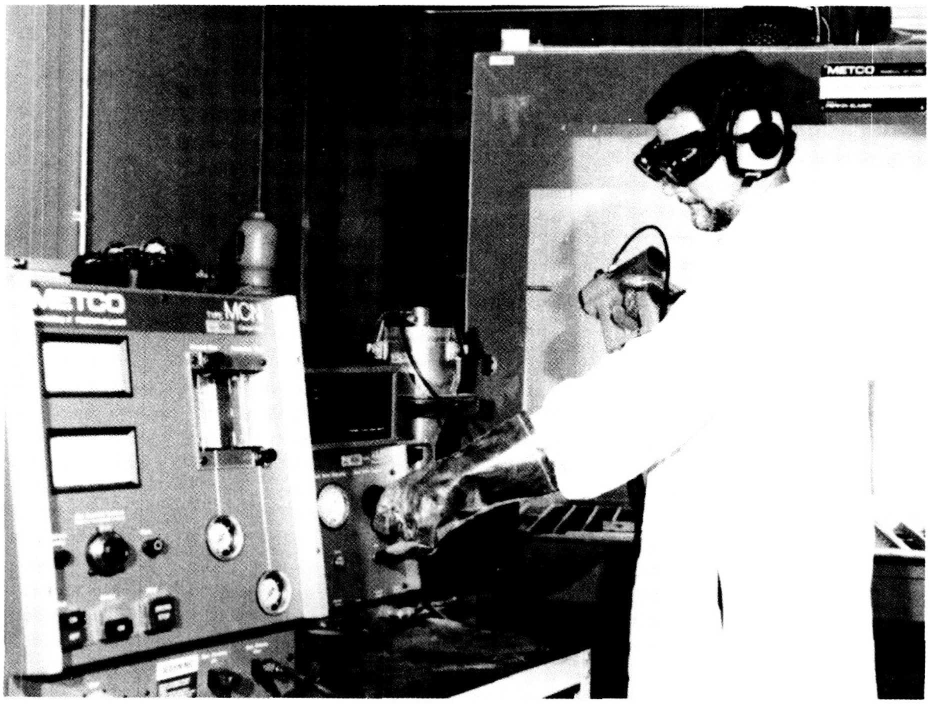

L-88-7767

Plasma spray system for high-temperature strain-gauge procedure.

High-Current DC Amplifier for Magnetic Suspension Wind Tunnel

The Langley Research Center 6-in. Magnetic Suspension and Balance System (MSBS) requires an independently controlled bidirectional amplifier for each of six positioning magnets. The original magnet power system, composed of motor-generator sets, magnetic amplifiers, and thyratron rectifier bridges, was bulky, prone to frequent component failure, and grossly inefficient. Considerable effort was required for maintenance and repair. Due to the use of voltage dropping resistors, the system consumed over 76 kW of power at less than 24 percent efficiency at full load, and nearly 6.4 kW at less than 20 percent efficiency for average loads. For these reasons, state-of-the-art replacement power amplifiers are required.

The new solid-state power amplifiers employ a digitally sequenced bidirectional MOSFET (metal oxide semiconductor field effect transistor) power transistor bridge design and can furnish up to ±90 A at ±90 V. Three instrument racks are sufficient to enclose the new equipment. Because of the inherent reliability of solid-state components and extensive fault protection designed into the new supplies, a low failure rate is anticipated. Indeed, elimination of dropping resistors, which increases efficiency to nearly 80 percent at full load and to over 70 percent at average load, is expected to reduce energy operating costs of the MSBS by 70 percent. The use of current feedback with integration provides highly linear power amplifier operation, and a zero steady-state controlled current error. Theoretical performance predicted by computer simulations has

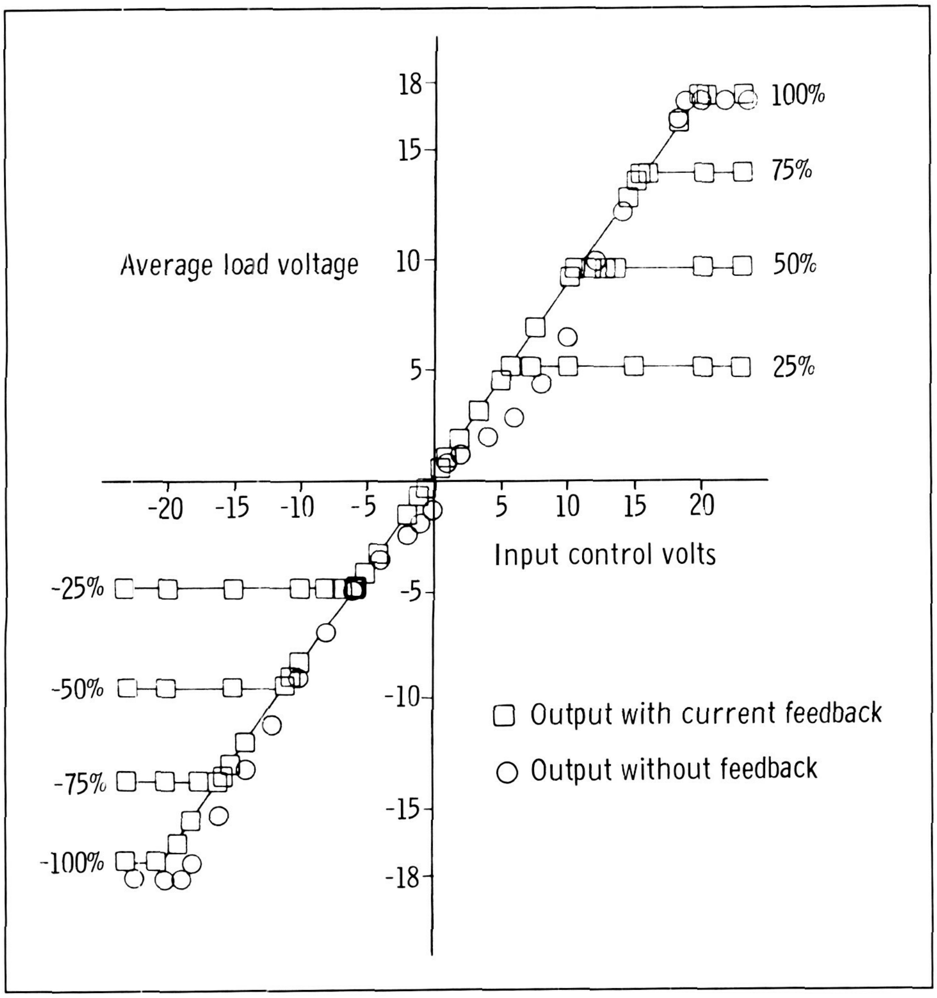

Dynamic response of dc power amplifier to steep ramp control input.

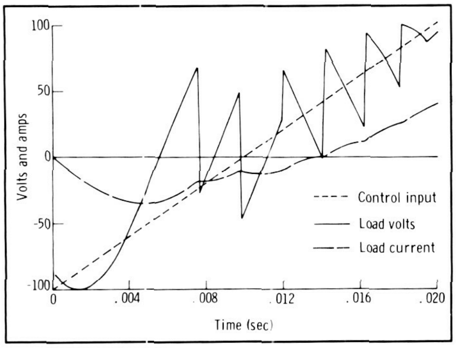

Amplifier linearity with and without current feedback at four current limit settings.

been confirmed experimentally via testing of a prototype dc power amplifier. Unlike the original system, the conductors from the power amplifiers to the positioning coils have grounded shielding, which should eliminate a troublesome source of 20 kHz interference in the electromagnetic model position sensing system.

(J. S. Tripp and T. S. Daniels, 3483)

Micro-Thin Hot-Film Transition Detection System

Of prime importance in many wind tunnel and flight experiments is a measure of the location of boundary-layer transition. This measure may not be so easily accomplished, however, in flows in which sensor thickness exceeds the critical roughness height on the model, in which model integrity precludes the use of probes that perforate the model surface, or in situations in which sensors aren't able to conform to three-dimensional models.

A micro-thin hot-film system has been developed at Langley Research Center to solve these problematic situations. The system, originally developed for use in the National Transonic Facility, consists of an array of micro-thin nickel films (8.66 μin.) which are vapor deposited on a parylene C/SiO_2 dielectric substrate (329.5 μin.) and which connect to the driving electronics through vapor-deposited aluminum leads (19.69 μin.). The films, substrate, and aluminum leads have a total roughness height of less than 400 μin. and can be deposited directly on the model to be tested.

The instrumentation that drives the films is a multichannel, simultaneous data acquisition system that can acquire and graphically display on-line the chordwise transition location.

The system has been demonstrated to detect the on-line, boundary-layer transition location in a low-speed test on a 12-in.-chord NACA 0012 airfoil in the Langley Research Center Instrument Re-

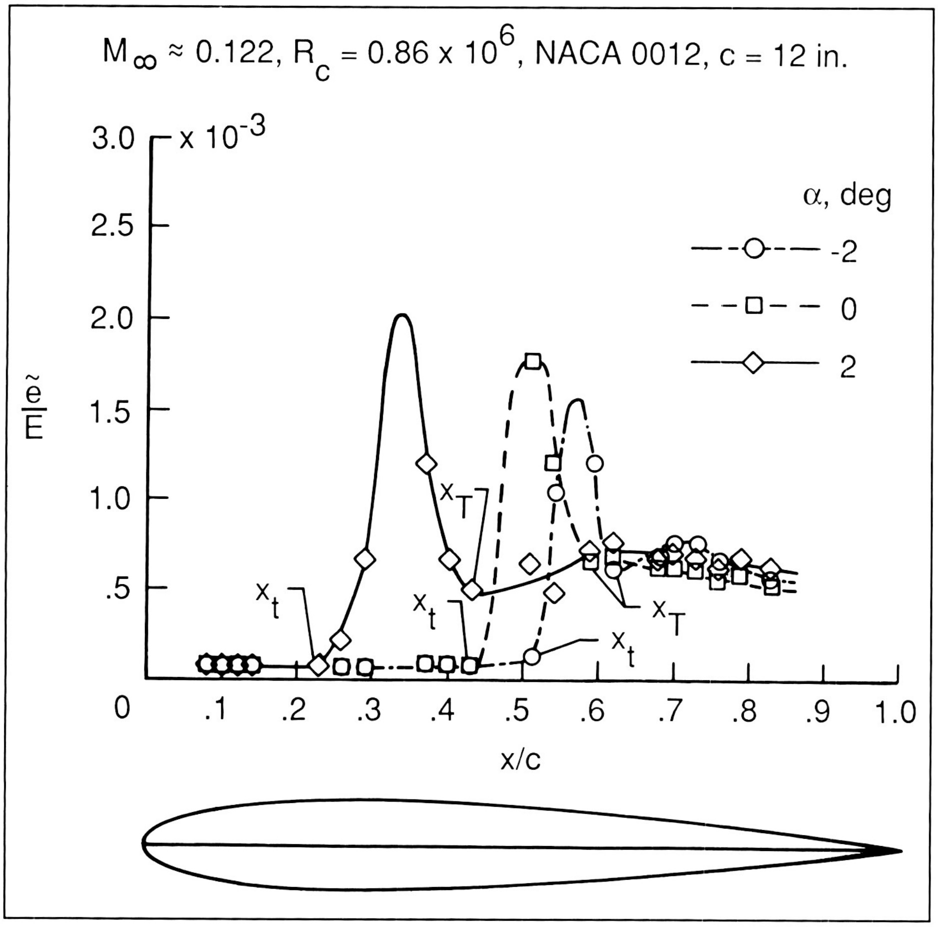

On-line chordwise fluctuating voltages for various angles of attack.

search Division small calibration facility. The figure shows a composite of the on-line results. The turbulence intensity level at each film (a function of the fluctuating voltage $\tilde{e}$, divided by the mean voltage E) is plotted against the film chordwise location x/c for various angles of attack ($\alpha = -2°$, $0°$, and $+2°$) at flow conditions of Mach 0.122 and chord Reynolds number of 0.86×10^6. Both beginning and ending transition locations, indicated by x_t and x_T, respectively, are clearly defined for each of the three sets of data. The test also demonstrated that films were capable of detecting the Tollmien-Schlichting waves at the onset of transition (the x_t location); this detection was validated by comparison of the measured frequencies with the predicted most-amplified frequencies from an incompressible stability computer code.

(D. L. Carraway, 3446, C. B. Johnson, and S. Q. Tran)

Thermal Shroud Design

Temperature sensors are often shrouded to protect the sensing element as well as to shield it from unwanted thermal radiation. Typically, shroud designs have been based upon trial-and-error testing.

Ventilated shrouds for a coaxial cylindrical sensor in cross flow have been studied at Langley Research Center.

Over a Reynolds number range from 2,000 to 20,000 (based on the sensor diameter), both the degree of shroud ventilation and the diameter influence the rate of convective heat transfer to the sensor. For shrouds ventilated with six rows of equally spaced circular holes, experiments showed that sensor heat transfer could be enhanced by up to 50 percent over its unshrouded level for a shroud ventilation factor of 0.35 (the fraction of shroud area that is open) when the shroud diameter was approximately 1.5 times the sensor diameter. An equivalent sensor diameter was developed as a function of ventilation factor and diameter ratio as shown in the figure. The equivalent diameter, which can be used in the design of shrouded thermal sensors, was defined as the corresponding sensor diameter that would produce the same rate of convective heat transfer as the shrouded sensor.

In order to determine the influence of ventilation hole shape on sensor heat transfer, a set of shrouds with six equally spaced slots was used which had the same ventilation factors and diameter ratios as the shrouds with circular holes. The internal flow was approximately two-dimensional in the slotted case. These tests showed that while the slotted shrouds behaved like those with circular hole patterns for ventilation factors on the order of 0.10 where heat transfer was retarded, heat transfer to the sensor was not enhanced for larger ventilation factors. Hence, shrouds that are ventilated with circular hole patterns improve sensor

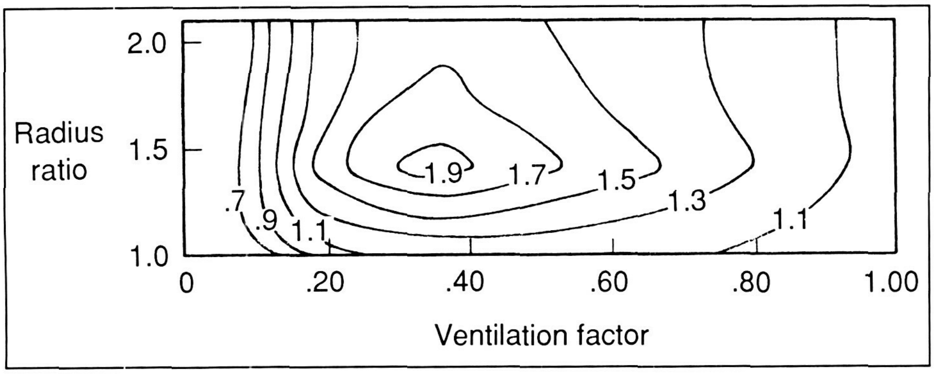

Constant equivalent diameter ratio contours as function of ventilation factor and radius ratio.

response because they create more three-dimensional internal flows.
(Kamran Daryabeigi and Robert L. Ash, 2466)

Power Transmission Characteristics of Polarization Preserving Single-Mode Optical Fiber (PPSMOF)

The transmission of a coherent optical field along a PPSMOF is important in both the instrumentation and the communication fields. An investigation of the transmission of high-power coherent optical fields along a PPSMOF waveguide has been conducted for the two main wavelengths of Ar ion laser radiation.

Waveguide transmission measurements have been performed to determine the power transmission efficiency, potentially adverse frequency generation, and polarization characteristics of a Panda-type PPSMOF waveguide at 488.0 and 514.5 nm. The two figures show the relationship between output power and input power for a 20-m-long fiber. The light input source was operated both in single- and multi-longitudinal modes. In the single-mode condition, a distinct saturated condition was experienced after a certain threshold input power level was exceeded. After the threshold power level was exceeded, additional frequency components were observed in the backward direction. The new frequency components are related to the frequency generated by the stimulated Brillouin scattering (SBS) process. It was experimentally demonstrated that optimization of the optical coupling as well as input polarization manipulation can shift the SBS threshold level to a higher value and consequently provide a higher transmission efficiency. The results show an improved performance compared

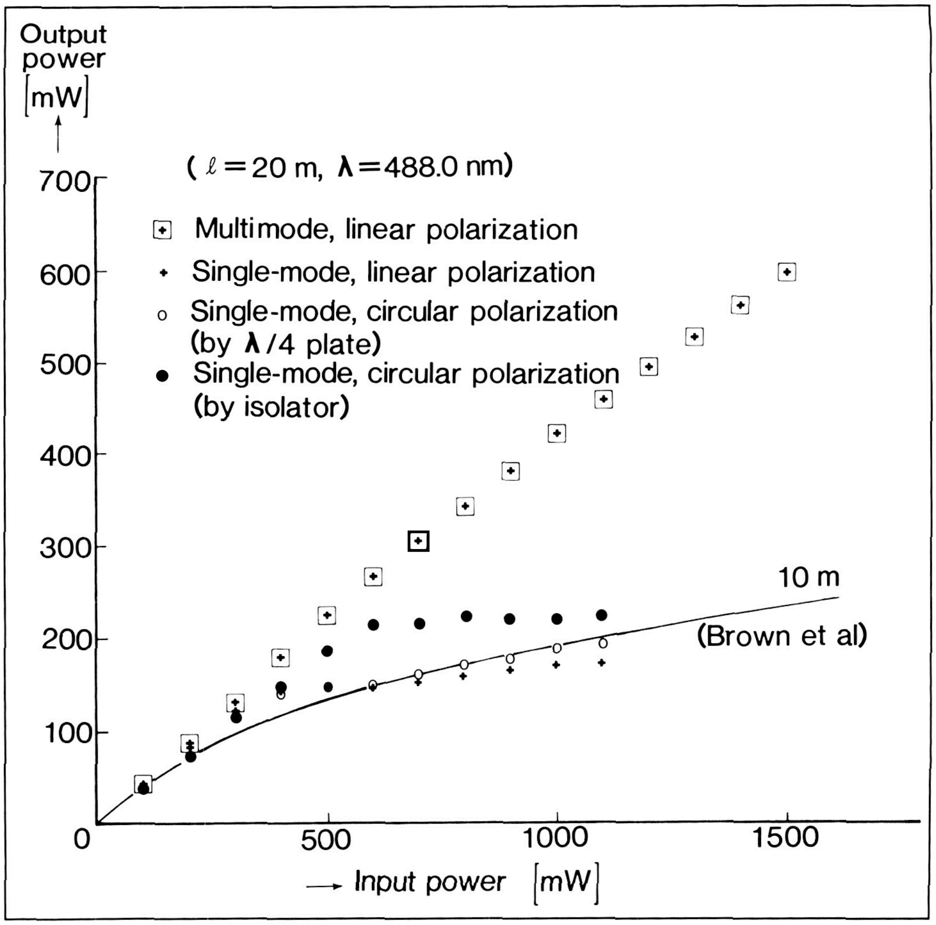

Experimental result for the relationship between output and input optical power, when the laser source wavelength λ is 488.0 nm and the PPSMOF length ℓ is 20 m.

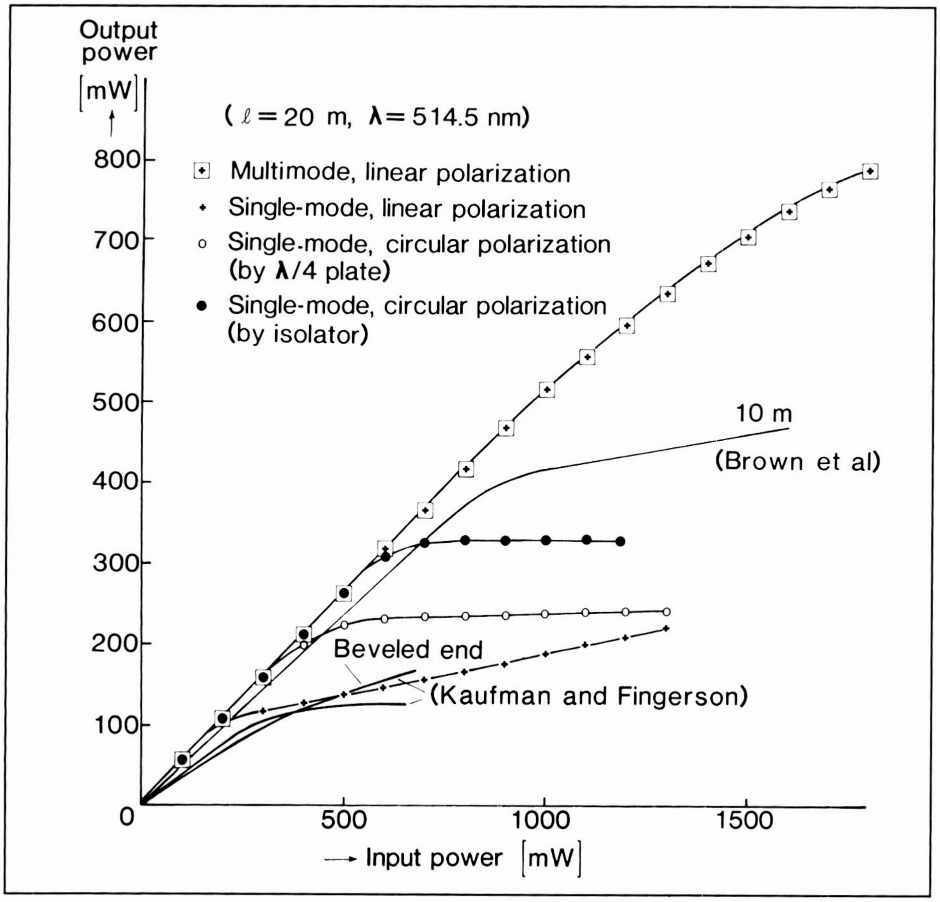

Experimental result for the relationship between output and input optical power, when the laser source wavelength λ is 514.5 nm and the PPSMOF length ℓ is 20 m.

to the previously published data (Brown et al., *ICO-13 Conference Digest* (1984) and Kaufman and Fingerson, *International Conference on Laser Anemometry-Advances and Application* (1985)).

These experimental results demonstrated the power transmission characteristics of a PPSMOF waveguide and its dependence on the polarization characteristics of the input light source. The initial use of this fiber as a transmission link for a high-power continuous wave light source in a laser Doppler system has been demonstrated in a laboratory situation.

(K. K. Tedjojuwono, 2791)

Miniature PCM Compatible Wideband Spectral Analyzer for Hypersonic Flight Research

Measurement of boundary-layer disturbances in hypersonic flight can be accomplished with emerging thin-film technology, but a bandwidth of 400,000 Hz per measurement limits the number of measurements that can be telemetered from a flight research vehicle. An electronic system to perform multichannel wideband spectral analysis for application in hypersonic rocket payloads has been developed. By employing state-of-the-art analog and digital electronics, this technique analyzes signals in the range of 10 kHz to 400 kHz and permits multichannel wideband measurements to be implemented within a miniature volume. The system provides a common digital or analog output proportional to the frequency along with the corresponding multiple analog outputs proportional to the power spectral density (PSD) for each channel. These multiple wideband measurements are

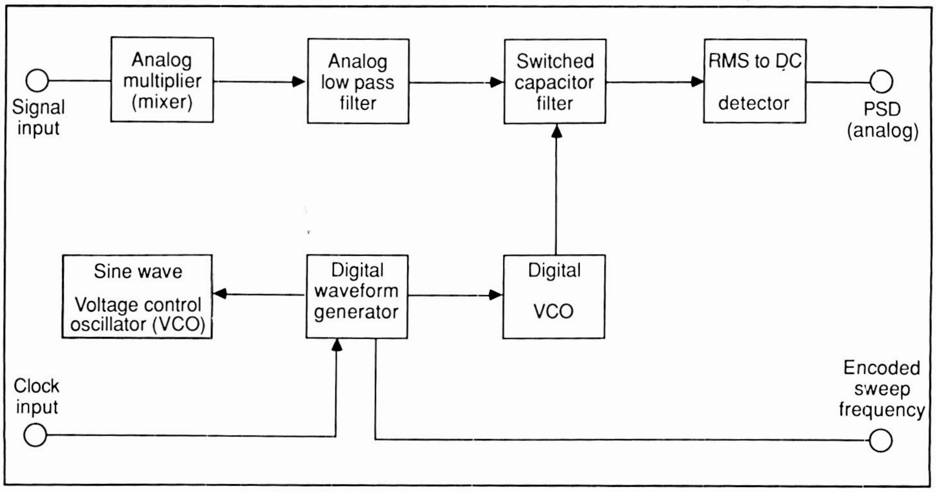

Single-channel spectral analyzer.

encoded in a pulse code modulation (PCM) mainframe with sampling rates as low as 2,000 samples per channel per second, which offers three orders of magnitude improvement in bandwidth compression. Although developed primarily for hypersonic boundary-layer transition research, this technique may find wider application in systems in which bandwidth compression of this nature is required.
(John K. Diamond, 3506)

Analysis of Positron Lifetime Spectra in Polymers

A new procedure for analyzing multicomponent positron lifetime spectra in polymers has been developed. This procedure requires initial estimates of the lifetimes and intensities of various components, which are readily obtainable by a standard spectrum stripping process. These initial estimates, after convolution with the timing system resolution function, are then used as the inputs for a nonlinear least-squares analysis to compute the estimates that conform to a global error minimization criterion. The convolution integral uses the full experimental resolution function, in contrast to the previous studies in which analytical approximations were utilized.

These concepts have been incorporated into a generalized computer program for analyzing positron lifetime spectra (PAPLS) in polymers. The validity of this program has been tested using several artificially generated data sets. These data sets were also analyzed using the widely used POSITRONFIT program. In almost all cases, the PAPLS program gives a closer fit to the input values. The new procedure has been applied in the analysis of several lifetime spectra measured in metal-ion-containing Epon-828 samples.
(Jag J. Singh, 3907)

Conservative Interfacing of Grids for Flow Field Calculations

Most computational fluid dynamics techniques used in aerodynamic flow simulations are computed with structured grids in an Eulerian formulation. It is extremely difficult, however, to devise a single structured grid topology that is suitable for all regions of a complex flow domain (i.e., the domain about an aircraft configuration). An approach that is desirable is to construct several blocks of grid points which have different topologies, depending on local geometry and anticipated flow phenomena. At the interfaces between blocks, it is necessary to transfer solution variables while conserving flow properties (mass, momentum, and energy). Heretofore, this concept has been successful for one-dimensional interfaces (two-dimensional flow domains), but the conservative transfer of flow field variables across two-dimensional interfaces (three-dimensional flow domains) has been less successful.

A procedure called the Ramshaw technique, originally developed at the Los Alamos National Laboratory for the conservative redistribution of flow variables in a Lagrangian formulation, has been adapted at Langley Research Center for computational fluid dynamics in an Eulerian formulation. The

Pressure contours for flow about and through the engine duct of an experimental fighter aircraft at Mach 2 and an angle of attack of 0°.

ORIGINAL PAGE
COLOR PHOTOGRAPH

technique simplifies the computation and storage of the relative areas of grid cells from two different grids at a common planar interface. The process is essentially an assembly line operation applied along the grid lines from the two sets of grid points. The ratios of the overlapping areas are used to specify the percentage of a conserved variable to be transferred from a cell in the first grid to a cell in the second grid.

The Ramshaw technique has been applied to several test aerodynamic configurations, one of which is the internal/external, inviscid, compressible flow about and through the engine duct of a fighter aircraft configuration. The grid topology for the internal domain is different from that of the external domain, and a conservative interface is applied at the inlet and at the outlet of the engine duct. Solutions have been obtained for the Euler equations at Mach 2 and angles of attack between 0° and 10°. From these calculations it has been found that the Ramshaw technique reduces programming complexity, saves computer time, and is viable for many conservative interface applications in fluid dynamics.

The figure shows the coefficient of pressure in the symmetry plane of a three-dimensional flow field about the fighter aircraft configuration. The figure depicts both internal and external flow.
(Robert E. Smith, 3978)

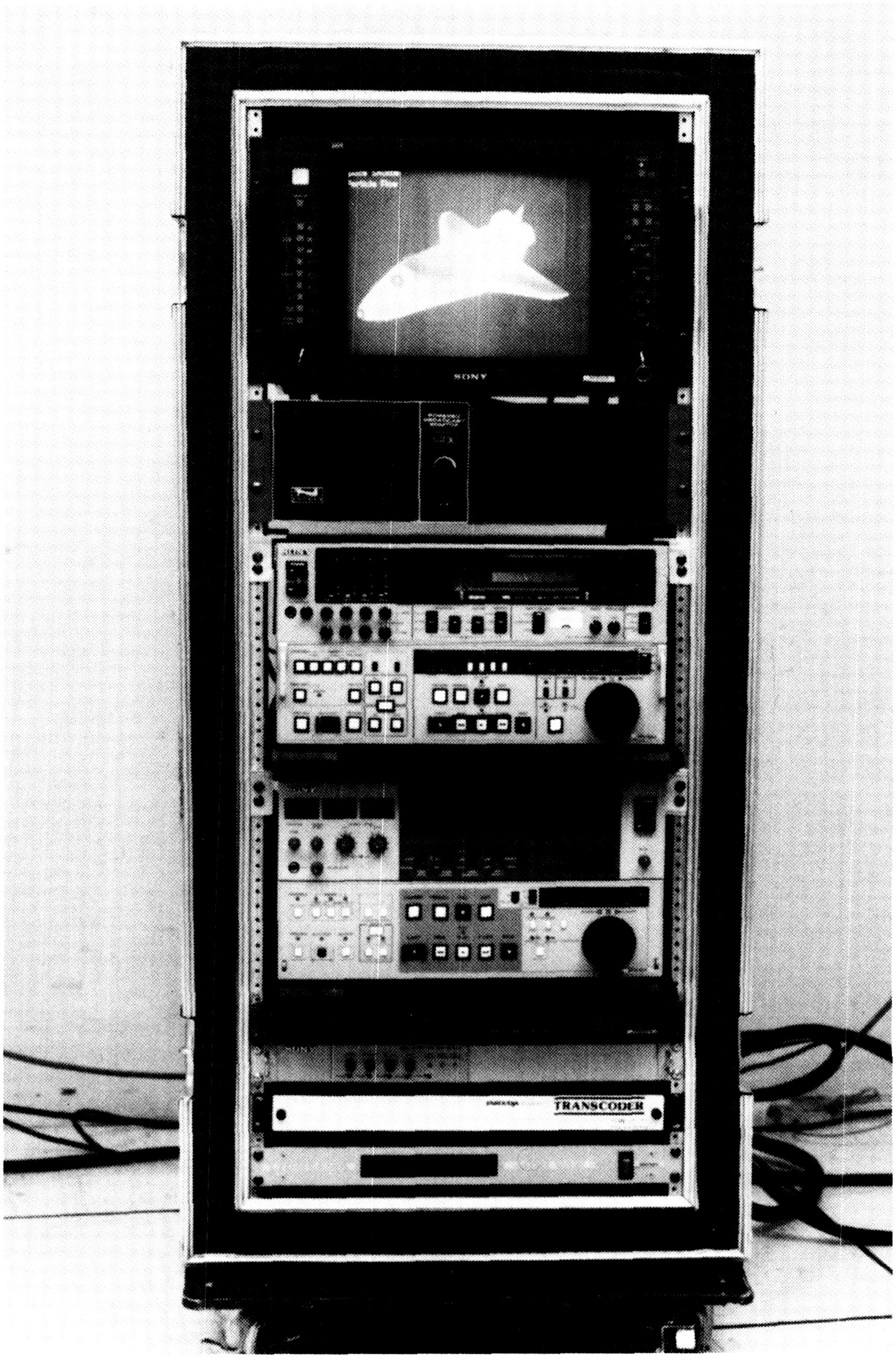

L-88-7418

Graphics workstation video recording system.

Videotaping System for Flow Field Simulation

To meet the growing demand for videotaping the results of computer simulations of complex time-dependent three-dimensional flow fields, a rack-mounted semiportable video recording system has been designed, implemented, and applied to several research applications. The system consists of a high-resolution color monitor, high-quality ½-in. Betacam and ¾-in. U-matic tape recorders, an animation controller, a

ORIGINAL PAGE
BLACK AND WHITE PHOTOGRAPH

broadcast monitor to provide sound, and a transcoder to convert the computer console red, green, and blue (RGB) input signals to video signals. The system is driven by a Silicon Graphics IRIS workstation that runs Numerical Aerodynamic Simulation (NAS) graphics and animation software to dynamically display aircraft grid generation, scramjet inlet flow, boundary-layer transition, and external flows over aircraft configurations.

The graphics software, executing on the IRIS, drives the animation controller, which regulates the frame-by-frame Betacam recording of the computer-generated display. Thus, the speed at which a video sequence may be replayed to give a realistic animation is not influenced by the time required by the computer to render a complex shaded image. The system permits tape duplication and simple sequential editing. An audio track of background music or an explanatory narrative may be added to enhance the presentation. The system may be used with any high-end color graphics workstation that has genlock synchronization, Institute of Electrical and Electronics Engineers, Incorporated (IEEE) standard RS-170A output at National Television Standards Committee (NTSC) resolution, and animation software with controller device driver to create the display and regulate its recording.
(D. L. Lansing, 2070)

Generation of Elastic Waves With Induction Heating

A new technique has been developed for thermally generating elastic waves to nondestructively evaluate metallic structures. Typical thermal sources for these applications are lasers or scanning electron or ion beams. These sources are appropriate for surfaces that have a coating which absorbs the laser radiation or for objects small enough to fit into a vacuum chamber. For larger metallic structures with reflective surfaces, these thermal sources may be ineffective.

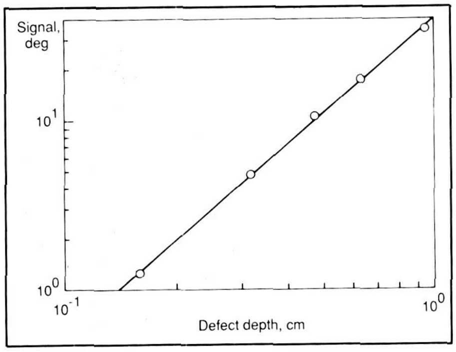

Signal level that is sensitive to defect size in induction heating experiment.

This technique makes use of induction heating of a metal surface with a small coil held near the surface. Induction heating is advantageous in that it requires no special coating of the surface or special environment for the testing. In addition, the power is easily modulated to generate a periodic elastic wave that is easily detected. A coil can be tailored to a particular application without much effort to reach into areas inaccessible by other techniques.

Measurements on samples with defects indicate that by scanning a coil over the surface and detecting the elastic wave at a remote location on the sample, both the size and location of a defect can be determined (as shown in the figure). The technique has the potential for nondestructively evaluating the integrity of a large structure by attaching the heating coil to a robotic scanner that can move over the structure.
(William P. Winfree, 3036)

Characterization of Bulk Residual Stress Generated by Fatigue Load Cycle

A new technique has been developed to interrogate material properties using the interaction between the magnetic domain and lattice systems of a ferromagnetic solid. The concept, called the magnetoacoustic technique, has been applied to measure bulk residual stress produced in pure iron polycrystalline samples after applying a certain number of tension-tension fatigue cycles. The technique is based on the two basic properties of a ferromagnet: magnetic domain structure-dependent elastic modulus and stress-dependent magnetic domain structure. An acoustic pulsed-phase-locked loop (P2L2) device was used to measure fractional changes in acoustic natural velocity as a function of net magnetic induction. The yield stress of the iron samples was estimated to be approximately 120 MPa from the stress-strain curve measurements.

The first figure shows the static stress measurement results for one sample. The purpose of these measurements is to provide a reference for the fatigue load cycle measurements. The label indicates the amplitude of static applied stress under which each curve was taken. The tension and compression curves in this figure are seen to be separated by the curve obtained without load, and the effect of stress on the natural velocity curve is apparent. The second figure shows the nat-

]

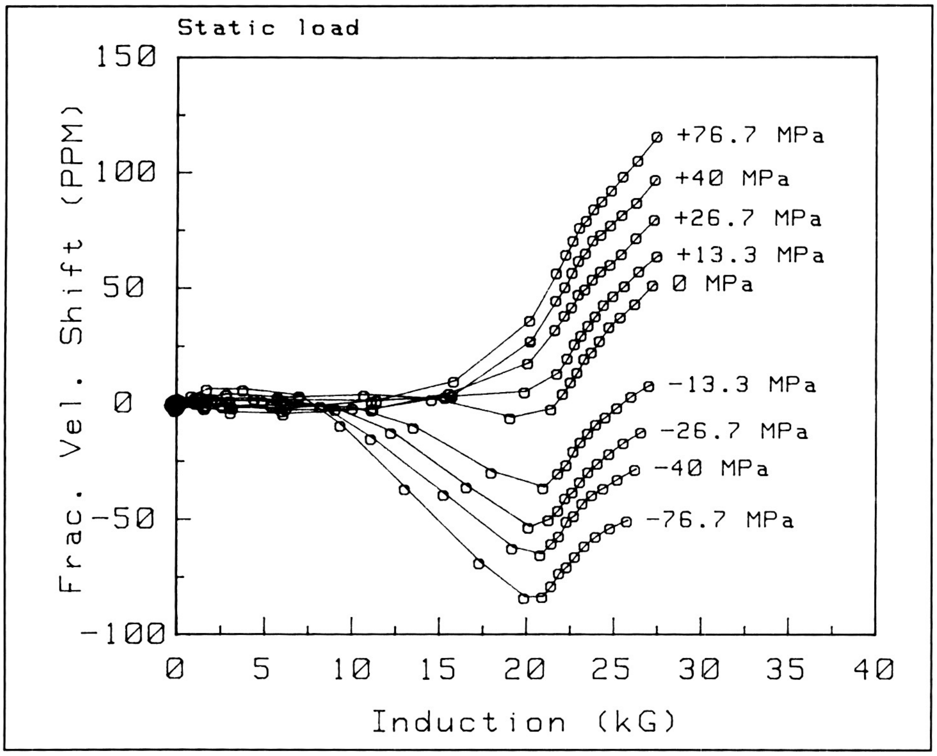

Velocity shift with magnetic field prior to loading.

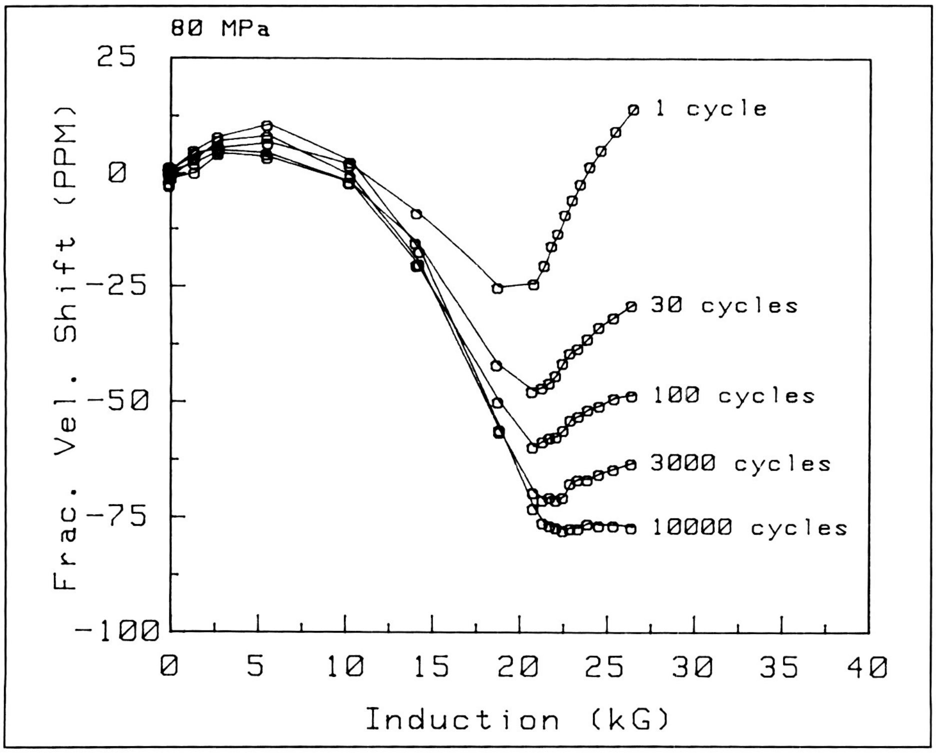

Velocity shift with magnetic field after cyclic loading.

ural velocity curves obtained for another sample after application of 80 MPa peak-to-peak load cycles. This figure shows clearly that bulk residual compression is built up in the sample as a result of tensile fatigue cycle application. At the end of 80 MPa load cycles, approximately 10 percent of the permanent tensile strain was produced in the sample. It is well known that permanent tensile deformation creates compressive residual stress, which is clearly consistent with the results in which approximately 70 MPa of residual compression is indicated after 10000 fatigue cycles. These and other measurements show that the physical basis of the magnetoacoustic technique applies to pure iron as well as to alloy steels.
(Min Namkung, 3036)

Smart Structures Research

Research on smart structures is being conducted in a cooperative effort with the United States Air Force Astronautics Laboratory at Edwards, California. Graphite/epoxy tubes with embedded optical fibers are fabricated at this laboratory and are tested at Langley Research Center.

The system used to interrogate the optical fibers is an optical phase-locked loop that was developed at Langley. The optical phase-locked loop uses a modulated laser to measure changes in the fractional length of an optical fiber to an accuracy to $\Delta L/L$ of 10^{-7}. The system has been tested with an embedded optical fiber in a composite tube approximately 3 ft long and 1.5 in. in diameter. Strain gauges were installed on the tube for com-

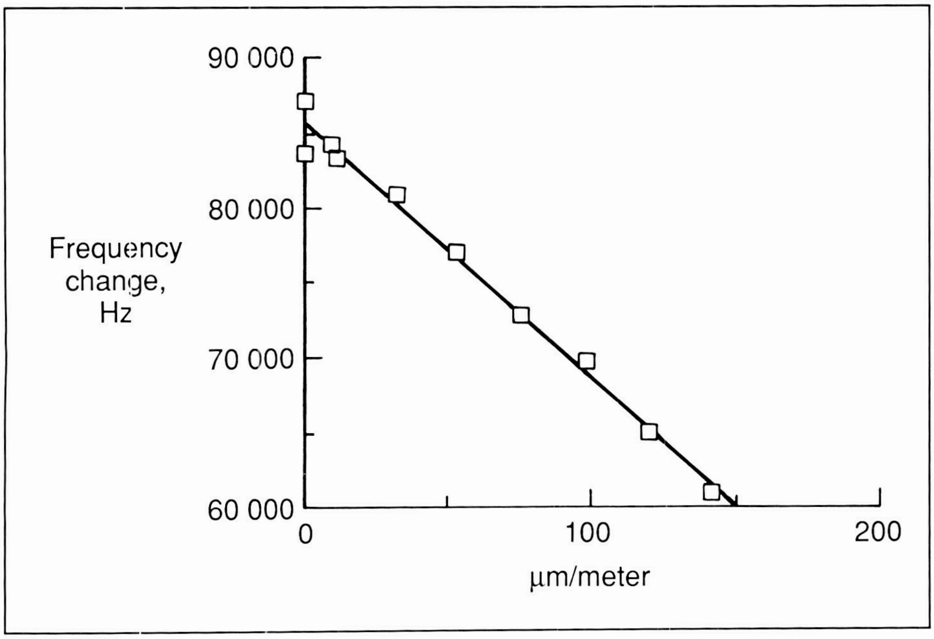

Correlation of optical fiber and strain gauge.

parison, and the tube was fixed at one end and loaded at the other to provide strain. Some recent data, shown in the figure, demonstrate the concept of using the phase-locked loop with an embedded optical fiber to measure strain and vibration.

The frequency change plotted in the figure is for a phase-locked loop operating at a nominal frequency of 300 MHz. The cumulative frequency change is due to the small change in the length of the optical fiber embedded in the composite tube under stress. The small increase in length causes a small change in the phase of the modulated light; this change is compensated for by a change in frequency of the voltage-controlled oscillator in the phase-locked loop. Vibration of the composite tube can also be measured by monitoring the voltage controlling the oscillator.
(Robert S. Rogowski, 3036)

Far-Infrared Narrowband Filter Technology

Remote sensing of atmospheric constituents (such as the very important OH and N205 from space in the far-infrared spectral region) involves, in general, the detection of a species signature in the presence of strong thermal background radiation from the Earth. Thus, narrowband photon-noise-blocking filters are essential performance-determining components of such instrumentation. These filters must be cooled to low temperatures and must be able to transmit the desired passband with good transmission while blocking the radiation (i.e., noise) at all other wavelengths. A solution is available, in principle, in the form of photolithographically produced metal mesh etalons assembled in precision-spaced Fabry-Perot-type assemblies, polarizers, and diplexer components. However, optical design models and fabrication processes do not yet provide well-engineered reliable solutions.

In a joint program with Queen Mary College, Langley Research Center is systematically combining prototype development, filter modeling, and photolithographic technique development. Linear grid polarizing elements of large aperture (12 cm) have been fabricated with line widths as small as 3 micrometers; this small line width provides good optical performance from low-frequency to 600 wavenumbers, or about a three times higher frequency than possible with conventional free-standing linear grids. This component technology is a key step in filling the critical measurement gap between the infrared and the microwave regions.
(I. G. Nolt, 3761)

Ultrasonic Preload Measurements in Space Shuttle Wheel Bolts

The pulsed-phase-locked loop (P2L2) ultrasonic interferometer technique has been used to determine the amount of axial load applied in critical fasteners during the tightening of wheel bolts on the Space Shuttle orbiter. This technique measures the fractional frequency shift necessary to satisfy the phase-locked conditions of acoustic interference with an accuracy of a few parts per million when the data acquisition procedure is fully computerized. To implement the P2L2 technique for the Space Shuttle wheel bolts, preliminary measurements were performed at The BF Goodrich Company site in Troy, Ohio.

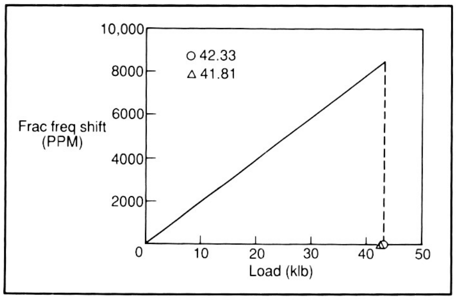

Frequency shift for increasing load (fastener tensioning).

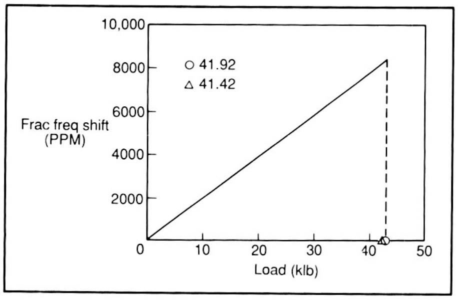

Frequency shift for decreasing load (fastener detensioning).

For the measurements, the Space Shuttle wheel bolts were mounted in The BF Goodrich Company specially designed load cell setup to measure the hydraulic pressure in a cylindrical bore. On this bore, the bolt acts like a piston. This hydraulic load cell technique is known to provide very accurate results, but it is not automated. The P2L2 measurements were compared with the load cell measurements. The first figure shows the results obtained while tightening the bolt. In this figure, the P2L2 measurement results are plotted as a nearly straight line consisting of about 120 data points. The horizontal position of each P2L2 reading was calculated by using a conversion factor separately obtained for this type of bolt prior to the present measurements. The maximum P2L2 reading was converted into an axial load of 42.33 klb (o) at the end of tightening. The figure also shows the axial load value of 41.81 klb (Δ) as indicated by the hydraulic pressure measurement. Subsequent measurements were performed to determine the amount of load removed by loosening the bolt. The results in the second figure show the removed load of 41.92 klb (o) and 41.42 klb (Δ) for P2L2 and hydraulic load cell measurements, respectively. Repeated measurements show less than 0.7 percent difference in axial load values obtained by the two methods.

(C. Gerald Clendenin, 3036)

Design Parameters for Two-Dimensional Pulse-Echo Phase-Insensitive Array for NDE of Layered Media

Ultrasonic inspection of interfaces in multilayered media is a common problem in the field of nondestructive evaluation (NDE). While inspection of flat and parallel layers is relatively straightforward, the presence of one or more rough or uneven interfaces offers a potentially complex set of difficulties, such as reflection of the beam away from the receiver and the phenomenon of phase-cancellation. Nonparallel surfaces can cause a reflected beam to partially miss the pulse-echo transducer, resulting in a signal loss unrelated to the integrity of the interface bonding. Phase-cancellation occurs when a phase-sensitive receiver (such as a piezoelectric transducer) is used to detect an ultrasonic field whose wavefronts do not match the geometry of the probe. Such wave distortions can result from transmission through or reflection from a rough, uneven surface. Under these conditions, the energy content of the output voltage generated by the probe is not proportional or simply related to the energy content in the acoustic field, thus resulting in invalid measurements.

One approach to these problems is the use of a large-aperture two-dimensional array of piezoelectric receivers whose output signals are summed phase-insensitively. Phase-insensitive summation provides reduced susceptibility to phase-cancellation, and large diameter two-dimensional sampling provides improved detection of reflections from nonparallel interfaces. In conjunction with Marshall Space Flight Center and Morton-Thiokol, Incorporated, design parameters were developed for a pulse-echo phase-insensitive array for the NDE of uneven bondlines in the inhibitor/propellant of the Space Shuttle solid rocket motor (SRM). Experimental results with a scanned-element pseudo-array indicate that the sensitivity of detecting total disbonds at a rough interface between two rubber-like materials can be improved by more than a factor of 2 by using phase-insensitive detection. A computer model was developed for evaluating the pulse-echo characteristics of various arrangements of pulse-echo arrays with coaxial transmitting and receiving arrays. This approach allowed flexibility for exploring various array configurations and independent selection of materials for optimizing transmit-and-receive characteristics.

The design that was chosen for fabrication is shown in the figure. The array consists of 31 piezoelectric elements positioned in a hexagonal arrangement within a circular aperture. All 31 elements

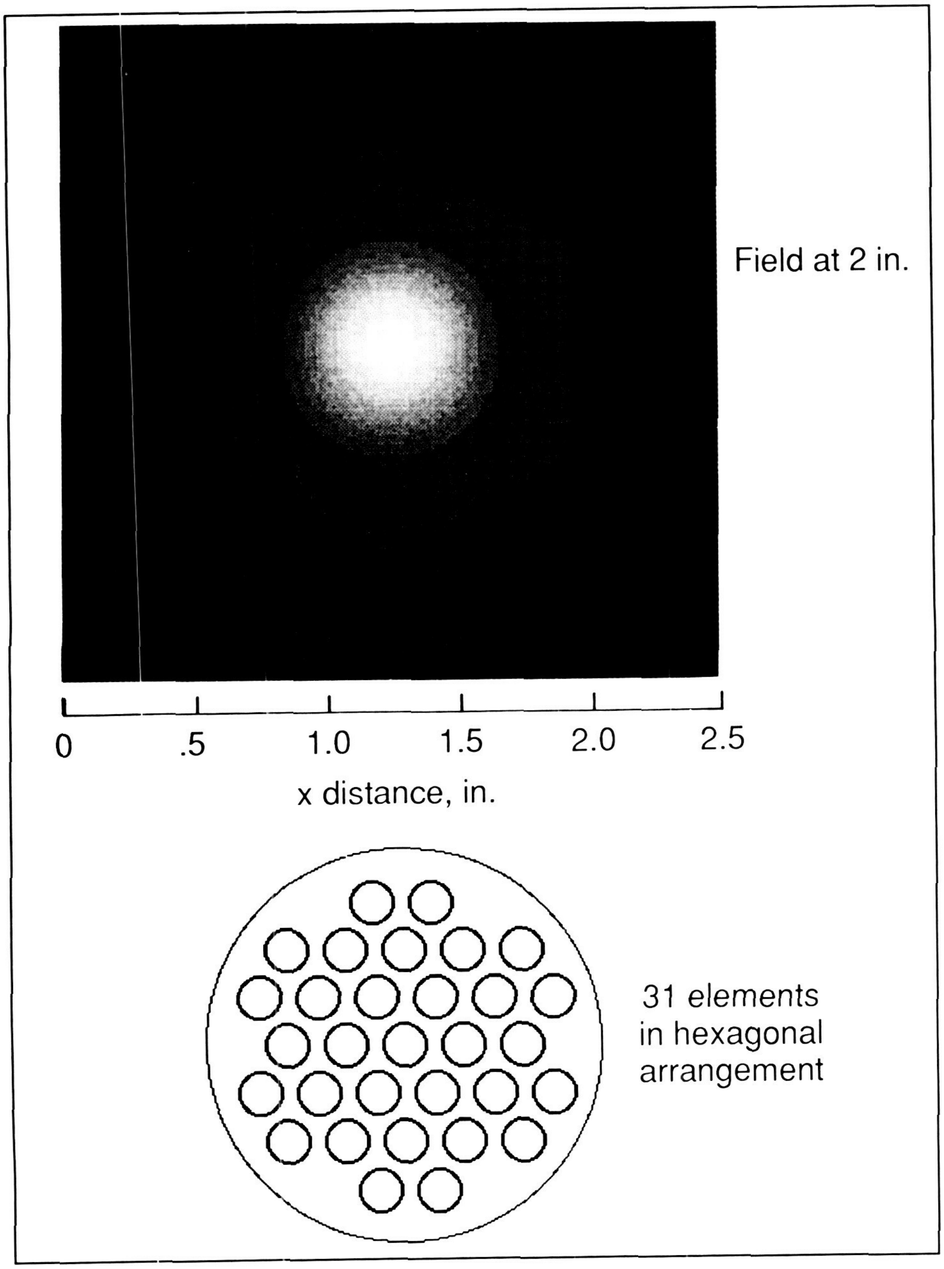

Acoustic energy field (top) produced by phase-insensitive pulse-echo array (bottom).

are driven to transmit an ultrasonic pulse into the inhibitor. The magnitude of the ultrasonic field at the array after one round trip through a 1-in.-thick inhibitor is shown. Analysis indicates adequate spatial sampling of the beam by the array elements. The signal from each of the elements is envelope-detected to remove the phase, and the 31 signals are summed to derive the phase-insensitive array response. **(Patrick H. Johnston, 3036)**

Reverberation Removal From SRM NDE Measurements by Signal Processing

Ultrasonic nondestructive evaluation of the integrity of multilayered material is achieved by transmitting ultrasonic waves into the material and investigating the reflections and scattering of the waves from discontinuities in the structure. In several cases it is advantageous, or even necessary, to investigate the material from one side only. A problem arises when the ultrasonic impedances of the layers are such that the first layer acts as an "energy trap" to the traveling waves, thus generating multiple reflections that mask most other events that arrive from deeper layers. This is the case in the solid rocket motor in which the casing is made from steel, filled with solid fuel, with a thermal insulation between them. Heavy reverberations in the steel layer interfere with the ultrasonic assessment of the integrity of the internal layers.

A digital signal-processing technique has been developed and tested. This technique, which analyzes the ultrasonic waveform and recognizes multiple reflection, is based on the idea that reflections are predicted events that relate to previous information, while reflections from acoustic discontinuities in the material are not. A mathematical operator is then obtained which can remove the reverberations component while leaving the other original events virtually unchanged. Information related to events deep in the material can then be investigated and analyzed. The figure shows an example of such a process. The top trace displays

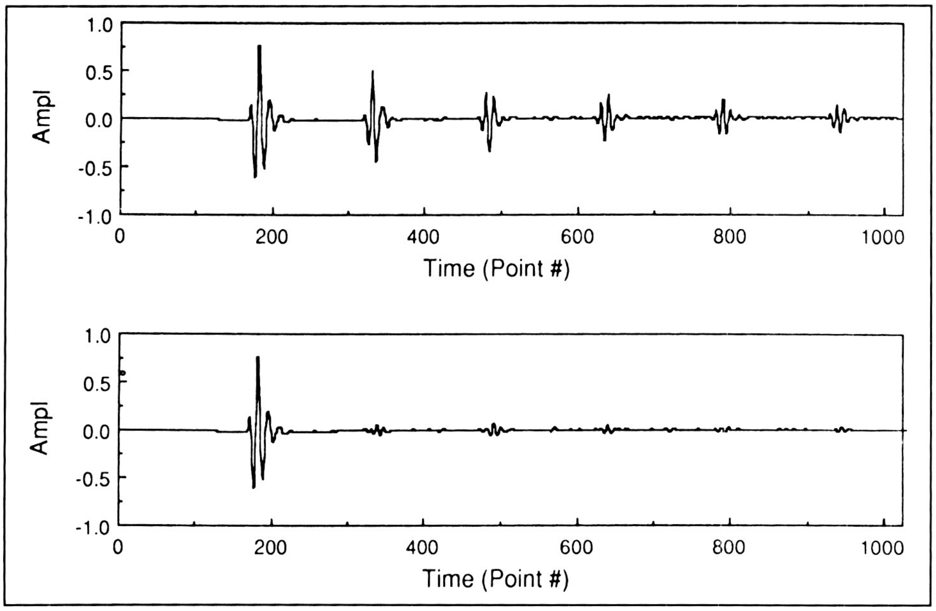

Reverberant ultrasonic trace before (top) and after (bottom) digital processing.

experimental raw data. Several reflections that are caused only by the repeated reverberation are clearly seen; these reflections override and obscure the later, small-amplitude reflections. The bottom trace shows the signal after the digital process; the reverberations are significantly reduced while maintaining the appearance of the other events, including the first reflection itself.

(Doron Kishoni; Joseph S. Heyman, 3036)

Energy Transfer Among Ions in Solid-State Laser Materials

Active remote sensing of the atmosphere from space is facilitated by the development of new, efficient solid-state lasers. Solid-state laser materials developed to date have consisted of a single optically active ion substitutionally doped into a crystalline or glass host; this ion absorbs the optical energy that is subsequently emitted as laser radiation. Recently, interest has existed in doping crystals with multiple ions so that ions of one element can absorb energy and transfer it to another element that will then lase. The energy transfer in crystals of yttrium, aluminum, and garnet (YAG) doped with chromium, thulium, and holmium has been studied. The Cr ions have broad absorption bands so that it is easy to get energy into the crystal. These Cr ions then transfer this absorbed energy to Tm ions, which, in turn, transfer it to Ho where it is emitted as laser radiation at about 2 μm. This is an important laser wavelength, not only for space-based atmospheric studies but also for wind shear Doppler lidar measurements.

A study of the energy transfer from Cr to Tm in samples of Cr,Tm:YAG has led to important insight into this process. The response of the Cr emission to pulsed excitation was measured at different temperatures from 78 to 360 K by exciting a $^4T_2$ band of Cr with 490 nm pulses from a dye laser.

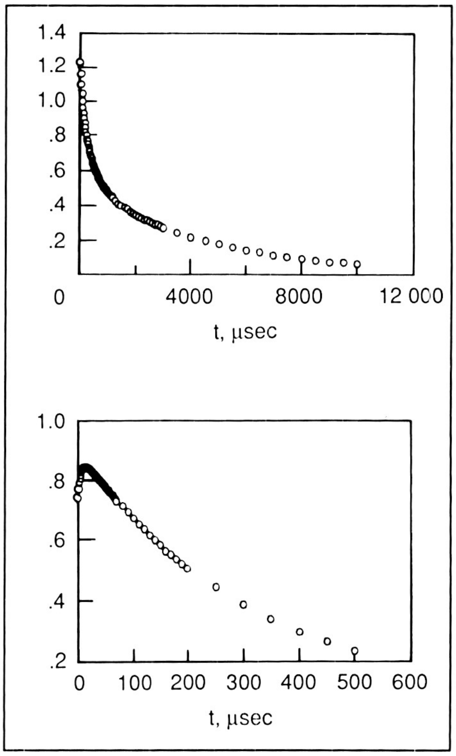

Time dependence of chromium emission (top) and thulium emission (bottom).

The decay of the Cr emission is seen to be nonexponential at all temperatures (as shown in the top figure). The rapid decrease in intensity at the early portion of the excitation indicates a transfer of excitation to Tm ions near to an excited Cr ion with subsequent slowing of the Cr decay rate as fewer Tm ions become available to receive the energy. The decay pattern of the Tm emission shows a rise at an early time in the decay curve corresponding to the rapid absorption of energy from Cr followed by a normal decay (as shown in the bottom figure). Integrated intensity measurements demonstrate the extreme

sensitivity of this transfer mechanism to temperature. This information is vital to the optimal design of flashlamp-pumped Cr,Tm:YAG or Cr,Tm,Ho:YAG lasers, which require sensitization with the broadband absorber, such as chromium. **(C. Byvik, 2818)**

Improved Birefringent Filter Design for Line Narrowing of Wideband Tunable Lasers

Some lasers, notably dye lasers and some solid-state lasers, offer wide frequency tunability. However, for many applications (including atmospheric remote sensing) a single well-defined wavelength within the continuous spectral output range must be selected. To achieve improved versatility in selecting a target line within a wideband laser output, a novel birefringent filter has been designed and incorporated into an existing Ti:sapphire laser.

The birefringent filter consists of several plates fabricated from an optical material that exhibits double refraction. Only those wavelengths that are transmitted through the filter without significant loss will manifest laser action. Birefringent filters are typically designed so that the thicknesses of the thicker plates are integral multiples of the thinnest plate thickness, *d*. For such a design, the separation of the maximally transmitted peaks is established by the thickness of the thinnest plate. The improvement to existing birefringent filter designs is achieved by recognizing that it is not necessary to actually fabricate a plate with thickness *d*, it is only necessary that *d* be the greatest common divisor of the thicknesses of the plates comprising the filter.

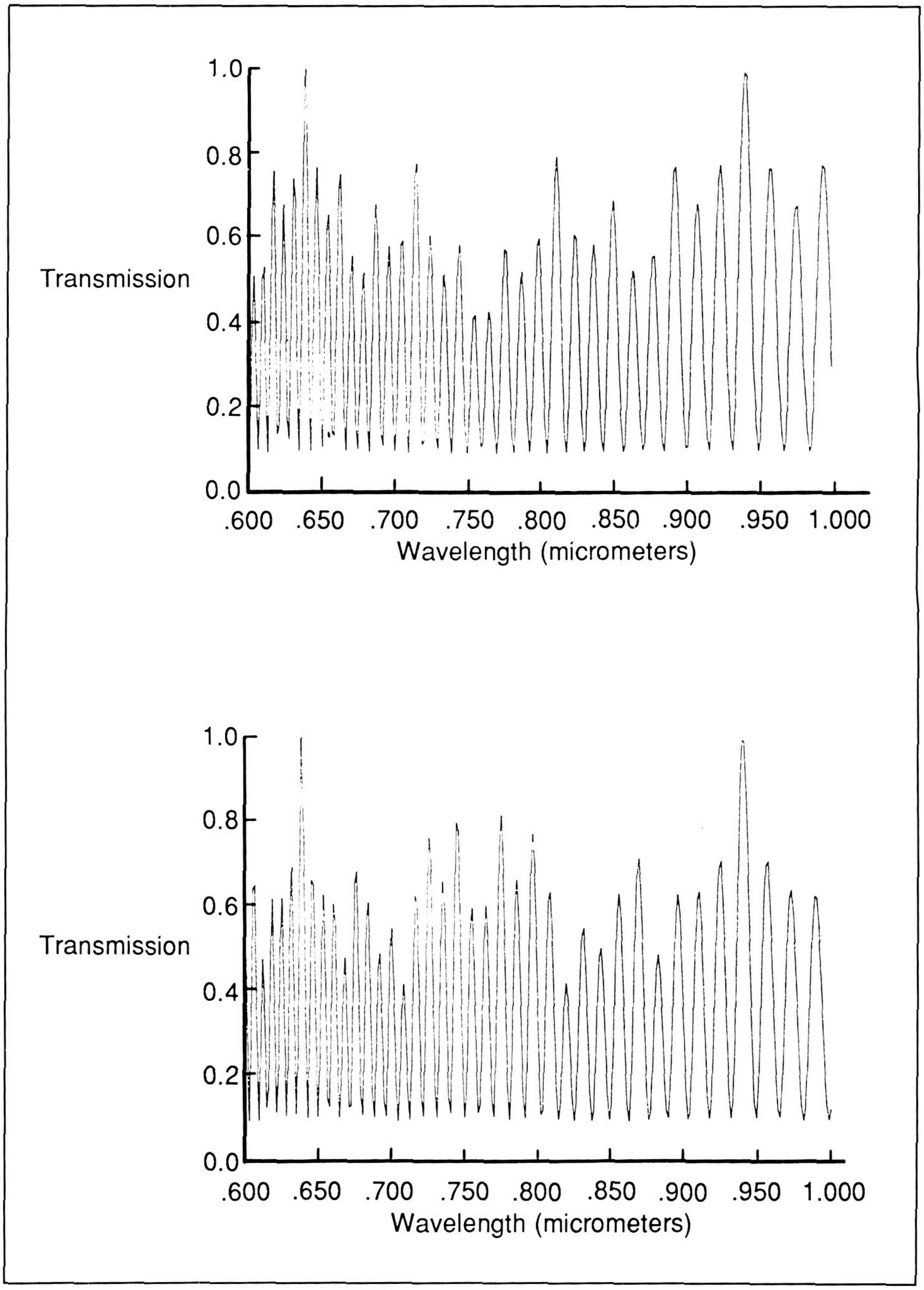

Plate thicknesses of 0.25, 0.5, 1.5, and 4.5 mm (top) and 0.5, 0.75, 1.5, and 4.5 mm (bottom).

The figure shows the calculated transmittance of two birefringent filters; the top section uses a traditional design, and the bottom section uses the improved design. In the traditional design, a plate with a thickness of 0.25 mm is used to obtain a separation between maximally transmitted peaks of 300 nm (0.3 μm). This same peak separation has been achieved in the improved design by substituting a

plate with a thickness of 0.75 mm for the 0.25 mm plate. Hence, the improved design avoids the fabrication of extremely thin plates that could result in questionable optical quality.
(C. H. Bair, 2818)

Spaceflight Optical Disk Recorder

The objective of this program is to develop a high-performance, erasable optical disk mass storage system that meets NASA spaceflight data storage and access requirements envisioned for the Space Station, Earth Observing System (EOS), and geostationary missions in the 1990s and beyond. This program is a part of the Civil Space Technology Initiative (CSTI) Data Systems Program within the NASA Office of Aeronautics and Space Technology (OAST). Features of the system include random access data playback; capacity to one terabit (120 gigabyte); rewritable optical media; and configurable, expandable architecture to satisfy various mission applications. The basic technology in magneto-optical write-read-erase capability was demonstrated in fiscal year 1987. The fiscal year 1988 effort involves both contractor and Langley Research Center in-house work in four key technology areas that include 14-in. magneto-optical media; 10-element diode laser arrays; multitrack electro-optic write-read-erase head; and versatile system controller architecture.

The recent accomplishments of this program include the development of the world's first individually addressable 10-element laser array and the world's first preformatted overcoated 14-in. magneto-optic disk on a single-sided aluminum substrate. Two of the 10-element diode laser arrays have completed 100 hr burn-in tests. The array and disk were incorporated into a developmental electro-optic write-read-erase head, and a demonstration of its performance was conducted. Four adjacent tracks simultaneously produced write-read-erase tones at 7.5 MHz while following a spiral pilot track. This demonstration scales to a maximum data rate of 133 megabits per second. An overall system architecture has been generated, and a system modeling activity has been begun at Langley Research Center.
(Reginald M. Holloway and Thomas A. Shull, 3541)

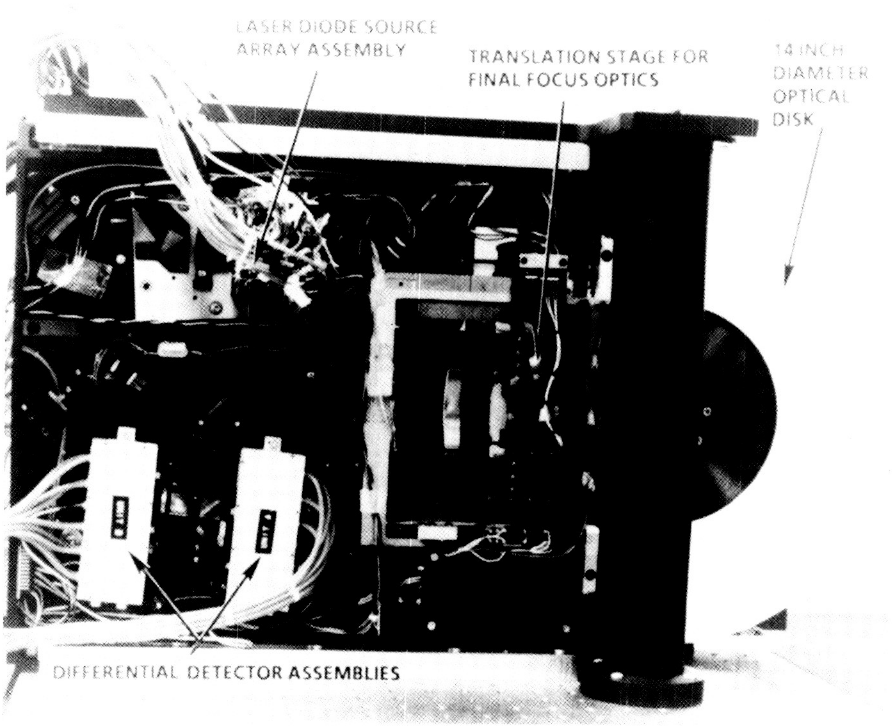

Optical disk buffer technology demonstration assembly.

Flight Systems Directorate

CLEARANCE ON REQ
CLRD TO GLD AS FILED
MTN 8000 FT, EXPT 12000 FT
10 MIN AFTER DEPARTURE,
DEP 128.05, SQUAWK 4324

REQUEST CLEARANCE
HDG ALT 08000

ORIGINAL PAGE
COLOR PHOTOGRAPH

The Flight Systems Directorate conducts basic research and development in the broad, multidisciplinary area associated with aerospace flight systems. This includes systems hardware and software architecture concepts and design guidelines, validation and verification methods for reliable flight control systems, advanced cockpit interfaces, advanced airborne systems technology, aircraft operating procedures, fundamental electronics research, automation and robotics technology, and aircraft and spacecraft guidance and control system design methods, guidelines, and criteria.

The Advanced Transport Operating Systems Program Office coordinates a wide-scale focused technology research and development effort aimed at developing and improving the technology base for transport aircraft operating systems and the integration of these systems into the current and future air traffic control environments. The office also provides a focus for research and development of improved airborne operations and procedures and operates the NASA Boeing 737 aircraft and associated simulator.

The Information Systems Division conducts research to provide an advanced technology base for future spacecraft and aircraft systems. Specifically, the division performs research in the areas of robotics and automation, fault-tolerant systems validation, reliable software, system architectures, electronic/optical subsystem technology, and software engineering. The scope of activities is broad and ranges from the highest level systems considerations to the investigation of solid-state physics phenomena.

The Guidance and Control Division conducts generic and applied research on aircraft and spacecraft guidance, control, and antenna systems. The research is directed toward the development of a technology base for advanced aircraft and spacecraft systems analysis and design methods, including validation and verification demonstrations of advanced concepts. The division also develops multidisciplinary computer-based tools and techniques which allow appropriate guidance, control, and antenna design issues to be considered through all stages of aircraft and spacecraft design.

The Flight Management Division conducts research to provide a viable technology base for future aircraft and spacecraft flight management systems. Specifically, the division provides technologies required by designers of crew station systems; defines and evaluates improved guidance and control procedures; and studies advanced airborne systems technology, traffic control strategies, and operating procedures for improving the efficiency of air traffic control operations. In addition, the division provides methodologies and criteria for measuring crew work load and stress.

The past year has been a year of significant technical accomplishments in the Flight Systems Directorate. Included in these accomplishments were the further development, flight testing, and airline community recognition of the Langley Research Center-developed Takeoff Performance Monitoring System. Significant progress was made toward a better understanding of the effects of wind shear on aircraft aerodynamic characteristics, development and initial evaluation of aircraft trajectory guidance concepts for flying around or through wind shears, and development of tools to study and simulate airborne Doppler radar as a sensor for detection of wind shear. In addition, the directorate accomplished the development and demonstration, under contract, of the first full-color thin-film electroluminescent (TFEL) display of practical size and resolution. A patent was presented to a Langley researcher for a two-layer full-color TFEL display that significantly enhances TFEL display brightness. Increased emphasis on and technical accomplishments in using artificial intelligence (AI) and expert systems include the development and evaluation of a prototype monitoring and diagnosis expert system called Faultfinder, the development of guidelines for expert systems that generated aircraft system status displays, and the flight test evaluation of an aircraft control mode panel whose logic had been programmed using AI programming techniques. The development and evaluation of tools and techniques for measuring surface conductivity characteristics for large deployable mesh antennas and adaptive-array compensation techniques to improve

performance of large antennas with reflector surface distortions were also accomplished. Multiple studies related to understanding and developing methods of controlling large flexible space systems, such as the space station, were undertaken through the use of models of the Spacecraft Control Laboratory Experiment (SCOLE) and optimized control algorithms.

Automatic Generation of Ada Code

The cost of designing, developing, testing, and maintaining avionics software is steadily increasing. Until recently, the lack of appropriate tools to aid in the creation of software has led to nonuniform development techniques and software that is often unreliable and difficult to maintain. A Computer-Aided Software Engineering (CASE) tool has been developed under Langley Research Center funding at the Charles Stark/Draper Laboratory (CSDL). This tool could dramatically improve the software development process and reduce production and maintenance costs. As a demonstration of this tool, the flight control system of the Boeing 737 autopilot autoland was produced at CSDL using the CASE system.

Specifications for the autoland design were reverse-engineered from inspections of FORTRAN flowcharts and source code. The software requirements were interactively specified in the form of hierarchical data flow block diagrams via the CASE highly flexible graphic interface. The requirements defined by these diagrams were checked for data-type consistencies by the CASE system, and captured in a centralized knowledge base. The knowledge base was then used to automatically produce executable Ada code and a formatted requirements document.

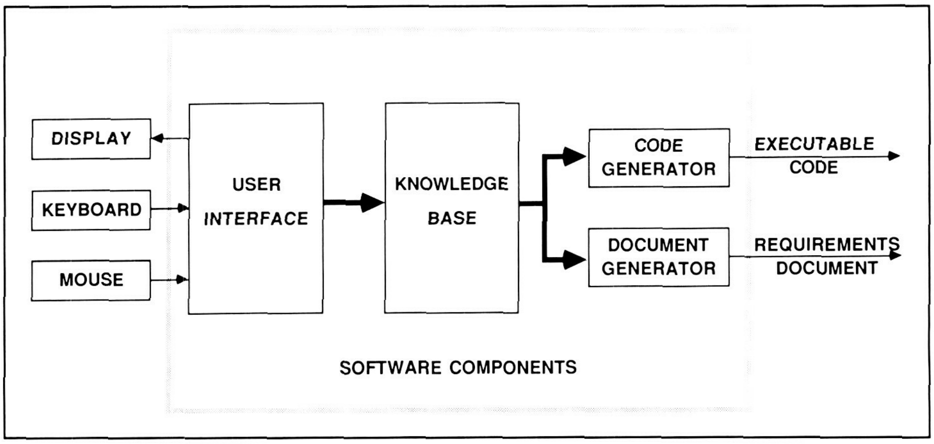

CASE system architecture.

In preliminary testing of the code, no errors were found; however, several ambiguities and inconsistencies were found in the specification as a result of using the CASE diagram methodology. These errors could have potentially led to serious errors in the software, had it been coded by hand. CASE has the potential to significantly increase the reliability of the generated code by checking for inconsistencies, ambiguities, and completeness of the specification; allowing users to specify software using engineering notation and block diagrams familiar to them; automatically performing the usually error-prone transformation to Ada code; and supporting the reuse of code.

(Carrie K. Walker, 3535 and Sally Johnson)

Computer-Aided System Design

A methodology to use a design and assessment tool and a computer-aided software engineering tool together has been developed for Langley Research Center. This methodology further automates the system design process. The Architecture Design and Assessment System (ADAS), developed at the Research Triangle Institute, is a set of computer-assisted engineering tools for the design and analysis of computer systems. The ADAS, which is based on directed graph concepts, supports the synthesis and analysis of software algorithms and hardware implementations. Additional control of the simulation is provided by the ADAS functional simulator. With the functional simulator, programs written in the programming languages Ada or C can be used to provide a detailed description of graph nodes. The CASE tool, developed at the Charles Stark/Draper Laboratory, automatically generates Ada code from data flow diagrams designed with an interactive graphic interface.

The user specifies the details of a graph node as a data flow diagram via the CASE graphical user interface. CASE generates code in the form of procedures contained within an Ada package.The user-defined code modules need to contain only a call to a procedure that was written by CASE. When the procedure call is performed, the code in the appropriate package is automatically located and executed. To demonstrate this new method, simulations were developed using both handwritten code and calls to CASE-written procedures to define the necessary user-furnished modules. The simulations were executed using the same data set, and the results were identical.

Benefits of the described method for functional simulation design include specifying software using block diagrams similar to familiar engineering notation and reducing the level of programming expertise needed by the user. The design techniques for functional simulation and for graphical modeling have been made similar. Both methods use graphical representations created with interactive interfaces. Also, the inclusion of CASE in the development cycle should shorten the development time for functional simulations.

(Carrie K. Walker, 3535)

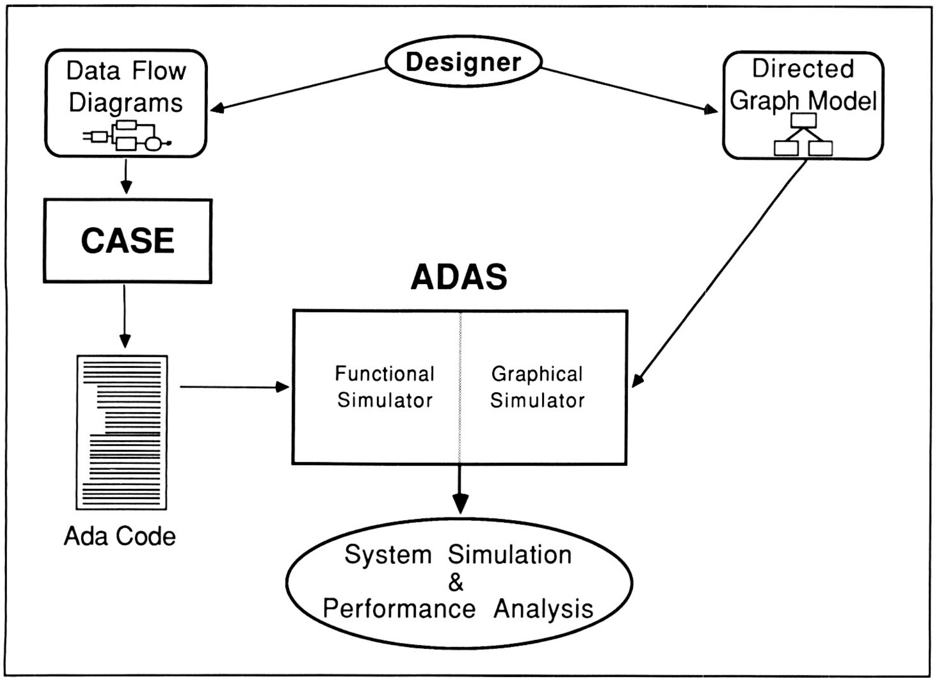

Automated computer system design methodology.

Improved Sensor Failure Detection and Isolation Using Fault-Tolerant Techniques

Safety concerns for advanced avionics generally dictate the use of redundant hardware in flight-crucial systems. Redundancy, based on fault-tolerant techniques, has also been proposed for improving the reliability of software, and this approach is currently being evaluated both theoretically and empirically. However, for certain applications in the flight domain, it is apparent that fault-tolerant techniques can improve functional performance as well. An experiment has been completed by Charles River Analytics under a Langley Research Center contract in which fault-tolerant techniques were applied to the redundancy management software for a simulated array of redundant skewed sensors. The experiment demonstrated that the use of three diverse algorithms for failure detection and isolation (FDI) improved functional performance by reducing the effective false alarm rate for failed sensors. A false sensor failure has the effect of causing the supposedly failed sensor to be configured out of service, thus needlessly reducing the level of hardware redundancy. For this particular application, for example, a false sensor failure reduces the functional performance of the sensor array for two sequential sensor failures from fail-op/fail-op to fail-op/fail-safe.

Three fundamentally different FDI algorithms (edge vector, parity, and multiple hypothesis) were independently developed and integrated into a triplex fault-tolerant structure. The status (failed or not failed) of the redundant sensors was determined by a majority vote of the individual algorithms. Because of the diversity of the algorithms, a sufficient number of the false alarms were uncorrelated, and their effects could be reduced using the triplex structure. This is shown in the figure as a function of the number of samples of sensor measurements used to make a determination of the status of the sensors. The data have been normalized to the average false alarm rate of the individual

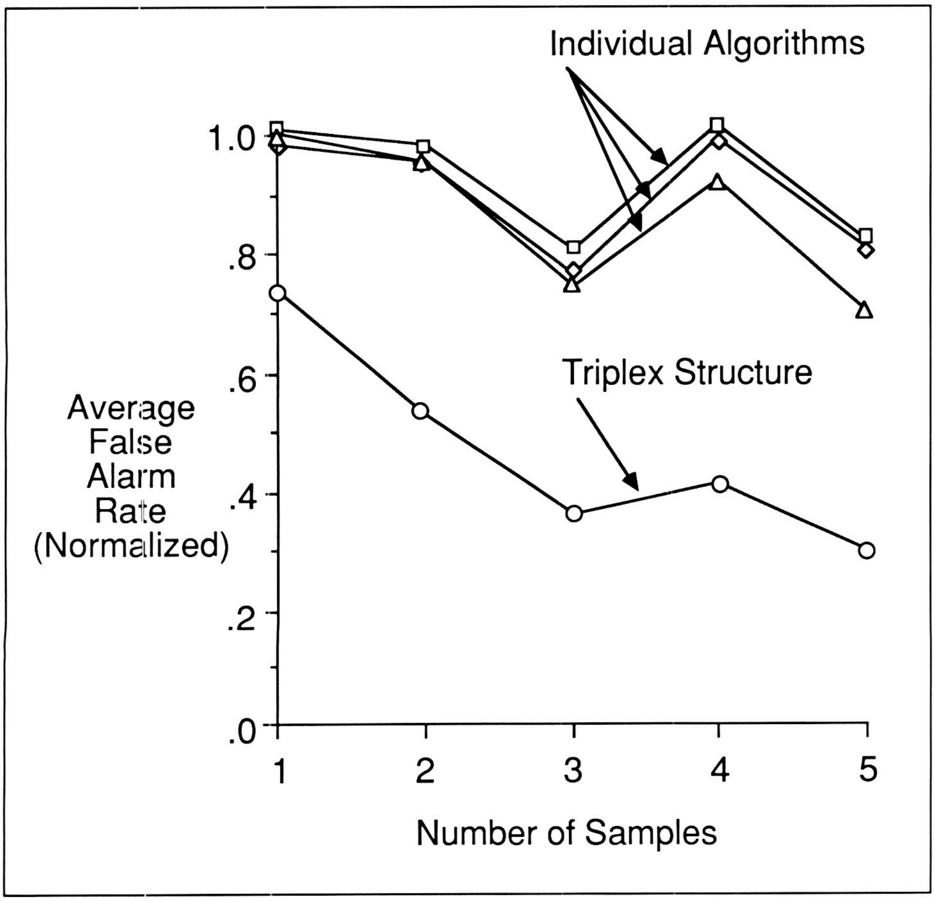

Reduced false alarm rate for triplex fault-tolerant structure with majority voting.

algorithms at one sample of sensor measurements. At five samples, the triplex structure reduced false alarms by approximately 60 percent compared to the individual algorithms.
(Dave E. Eckhardt, 3535)

Automated Software Development

It is widely acknowledged that software development is a time-consuming, costly process, often with questionable quality in the end product. Researchers are looking for ways to reduce software production costs and at the same time improve the quality of software. One solution to the problem is the creation of an automated, integrated programming support environment. Although there are many automated software tools on the market, relatively few of these exist in an integrated environment.

Under a grant titled SAGA (Software Automation, Generation, and Administration) at the University of Illinois, a number of software engineering concepts were studied, and experimental special-purpose tools were developed based on these concepts. The goal of the project was to design a practical software development environment that supports and aids all major phases of software life cycle activities. Prototype tools include a syntax-directed, language-oriented editor; a compiler generator; a tree editor; an electronic bulletin board; an executable specification language; a configuration management system; and a project management system. These tools and techniques were used to

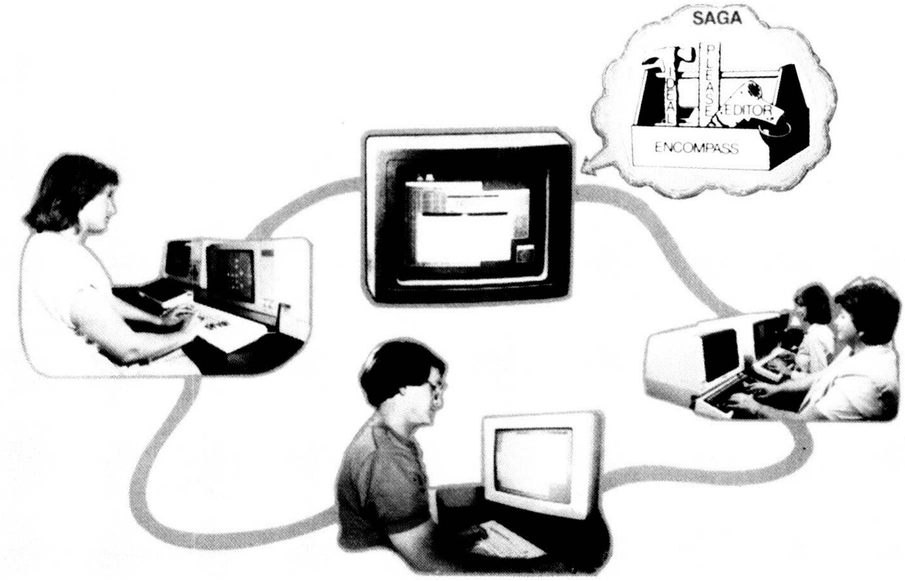

Automated software development and management.

develop ENCOMPASS (Environment for the Composition of Programs and Specifications), a prototype software development environment. ENCOMPASS demonstrates the validity of many of the concepts on which SAGA is based. A number of software engineering concepts were studied during the development of ENCOMPASS. Based on the idea of development by incremental refinement, ENCOMPASS includes an executable specification language, testing tools, and formal verification techniques. A number of these prototype tools have been installed on a UNIX-based, software engineering test bed at Langley Research Center for evaluation. In addition, several of the SAGA tools have been distributed to other educational institutions. The concepts and ideas explored during the early part of the SAGA project influenced the development of the NASA Software Acquisition Life Cycle (SALC), which is now used as the guideline for software development at NASA. In turn, the SALC influenced the development of ENCOMPASS.
(Kathryn A. Smith, 3535)

Order Reduction in Controller Synthesis

This research addresses order reduction and error characterization issues that are of importance in the synthesis of implementable robust controllers. The objective is to develop and evaluate procedures for plant order reduction which will make it practical to use a frequency domain methodology known as the H_∞ design approach to realize low-order robust controllers. Although the primary emphasis of this research is with respect to plant order reduction, the methods also apply to controller reduction from established higher order designs.

Use is made of the fact that feedback desensitizes the closed-loop response to model uncertainties occurring in specific frequency ranges and makes both plant and controller reduction feasible. Reduction of both plant and controller order requires some type of frequency-weighted approximation based on desired closed-loop system characteristics. For controller reduction, frequency weighting is directly available via the stability robustness theorem. However, this is not so in plant reduction. As illustrated in the figure, an approach has been developed which provides frequency-weighting appropriate for plant order reduction. A reduced-order model (ROM) is produced which matches the evaluation mode in the desired frequency range and also has the desirable attribute of preserving unstable plant poles.

The internally balanced approach has been extended to handle order reduction when some or all of the poles of the approximation are taken from the original plant. In the frequency-weighted form of this new procedure, unlike the current partial-fraction-expansion approach, the residues of the retained unstable poles are allowed to vary in order to enhance the resulting frequency-weighted approximation. A paradigm, which makes use of the desired closed-loop response and the inverse representation of the plant, has also been provided for constructing the appropriate frequency weighting.

The research is motivated by the need to obtain implementable control designs that stabilize and reach an acceptable level of performance in the face of modeling uncertainties. The H_∞ design approach readily admits embedding multiloop stability and performance robustness measures into its cost functional; however, the resulting H_∞ controller can have an order up to six times that of the plant design model. Therefore, the plant reduction procedure that has been developed is essential to the achievement of H_∞ designs that are, in addition

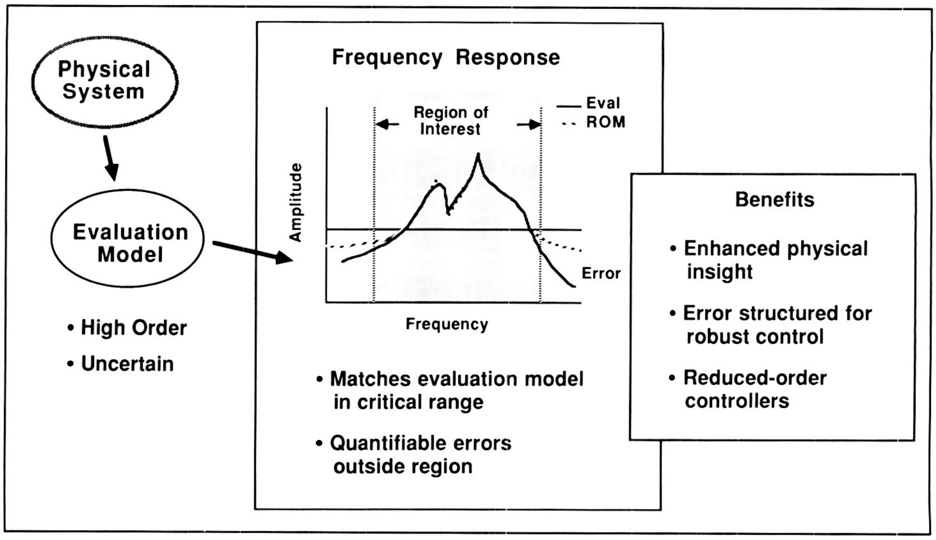

Plant order reduction for controller synthesis.

to being robust, of sufficiently low order to be implementable.
(Barton J. Bacon, 3934)

Quantifying Icing Effects on Aircraft Stability and Control Through Flight Test Data

The purpose of this work was to quantify the effect of ice on aircraft stability and control using flight test data, thus allowing for the first-time direct comparison of flight test results with analytical predictions and wind tunnel measurements. This work was conducted in support of the National Aircraft Icing Technology Plan.

A flight research program comprising two thrusts was planned using the NASA deHavilland Twin Otter icing research aircraft. The first thrust was to determine the accuracy with which the aircraft stability and control derivatives could be estimated. To this purpose, 45 maneuvers were performed at the same flight condition to acquire data as a basis for a statistical ensemble of stability and control derivative estimates. The second thrust was to determine longitudinal stability and control derivatives for the aircraft both in clean and "artificially" iced conditions. The artificial ice is a strip of plastic molded into a generic ice shape seen in flights and the Lewis Research Center icing research tunnel; this constant shape allows for strict repeatability of icing conditions. All flight data were analyzed using the modified stepwise regression algorithm developed at Langley Research Center and previously reported in NASA TP-1916.

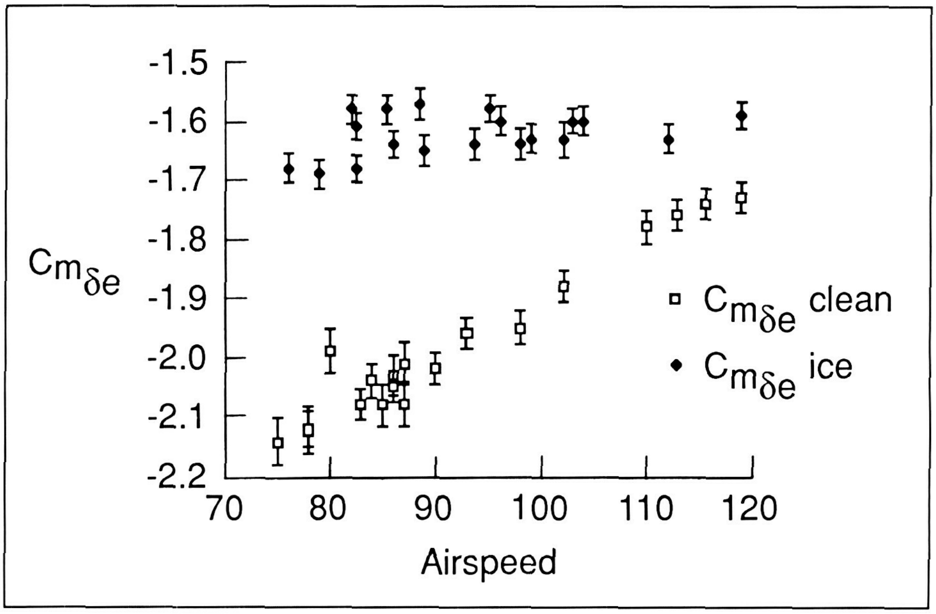

Comparison of elevator effectiveness $C_{m_{\delta e}}$ for artificially iced and clean baseline airplane.

Over 200 maneuvers were planned and performed during four flights in December 1987. The resulting recorded data have now been analyzed as to short-period longitudinal stability and control derivatives. A relationship between the ensemble standard deviation and estimated standard deviation of the main derivatives was developed. Significant differences were detected between the derivatives for the iced and uniced airplane. An example of this is shown in the figure for the elevator effectiveness derivative $C_{m_{\delta e}}$. Results of this program indicate that the effect of ice accumulation on this aircraft is quantifiable in the form of stability and control derivatives. Such comparison can give confidence bounds to ground facility measurements resulting in increased efficacy of those measurements for the preliminary design phase of aircraft. Additionally, simulation math models can be upgraded to include realistic aerodynamic models for icing scenarios.
(James G. Batterson, 4887)

Completion of Interactive Graphics Editor for Rapid Development of Flight Display Software

Development of flight display applications software for high-performance programmable display generators (PDGs) used in research simulator and flight applications can be quite costly. These high developmental costs are incurred because the more sophisticated, flexible, and efficient the PDG, the lower the level of available programming tools, and the harder it is to program. The research objective was to develop an interactive editor for rapid development of two- and three-dimensional (2-D/3-D) flight display software.

The Air Force (AF) Avionics Laboratory and Langley Research Center jointly funded the Research Triangle Institute (RTI) to develop the interactive graphics editor (IGE) for application to the AF

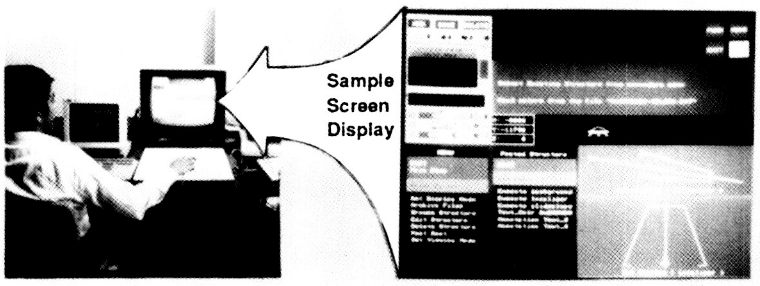

INNOVATIONS INCLUDE:

- PHIGS Graphics Standard
- Concurrent Process Window Manager
- Automatic Code Generation & Partition
- Specification of Animations
- 2D/3D Object Editor
- Self-Editing Dynamic Menus
- Preview Animation Capability
- Interactive Color Editing

L-87-10,531

Reduced developmental time and costs for two- and three-dimensional flight display software through use of interactive graphics editor.

Simplified Automated Layout Center (SALC) and the Langley Crew Station Systems Laboratory. Both laboratory environments are based on the use of a VAX/MICROVAX host and Adage 3000 color PDG environment for the generation of real-time experimental 2-D/3-D electronic flight displays.

An IGE has been developed which provides the capability for rapid development of 2-D/3-D flight display software. The IGE is a complex software system that provides many innovations and has been installed and demonstrated within the SALC of the Avionics Laboratory and will be installed at Langley. In the demonstration, the IGE was used to rapidly modify a 2-D/3-D pictorial glideslope/localizer instrument landing system (ILS) display and to create 3-D objects. By reducing development time from months to weeks (complex formats) and from weeks to days (simple formats), the IGE provides the basis for reducing the development costs of flight display software by an order of magnitude.

(Jack J. Hatfield, 3917 and Russell V. Parrish)

Patent Award for Two-Layer, Full-Color Thin-Film Electroluminescent (TFEL) Display

TFEL flat-panel displays have the potential for replacing cathode-ray tubes (CRTs) in future aircraft and spacecraft because of greater flexibility and reliability, lower weight, space, and power consumption, and graceful degradation characteristics. However, for any flat-panel display technology to replace the CRT, it must have full-color capability. Although full-color TFEL display capability has been achieved, there is a need to overcome a major shortcoming of low brightness in the blue phosphor.

Full-color displays require the use and control of the three primary colors (red, green, and blue). The brightness of the display is limited by the weakest color phosphor (blue). Two leading designs for full-color TFEL displays include the

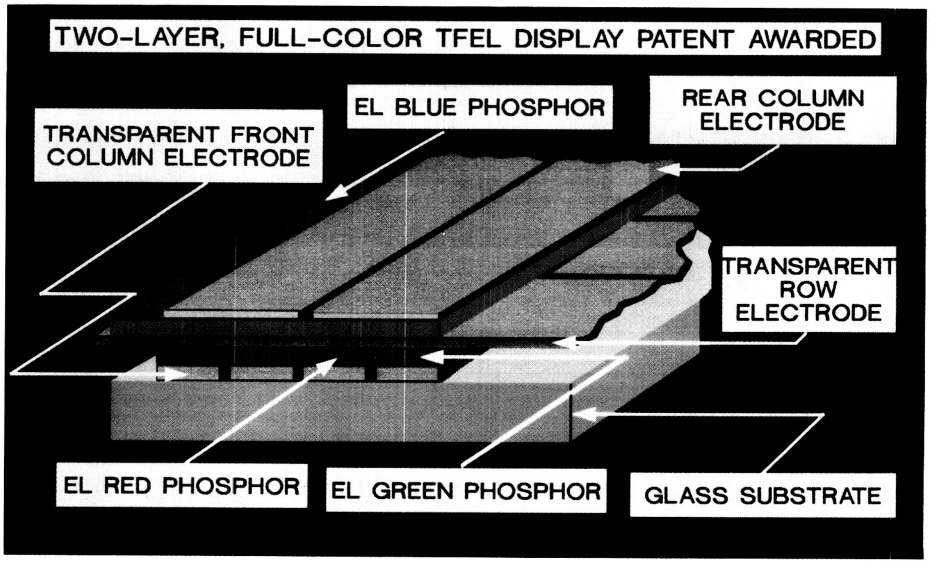

Design for increasing blue phosphor brightness for full-color TFEL displays.

ORIGINAL PAGE
BLACK AND WHITE PHOTOGRAPH

alternating color stripes deposited in the same layer, and a separate phosphor layer for each primary color. An alternate design for fabrication of full-color TFEL displays was conceived. The design, called the Two-Layer, Full-Color TFEL Display, is composed of a one-color, single-layer display superimposed upon a two-color, single-layer display. The size and shape of a picture element (pixel) in the one-color phosphor layer is equivalent to the size and shape of two subpixels (side by side) in the two-color layer.

The new display design offers an increased display brightness by doubling the active area of the dimmest color phosphor (blue). In the case in which the display resolution (pixels/inch) is limited by the minimum width of the electrodes, the new design allows for a 50-percent greater resolution compared to the single-layer, patterned-phosphor design. The new design also requires roughly one-third fewer interfaces and creates less undesirable capacitance than do present three-layer designs. **(James B. Robertson, 4682)**

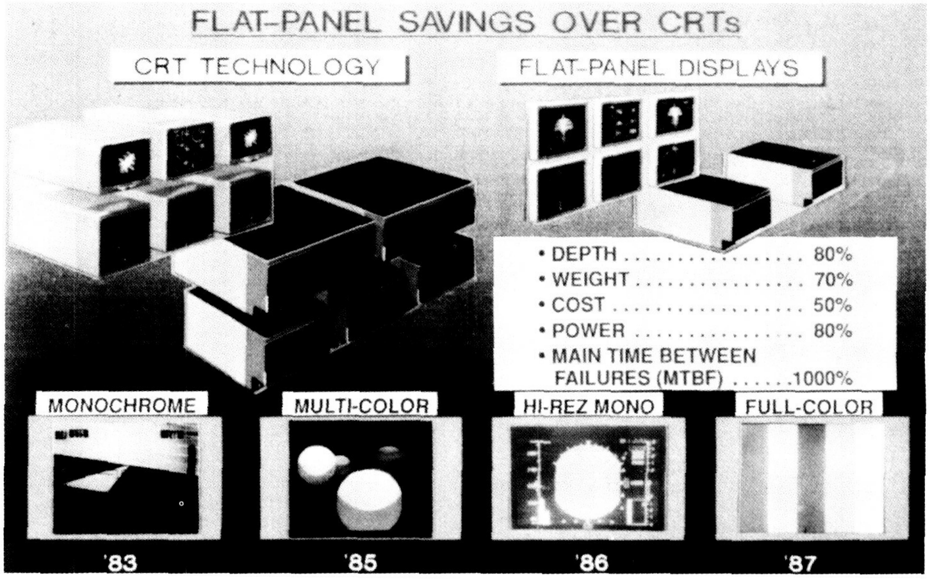

Evolution of TFEL flat-panel display technology.

Achievement of Full-Color Thin-Film Electroluminescent Flat-Panel Display

The objective of this research was to develop technology and fabrication methods for full-color TFEL flat-panel displays of practical size and resolution (as shown in the first figure). Full-color flat-panel displays are needed to replace the CRTs now in aircraft flight decks and to enable spacecraft applications (because of the potential of flat panels) to reduce weight, space, and power consumption; improve flexibility and reliability; and provide graceful degradation. Prior achievements have developed standard and high-resolution monochrome panels and multicolor (two-color primaries) TFEL prototypes of practical size.

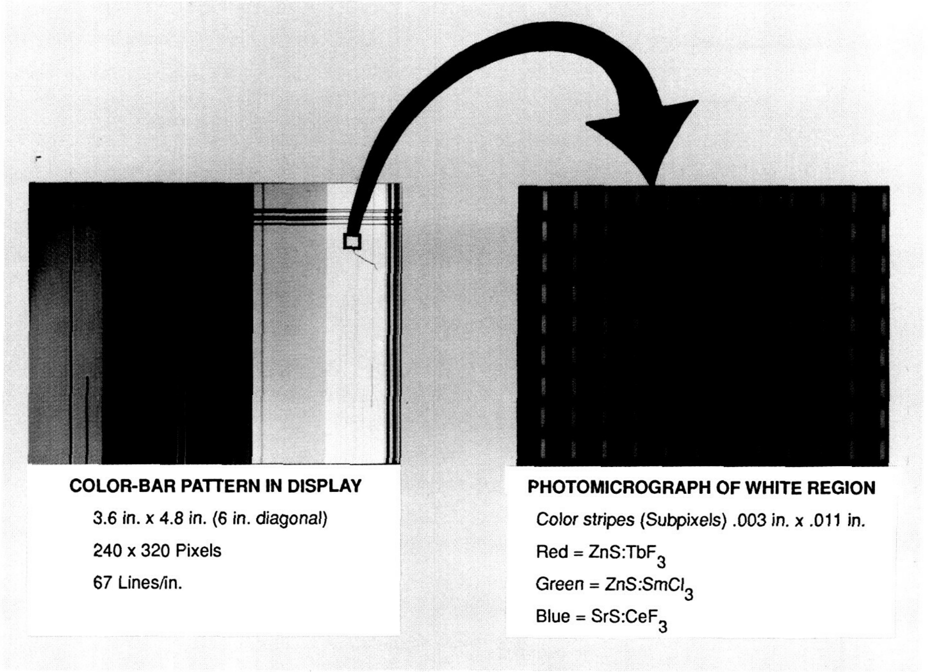

L-87-11,497

Photomicrograph of full-color thin-film electroluminescent panel.

The United States Army LABCOM and Langley Research Center jointly funded a research contract with Planar Systems, Incorporated to develop needed display technology and fabrication methods. The approach chosen was to deposit three separate electroluminescent primary-color phosphors (red, green, and blue) in the same layer in a pattern similar to that of a vertically striped color TV screen (as shown in the second figure). The vertical color stripes were fabricated in sequential steps using vacuum deposition, photolithography, and etching. Culminating a 4-year intensive applied research effort, a prototype full-color TFEL flat-panel display has been achieved. The experimental display is 3.6 in. by 4.8 in. (6 in. diagonal), and has 240 rows and 320 columns with a resolution of 67 pixels/in. The display panel, without addressing electronics, is less than 0.5 in. in thickness.

This is the first electroluminescent display to achieve full color, without the use of filters, and the first full-color TFEL display of practical size and resolution. This technology should provide the basis for future applications of full-color, flat-panel displays in aeronautical and space applications.

(James B. Robertson, 4682)

Effectiveness of Stereo and Pathway Cues in 3-D Primary Flight Display Showed by Reaction-Time Data

Recent advances in liquid-crystal (LC) shuttered stereo view-

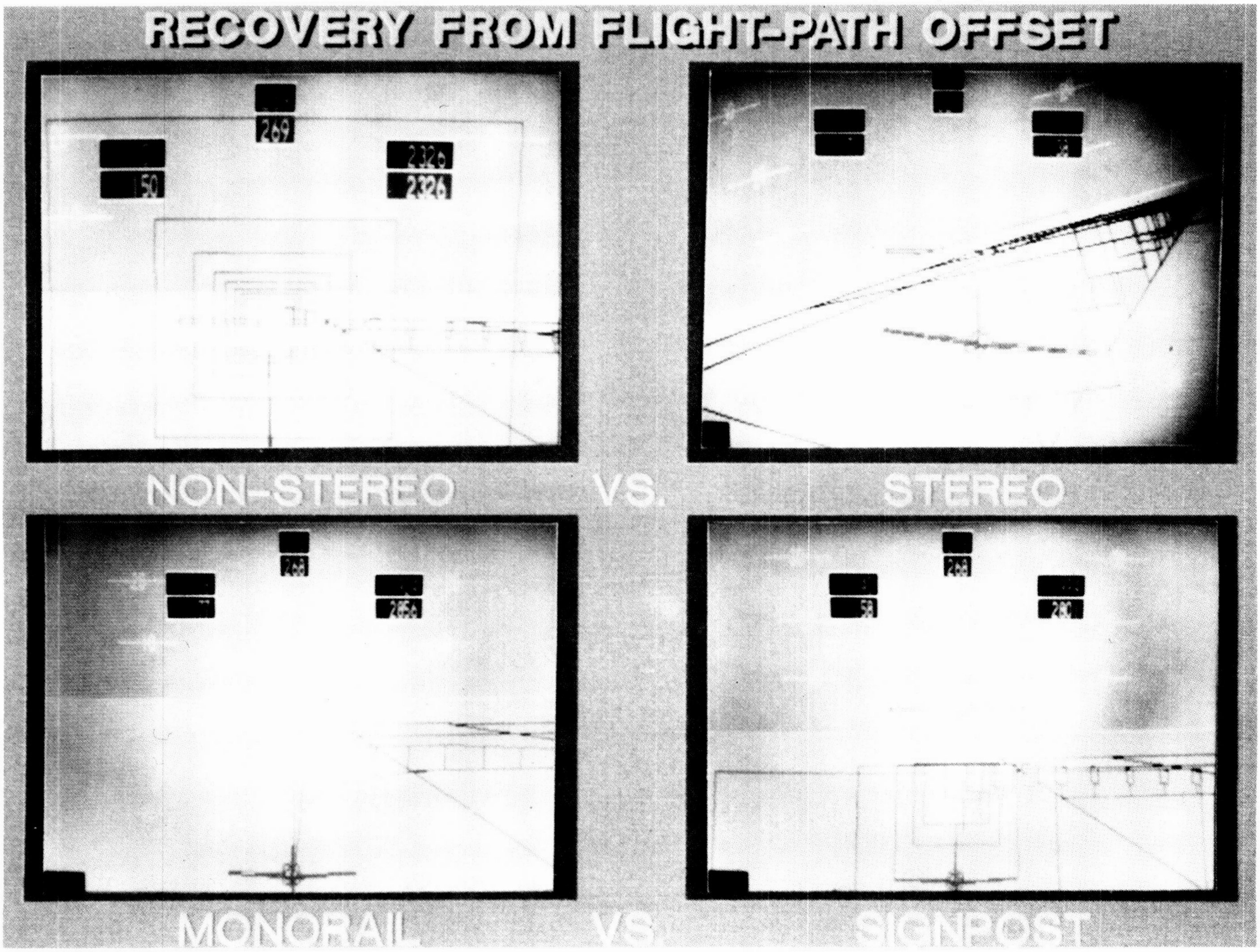

Situation-at-a-glance display using stereo 3-D technology evaluated by pilots.

ing systems, coupled with high-performance computer graphics, have made possible the generation of integrated, 3-D pictorial primary flight displays having a unique depth cue, called stereopsis. Exploitation of that technology provided the basis for the present research in the form of a stereo 3-D real-world primary flight display having, as primary features, curved "pathway-in-the-sky" and "follow-me" aircraft symbols designed for curved approach-to-landing piloting tasks. The overall goal of this research is to achieve situation-at-a-glance pilot awareness; the specific goals of the reported research were to determine the value of stereopsis and pathway cues for flight control.

Reaction times were used in a piloted simulation study designed to determine the effectiveness of stereo and pathway cues. The use of stereo 3-D capability was expected to decrease reaction time in correcting flight-path offset. In addition, two different pathways, a monorail and a signpost (as shown in the first figure), were used. Eight United States Air Force pilots served as subjects. At the start of each trial, pilots were initiated on the nominal flight path. After 2 sec, they were offset to one of eight positions or had no offset. As soon as the pilots detected an offset, they were required to make the initial stick input to fly toward the nominal flight path. After their initial input, the trial was over. The pilots responded faster with the stereo 3-D display, indicating improved situational awareness with stereo. The significant interaction of stereopsis with pathway also has implications for designers of pseudo 3-D (monocular) pictorial displays. The second figure clearly shows that pilots responded faster with the signpost pathway. It also shows that the difference in reaction times was much greater when the pseudo 3-D display was used instead of stereo 3-D. This means that it is potentially even more critical for designers of pseudo 3-D displays to carefully evaluate the effectiveness of their pathway cues.

(Lt. Col. Mark Nataupsky, 3917 and Lucille Crittenden)

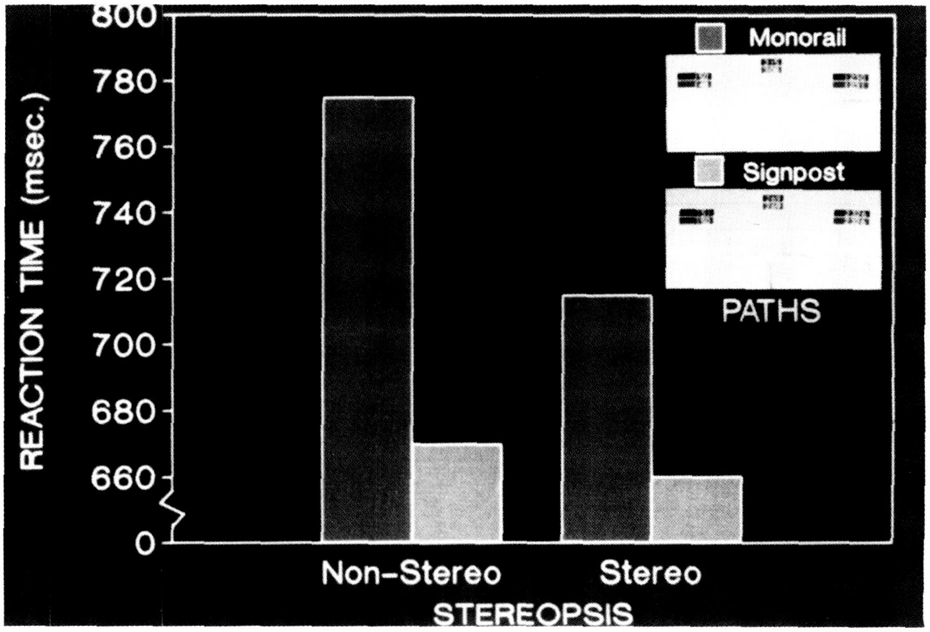

L-88-7153

Reaction times of pilots for various test conditions.

Results of Software Error-Data Studies

In order to evaluate existing software reliability models and proposed modeling approaches, a search was conducted for data on the software failure process. This search revealed that the data necessary for this evaluation were not available. As a result, a research effort was initiated by Langley Research Center to generate data on which to base the development of credible methods for assessing the reliability of software targeted for flight-crucial applications.

Two sets of software error-data experiments were conducted for Langley by Boeing Computer Services (BCS) and the Research Triangle Institute (RTI). The results of these experiments were consistent and have made significant contributions to the area of software reliability. The significance is at two levels. First, much has been learned about specific trends and behaviors that contribute to software failure. Different faults in a program were found to produce errors at widely varying rates. Program failure rates were found to follow a log-linear trend with respect to the number of faults corrected. Some of the faults identified were found to interact with each other in concealing and revealing ways. Points in the input space that cause a fault to produce errors can tend to cluster and form regions called error crystals.

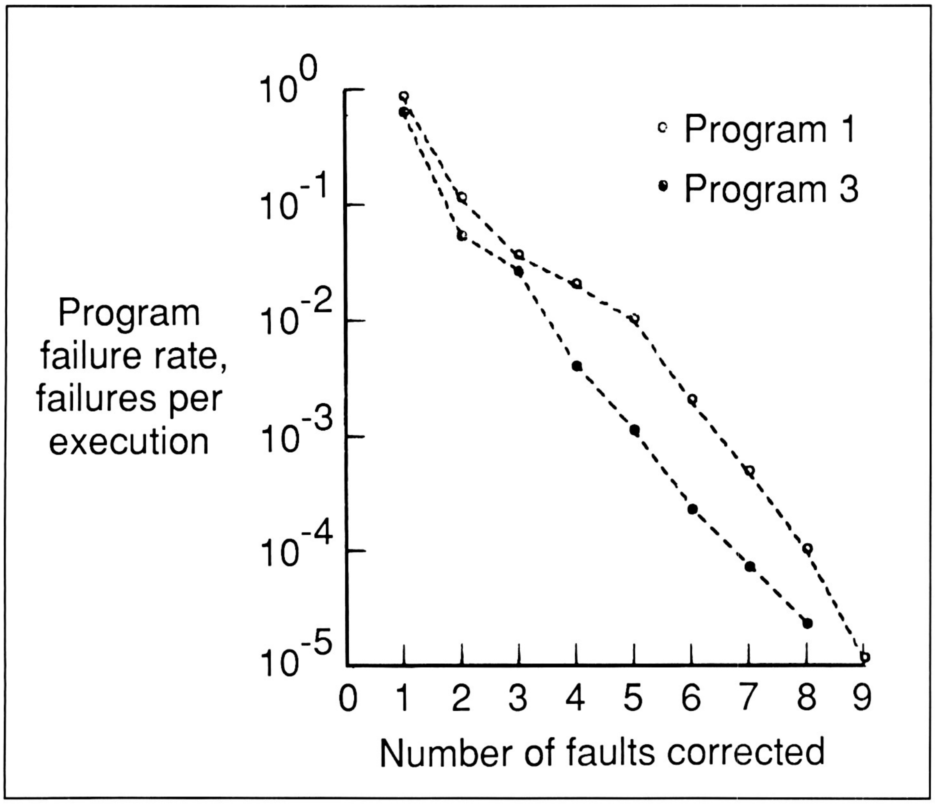

Log-linear trend of program failure rate.

Collectively, these experiments have produced information on software failure that must be accounted for in software reliability modeling approaches.

The second level of significance pertains to knowledge that has been accumulated concerning the execution of controlled experiments to generate software error data. The repetitive run approach introduced by BCS was demonstrated to be an expedient way of producing sets of data from which statistically good parameter estimates can be obtained. The automated execution of error detection, identification, and correction developed by RTI proved to be an efficient way of generating large amounts of data.

(George B. Finelli, 3681)

Performance Assessment of Quadruply Redundant Fault-Tolerant Processor

The Fault-Tolerant Processor (FTP) was designed and developed for Langley Research Center as an architecture for advanced flight control systems. The FTP attempts to provide high reliability without sacrificing an extensive amount of computational power. High reliability ($10E^{-7}$ failures/hr) is attained by implementing the system as four separate processors that execute the same software at the same time, thus providing four redundant copies of data. These data are then compared (voted) to determine if any discrepancies have occurred. When one of the processors is seen to be producing erroneous data, it can be masked out of the configuration, and the system will continue to function correctly with one less redundant processing site.

Despite the fact that a high level of reliability must be maintained in advanced fly-by-wire flight control systems, a high level of performance must also be maintained to ensure the stability of the aircraft/spacecraft. The FTP attempts to minimize the operating system and redundancy management overhead by tightly synchronizing the four processors at the instruction level via hardware, and by giving many of the fault coverage routines a low priority with respect to task scheduling. Results of laboratory experiments have shown that the overhead incurred during every 40-ms frame (the basic frame rate of the FTP under test) due to the operating system and the high-priority fault coverage routines is 5.445 ms. This corresponds to a 13.6 percent reduction in system throughput for a 40-ms (25-Hz) sampling rate. Note that this number will rise if higher sampling rates are required.

Using a representative instruction mix as a work load model and subtracting the overhead mentioned, the FTP was found to perform at 318 kips (kilo-instructions/sec). This rate will be further degraded depending on the number of votes executed per frame. The results of this research reveal that despite the FTP's high reliability, it cannot meet the high operating speed requirements for current advanced systems. By modifying existing subsystems in the FTP where bottlenecks occur (voting, I/O, and memory accessing), the FTP can

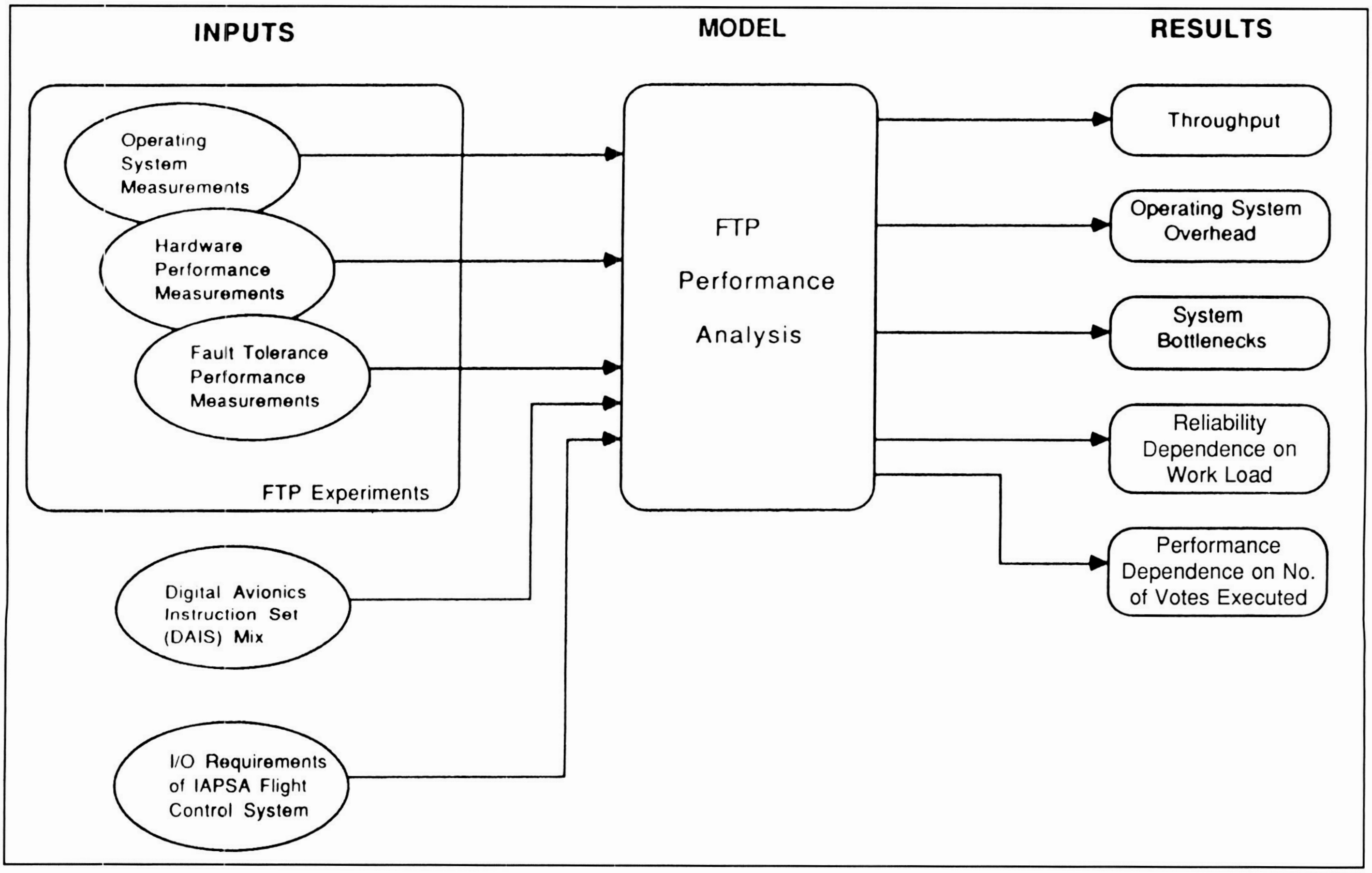

FTP performance assessment experiment.

evolve into a usable control system for many advanced applications.
(Steven D. Young and Carl Elks, 3535)

Automated Generation of Reliability Models

Because of their flexibility, semi-Markov models can be used to analyze the reliability of virtually any fault-tolerant system. Recently developed mathematical methods, such as the Semi-Markov Unreliability Range Evaluator (SURE) computer program, have greatly advanced the semi-Markov approach to the reliability analysis of fault-tolerant architectures. However, the process of delineating all of the states and transitions in the model of a complex system is tedious and error-prone.

The Abstract Semi-Markov Specification Interface to the SURE Tool (ASSIST) computer program was developed to allow analysts to automatically generate reliability models. Rules describing the failure and fault-recovery behaviors of a system are input to ASSIST in an abstract language, and ASSIST automatically generates the semi-Markov model from the rules. The model output is in the format required for input to the SURE reliability analysis program.

Because no assumptions are made about the system being modeled, the ASSIST program can be used to generate models describing the behavior of any type of system. A small number of statements in the abstract language can be used to describe a very large, complex model. Furthermore, changing only one line in the model definition, such as the number of initial spares, can result in a large increase in the size of the generated model. The analyst can use various model reduction techniques with ASSIST to reduce the size of the model before it is generated.
(Sally C. Johnson, 3681)

Investigation of Wind Shear Influence on Aerodynamic Characteristics of Aircraft Using Vortex-Lattice Method

The flight simulator is an important tool used to address the airborne aspects of wind shear research and training. The fidelity of the analytical models that represent the airplane and the atmosphere within the flight simulators is, therefore, of critical importance. The bulk of the simulation and analytical studies conducted to date has concentrated on determining the effect of the changing free-stream velocity vector on the airplane performance, and on developing higher fidelity wind shear models. Very little work has been done to determine the effect of the spatial variation of the wind field on the airplane's aerodynamic characteristics. It is important that these aerodynamic effects are characterized and presented in a form that can be incorporated into research and training simulators. The objective of this study was to investigate and characterize the aerodynamic effect of shear flow in a series of sensitivity studies of the wind velocity gradients and wing planform geometry parameters.

Formulation of new aerodynamic coefficients for the presence of wind shear was computed using a modified vortex-lattice computer program. A series of sensitivity studies was used to explore the variation of the wind shear aerodynamic effect with planform geometry. A method of computing the aerodynamic effect of a spatially variant wind field and of characterizing the effect in the form of wind shear aerodynamic coefficients was developed. The magnitude of the aerodynamic effect was demonstrated by computing the resultant change in the aerodynamics of a conventional wing and tail combination on a fixed flight path through a simulated microburst.

The results of this study indicate that a significant amount of the control authority of the airplane may be required to counteract the wind shear induced forces and moments in the microburst environment. It is important to note that these forces and moments are due only to the spatial variation of the wind field, and are not currently accounted for in today's research and training simulators (as shown in the figure).

(Dan D. Vicroy, 3621)

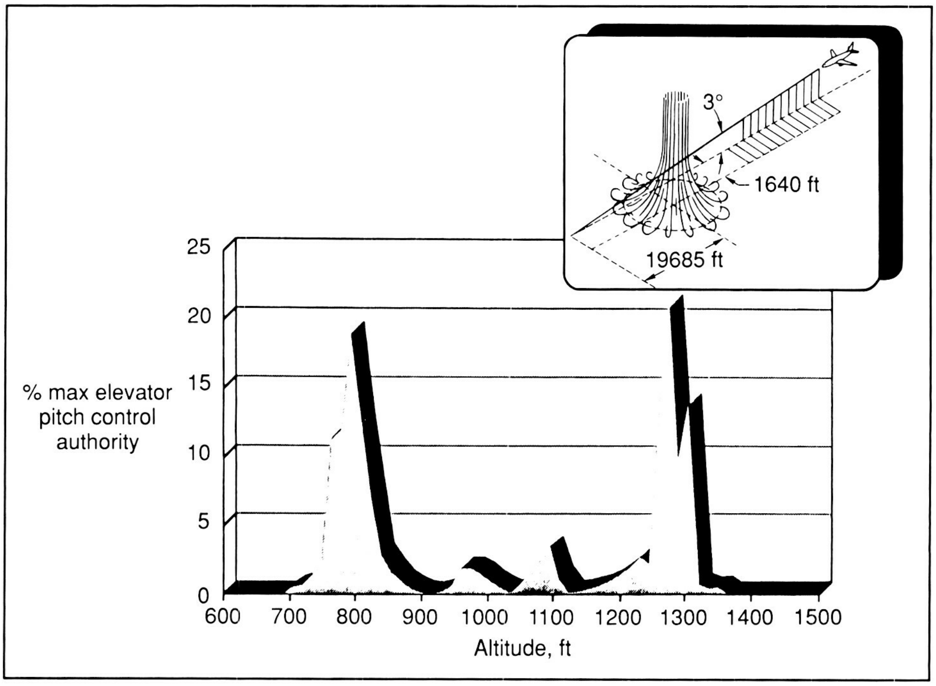

Percent elevator control required to counteract pitching moment induced by spatial variation of wind field.

Potential to Improve Airport IFR Throughput for Conventionally Equipped Aircraft by Use of Simulation and Flight Evaluations

A time-based concept, called TIMER (Traffic Intelligence for the Management of Efficient Runway-scheduling), has been developed to improve instrument flight rules (IFR) throughput. This concept integrates en route flow control, runway scheduling, and spacing, together with fuel-saving flight-idle descents to both fully utilize runway capacity and improve fleet efficiency. TIMER was designed for evolutionary integration into today's manual, voice-linked air traffic control (ATC) system by generating suggested speed and vector instructions to assist the controller in delivering non-four-

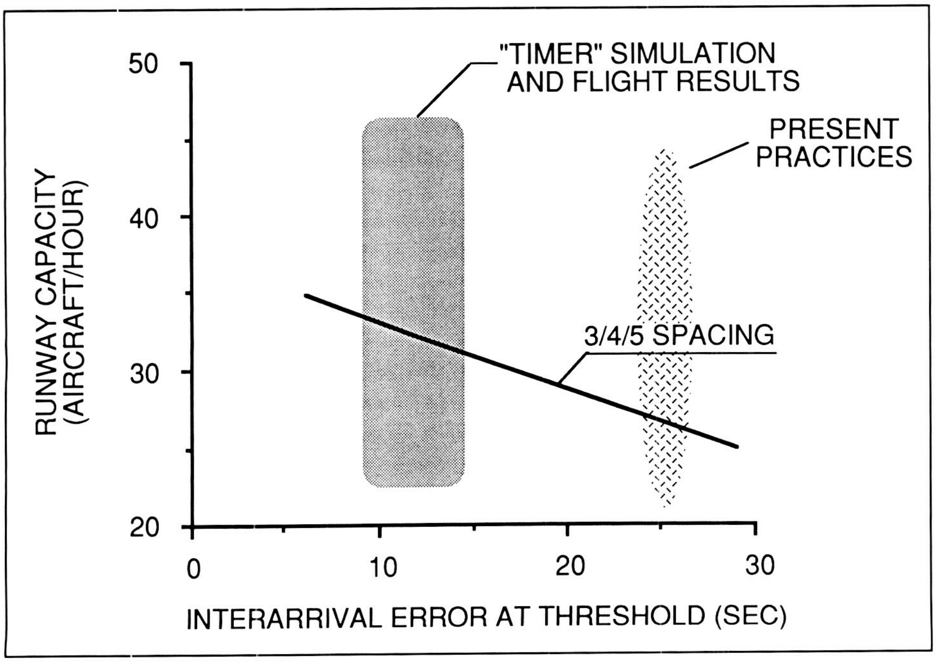

Comparison of TIMER-based controller versus present-day manual control.

dimensional (4-D) aircraft to their scheduled times. TIMER was incorporated into the Terminal Area Air Traffic Model (TAATM) for fast-time evaluation. A real-time version was developed and linked with a transport cockpit simulation for crew-in-the-loop, conventional aircraft performance measurement. Verification flight tests were conducted with the Advanced Transport Operating Systems (ATOPS) B737 flying under TIMER control at Wallops Flight Facility.

Based on results from a fast-time parametric sensitivity evaluation of the TIMER concept to determine the effects of key system variables, real-time simulation tests, using airline crews, were conducted with the full work load DC-9 cockpit simulator, and a certified ATC controller. Test results have demonstrated that conventional non-4-D aircraft can be delivered to the runway with an interarrival error standard deviation in the region of 10 to 15 sec. As the figure shows, this translates to about an 18-percent arrival capacity improvement over the 26 sec achieved in present practice. Flight tests at Wallops Island using the forward cockpit of the ATOPS B737 flying under real-time TIMER control have verified these findings.

The simulator and flight test results demonstrate that a significant part of the capacity benefits possible from an extended-terminal time-based ATC flow-control system can be realized before the airline fleet is equipped with 4-D flight management systems.

(Leonard Credeur, 3621)

Comparison of Airplane Trajectory Guidance Concepts for Wind Shear Encounters

Microbursts and low-level wind shear pose a significant threat to transport category airplanes during takeoff and landing. A critical issue is how best to manage available airplane performance during inadvertent encounters with microburst winds for the case when the wind field ahead of the airplane is not known. The objective of this effort was to evaluate the piloting factors and performance of a candidate set of wind shear recovery techniques in a piloted simulation environment. Batch simulations were used to develop suitable recovery techniques. Three recovery techniques were implemented as flight director guidance algorithms in the Visual/Motion Simulator, programmed with the math model of a Boeing 737-100 airplane. A total of 252 data runs were flown by three research pilots; each run consisted of a wind shear encounter shortly after takeoff.

The batch and simulator results indicate that the characteristics of a recovery procedure that maximizes airplane performance (in a takeoff wind shear encounter) include an initial reduction in pitch attitude to reduce the climb rate, the use of the smallest acceptable climb angle, and, late in the encounter, an increase in pitch to the stick-shaker angle of attack. Stick-shaker activation must be delayed as long as possible. Flight-path-angle-based guidance was less sensitive to variations in the wind shear and had better overall performance when compared to constant pitch and acceleration-based guidance. The

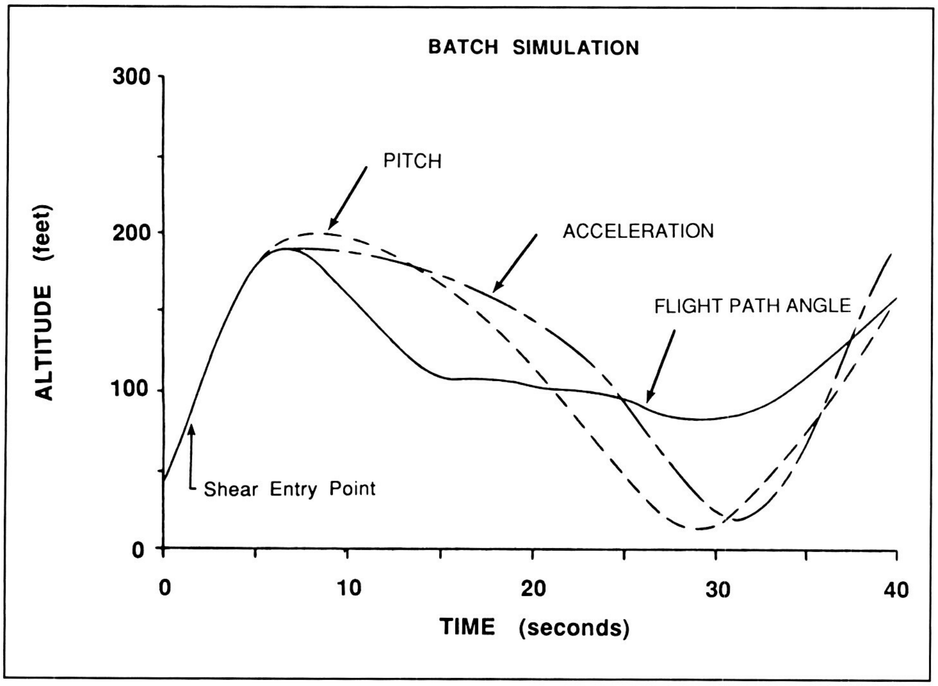

Comparison of three airplane recovery strategies.

figure shows a comparison of the three techniques in a batch simulation. The results of the batch and piloted simulations generally agreed, but the difference in performance between the recovery techniques was less in the piloted simulation than was predicted by the batch simulation. The experimental variation in performance between piloted runs was generally greater than the difference in performance between recovery techniques.

The results indicate that the performance increase of advanced recovery techniques predicted by batch simulations will not always be realized in a piloted environment. However, flight-path-angle-based guidance shows the most promise for further development.
(David A. Hinton, 3621)

Path Redefinition Algorithms for RNAV/MLS Transition

The objective of this research was to reduce large, undesirable, autopilot-induced aircraft pitch and roll maneuvers (for an autopilot operating in the three-dimensional, or 3-D, mode) which result from large guidance errors produced at transition from radio navigation (RNAV) to microwave landing system (MLS) navigation. The MLS, which is planned to replace the instrument landing system (ILS), will provide precision navigation in a greatly expanded area of the airport which can be used to safely reduce aircraft spacing and thus increase airport capacity and relieve congestion. However, satisfactory autopilot operation is needed to effectively use the MLS for this purpose.

Three algorithms, which modify the 3-D path to produce insignif-

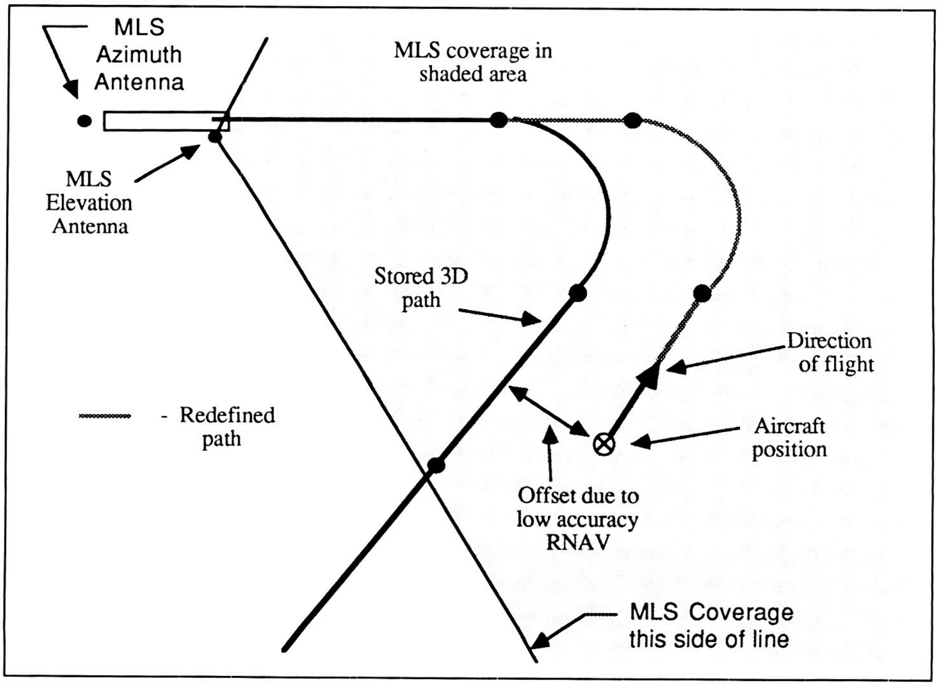

Illustration of typical new 3-D path segments at RNAV/MLS transition.

icant errors at MLS transition, were developed in batch simulation. Each algorithm defines a new 3-D path segment that begins at the current aircraft position and merges with the previous path, stored in the flight computer, in one of three ways depending on the algorithm being used. The first figure illustrates typical new path segments that are computed by the algorithms for joining with the stored 3-D path at MLS transition. A cathode-ray tube (CRT) display was also developed which shows the stored 3-D path and new 3-D path segments to the pilot. The first figure closely resembles the presentation to the pilot.

The software for these algorithms and the CRT display was implemented and flight-tested in the flight control computers of the Boeing 737 Transport Systems Research Vehicle (TSRV) operated by the Advanced Transport Operating Systems (ATOPS) Program Office at Langley Research Center. Each algorithm was tested during the course of two flight tests.

The flight test data showed that each algorithm significantly reduced roll maneuvering. The second figure shows a plot of the aircraft roll attitude, from flight data, with and without path redefinition at MLS transition for the flight path illustrated in the first figure. Pitch maneuvering was reduced to the degree that it was barely discernible. This research has also shown that development of logical functions will probably be needed for an operational implementation in order to select the algorithm that is best suited for use in a particular air traffic control situation.
(Richard M. Hueschen, 3540)

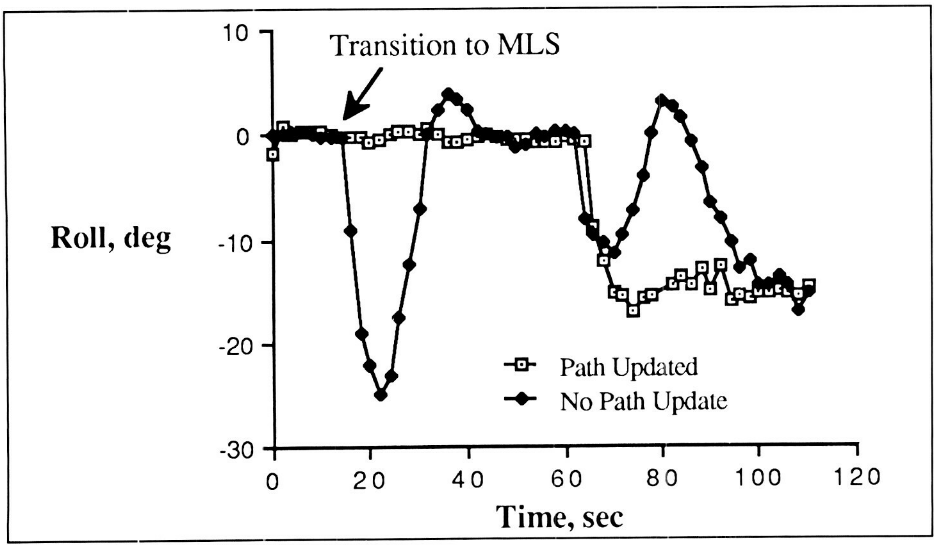

Aircraft roll attitude with and without path definition.

Takeoff Performance Monitoring System

The purpose of this work is to develop and evaluate an aircraft cockpit aid that will help reduce takeoff accidents due to undetected or uncertain performance deficiencies by providing valuable information pertinent to the pilot's decision to continue or to abort a takeoff attempt.

An algorithm was developed to compute, organize, and send such information to cathode-ray tubes on the pilot's instrument panel and also to a head-up display (projected in the windshield area). The TOPMS head-down display consists of a runway graphic with overlaid symbols and numbers. The photograph shows a case in which the airplane has reached an 88-knot airspeed and the right-side engine has failed. The engine-pressure-ratio (EPR) bar on the right side of the runway graphic turned red and dropped well below its reference value of 1.95. (The EPR bar on the left is at the reference level.) The TOPMS algorithm has determined that the airplane is below "decision speed" (V_1, the airspeed at which the pilot must decide to continue or abort the takeoff) and that with maximum braking the airplane can be stopped at the "X." Therefore, an immediate abort (a large "STOP" sign appears at the end of the runway symbol) is being advised. The apex of the shaded triangle indicates where the airplane would reach rotation speed (V_R = 128 knots) in the unlikely event that the takeoff were continued. The unshaded triangle marks the pretakeoff prediction of the rotation point. Also shown are second-segment-climb speed (V_2 = 134 knots), runway length (6000 ft), runway number (22), and relative wind vector (15-knot quartering headwind). Similar but simpler information is presented on the TOPMS head-up display.

The TOPMS displays have been "flown" and evaluated by 41 United States Air Force, airline, NASA, Federal Aviation Administration, and industry pilots on the Trans-

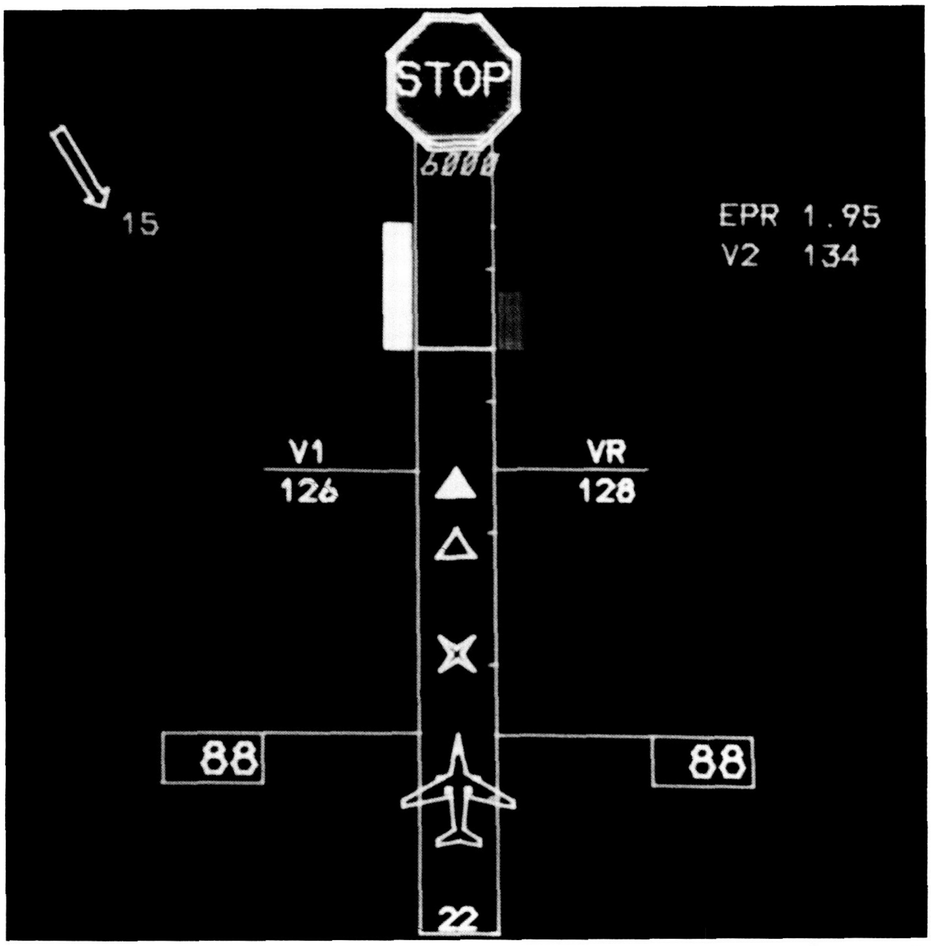

TOPMS display that advises abort.

L-87-12,381

port Systems Research Vehicle B-737 real-time simulator. The system was well received. The evaluation pilots said that using the display required low mental effort and that they felt the system would materially aid them in making critical takeoff/abort decisions and thus increase safety of the takeoff operation. Currently, a TOPMS head-down display is being flight-tested on the Langley B-737 research airplane.

(David B. Middleton, 3595)

Reduction of Pilot Stress and Work Load by Data Link Between Air Traffic Control and General-Aviation Aircraft

The Air Traffic Control (ATC) Mode-S transponder, planned for operational use in the next decade, will provide the capability of digital communications between ATC and individual aircraft. The objective of this study was to determine the potential benefits and liabilities of various levels of data link capability in general-aviation, single-pilot instrument flight rules (IFR) operations. A research prototype data link interface was fabricated (see figure) and installed in the Langley General Aviation Simulator. The Mission Oriented Terminal Area Simulation (MOTAS) facility simulated the Denver Stapleton ATC environment as pilots flew arrival and departure scenarios. The scenarios extended from the runway to Denver Air Traffic Control Center airspace, about 30 miles from the airport, and included all handoffs, vectors, initial clearances, and automatic terminal information service (ATIS) reception. The communication levels tested were voice baseline, uplink of only assigned heading and altitude, uplink of heading and altitude plus textual information, and uplink of all of the previous plus downlink capability to request clearances and weather information. Voice communication with ATC remained available with all data link levels.

The four subject pilots were enthusiastic about the data link capability and indicated that pilot stress and work load were reduced. The mixed use of both voice and data link communications in a given scenario seemed natural to the pilots. The continuous display of last-assigned heading and altitude was considered beneficial, and the lower levels of data link capability were liked almost as well as the highest level. The downlink capability was rarely used in the terminal area, except to request ATIS information and the initial departure clearance. This fact suggests the feasibility of designing simple, inexpensive data link interfaces. The pilots did not like the use of data link in situations where the pilot's visual channel was already highly loaded or for receiving takeoff clearance. Voice communication with the local controller for takeoff was

L-86-10,500

Data link interface used in research.

considered essential. The pilots did not acknowledge ATC clearances as rapidly with the data link as with the voice technique. A voice transmission requires real-time processing by the pilot. Data link transmissions, on the other hand, often were not acknowledged until the pilot read the entire message, a task which was time shared with basic airplane control.

(David A. Hinton, 3621)

Development of Preliminary Guidelines for Displaying Aircraft System-Status-Information Generated by Expert Systems

As increasingly capable onboard diagnostic systems that utilize expert systems technology are developed for transport aircraft, the question arises of how to present the resulting system status information to the flight crew in a comprehensible form. The objective of this research study was to investigate display issues associated with providing system status information and to provide preliminary guidelines for displaying such information.

A fast-time simulation study was conducted that investigated four system status display issues: display type, hypothesis presentation style, information presentation style, and parameter presentation style. To address the issue of display type, picture-based displays (iconic representations of the device) were compared to symbol-based displays (geometric shapes with no intrinsic meaning) and to text-based displays (alphanumeric representations). The hypothesis presentation style addresses the level of detail at which hypotheses are presented; this was investigated by comparing presentation of hypotheses describing the individual components to hypotheses describing only the subsystems. Information presentation style is concerned with which parameters to present to the pilot. In this study, two styles were compared: presentation of abnormal parameters only versus presentation of all parameters, normal and abnormal, in affected subsystems. The parameter presentation style issue was investigated by comparing a bar graph to an alphanumeric format. The figure shows a montage that illustrates the formats tested for the different display issues. Reaction time and error in identifying faulted subsystems and abnormal sensors were measured.

The results of the study show that pilots responded more quickly

ORIGINAL PAGE
BLACK AND WHITE PHOTOGRAPH

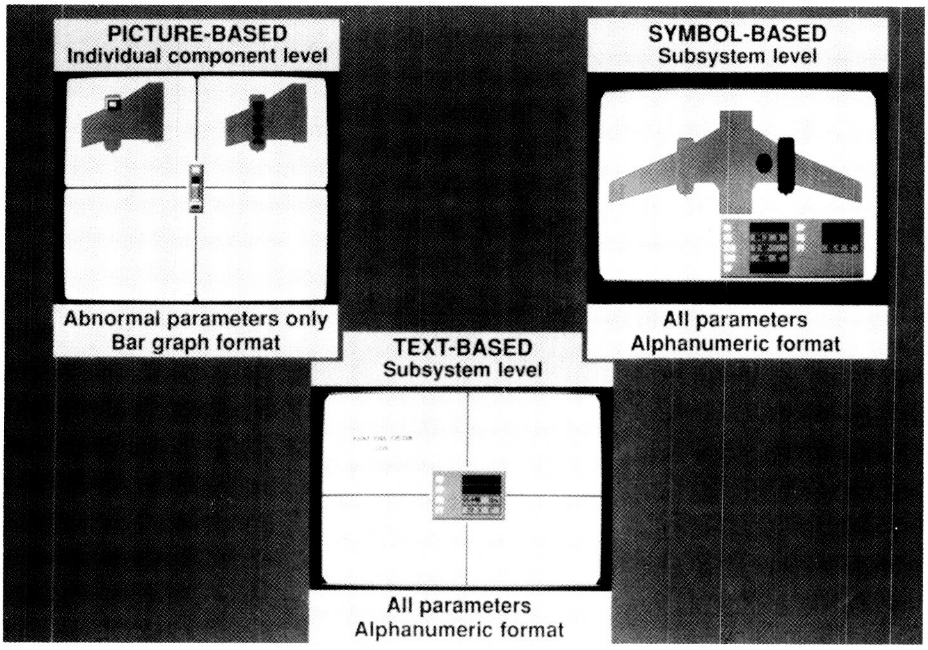

System monitoring displays.

L-88-7899

and made fewer errors when system status was presented in the picture-based or the text-based display style at the subsystem level of detail, and when only abnormal parameters were displayed. Preliminary guidelines that incorporate these results were developed. **(Kathy H. Abbott, 3621)**

Control Mode Panel Logic

The objective of this research is to develop, evaluate, and demonstrate methods for applying artificial intelligence (AI) programming tools for the implementation of guidance and control functions within advanced aircraft flight control systems (FCS). The research will evaluate the potential of these methods to reduce the cost and time of FCS design and software development, to simplify the implementation of complex FCS, and to increase the functional capability and reliability of the FCS.

An initial project of this research was to implement a logic-intensive software function of a modern FCS because a large portion of its software is logic (estimated to be at least 80 percent), and AI tools are well-suited for logic implementation. The complex logic associated with the control mode panel (CMP) on the Transport Systems Research Vehicle (TSRV), a modified Boeing 737 aircraft operated by the Advanced Transport Operating System (ATOPS) Program Office at Langley Research Center, was selected for this project. The CMP allows the pilot to set control modes in the TSRV fly-by-wire control system.

The CMP logic was implemented with the symbolic processing language LISP using typical AI programming techniques. Additionally, by taking advantage of the AI software structure, a message feedback, fail-engagement advisor (FEA) was easily developed and added to the CMP logic to assist the pilot in operating the panel. The figure shows the tie-in of the logic and FEA to the aircraft sensors, control laws, and CMP. The list processing (LISP) code was subsequently translated into C code, a high-level

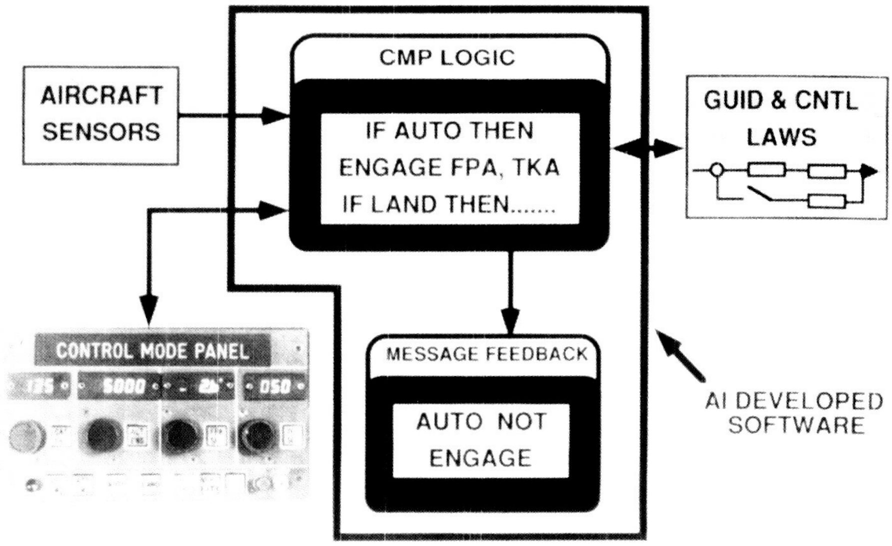

procedural language, for real-time implementation. The C code was installed in the TSRV flight computers and ground-tested for proper operation. It was recently successfully flight-tested, thus becoming the first real-time flight crucial AI-based system to be tested on a commercial-type aircraft.

This research project has shown that the potential exists for an order-of-magnitude reduction in the software development time for complex logical functions. Additionally, the development and incorporation of the message feedback advisor demonstrated that modifications to existing AI software are significantly easier to program than conventional methods.

(Richard M. Hueschen and John W. McManus, 3540)

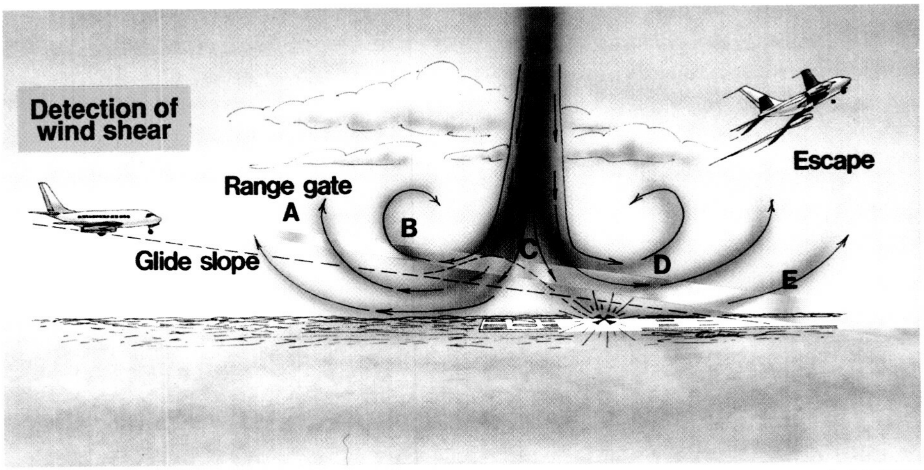

L-88-8986

Microburst wind shear hazard for approaching aircraft being probed by radar beams.

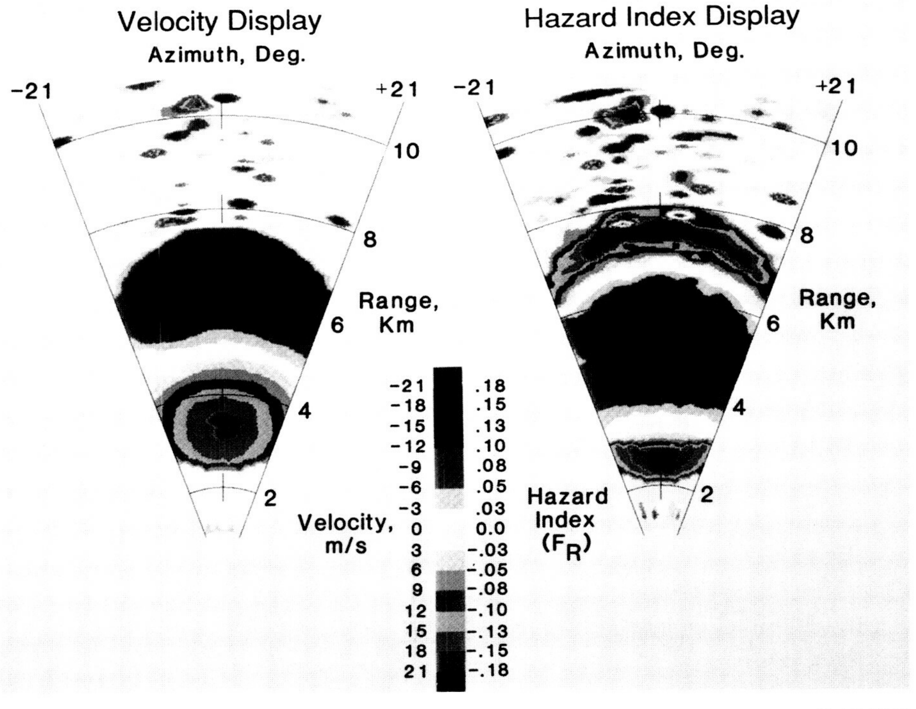

L-88-9165

Range-azimuth display of wind velocity contours and hazard index contours for "wet" microburst.

Airborne Doppler Radar Detection of Microburst Wind Shear Microburst/Clutter Radar Simulation Program

The purpose of this research is to develop airborne Doppler radar technology for the detection of low-altitude microburst wind shear and to assess the capabilities and limitations of the Doppler radar as a forward-looking sensor for detecting wind shear during aircraft landing or takeoff.

One specific goal has been to develop a microburst/clutter/radar simulation program that accurately calculates the expected output of an airborne pulse-Doppler radar system viewing a low-level microburst along or near the approach path of the aircraft with a background clutter environment.

A comprehensive computer program has been developed which simulates the operation during landing approach of an onboard Doppler radar sensing returns from a microburst wind field and an airport clutter environment. The program incorporates wind field and reflectivity data bases derived from a numerical wind

ORIGINAL PAGE
COLOR PHOTOGRAPH

ORIGINAL PAGE
COLOR PHOTOGRAPH

shear model, clutter maps derived from Synthetic Aperture Radar backscatter data, and various radar configurations and signal processing concepts. Output displays of various radar parameters detected, such as wind speed and wind shear, provide information on radar performance. A preliminary performance assessment study of a radar concept sensing both "wet" and "dry" microbursts has been conducted using this simulation program. This assessment was presented at the AIAA meeting on Sensor and Measurements Technology, Atlanta, Georgia, in September 1988.

This comprehensive simulation program provides an analytical tool for accurately evaluating the performance of airborne radar concepts and signal processing techniques that may be proposed for detecting microburst wind shear during aircraft landing or takeoff.

Utilizing this simulation program, a full range of microburst/clutter environments will be investigated and extensive tradeoff and optimization studies conducted on various Doppler radar concepts. Improvements in the program will also be made to investigate more sophisticated signal-processing techniques, more severe ground clutter environments, improved displays for evaluating performance, and methods for evaluating the efficiency of hazard detection.
(Emedio M. Bracalente, 3631)

Tactical Maneuver Simulator (TMS)

Future fighter aircraft will have enhanced agility (maneuverability and controllability combined) throughout the flight envelope. To date, increased levels of agility have been postulated as tactically advantageous, but no capability exists to study maneuvers that use agility. The objectives of this research are to identify maneuvers that effectively exploit agility and to evaluate the impacts of different control laws on the tactical use of agility.

The Tactical Decision Generator (TDG) is being developed as a knowledge-based system that generates aircraft maneuver commands based on the tactical status of a one-versus-one engagement ("dogfight"). The Tactical Maneuver Simulator (TMS) is being constructed as a simulation tool to permit development and evaluation of air combat rules and scoring algorithms that comprise the TDG. The TMS consists of two computers that communicate as shown in the figure. The symbolic computer contains the user interface and the TDG; the numeric computer contains the aircraft models and also solves the equations of motion.

Air combat rules and scoring algorithms have been implemented in the TDG. The current TDG has been used to validate basic concepts and provides a baseline against which future improvements can be compared. A technique for interprocess data transfer between a numeric and symbolic computer has been developed. This technique is the first step toward a real-time simulation interface. A graphic display has been implemented that shows aircraft trajectories from any orientation, promoting a natural, qualitative analysis of engagements. The TDG engagement trajectories were "flown" by the Differential Maneuvering Simulator (DMS) target aircraft (as shown in the figure) to obtain pilot impressions of TDG-generated maneuvers. A simple situation assessment module was developed to determine either aggressive, defensive, neutral, or evasive piloting strategies.
(P. Douglas Arbuckle, 2132)

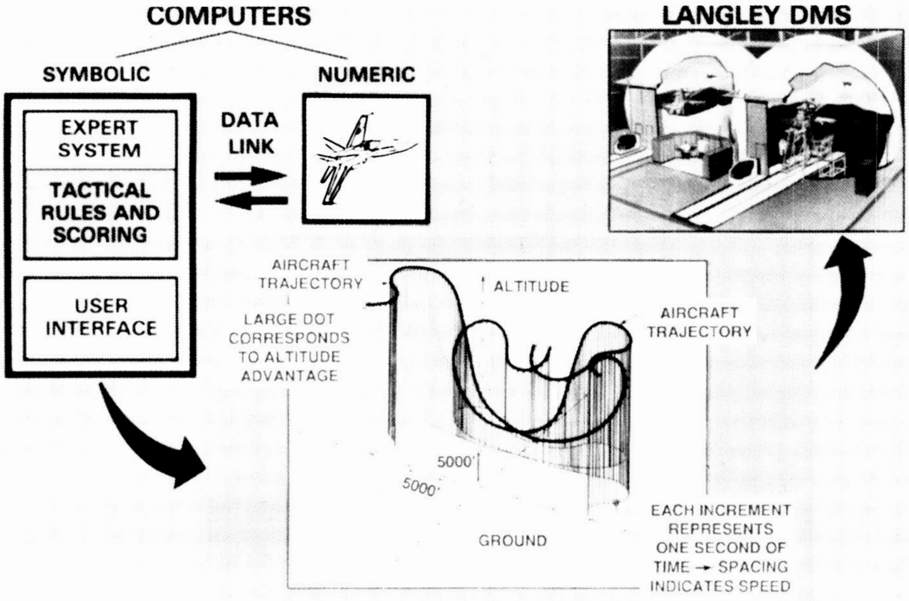

Schematic of TMS showing graphic display and relationship to DMS.

Evaluation of Prototype Diagnostic Expert System Using National Transportation Safety Board Accident Cases

A research prototype of an onboard fault-monitoring and diagnosis expert system has been developed to demonstrate the use of artificial intelligence techniques in providing aid to the flight crews of civil transport aircraft. This prototype, called Faultfinder, detects and provides diagnoses of failures in the engine and hydraulic subsystem of a generic aircraft. The diagnosis process is performed in two stages. The first stage uses rules to diagnose known faults. The second stage uses model-based reasoning to diagnose faults that were not included in the rules. The objectives of this evaluation, using data from actual aircraft accident cases, were to perform a preliminary assessment of the performance of the expert system, to determine the validity of the concept, and to identify future areas of research and development.

Eight accident cases, obtained from the National Transportation Safety Board (NTSB), were selected to evaluate Faultfinder. These cases were reconstructed to produce a simulation of the accident, and the expert system was run using the simulations to produce hypotheses for the probable cause of the failure for each test case. The hypotheses produced were then compared to the correct diagnosis of the failure as determined by the NTSB. Finally, the results of this comparison were analyzed to assess the system performance.

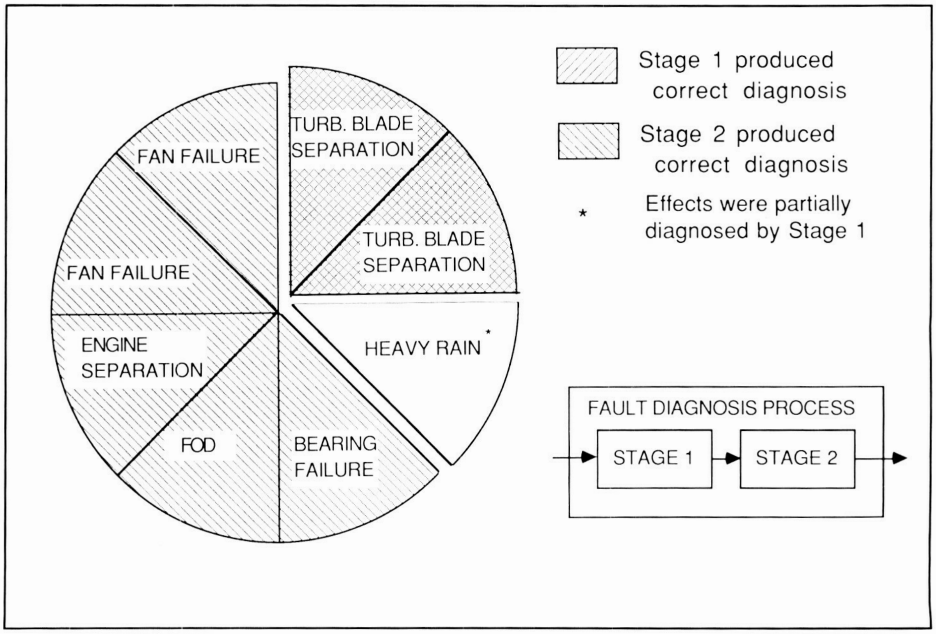

NTSB cases reconstructed for Faultfinder evaluations.

The results of this evaluation showed that the implementation was able to correctly diagnose seven of the eight test cases that were reconstructed. As the figure shows, the first stage of the diagnosis process correctly diagnosed two of the eight test cases, while providing a partial diagnosis for a third. The partial diagnosis described a portion of the fault's effects. The second stage correctly diagnosed seven cases. In several cases, multiple hypotheses were produced. Such situations may result in ambiguity in the selection of the appropriate response by the flight crew. Enhancements to the knowledge base and inference structures are expected to reduce the number of multiple hypotheses. The evaluation demonstrated that the concept has potential for providing onboard aid to the flight crew in performing fault diagnosis.

(Paul C. Schutte, 3621)

Demonstration of Intelligent Decision-Aiding Concept for Air Traffic Control Diversions

A current problem in flight operations is the excessive pilot work load required while responding to flight plan diversions during critical flight phases. The objective of this research was to develop concepts and guidelines for applying artificial intelligence (AI) techniques for reducing pilot work load while generating new or revised flight plans, and to integrate these AI techniques into current and future flight management systems. Through surveys of airline crews, concepts and candidate functions for an airborne crew decision aid for flight plan diversions were investigated. Available AI tools and architectures were reviewed, and a systems design was implemented as a research prototype, DIVERTER, on a Symbolics LISP machine. DIVERTER pro-

vides decision information to the crew regarding alternate airfields and routes based on weighted factors such as weather, safety of operations, economy, schedule, and facilities. Exploratory research is being conducted through a series of prototype states in which knowledge bases are expanded, and crew and other onboard systems are integrated.

Two separate demonstrations of the research prototype DIVERTER system have been accomplished. The first demonstration included a skeletal system architecture based on a blackboard concept, with a relatively simple rule-based system to represent the decision logic. The system was demonstrated to accept a severe weather message that necessitated a diversion, and then to select and rank the available alternate airfields. Predetermined map displays were provided on the Symbolics terminal screen to show the user the change in route to the airfield that was chosen. The second demonstration, instead of using a set of predetermined routes to alternate airfields, planned these routes through the High-Altitude Jet Airway system using an AI search technique called A-Star. This planning was conducted with the additional factor of altitude necessary for passage through mountainous terrain.

This research effort demonstrated the feasibility of decision aiding for flight plan diversions. It provided the research prototype system, DIVERTER, which has been demonstrated to select and rank alternate airfields. DIVERTER also plans the best route to the chosen airfield considering the airway system, topography, weather, safety of operations, and economy. Expected benefits are enhanced flight safety and a reduction in peak crew work load.

(Michael T. Palmer, 3621)

Strong Designer Endorsement of Evaluation Phase of Knowledge-Aided Display Design (KADD)

The primary objective of KADD has been to provide a computer-based display design system that enhances the design process and products by providing on-line assistance through an expert system with knowledge in human factors, ergonomics, and display formats. The objective of the evaluation phase has been to compare KADD to other graphics tools widely used by industry for display design. Part I evaluated the utility of KADD by comparing human "time-to-design" performance for KADD with two other graphics packages. Part II solicited qualitative assessments of KADD from experienced crew system designers by having them use the system. Part I utilized only the display editor portion of KADD with no on-line assistance provided by the expert system. KADD was compared to two PC-based graphics editors: PC PAINTBRUSH and IN-A-VISION. Part II allowed the participants to use the full capabilities of KADD.

The results of Part I of the evaluation plan are illustrated in the figure. The data were averaged across subjects and tasks (create or modify) and show that KADD excels when the display uses predefined graphic elements but suffers when the display design requires manipulations of graphical primitives as the "Display 3" did. Although the time-to-design with KADD was greater for "Display 3," the time-to-modify "Display 3" was substantially less. In Part II of the evaluation, the subjective responses

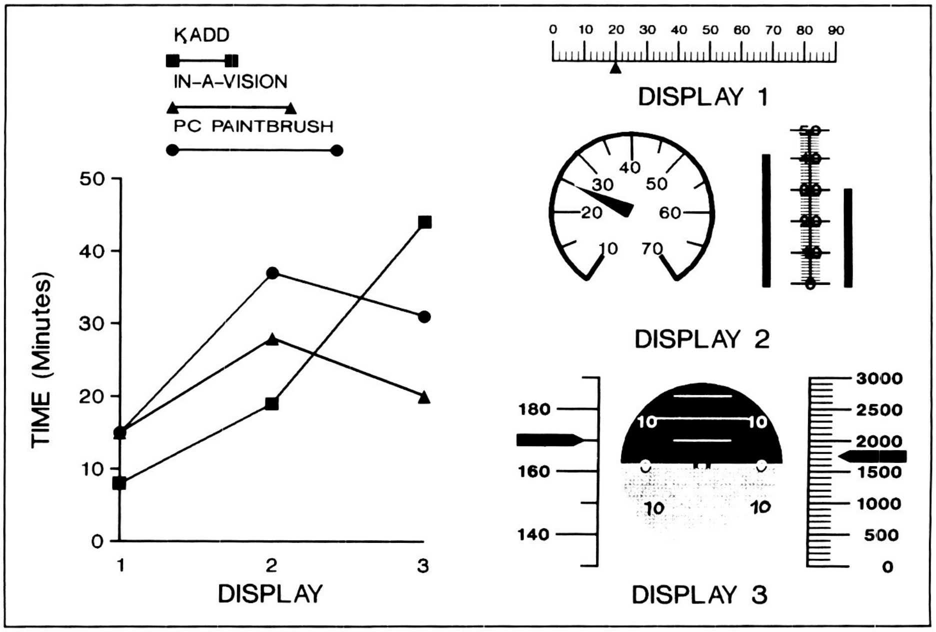

Comparison of graphic design tools.

to KADD were highly positive, although the designers felt the depth of the knowledge base was too shallow. Also, the designers wanted the ability to easily define three-dimensional displays, some sort of simulation capability, and the ability to evaluate displays across display elements and formats.
(James R. Burley and Terence S. Abbott, 3917)

Improved Radiation Patterns of Distorted-Surface Reflector Using Adaptive-Array Compensation

The objective is to develop methods and computer codes in order to enable the determination of complex excitation coefficients of array feeds, which will improve the electromagnetic performance of large space deployable reflector antennas whose surface distortion has unacceptably degraded its performance.

Geometrical optics with aperture-integration techniques have been shown to give good results for reflector antennas whose surfaces are slowly varying (IEEE AP-S 1987 Symposium, pp. 764–767). Earlier, an efficient and accurate technique (NASA TM-87644) was developed which models the aperture as overlapped arrays of subapertures.

Recently, a new method (NASA TM-100652) was developed which utilizes the previously mentioned techniques in a least-squares procedure. This approach determines the complex excitation coefficients for the elements of an array feed which will, when illuminating a distorted reflector, produce a secondary radiation pattern approximating the performance of an ideal reflector. This technique has been applied to a practical feed array to determine the excitation coefficients that will compensate for the surface distortion of the 15-m hoop/column antenna as measured in 1985 (see the figure).

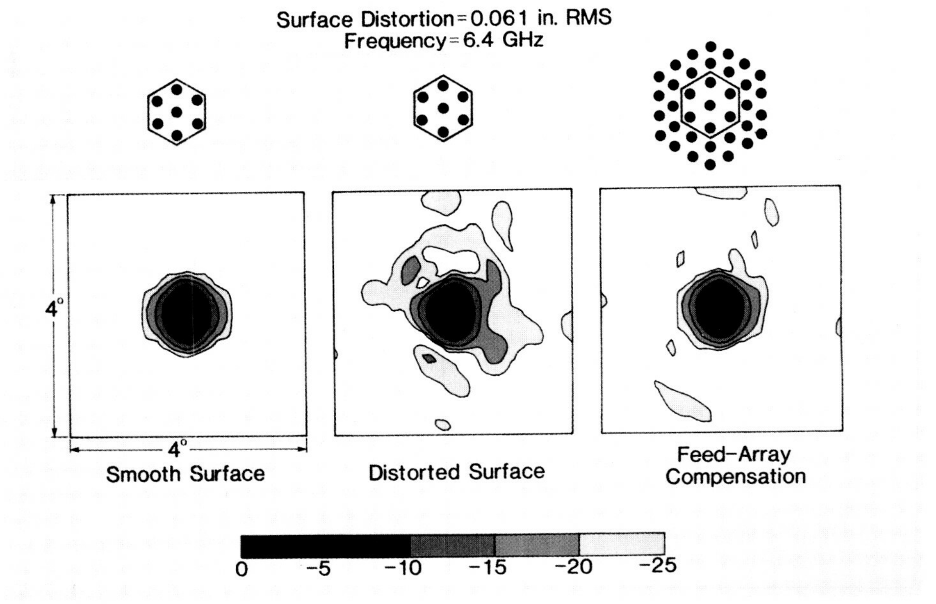

L-88-7723

Calculated radiation pattern contours for 15-m hoop/column antenna.

This technique will enable the use of electronic means to improve the electromagnetic performance of large space deployable reflector antennas whose performance has become unacceptably degraded. The technique will provide a means to fine-tune the performance after possible mechanical surface adjustments have been implemented.

Using computer simulations, tradeoffs will be made to determine the relative improvements to be realized by electronic compensation versus mechanical adjustments for the 15-m hoop/column antenna using actual measured surface distortions. Computer simulations will also be conducted to determine possible improvements using a combination of electronic and mechanical compensation.
(M. C. Bailey, 3631)

Grating-Surface-Emitter Phased-Array Lasers for Optical Communications

The research task is to develop and demonstrate semiconductor lasers with single spatial and spectral modes, and high-power and high-speed modulation for both near-Earth and deep-space optical communications applications.

Aluminum/gallium/arsenide semiconductor laser technology and the coupled mode theory have been utilized to phase together the outputs of a number of semiconductor lasers. By coupling many lasers together, the overall emission from a

C-2

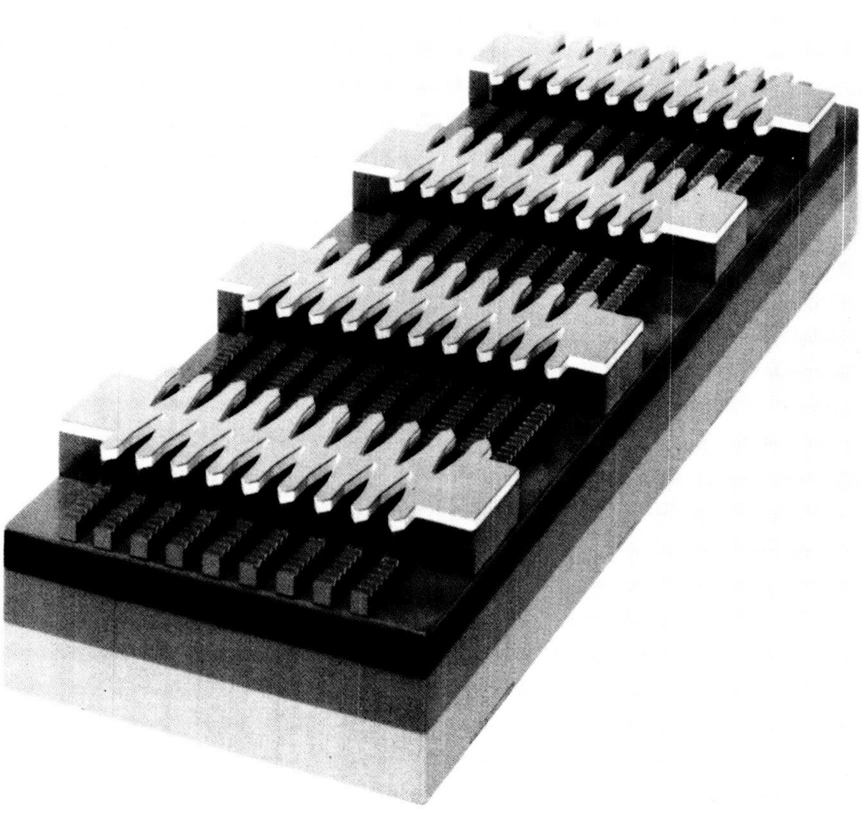

Physical model of y-coupled grating-surface-emitter phased-array laser.

laser array can be increased. The physical model of a device that has been demonstrated is shown in the figure. The gray sections are the y-coupled regions that are used to transversely couple the lasers. By electrically pumping these gain regions of the lasers, 830 nm (near-infrared) optical energy is produced. The emission is directed via the white waveguide region into the output gratings (thus the term grating-surface-emitter laser) shown next to the ridges. The laser emission is coupled perpendicular to the laser surface.

Research achieved in the development of initial phased-array lasers using this approach has shown the single-lobe output, high power, and modulation speed. Recently the y-coupled grating-surface-emitter phased-array laser has demonstrated 1.1 W of output power, a diffraction limited single-spatial mode, a single-spectral mode line width of < 1Å, and multi-GHz modulation capability.
(Herbert D. Hendricks, 3777)

Robust Model-Based Controller Synthesis for SCOLE Configuration

A multivariable frequency domain compensator design approach that produces controllers meeting performance requirements has been developed for use on flexible spacecraft. A modification of the linear quadratic Gaussian/loop transfer recovery method with a frequency domain stability robustness criterion has been applied to a finite dimensional model of the Spacecraft Control Laboratory Experiment (SCOLE) using optimal regulator

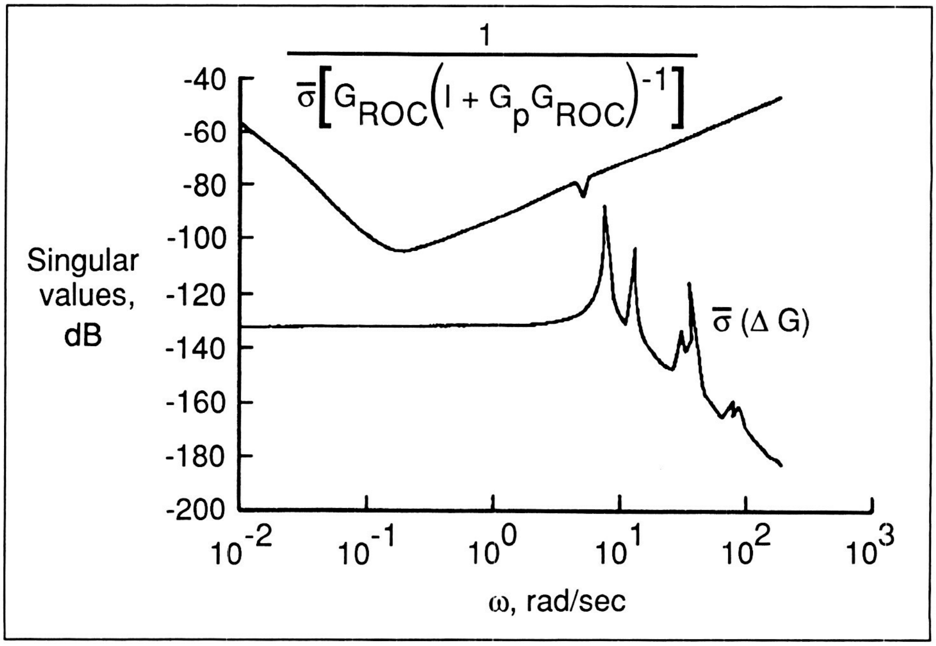

Stability robustness with reduced-order compensator.

algorithms for the control of linear systems (ORACLS) and a multivariable frequency domain compensator design approach.

Results indicate that a tenth-order, reduced-order compensator can be used to meet a representative set of stability-performance-robustness conditions for the twenty-sixth-order SCOLE model without destabilizing spillover effects. It was discovered that order reduction can cause a reduction in stability robustness margin as illustrated in the graphic. The graphic depicts the stability robustness criterion. The distance between the upper and lower curves gives a measure of robustness margin. The dip in the upper curve at 5.1 rad/sec (the frequency of the SCOLE third elastic mode) was not present prior to order reduction.

These techniques allow for the relatively systematic design of control systems for flexible spacecraft that meet prescribed performance requirements. Since the SCOLE configuration is representative of many proposed spaceflight experiments, the results and design techniques developed in this program are applicable to a wide range of large space structure control problems.
(E. S. Armstrong, S. M. Joshi, and E. J. Stewart, 4591)

Algorithm-to-Architecture Mapping Model

An algorithm-to-architecture mapping model (ATAMM) was developed for dynamically assigning graph nodes of an application algorithm graph to processors in a parallel processor architecture.

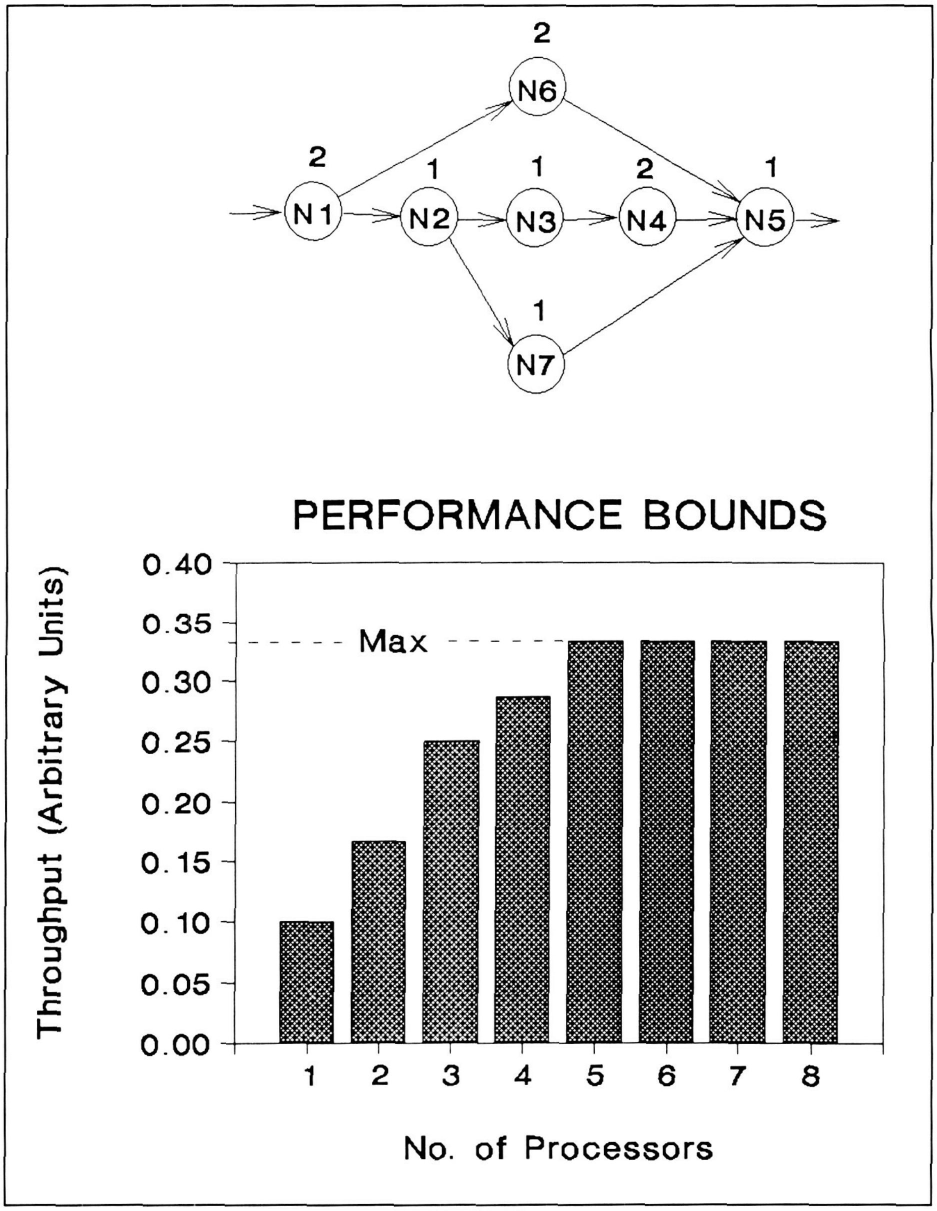

Algorithm graph.

The ATAMM, developed by Old Dominion University on a Langley Research Center grant, is based on the Petri Net theory and is applicable to data-driven applications with predetermined graph node interconnections such as are typically required in flight control systems.

The data flow graph management methodology embodied in ATAMM employs both the forward flow of data and backward flow of control information needed to ensure proper operation of the graph. The model assumes that each processor has identical software and can execute all of the algorithm modes. The ATAMM provides a new multiprocessing capability set consisting of the operating system rules

to manage the assignment of graph nodes to processors; mathematically proven deadlock-free performance; and prediction of a graph's performance bounds. Performance prediction is illustrated for an example graph, which consists of seven nodes named N1 through N7, with each node having a latency execution time of either one or two relative time units. Operation of the graph may occur in any part of the shaded portion of the histogram. For the graph example, ATAMM has determined the maximum attainable throughput, the number of processors needed to execute the graph at the maximum throughput, and the dependence of throughput on the number of available processors.

The ATAMM is a potential major new tool for the design, development, and implementation of application algorithms and is being further explored for inclusion in NASA fault-tolerant onboard multicomputer systems.
(Paul J. Hayes, 3777)

Technique for Measuring Surface Conductivity Characteristics for Large Deployable Mesh Antennas

L-88-7728

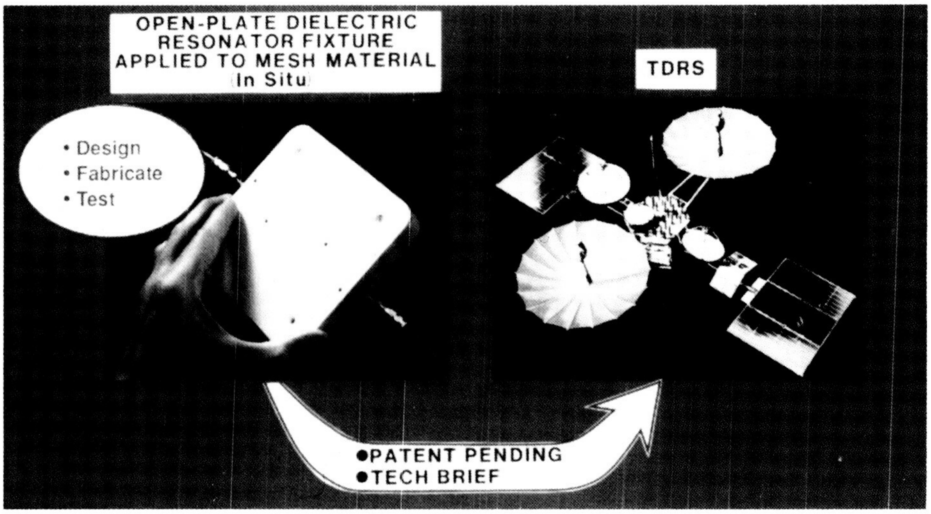

Nonobjective technique developed for measuring surface conductivity characteristics for large deployable mesh antennas.

The objective of this research is to devise a method for nondestructively measuring the microwave surface conductivity of large space deployable antenna mesh materials. The nonrigidity of the mesh materials precludes the application of conventional resonant cavity techniques that require a volume totally enclosed by conductive walls. A dielectric resonator element operated in the parallel-plate configuration can be applied to this problem, as the test fixture is open ended and uses plates of finite extent. The Q factor of the fixture is measured with the mesh as one of the conducting plates and then with other materials whose conductivity is known. The conductivity of the mesh can then be obtained by interpolation.

Two experimental test fixtures have been fabricated and are undergoing evaluation. An automated technique for measuring the Q factor with a vector network analyzer is being developed to support the test program. A patent disclosure has been filed for this measuring technique, which should be useful to other applications involving nonrigid, high-conductivity materials for which microwave surface conductivity is sought.

The application of less-sophisticated, Q-measurement methods will be studied in the hope of developing a truly portable "measurement package," thereby freeing the technique from laboratory instrumentation.
(Chase P. Hearn, 3631)

Single-Step Optimal Control Validation on Computer Model of SCOLE

Tests have been conducted on a mathematical representation of the Spacecraft Control Laboratory Experiment (SCOLE) in order to develop and validate control concepts for flexible space structures that can readily be implemented on real-world hardware. These control algorithms must be capable of utilizing a complement of actuators composed of a mixture of on-off thrusters (nonlinear actuators) and saturation-limited, proportional reaction wheels (linear actuators) in an efficient manner.

Two control algorithms based on Single-Step Optimal Control (SSOC), found in the literature, have been adapted to evaluate their effectiveness for vibration supression. SSOC treats the optimization problem as one of parameter optimization. The given time interval of control interest is divided into

ORIGINAL PAGE
BLACK AND WHITE PHOTOGRAPH

L-87-7321

Spacecraft Control Laboratory Experiment.

subintervals, and a cost function for each subinterval is defined. For SCOLE, the cost function is the total vibrational energy and control effort. This cost function is minimized, without constraints, with respect to the control over each subinterval. The constraints on the individual control inputs are taken into account by replacing the calculated values with the bounded values whenever the bounds are reached.

This research has demonstrated that minimum control effort control laws employing a mixture of on-off and proportional actuators can be implemented. The need for such control approaches is evident since future large space structures will utilize a mix of actuators for maneuvering as well as for fine pointing and articulation.
(D. W. Sparks, Jr., 4424 and J. P. Williams)

Linear Quadratic Gaussian (LQG) Control for Mini-Mast Experiment

In order to develop a viable test facility for the experimental evaluation of control system concepts for large flexible space structures, a "pathfinder" control law was developed for the Mini-Mast Experiment. The Mini-Mast is a 20-m, joint-dominated, three-longeron beam made of graphite/epoxy tubes with sensors and actuators distributed along its length.

Using a finite-element model of the Mini-Mast, the mode shapes and frequencies for the first 10 modes were derived. These, in addition to the actuator/sensor complement attendant to this test article, were employed in the definition of the "pathfinder" control algorithm. Using the linear quadratic regulator (LQR) method, control gains were then derived. State estimates were derived with Kalman filters from the noisy sensor inputs. Due to reaction mass actuator characteristics, the local controllers and the command algorithms that convert force commands to position commands had to be developed and implemented.

A computer simulation of the test facility was employed to validate this "pathfinder" control concept to verify the process for future candidate guest investigators. The structure was excited by commanding one of the reaction mass actuators. Four of these

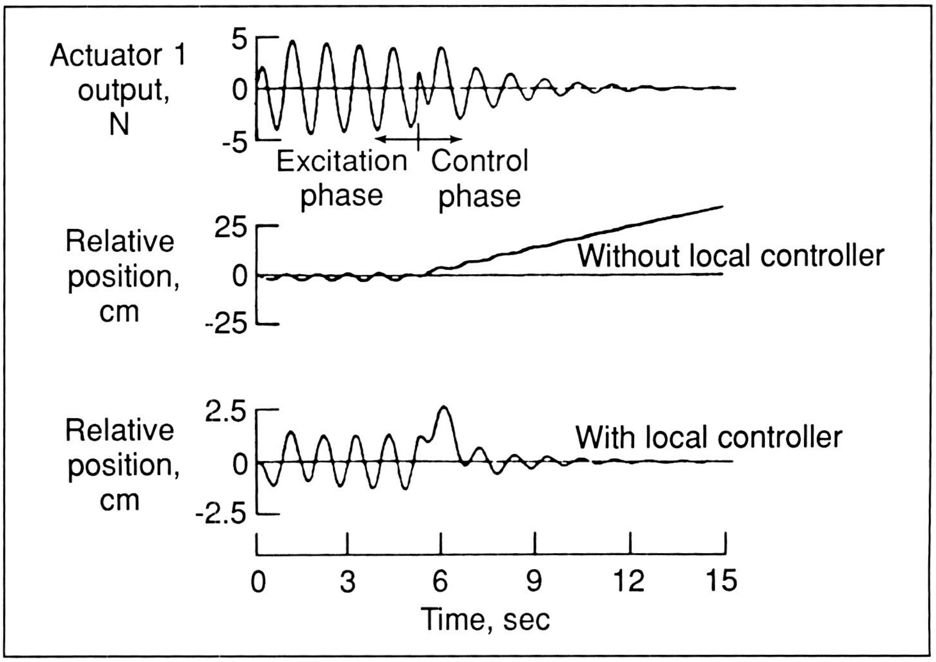

LQG control simulation for Mini-Mast Experiment.

actuators and one reaction wheel were then used to damp out the vibrations induced in the beam. As is noted in the figure, the induced vibration was readily damped. It is also noted that without proper attention to the physical characteristics of the actuator, control effectiveness can be lost as the actuator drifts to the end of its displacement range. This effect has been overcome through the proper design of local controllers.

(R. C. Montgomery and D. Ghosh, 4591)

Response of Hypersonic Vehicles to Atmospheric Disturbances

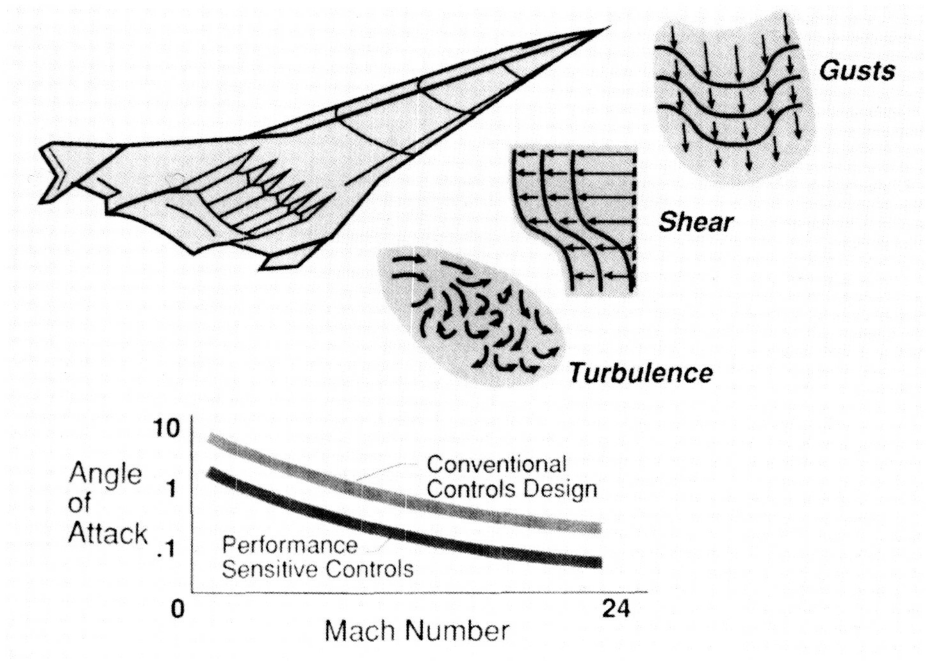

Vehicle response to atmospheric disturbances.

Hypersonic vehicles that use air-breathing engines will require unprecedented attitude and flight path stability to maintain near nominal trajectories so that aerodynamic/propulsive system performance can be optimized and maximum payload to orbit may be achieved. One objective of this program is to determine the response of a hypersonic vehicle to atmospheric disturbances during ascent. A second objective is to define control power requirements and to determine the induced drag along a constant dynamic pressure trajectory.

The problem of transatmospheric vehicle encounters with atmospheric disturbances during ascent was addressed to estimate the angle of attack and control deflections along constant dynamic pressure trajectories. The vehicle longitudinal dynamics were modeled and analyzed. A control system, which used aerodynamic effectors, was designed to enhance vehicle stability, to reduce angle of attack and load factors, and to provide good handling qualities. Turbulence, gusts, and wind shear disturbance models were developed for examination of 10 flight conditions from Mach 0.7 to Mach 24.

Vehicle response to severe levels of atmospheric turbulence and gusts resulted in excessive levels of angle of attack and load factor, particularly in low Mach numbers. It was shown that these responses could be reduced through tighter control at the expense of greater control activity and larger control deflections. The figure shows peak angle of attack experienced over the Mach number range for two control system designs; one is for a "conventional" design and one is for a design in which payload performance was a consideration (a "performance sensitive" design).

The risks associated with atmospheric disturbance encounters during the ascent phase of transatmospheric vehicles that make use of air-breathing engines can be reduced through improved control design strategies. At hypersonic speeds, vehicle drag and propulsion system performance are adversely affected by only moderate angles of attack. This study indicates that optimal control strategies can be used to find minimum drag-maximum engine performance compromises that will maximize the payload to orbit.

(John D. Shaughnessy, 3321 and David L. Raney)

Space Directorate

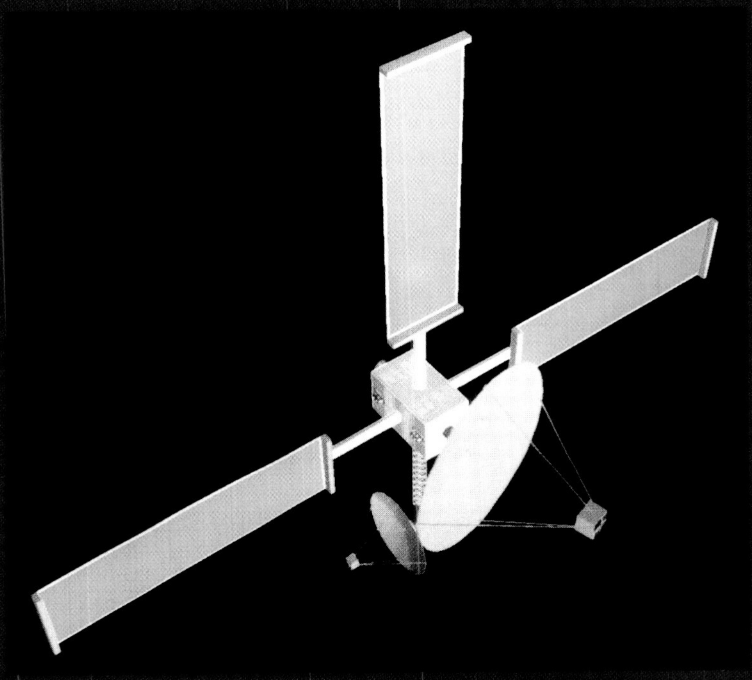

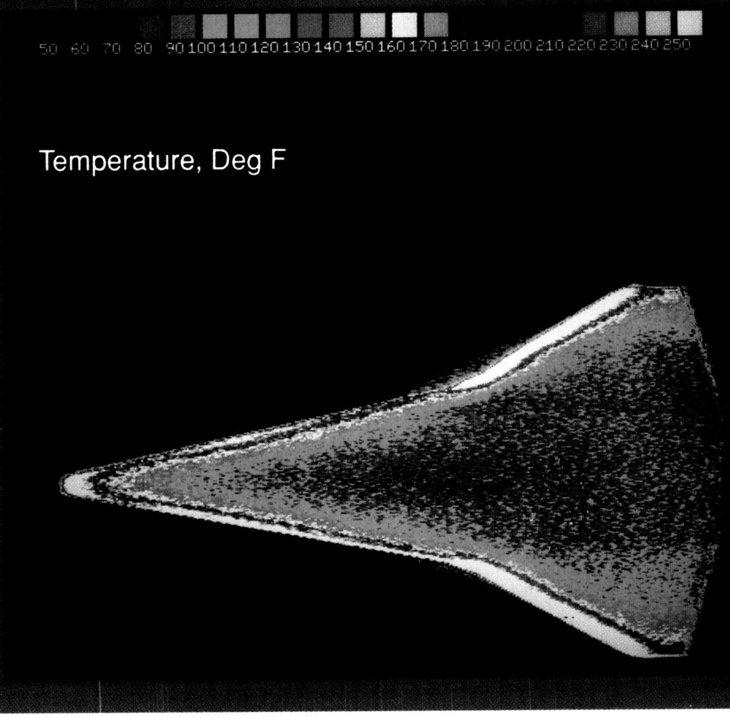

The Space Directorate conducts research in atmospheric and Earth sciences, identifies and develops technology for advanced transportation systems, conducts research in energy conversion techniques for space applications, and provides the focal point for conceptual design activities for both large space systems technology and space station activities.

The Atmospheric Sciences Division is a leader in the area of atmospheric sciences. Its researchers are involved in seeking a more detailed understanding of the origins, distributions, chemistry, and transport mechanisms that govern the regional and global distributions of tropospheric and stratospheric gases and aerosols, and in the study of the Earth radiation budget and its effect on climate processes. The research seeks to better understand both natural and anthropogenic processes and covers a wide spectrum of activities, including the development of theoretical and empirical models; collection of experimental data from in situ and remote-sensing instruments designed, developed, and fabricated at Langley Research Center; organization of extended field experiments; and development of data management systems for the efficient processing and interpretation of data derived from airborne and satellite instruments.

The Space Systems Division conducts research and systems analysis studies of advanced transportation systems, large space systems, and space station concepts; analytical and experimental research in hypersonic aerodynamics and aerothermodynamics; hypersonic computational fluid dynamics code development and studies; and basic research on energy generation and conversion techniques for potential use in space. The division is a leader in the development of highly interactive computer-aided design tools that enable rapid conceptual design and evaluation of space vehicles and spacecraft and identification of technologies needed to develop these space systems. Space systems such as Earth-to-orbit launch vehicles, Shuttle II, utility vehicles, and orbital transfer vehicles are developed and evaluated. Flight experiments are developed that use the Space Shuttle orbiter as an orbital platform and reentry research vehicle and that use entry vehicles launched from the Space Shuttle to study aerothermodynamic and aerodynamic characteristics. The results provide a data base for development of advanced vehicle systems.

The Space Station Office is the focal point for Langley Research Center's involvement in the Agency-wide Space Station Program and is responsible for the implementation and coordination of Langley's direct support of this program. The Space Station Office is NASA's lead office for the identification, definition, and evaluation of the evolutionary space station capabilities and for the identification of technology and advanced development required for long-term evolutionary development. The office represents the engineering community as technology users of the space station. It also advocates flight experiments on future Space Shuttle flights which contribute to space station technology use as well as flight experiments from technology programs which can contribute to both the initial operational capability and the evolutionary space station. The office provides Langley Research Center support to the NASA-wide in-house space station systems engineering and integration in areas consistent with demonstrated Langley capabilities and expertise.

The Space Directorate has had a significant number of major accomplishments this year. Two important experiments designed to provide new insights into chemical and dynamical processes in the atmosphere have been accomplished by the Atmospheric Sciences Division. The Global Tropospheric Experiment (conducted over the Amazon Basin) has shown the very important role of biosphere-atmospheric interactions in determining atmospheric chemical processes over undisturbed rain forests. The NASA/NOAA (National Oceanic and Atmospheric Administration) experiment to investigate the ozone hole over Antarctica used the Langley Research Center airborne differential absorption lidar system to successfully measure large-scale cross sections of ozone and polar stratospheric clouds in the ozone hole.

The Space Systems Division has conducted extensive system studies in the areas of advanced transportation systems and large space systems. These systems studies

identified advanced technology requirements and assessed the impact of varied mission options. Unique concepts of using solar-pumped lasers for space energy transmission have been identified. Particle radiation protection methods have also been identified. Significant advancements have been made in aerothermodynamic computational techniques with thermal and chemical nonequilibrium effects, for both continuum and rarefied flow regions. In addition, experimental data were obtained and assessed for expanding the heating and aerodynamic data base for the Aeroassist Flight Experiment and new hypersonic wind tunnel testing techniques were developed. The Space Station Office developed requirements and representative configurations for a number of alternative evolutionary paths for the space station that included research and development growth and growth into a transportation node in support of human missions to the Moon and Mars. Based on these analyses the evolutionary space station resource, capability, and "scar" (a hardware design accommodation to enable and/or enhance the addition or update of systems and capability at some future time) requirements were established. Other studies included definition of early man-tended configurations, enhanced Space Shuttle utilization, and Industrial Space Facility utilization. In addition, the Space Station Office led the Office of Aeronautics and Space Technology (OAST) "outreach" program to develop new technology experiments in industry and academia. Details of the accomplishments of the Space Directorate follow.

Spatial Structure of Radiation, Vapor, and Liquid Water in the Atmosphere

Satellite radiometry permits the retrieval of many basic tropospheric constituents. The fields of reflected and emitted radiation, water vapor, precipitation, and cloudiness all interact thermodynamically to drive global weather. Atmospheric models indicate that better observation of these fields will facilitate the statistical prediction of climate variations on the scale of a few months.

Data from the *Nimbus 7* spacecraft have been processed to display the basic spatial structure of tropospheric constituents using the empirical orthogonal function (EOF) analysis on a monthly scale. The EOF analysis permits data to be compacted and expressed in a small number of eigenvectors; physical relationships between fields may then be more easily elucidated. The column loading of the water vapor field (labeled "vapor" in the figure) generally has a simple geographical structure over the tropical and mid-latitude oceans; the first few eigenvectors can explain more than 80 percent of the monthly variance. The field of suspended atmospheric liquid water (labeled "liquid" in the figure), composed of mostly precipitation-sized particles, is more chaotic; several eigenvectors are needed to describe one-half of the variance. The spatial structure of the outgoing thermal infrared radiation is also less ordered than that of the water vapor. Langley Research Center scientists are presently using EOF analyses of water vapor, radiation, and other fields in studies of long-range atmospheric prediction. **(Thomas P. Charlock, 2977)**

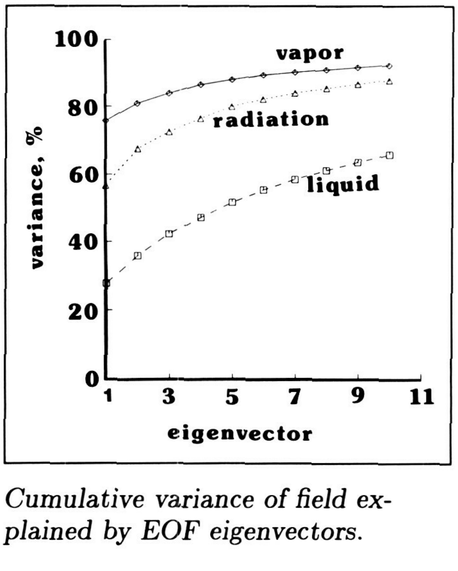

Cumulative variance of field explained by EOF eigenvectors.

Satellite Studies of Upper Free Tropospheric Aerosols

The nature and optical scattering characteristics of aerosols in the upper free troposphere are not well understood at the present time. Little in situ sampling has taken place, and the relatively low aerosol concentration makes remote sensing difficult. Considerable current interest in this region does exist due to the Laser Atmospheric Wind Sounder (LAWS) program, which hopes to develop an instrument to measure wind velocity on a global scale. This instrument would use, as part of its operation, the backscatter from atmospheric aerosols and, therefore, there is a need to know the expected magnitude of this backscattered signal.

The SAM II/SAGE I/SAGE II series of satellites were designed to measure, using solar occultation techniques, the optical extinction produced by stratospheric aerosols

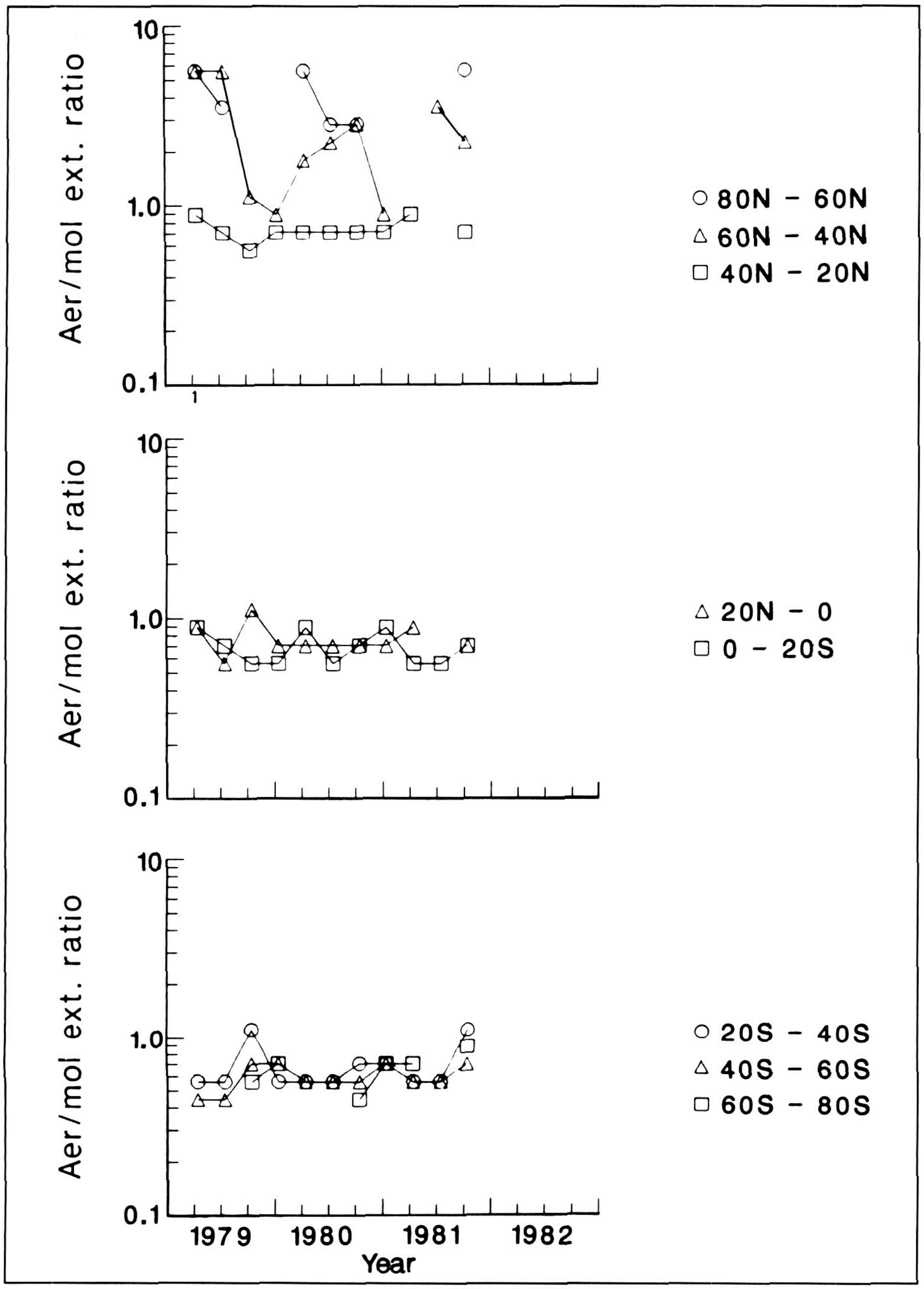

Temporal variation of average 1.0-μm background aerosol extinction ratio mode in the upper free troposphere. Data shown for 1979 to 1981 are from the SAGE I satellite. Data for 1984 onward are from the SAGE II satellite.

at a wavelength of 1 μm. However, in the absence of high-altitude clouds, these measurements extend downward into the troposphere. Therefore, the SAGE I data set from 1979 to 1981 and the SAGE II data set from 1984 to 1987 have been studied in order to determine the extinction characteristics of the upper tropospheric aerosol, as a function of altitude, latitude, and time. The aerosol extinction at 1 μm wavelength has been analyzed in terms of its ratio to the molecular extinction at the same location and time. This ratio is found to have distinct modal characteristics and the principal mode, which is well defined, is believed to be a good descriptor for the aerosol optical properties.

The principal extinction ratio mode, at a wavelength of 1 μm, is found to be fairly constant with altitude, from 5 km to approximately 3 km below the tropopause. Its value does, however, depend upon latitude, season, and volcanic activity. This fact is illustrated in the figure, which shows SAGE I and SAGE II data, divided according to latitude band and season. SAGE II data have a greater signal-to-noise ratio than those from SAGE I and show a distinct seasonal variation that is in antiphase in the northern and southern hemispheres. There is also a temporal decrease between 1984 and 1987, due to decay of the aerosol enhancement that occurred in the stratosphere and in the upper troposphere following the eruption of the El Chichon volcano in April 1982. Both SAGE I and SAGE II data show that the aerosol extinction north of 40°N is considerably greater than that south of 40°N latitude. It is not yet known if this variation is determined by the global distribution of land mass, or if anthropogenic sources are the driving influence.

(M. P. McCormick, 2065)

Airborne Lidar Measurements of Ozone and Aerosols During 1987 Antarctic Ozone Experiment

The Langley Research Center airborne differential absorption lidar (DIAL) system was operated from the Ames Research Center DC-8 aircraft to obtain profiles of ozone and polar stratospheric clouds (PSCs) in the lower stratosphere during the 1987 Airborne Antarctic Ozone Experiment (AAOE). A total of 13 long-range flights were made over Antarctica from Punta Arenas, Chile, from August 28 to September 29, 1987. During the development of the ozone hole over Antarctica, DIAL measurements of ozone and aerosol profiles were obtained in the altitude region from 11 to 22 km. An example of the measurement of the depletion of ozone over Antarctica is shown in the figure. The primary altitude region of the ozone reduction was found to be between 15 to 22 km. Over the period of this field experiment, the average ozone concentration at high latitudes (> 75°S) decreased by more than 50 percent. Along with ozone, PSCs were detected in the altitude region from 11 to 21 km. Many of the PSCs were found to be very large in vertical and horizontal extent. Some of the larger PSCs extended more than 5 km in altitude with considerable vertical structure. The horizontal extent of larger PSCs was greater than 10° latitude (> 1000 km). The PSCs have been associated with the depletion of ozone and exist in the coldest regions (< 195 K) of the Antarctic stratosphere.

(Edward V. Browell, 2576)

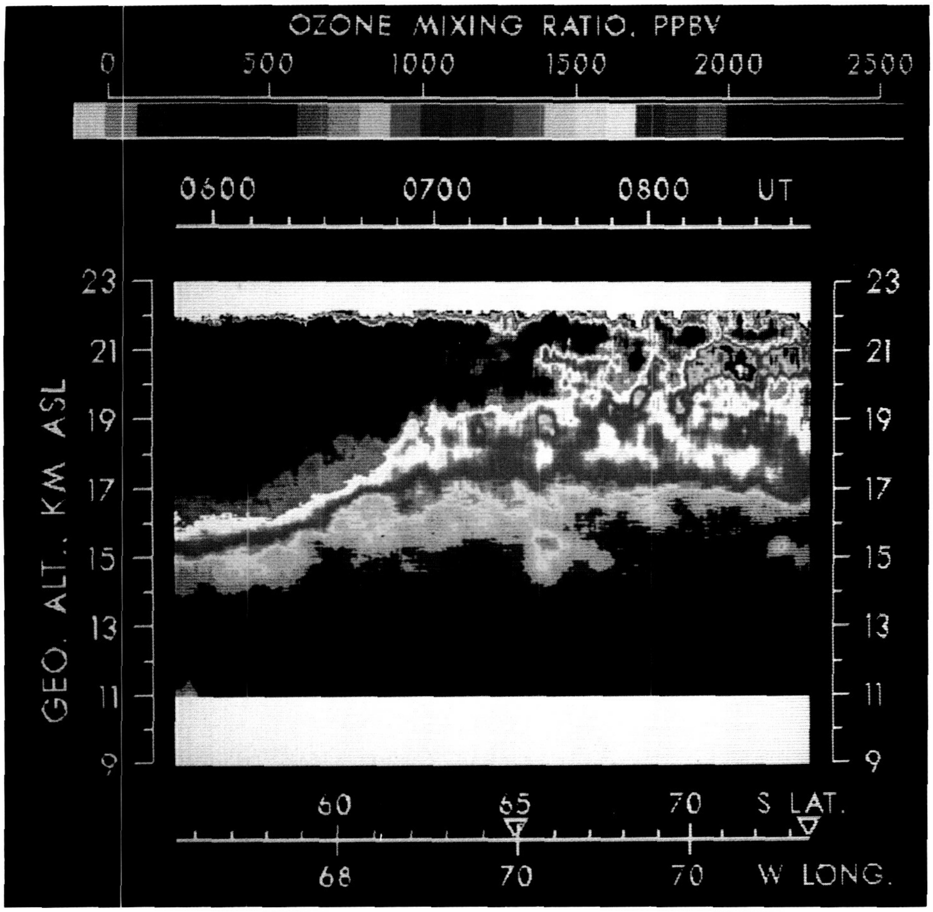

Airborne lidar measurements of ozone depletion over high latitudes (>63°S) in Antarctica on September 26, 1987. The ozone concentrations are mapped according to the color scheme on the top of the figure.

Tropospheric Ozone: Antarctic Ozone Hole

While emphasis has been placed on studying the stratosphere, its chemistry and dynamics associated with ozone hole formation and growth, and the net effect on global stratospheric ozone, it is also necessary to consider tropospheric effects. Such questions as the extent to which the ozone hole penetrates into the troposphere, the net mass exchange between the troposphere and the stratosphere, and whether the events in the stratosphere result in a net ozone change in the troposphere are important to understand ozone hole chemistry and the dynamics and net global effect of the hole.

Tropospheric ozone data obtained during the fall 1987 flights of the Ames Research Center DC-8 aircraft over Antarctica suggest that while tropospheric ozone changes are noted at flight altitudes from 10 to 12 km, these changes appear to be restricted to altitudes above approximately 9 km and localized to the vicinity of the hole. Ozone data at Punta Arenas, Chile, over a 1-month time frame, suggest little net change in background tropospheric

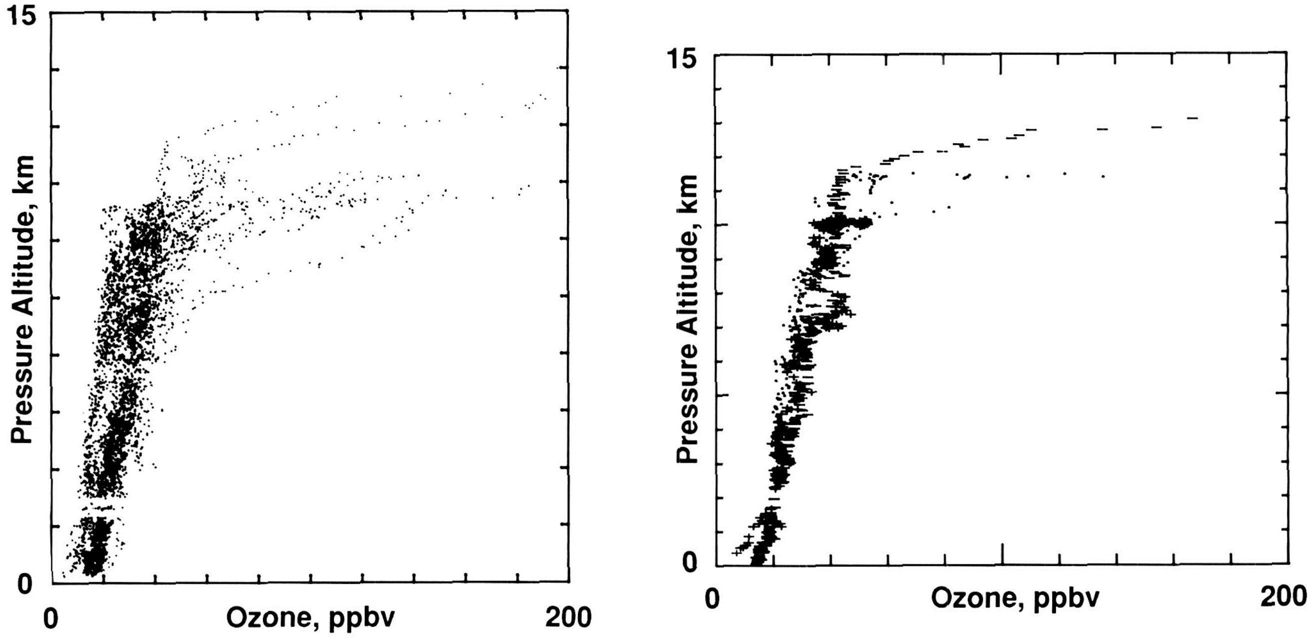

Landing and takeoff profiles (left) at Punta Arenas include 24 profiles taken from August 28 to September 21, 1987. Profiles (right) of September 21, 1987 include takeoff and landing at Punta Arenas, and ascent and descent at the South Pole.

ozone, if it is assumed that data at Punta Arenas (53°S) are representative of southern hemispheric ozone and that synoptic changes in tropospheric ozone would be detected at 53°S with the northern boundary of the hole at 65°S to 70°S. In addition and as shown by the single data set, ozone at the South Pole and ozone at Punta Arenas are nearly identical.

These results should not be interpreted as the troposphere being completely decoupled from stratospheric ozone hole effects. Locally and beneath the hole boundaries, tropospheric ozone shows sizable variation ranging from nominal background values of 20 to 50 ppbv to several hundred ppbv in "patches" or "pockets" of descended tropopause or stratospheric air. The ozone beneath the hole can average two to three times the background values. These pockets of descending air occur with high frequency beneath the hole boundary. In addition, the frequency of occurrence increased as the ozone hole deepened or grew from late August to early October. While more tropospheric data are required to conclusively answer these questions, initial observations suggest that the troposphere effects are restricted to the localized areas near the hole and then only to altitudes above approximately 9 or 10 km. **(Gerald L. Gregory, 4341)**

Amazon Rain Forest: An Ozone Sink

Tropical ecosystems are of considerable importance for atmospheric chemistry. Forested and wetland environments in the tropics store and cycle a significant fraction of the total carbon and nitrogen in the Earth's biosphere-atmosphere-ocean system. The biosphere acts as a source and/or sink for numerous atmospheric gases, some of which are major participants in photochemical and radiative transfer processes that determine the atmospheric chemical composition and climate of the Earth.

Data have shown the rain forest to be a significant sink for tropospheric ozone. Even during periods of significant biomass burning

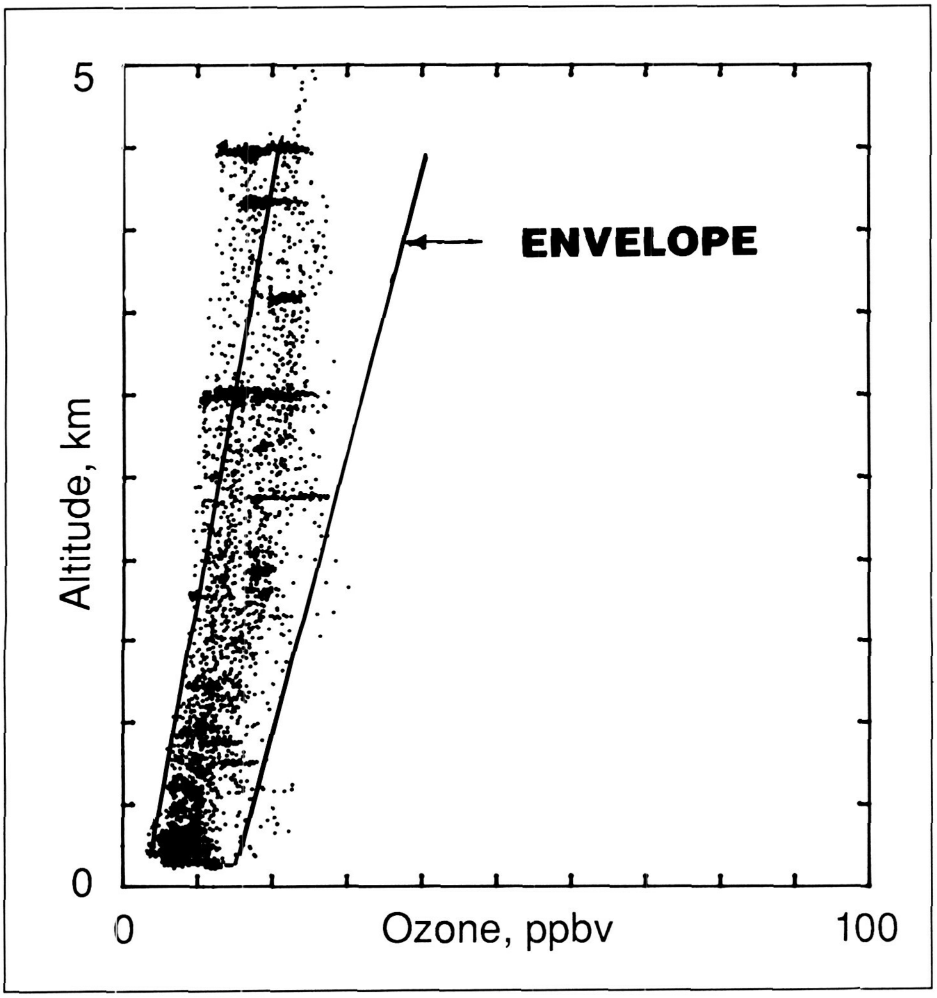

Ozone profiles of Amazon tropical rain forest from the wet season period of April 14 to May 8, 1987. Data are 1-min averages. The indicated envelope encloses the dry season data of July 18 to August 9, 1985.

in which photochemistry results in a net production of ozone in the mixed layer, the role of the forest sink does not go unnoticed. This sink is effective across the entire Amazon Basin. In the absence of significant biomass burning and resultant photochemistry, the surface sink is the dominant reaction affecting ozone in the tropical troposphere below the trade wind inversion. This reaction is largely the result of the consistency and strength of the sink and the constant mixing of the tropical troposphere as the result of the continuously forming, growing, and decaying convective cloud systems. The effectiveness of the surface sink can be seen by the consistency in which ozone profiles over the forest exhibit a negative gradient to the surface. The consistency of the surface sink itself is suggested by the observation of limited variability (excluding the biomass burning case) of ozone diurnally and on a day-to-day basis. As indicated, ozone at a given altitude and for a given season lies within about an envelope of 10 to 15 ppbv. Data show that in terms of lowering tropospheric ozone, the net effect of this surface sink is greater in the wet season than the dry season. This condition is probably more the result of improved mixing (i.e., improved communication between the surface and the overriding troposphere) associated with enhanced convection during the wet season rather than any magnitude increase in the strength of surface sink mechanisms.
(Gerald L. Gregory and Linda Warren, 4341)

Fire and Biogenic Emissions of Methane

Methane (CH_4), only a trace gas in the atmosphere, is a key player in the chemistry of the lower and upper atmosphere. In addition, methane is a greenhouse gas that impacts the global temperature of our planet.

Most of the world's supply of atmospheric methane is produced by microorganisms living in oxygen-deficient environments, such as wetlands and swamps. Recently, researchers at Langley Research Center discovered that the biogenic emissions of methane were significantly enhanced after a fire spread through a wetlands. The controlled fire took place at the Kennedy Space Center on November 9, 1987. Prior to the fire, biogenic emissions of methane from the wetlands were below the sensitivity threshold of the instrumentation. After the fire, both measurement sites containing diverse wetlands vegetation (Site 1: Juncus Effusus and Site 2: Spartina Bakeri) showed significantly enhanced methane emissions. No methane emissions were detected from the unburned controlled sites. All of these wetlands

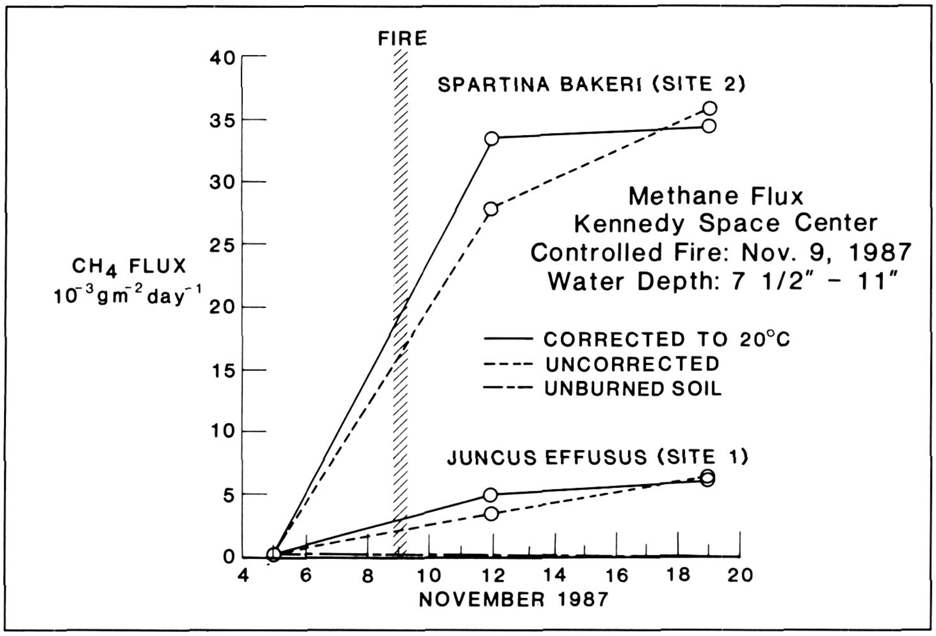

Biogenic emissions of methane from wetlands, before and after a controlled fire at Kennedy Space Center.

sites had 7½ to 11 in. of standing water during the measurements. The methane fluxes before and after the fire are shown in the figure. The broken line represents the measurements uncorrected for water temperature effects; the solid line represents the temperature-corrected measurements.

These measurements are the first data to show the significant effect that fire has on the biogenic emissions of methane. This is very important since the world's wetlands are very susceptible to burning from lightning-induced wildfires. These measurements identify another important link in the biogeochemical cycling of trace gases between the biosphere and the atmosphere. This research was performed in collaboration with personnel from the Kennedy Space Center and the United States Fish and Wildlife Service.
(Joel S. Levine, 2817 and Wesley R. Cofer III)

Trace Gas Emissions From Wildfires, Agricultural Burning, and Deforestation

Recently the National Academy of Sciences (1984 and 1986) recommended that major research efforts be undertaken to better characterize trace gas emissions from biomass (vegetation) burning. Emissions from large fires may contribute substantially to the global atmospheric budgets of carbon dioxide (CO_2), carbon monoxide (CO), methane (CH_4), nitrous oxide (N_2O), other oxides of nitrogen (NO_x), hydrogen (H_2), and numerous other trace gases. Many of these trace gases are very important in atmospheric chemistry and photochemistry (e.g., N_2O is responsible for most of the destruction of ozone in the stratosphere) and several (CO_2, CH_4, and N_2O) are greenhouse gases that are instrumental in regulating radiative transfer in the lower atmosphere, thus ultimately influencing our global climate.

Helicopters were used at low altitudes ($\approx$ 50 m above the fires) to collect smoke samples during several large ($\geq$ 500 acres) prescribed fires of dissimilar vegetation to assess the role of vegetation type on the nature of the trace gas emissions. Gas collections were made above burning chaparral in southern California, boreal forest in northern Ontario, Canada, and grassy wetlands in Florida. CO_2-normalized emission ratios for the primary trace gases

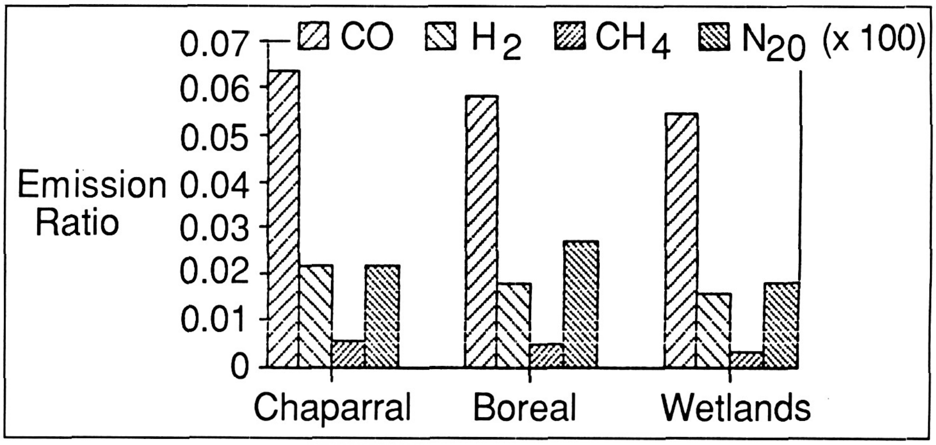

CO_2 normalized emission ratios for chaparral, boreal forest, and wetlands fires.

($\Delta X/\Delta CO_2$; V/V; X = trace gas) produced in these fires are shown in the figure. CO_2-normalization allows the comparison of reduced gas production during combustion from each vegetative type with the primary and fully oxidized combustion product, CO_2. As can be seen in the figure, emission ratios determined for CO, H_2, CH_4, and N_2O over vastly different vegetative habitats have revealed small differences. Although these results are based on a small sampling of vegetation, they do tend to suggest that vegetation type is not a major parameter in determining the composition of trace gas emissions from biomass fires. If so, modeling fire emissions on a global scale will be facilitated since vegetation type (which varies substantially on a global scale) should be of less consequence in determining the nature of the emissions than previously felt.

(W. R. Cofer III, 4372 and J. S. Levine)

Hypervelocity Aerophysics Facility Workshop

As part of an effort to assess the viability and technology requirements of a bold concept for greatly expanding the Nation's hypervelocity test capability, a workshop was held on May 10 to 11, 1988, at Langley Research Center for the purpose of conducting a critical review of a concept for a large hypervelocity ballistic range test facility. The facility would utilize Department of Defense (DoD)-sponsored electromagnetic launcher (EML) technology to launch large (on the order of 12 to 16 in. diameter) instrumented models into test chambers prepared to duplicate the densities and gas constituencies of the Earth's atmosphere and those of other planets. Key United States experts in the areas of hypersonic aerodynamics and aerothermodynamics, EML technology, and ballistic range technology defined specific experiments that could be conducted in such a facility, deemed the facility to be technically achievable, and outlined the research and development efforts required to assure success.

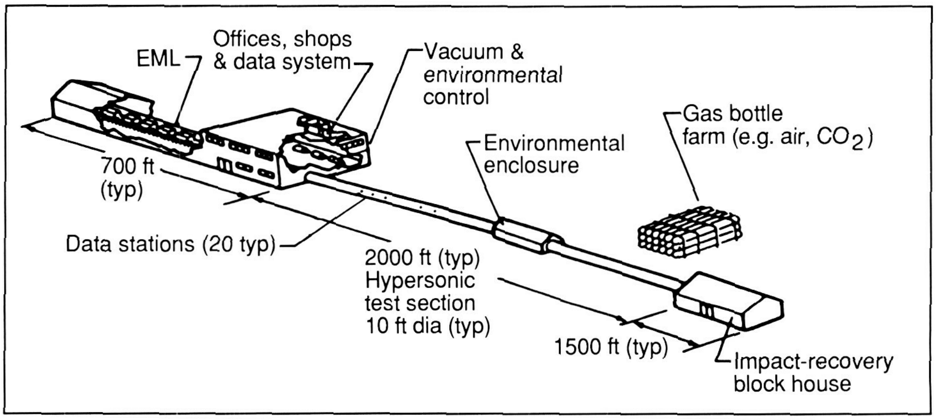

Diagram of proposed hypervelocity aerophysics facility.

The recommended approach for the launcher was the conventional rail gun. Workshop participants who were expert in EML indicated that the key technical issues regarding the application of rail gun technology to such a facility could be resolved, without enormous expense, through a series of experiments addressing relatively low-pressure, low-acceleration rate armatures. A tracked range (one in which the test model is guided through the test section by the use of constraining tracks) was also recommended, with the option of providing free-flight capability. Miniaturization and electromagnetic hardening of model instrumentation were also cited as technological needs.

(William I. Scallion and Robert D. Witcofski, 3984)

LDEF Reentry Predictions

Orbital lifetime analyses have been conducted by the Langley Research Center Space Station Office in support of proposed NASA-wide projects such as the space station, as well as currently operating spacecraft, such as the Langley Long-Duration Exposure Facility (LDEF). For each of these applications, orbit decay is simulated with the Orbital Lifetime Computer Program (OL). The atmospheric density for the OL is obtained using a Jacchia 1970 computer model, which includes density variations with altitude and is characterized by a nominal 11-year solar activity and geomagnetic activity cycle. In order to bound predicted reentry time, OL uses both nominal and two-sigma forecasts of solar and geomagnetic activity data which are published bimonthly by the Atmospheric Science Division of the Marshall Space Flight Center (MSFC).

Recent observations analyzed by MSFC resulted in a 19-month back-

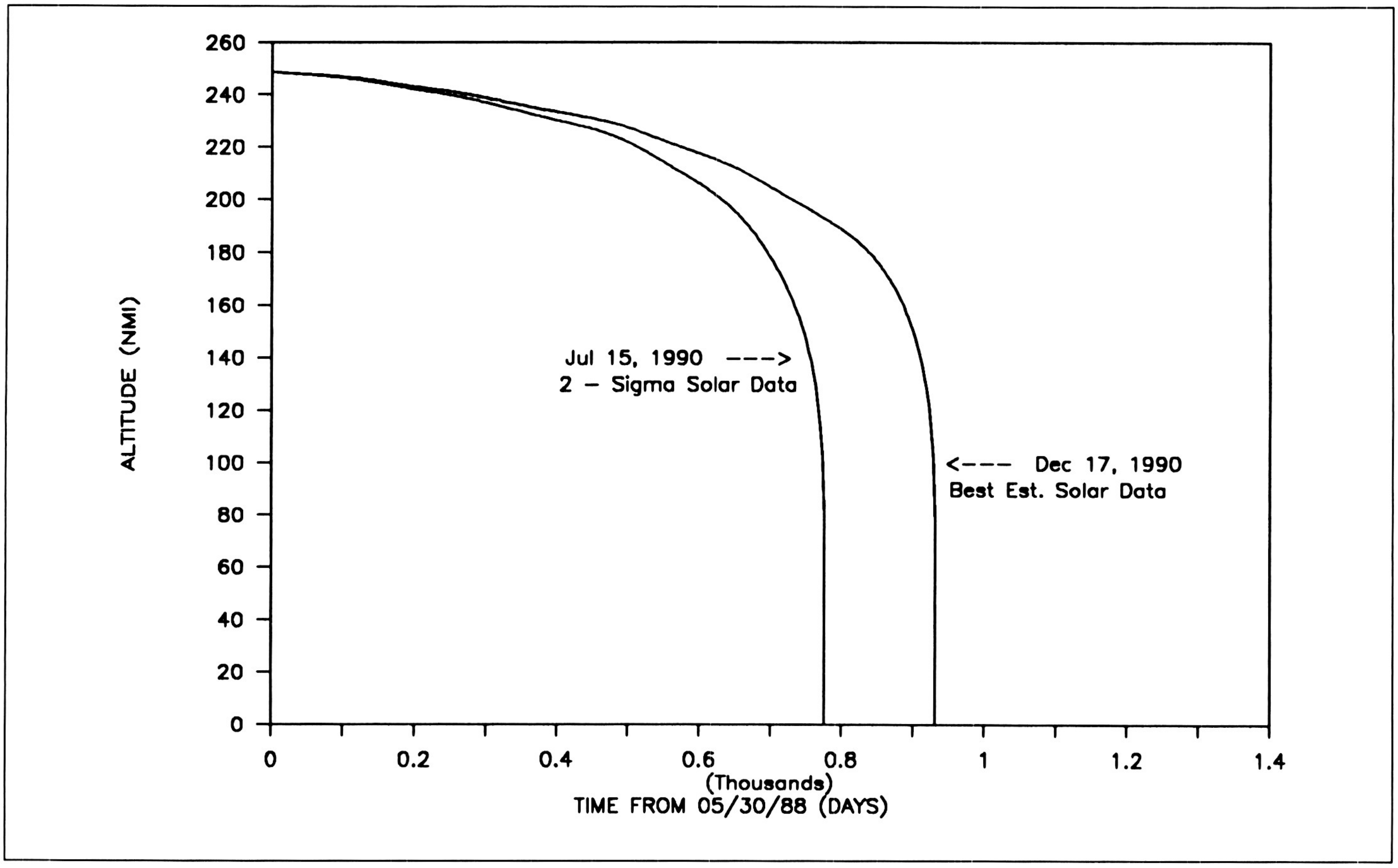

LDEF reentry altitude profiles.

ward shift in the predicted time of maximum solar activity from May 1992 to October 1990. The time shift has positive implications for the space station in that the 1995 to 1998 assembly period becomes one of lower solar activity than previously predicted. The remaining lifetime for LDEF, which was launched from the Space Shuttle orbiter in 1984, was adversely affected, however, due to the revised forecasts. LDEF had been manifested for retrieval by the Space Shuttle in 1991. Based on analysis performed using the Langley OL program, the LDEF reentry time period corresponding to the revised solar activity predictions was moved forward. This analysis included development of the "measured" altitude profile of LDEF from the time of its launch to the time of the most recent orbit determination provided by the North American Air Defense Command (NORAD); estimation of the effective ballistic coefficient needed to match the actual orbital decay using OL; and lifetime predictions based on the derived ballistic coefficient and the current MSFC solar activity data. As shown in the figure, the LDEF reentry time interval (obtained using the best estimate and two-sigma solar and geomagnetic data from the MSFC April 1988 report and initial conditions defined by the NORAD May 30, 1988 orbit solution) is mid- to late 1990. As a result, the Space Shuttle Transportation Systems office has been informed, and a revised manifest has been proposed. **(G. Mel Kelly; L. J. DeRyder, 4826)**

Articular Dynamic Analysis of Spacecraft Systems

The dynamic environment onboard the space station is an issue of concern to NASA engineers. Onboard operations, such as the Space Shuttle orbiter berthing, payload retrieval, and deployment using the remote manipulator system (RMS) arms; Mobile Servicing Center motion; and large area solar array Sun-tracking must be evaluated in

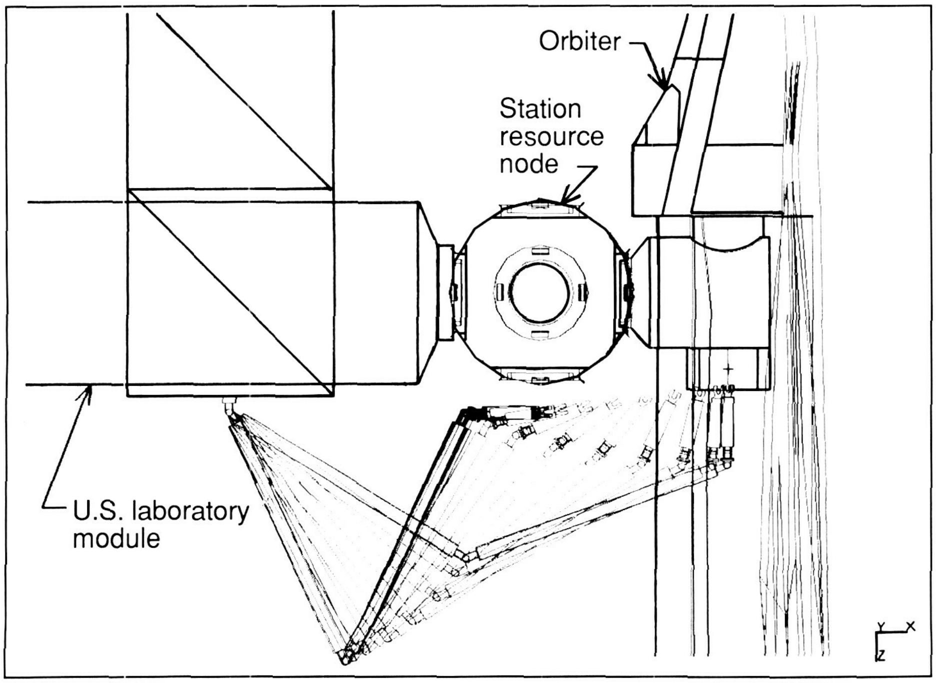

Space station RMS retrieves payload from Space Shuttle orbiter cargo bay.

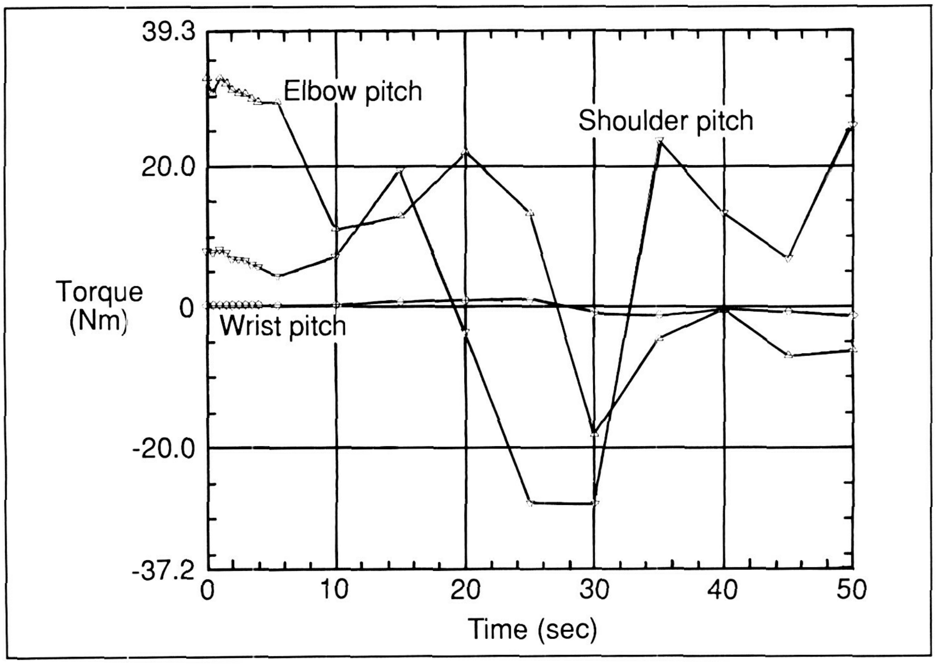

Space station RMS applied torque during payload retrieval.

terms of flight controllability. Furthermore, prospective space station customers have specific microgravity environment and payload pointing accommodation requirements for proposed experiments. The Articular Dynamic Analysis of Spacecraft Systems (ADASS) software has been developed and integrated into the space station multidisciplinary engineering and analysis software package, IDEAS^2, in order to simulate the space station articular dynamic environment. ADASS models the force and motion behavior of articular dynamic Earth-orbiting spacecraft undergoing large displacements. ADASS can be used to assess spacecraft attitude performance and requirements and to compute the rigid-body response (microgravity environment) resulting from modeled system dynamics. Forcing functions can be generated for use in structural dynamic studies. The RMS-transmitted joint control and reaction forces and torques, as well as structural part clearances during prescribed kinematic paths, can be determined.

ADASS has been developed by integrating the kinematic and dynamic solver software package called Automatic Dynamic Analysis of Mechanical Systems (ADAMS) into IDEAS^2. The six-degree-of-freedom software package models the orbital environment (gravity, gravity gradient, aerodynamic, and solar pressure) forces and torques. A closed-loop flight attitude control system and articulating appendage Sun-tracking (alpha, beta) logic and control system have been modeled to allow dynamic spacecraft simulation. Preprocessors and postprocessors have been developed to facilitate a user-friendly simulation setup and quick and clear graphical results interpretation, all of which are accessed through a common relational data base. A time-elapsed ADASS generated picture illustrates a space station RMS retrieving a payload located in the Space Shuttle orbiter cargo bay. The applied RMS joint torque required for the prescribed motion is illustrated. **(Brent P. Robertson and L. J. DeRyder, 4826)**

Space Station Steady-State Microgravity Environment

One of the principal functions of the space station is to provide a low-gravity research facility for scientific and industrial utilization. As currently configured, the space station contains three pressurized laboratory modules (two of which are provided by our international partners) in which microgravity experiments can be performed and tended by man. The microgravity requirements of the experiments range in level from 100 μg to 1 μg with durations as long as 30 days. To ascertain the feasibility of obtaining the low-acceleration environment, the Langley Research Center Space Station Office simulated the steady-state environmental forces that act on the modeled space station configuration to determine the resultant sensed microgravity environment.

The steady-state microgravity environment sensed on the space station is due to the gravity gradient field, aerodynamic drag, station attitude, and rotational motion. These factors make it highly dependent on the space station configuration. The Articulated Rigid Body Control Dynamics (ARCD) module of the IDEAS^2 software package was used to compute the steady-state microgravity environment. The figure shows a closeup of the laboratory modules as seen in a front and side view of the November 1987 reference space station configuration flown at torque equilibrium attitude with atmospheric conditions as indicated in the figure. Superimposed are the 1-μg and 2.3-μg contours resulting from the environmental forces. It is a goal to provide a 1-μg steady-state environment to the laboratory modules; however, as seen in the figure, portions of the United States laboratory module experience up to 2.3 μg over an orbit for the conditions and configuration studied. Based on the microgravity results obtained, alternate space station configurations are being examined to reduce the steady-state microgravity environment. The most promising solutions involve relocation of the center of mass to fall within the laboratory module.

(Laura Waters; L. J. DeRyder, 4826)

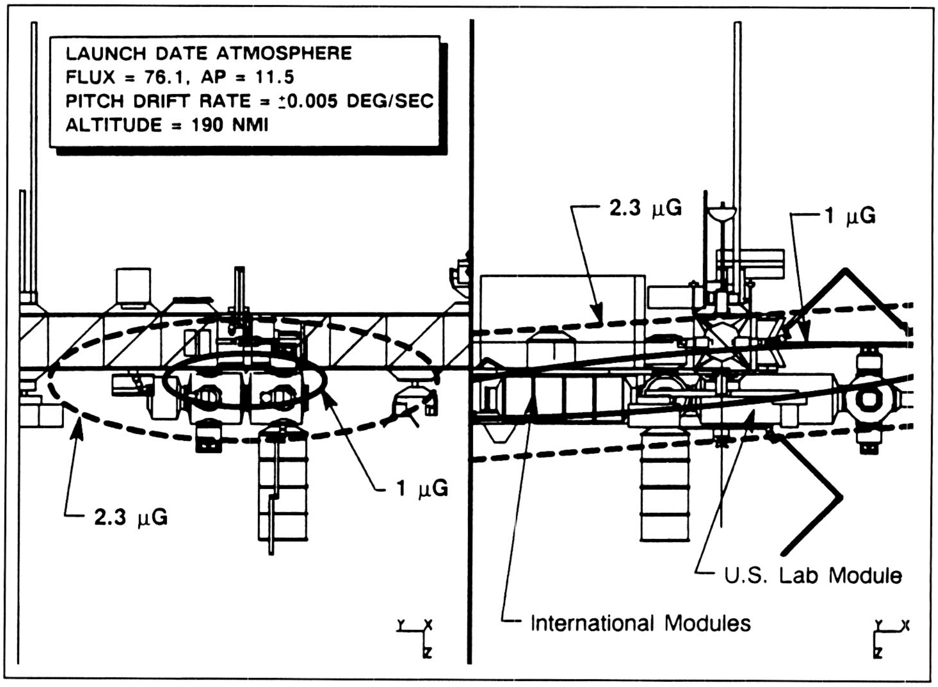

Steady-state microgravity profiles on space station.

Stationkeeping Platform Utilization for Space Station Assembly

The Langley Research Center Space Station Office has been evaluating alternate space station assembly configurations in an attempt to accommodate the conflicting constraints imposed by the lift capacity of the Space Shuttle orbiter, and the requirement that each station assembly flight be a complete spacecraft. Following each orbiter departure, multiple subsystems must be operational in order to assure space station survivability. To this end, consideration was given to the utilization of a stationkeeping platform (SKP).

As shown in the figure, the SKP is a stand-alone, prevalidated "utility bus," complete with power provided from the gimballed solar arrays, a propulsion reboost system, attitude control, communication capability, thermal system, and a payload accommodation platform. Launched prior to the first assembly flight of the space station, it nominally operates in close proximity and docks with the completed operational space station every 3 months for payload recycle.

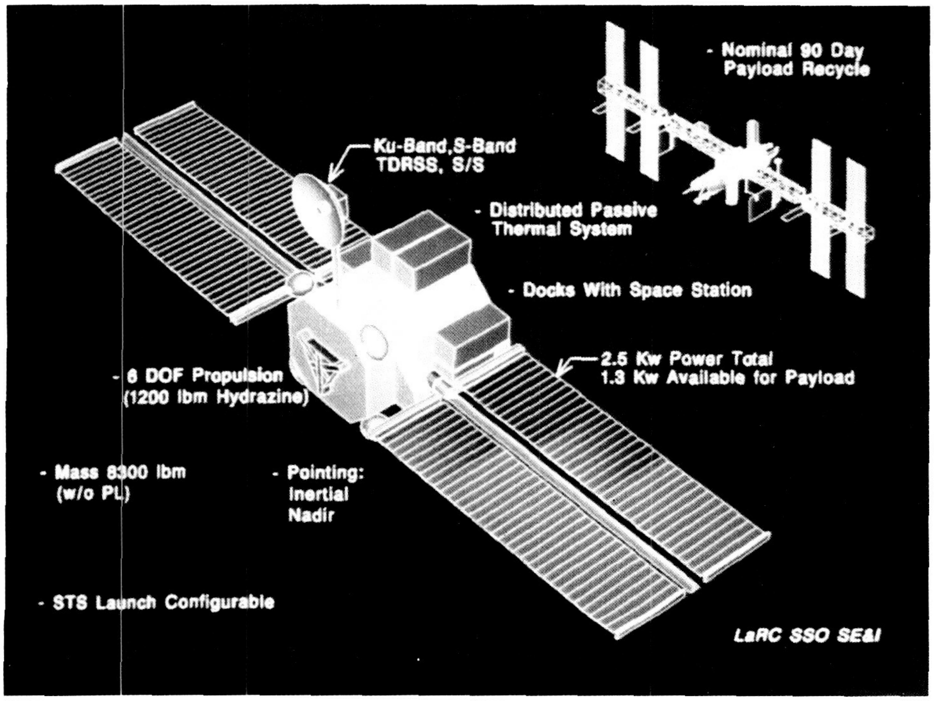

Stationkeeping platform.

The SKP analysis was performed using the multidisciplinary computer-aided engineering software package IDEAS[2]. Results indicated that the SKP could provide the necessary resources to sustain the early space station flights. For example, while mated to the station, it could provide power, reboost, and communication. Assembly could take place at lower altitudes (since the SKP propulsion system will already have been flight verified), thus allowing the Space Shuttle to manifest additional mass. Complete subsystems (e.g., preintegrated nodes, photovoltaic array pairs, integrated structure, utilities, and avionics) may be independently assembled and verified on-orbit. In the event of a premature orbiter departure, the SKP was shown to have sufficient propellant reserves to serve as a contingency backup to maintain attitude control and provide orbital reboost.

Two flight attitude modes were studied. With the SKP mated at the end of the transverse boom opposite the solar arrays, the "arrow" configuration had the minimum area along the velocity vector. The gravity gradient attitude had the transverse boom aligned along the local vertical. The 90-day SKP reaction control system (RCS) attitude-control propellant requirements were 45 lb and 85 lb for the arrow mode and gravity gradient mode, respectively. The 90-day orbit reboost requirements were 225 lb and 240 lb, respectively. With a total capacity of 1200 lb of fuel, this would allow up to five 90-day reboost cycles. Therefore, neither flight mode was superior to the other.

(Michael Heck; L. J. DeRyder, 4826)

Offset Truss Space Station Configuration

The currently baselined space station has a configuration geometry characterized by asymmetrical physical properties. The environmental forces and torques acting on a low-Earth-orbiting spacecraft like the space station must be accommodated by the onboard flight control system. Asymmetric physical characteristics generally increase attitude control sizing requirements. In particular, the space station configuration has a 4-m offset between the center of aerodynamic pressure CP and the center of mass CM which results in an aerodynamically induced positive torque about the station's pitch axis. In general, gravity gradient torque can be used to offset the aerodynamic torque about the pitch axis; however, the space station configuration with its cylinder-like inertias yields little gravity gradient torque about the pitch axis. The attitude at which the environmental torques balance each other yielding the minimum control momentum requirements is defined as the torque equilibrium attitude (TEA). The space station has a pitch TEA that will vary from $-6°$ to $-16°$ from a local vertical local horizontal (LVLH) attitude during the lifetime of the configuration. This variation in attitude is directly related to the station operating altitude as well as the 11-year solar cycle and to their impact on atmospheric density and the associated induced aerodynamic torque resulting from the station's CP/CM offset.

Current payload pointing requirements have been established for the space station program which require attitude stability to within 5° of the LVLH attitude. These requirements

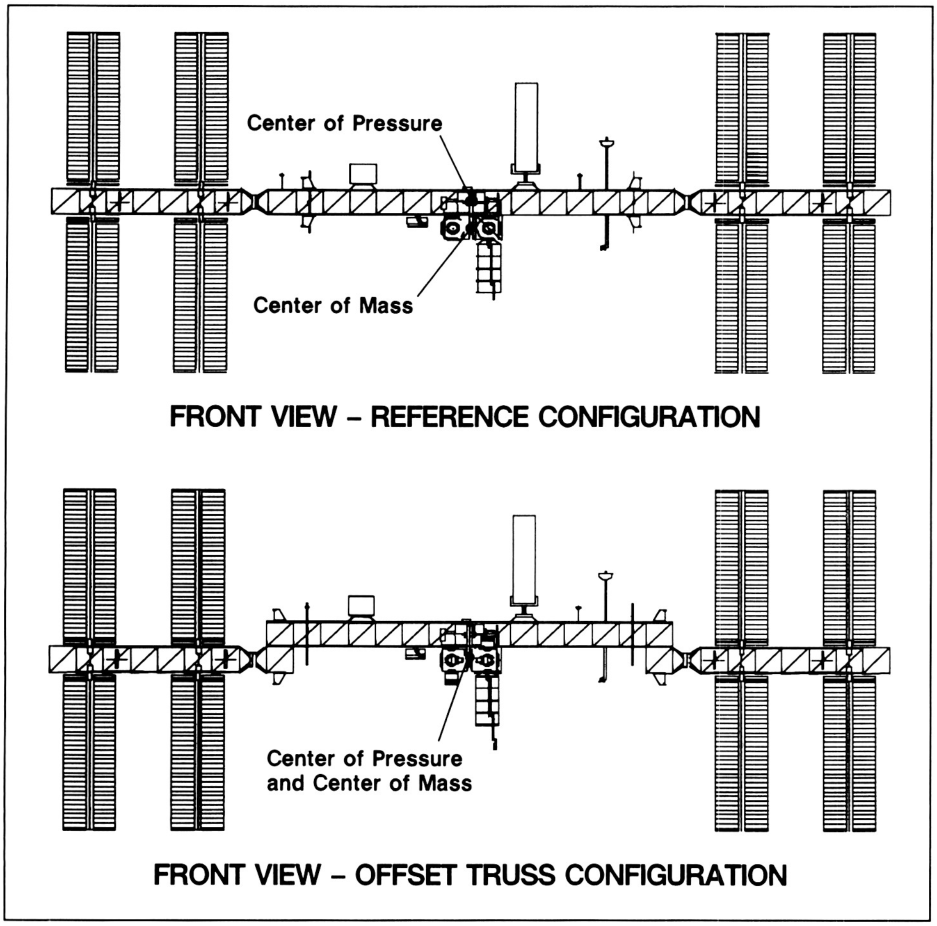

Configuration comparison.

cannot be satisfied by the current space station configuration using angular momentum storage devices such as control moment gyroscopes. The Langley Research Center Space Station Office has proposed reducing the pitch TEA on the space station configuration by lowering the truss outboard from the alpha joints by 5 m so that the centers of the solar arrays are aligned with the station's center of mass, thus greatly reducing the CP/CM offset. For a given launch date and altitude, this offset truss configuration produces a pitch TEA of only –2.7° compared to –16° for the configuration; this TEA is provided without adversely impacting other existing system requirements. Furthermore, the variation in the offset truss configuration attitude over its lifetime is also reduced to less than 2° in pitch since the station is no longer as sensitive to aerodynamic variations. Another enhancement resulting from the offset truss configuration is that the station's center of mass is moved closer to the center of the laboratory module and results in lower steady-state microgravity accelerations sensed by laboratory experiments. The offset truss configuration greatly reduces the aerodynamic asymmetry resulting in lower control requirements, a smaller pitch TEA, and enhanced payload accommodations.
**(Patrick A. Troutman;
L. J. DeRyder, 4826)**

Space Station Accommodation of European Hermes Vehicle

The Langley Research Center Space Station Office has identified and assessed potential space station docking port locations to accommodate the European Space Agency's Hermes spaceplane. The Hermes vehicle will weigh approximately 21 metric tons with a length of 15.5 m and a wing span of approximately 10.5 m. The docking port is located in the rear with cold-gas thrusters used for the rendezvous phase.

The spacecraft modeling and analysis for this study was performed with the IDEAS^2 computer program. In particular, the Geomod (geometry modeling) module was utilized to construct the solid geometry and to ascertain docking clearances with respect to the space station; the SSPLIMP (Space Station Plume Impingement Program) module was used to evaluate plume impingement station impacts due to the docking Hermes; and the Articulated Ridge-Body Control Dynamics (ARCD) module was used to assess the impact of the docked Hermes on space station flight control.

Ten potential docking port locations were selected and evaluated with respect to several criteria, such as the clearance between the station's elements and Hermes, the complexity of approach rendezvous and proximity operations, the impact of Hermes on the flight characteristics of the space station, and the station's remote manipulator system access for final berthing operation via the grapple. These locations were labeled from 1 to 10 and are shown in the figure. Two docking locations (front

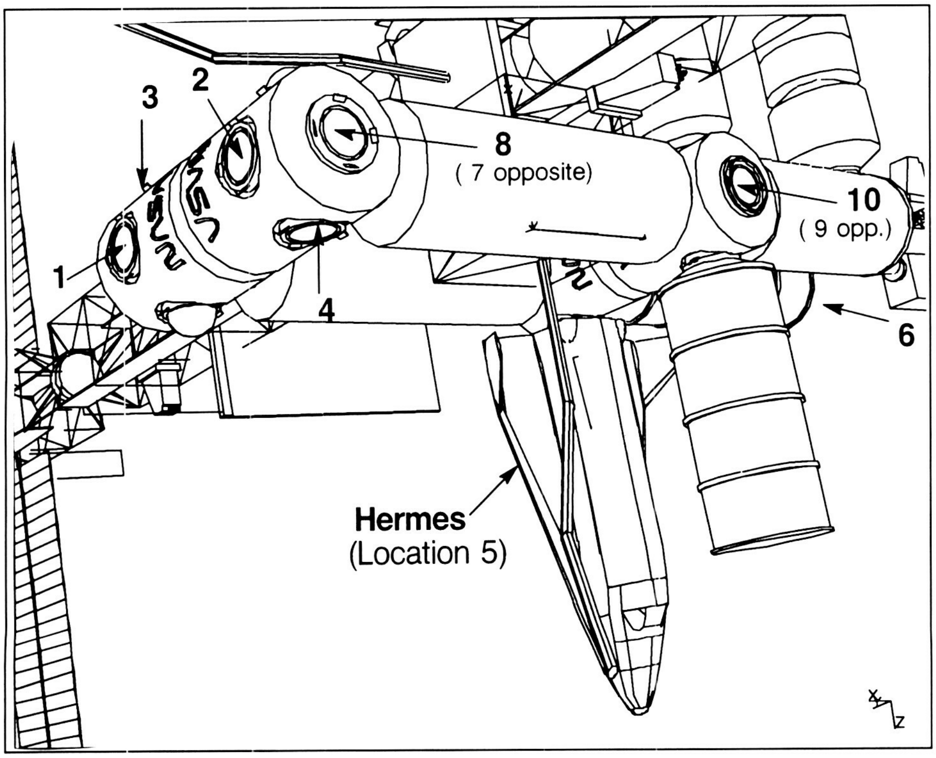

Hermes spaceplane docked at bottom of starboard aft node.

of the starboard forward node and front of the port forward node, i.e., locations 1 and 2, respectively) appeared to be the best all-around choice since there were no clearance problems. The approach path was unobstructed along the $+X$ axis (i.e., along the station's velocity vector). Furthermore, no negative impact was found on the station's attitude and control. However, Hermes cannot use these locations while the Space Shuttle orbiter is docked (location 2 is the primary orbiter docking port), and the Hermes docking port must work with the Space Transportation System docking adapter. Location 3 was found viable in the presence of a concurrent docked orbiter. The most unfavorable locations were found to be on the side of the starboard aft node and the side of the port aft node (i.e., locations 9 and 10, respectively). These docking locations had serious clearance and docking operation problems.
(Zoran N. Martinovic; L. J. DeRyder, 4826)

Evolution Requirements Definition for Space Station Preliminary Requirements Review

The Space Station Program initiated its Preliminary Requirements Review (PRR) for the design and development phase in April 1988. The objective was to adopt a consistent set of system requirements, thereby allowing the work package centers and contractors to proceed with the development of preliminary designs for the various elements and subsystems. The Langley Research Center Space Station Office (SSO), in the role of technical lead for the space station evolution definition, was responsible for developing and advocating requirements for the space station and platform growth at the PRR. In this capacity, mission and systems analyses were performed at Langley to identify growth requirements necessary for the principal evolutionary paths or options for the space station. One future option addresses the accommodation of bold new initiatives as identified by the National Commission on Space and the Sally K. Ride report, "Leadership and America's Future in Space."

To support initiatives such as the Humans to Mars and Lunar Base projects, the space station serves first as a facility for life science research and technology development and eventually as a transportation node for vehicle assembly and servicing. Another viable evolutionary path involves continued growth of the space station as a multipurpose research and development (R&D) facility for science, technology, and commercial endeavors. For these options, mission and systems analyses were conducted by the Langley SSO to determine primary resource requirements such as power, crew, and volume. For example, studies of multidiscipline, R&D growth at the space station involved analysis of a number of considerations, each of which emphasized a particular discipline on the space station (e.g., microgravity research). Resource levels constrained by lift capability were determined utilizing transportation models with expendable and heavy lift launch vehicles as well as the Space Transportation System. These data, along with those from the transportation node analyses performed at the Langley SSO, comprised the foundation for

	Crew		Facilities	
Science, commercial technology R&D accommodation	User: 20	Total: 24	4 U.S. labs:	1 human life science; 1 animal & plant science; 2 materials processing <u>or</u> 1 mat processing + closed environmental life support system (CELSS)
	Power (kW)			
	User: 170	Total: 275	1 European Space Agency lab (ESA) 1 Japanese Experiment Module (JEM) 3 HABS	3 attached press. payloads 1 servicing bay (+ Orbital Maneuvering Vehicle) 1 Orbital Transfer Vehicle hangar
	Crew		Facilities	
New initiatives accommodation	User: 17-20	Total: 21-24	3 U.S. labs:	1 assembly/serv. lab 1 human life science 1 CELSS
	Power (kW)			
	User: 110-130	Total: 205-225	1 ESA lab 1 JEM 3 HABS	2 attached press. payloads 1 assembly hangar 1 servicing bay (+Orbital Maneuvering Vehicle)

Space station resource requirements derived for mature operational phases of principal evolution options.

evolutionary requirements derivation. Inputs from other sources were assessed and integrated at an intercenter working session hosted at Langley in February of 1988. Primary Phase I design accommodations for evolution were identified. The table presents the power, crew, and facility requirements selected by the Langley SSO for the two principal evolution options. Due to these results, Langley recommended that the Phase I space station be capable of growth to 275 kW of power, a crew of 24, three habitat modules, six laboratory modules, three mini-laboratories, a servicing bay, and an assembly hangar.
(Barry Meredith, 4830)

Space Station Accommodation of Human Expeditions to Mars

The NASA Office of Exploration is developing plans and options that meet the National Space Policy directive of "expanding human presence and activity beyond Earth orbit into the Solar System." Langley Research Center studies have focused on the use of the space station as a transportation node where the space transportation systems are assembled, checked out, and fueled. In one study the requirements for support of a set of three missions to Mars have been established. These missions use the "split sprint" approach of sending a cargo vehicle ahead to Mars orbit on a low-energy trajectory followed

by a piloted vehicle on a fast, high-energy trajectory. (Total crew trip time is 14 months.)

The space station is used for precursor research and technology development, beginning at the permanently manned capability (PMC). A life sciences program has been established to determine countermeasures for the deleterious effects of the zero-g environment (cardiovascular system deterioration and bone mass loss are two major effects). This program is initiated at the PMC and requires an additional laboratory module plus a pressurized facility containing a 4-m centrifuge.

The most important technology development activity is the establishment of the capability to assemble and check out large, complex vehicles (including large aeroshells) in the 1- to 2-million-lb class. Other systems requiring on-orbit test and validation include environmental control and life support system (closed air and water); automation and robotics, automated rendezvous and docking systems; cryogenic storage and transfer systems; extravehicular activity (EVA) equipment; automated communications and tracking systems; and electrical power systems.

The space station must rapidly grow to accommodate these activities. Crew size must increase to 14 and power levels to 150+ kW. At least one additional laboratory and one additional habitation module are required. Once assembly of the Mars vehicle begins, additional resources must be added. The assembly crew is currently estimated at six. This number assumes major application of telerobotics and highly automated systems with self-check and fault-tolerant capabilities. Extensive studies are currently under way to define more precisely the resources required to perform this function. The total resources for the space station as a mature transportation node to support the Mars case study include an 18-person crew, five laboratory modules (including the European Space Agency (ESA) and the Japanese Experiment Module (JEM) laboratories), three habitat modules, two attached pressurized payloads, one assembly hangar, one servicing bay (with orbital maneuvering vehicles), and 225 kW of power.

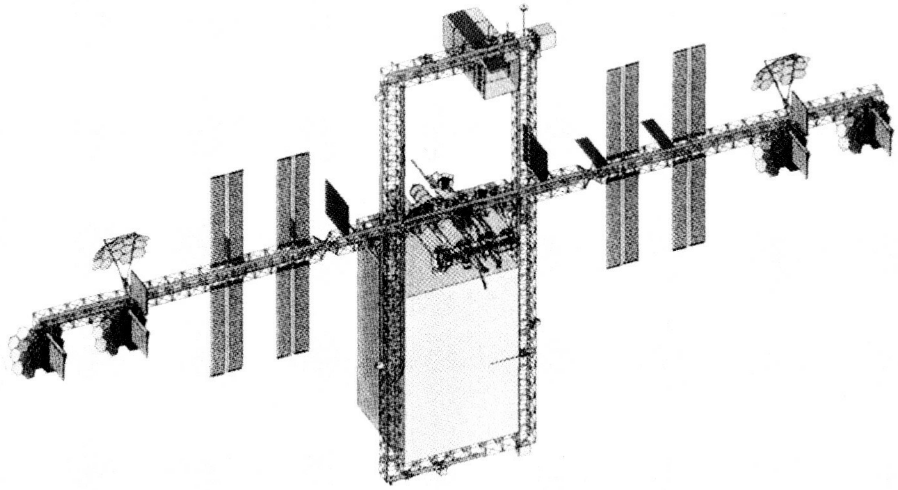

Mars transportation node concept.

One concept of the space station with these capabilities is shown in the figure. This concept adds dual keels to the space station to serve as locations for attaching the large Mars vehicle hangar and the servicing bay (used to service platforms and free flyers and to accommodate the orbital maneuvering vehicles). Observational instruments can be accommodated on the upper and lower booms. As shown in the figure, power growth is through the addition of 25 kW solar dynamic power units. The mass of this system is about 470 metric tons (without the Mars vehicle), which is more than double the mass of the Phase I space station.

Additional concepts of the space station as a transportation node will be developed as the Mars vehicle concepts are further defined. On-orbit assembly and processing studies will establish the impacts of these activities on the space station research program.
(E. Brian Pritchard, 4830)

Development of Thermal Imaging Technique Using Two-Color Thermographic Phosphors

A thermal imaging technique has been developed for wind tunnel surface temperature mapping using thermal luminescent characteristics of a temperature-sensitive phosphor coating. The technique has potential for quantitative surface temperature measurements to provide temperature-time data necessary for

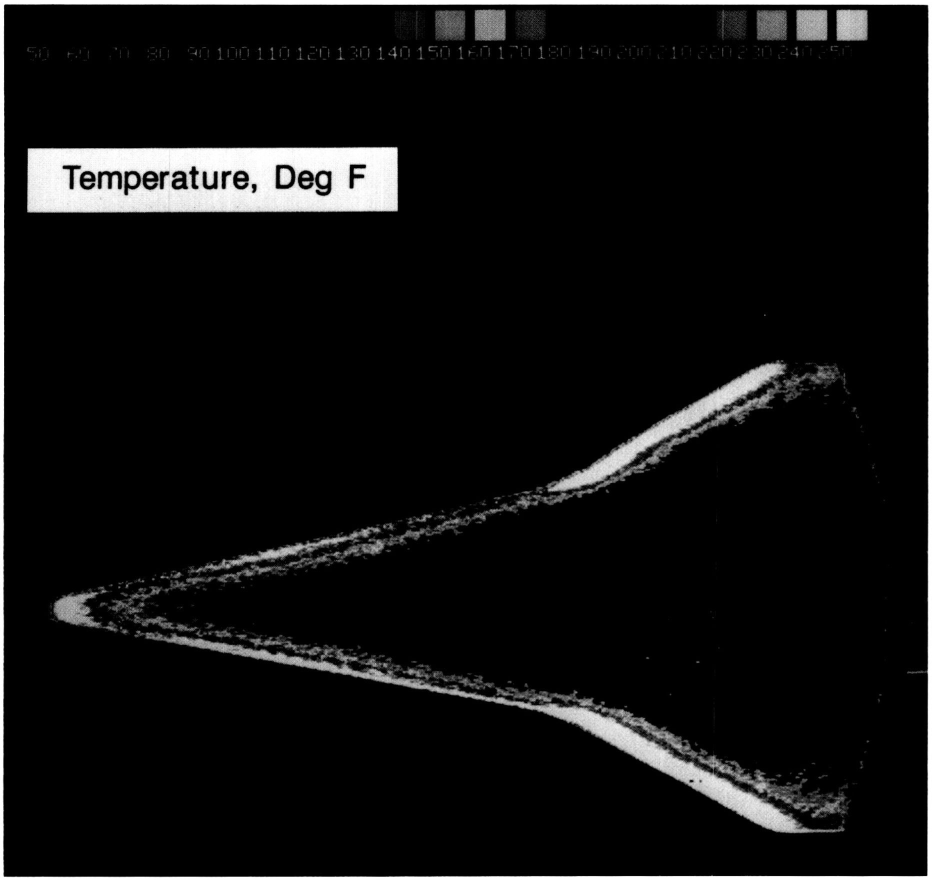

Windward surface temperature mapping on a transatmospheric model in 31-Inch Mach 10 Tunnel.

thin-film heat transfer calculations. With this technique, aerothermodynamic hypersonic wind tunnel test models can be constructed at a fraction of present model costs, and much more quickly, since intricate thermal instrumentation and wiring of these small models can be replaced by a simple coating. Also, since the phosphor mechanism is completely reversible, model test setup times are significantly reduced in comparison with phase-change paint techniques and other commonly used thermal chemical coatings because a given model can be tested over and over again with only a single coating.

The technique is implemented by using a ratio of the measured blue-to-green (450, 520 nm) emission from a phosphor coating excited by an ultraviolet (365 nm) source. Separately filtered images are recorded from a three-tube color camera, utilizing off-the-shelf front-end video optics to discriminate wavelengths. Digital processing is used to calculate surface temperature profiles from video image data.

Tests demonstrating the Thermal Imaging System (TIS) were performed in the 31-Inch Mach 10 Tunnel using phosphor-coated cast ceramic models. Shown in the figure is a windward surface temperature mapping on an 11-in. strake/wing transatmospheric vehicle. Tests also included a 12.84°/7° straight biconic with a 3-in. base, and a 9.5-in. slender blunted cone. Image data were recorded on $^3/_4$-in. videotape and processed at the Langley Research Center Image Processing Laboratory.

Feasibility of the technique has been successfully demonstrated with the available equipment for recording and processing image data. Work is currently under way to develop a dedicated digital acquisition/image processing system that will provide much higher data quality along with on-site data processing capability.
(Gregory M. Buck, 3984)

Supersonic Characteristics of Modified Circular Body Vehicles

One concept now under study as an advanced Space Transportation System is based on the requirement of full reusability. This results in a single-stage-to-orbit vehicle that carries propellant internally, is launched vertically, and lands horizontally. The basic configuration consists of a fuselage having a circular cross section, a cropped delta wing, and a large vertical tail. The circular body vehicle is 197 ft long, which is about twice the size of the Space Shuttle orbiter. This study has been expanded to ascertain the effects of two alternate versions on the aerodynamic characteristics. One version employed wing tip fins instead of the vertical tail, whereas the second version used a small nose-mounted dorsal fin with fuselage side brakes. Force-and-moment tests were conducted in the Unitary Plan Wind Tunnel at Mach numbers of 2.3, 2.96, 3.9, and 4.6. Data on the basic vehicle

ORIGINAL PAGE
COLOR PHOTOGRAPH

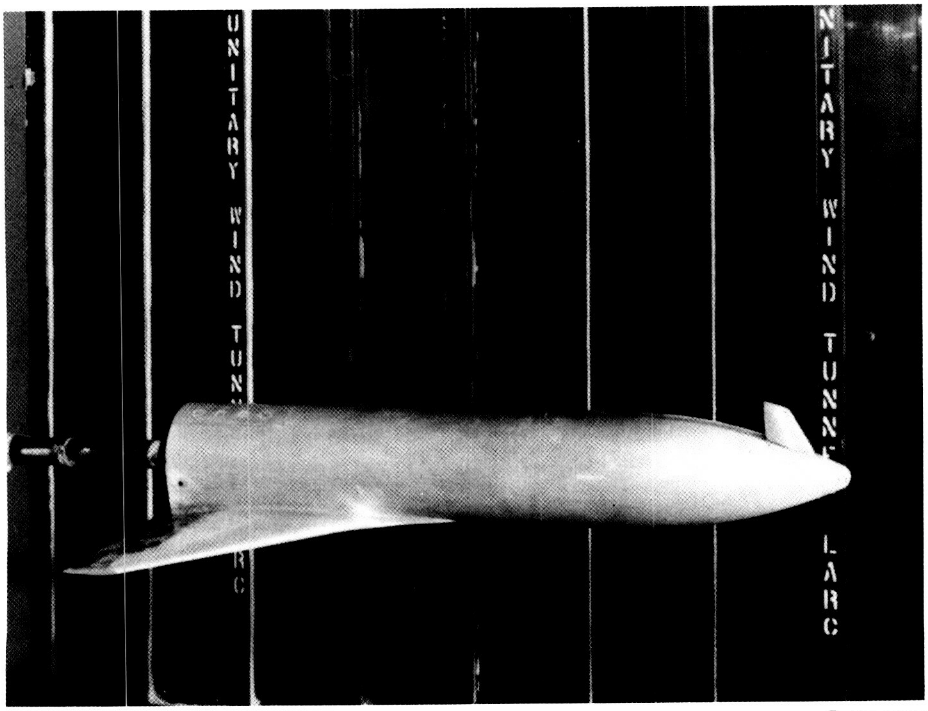

L-87-4420

Dorsal fin model mounted in Unitary Plan Wind Tunnel.

and the two alternate versions were obtained over an angle-of-attack range of 0° to 22° at a Reynolds number of 4.3×10^6, based on fuselage length.

For all three models, stable trim conditions were obtained at $M = 3.9$ and 4.6 by using elevon controls. The vertical-tail model yielded stable trim at the two lower Mach numbers. The tip fin and dorsal versions generally had only neutral stability for $M = 2.96$. At $M = 2.3$, the dorsal model indicated stable conditions at the operational angle of attack of 10°, whereas the tip fin model was unstable. With the center of gravity located at 72 percent of the fuselage length, the tip fin and dorsal versions were directionally unstable. Directional stability existed for the vertical-tail model, but only at angles of attack below approximately 10°. A positive effective dihedral was obtained over the angle-of-attack range of 0° to 22° for the vertical-tail model. For the other two versions, a positive dihedral was indicated at angles of attack above approximately 10°. In general, it appears the basic model with the large vertical tail yielded better longitudinal and directional stability characteristics when compared with the alternate versions.

(P. T. Bernot, 3984)

Low-Density Flow in Langley Hypersonic CF_4 Tunnel

Some of the aerodynamic effects of air dissociation ("real-gas effects") between the shock and body of an entry vehicle during flight can be simulated by reproducing the density ratio across the normal shock in a wind tunnel. The Langley Hypersonic CF_4 Tunnel uses tetrafluoromethane (CF_4) as a test gas, which allows a partial simulation of real-gas effects by producing a normal shock density ratio of approximately 12, which is closer to the flight value (approximately 17) than the ratio obtainable in an air or nitrogen tunnel (approximately 6). Some vehicles not only fly at very high velocity, which results in shock-induced dissociation, but at very high altitude as well. This high-altitude flight occurs in a low-density flow field that is not generally available as a test condition in this Nation's hypersonic facilities. These low-density effects can change vehicle aerodynamic characteristics dramatically, particularly for blunt-body configurations. (An example of a class of high-velocity, high-altitude flight vehicles with blunt configurations is the aeroassisted orbital transfer vehicle, AOTV.)

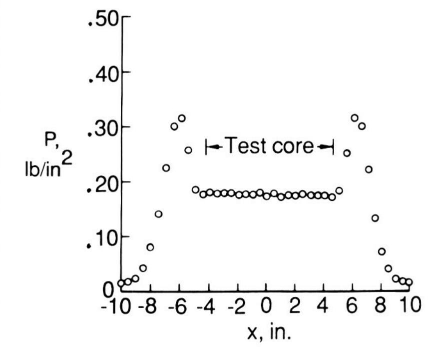

Test stream pitot pressure profile in Langley Hypersonic CF_4 Tunnel at reservoir pressure of 133 lb/in^2.

In an attempt to better simulate the high-altitude, low-density flight conditions, the Langley Hypersonic CF_4 Tunnel has now been successfully operated at a reservoir pressure as low as 100 lb/in^2. The normal reservoir operating pressure is in the range from 1500 to 2000 lb/in^2. Measurement with a

pitot rake at the low-pressure condition indicated a nearly constant pitot pressure distribution over an 8-in.-diameter core, which is comparable to the high-pressure test core size.

Much work will be required to assure that flow conditions are correctly calculated and that all types of wind tunnel testing can be carried out in this low-density environment. However, results obtained so far suggest that the effects of a high value of normal shock density ratio and low test stream density may be obtained in the same test environment.

(R. E. Midden and W. L. Wells, 3984)

Miniaturized Water-Cooled Pitot-Pressure Probe for Flow Field Surveys in Hypersonic Wind Tunnels

Pitot pressure is among the measurable parameters that are useful for defining the flow conditions about an aerodynamic configuration, and, in general, a pitot-pressure probe is among the simplest to fabricate and use. However, the need for accurately measured pitot-pressure profiles in the relatively thin shock layer about models at hypersonic speeds, to evaluate and calibrate computational fluid dynamic computer codes, places constraints on tube size, pressure settling-time, and transducer temperature.

By locating the pressure transducer within the probe body and cooling it, a pitot-pressure survey probe has been reduced in size to minimize its intrusive interference effect on the flow field and simultaneously maintain a relatively fast response.

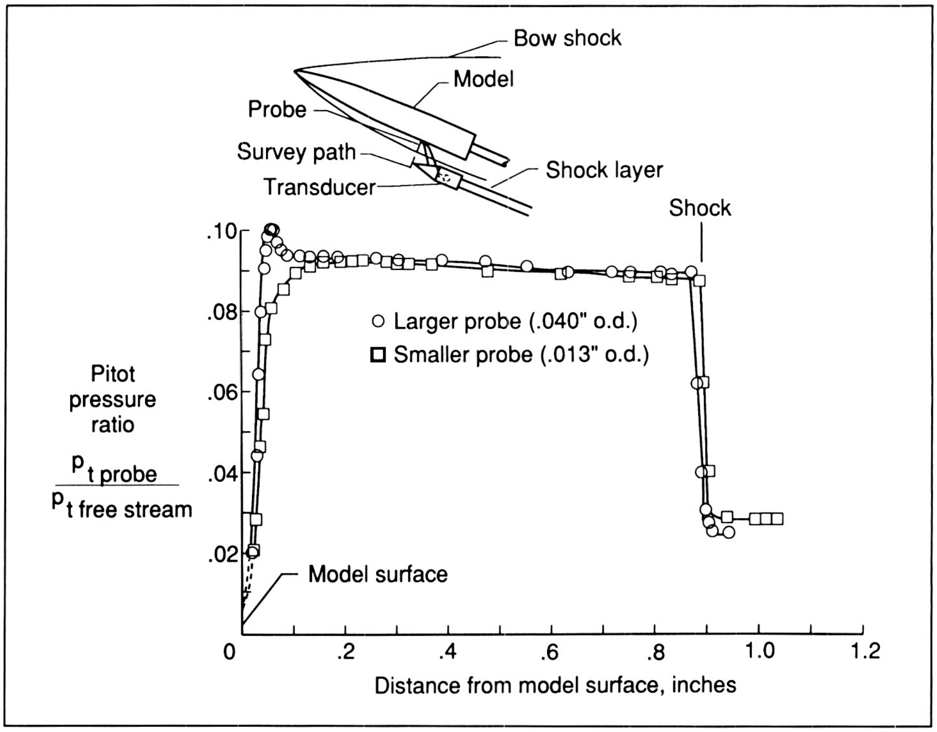

L-6892-4

Comparison of pitot-pressure profiles obtained with miniaturized probe and larger probe in flow field about 2:1 elliptical cone in Langley 20-Inch Mach 6 Tunnel.

The probe, which has an 0.013-in. outside diameter, has an internal chamfer of 60° to minimize flow angularity effects and an oval shaped tip for aerodynamic efficiency. The transducer is located approximately 2.50 in. from the probe tip for rapid response. Water cooling reduces the temperature at the transducer during the tunnel tests from 325°F to 103°F, which is normally low enough to avoid thermal effects on the accuracy of the transducer.

Comparison of the pitot-pressure profiles in the flow field about a 2:1 elliptical cone in the Langley 20-Inch Mach 6 Tunnel, obtained with the subject probe and with a larger probe, shows the elimination of the intrusive pressure peak near the model surface by the use of the smaller probe.

(George C. Ashby, Jr., 3984)

ACRC Daylight Landing Study

An assured crew return capability (ACRC) is being proposed for the space station. This would entail missions of crew evacuation, rescue, or emergency return. Several vehicle configurations for providing the capabilities are under study at Langley Research Center and Johnson Space Center. Under one plan, the vehicle would land in the water by parachutes with recovery made during daylight hours.

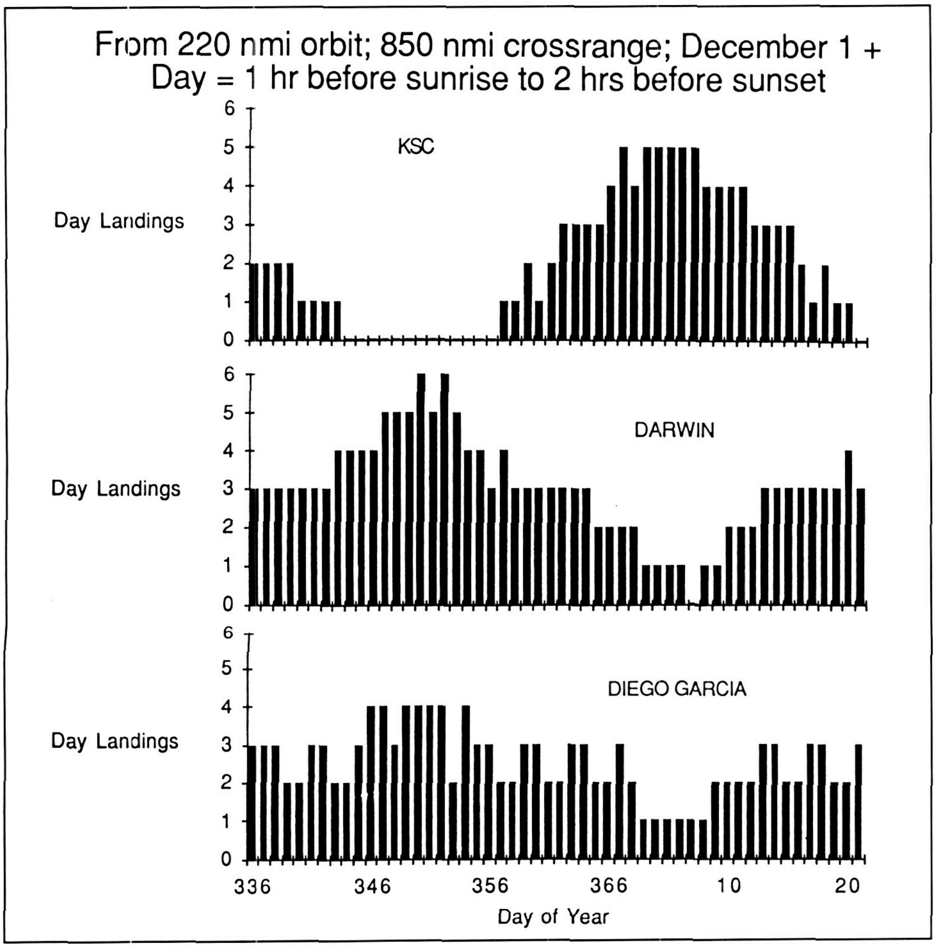

Frequency of day landing opportunities during winter months for ACRC lifting-body vehicle for northern and two southern latitude landing sites.

The ACRC daylight landing study is examining the frequency of occurrence of daylight landing opportunities available at specified landing sites as influenced by the effects of vehicle crossrange capability, season, and site selection. Precessional effects on the space station orbit lead to periods in which no daylight landings are possible for northern latitude landing sites such as offshore Kennedy Space Center (KSC) or Hawaii. Southern latitude sites, such as Darwin, Australia, or Diego Garcia in the Indian Ocean, must be included to ensure year-round daylight recovery coverage. Seasonal effects have only a slight effect on the number of landing opportunities. The amount of crossrange capability available during the return of the ACRC vehicle to Earth, however, strongly influences the results. For the Langley lifting-body ACRC vehicle, with 850 nmi of crossrange, two to seven daily landing opportunities exist depending on season and site selection. Vehicles with limited crossrange are more severely restricted in the frequency of such opportunities.

(T. A. Talay, 2768)

Lifting-Body Assured Crew Return Capability Vehicle

With a permanently manned space station in orbit, assured crew return capability missions become an important consideration. The envisioned missions will provide emergency evacuation capability from the space station, rescue capability for the Space Shuttle on a space station delivery mission, rescue capability for a space station crewman stranded during extravehicular activity, and alternate manned and unmanned access to the space station using an expendable launch vehicle. Several vehicle concepts, also identified as crew emergency return vehicles (CERVs), have been examined for this role in a Phase-A type study being conducted by an in-house team involving Langley Research Center, Johnson Space Center, and Kennedy Space Center. Langley has developed a lifting-body concept for this role to be compared with water landing capsule configurations proposed by Johnson Space Center.

In the Langley study, the major subsystems for the lifting-body configuration were identified for each of the missions. Weights, internal layouts, and costs have been generated in the analysis. The configuration has been shown to satisfy all the mission requirements, to have a significant advantage over other configurations because of its 850-nmi usable crossrange, and to be cost competitive with the other configurations.

Recent wind tunnel tests have shown that the lifting-body configuration has the ability to be statically stable, trimmed, and controllable at modest landing speeds. Six-degree-of-freedom simulations have

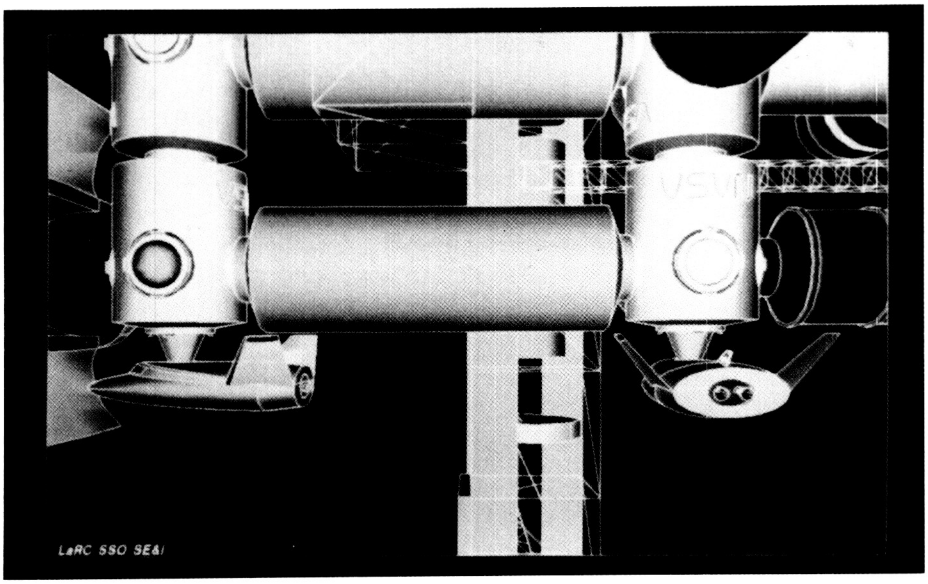

View of attached CERVs from lower boom.

also demonstrated good flying qualities at hypersonic and supersonic speeds.
(H. W. Stone, 4960)

Viscous Shock-Layer Solutions With Nonequilibrium Chemistry for Hypersonic Flows Past Slender Bodies

Proposed transatmospheric vehicles (TAVs), whose trajectories encompass a large range of free-stream conditions, have increased interest in improving both the understanding of viscous flow field phenomena and also the computational capability for application to hypersonic slender bodies. The low-altitude ascent conditions of a TAV should determine the thermal protection system of the vehicle. An understanding of the higher altitude ascent and the entry conditions (probably characterized by nonequilibrium chemistry) should be important to assess if surface reradiation alone is sufficient to maintain the desired material temperatures. Since extensive nonequilibrium studies exist only for the Space Shuttle vehicle class, the present study was conducted to enhance the existing information base for nonequilibrium laminar heating effects to slender vehicles with particular emphasis on effects of vehicle and free-stream parameters on nonequilibrium flow. The calculated results of the study are presented as a ratio of the noncatalytic $\dot{q}_{NC}$ to fully catalytic $\dot{q}_{FC}$ heating rates to illustrate the maximum potential for a heating reduction in dissociated nonequilibrium flow.

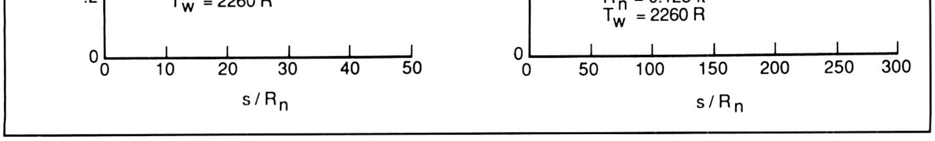

Cone-angle effect on nonequilibrium heat-transfer distributions, fore cone (left) and aft cone (right).

An effect of cone angle on the heating ratio is shown as a function of the normalized wetted distance at a Mach number of 25, a nose radius of 0.125 ft, and a wall temperature of 2260°R. Downstream of 100 nose radii (aft cone), the results are generally as expected, i.e., the largest nonequilibrium effects (as suggested by a lower value of the ratio) are computed for the largest cone angle. Note, however, that for the smaller half angles, relatively small nonequilibrium effects are computed at these distances. However, in the fore-cone region downstream of the tangency point, an unexpected and interesting reversal of the trend was obtained.
(Vincent Zoby, 2707)

Three-Dimensional Thermal and Chemical Nonequilibrium Flows

Future plans for space transportation and exploration call for mission trajectories with sustained and/or maneuvering hypersonic flight in the Earth's atmosphere at altitudes > 70 km and velocities > 9 km/sec. Aeroassisted orbital transfer vehicles will use this domain in returning from geosynchronous Earth orbit to low Earth orbit for rendezvous with the space station. Lunar, planetary, and comet sample return missions will utilize the Earth's upper atmosphere for aerobraking as well. Hypersonic, air-breathing cruise vehicles may ultimately be called on to fly through this domain. Substantial portions of these mission trajectories, in the transitional regime between free molecular and continuum, will carry the vehicle through conditions resulting in chemical and thermal nonequilibrium within the surrounding shock layer.

Nonequilibrium processes in the shock layer and near wake of hypersonic vehicles alter the flow field in three important ways. Radiative energy transfer rates are sensitive to the electronic temperature. Shock standoff distances and potential shock-body interactions are sensitive to the degree of dissociation. Local sound speeds, which influence pressure levels over aerodynamic expansion and compression surfaces, are sensitive to the partition of energy among the translational, rotational, and vibrational modes.

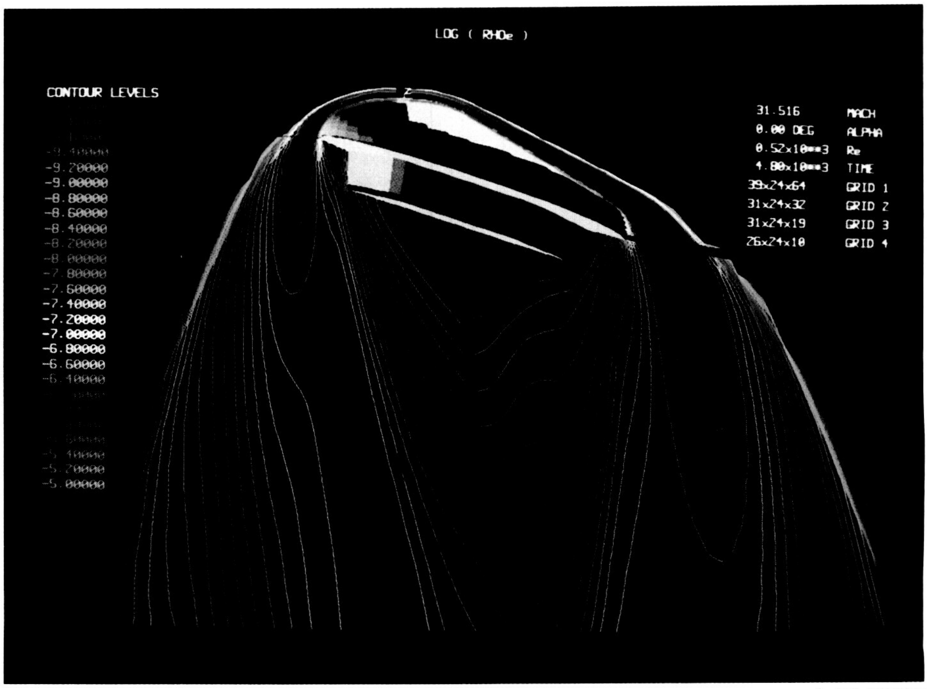

L-88-06327

Electron number density contours over AFE configuration.

Modifications to Program LAURA (Langley Aerothermodynamic Upwind Relaxation Algorithm) now permit the simulation of both chemical and thermal nonequilibrium over real three-dimensional configurations, such as the Aeroassist Flight Experiment (AFE) vehicle shown here. Four computational domains (forebody, outer wake shell, free shear layer, and inner wake core) permit a more efficient allocation of computational resources and improve convergence. "Freezing" of inverse Jacobian matrices significantly decreases time to convergence compared with earlier versions of LAURA. The electron density contours presented in the figure show nearly parallel, closely packed lines in the free shear layer, emanating from behind the circular shoulder of the AFE. These lines separate recirculating flow in the base wake core from the hypersonic expanding flow in the outer shell. In this case, the free electrons are at a different temperature than the heavier atoms, molecules, and ions in the flow because of the effects of thermal nonequilibrium.

(Peter A. Gnoffo, 2921)

Shock Interference Heating in Rarefied, Hypersonic Inlet Flow Fields

The direct simulation Monte Carlo (DSMC) method has been used to study shock interference heating problems under rarefied flow conditions for a hypersonic inlet at reentry velocities. Previous experimental evidence indicates that under continuum conditions, more than an order-of-magnitude increase in peak local heating rate may be expected for shocks impinging on leading-edge surfaces such as inlet cowl lips. At the lower densities of high-altitude reentry, the shocks are more diffuse, and the interactions are expected to be weaker than for continuum flows. However, because of the lack of experimental data and the difficulties in analyzing these highly viscous, nonequilibrium flows, little

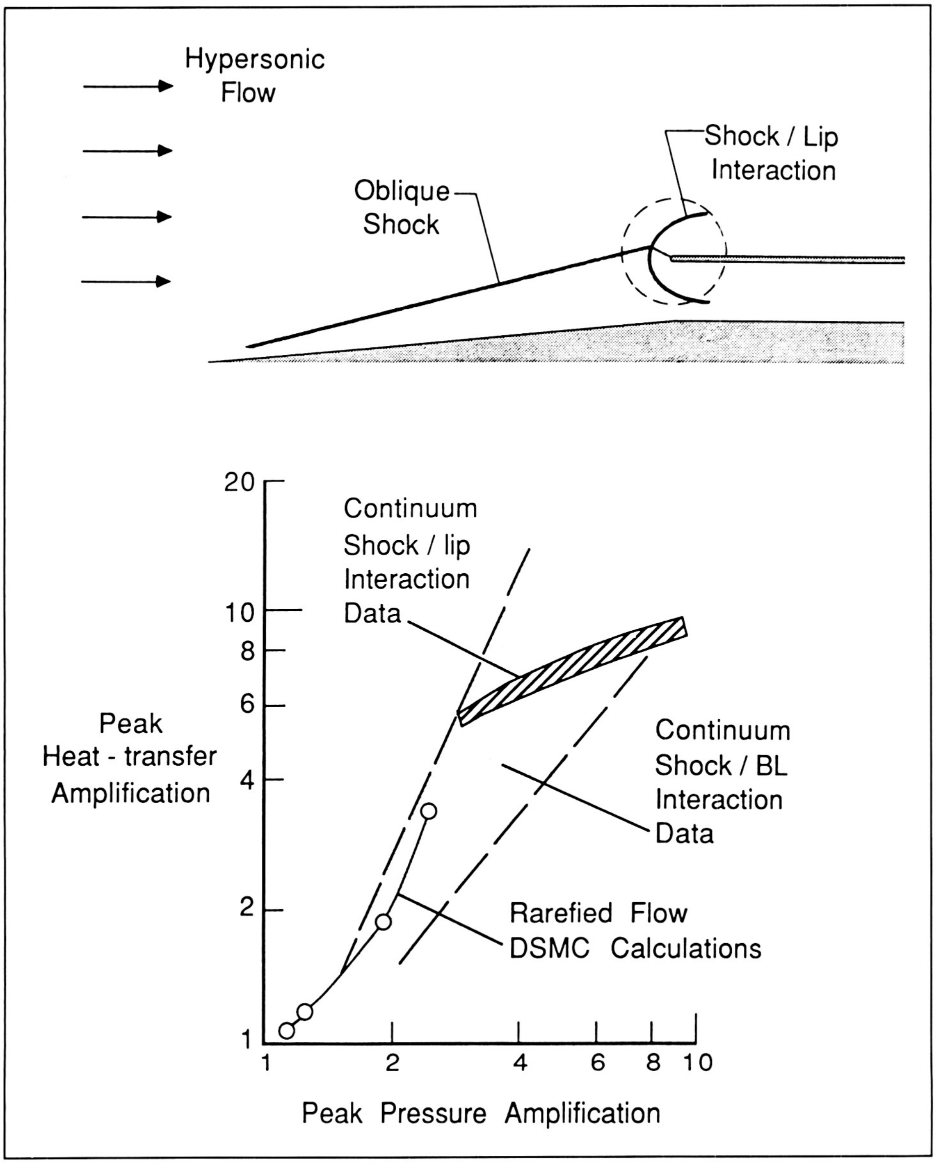

DSMC predictions of rarefied, shock/lip interactions in hypersonic inlet.

is known about the details of shock-induced heating under rarefied flow conditions. This study represents a first attempt at modeling such interactions through the application of the DSMC method.

Results obtained for a two-dimensional, inlet-type geometry show that the peak heat transfer on a circular-shaped inlet lip can be amplified significantly over the isolated stagnation value even under rarefied conditions. Calculations at a reentry velocity of 7.5 km/sec over an altitude range of 75 to 90 km show a correlation of the peak heat-transfer amplification with the peak pressure amplification that is roughly the same as that for continuum shock/boundary-layer interaction data. Although the amplification factors are lower than those seen in typical shock/lip heating data obtained under continuum flow conditions, the DSMC results indicate that shock interference heating is an important design factor to be considered over a wide range of flight conditions. The study further shows that the DSMC method provides a useful analysis tool for bridging the gap between the continuum and free-molecular flow regimes.
(R. G. Wilmoth, 4953)

Three-Dimensional Direct Simulations of AFE Flow Field

The direct simulation Monte Carlo method has been used to calculate the hypersonic rarefied flow about the Aeroassist Flight Experiment vehicle. The simulation accounts for translational, internal, and chemical nonequilibrium effects for a five-species dissociating gas. The calculations were made for an entry velocity of 9.9 km/sec over an altitude range of 120 to 200 km, that is, the more rarefied portion of the transitional flow regime. This study is the first application of a general three-dimensional DSMC code to simulate the flow about a full-scale space vehicle. The extent of the flow field over the AFE configuration at a 120-km altitude is illustrated by the translational temperature contours presented in the first figure.

Of particular interest for the transitional flow regime are the extent of rarefaction necessary to achieve collisionless flow and the large variations in aerodynamic coefficients. The second figure illustrates the variation of the lift-to-drag ratio as a function of altitude. Clearly, the DSMC results approach

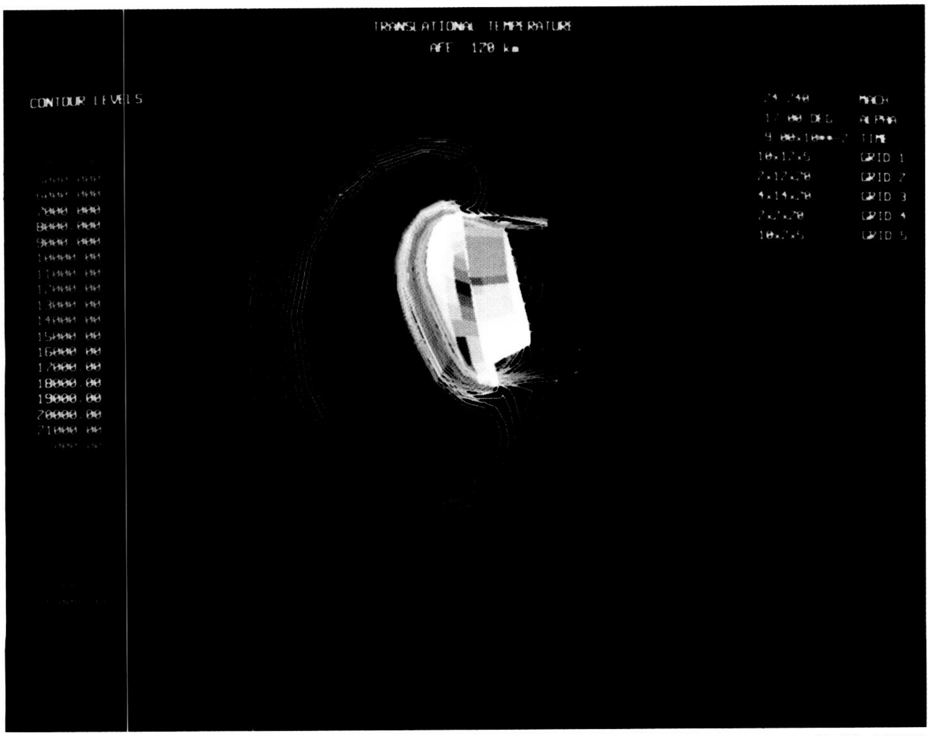

L-88-06522

Translational temperature contours over the AFE configuration at 120-km altitude.

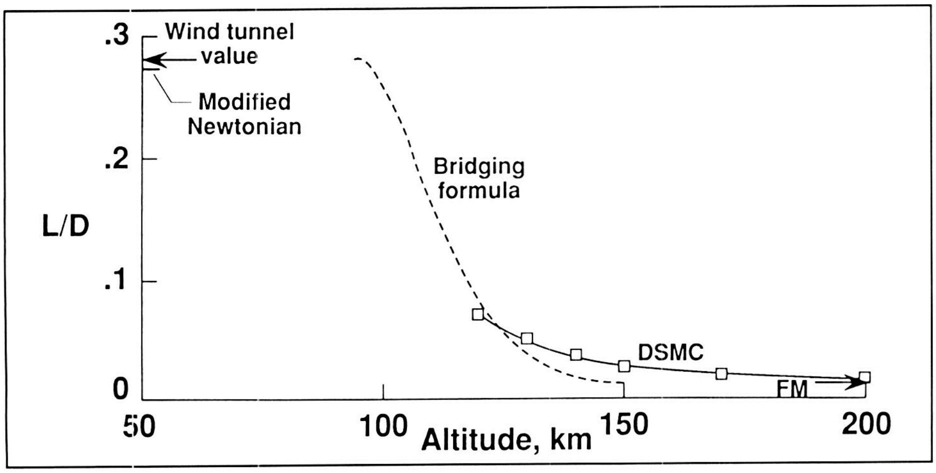

Lift-to-drag variation for AFE vehicle.

the free-molecule (FM) limit very slowly at higher altitudes, and even at a 200-km altitude, the flow is not completely collisionless. Prior to this study, it was generally acknowledged that FM flow existed for the AFE vehicle for altitudes near 150 km, but this study shows that the transitional effects are significant at these altitudes and influence the overall aerodynamic coefficients. Also shown in the figure are the calculated Modified Newtonian results and the continuum data obtained in hypersonic wind tunnels at Langley Research Center. In addition, the figure demonstrates the limitations of bridging formulas that are used in the absence of transitional flow calculations to empirically connect the continuum and FM limits. Results of this study have important implications for the interpretation of aerodynamic coefficients extracted from flight measurements under rarefied conditions.

(M. Cevdet Celenligil; James N. Moss, 3770)

Direct Simulation of AFE Forebody and Wake Flow With Thermal Radiation

Results for the flow field structure and surface quantities have been calculated for an axisymmetric representation of an Aeroassist Flight Experiment vehicle. The direct simulation Monte Carlo method is used to perform the calculations, since the flow is in a highly nonequilibrium state during both the compression and expansion phases about the vehicle. Free-stream conditions correspond to an altitude of 90 km and a velocity of 9.9 km/sec. The calculations account for nonequilibrium in the translational and internal modes, dissociation, ionization, and thermal radiation. The degree of dissociation is large, but the maximum ionization is only about 2 percent by mole fraction.

The figure displays selected contours of the local density, expressed as a ratio to the free-stream value, for the forebody and near-wake region. In the stagnation region, the

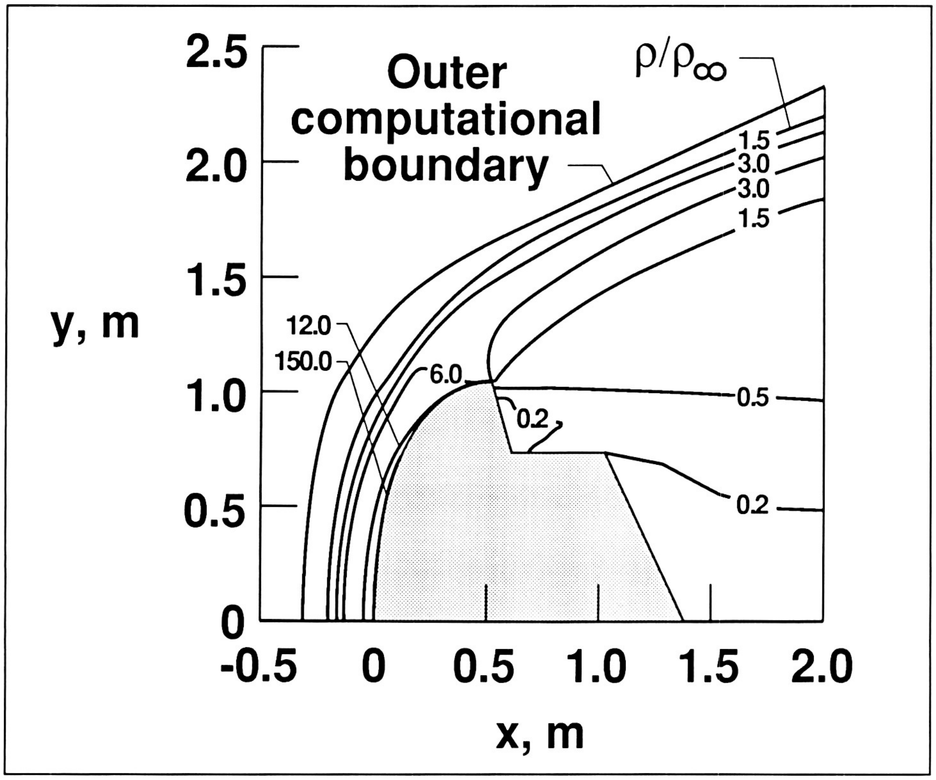

Density contours about AFE vehicle.

compression combined with a relatively cool wall produces a density that is slightly greater than 150 times the free-stream value. In the afterbody region, the density is only a small fraction of the free-stream value. The blunt forebody flow experiences a high degree of thermal nonequilibrium in which the translational temperature is generally greater than the internal temperature. However, as the flow expands about the aerobrake and afterbody, the internal temperature is generally greater than the translational temperature. Furthermore, the calculated results clearly show mass separation effects in the wake with a preferential increase in the concentration of the light (atomic) species relative to their values at the corner expansion. Forebody heating is dominated by the convective component; however, the stagnation point radiative heating under the assumption of no absorption is about 12 percent of the convective value. Afterbody heating is very small compared with the forebody values.

(James N. Moss, 3770)

Aerothermal Loads for Aeroassist Flight Experiment Vehicle

Calculated convective heating rates have been obtained for hypersonic flow about an axisymmetric representation of an Aeroassist Flight Experiment (AFE) vehicle using the direct simulation Monte Carlo method. The body configuration is an elliptically blunted cone with a 60° half angle and a stagnation radius of curvature of 2.3 m. The free-stream conditions correspond to selected points along the entry, aerobraking, and exit phases of the AFE trajectory, where the altitude and velocity ranges considered are 130 to 78 km and 9.9 to 7.5 km/sec, respectively. The figure presents the calculated stagnation-point convective heating as a function of time from an altitude of 122 km. For altitudes of 90 km and greater, a five-species dissociating air model was used, and the surface was assumed to promote atom recombination at the rate appropriate for the Space Shuttle thermal protection tiles. For the higher free-stream density conditions (90 km and below), only quasi-one-dimensional calculations

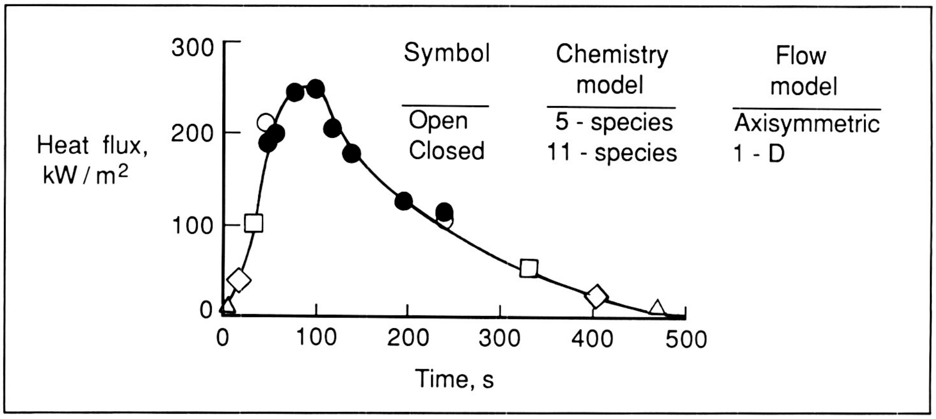

Stagnation-point convective heating rate history for AFE atmospheric encounter.

were made to simulate the stagnation streamline flow. For these conditions, an 11-species dissociating and ionizing gas model for air was used that included 41 chemical reactions but no atom recombinations at the surface.

These calculations are the first to define the heating for an AFE trajectory that includes both transitional and continuum flow conditions. The DSMC calculations show that thermal diffusion effects are present and produce a noticeable change in the gas composition near the surface. Such effects are not normally included in continuum calculations.

(James N. Moss, 3770)

Rarefied Flow Past Flat Plate at Incidence

The direct simulation Monte Carlo method has been used to calculate the flow field, surface quantities, and aerodynamic characteristics of rarefied flow about a flat plate at 40° incidence. Previous studies have shown that the Space Shuttle orbiter lift-drag ratio for free-molecular flow can be approximated well with a flat plate at 40° incidence.

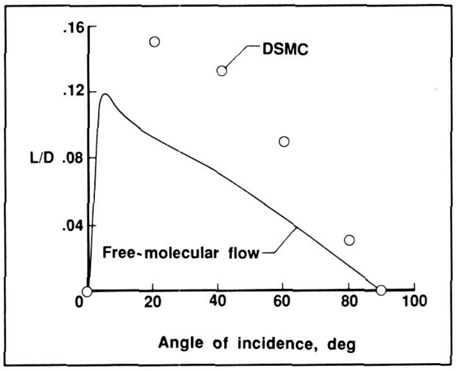

Transitional effects on lift-drag ratio for a flat plate at incidence (Knudsen number = 8.4).

The range of free-stream Knudsen number considered was 0.02 to 8.4, which corresponds approximately to an altitude range of 100 to 175 km for the Space Shuttle orbiter during reentry. The calculations show that the transitional effects are significant for all cases considered. Even for the largest free-stream Knudsen number condition, transitional effects remain quite pronounced where the flow is generally considered to be free-molecular. These results have important implications for the interpretation of flight measurements used to deduce aerodynamic coefficients under rarefied conditions. At altitudes of 160 km and above, the conventional procedure has been to interpret the Space Shuttle flight measurements using the free-molecular flow calculations with a fraction of the gas-surface interaction as specular. This study has shown that transitional effects at 175 km would increase the Space Shuttle orbiter lift-drag ratio by 90 percent over the free-molecular value. This is clearly demonstrated in the figure for a flat plate at 40° incidence. Thus, the interpretation of aerodynamic flight data for space vehicles at higher altitude must be done in concert with calculations that describe the transitional effects. Failure to account for this effect could significantly distort the interpretation of the gas-surface interactions under highly rarefied conditions.

(V. K. Dogra; James N. Moss, 3770)

Master Oscillator-Power Amplifier System for Laser Power Transmission in Space

Future space activities call for large power consumption by widely distributed satellites on various missions. A novel concept for using the Sun as the prime power source is that of orbiting solar-pumped laser power stations beaming high-quality energy to multiple users for such purposes as propulsion and generating electricity. The lasers must have at least 1 MW output with good beam quality for efficient transmission over distances > 1,000 km.

Several important milestones have been reached for direct solar-pumped iodine lasers, including the identification of the iodide t-C_4F_9I as the best laser medium and demonstrations of over 10-W continuous wave and 150-W Q-switched operations. However, continued scaling of single lasers to megawatt levels, while retaining high-quality beams, is far more difficult and less efficient than using a master oscillator-power amplifier (MOPA) system. The laser oscillator in this arrangement needs to only provide a low-power coherent beam, the amplification of which preserves the transmission quality.

The first figure schematically illustrates the system architecture envisioned for the solar-pumped MOPA system. The laser medium used in the power amplifier must have a long upper-state lifetime for high-energy storage before it is extracted by the injection of the oscillator pulse. The duration of the oscillator pulse must be short (typically submicrosecond) to produce extremely high peak power from the amplifier, which also means high average power when the system is operated at a high repetition (rep) rate. The MOPA system enables generation of good beam quality because the beam profile of the amplifier output is

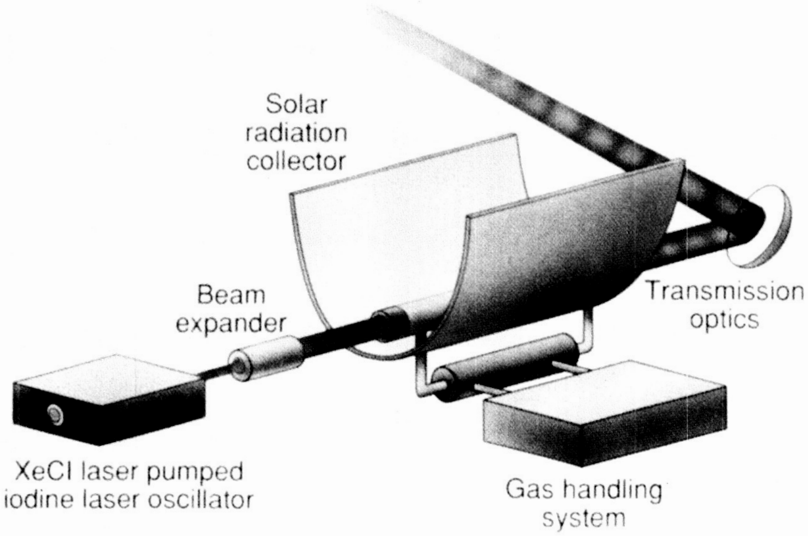

L-88-6062

Master oscillator power amplifier.

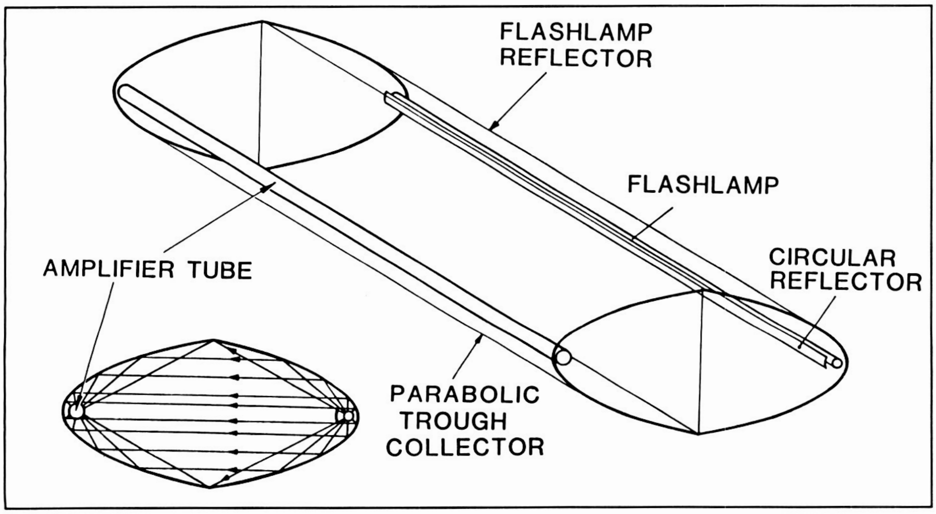

Diagram of amplifier experiment.

controlled by the oscillator beam profile, which is easily determined by spatial filters. The kinetics of iodine photodissociation lasers indicate that they are well suited for high-power MOPA systems.

The characteristics of a long-pulse iodine laser amplifier have been investigated in order to evaluate the adaptability of a MOPA system as a high-energy solar-pumped laser system. Long storage time ($> 500\ \mu$sec) and substantial amplification (> 3) were observed to confirm that developing such a system is indeed feasible. The experimental arrangement is shown in the second figure. To simulate the beam pattern of the solar radiation with a long flashlamp, a pair of 1-m-long parabolic troughs was used. One of the troughs surrounds the flashlamp and reflects a parallel beam to the other trough, which acts as a beam collector for the laser tube placed along the focal line. The laser oscillator is a low-power flashlamp-pumped iodine laser. This arrangement was used to evaluate different iodide lasants such as i- and n-C_3F_7I, n- and t-C_4F_9I; t-C_4F_9I was identified as the best material (highest efficiency).

Since high-rep-rate operation of the MOPA system is necessary for obtaining high average power, an XeCl-laser-pumped oscillator (308 nm) with t-C_4F_9I was recently developed in order to operate beyond the maximum rep rate (≈ 1 Hz) of a flashlamp-pumped oscillator. An oscillator output of 3 mJ with a pulse duration of 25 ns was generated at a rep rate exceeding 5 Hz; these results are limited only by the power supply capacity. The oscillator output is temporally steady and short enough for incorporating into the MOPA system. Preparations are currently under way to construct a MOPA system with this oscillator and a solar-simulator-pumped power amplifier. The power amplifier will be pumped by a Vortek argon arc that provides an irradiance equivalent to 1,250 solar constants with a solar-simulated spectrum. This system is expected to produce continuous kilowatt-level peak-power output at a rep rate of 5 Hz to enable experimental studies of far-field beam profiles and evaluation of long-distance transmission efficiency.

(J. H. Lee, 4332)

Space Shuttle Orbiter Hypersonic Rarefied-Flow Pitching-Moment and Elevon Effectiveness Measurements

Flights of the Space Shuttle have provided the first measurements that allow calculation of the pitching moment coefficient C_m and elevon effectiveness $\partial C_m/\partial \delta_E$ for a delta-wing reentry vehicle in hypersonic rarefied flow. Knowledge of aerodynamic moment behavior in the high-altitude, high-speed regime should enhance the design of future reentry and aerobrake missions. Advanced Space Transportation Systems design will also benefit in terms of reduced control-jet fuel margins (increased payload) because the transition process from spacecraft to aircraft is better understood.

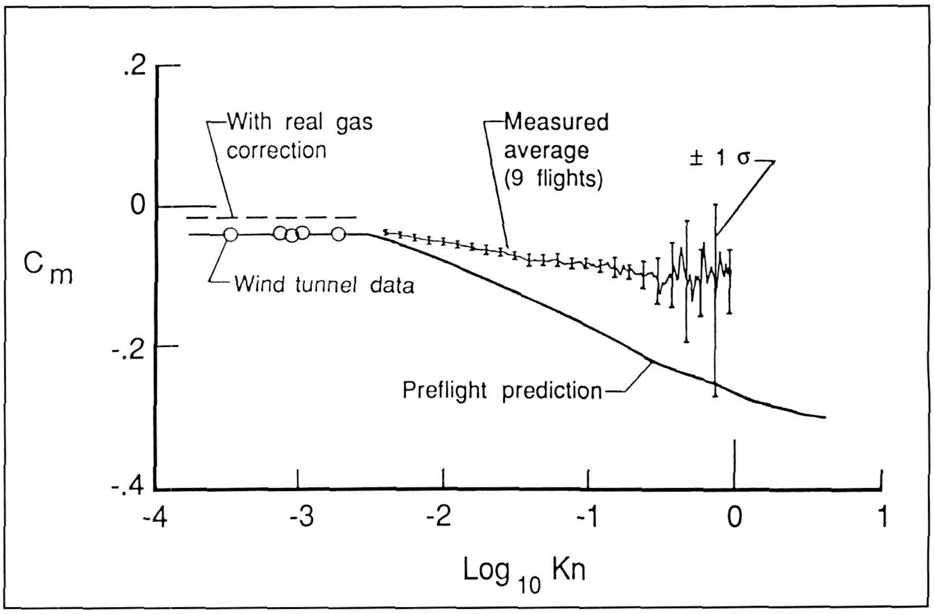

Space Shuttle orbiter pitching-moment coefficient with baseline CG, $\alpha = 40°$, and $\delta_E = \delta_{BF} = 0°$.

The orbiter control surfaces are activated for aerodynamic control at approximately a 95-km altitude. Above 95 km, the control surfaces are fixed, and attitude is controlled with jets, allowing for the direct determination of C_m from onboard rate gyro data. Also, $\partial C_m/\partial \delta_E$ can be obtained because the elevons are fixed at different angles for each reentry mission. Values of C_m were calculated for nine orbiter reentries between 95 and 130 km and adjusted to a baseline center-of-gravity (CG) location, angle of attack α of 40°, and 0° body flap deflection δ_{BF}. This allowed for the calculation of $\partial C_m/\partial \delta_E$ with increasing altitude. Using the flight-derived $\partial C_m/\partial \delta_E$, estimates were made of the control surface deflections required to zero the pitching moment. The calculated elevon deflections exceeded the heating limit at 100 km and the mechanical limit at 110 km. Aerodynamic control authority would therefore be marginal or inadequate for forward CG loading until the orbiter descended to about 95 km. The measured C_m for the nine flights is referenced to 0° elevon deflection using the flight-derived elevon effectiveness. The average values and standard deviation for the nine flights are presented in the figure as a function of Knudsen number. The preflight prediction for the same reference conditions is also shown along with preflight Calspan wind tunnel data and the real-gas correction to the prediction in the hypersonic continuum. Clearly seen in the results are the viscous interaction effects that cause a more negative C_m as altitude increases, corresponding to an aft shift in the center of pressure. The flight-derived average appears to be converging on the real-gas corrected prediction in the continuum regime. However, the pitching moment is increasingly overpredicted in the transition region, with the likelihood that the overprediction would occur in the free-molecule regime also.

(Robert C. Blanchard, 3031)

International Cooperative Effort on Propulsion Evaluation for Earth-to-Orbit Vehicles

A capability to evaluate rocket engine cycles for single-stage Earth-to-orbit vehicles has been developed as a result of an international cooperative effort between Langley Research Center and the DFVLR (Deutsche Forschungs- und Versuchsanstalt für Luft und Raumfahrt, German Aerospace Research Establishment). The effort included a 1-year visit to Langley Research Center by Dr. Detlef Manski from the Institute for Chemical Propulsion and Chemical Engineering, Lampoldshausen, West Germany.

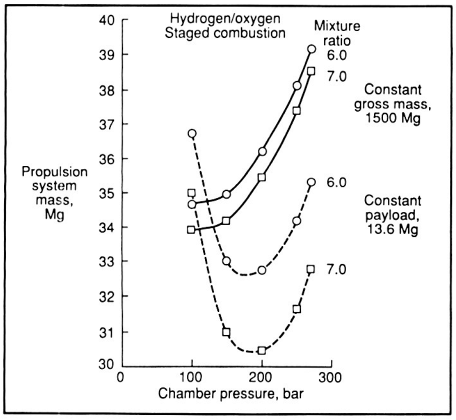

Effect of propulsion system mass on chamber pressure optimization.

The new capability was built from existing parts. The rocket engine analysis from DFVLR, including combustion data, power balance, and engine mass, was combined with the vehicle analysis from Langley Research Center, including trajectory optimization, vehicle mass, and sizing, to meet the design requirements.

One of the interesting results in the study was found while trying to optimize the chamber pressure. It was found that the specific impulse improves with increasing chamber pressure, but the engine mass has a minimum. When the gross mass of the vehicle is fixed, the engine mass is minimum at a low chamber pressure, but when the vehicle is sized for the required payload, the engine mass minimum is at a moderately high chamber pressure. With the effect of specific impulse, the final optimum chamber pressure is even higher than the chamber pressure that minimizes the engine mass.

The resulting capability has been used to compare several cycles and propellant combinations. The staged-combustion cycle used in the Space Shuttle main engine was found to be the best cycle with hydrogen fuel. A more complicated engine with two combustion chambers and two fuels, hydrogen and propane, was found to provide the best performance overall.

(James A. Martin, 4964)

Interplanetary Mars Mission Analysis

Through project Pathfinder, NASA is performing research aimed at future manned and robotic missions to Mars. The success of these missions depends greatly upon minimizing the initial vehicle mass in low Earth orbit (LEO). In this analysis, several flight path options were explored to determine their effects upon mission feasibility. These options include trip times ranging from 1 to 3 years, performance of a planetary swingby, and high-energy aerobraking. The figure shows a possible vehicle configuration that would satisfy all these options.

Although unimportant in a robotic mission, the total trip time is a significant parameter in a manned mission. Because trips of under 1 year were found to be impractical from a mass standpoint, an artificial gravity device is probably warranted. Note the two rotating, retractable habitation modules shown in the figure. Two different types of Mars missions were studied; these include the relatively short initial manned excursion mode (1 to 2 years), and a more efficient but longer duration colonization or cargo resupply mode (2 to 3 years). The most efficient missions from a weight standpoint were found to range from 2 to 2.5 years in duration (including a 60-day stay at Mars).

By performing a Venus swingby en route to Mars (outbound swingby) or prior to Earth return (inbound swingby), a spacecraft can take advantage of the Venus gravitational field to tailor its interplanetary trajectory. In this manner, energy may either be gained

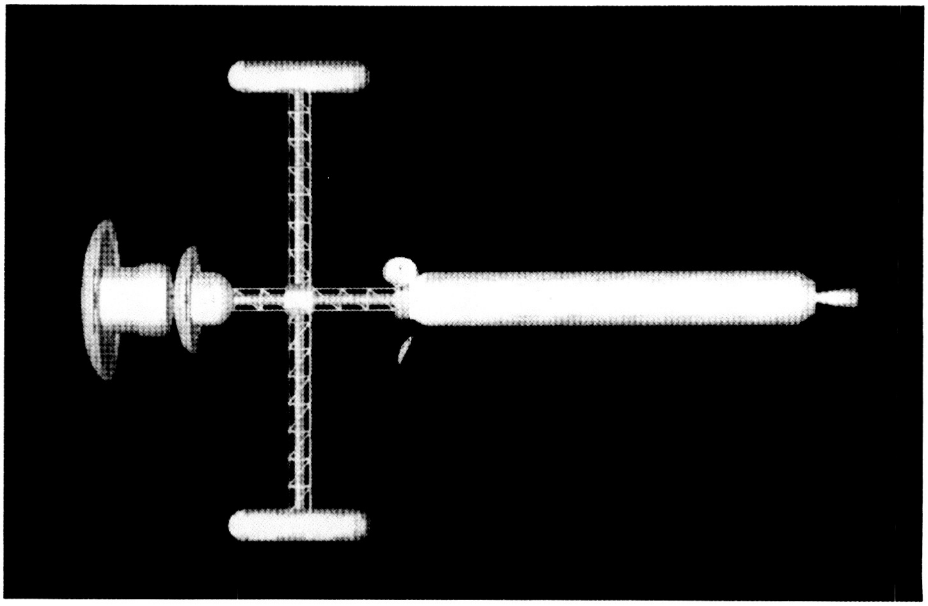

Potential manned Mars vehicle.

or lost relative to the Sun without performing a propulsive maneuver. Although the LEO launch opportunities are less frequent because of the involvement of a third planet, the use of a Venus swingby was found to significantly lower the required initial weight. Furthermore, the use of a swingby prior to aerobraking at the target planet was shown to yield greatly reduced atmospheric entry velocities. This result was particularly important during Earth return where reentry speeds became quite high (11.5 to 21.0 km/sec). By correctly performing an inbound swingby, this range of reentry was shown to narrow to 11.5 to 15.5 km/sec.

High-energy aerobraking requires a vehicle to withstand a much more severe flight environment than that of either Apollo or the Space Shuttle. However, preliminary studies have shown that use of this technology yields a potential weight reduction on the order of 25 to 50 percent depending upon LEO launch date and total trip time. Because of this tremendous payoff, the present analysis focused particular attention on defining the flight conditions during both Mars entry and Earth reentry. Both a Mars and an Earth aerobrake are displayed in the figure. With a better understanding of these flight envelopes, as well as the effect of a Venus swingby, a detailed entry analysis is currently being performed.

(Robert Braun, 4900 and J. W. Youngblood)

Automatic Generation of Finite-Element Models

The Solid Modeling Aerospace Research Tool (SMART), developed at Langley Research Center, is being used to generate geometric representations of advanced launch systems such as Shuttle II and the National Aero-Space Plane (NASP). SMART uses bicubic patches to model the surface of a vehicle. The surface definitions can then be sent to aerodynamics and structural programs for analysis. Structural analysis programs allow the user to create a finite-element model from the surface definition.

Defining the elements of a finite-element model has always been a cumbersome and time-consuming task, often taking weeks to model a vehicle. A capability has been developed in SMART to interactively and dynamically specify the element grid pattern and then calculate the actual elements from the pattern and the original surface definition.

The figure is a typical display from the finite-element generation from SMART. On the right-hand side of the screen is a planform outline of a wing that was created in SMART. The wing is made up of three-dimensional (3-D) bicubic surface patches. The rib and spar pattern can be generated automatically or manually. Planar surfaces through rib and spar lines are used to cut the surface patches. The resulting intersections form the edges of the finite elements. The result of this operation is illustrated on the left-hand side of the screen. To generate the original 3-D wing in SMART took 30 sec, specifying the rib and spar pattern took approximately 1 min, and the calculation of the intersections and generation of the finite elements took approximately 1 min.

(Joe Rehder, 4967)

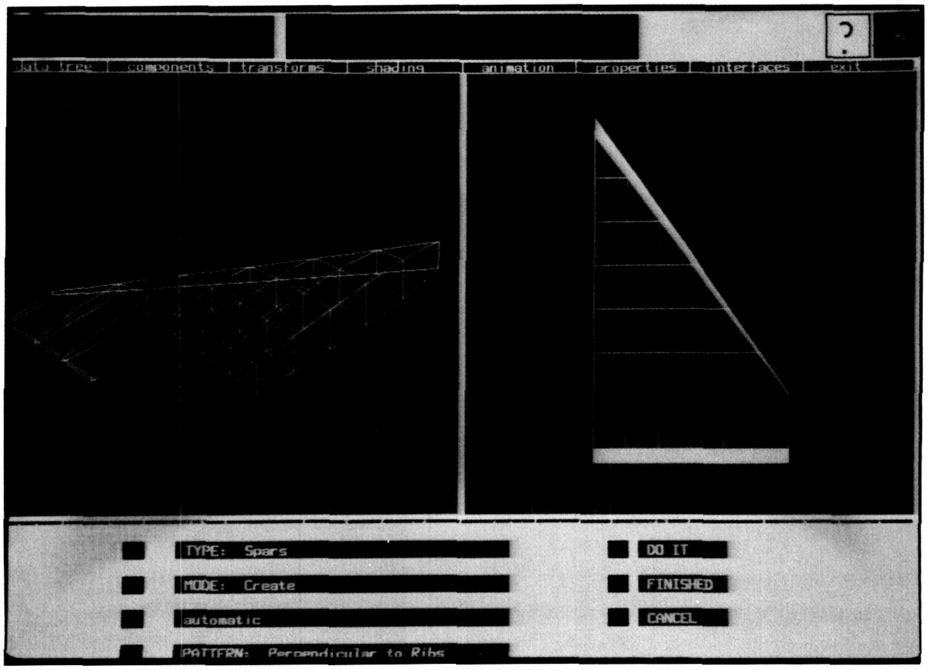

TYPE: Spars

MODE: Create

automatic

PATTERN: Perpendicular to Ribs

Typical display from SMART finite-element generation.

Lunar Orbiting Station in Support of Manned Mars Missions

Future missions to Mars and its moons need large quantities of propellants, and Earth sources require numerous large-tanker launches. An alternate source for oxygen (O_2) is the extraction from lunar minerals at a lunar surface facility. Lunar samples show O_2 at recoverable concentrations, and mission studies have shown a logistic advantage from lunar O_2. A lunar liquid O_2 (LLOX) supply requires a transportation system in which one element could be a lunar orbiting propellant depot, as a Lunar Node in the system. The Lunar Node can provide temporary storage and subsequent transfer of LLOX to a Mars-bound spacecraft. Additional roles provide a way-station for lunar-bound cargo and crews and a temporary safe haven for a stranded crew in the lunar vicinity.

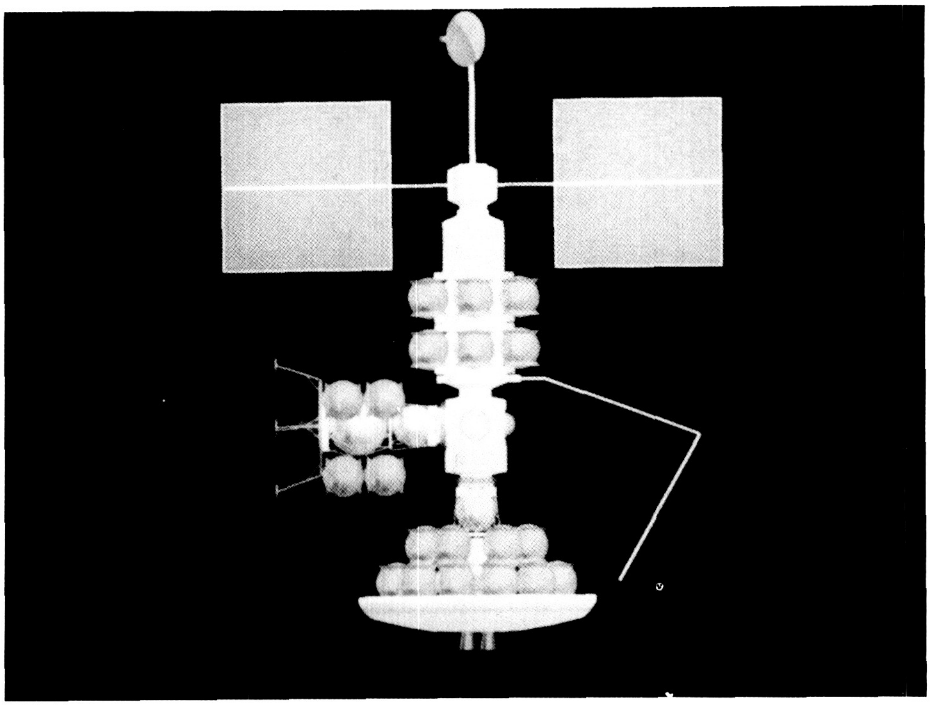
Lunar Node with STV and LADV docked.

A Lunar Node concept was formulated which could support LLOX production and distribution. The Node is composed of a propellant tankage array, a crew operational and safe-haven habitat, a docking module and manipulator, and a solar-photovoltaic power array. All of these components are within a truss structure. The Node operates in low polar lunar orbit (LLO) and can rendezvous with a lunar ascent-descent vehicle (LADV) or a space transfer vehicle (STV), as shown in the figure. The Lunar Node concept provides for storage and transfer of both H_2 and O_2 propellants. Remotely manipulated interchangeable tanks expedite the exchange.

The Lunar Node has the capacity to support a crew of 2 during operational periods, with an emergency capacity to support 14 persons for over 100 days as a safe haven. The Lunar Node concept can be evaluated for Mars staging sites at LLO, and at Earth-Moon libration points. Mission-specific input is required to define the safe haven and the propellant storage for a particular Mars mission. Methods for on-orbit exchange of propellant require further evaluation.

(L. Bernard Garrett, 3667)

Conceptual Design of Lunar Base Thermal Control System

Conceptual thermal control system (TCS) designs were evaluated to enable man to survive for extended durations on the lunar surface at four candidate base sites: Lacus Veris, the South Pole, the *Apollo 17* landing site, and the Mare Nubium. Space station (SS) and alternate active thermal control technologies were evaluated for use at these sites.

The SS thermal acquisition technology evaluated for the removal of sensible and latent heat loads from the inside of a lunar base consisted of two single-phase pumped water loops, one operating at 2°C and one at 21°C. Two-phase pumped ammonia loop technology was evaluated to transport the heat from the base to a series of individual SS ammonia heat pipe radiators for the rejection of heat to the lunar environment. The SS acquisition technology proved compatible with the lunar base internal requirements at all four base sites. The SS transport and rejection systems proved compatible with the environment at the South Pole, but incompatible

ORIGINAL PAGE
BLACK AND WHITE PHOTOGRAPH

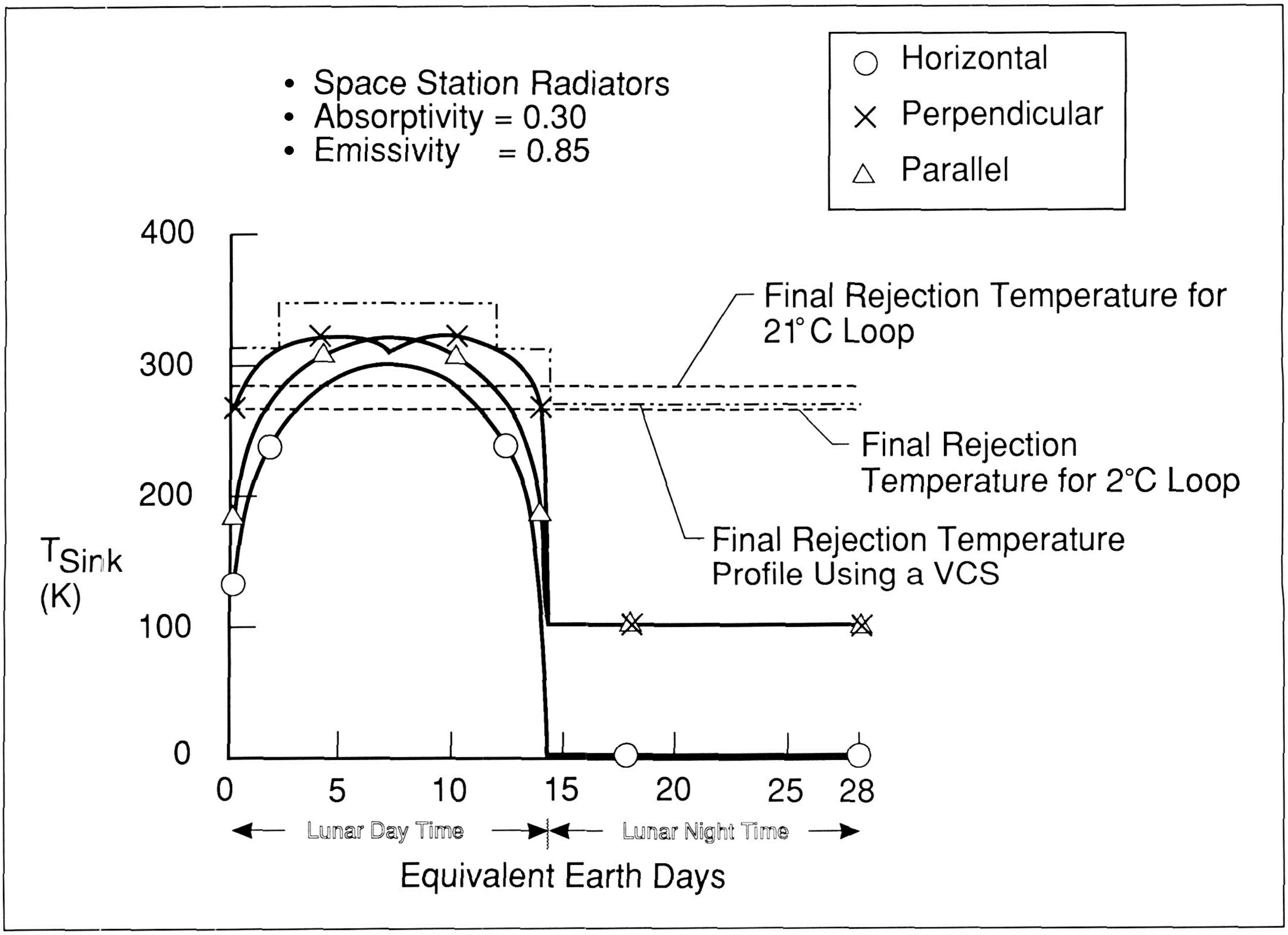

Sink temperature profile for radiators at Lacus Veris.

with the environment at the other three sites because of the dramatic changes in the solar flux and lunar surface temperature over the lunar day/night cycle. Variations in the sink temperature (which represent the added effects of cold space, the solar flux, and the infrared flux from the lunar surface) for radiators over the lunar day were determined for three orientations: a horizontal radiator and vertical radiators either perpendicular or parallel to the plane of the solar ecliptic. As shown in the figure, the final rejection temperatures of the two acquisition loops (assuming an 8°C drop to the radiator) for all orientations at Lacus Veris were well below the sink temperatures for a large portion of the lunar day and well above the sink temperature during the lunar night; therefore, modifications to the system were required. A two-loop cascaded vapor cycle heat pump system was selected as a means to increase the final rejection temperature of the vertical SS radiators oriented parallel to the plane of the solar ecliptic significantly above the sink temperature for lunar day operation. A bypass compressor loop was selected to prevent overrejection of heat during lunar night operation. One two-phase pumped Freon 12 loop operating at –3°C was selected to transport the heat from both acquisition loops in the base to the heat pump system. This system design can also be used at the *Apollo 17* site and the Mare Nubium because of their similar distances from the equator.

(L. C. Simonsen; J. B. Hall, Jr., 4982)

Second-Generation Space Station Technology Studies

A feasibility study has been conducted to determine enabling technologies for a second-generation space station. The space station is not only capable of supporting in situ research and development, but also serves as a platform for civil, military, and commercial applications. Primary functions include supporting visiting crews and vehicles; relaying power, communications, and data between spacecraft; and providing variable gravity adaptation facilities for transient crews and researchers. The baseline space station was designed to accommodate a standard crew of 60 persons, produce a total of 2.5 MW of electrical power, and adhere to the National Commission on Space recommendations.

The products of the study are represented in the form of a list of twenty-two major enabling technologies in eight fields: structures, mechanisms, and materials; power and thermal control; propulsion; crew systems; rigid- and flexible-body controls; environmental control and life support systems; transportation systems; and assembly and operations. These items are shown in the table.

Each item was assessed in a twofold ranking. First, the item was ranked in terms of its criticality to the development of the space station configuration, and second, the item was ranked in terms of the current state of technological readiness.

(Melvin J. Ferebee, Jr., 3440)

Structures, Materials, and Mechanisms
1.) Improved Structural Design and Analysis Methods
2.) Lightweight Industrial Equipment
3.) Large Articulated Airlock Doors and Seals
4.) Large-Diameter Gas Seals for Rotating/Moving Joints
5.) Large-Diameter Rotating Joints and Drives
6.) Filament-Reinforced Structural Composites
7.) Expandable and Modular Structural Composites

Power/Thermal Control
8.) High Specific Power, Power Generating Systems
9.) Improved Thermal Control Devices and Radiators

Propulsion
10.) High-Performance, Non-contaminating, Intermediate Thrust Attitude Control Thrusters

Crew Systems
11.) High-Motility, No-Prebreathe Space Suits

Rigid-Body/Flexible-Body Control
12.) Predictions of Dynamics and Control of Large Space Vehicles with Flexible, Rotating Components
13.) Advanced Momentum Storage/Management Systems

Environmental Control and Life Support
14.) High Degree of Closure in Air, Water, and Waste Cycles
15.) High-Performance, Long-Duration Environmental Control and Life Support (ECLS) Systems
16.) Improved Ability to Remove Contaminants From Atmosphere and Water
17.) Operating an Ambient Atmosphere
18.) Artificial Gravity Environment

Transportation Systems
19.) Heavy Lift Launch Vehicle (250,000 lbm to low Earth orbit (LEO))

Assembly and Operations
20.) Telerobotic Assembly Machines and Orbital Maneuvering Vehicles
21.) On-Orbit Assembly Techniques
22.) Autonomous Operations Capability

Major technology requirements for second-generation space station.

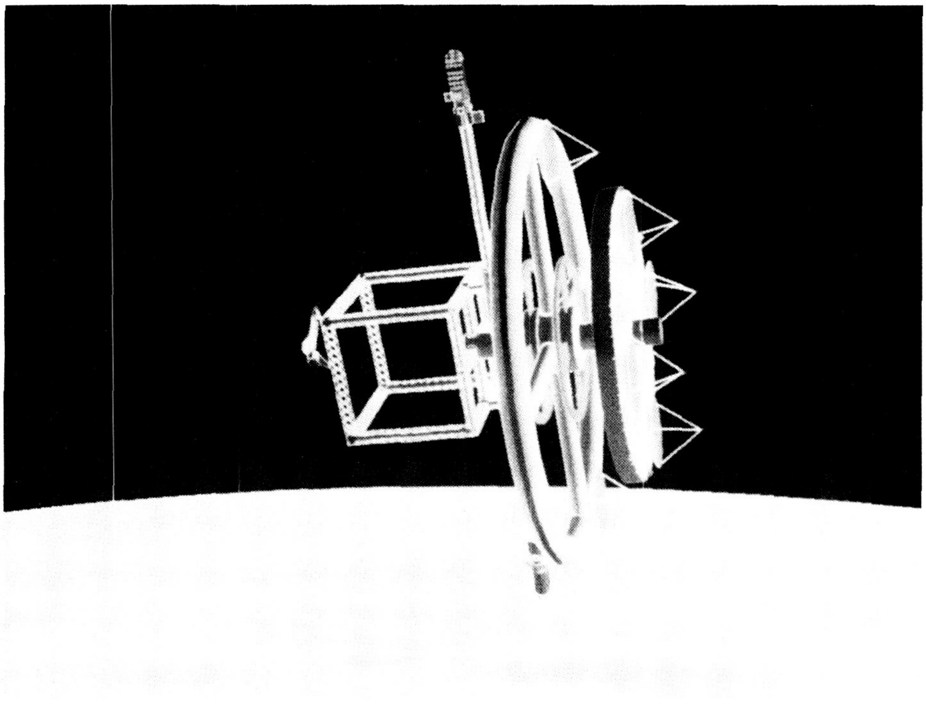

Second-generation space station.

Radiation Shielding for Lunar Habitation Modules

As establishment of a manned lunar outpost enters the mission planning phase, factors pertinent to crew safety and health maintenance receive more critical attention. One such factor involves protection from the ionizing radiation environment, which at times can be extremely hazardous on the lunar surface. For short-duration missions, the principal radiation danger results from large solar proton events that can produce high fluxes of energetic protons. In the absence of adequate shielding, resultant radiation dose levels can be mission disabling or even lethal. Consequently, a determination of radiation protection requirements is essential.

Known physical characteristics of the lunar regolith suggest that it may be a serviceable and convenient material for shielding. A recent study has been conducted with this purpose in mind. A comprehensive and computationally efficient nucleon transport code developed at Langley Research Center has been applied to a typical proton flare flux spectra incident on a regolith shield. The lunar soil model adopted is based on Apollo sample return compositions. The flux of nucleons through the regolith is computed and used as input for a geometry code applicable to a specified configuration. Predictions of resultant dose levels are made by integration of the anisotropic radiation fields over all directions at a number of target points within the shielded volume. The figure shows a sample isodose map for a half-buried spherical habitation module of 15.2-m diameter. The portion of

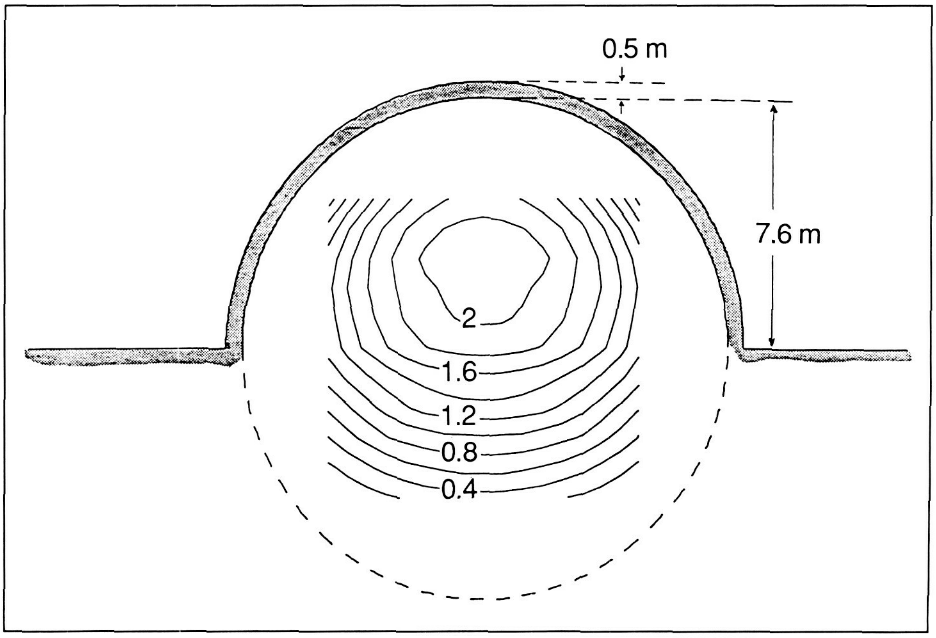

Isodose map for half-buried 15.2-m-diameter spherical habitation module with 50-cm overhead regolith shield thickness. Doses are in rem at 5-cm body tissue depth; input flux spectrum corresponds to that of the large flare of November 1960.

the sphere extending above the lunar surface is shielded with a 50-cm regolith layer. The resultant dose patterns exhibit the nonuniformity of the interior dose rates. Such results can have an influence on location of sleeping quarters and placement of equipment and supplies for added shielding.
(John E. Nealy, 4983)

Conceptual Design of Communications Satellite for Future Mars Exploration Missions

The Synchronous Mars Telecommunications Satellite (SMARTS) has been designed as a relay station to provide all of the necessary communication links for future Mars missions. SMARTS would orbit the planet with a period equal to one Martian day (aerosynchronous orbit), thus providing constant spot coverage over several proposed landing sites.

The procedure used for this preliminary design is one of systems analysis and integration. The design of the antenna reflectors and feed arrays is based on trade studies of spacecraft mass and power requirements. Bandwidths selected use Deep Space Network allocations, supporting technology readiness levels, and minimum power requirements. Data storage capabilities are provided for use during periods of occultation, when direct communication with Earth is not possible. The supporting spacecraft structure and subsystem designs were defined by the needs of the communications system.

The figure shows the design configuration of SMARTS, developed using IDEAS^2 software. The satellite is unmanned, solar-powered, three-axis stabilized, and has a solar inertial orientation. The larger antenna is 8 m in diameter and is oriented toward the Earth. It is a deployable structure of radial-rib design with a gold-plated molybdenum mesh reflective surface. The smaller antenna is a 3-m-diameter rigid structure and points toward the Martian surface.

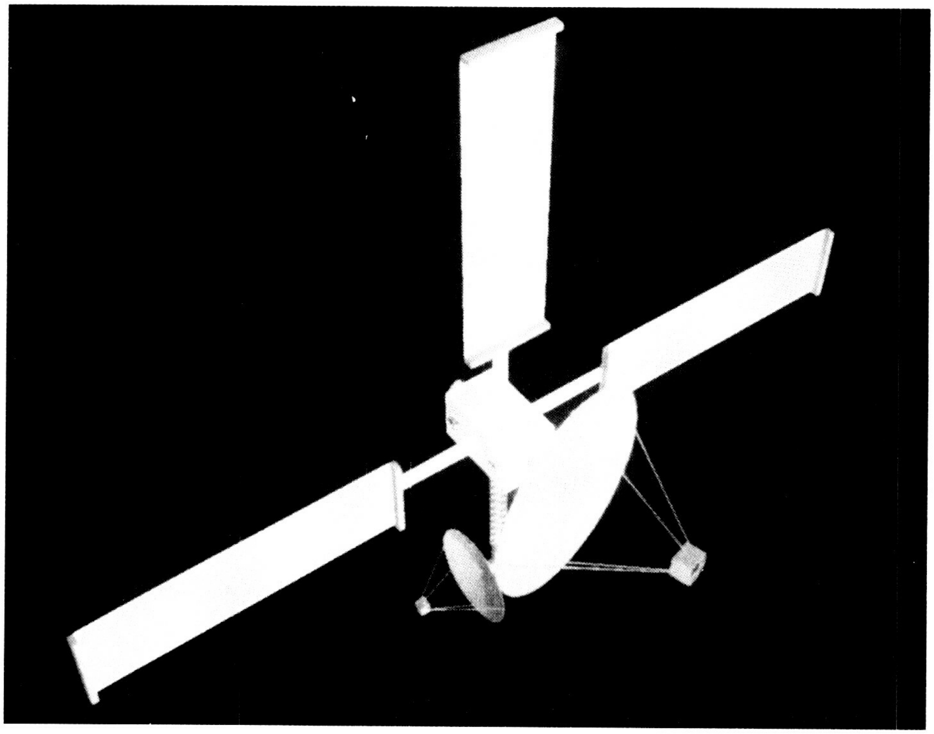
Synchronous Mars Telecommunications Satellite.

The design of SMARTS is based primarily on current, flight-ready technology. Those items that are not currently available are in the design and development stages. Continuation of the technology development could enhance the satellite's availability for inclusion in the overall Mars exploration infrastructure as early as the first proposed Mars excursions of the 21st century.
(Deborah M. Badi, 4982)

Shuttle II Concept With Airbreather First Stage

Candidate launch vehicles are being studied to complement and replace the current Space Transportation System. One potential Shuttle II concept, shown in the figure, is a two-stage, horizontal-takeoff, horizontal-landing vehicle. The first stage utilizes an airbreathing propulsion system called an air turborocket (ATR), and the second stage uses conventional rocket engines similar to those on the present Space Shuttle. The second stage separates from the booster at Mach 6, which is the operational limit of the ATR, and the booster flies back to the launch site.

The ATR uses liquid hydrogen and oxygen as its propellants. The propellants are pumped to small rockets inside the ATR engine.

ORIGINAL PAGE
BLACK AND WHITE PHOTOGRAPH

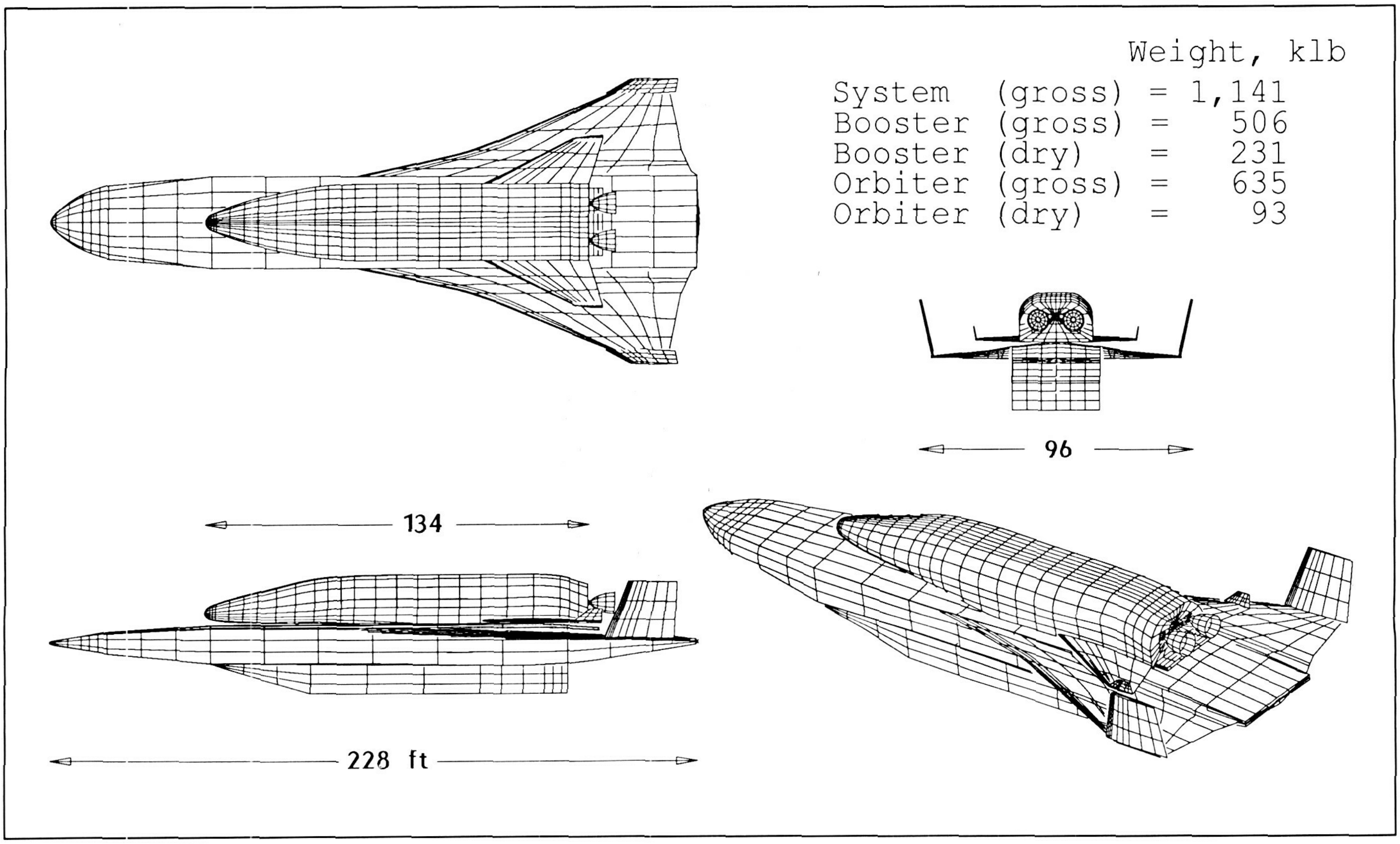

		Weight, klb
System	(gross) =	1,141
Booster	(gross) =	506
Booster	(dry) =	231
Orbiter	(gross) =	635
Orbiter	(dry) =	93

Shuttle II airbreather/rocket concept with 12,000-lb payload to polar orbit.

The exhaust from the small rockets drives a turbine that is connected to a compressor. The compressor entrains air from the atmosphere and burns additional hydrogen to produce thrust. At higher speeds (between Mach 4 and 6), the ATR works similar to a ramjet. The advantages of the ATR are that it is efficient in the atmosphere, and less oxygen is required on the booster, since it burns the oxygen from the air. This reduction in the amount of stored oxygen yields a lower gross weight for the vehicle, which allows the vehicle to take off unassisted from a conventional runway. The ATR's thrust-to-weight ratio, however, is low, which causes both the engine weight and the dry weight of the vehicle to be high.

The orbiter is aerodynamically tailored so the vehicle can accelerate through the transonic drag pinch. Because of the high staging Mach number, the orbiter is relatively small. This will enable on-orbit maneuvering to be accomplished with less fuel. The payload bay is designed to be loaded like a containerized cargo transport vehicle. This concept is used throughout the Shuttle II study.

This vehicle will be assessed with the other vehicles in the Shuttle II Program. The results of the study will hopefully provide insight for selecting the next launch vehicle for the United States.

(Mark J. Cunningham, 4954)

Shuttle Crew Escape Tube Study

The Presidential Commission on the Space Shuttle *Challenger* Accident asked NASA to investigate means of successful crew bailout from the Space Shuttle orbiter. "Recommendation VII–Launch Abort and Crew Escape" states that the Agency should "make all efforts to provide a crew escape system for use during controlled gliding flight." This recommendation covers a situation during an abort on ascent in which the orbiter has safely separated from the external tank and solid rocket boosters and slowed to subsonic speeds, but cannot reach a suitable landing site. A similar situation may also occur

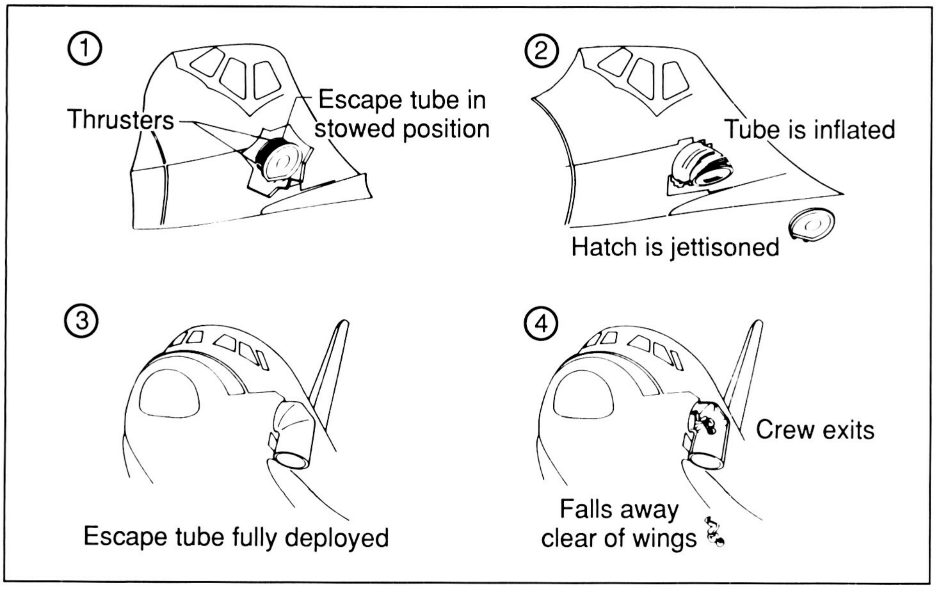

Escape tube system.

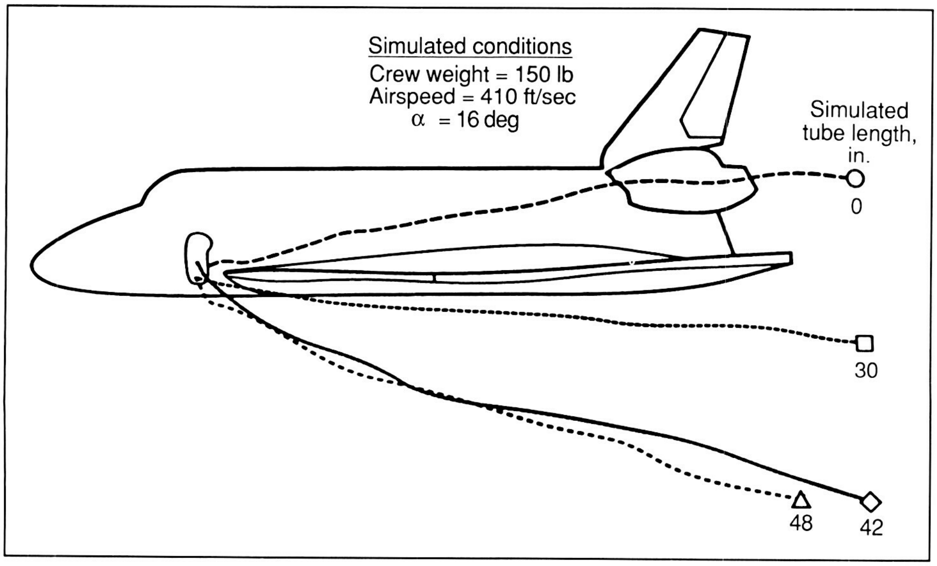

Effect of escape tube length on crew bailout trajectory.

during an entry in which a guidance or other malfunction has occurred, and a safe landing is impossible.

A previous investigation conducted at the Langley Research Center indicated that successful unassisted crew bailout from the orbiter may not be possible. Therefore, current work has concentrated on augmenting crew egress. One proposed escape system uses an inflatable elastic/fabric Airmat tube that is deployed out of the orbiter's main hatch and down the side of the fuselage. The crew members slide through the tube and exit below the wing (as shown in the first figure).

Two wind tunnel tests have been conducted. The first test, in the Langley 12-Foot Low-Speed Tunnel, determined that safe bailout could be accomplished if the tube extended at least 42 in. below the hatch (as shown in the second figure). This places the opening of the tube 12 in. below the centerline of the wing leading edge. The second test, in the Low Turbulence Pressure Tunnel, determined that the deployed escape tube had only a minor effect on the aerodynamics of the orbiter. Small control adjustments could easily compensate for the presence of the tube. Measurements indicated that the air loads on the tube were within the capabilities of the Airmat structure.
(George M. Ware, Bernard Spencer, Jr., Joseph D. Pride, Jr., Andrew S. Wright, Jr., and Homer F. Rush, Jr., 3984)

Heating Distributions in Wake of Aeroassist Flight Experiment Vehicle Configuration

As part of an extensive experimental program to develop an aerodynamic and aerothermodynamic data base for the Aeroassist Flight Experiment (AFE) configuration, a test series has been conducted in hypersonic wind tunnels to determine heating distributions and streamline directions on a cylindrical surface in the near wake of the AFE aerobrake configuration. The flow immediately downstream of the aerobrake is in a region of much interest because it is here that manned and unmanned payloads will be carried by future aeroassisted orbital transfer vehicles (AOTVs). The flow field is very

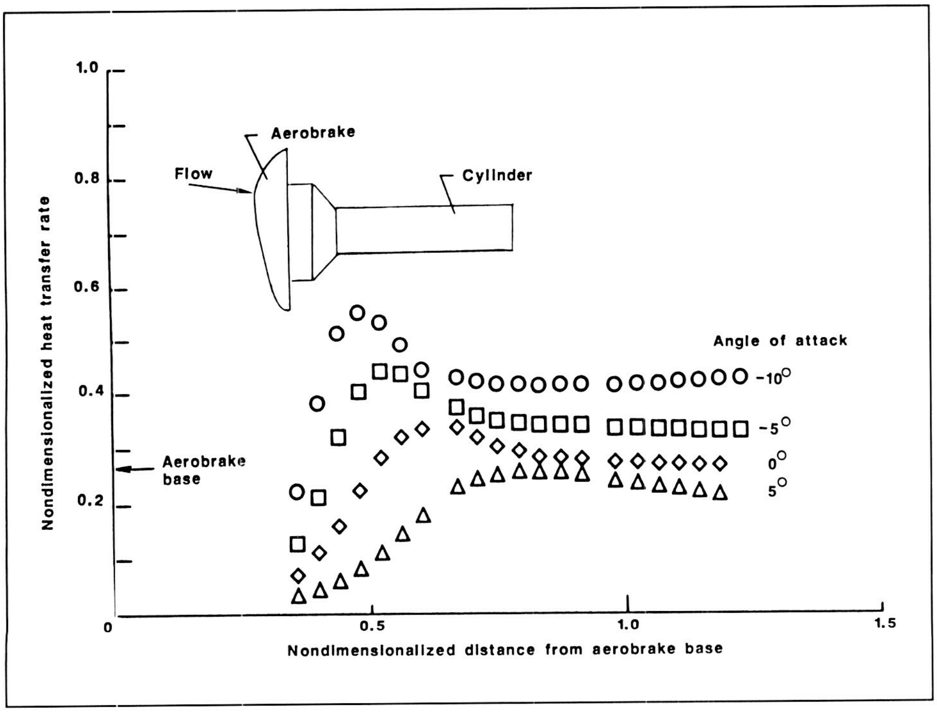

Measured heating distributions on cylinder in wake of AFE aerobrake in air at $M_\infty = 10$ *and unit* $Re = 0.25 \times 10^6/ft$.

complex in this near-wake region in which one of the primary features is the free shear layer that expands from around the periphery of the aft edge of the aerobrake and converges at approximately one to two aerobrake diameters downstream. Within the shear-layer envelope, the flow recirculates in the lee of the aerobrake, while exterior to the envelope, supersonic flow continues downstream. Impingement of the high-energy shear layer on a surface (e.g., a payload) can result in localized high heating.

The experimental test results revealed that heating was greatest along the upper surface of the cylinder in the symmetry plane of the aerobrake and decreased monotonically around the cylinder in the direction of the lower surface. Along the length of the cylinder, maximum heating occurred at the shear-layer impingement location and increased in magnitude as the impingement location moved upstream with decreasing angle of attack. At a given angle of attack, a decrease in Reynolds number moved the impingement location downstream, decreased the value of maximum heating, and spread the heating over a larger surface area.

(William L. Wells, 3984)

Experimental and Predicted Pressure and Heating Distributions for Aeroassist Flight Experiment Vehicle in Air at Mach 10

Development of an extensive aerodynamic and aerothermodynamic data base for the AFE is in progress at the Langley Research Center. This data base will provide a better understanding of the AFE vehicle performance and is expected to be of great importance to the designers of the AFE aeroshell, the principal investigators of the onboard experiments, and the computational fluid dynamics (CFD) community. In addition, the present results will be used to validate CFD codes and ground-to-flight extrapolations for use in future aeroassisted orbital transfer vehicle (AOTV) designs.

Recently, tests were performed in Mach 10 air, over a range of Reynolds numbers, on 0.022-scale (3.67-in. diameter) models of the AFE to obtain detailed pressure and heating distributions. Results indicate a negligible effect of Reynolds number on measured pressure and heat-transfer distributions for the present test conditions. Good agreement was noted when predictions from an inviscid flow field code, known as HALIS (High Alpha Inviscid Solution), were compared with these experimental data. Modified Newtonian theory was also compared with these data and found to be in good agreement over the nose and skirt of the configuration, but in poor agreement over the cone section. For heat-transfer distributions, decreasing α from 15° to −10° caused a movement of the stagnation region up and around the nose and onto the skirt. Heat transfer rates predicted with Program LAURA (Langley Aerothermodynamic Upwind Relaxation Algorithm, a Navier-Stokes solver) and AA3DBL (Axisymmetric Analogue 3-Dimensional Boundary Layer, a viscous boundary-layer solver) were generally lower than measured values; however, both codes qualitatively captured the heating trends of the data with angle of attack.

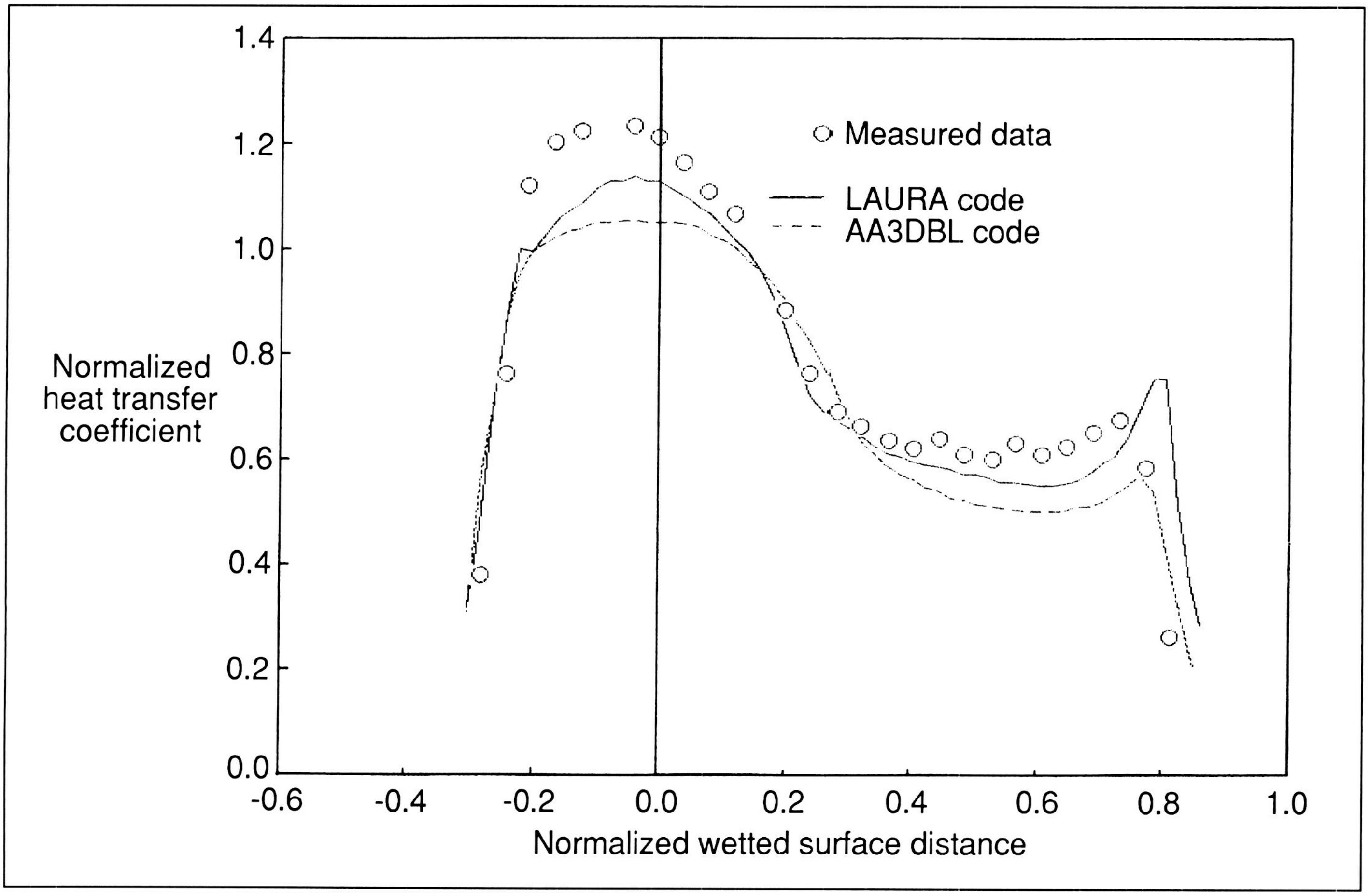

Comparison of experimental and predicted heat transfer distributions in air at $M = 10$, unit $R_e = 0.5 \times 10^6/ft$, and $\alpha = 0°$.

Predictions of LAURA were generally in better agreement with measurement, as shown.

(John R. Micol, 3984)

Airborne Lidar Observations of Arctic Polar Stratospheric Clouds

Polar stratospheric clouds (PSCs) have been observed frequently during both polar winters since 1979 by the orbiting SAM II (Stratospheric Aerosol Measurement II) sensor. The clouds occur in regions of very cold stratospheric temperatures (below approximately 195 K) and, in Antarctica, are often large in spatial scale and persist over the entire winter and into spring. Recent evidence points to PSCs as a major catalyst in the development of the springtime Antarctic ozone hole. Hydrated nitric acid (Type I) PSCs forming at temperatures above the frost point may consume a large fraction of the local gaseous odd nitrogen supply and subvert the otherwise rapid formation of inert chlorine reservoirs such as chlorine nitrate. At temperatures below the frost point, Type I particles can serve as nuclei for the formation of Type II PSC particles, which are predominantly water-ice and can grow to sizes such that gravitational settling (i.e., removal of the condensed nitric acid and water vapor) is significant. In addition, both Type I and Type II particles are thought to provide favorable surfaces for heterogeneous (mixed-phase) chemical reactions that liberate active (ozone-destructive) chlorine species.

In cooperation with the European CHEOPS 2 (Chemistry of Ozone in the Polar Stratosphere) campaign, a PSC formation was probed in the 21- to 24-km altitude range north of Greenland (82°N to 84°N, 0°W to 25°W) on January 29, 1988, using a dual-polarization, 0.532-μm

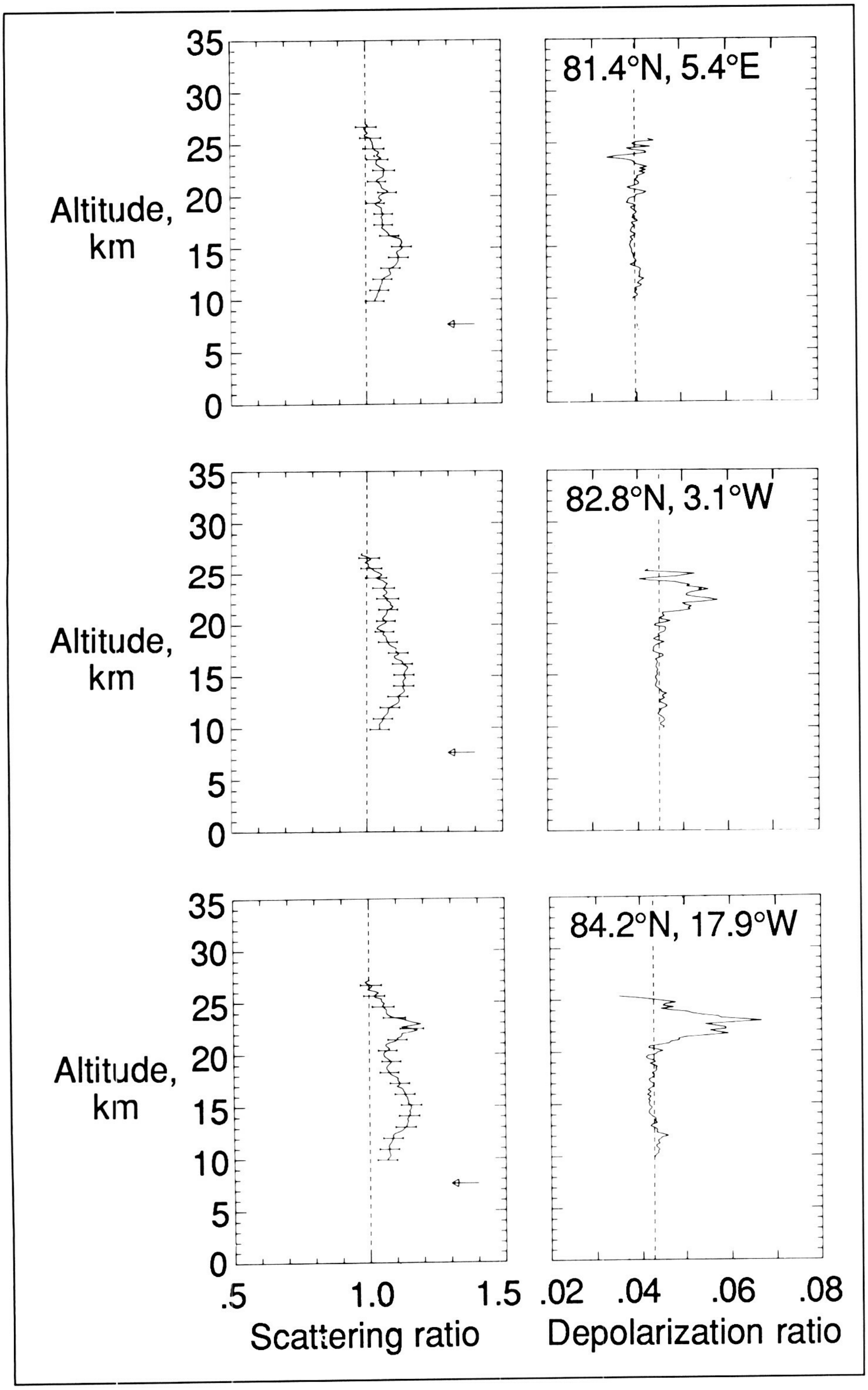

Profiles of backscatter ratio and depolarization ratio measured by airborne lidar on January 29, 1988.

wavelength lidar system mounted aboard the NASA Wallops P-3 aircraft. Temperatures near the 22-km level were between 191 K and 193 K, which is well above the estimated frost point temperature of 185 K. These temperatures indicate that the PSCs were of the Type I, hydrated nitric acid class. Peak scattering ratios of 1.1 to 1.2 were measured in the PSC layer, compared to values near 1.05 for the ambient stratospheric aerosol over the same altitude range. Profiles of the depolarization ratio distinctly showed the PSC layer, but maximum values were in the range of 0.06, only slightly greater than the value measured in cloud-free regions (0.04) and well below the value typical of cirrus clouds and small ice crystals (0.3). This signature suggests that the observed Type I PSCs were composed of small, solid particles having radii on the order of 0.5 μm; this corroborates recent theoretical calculations and experimental observations of Type I PSCs in Antarctica.

(L. R. Poole, 2065)

Improved Understanding of Shortwave Reflectance Patterns

The Earth Radiation Budget Experiment (ERBE) has provided a unique opportunity to study the distribution of shortwave radiation as it is viewed from space. The scanning radiometer on the ERBE spacecraft has been operated in an "alongtrack" scanning mode that provides a nearly instantaneous view of any location along the groundtrack over the entire available range of viewing zenith angles. This scanning pattern not only pro-

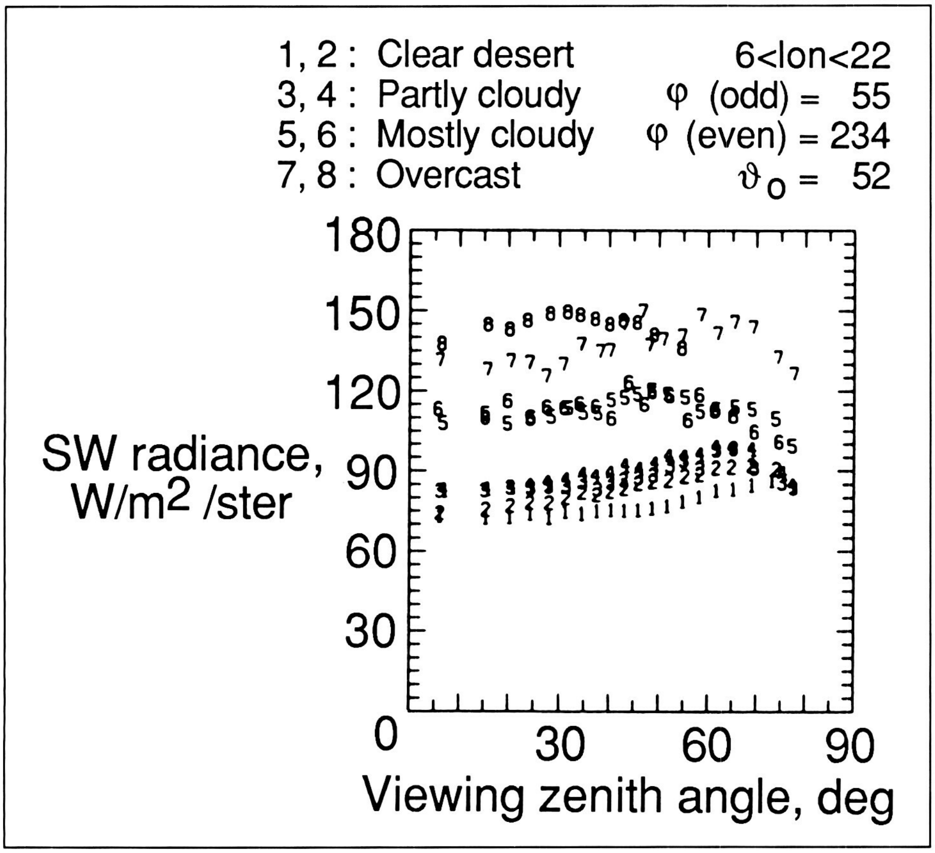

Shortwave radiance as function of viewing zenith angle for ERBE radiance measurements taken over the Sahara Desert, August 13, 1985.

vides a complete "slice" through the radiance distribution at essentially constant solar zenith angle and at a pair of nearly constant relative azimuth angles, but also provides a detailed view of how the function must behave under a well-specified set of angular conditions.

The figure illustrates a set of radiances measured over the Sahara Desert on August 13, 1985, at a solar zenith angle θ_o of 52°. Each ERBE-defined scene category is represented by a pair of numbers which represents the forward- and backward-looking portions of the instrument scan. The clear surface radiances have significant variability as a function of relative azimuth angle; this is caused by a combination of surface-related effects and molecular and aerosol scattering in the atmosphere, and is in qualitative agreement with theory. The mostly cloudy and overcast scenes are substantially brighter and more variable than the other two scenes. Because of the highly variable nature of cloud cover, the theoretical distribution of radiances from cloudy scenes is less well understood than for clear scenes.

(David R. Brooks, 2977)

Variability in Solar Constant: Climate Forcing Function

The solar constant is one of the most important forcing functions in the Earth climate system and the primary energy source for the Earth. A series of Earth Radiation Budget Experiment active-cavity-type radiometers, called the solar monitor, has been used successfully to detect variability in the solar constant. These monitors were placed aboard the NASA Earth Radiation Budget Satellite (ERBS) and the National Oceanic and Atmospheric Administration (NOAA) 9 and 10 spacecraft platforms during October 1984, December 1984, and September 1986, respectively.

In the figure (p. 128), recent measurements of the ERBE solar monitors are presented as a function of time. The most obvious features in the combined time series are the decreasing trend before September 1986 and the increasing trend thereafter. Since September 1986 marks the start of sunspot cycle number 22 and the reversal in the magnetic poles of the Sun, the trends in the time series may be correlated with either the 11-year sunspot cycle or the 22-year solar magnetic cycle.

The ERBE measurements suggest that a data base of at least 44 years is needed to separate the climatically forcing changes in the solar constant from those cyclic changes that are associated with the 11-year sunspot or 22-year solar magnetic cycle.

(R. B. Lee III, 2977)

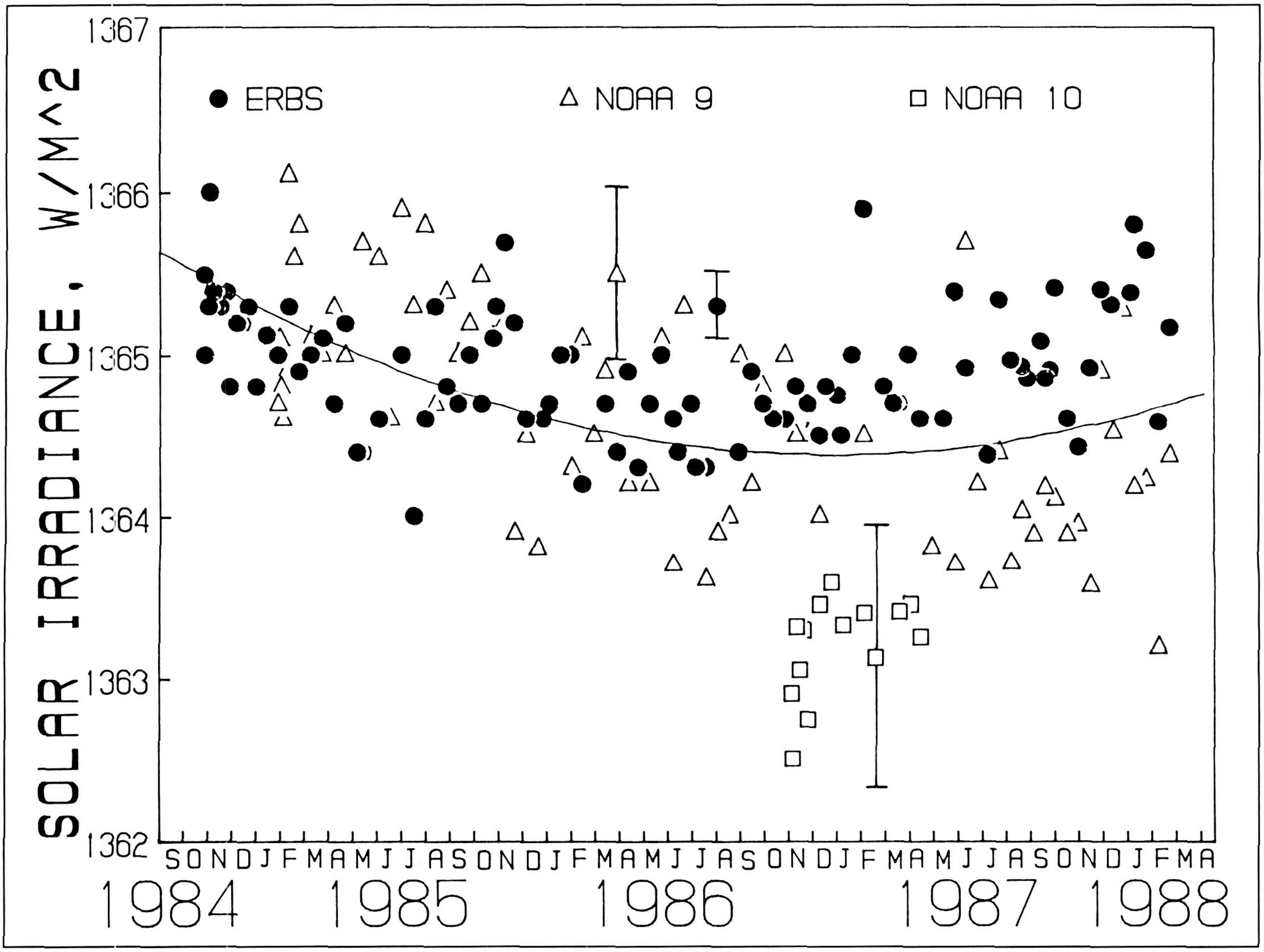

Solar constant values derived from ERBE solar monitors presented as a function of time. The solid curve represents a second-order polynomial fit through all of the data. September 1986 represents the beginning of the sunspot cycle number 22 and of another Hale solar magnetic cycle.

Change in Mid-Latitude Ozone Profile

In late 1986, the Ozone Trends Panel was formed by NASA in cooperation with several national and international agencies to critically review all ground-based and satellite ozone measurements. The motivation for the formation of the panel stemmed from analyses of the Solar Backscatter Ultraviolet (SBUV) and Total Ozone Mapping Spectrometer (TOMS) satellite data that indicated large negative trends in global ozone had occurred over a period of approximately 7 years. The magnitude of the change in ozone concentration at 50 km, for example, was calculated as 3 percent per year from the SBUV measurements, while TOMS showed global column decreases since 1979 were approximately 1 percent per year. Data from the ground-based Dobson network also indicated that the total column ozone had decreased on a global scale significantly but to a lesser extent than reported by the aforementioned satellite data. The urgency of the situation was exacerbated by the large decreases found during the Antarctic springtime.

One of the final conclusions of the Ozone Trends Panel was that the trends observed in the SBUV data were caused by incorrect modeling of the degradation of an optical component necessary for the instrument's calibration. Major evidence for this conclusion came from the analysis of the self-calibrating SAGE I (Stratospheric Aerosol and Gas Experiment) and SAGE II ozone data sets over the period of time coincident with the SBUV measurements.

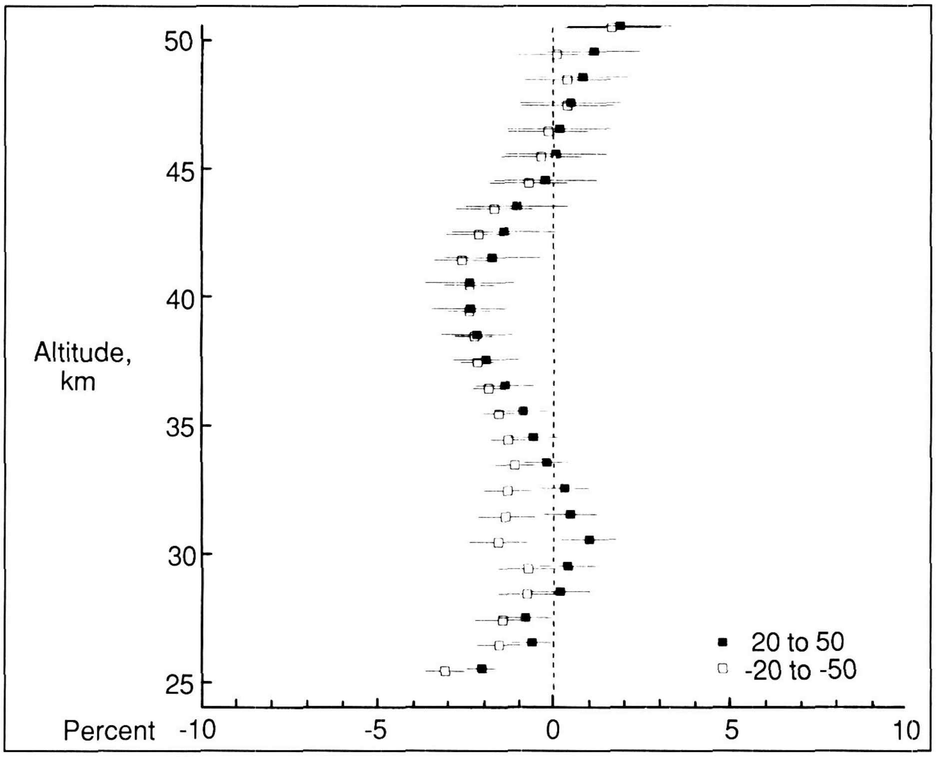

Difference between SAGE II and SAGE I O_3 measurements at 20° to 50° latitude in each hemisphere based on measurements from October 1984 to November 1987 and from February 1979 to November 1981, respectively.

The change in ozone measured by SAGE I (February 1979 to November 1981) and SAGE II (October 1984 to November 1987) was computed so that biases due to the natural interannual ozone variability would have a minimal impact on the trend estimate. Ozone profiles were grouped into latitude bands 10° wide centered on the equator, latitudes of 20°N, 30°N, 40°N, and 50°N, and 20°S, 30°S, 40°S, and 50°S. SAGE I and SAGE II profiles were used when both data sets contained measurements occurring within the same month in the year. The percentage difference profile was computed for each month using SAGE I as the reference point. The collection of all monthly percentage difference profiles spanning the latitude bands in each hemisphere between 20° and 50° was averaged to obtain the mean percentage difference profile. The combined sample contained on the order of 2500 SAGE I profiles and 6000 SAGE II profiles for each hemisphere. The resulting ozone change profiles appear in the figure. Note that the ozone change is only between −3 and +1 percent and that both hemispheres show essentially the same vertical structure. The systematic error between SAGE I and II is estimated to be no more than ±4 percent. Thus, these results do not support the large O_3 changes reported based on SBUV data. Further, they support the altitude shape and magnitude of model results for O_3 change. In addition, the SAGE results are consistent with the observed temperature changes in the tropics.

(M. P. McCormick, 2065)

Interim Reference Model for Middle Atmosphere Water Vapor

Water vapor is an important minor constituent in studies of the middle atmosphere for a variety of reasons, including its role as a source for active hydrogen-oxygen chemical radicals that affect ozone and its use in analysis of transport processes. Until recently, only estimates of the actual water vapor profile were available. Enough data have been obtained now by two different remote measurement techniques that an interim reference profile can be reported for Northern Hemisphere mid-latitudes during springtime and from a pressure-altitude range of 100 mb to 0.01 mb (about 15 km to 80 km in height, respectively). First, the *Nimbus 7* Limb Infrared Monitor of the Stratosphere (LIMS) data obtained during 1979 yielded results from 100 mb to 0.5 mb. Then an extensive series of ground-based, microwave-emission radiometer measurements at the Jet Propul-

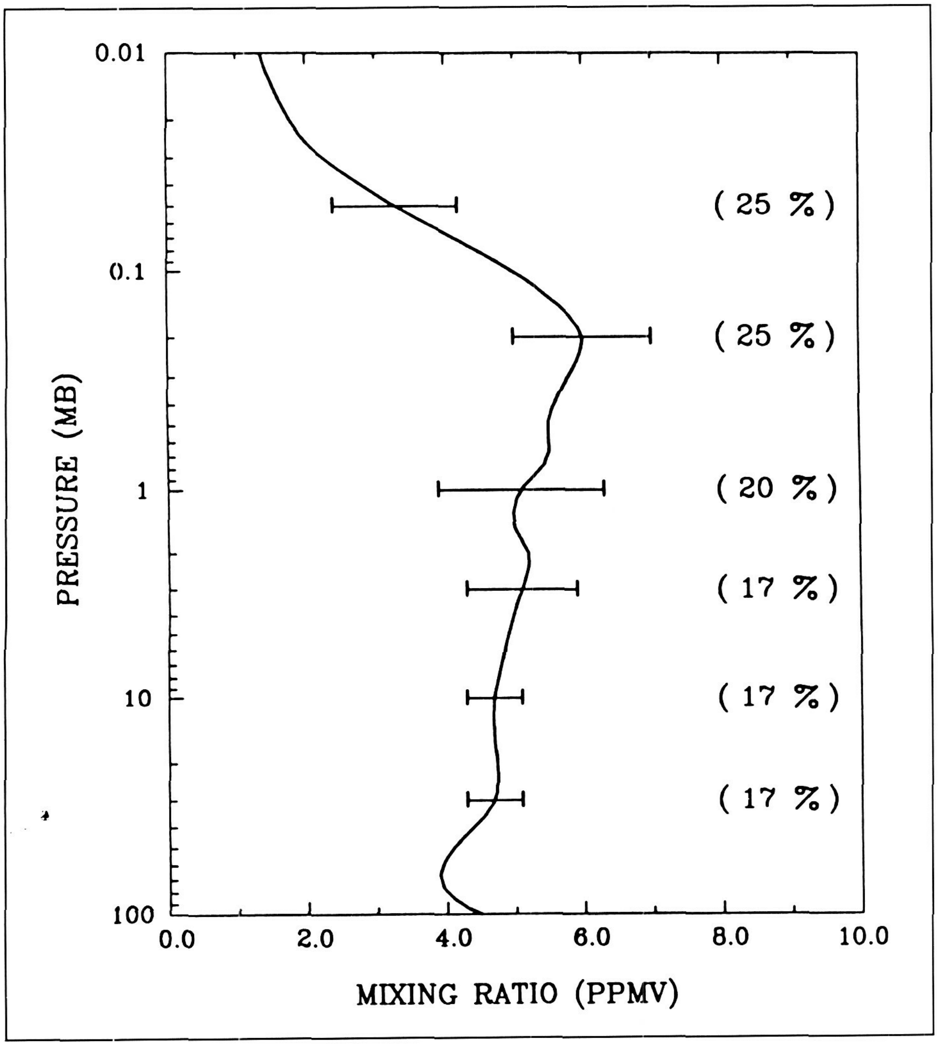

H_2O interim reference profile for Northern Hemisphere mid-latitude during springtime. Bars represent variability of the data. Numbers in parentheses represent estimated accuracies.

sion Laboratory at Penn State University during spring 1984 were employed to extend the results from 0.2 mb to 0.01 mb. The combination of those two different data sets yields the water vapor profile in parts per million by volume (ppmv) in the figure. The horizontal bars represent the observed variability of the data, while values in parentheses indicate accuracies for the mean profile.

Gradual increases of water vapor from the mid-stratosphere (10 mb) to the lower mesosphere (0.5 mb) are consistent with ideas about the formation of water vapor from the oxidation of methane. The decrease from 0.1 mb to 0.01 mb is due primarily to the photodissociation of water vapor by ultraviolet light and Lyman-alpha radiation. The position of the peak mixing ratio near 0.2 mb is not known as well, and its value is uncertain by 25 percent. Data from other latitude ranges and seasons are needed, particularly in the mesosphere, to determine whether this interim profile is representative of the global annual average.

(Ellis E. Remsberg, 3306 and James M. Russell III)

Exploratory Hypersonic Helium Tests on Inlet

The emphasis on the National Aero-Space Plane (NASP) has generated the need to extend simple inlet testing to high Mach numbers. A variety of simple inlet models existed that had been tested at $M = 4$ in air. One was adapted for installation in the Langley Hypersonic Helium Tunnel with modifications to provide for additional parametric variations. Contraction ratio, cowl position and sweep, and Reynolds number were among the test variables considered. Measured data included pressures on the centerline and at two locations on the side walls. Flow visualization was provided by the electron beam technique. Concerns included the possibility of an unstarted tunnel or inlet because there was no previous test experience either in this facility or others at these high Mach numbers ($M = 20$). Test objectives included determining our ability to test reasonably sized inlets at $M = 20$ in helium and to generate sufficient data for computational fluid dynamics (CFD) calibration.

Tunnel flow conditions were fully established for the extremes of tunnel operation ($M = 18$ to 22 and Reynolds number $= 2 \times 10^6$ to 12×10^6). Measured pressures and flow visualization data were obtained for both started and unstarted inlets, depending on inlet

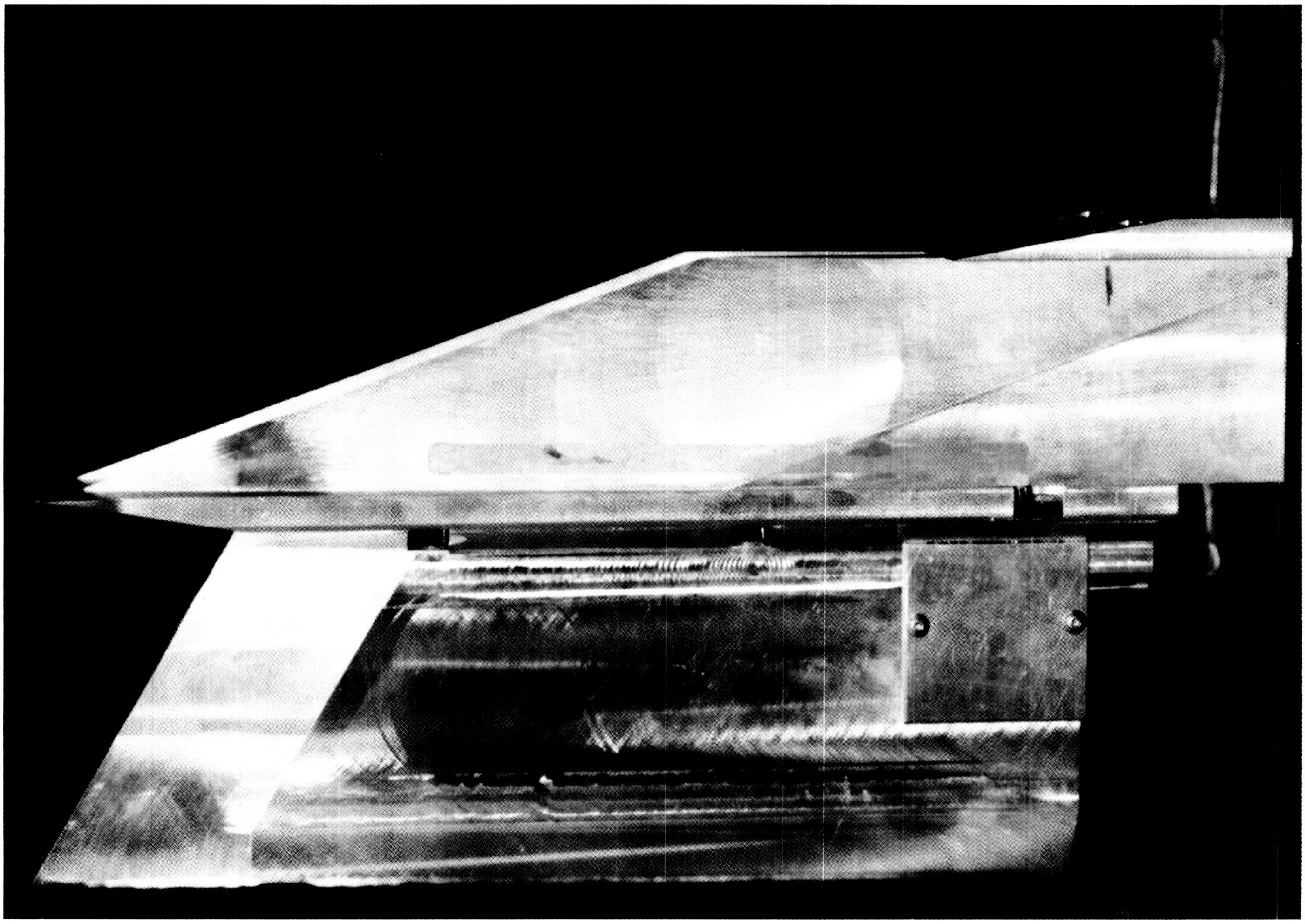

L-87-7809

70° swept simple hypersonic inlet installed in Langley Hypersonic Helium Tunnel (22-in. leg).

configuration and test conditions. Both 30° and 70° swept inlets appeared to start at contraction ratios of 4 and 5 with the cowl at the throat. Moving the cowl forward produced unstarted flow for the 30° inlet, but the 70° inlet remained started at the lower contraction ratio. All configurations exhibited possible corner flow effects and flow separation. Results confirm our ability to determine internal pressure, shock structure, surface flow structure, and mass flow of a variety of inlet configurations at $M = 20$ for CFD calibration.
(W. C. Woods, 3984)

Advanced Manned Launch Vehicle Study

The Langley Research Center Shuttle II study has focused on the concepts, technologies, and operations of next-generation advanced manned launch systems. The basic underlying reason for examining such systems includes the need for routine, low-cost manned access to space in the post-Space Shuttle era. Past launch system designs have generally been performance driven because of technology limitations, restricted development budgets, and the desire to maximize payload to orbit. Often, this has led to increased costs of launch operations. In the Langley Shuttle II study, an approach has been adopted whereby the use of advanced technologies permits vehicle designs to be driven by operations, safety, and low-cost considerations.

Several candidate Shuttle II concepts have been studied (see p. 121 in this report). The reference configuration is a two-stage, fully reusable rocket system, but other concepts include partially reusable

ORIGINAL PAGE
BLACK AND WHITE PHOTOGRAPH

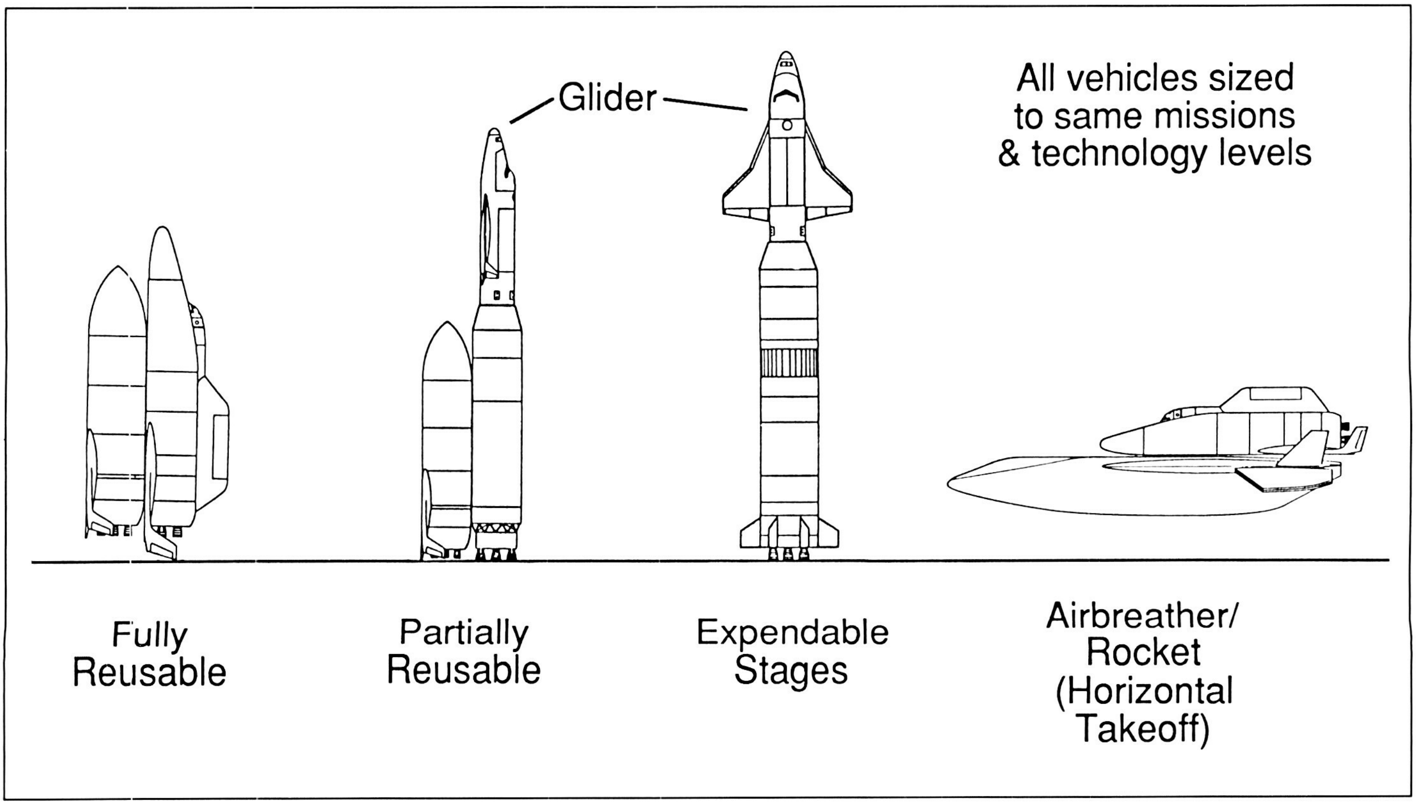

Advanced manned launch vehicle (Shuttle II) concept options.

and expendable stage systems with an unpowered manned glider stage, and a horizontal takeoff version with an air-breathing first stage and rocket second stage.

Technologies play a key role in concept and subsystem selection. For example, fully reusable launch systems require the development of reusable cryogenic propellant tanks. Safety requirements for manned launch systems will require stringent inspection procedures to qualify these tanks for each flight. Operational costs under these conditions must be compared with concepts employing expendable propellant tanks. Also under consideration is the all-hydrogen-fueled vehicle compared with systems that use a hydrocarbon-fueled booster element. Studies indicate large benefits in the development and operations of a common propulsion system when traded against the slight increase in vehicle size.

(T. A. Talay, 2768)

[illegible]

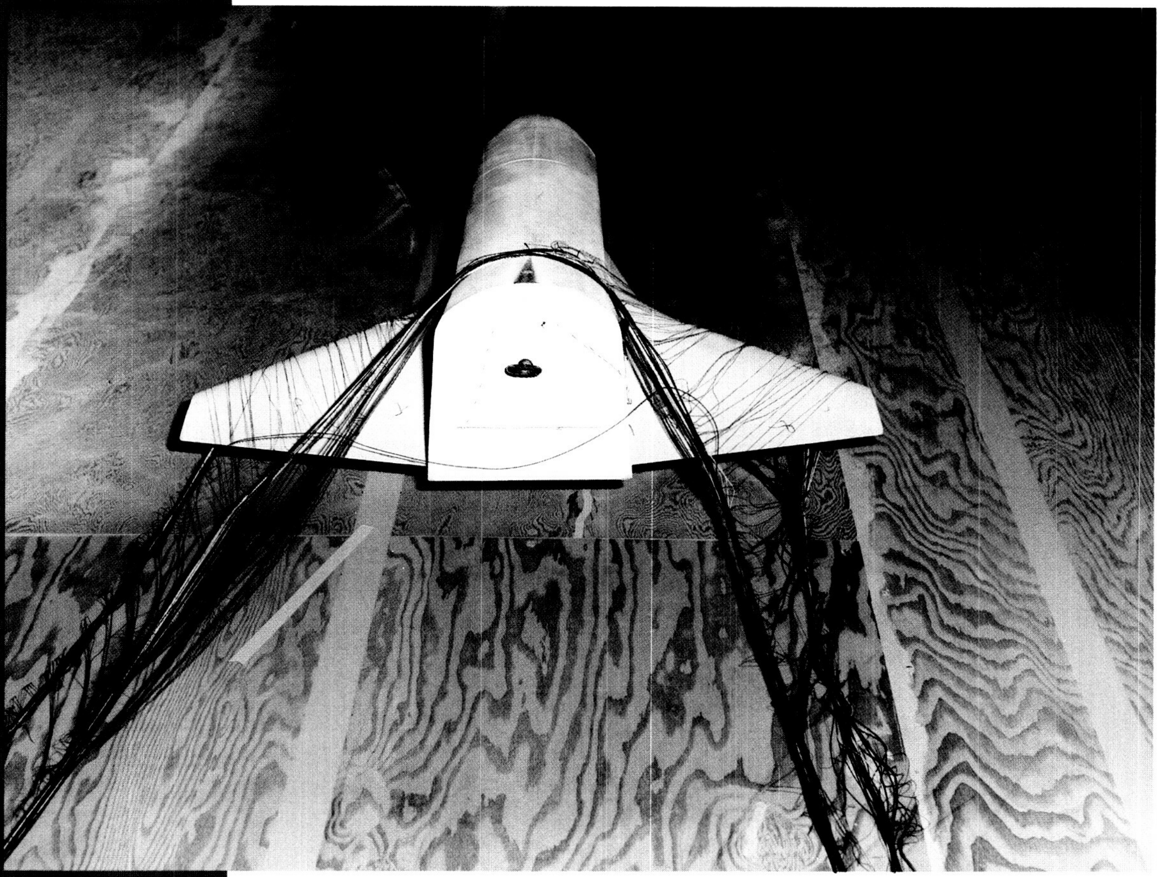

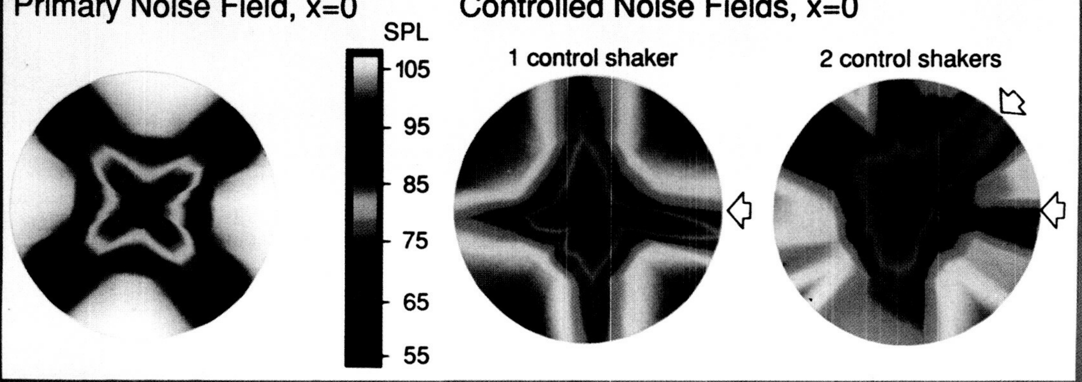

PRECEDING PAGE BLANK NOT FILMED

ORIGINAL PAGE
COLOR PHOTOGRAPH

PRECEDING PAGE BLANK NOT FILMED

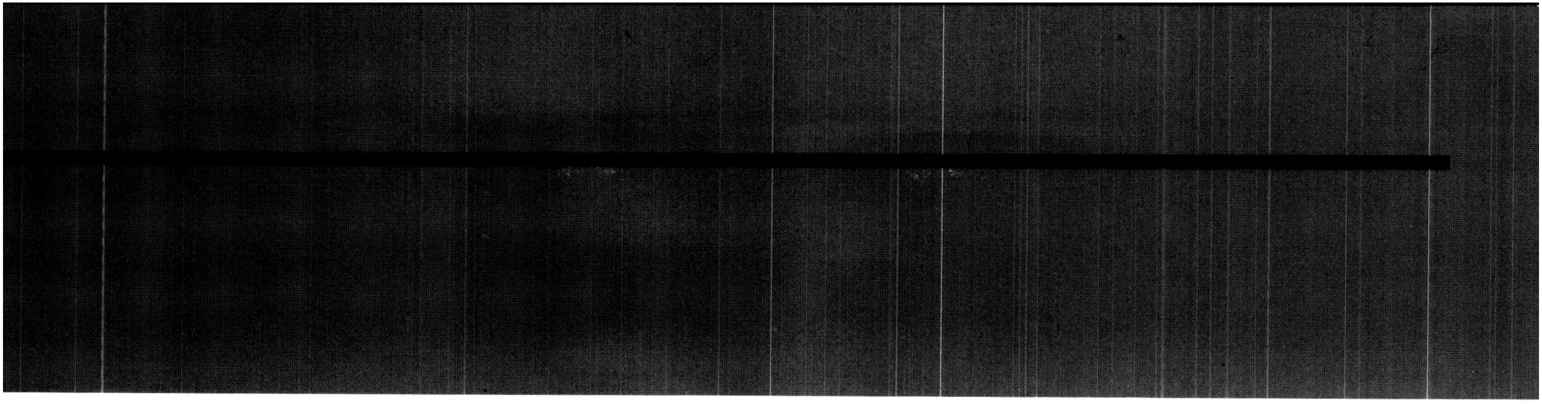

The Structures Directorate conducts basic research and develops technology in the areas of advanced aerospace materials and structures, structural loading and aeroelasticity, noise generation by aircraft propulsion systems and its interaction with structures, and methodologies for interdisciplinary design and optimization. This technology development is directed toward reduction in both weight and cost of aircraft and space structures along with an increase in their reliability and service life. The technology developed also provides improved design capability through more accurate prediction of aerostructural loads, vibration, and noise.

The Materials Division conducts research on advanced materials and their application to aircraft and space structures. The division also develops novel polymeric, metallic, and carbon-carbon materials for these applications. The materials processing and fabrication sciences are developed, and the application of materials to specific flight and space structures is demonstrated. The division conducts research on thermal protection materials and hot structure systems for application to hypersonic and transatmospheric vehicles. The fatigue and fracture behavior of materials is studied in specialized laboratories to provide practical methods for ensuring structural integrity. Specialized facilities are also used to study the behavior of materials under extreme conditions of high and low temperature, pressure or vacuum, and electron radiation.

The Structural Dynamics Division conducts research on aeroelasticity, unsteady aerodynamic loads, aeroservoelasticity, structural dynamics and controls for spacecraft, and landing and impact dynamics for aircraft safety and ground handling. Analytical methods are developed for calculating aeroelastic deformation and instabilities, for active control of dynamic behavior of aircraft and spacecraft, and for dynamic stresses and strains in large space structures. Unique facilities are employed in experimental studies of unsteady aerodynamics, aeroelastic behavior, dynamics of aircraft under simulated landing and crash conditions, and dynamic response and control of large space structures.

The Structural Mechanics Division conducts research on structures and mechanics for advanced aircraft, spacecraft, and automated construction of the space station. Research is conducted on aerothermal loads and high-temperature structures to support technology development for hypersonic vehicles and advanced launch systems. Analytical methods are developed to predict stresses and strains in complex aerospace structures, behavior of composite structures, thermal responses of structures, and aerothermal loads. The division develops new structural systems for aircraft and advanced computational methods for structural analysis and design.

The Acoustics Division conducts research on the generation and propagation of aircraft noise and seeks to understand the relationships between unsteady aerodynamics, structural dynamics, and noise generation by the interaction of fluids with solid surfaces. This research is directed toward predicting and reducing the noise from helicopter rotors, conventional and advanced aircraft propellers, and turbofan engines. Research is conducted on the propagation of noise from its source through the atmosphere and through aircraft structures.

The Interdisciplinary Research Office develops methodologies for aircraft and spacecraft design which will provide a means of understanding and quantifying interactions among multiple engineering disciplines. The goal is to control and exploit these interactions for improved vehicle performance and increased efficiency of the design process. This research has focused on the development of algorithms and techniques for integrating strength and stiffness designs of large-aspect-ratio wing transport aircraft and of rotorcraft. The methodology has been developed for the optimization of space antenna dish shapes subjected to thermal loadings. Controls, structures, and structural dynamics have been integrated for use in the design of space station type structures.

Significant research accomplishments have been made in the Structures Directorate in 1988 in all research areas. Highlights included in this report are representative of the research accomplished in support of the NASA missions in both

aeronautics and space. These highlights illustrate the broad range of the research activities conducted in the Structures Directorate which includes materials and structures, mechanics and dynamics, aeroelasticity, acoustics, and interdisciplinary design and optimization.

B-1B Engine Exhaust Plume Noise Reduction

Twin engine installations, such as those used on the B-1B aircraft, experience structural fatigue failure to their outer nozzle flaps. The dynamic loads associated with these failures are believed to be caused by jet plume shock noise processes. Previous model-scale investigations have shown that satisfactory reduction of this component can be achieved by inserting a tab-like device into the exhaust flow at the nozzle exit. This method, however, may be impractical for the high-temperature exhaust of an F-101 engine with afterburner. Application of a small supersonic auxiliary air jet at the nozzle exit represents an alternate method for shock noise suppression which is free of any heat-related problems.

In order to investigate the capability of the auxiliary air jet to reduce shock noise, an experimental investigation was undertaken in the Langley 16-Foot Transonic Tunnel using a 6-percent full model of the B-1B. The model was instrumented with 24 dynamic sensors on the nozzle outer flaps to assess the success of the tube jet suppressor. The tube jet suppressor consisted of a small tube with a diameter equal to 0.025 times the jet exit diameter. Tube exhaust Mach numbers to 1.5 could be achieved.

Narrowband surface pressure spectra on the nozzle outer flaps contain high-amplitude tones associated with jet plume resonance as shown for the unsuppressed condition. Application of the tube jet suppressor clearly shows that this shock noise component can be controlled. The study shows that the tube jet suppressor must be capable of penetrating into the supersonic portion of the main exhaust flow to achieve reduction.

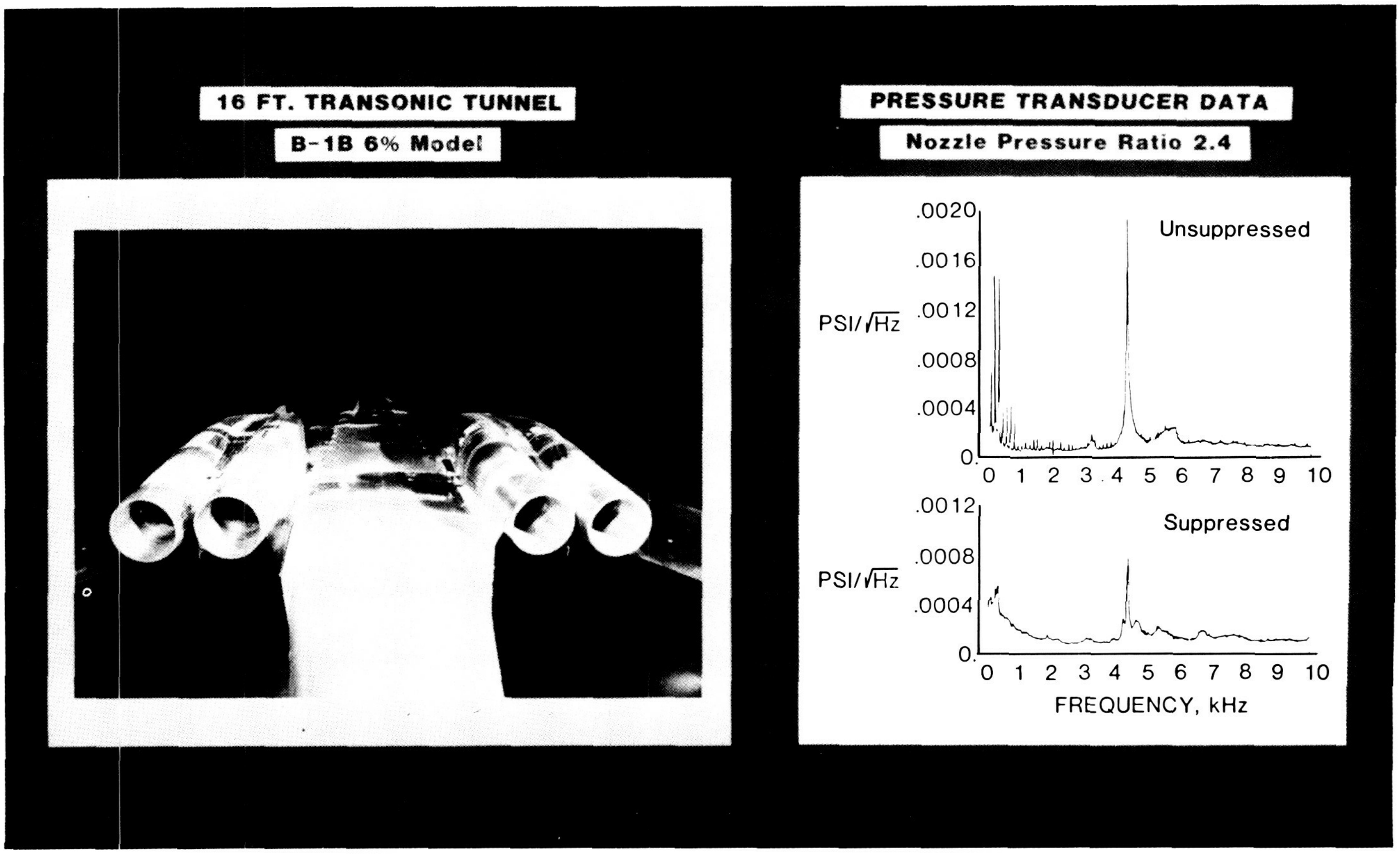

B-1B twin jet engine noise reduction.

L-88-8291

At full scale, the air supply for the small tube jet suppressor could come from the high-speed compressor and be used only when necessary for shock noise control. **(John M. Seiner, 3094)**

Fluctuating Pressure Loads Under Hypersonic Boundary Layer

High-frequency fluctuating pressure loads are an important consideration on supersonic and hypersonic flight vehicles. These loads must be ascertained experimentally with instrumentation capable of withstanding the adverse environment associated with such flows. To aid in this measurement technology development, an experiment was conducted on a flat-plate, boundary-layer survey model in the Langley 8-Foot High-Temperature Tunnel to measure surface pressure fluctuations underneath a hypersonic boundary-layer flow. A 6-in.-square, water-cooled insert was instrumented with an array of piezoresistive sensors (0.093 in. in diameter) as indicated by the photograph at the left of the figure. The insert was installed in the 107- by 51-in. test model as indicated. The model was then inserted into a Mach 4.6, 2840°F total-temperature flow. Data were taken for 4 sec at a sampling rate of 125 kHz and stored on a hard disk for posttest analysis.

A power spectrum of the fluctuating pressure over the frequency range from 100 Hz to 40 kHz is shown at the right of the figure for the test conditions stated. Except for the low-frequency range to approximately 3 kHz, the spectrum falls off exponentially with frequency. The total spectrum level,

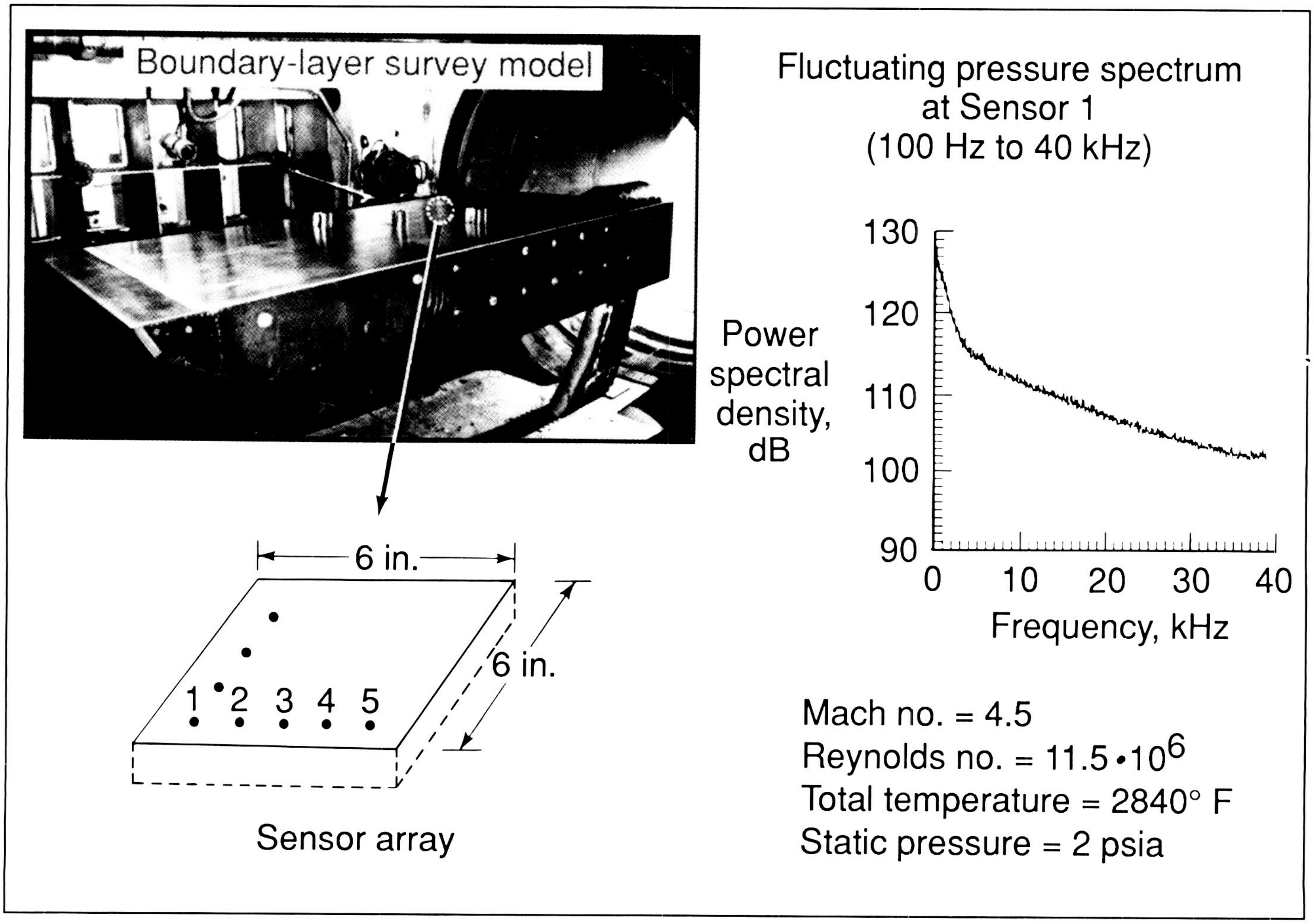

Hypersonic fluctuating pressure loads.

L-88-9398

obtained by integrating under the spectrum curve, is approximately 147 dB. Not shown are the cross-spectral densities for the different microphone pairs. The completion of this experiment demonstrates the ability to measure high-frequency loads in a high-temperature, high-speed flow environment. Particular elements of concern were sensor installation, data acquisition, and calibration. This measurement capability is essential in defining fluctuating pressure loads on high-speed vehicles.

(Tony L. Parrott, 4310)

Damage-Tolerant Cover Panel for High-Aspect-Ratio Wing

Advanced-concept composite structures have an exciting potential for use as primary aircraft structures. These advanced-concept structures exploit the unique features of composite materials, and the results are innovative and affordable structures fabricated using the latest materials and material forms. An example of an advanced-concept composite structure is a blade-stiffened cover panel that satisfies the design requirements for a stiffness-critical, high-aspect-ratio wing for a transcentury transport aircraft. The blade is a simple stiffener configuration that lends itself to cost-effective fabrication techniques. This structure was fabricated using the damage-tolerant IM6/1808I interleaved material. The structure was severely impacted with 100 ft·lb of energy and was subsequently compression loaded to validate the damage-tolerant design.

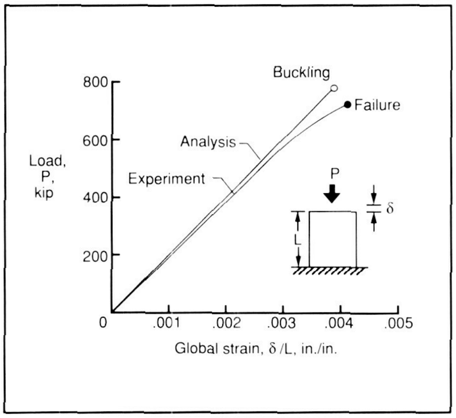

Response for compression-loaded, blade-stiffened panel.

Experimental and analytical results for load as a function of the global failure strain are shown in the figure for the blade-stiffened cover panel. Panel buckling initiated panel failure, and the nonlinear load-global strain behavior in the figure shows the experimental response. A linear finite-element analysis was conducted to predict both load-global strain response and panel buckling. The linear analytical results agree reasonably well with the experimental results and predict that panel buckling occurs prior to panel failure. The measured global strain at failure for the cover panel exceeded 0.004 in./in. despite the severe impact event, and the local damage caused by the impact did not affect the global panel response. This failure strain is approximately 33 percent higher than the failure strain for impact-damaged panels fabricated using brittle material systems. This cost-effective, damage-tolerant cover panel for a high-aspect-ratio wing illustrates the potential of composite materials for advanced-concept primary aircraft structures.

(M. J. Shuart, 2813 and C. B. Prasad)

Improvement of Structural Analysis by Exploiting Supercomputer Architecture

Modern supercomputers such as the Numerical Aerodynamic Simulation (NAS) CRAY-2 offer enormous potential for structural analysts. The 256-million-word memory of the CRAY-2 and its maximum computation rate of several hundred million operations per second make possible the solution of problems that would not have been attempted a few years ago. However, a major impediment confronts structural engineers who wish to exploit supercomputers: Most structural analysis codes do not take full advantage of the architectural features of advanced computers and typically achieve only 5 to 10 percent of the maximum computation rate on realistic structural analysis problems. One difficulty that is being addressed successfully is the computationally intensive solution of very large systems of equations of the type that occur in structural analysis applications.

Two new equation solution routines that exploit supercomputers were developed and incorporated in a large, finite-element structural analysis code for evaluation. This code, denoted the Computational Structural Mechanics Testbed, was used to solve several large structural analysis problems on the NAS CRAY-2. The new equation solution routines reduced the equation solution time by more than a factor of 10 when compared to the initial solver (a sparse Choleski method) in the Testbed code. Direct and iterative methods were implemented in the two new routines, and the methods were compared to deter-

mine classes of problems for which each method is best suited.

The direct methods achieve computation rates in excess of 150 million operations per second by integrating various forms of banded and profile storage (a technique known as loop unrolling) and by the use of fast local memory. The iterative methods, while not achieving such high computation rates, require less memory and for some problems also require less time than the direct methods. The figure illustrates the relative performance of the initial sparse Choleski equation solver and the best new direct and iterative methods. For the static analysis of a composite blade-stiffened panel, a direct method was fastest. For the three-dimensional cube problem, which is representative of detailed local analysis around high stress regions in the panel, an iterative method was fastest. The new equation solvers were also used to carry out a linear elastic static analysis of the Space Shuttle solid rocket booster. For this very large problem, the fastest direct method, a profile Choleski solver, was more than 10 times faster than the initial solver in the Testbed code.

The development and implementation of the new equation solvers within an existing large finite-element code demonstrated that existing computer codes can be substantially improved to take advantage of advanced computer architectures without rewriting the entire code. The comparison of the solvers on a wide variety of structural analysis applications has helped to identify classes of problems for which the various solvers perform best. **(Eugene L. Poole and Andrea L. Overman; W. Jefferson Stroud, 3939)**

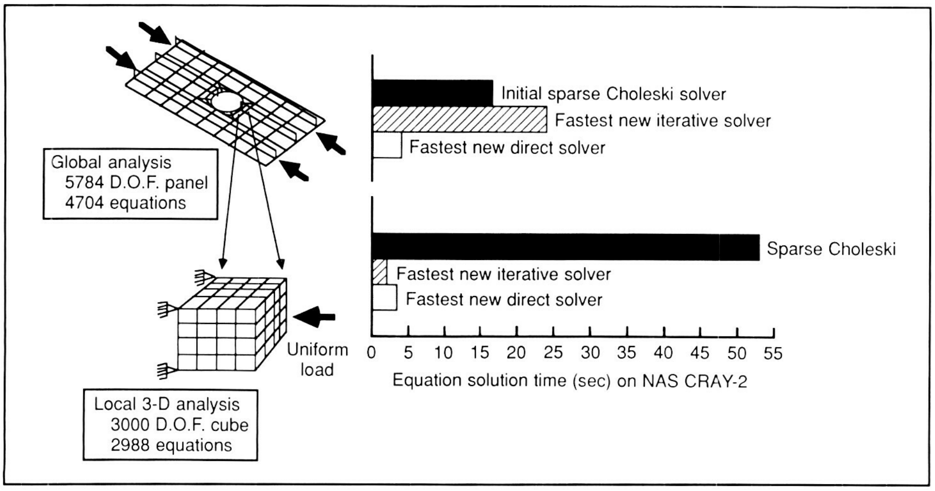

Comparison of equation solvers for two structural analysis example problems.

Tests and Analyses of Composite Z-Frame Subfloor Sections

Composite materials are presently being investigated as the primary structural material for the next generation of airplanes. Consequently, a program has been initiated at Langley Research Center to address the behavior of composite aircraft structures under crash conditions through detailed experimental and analytical studies of structural subcomponents.

Two circular 6-ft-diameter graphite/epoxy fuselage floor sections have been statically tested as an initial step in assessing the response of such structural subcomponents to vertical impact loads. Both sections have an identical skeletal framework, shown in the photograph, consisting of three graphite/epoxy, 6-ft-diameter, semicircular Z-cross-section frames (Z-frames), three aluminum floor beams, and fifteen graphite J-stringers. Notches machined into the outside of the Z-frames accommodate stringers that are attached to the frames with aluminum shear clips and rivets. One specimen had a graphite/epoxy skin bonded and riveted to the frames and stringers. The other specimen did not have the graphite/epoxy skin (skeleton specimen). This skeleton specimen, originally 39 in. in height, was statically crushed approximately 12 in. Some results from this test are shown in the figure. (For presentation in the figure, the load-deflection response for the skeleton floor section was reduced to one-third of its value to facilitate comparison with the load-deflection data obtained from the tests of an individual frame.) For the single frame test, the frame was sandwiched between two fences that limited the degree of twisting and out-of-plane bending along the entire length of the frame. The equivalent one frame load from the floor section load agrees well with load-deflection data obtained from the tests of the single frame. For a static test of the skinned subfloor specimen, the stiffness from

Failed skeleton subfloor section. L-88-2459

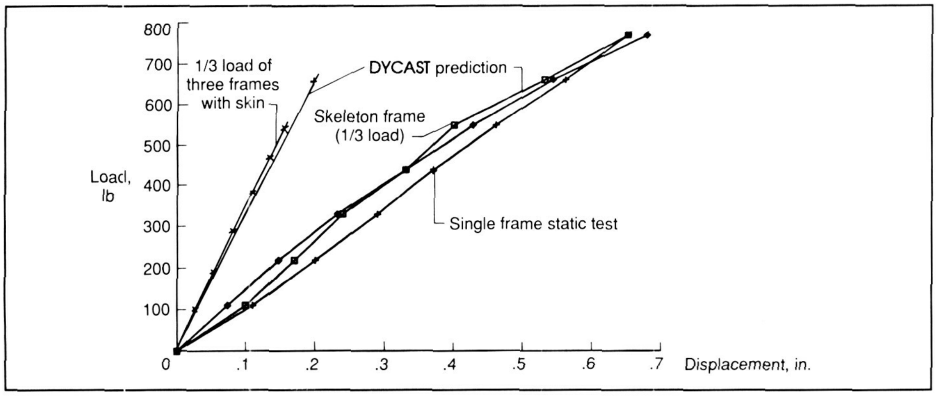

Results from vertical impact loads on simulated fuselage floor sections.

the load-deflection data was approximately four times larger than the stiffness of the skeleton specimen. Also included in the figure for comparison purposes are analytical results obtained by using the DYCAST (Dynamic Crash Analysis of Structures) finite-element computer code. The agreement between experiment and analysis is good. **(Richard L. Boitnott, 3795 and Edwin L. Fasanella)**

Fiber/Matrix Separation in Silicon Carbide/Titanium Matrix Composites

Recent interest in hypersonic flight vehicles has required the development and characterization of materials capable of retaining high stiffness and strength at temperatures in excess of 1000°F. One such class of materials is metal matrix composites.

The material system studied in this investigation consisted of a titanium (Ti 15-3-3-3) matrix reinforced by continuous silicon carbide (SCS_6) fibers. Room temperature quasistatic tension tests were performed on matrix material, and on $[0]_8$, $[90]_8$, $[0/90]_{2s}$, $[0/\pm 45/90]_s$, and $[0_2/\pm 45]_s$ composite laminates in order to evaluate an existing elastic-plastic model that had successfully predicted the response of other metal matrix systems. The initial moduli and Poisson ratios were found to be in good agreement with those predicted by the model. However, the laminates containing off-axis plies exhibited nonlinear mechanical response at stress levels that were significantly lower than the onset of yielding predicted by the model. The edge replication technique was used to document damage development in the laminates. In the edge replication technique, a permanent impression of the specimen edge is produced in a cellulose acetate film. Edge replicas were taken at various stages of the quasistatic load history of a specimen, and were subsequently examined via scanning electron microscopy.

Studies found that after sufficient load was applied to specimens containing off-axis plies (usually 20 to 30 ksi), fibers began to separate from the matrix material. Upon unloading, the fiber and matrix were again in contact. The figure shows a representative stress-strain curve for a $[0/90]_{2s}$ laminate that was reloaded after fiber/matrix separation had occurred. The micrograph at the left shows the fiber and matrix in contact at low stress, while the micrograph at the right shows evidence of

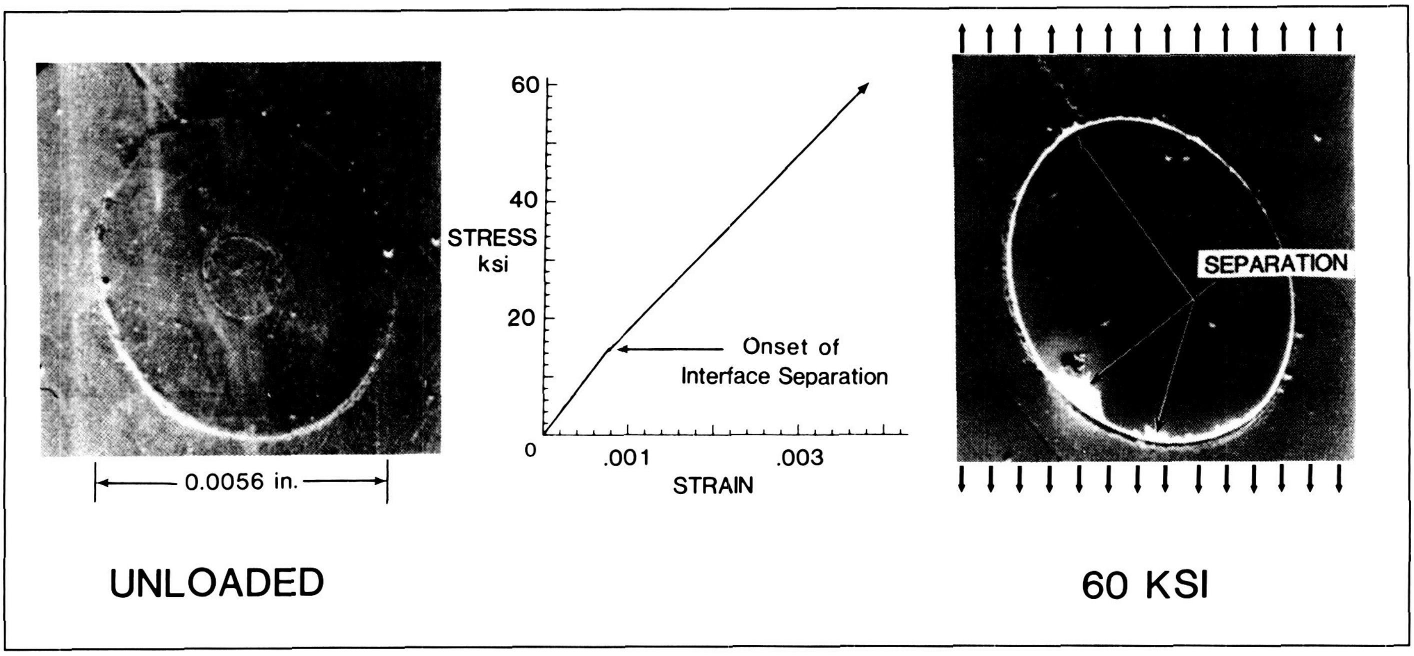

Fiber/matrix interface failure in SCS_6/Ti-15-3.

separation at high stress. More detailed evaluation revealed that the separations occur primarily in the reaction zone between the silicon in the fiber and the titanium in the matrix. The "knee" in the stress-strain curve is indicative of the loss of stiffness that occurs when fibers in off-axis plies are no longer in contact with the matrix, and therefore no longer carry load.

The results of this study indicate that the fiber/matrix interface in the silicon carbide/titanium system is quite weak. Improved bonding between the fiber and matrix is needed in order to raise the operating stress level of this material to a desired level. This fiber/matrix separation has been incorporated into strength prediction models.
(W. S. Johnson, 2715)

Damage Tolerance Analysis for Composite Materials and Structures

Composite materials are beginning to be used for primary aircraft structural components. In order to ensure that these composite structures are both sufficiently durable for economy of operation, as well as adequately fail-safe or damage tolerant for flight safety, a damage tolerance methodology similar to the one that exists for metallic structures is needed. To this end, a methodology for predicting damage onset and growth in composites and assuring that the composite is fail-safe in the damage condition was developed. This damage-threshold/fail-safe methodology includes the following steps. First, cracks are assumed to exist in the matrix of all plies whose fibers are not aligned with the load direction. In addition to any structural discontinuities that are present in the structure (such as edges, holes, or internal plies that are dropped to taper thickness), matrix cracks are common sources for delamination, which is a separation of the composite plies. Next, delamination onset is predicted using fracture mechanics. The strain-energy-release rate associated with the delamination is calculated and plotted as a function of the number of cycles to delamination onset. Then, delamination growth may be accounted for in one of three ways: by using delamination growth laws in conjunction with strain-energy-release rate analyses that incorporate delamination resistance curves; experimentally, by using measured stiffness loss; or conservatively, by assuming that delamination onset corresponds to catastrophic delamination growth. The composite can be shown to be fail-safe by accounting for the accumulation of delaminations through the thickness and calculating the influence of delaminations on residual properties.

To illustrate how this approach may be implemented, the tension

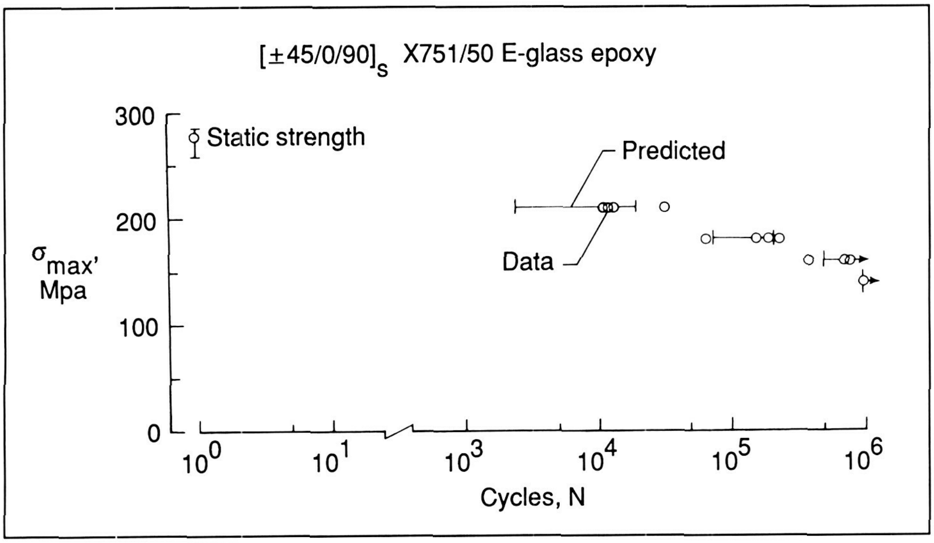

Fatigue life prediction based on local delamination accumulation through thickness.

fatigue life of composite laminates was predicted. A fracture mechanics analysis of delaminations that initiate at the edge of the composite was used to generate a delamination onset criterion for the material as a function of fatigue cycles. Then, strain-energy-release rates were calculated for local delaminations that formed at matrix ply cracks through the laminate thickness and were compared to the criterion to predict local delamination onset. Delamination growth was accounted for experimentally using measured stiffness loss. Finally, fatigue failures under constant cyclic stress σ_{max} were predicted, as shown in the figure, by accounting for the local strain concentration on the 0° plies resulting from delaminations forming at matrix cracks through the laminate thickness.

Although the results shown are for a relatively simple structural configuration and loading, the damage-threshold/fail-safe methodology developed in this study provides a generic framework for analyzing the damage tolerance of composite structures under a variety of loading situations.

(T. Kevin O'Brien, 2093)

Damage-Tolerant Composite Material Concepts

Damage tolerance is an essential requirement for composite materials to be used in commercial aircraft. Moreover, in today's aircraft market, the use of composite material must be justified on the basis of cost. Stitching of dry fiber layers, followed by resin infusion, may provide a means to achieve composite material that combines outstanding damage tolerance with the potential for cost-effective manufacturing.

A study of stitching was conducted using test plates produced by stitching layers of dry AS4 graphite fabric with closely spaced threads followed by resin infusion of 3501-6 epoxy-matrix material. In this construction, the graphite fabric forms a two-dimensional array of 0°, ±45°, and 90° fibers (quasi-isotropic) while the stitching threads provide through-the-thickness reinforcement. Compression failure strain achieved by the stitched plate is compared to other material combinations in the figure.

A failure strain level of 0.006 is an accepted measure of merit in the compression-after-impact tests. The AS4/3502 material is representative of the brittle composite materials in current use. The IM7/8551-7 material (Hercules Corporation) is representative of the best available commercial composites. The T300/8551-7 material incorporates a special fabric to improve damage tolerance.

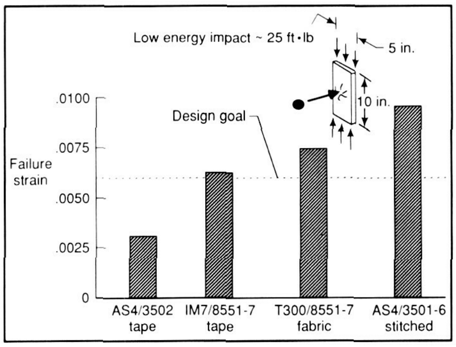

Compression-after-impact failure strain of quasi-isotropic graphite/epoxy laminates.

The materials incorporating the 8551-7 resin matrix offer significant improvements in damage tolerance, but current costs do not favor extensive application. Without stitching, the AS4/3501-6 would perform at the same level as AS4/3502 since both are brittle composite materials. With stitching, the AS4/3501-6 material demonstrated outstanding performance in this test.

It is shown by this study that stitching composite materials in a textile process offers improved damage tolerance and, in combina-

tion with resin infusion molding, has the potential for cost-effective fabrication.
(M. B. Dow, 2850)

Significance of Small-Crack Effect for Fatigue Design

Current standard tests to evaluate fatigue-crack-growth rates use specimens with crack sizes > 1 mm. For these large cracks (> 1 mm), the crack-growth-rate data at different stress levels and crack lengths are correlated very well by the stress-intensity-factor-range parameter ΔK. Design calculations of crack-growth life are based on the assumption of a unique growth rate against the ΔK relationship. However, in recent years it has been found that in some materials, small cracks (< 0.5 mm) grow faster than large cracks at the same ΔK level. To assess the significance of this small-crack effect on fatigue design calculations for an airframe aluminum alloy (2024-T3), crack-growth lives computed using only the large-crack data were compared to lives computed using a combined small-crack and large-crack data base.

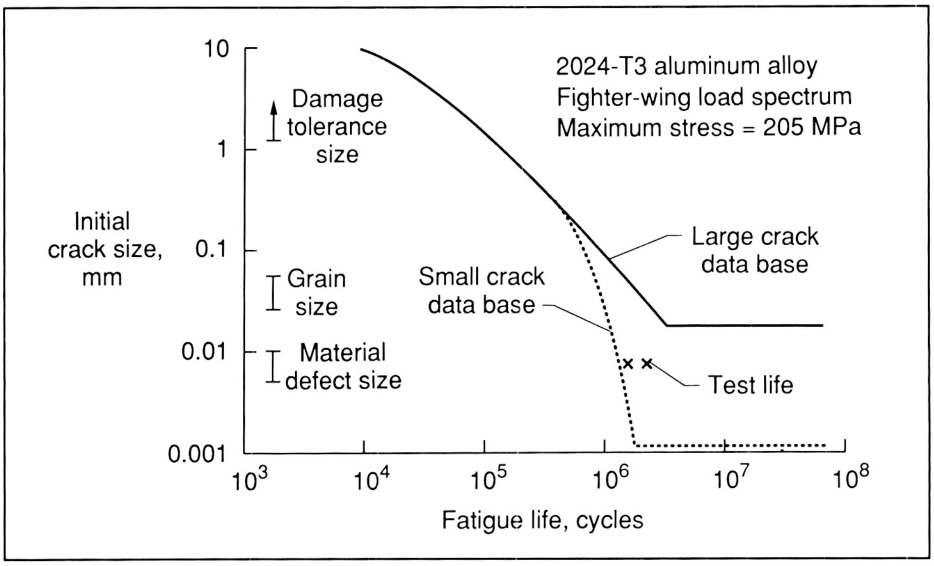

Effect of small-crack behavior on calculated crack growth lives as function of initial crack size.

The figure shows the crack-growth lives computed for test specimens subjected to a fighter-aircraft loading spectrum as a function of the initial crack size assumed in the analysis. The solid line was computed using only the large-crack data, and the dotted line was computed using the combined data base. Also shown in the figure are the lives from two tests of initially crack-free specimens. The test lives are plotted at the crack size where the cracks were first measured in the tests, that is, a size just larger than the inclusion particles where the cracks initiated. The results show that for assumed initial crack sizes below approximately 0.3 mm, the lives computed using the small-crack data were lower than those computed using the large-crack data. The life computed using the small-crack data agreed well with the test lives, whereas the large-crack data predicted infinite life. This study indicates that crack-growth lives calculated using conventional, large-crack data are nonconservative when small initial cracks are assumed in the analysis. Current damage tolerance design analyses (crack sizes > 1 mm) are not affected by the small-crack effect.
(E. P. Phillips and J. C. Newman, Jr., 3192)

Flight Service Experience With Composite Spoilers

The influence of operational environments on the long-term durability of advanced composite materials and aircraft components fabricated from them is an ongoing concern of aircraft manufacturers and airline operators. Some of the uncertainties include the effects of moisture absorption, ultraviolet radiation, aircraft fuels and fluids, long-term sustained stress, fatigue loading, and lightning strike.

In the early 1970s, the Langley Research Center initiated a series of composite flight service programs to evaluate the long-term durability of several advanced composite materials and structural components. The largest data base has been acquired with composite spoilers on B-737 aircraft. A total of 108 spoilers with graphite/epoxy skins bonded to aluminum substructure were installed on B-737 aircraft in 1973. Since then, the composite spoilers have accumulated 2.5 mil-

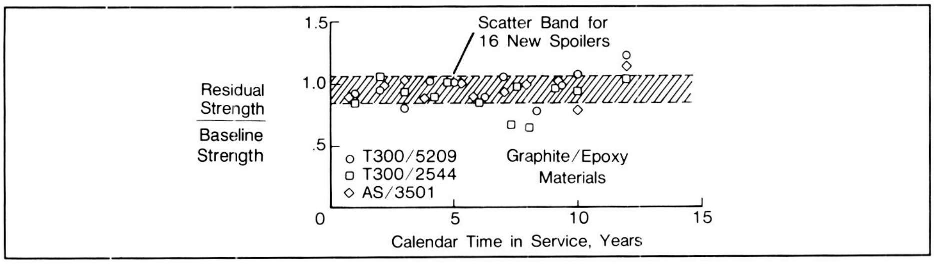

Residual strength of B-737 graphite/epoxy spoilers.

lion flight hours, with the high-time spoiler having accumulated over 40,000 flight hours. The spoilers were fabricated with three different graphite/epoxy systems and have been flying in worldwide environments with the following airlines: Piedmont, Frontier, Aloha, Pacific Southwest, Air New Zealand, Lufthansa, and VASP (Brazil).

A total of 35 spoilers have been removed from service and tested, and the residual strength results are presented in the figure for service times up through 12 years. The residual strength of most spoilers falls near or within the strength scatter band for the baseline spoilers. However, spoilers with significant corrosion damage indicated a 35-percent strength reduction after 7 and 8 years. The corrosion damage to the aluminum substructure was initiated by moisture intrusion through cracked paint and sealants. The corrosion damage and subsequent strength loss can be prevented by design changes and improved sealing methods.

The results of this program indicate that composite materials have good long-term durability in commercial transport operating environments. Aircraft manufacturers have started to make production commitments to composite structures for transport aircraft.

(H. B. Dexter, 2869)

Unique 7475 Aluminum Structural Concept Fabricated by Superplastic Forming

Recent advances in the state of the art of superplastic forming (SPF) of certain titanium and aluminum alloys have made it possible to fabricate design shapes that were unattainable in the past.

Superplasticity is the ability of a material to undergo very large strains prior to localized necking and fracture. The 7475 aluminum, for example, when heated to 960°F and subjected to a tensile stress of 250 to 300 psi, will exhibit strains to failure of 700 to 900 percent. The ability of the material to readily deform at elevated temperatures when subjected to low stresses makes it possible to blow mold or superplastically form the material into a mold cavity using gas pressures of 50 to 100 psi. Unfortunately, due to the metallurgical nature of the 7475 aluminum alloy, superplastic deformation creates internal voids or cavities within the material. Therefore, studies were conducted to alleviate cavitation resulting from SPF in order to maximize post-SPF mechanical properties. Results showed that the cavities created during SPF could be healed through the application of postforming pressure.

Analytical studies were conducted to assess the potential of increasing structural efficiency through the design of unconventional SPF structural concepts. As a result, the curved-cap beaded-web compression specimen shown in the figure was designed to offer a higher structural efficiency than a honeycomb-core

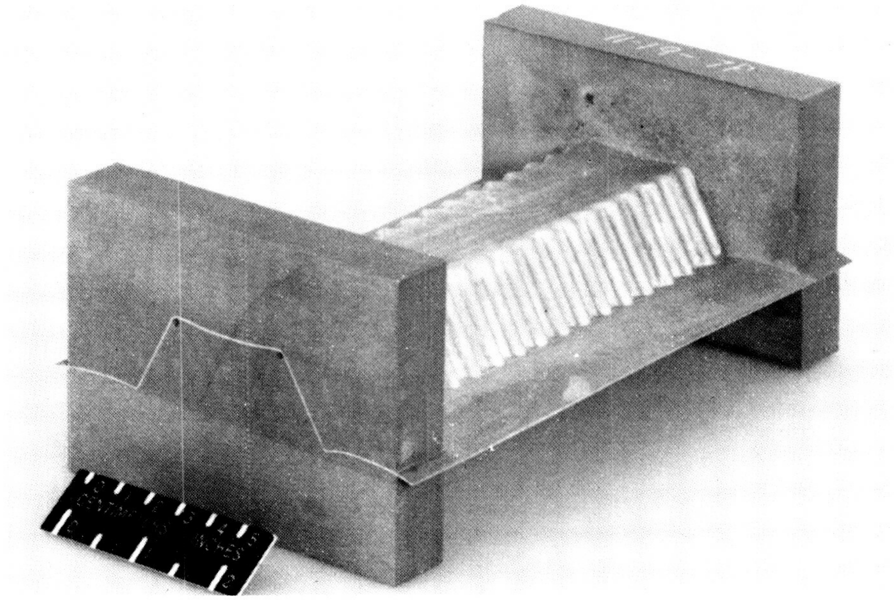

Superplastically formed 7475 aluminum curved-cap beaded-web compression specimen.

L-87-12114

ORIGINAL PAGE IS
OF POOR QUALITY

sandwich panel. The specimen was superplastically formed using an 0.020-in.-thick fine-grained 7475 aluminum alloy sheet. Time-temperature-pressure profiles were established to blow mold the specimen into a tool cavity at a temperature of 960°F. Following contact of the sheet material with the tool, the postforming gas pressure was increased to 300 psi and maintained for 30 min to heal the cavitation. The ends of the specimens were then potted and machined for testing. The test results obtained agreed favorably with analysis, demonstrating that SPF does offer the potential to improve structural efficiency through the forming of uniquely shaped structural components that would be impossible to fabricate using conventional processes.
(T. T. Bales, 3405)

Shape Sensitivity Analysis of Wing Characteristics

The objective of this proof-of-concept study is to determine the changes in elastic wing characteristics with respect to changes in wing shape parameters, accounting for structures-aerodynamics coupling.

The wing lift distribution and related quantities are calculated by combining the Weissinger L-method and the Giles equivalent plate analysis method. The derivatives of the resulting analysis equations with respect to the wing shape parameters are found analytically and yield the sensitivity parameters of interest.

The results in the figure show the sensitivity of the trim angle of attack of a forward-swept wing to changes in the sweep, and the strong coupling effect responsible for the opposite slopes of the rigid and elastic curves. Comparison between sensitivity curves generated by repeated analyses and linear extrapolations based on sensitivity analysis at the baseline sweep attest to the accuracy of the method. Further, it indicates that, at least in this aerodynamic regime, the change in trim angle of attack is linear enough that it can be accurately predicted by sensitivity derivative-based extrapolations over a range of ±50 percent change in the sweep angle.

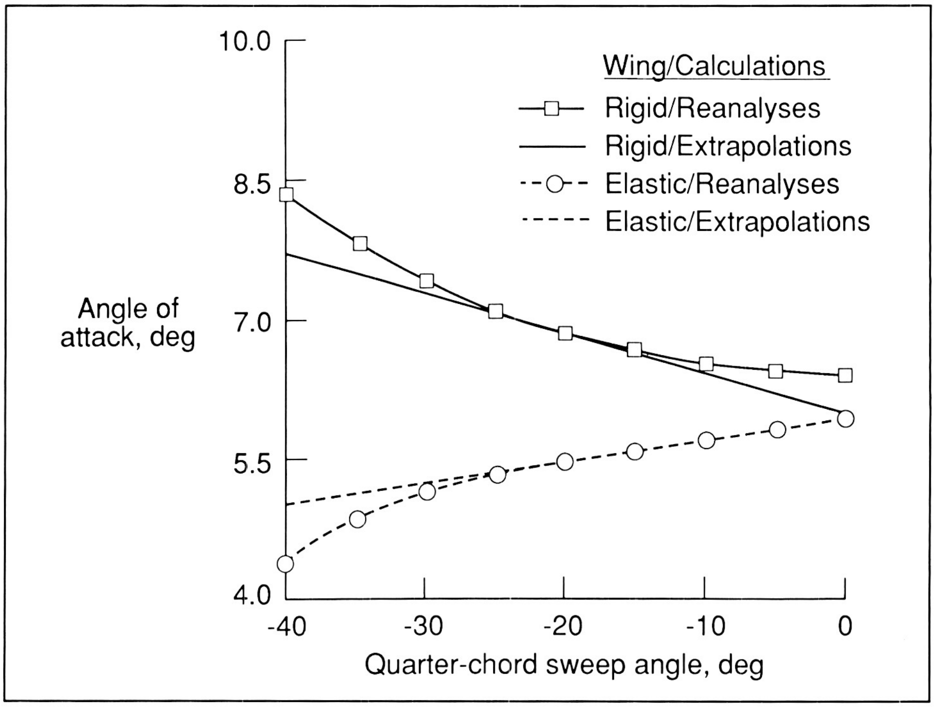

Angle of attack versus sweep angle results.

The application of formal shape optimization methods to aircraft design has been hampered by the lack of analytical sensitivity capabilities for aerodynamic and aeroelastic responses. This effort demonstrates that such analytical capability can be developed. The resulting derivatives are generated at lower cost than with the traditional finite-difference approach. Further, at least for the subcritical flight regime, these derivatives can be used to extrapolate the wing aeroelastic response over a wide range of variation of the shape.
(Jean-Francois M. Barthelemy, 2887)

Unsteady Transonic Small-Disturbance Theory With Entropy and Vorticity Effects

Modifications have been made to the Computational Aeroelasticity Program-Transonic Small Disturbance (CAP-TSD) code to more accurately treat attached flows with strong shock waves involving entropy and vorticity generation. The CAP-TSD code solves the transonic small-disturbance potential equation

and has been developed for aeroelastic analysis of complete aircraft configurations in the flutter-critical transonic speed range. Because the classical TSD theory is only applicable to cases involving mild shock waves, the code was modified to include the effects of shock-generated entropy and vorticity which are important for strong shock cases. The modified code includes these effects while retaining the relative simplicity and cost efficiency of the TSD formulation.

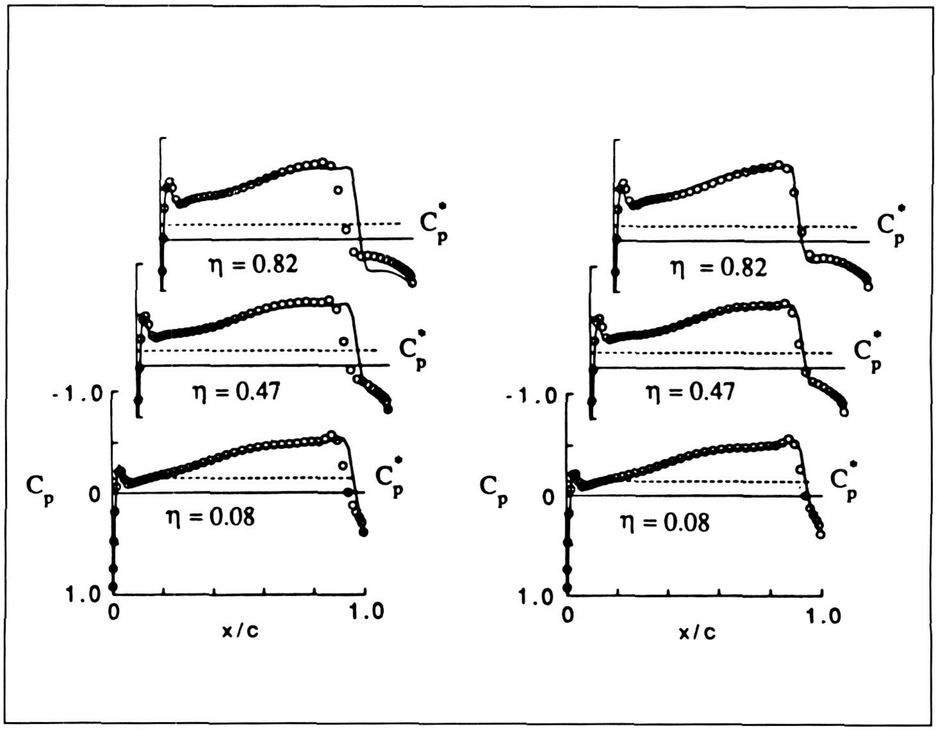

Comparison of chordwise pressure coefficients for unmodified (left) and modified (right) theories.

To test the modified TSD theory, calculations were performed for the ONERA (Office National d'Etudes et de Recherches Aerospatiales) M6 wing. The M6 wing has an aspect ratio of 3.8, a leading-edge sweep angle of 30°, and a taper ratio of 0.562. Results were obtained at the free-stream Mach number of $M = 0.92$ with the wing at an angle of attack of 0°. The figure shows the steady pressure coefficient C_p distributions versus fractional chord x/c for three values of the fractional semispan of the wing η. For this case, the flow is symmetric about the wing with shocks on the upper and lower surfaces. As shown at the left of the figure, the results from the unmodified theory indicate that the shock is located too far aft and is too strong outboard near the tip in comparison with an Euler calculation (circular symbols). When the entropy and vorticity corrections are included in the calculation, the shock is in excellent agreement with the Euler results in both strength and location, as shown at the right of the figure. Consequently, the steady pressure distributions from the modified TSD theory compare very well with the Euler pressures. The entropy correction alone produces a shock that is still downstream of the Euler location, approximately halfway between the two sets of CAP-TSD results shown in the figure. Therefore, both entropy and vorticity corrections are required to give Euler-like accuracy. The capability now provides the aeroelastician with an affordable method to analyze relatively difficult transonic cases consisting of attached predominantly streamwise flows with strong shocks, without resorting to solving the computationally more expensive Euler equations.

(John T. Batina, 4236)

Agreement of Improved Boundary-Layer Method for Unsteady Potential Flow With Navier-Stokes Solution

Unsteady transonic flow fields are routinely calculated with computer codes based upon the Transonic Small Disturbance (TSD) potential theory. Results are quite accurate for thin bodies as long as viscous effects are small. As moderate-strength shock waves develop, the inclusion of viscous effects is essential for accurate predictions of aerodynamic loading. For attached flows, techniques are available for interacting a boundary-layer analysis (such as the integral method of Green) with the inviscid solution algorithm. For separated or nearly separated flows, this interactive approach fails due to a singularity in the boundary-layer equations. This singularity can be circumvented by solving the boundary-layer equations in inverse form as has been demonstrated by Carter and others (AIAA Paper Number 79-1450). This improved interactive boundary-layer technique has been implemented in the unsteady tran-

sonic small disturbance computer code XTRAN2L so that separated flows can be calculated. This code uses Carter's relaxation method to update the boundary-layer displacement thickness.

Some illustrative results of the application of this code to an NACA 0012 airfoil oscillating in pitch are shown in the figure as the variation of lift coefficient with angle of attack. The flow is close to separation at the larger angles of attack. Transition is specified to be at 20 percent chord for the inverse boundary-layer calculations. Calculated results with the improved interactive (inverse) boundary-layer method agree very well with the CFL2D Navier-Stokes code calculations. The differences between the calculated and experimental results are believed to be due to wind tunnel wall effects.

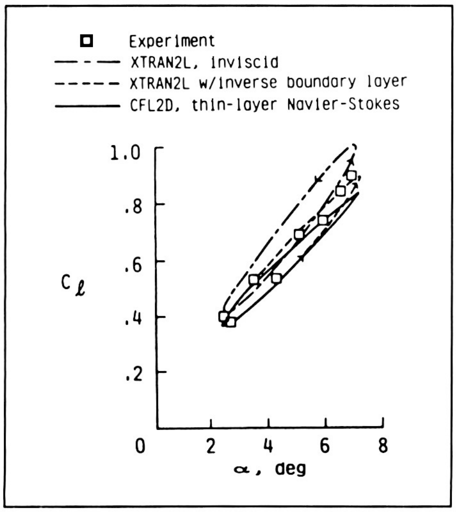

Comparison of calculated and experimental variations of lift coefficient with angle of attack.

The results obtained indicate that the TSD theory combined with the improved interactive boundary-layer method can be successfully applied beyond the traditional limits associated with small disturbance assumptions. This increases the range of conditions which can be treated with the less expensive TSD methods; this is a significant advantage of applications to aeroelastic analysis in which many conditions must be computed.

(James T. Howlett, 4236)

Comparison of SDG and PSD Methods for Gust Response

The Federal Aviation Regulations (FAR) require that, unless a more rational method is used, an airplane manufacturer must use the power spectral density (PSD) method to establish the dynamic response of its airplanes to atmospheric turbulence. In recent years many foreign civil airworthiness authorities, foreign transport manufacturers, and some United States transport manufacturers have looked to the Federal Aviation Administration (FAA) to encourage research into alternate means of compliance with the FAR. The statistical discrete gust (SDG) method is a candidate for an alternate means of compliance. The developer of the SDG method, J. G. Jones of the Royal Aerospace Establishment (RAE), claims that, under certain conditions, the SDG and PSD methods produce essentially the same numerical results. Before the FAA will approve a new method as a means of compliance, it must satisfy itself that the new method is valid and that the claims made concerning the method are true. In an effort to gain this satisfaction, the FAA requested and obtained NASA assistance in investigating the claim made by Jones regarding the SDG and PSD methods.

The essential elements of both the SDG and PSD methods are shown in the figure. The SDG method is performed in the time domain. The output response is given by the term $\bar{\gamma}$. Letters A and B in the figure refer to two input/response pairs. The PSD method is performed in the frequency domain. The output response is given by the term $\bar{A}$, which is defined in the figure as the square root of the ratio of the areas. Jones' claim about the SDG and PSD methods is expressed quantitatively by the equation in the figure. The SDG and PSD methods were

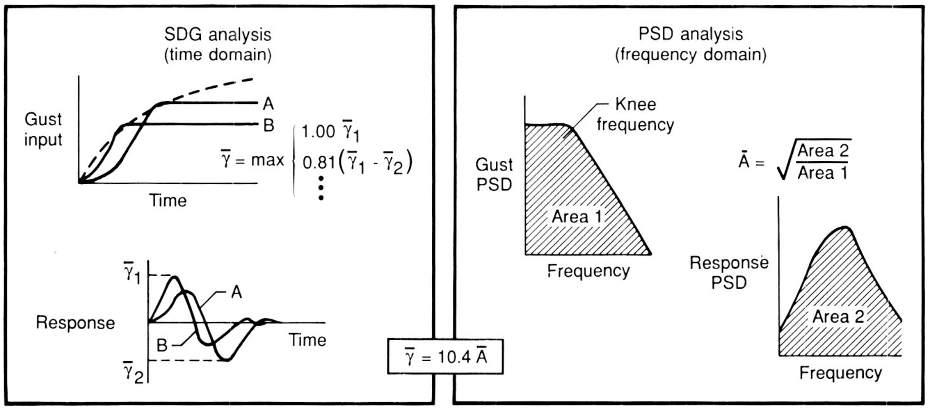

Schematic representations of two gust response analysis methods showing interrelationship.

applied to several configurations, and the corresponding responses were compared to see if the two methods were related by the 10.4 factor as shown in the figure. These comparisons showed that the factor 10.4 was approached when the airplane short-period frequency exceeded the knee frequency of the gust spectrum. At lower frequencies, the relationship began to diverge from the 10.4 relationship. Results from studies such as this one are invaluable to the FAA in evaluating the usefulness of new gust response methods.
(Boyd Perry III, 3323)

Correlation of Flexible Wing Response With Changing Flow Conditions in Transonic Range

The initial test of the second aeroelastic research wing (ARW-2) in the Transonic Dynamics Tunnel (TDT) resulted in the prediction of what appeared to be a wing first-bending mode instability at dynamic pressures well below the predicted classical flutter boundary. A second test, which was conducted to explore the predicted instability, found no "hard flutter" conditions but rather a narrow transonic region of high dynamic wing response. During the second test, continuous time history measurements of unsteady wing surface pressures were obtained for evaluation to determine if a physical understanding of the flow conditions could be developed.

The ARW-2 is a flexible supercritical wing designed for a cruise Mach number of 0.80. The drag rise occurs in the Mach number range from 0.81 to 0.83. (Drag rise is con-

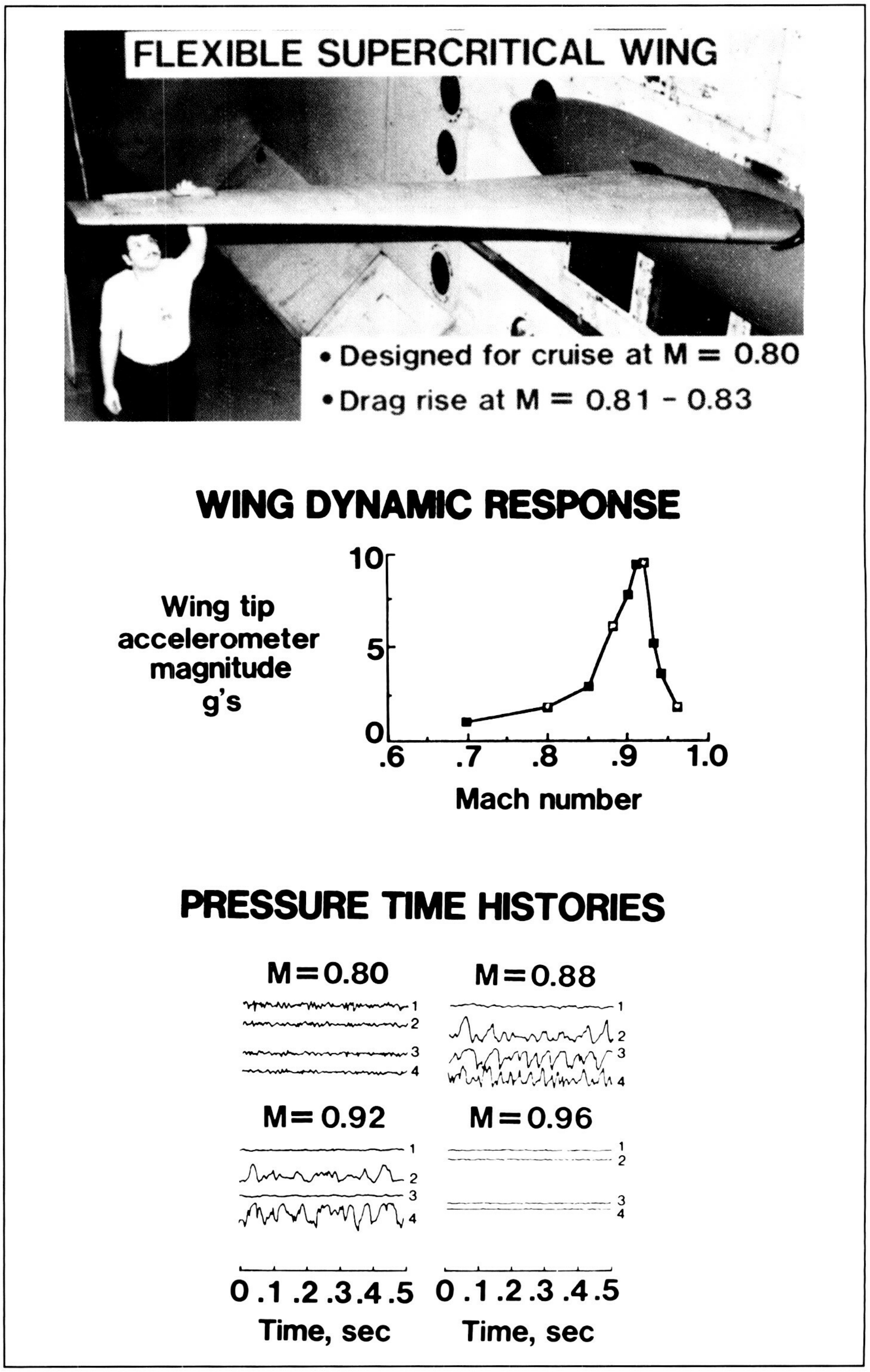

Comparison of dynamic response and unsteady pressures for flexible supercritical wing.

sidered a strong indicator of the onset of a breakdown in steady flow conditions followed by the development of a strong recompression shock with associated boundary-layer flow separation.) Shown in the figure are sample surface pressure time histories measured on both the upper and lower surfaces of the wing at an 87-percent span for a range of Mach numbers. Traces labeled 1 and 2 (bottom figure) were on the upper surface; traces labeled 3 and 4 were on the lower surface. Also presented in the figure is the variation of the magnitude of wing-tip acceleration with Mach number. A comparison of the pressures to the response clearly shows a strong correlation. These pressure time histories are indicative of strong oscillating shocks that are moving aft over the wing in the Mach number range shown.

This investigation showed that the magnitude of the flexible-wing dynamic response in the transonic region correlates closely with the variations in unsteady flow conditions which occur during the transition from subcritical attached flow to supercritical flow with a strong recompression shock and associated separation of boundary-layer flow aft of the shock location. **(Clinton V. Eckstrom, Maynard C. Sandford, and David A. Seidel, 2661)**

Scale-Model Shuttle Orbiter Arrestment Studies

A number of landing sites are designated for use by the Space Shuttle orbiter. Although these sites are all within the capabilities of the orbiter, there is, of course, a possibility of landing anomalies that could lead to a hazardous runway overrun incident. A runway overrun has the potential of significantly damaging the orbiter and the possibility of injury or loss of crew. A properly designed Space Shuttle Orbiter Arrestment System (SOAS) can bring the orbiter to a safe stop with a minimum of damage.

Scale-model tests of the SOAS have been completed using the 1/27.5-scale model shown in the figure. The purpose of these tests was to verify that the net configuration was appropriate for complete penetration of the forward fuselage and proper wing envelopment. Scale-model dynamic tests were conducted at model speeds proportional to full-scale speeds of 20 to 100 knots using four different net configurations. The 36-element net was fabricated from nylon string and suspended between two supports. Dragging chains, which were attached to the horizontal net bundles with nylon cording guided by sheaves in line with the net, were used as the energy absorbers.

Initial tests indicated a problem with underwing engagements for cases when the top horizontal net bundle fell below the wing for slow-speed engagements. This problem was corrected by installing zipper tearaways between the suspension chord and the net supports. In addition, the sheaves of the energy absorbers were moved upstream 7.27 ft, which is proportional to 200 ft full scale. These tearaways held the net up until full penetration by the forward fuselage had occurred and the moving of the sheaves changed the pull angles of the horizontal net bundles resulting in complete wing envelopment even for slow speeds. **(Pamela A. Davis and Sandy M. Stubbs, 2796)**

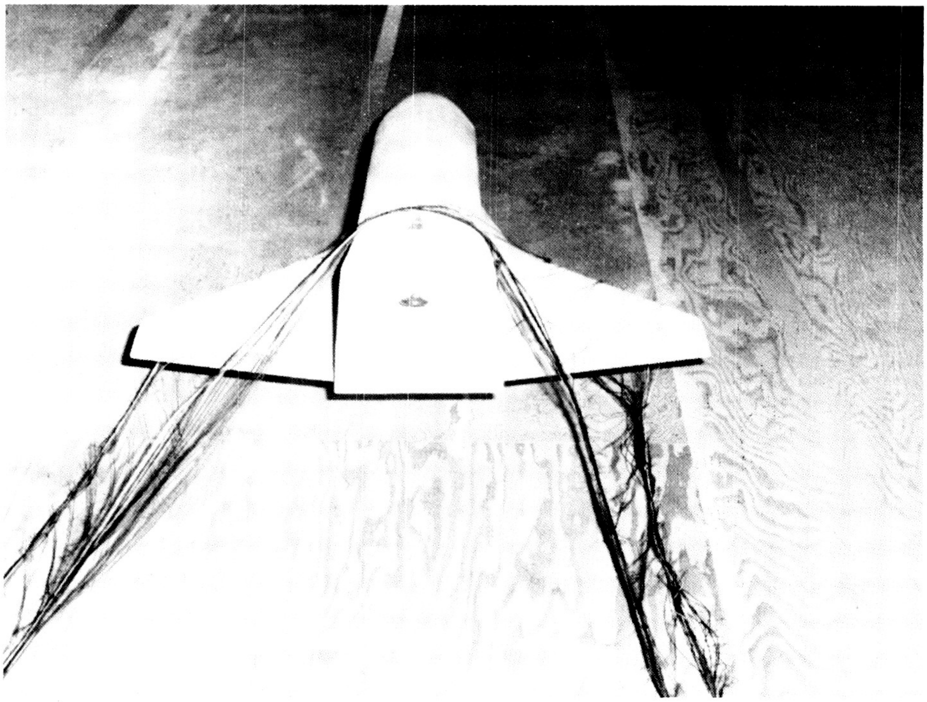

L-86-9367

Scale model of Space Shuttle orbiter shown after successful arrestment.

ORIGINAL PAGE IS OF POOR QUALITY

Definition of Rotor Blade-Vortex Interaction Noise Directivity Patterns

Of the many types of rotorcraft noise sources, probably the most offensive is blade-vortex interaction (BVI) noise. This noise source is due to the aerodynamic interaction of the rotor blades with the previously shed blade tip vortices. The resulting impulsive aerodynamic loading of the blade creates a strongly impulsive, high-amplitude acoustic signal. The earliest experimental research in this field gave indications that the signal was a directional noise source, and that the amplitude was dependent on rotor operating condition.

To investigate this phenomenon further, an extensive data base of rotor BVI noise data was obtained for a 40-percent model-scale BO-105 main rotor in the DNW (Duits-Nederlandse Windtunnel/ Deutsch Niederlandischer Windkanal (German/Dutch)) large open-jet aeroacoustic wind tunnel. The acoustic radiation pattern of the rotor was finely mapped in a plane representing the vehicle flight path, by acquiring acoustic data with a traversing multimicrophone array. One such directivity pattern is illustrated in the figure, for a low rotor flight speed (advance ratio $\mu = 0.116$) at a moderate descent rate. Here, α_{TPP} is the tip-path-plane angle and C_T is the thrust coefficient. The figure displays contours of equal peak-to-peak acoustic pressures, a noise "metric" that reflects the BVI impulsive content of the acoustic signal. The acoustic data have been normalized to the same propagation distance D to remove the natural effect of power decay with increased distance from the source.

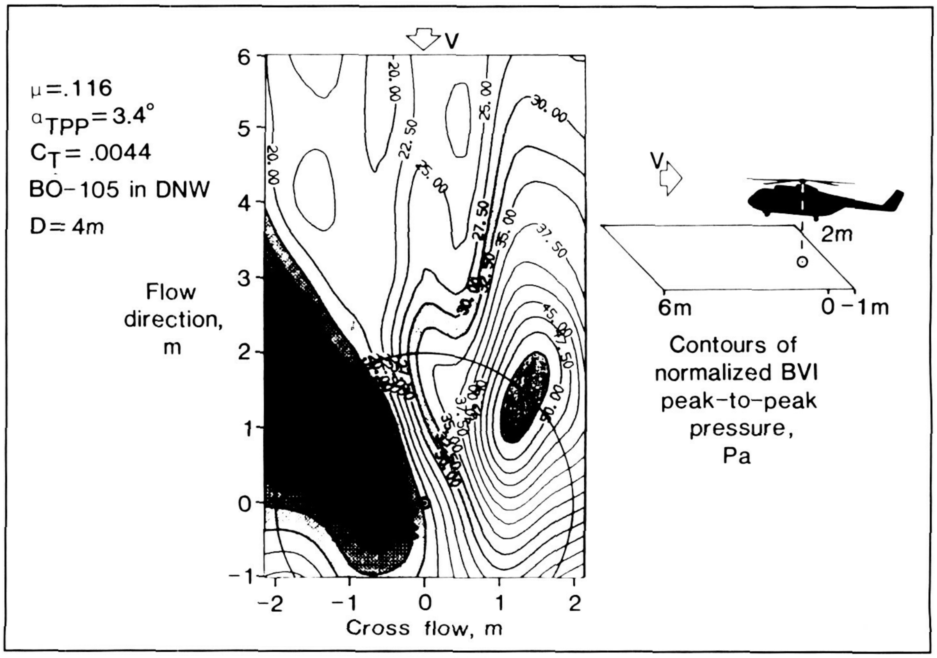

Rotor BVI noise directivity.

L-87-7568

The figure clearly shows the strongly focused directivity of the BVI signal, in this case toward the right and downward from the aircraft's flight path. Directivity mappings were made for several flight speeds V, at the descent condition exhibiting the highest BVI noise levels, to document the change in radiation pattern with rotor operating condition. Significant differences in both the primary radiation direction and in the noise level were found with changes in flight condition. Further research has been able to correlate these directivity and amplitude changes with the variation of BVI noise source location on the rotor disk, and with the changing geometry of the interactions.

(Ruth M. Martin, 2645)

ROTONET Prediction Code Validation

ROTONET is a comprehensive helicopter noise prediction code in its second phase of development. The code structure is divided into four parts: main- and tail-rotor blade geometry, rotor performance calculations, source noise calculations, and source-noise-to-observer propagation. A Phase II system, which has been distributed to the four major helicopter manufacturers, includes a nonuniform inflow model, a higher harmonic blade and loads analysis, a full-surface tone noise model, and a broadband noise model. NASA and the McDonnell Douglas Helicopter Company (MDHC) have made accurate far-field acoustic measurements of a MDHC 500E helicopter to create an accurate data base for comparison with the results of ROTONET predictions. The 500E data base has been completed and

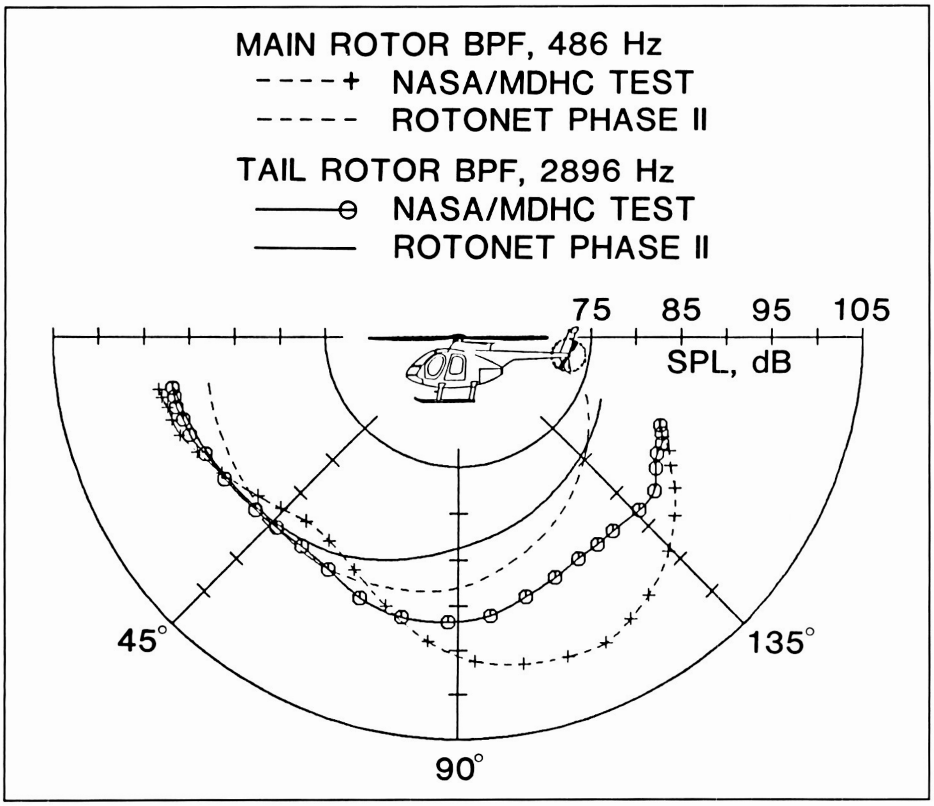

Initial ROTONET validation with MDHC-500E flight data.

contains data for simultaneous measurements of the aircraft dynamic state, six degree-of-freedom flight path, weather conditions up to the aircraft flight altitude, and far-field narrowband acoustic spectra.

The figure shows a comparison between ROTONET predictions and sound pressure level (SPL) data for the main- and tail-rotor blade-passage frequencies (BPF). The test conditions are for a 3000-lb helicopter with a five-bladed main rotor and a two-bladed tail rotor flying at an altitude of 250 ft at 95 knots. The SPL data correspond to measurements made in the vertical plane of symmetry as the helicopter approaches from 15° above the horizon, passes over the microphone measuring point at 90°, and continues to 15° above the downrange horizon. The experimental data have been corrected to a distance of five main-rotor blade radii ($\approx$ 66 ft). As the figure indicates, the agreement is good in the forward arc but becomes increasingly worse in the aft arc. The discrepancy in the main rotor predictions suggests the presence of an unknown noise source radiating to the aft arc. **(Robert A. Golub, 3842)**

Structural Feasibility of Extension-Twist-Coupled Rotor Blade Concept

Currently there is a compromise in the design of the rotor system of a typical tilt-rotor aircraft because of the difference between forward flight (airplane mode) and hover (helicopter mode) requirements. The blade design for a typical tilt rotor has a twist distribution that produces acceptable hover performance at the cost of a lower flight propulsive efficiency. One solution to this problem would be to vary the blade twist between the airplane and helicopter modes. This variation could be achieved by using an extension-twist-coupled rotor blade.

The structural feasibility of an extension-twist-coupling concept was determined through the following approach, which is to determine the maximum twist deformation required to produce the desired twist changes between helicopter and forward flight modes for a typical full-scale design; to fabricate specimens using realistic material, wall thickness, and laminate to both simulate a full-scale rotor blade cross section and achieve desired twist changes; to perform static tension tests on specimens to determine twist deformations as a function of axial load; and to determine the twist deformation at the design load and compare to the required twist deformations for a full-scale blade.

An extension-twist-coupled tilt-rotor blade design was developed based on a theoretical optimum-twist model. The design showed that the maximum twist deformation required rotor was on the order of 0.4°/in. Static test specimens were fabricated using T300/5208 Gr/E and IM6/R6376 Gr/E composite materials. One set of results is shown in the figure as the variation of twist rate with axial load. These data show that at the design limit loads, the corresponding twist rates are at and above the 0.4°/in. value desired for the theoretical

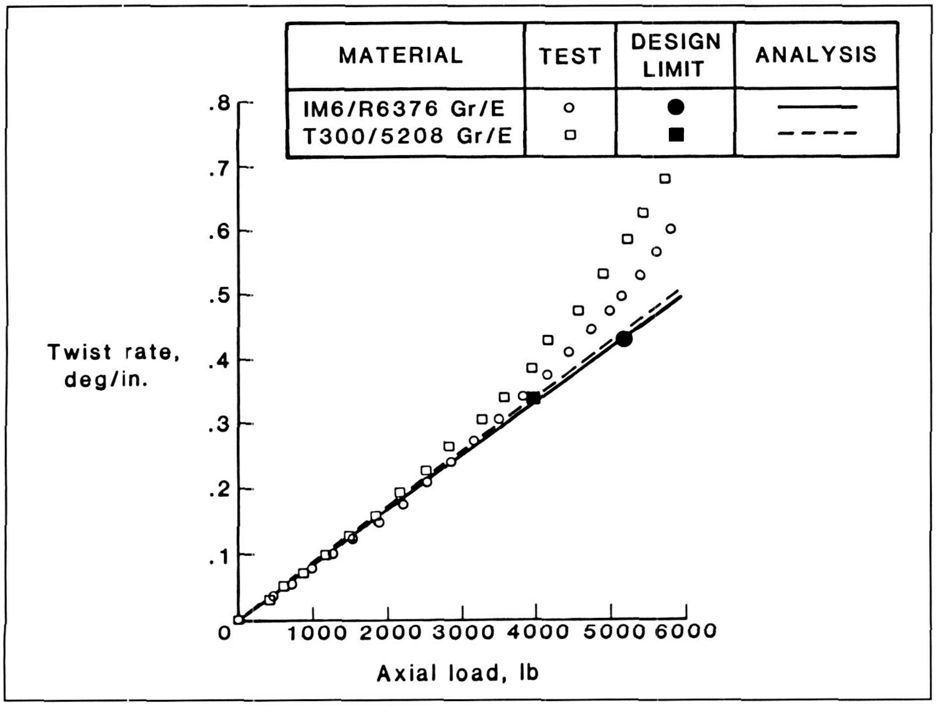

Comparison of measured and calculated variations of twist rate with axial load.

tilt-rotor blade. Thus, the aerodynamically beneficial extension-twist-coupled rotor blade concept is structurally feasible statically. **(Mark W. Nixon, 2661)**

Initial Evaluation of Industry Codes for Calculation of Coupled Rotor-Airframe Vibrations

One of the critical considerations in the design of any new helicopter is vibration. With only a few exceptions, helicopters have been designed to performance requirements by past experience with vibrations taken into account and with new vibration problems being solved during flight tests and operation. Because of increasing demands for further reduction of vibration to achieve the goal of a "jet-smooth" ride, it is now recognized that analysis methods that accurately account for the coupling between the rotor and the airframe in producing vibrations must be employed in design. The Langley Research Center has under way a program, designated DAMVIBS (Design Analysis Methods for Vibrations), with the overall objective to establish the foundations for developing a superior design analysis capability for vibrations within the United States industry. One of the activities being conducted under the DAMVIBS program is to evaluate existing analysis methods for calculating coupled rotor-airframe vibrations for the purpose of supporting helicopter airframe design work.

In an initial effort, Bell Helicopter Textron, Boeing Helicopter Company, McDonnell Douglas Helicopter Company, and Siko-

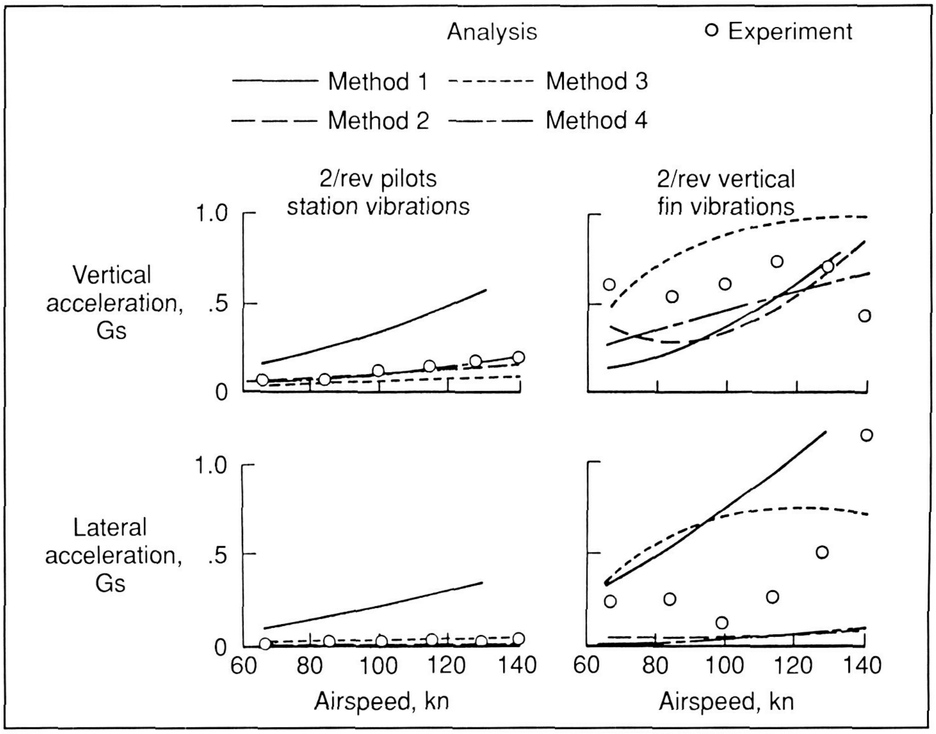

Comparison of flight and calculated vibratory accelerations for Bell AH-1G helicopter.

rsky Aircraft have applied existing company-developed methods to calculate the coupled vibrations of the Bell AH-1G helicopter. Comparisons also have been made with existing data from an Army Operational Loads Survey. An illustrative example of the type of results obtained is given in the figure, which shows a comparison of the calculated and measured 2/*rev* (two times the rotor rotational speed, the primary main rotor excitation in the airframe for this helicopter) vertical and lateral vibrations as a function of airspeed for two locations on the airframe. The analytical results obtained by the four companies for the 2/*rev* vibrations are in fair to poor agreement with measured data. In general, the best agreement was obtained for vertical vibrations; the worst agreement was for lateral vibrations. These studies on the Bell AH-1G represent the first comparative evaluation of industry codes applicable to the computation of coupled rotor-airframe vibrations.

(Raymond G. Kvaternik, 2661)

Reduction of Helicopter Rotor Blade Response by Selection of Optimum Locations for Tuning Masses

The concept of modal tailoring through proper placement of tuning masses is of increasing interest in the design of helicopter rotor blades to achieve reduced vibration. Optimal placement of the masses tailors the mode shapes such that they approach orthogonality to the air loads, thus reducing generalized force and response of the blade. Conventionally, the optimum magnitudes of the masses at fixed-blade spanwise locations are determined by trial and error. A Langley-developed optimization procedure, however, systematically determines not only the magnitudes but also the locations of masses that minimize blade root vertical shear while avoiding a large mass penalty.

The procedure was applied to the determination of the magnitudes M_1, M_2, M_3, and locations X_1, X_2, X_3 of three tuning masses along a 193-in. rotor blade model shown in the figure. The shear corresponding to typical air load distributions at frequencies of three, four, and five times the rotational speed Ω of the blade (3/*rev*, 4/*rev*, and 5/*rev*) was minimized for the first and second elastic flapwise modes.

The table in the figure gives the magnitudes and the locations of the masses along the blade before and after optimization. Initially, three tuning masses (totaling 18.4 lbm) were placed at three arbitrary outboard locations. In the final design, the masses have all been moved to approximately 80 percent of the blade span, and the total tuning mass is 26.85 lbm. For the initial and final designs, the figure shows the graphs of the shear plotted as a function of azimuth for a revolution of the blade. The peaks have been reduced dramatically. For example, the change in the masses and locations reduced the maximum peak shear S_{max} from −78.00 lbf to −0.576 lbf.

(Jocelyn I. Pritchard and Howard M. Adelman, 2887)

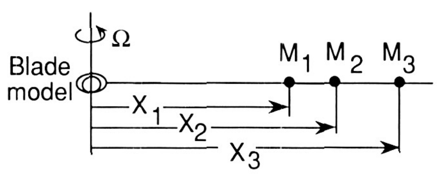

		Initial	Final
X_1	(in)	135.0	153.0
X_2	(in)	154.0	154.0
X_3	(in)	174.0	154.0
M_1	(lbm)	5.2	7.9
M_2	(lbm)	6.5	9.7
M_3	(lbm)	6.6	9.2
M_{tot}	(lbm)	18.3	26.8
s_{max}	(lbl)	-78.0	-0.60

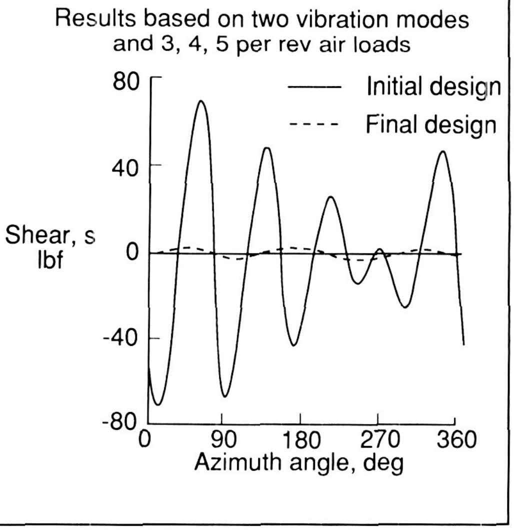

Helicopter rotor blade dynamic response reduced through optimum locations for tuning masses.

Benefits of Sonic Boom Shaping

Studies have indicated that the distribution of the volume and lift of a supersonic transport may be manipulated in order to shape the pressure-time signature of the resulting sonic boom. Proper shaping of the sonic boom will reduce adverse human response. Since, from a human perspective, the most fundamental attribute of a sound is loudness, this characteristic was chosen as the basis for estimating the potential benefit of sonic boom shaping. Using a well-developed theory of loudness (Stevens Mark VII), calculations were performed for a range of those parameters which describe a conventional N-wave sonic boom and a shaped sonic boom.

The upper part of the figure indicates that, for an N-wave sonic boom, loudness is dependent on peak overpressure and rise time. The lower part of the figure illustrates a shaped sonic boom that has a rapid rise to the initial shock amplitude A and a more gradual rise to the peak overpressure B. For illustrative purposes, the rise times of the initial shock and the peak overpressure have been held constant. The effects of the initial shock amplitude and the secondary rise time T_2 are illustrated. The loudness of a flat-top shaped boom $A = B$ is independent of T_2 and equivalent to an N-wave of overpressure B and rise time of 1 msec. However, for values of the initial shock amplitude less than B there is a predicted decrease in loudness for increasing T_2. Based on these predictions, for a constant peak overpressure, the loudness of a shaped boom may be reduced by reducing the initial shock amplitude and increasing the secondary rise time.

(Kevin P. Shepherd, 3561)

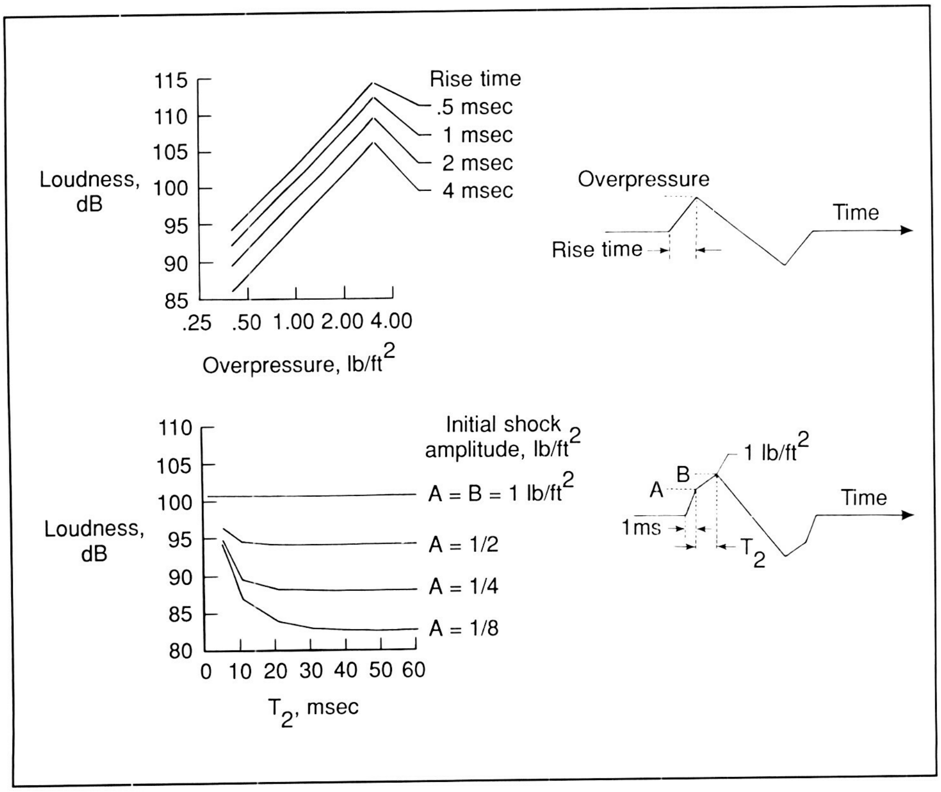

Loudness of N-waves and shaped sonic booms.

Improved Polymer Properties Provided by Semi-Interpenetrating Network Polyimide

PMR-15 is a widely used composite matrix resin that retains good elevated temperature mechanical performance and is readily processible using conventional autoclave technology. This polymer system suffers, however, from a lack of toughness and microcracking resistance.

A new semi-interpenetrating network polyimide (LARC-RP40) was synthesized from thermosetting PMR-15 and a thermoplastic, NR-150B2. This new matrix resin showed significant property improvements over PMR-15 in three areas. Toughness, as reflected in fracture energy G_{Ic} measurements, showed a 322-percent increase. A significant increase in microcracking resistance after 1000 thermal cycles was also seen. In addition, the glass transition temperature of the semi-interpenetrating polymer network (IPN) system was 369°C (30°C higher than that of PMR-15). The development of LARC-RP40 demonstrated the feasibility of attaining both improved toughness and increased glass transition temperature, a combination of properties that is difficult to achieve by conventional synthetic routes.

(Ruth H. Pater, 3041)

Neat resin fracture surfaces

Rough ← Fracture propagation   Smooth ← Fracture propagation

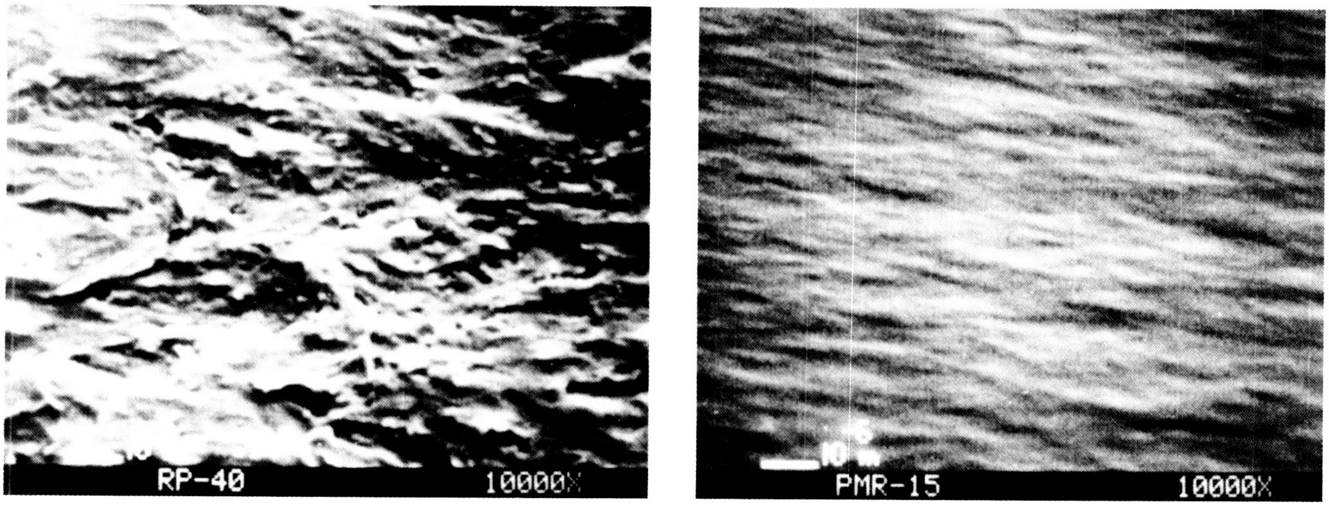

	LaRC-RP40	PMR-15
G_{Ic}, J/m^2	368	87
Microcracks after 1000 thermal cycles, cracks/in.	0	58
316° C flexural strength, ksi	174	159

LARC-RP40, a new, tough high-temperature matrix resin.

In Situ Fiber Optic Sensor for Monitor Composite Cure Cycles

The lack of repeatable processing and manufacture of advanced composite materials is perhaps the major obstacle inhibiting the widest possible acceptance of resin matrix composites as major aircraft structural elements. Considerable research and development effort has been expended in government, university, and aerospace laboratories to improve the quality and reliability of this class of materials. Langley Research Center has made a significant advance toward resolving these problems by demonstrating that infrared (IR)-transmitting optical fibers can be used to remotely sense and transmit IR spectra that indicate the chemical state-of-cure of graphite fiber/polymeric resin materials.

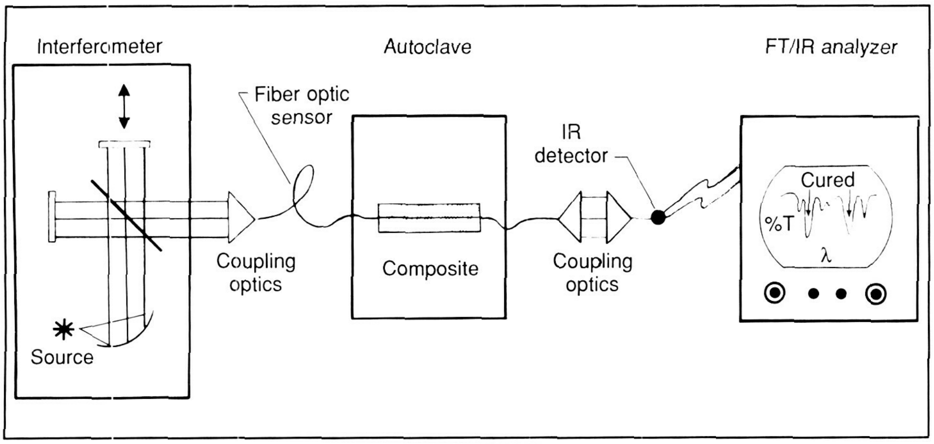

Fiber optic composite cure monitoring.

A portion of cladding is removed from the small diameter (0.1 mm) fiber to expose the sensor element. The sensor is then embedded during layup in the material to be monitored. The IR beam is carried outside the interferometer by the optical fiber, through the composite where selected wavelengths are absorbed, and finally focused onto an IR detector. Fourier transform (FT) of the detector information results in an IR spectrum that relates to the chemical state of the manufactured part. Feedback to control the processing parameters is the next development step to be taken. Additional potential applications for this new technology include monitoring the integrity of materials in the in-service environment (the smart skins concept), the remote sampling of hazardous materials, and the examination of processes in furnaces and reactors.

(Philip R. Young, 3041)

New Thermosetting Structural Resins

Thermosetting polymers have been widely used as composite matrices and adhesives on aerospace vehicles because of their excellent processibility, solvent resistance, and low cost. However, until recently, these highly crosslinked systems lacked toughness and hot and wet strength. New polymer blends have been developed which retain the ease of processibility and solvent resistance of state-of-the-art brittle epoxies but possess significantly improved toughness and adhesive properties.

The new thermosets were prepared by blending various structurally different acetylene terminated aspartimides (ATA) and imidothioethers (ITE) with acetylene terminated arylene ether oligomers (ATAE) of differing chemical structure and molecular weight. The fracture toughness K_{Ic} and the adhesive strengths of these blends were significantly higher than those of a 177°C curing epoxy.

Unidirectional carbon fiber laminates of an acetylene terminated

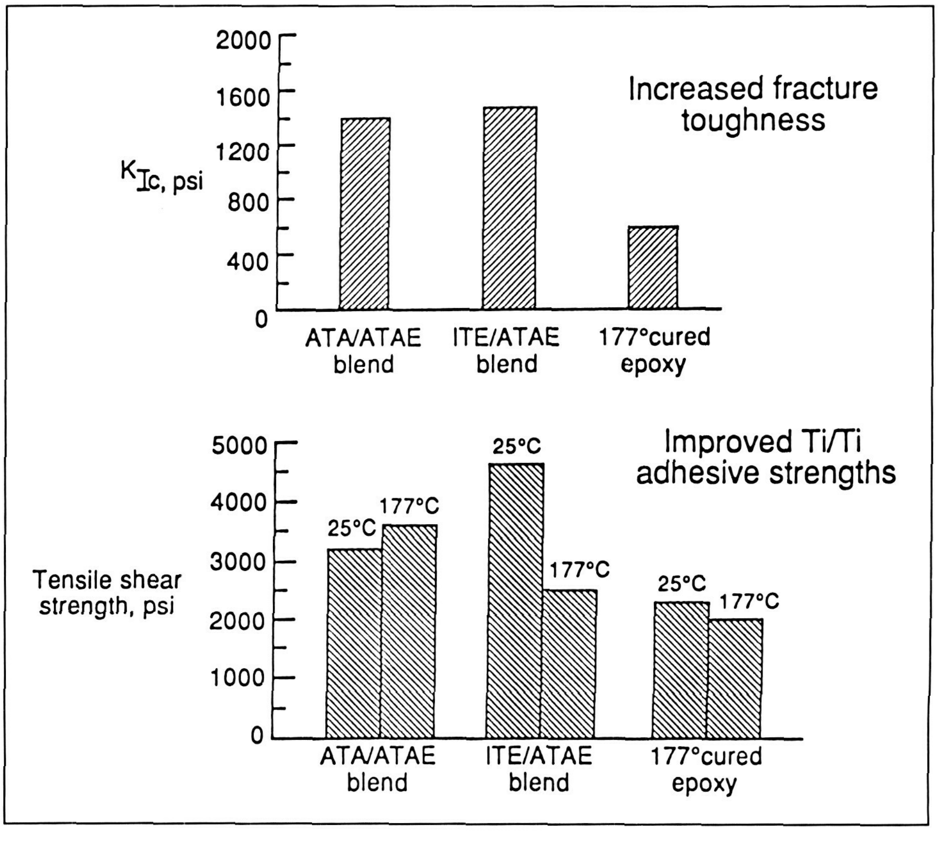

Mechanical properties of thermoset blends.

imidothioether/acetylene terminated arylene ether blend exhibited flexural strength and modulus at 25°C comparable to state-of-the-art 177°C curing epoxy composites. However, the mechanical properties of composites from the blend at 150°C after aging for 1000 hours at 200°C in air were significantly better than those of epoxy laminates.

Further work is under way to optimize the composition of the blends in an attempt to obtain the best overall combination of properties. Composites from new commercially available toughened epoxy systems currently offer excellent impact resistance and other mechanical properties at temperatures to 82°C. These new blends extend the use temperatures to 177°C.

(Paul M. Hergenrother, John W. Connell, and Stephen J. Havens, 3041)

END CRACKS IN A P75/934 $[\mathrm{Al/Ad}/+15/0/\pm 10/0/-15]_s$ TUBE AFTER 3000 THERMAL CYCLES

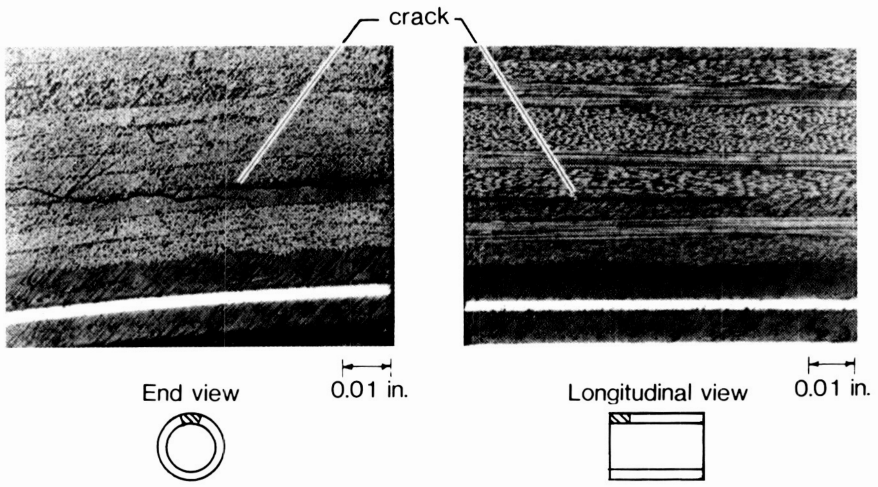

Thermal-cycling-induced damage in composite tubes.

Thermal Cycling Effects on Composite Tubes

Composite tubes will be the primary building elements of the space station truss structure because of their high specific stiffness and low coefficient-of-thermal expansion. Changes in these properties due to the repeated thermal cycling experienced on-orbit of the space station (175,000 cycles over 30 years) are important design considerations. A study to determine the effects of long-term thermal cycling on composite tubes has been conducted. Tubes of several different graphite/epoxy material systems were examined for damage and tested to determine changes in properties after 3000, 7000, and 9000 thermal cycles between ±150°F. All the tubes had a laminate configuration designed to maximize longitudinal stiffness and minimize thermally induced internal stresses. Aluminum foil was adhesively bonded to the inner and outer surfaces of the tubes to serve as thermal control and atomic oxygen protective coatings.

No significant changes in axial compressive modulus were observed in any of the tubes after 3000, 7000, or 9000 thermal cycles. However, cracks and delaminations at the tube ends were observed after 3000 cycles. A photomicrograph of an end view of this damage in a P75/934 graphite/epoxy tube is shown in the figure. A longitudinal view of the same location shows that the crack extends only about 0.07 in. along the length of the 10-in.-long tube. Further examinations showed that all the damage was confined near the end of the tube. This damage did not grow with additional thermal cycling. The type and the extent of the observed damage were consistent with results from a finite-element stress analysis that predicted large interlaminar stresses at the free end of the tube. These stresses had magnitudes comparable to the interlaminar shear strength of the material and decreased to zero, approximately 0.2 in. away from the free end of the tube.

This study indicates that thermal-cycling-induced damage is confined to a small region near the end of the tube and does not grow into the interior with additional thermal cycling. This type of damage had no significant effects on the longitudinal stiffness of the composite tubes.

(D. E. Bowles, 4558)

Prediction of Hypersonic Vehicle Fuel Stratification Using Blatt's Correlation

The natural buoyancy of liquid warmed by heated walls, within

a closed container, results in a phenomenon termed thermal stratification. The warm liquid flows over the top of cooler liquid, and it is the vapor pressure of the warm liquid that determines the rise in the tank pressure. This process has particular importance in the design of tank structures and insulation for cryogenic fuel (liquid hydrogen) systems of hypersonic, air-breathing vehicles such as the National Aero-Space Plane (NASP). Any fuel that needs to be vented (and thus wasted) to prevent tank overpressurization can result in a large penalty in the overall vehicle weight and volume.

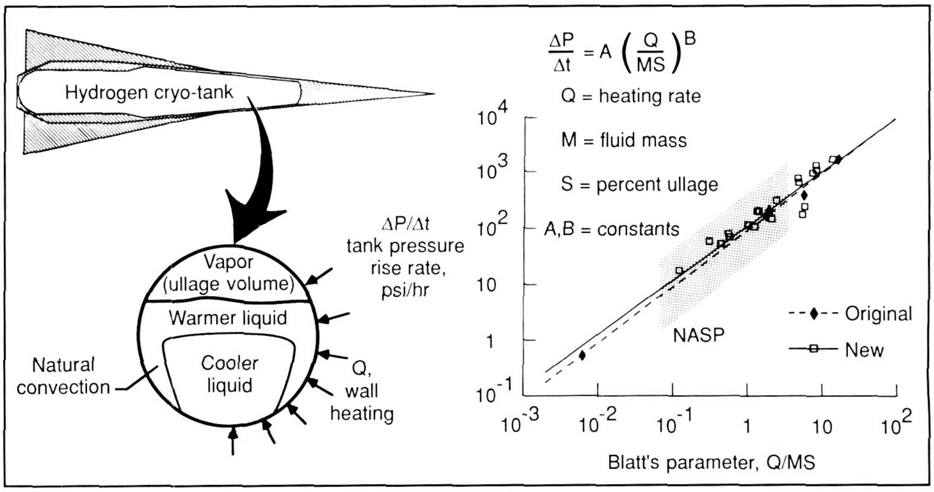

Cryo-tank thermal stratification and pressure rise rate correlation.

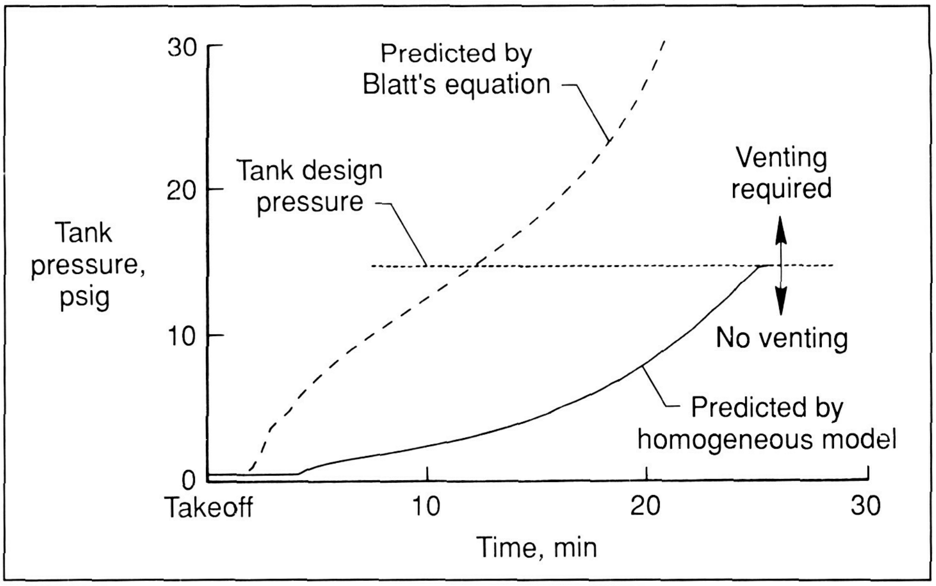

Analytically predicted cryo-tank pressure during NASP vehicle ascent trajectory for homogeneous and stratified tanks.

The majority of previous experimental and analytical work on thermal stratification was directed toward specific vertical launch vehicle cryo-tanks, and could not be confidently applied to NASP-type horizontal tanks. However, one relatively simple correlation, originally proposed by Blatt (*J. Spacecraft,* Vol. 5, No. 6, June 1968), was identified and appeared to be applicable to various tank geometries and sizes. Blatt correlated data from five liquid hydrogen tanks, both spheres and vertical cylinders. During the present effort, results from 21 additional stratification tests, including those from four horizontal cryo-tanks, were added to the Blatt data. These new data and the original data are shown on the right side of the first figure. Much of the additional data fell within the region applicable to NASP and permitted greater confidence in the use of the correlation on cryo-tank designs for NASP-type geometries, trajectories, and conditions.

The effect of thermal stratification was investigated for a generic NASP vehicle and cryo-tank design, by examining the tank pressure response to fuel withdrawal and aerothermal heating of the tank walls during an ascent trajectory. Two cases were considered: In the first, the tank contents were assumed to be warmed uniformly (homogeneous model), while in the second case, Blatt's correlation was used to calculate the tank pressure. Results from the study are presented in the second figure and show that a tank design (including insulation weight) based on the homogeneous model is nonconservative and that stratification will require venting of fuel relatively early in the flight trajectory.

These results emphasize the importance of thermal stratification on hypersonic vehicle design, insulation weight, and fuel volume.

The modified Blatt's correlation provides a tool for the designer to examine its effect on tank pressurization, fuel venting, and insulation requirements.

(N. R. Baker; J. C. Robinson, 2291)

Blade-Stiffened Carbon-Carbon Compression Panels

Carbon-carbon composite materials are being considered for use as hot structures on advanced aerospace vehicles. Stiffened panels are basic to most aerospace vehicle structures, and understanding their behavior in compression is essential for the design of efficient carbon-carbon structural components. The objective of the present research is to develop the technology to design and fabricate efficient carbon-carbon-stiffened compression panels.

The approach used in this study is to use the structural Panel Analysis and Sizing Code (PASCO) to determine efficient carbon-carbon panel designs and then to fabricate full-size carbon-carbon panels of one of the designs to develop the fabrication techniques and to provide test specimens. The panel specimens are instrumented and loaded to failure in compression to determine the failure modes and strength of the fabricated panels. The panels are analyzed using the finite-element code, Engineering Analysis Language (EAL), and the predicted results are compared with the results obtained from the tests.

Several blade and T-stiffened carbon-carbon panel concept designs have been analyzed and evaluated. A blade-stiffened minimum gauge design has been selected, and four uncoated advanced carbon-carbon-4 panels have been fabricated. One of the panels is shown in the figure. The panels are 12.5 in. wide by 20 in. long, and have four blade stiffeners 0.75 in. high spaced 3.50 in. apart. The panel skins and stiffeners are composed of six plies of Thornel-300 graphite fibers woven into eight-harness satin weave fabric. Two of the panels have a single row of stitching along each side of the stiffeners to determine if stitching will improve the failure strength of the panels. The panels have been analyzed and are expected to have buckled skins when loaded to failure.

The capability to design, fabricate, and analytically predict the behavior of carbon-carbon-stiffened compression panels will supply some of the technology required for the structural applications of carbon-carbon material.

(James Wayne Sawyer, 4201)

LARCNESS in Good Agreement With Mach 8 Experiment for Cowl Aerothermal Loads Amplified by Shock-On-Lip

Langley Adaptive Refinement Code Navier-Stokes Solver (LARCNESS) is a finite-element analysis code with an adaptive unstructured remeshing capability that conforms the computational mesh to the physics of the flow field. The ability of the code to predict the shock-on-lip amplified aerothermal loads on a scramjet engine cowl has been demonstrated by comparison with experimental data for incident shock heating on a blunt cylindrical leading edge. The

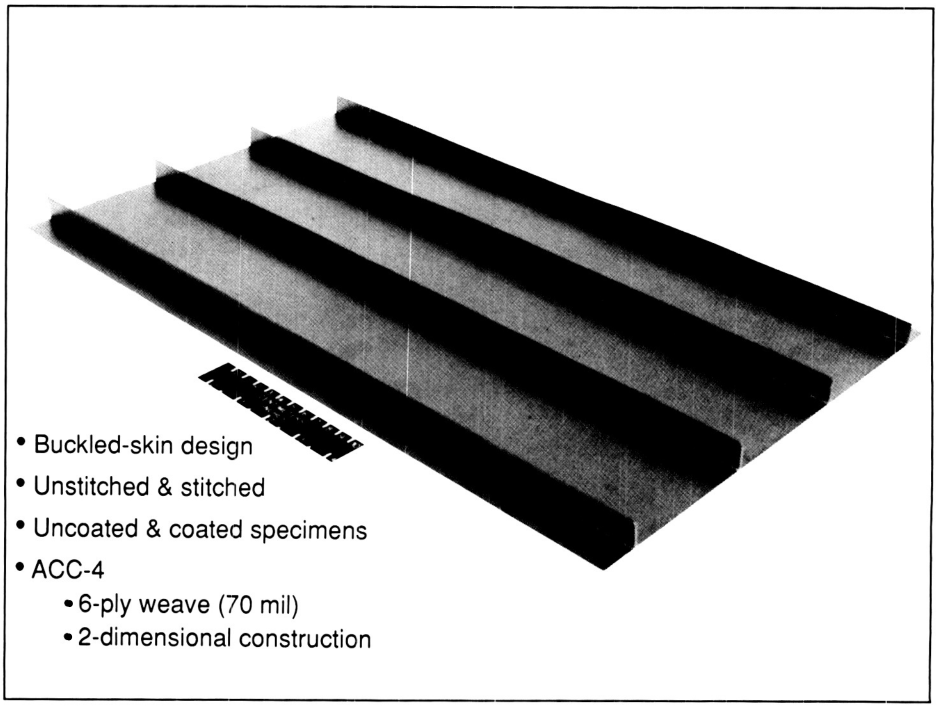

- Buckled-skin design
- Unstitched & stitched
- Uncoated & coated specimens
- ACC-4
  - 6-ply weave (70 mil)
  - 2-dimensional construction

Example of typical blade-stiffened carbon-carbon panel. L-87-4663

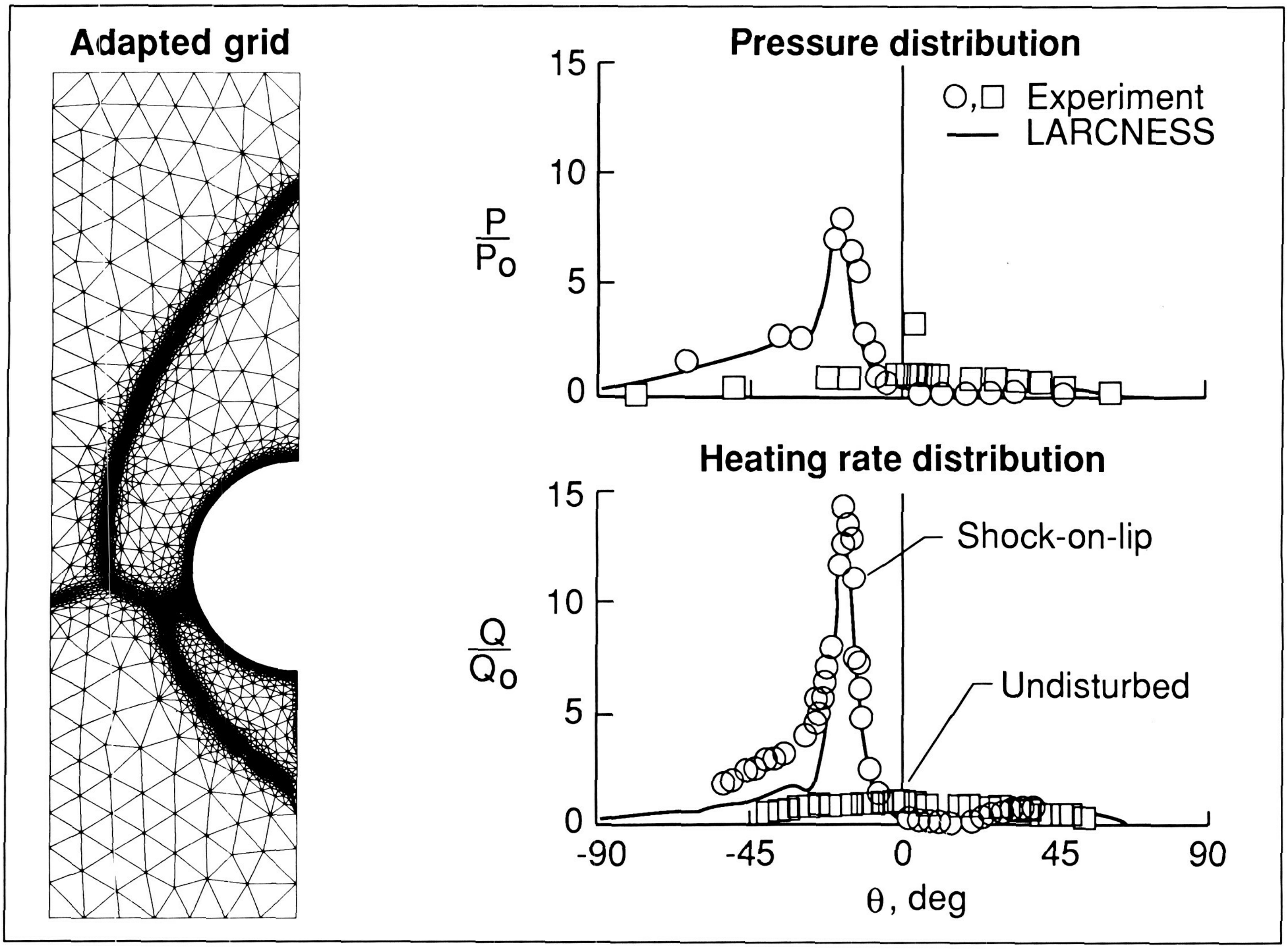

Comparison of analytical and experimental results.

experimental configuration analyzed was a 3-in.-diameter cylinder in Mach 8.03 flow with a 10° turning angle shock forming a supersonic jet that impinges on the leading-edge surface and causes severe heating rate and pressure augmentation.

LARCNESS computations were begun on a coarse initial mesh with an approximately uniform triangular mesh in the essentially inviscid region and a stretched rectangular mesh in the near-wall region (to encompass the boundary layer). The computations were continued on the initial mesh until the flow features were well defined. Then, utilizing one or more of the computed flow field gradients (such as density and Mach number) the triangular meshed inviscid region was remeshed to place smaller elements in the regions of high gradients and larger elements in regions of small gradients. The near-wall rectangular mesh was maintained constant in the stretched direction, normal to the wall, and was refined parallel to the wall to match the triangular mesh. Computations were then continued on this solution-adapted mesh, and the remeshing process was repeated. Three remeshing cycles provided excellent definition of the shock interaction with the adapted grid conforming to the flow field physics as seen by comparing the experimental schlieren photograph with the final adapted mesh shown in the figure.

The complex Type IV supersonic jet shock interaction was captured with 8800 grid points (other codes require on the order of 20,000 grid points) and elements that

varied in size by a factor of 1000:1. Wall pressure P and heating rate distributions Q, normalized by the undisturbed (no incident shock) stagnation point levels P_o and Q_o, respectively, and plotted as a function of the circumferential position θ on the cylinder (positive values of θ are on the upper half of the cylinder), are shown. The computational results capture the sharp peaks of the locally amplified loads and are in good agreement with the experimentally measured values.

(Ken Morgan and Rajiv Thareja; Allan R. Wieting, 3423)

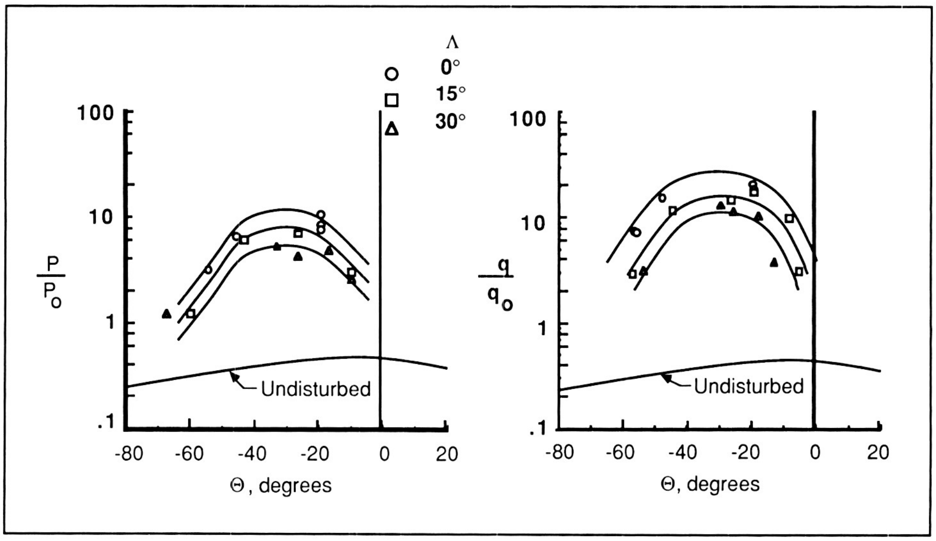

Pressure and heating rate amplification due to shock interaction on swept cylinder.

Reduction of Peak Pressure and Heat Transfer Rate by Leading-Edge Sweep

Shock-wave interference heating on the cowl-lip of an airbreathing hypersonic engine is a critical thermal structural design problem. A generic wedge (incident-shock generator)/cylinder (bow-shock generator) shock-wave interference model has been tested at 0° sweep, and the experimental results show that extremely high-pressure and heat transfer rate amplification occurs in highly localized regions on the cylinder surface due to shock-wave interference. A swept wedge/cylinder shock-wave interference model was tested to provide experimental data to compare with existing unswept data and to show reductions, if any, in surface pressure and heat transfer rate as a means of decreasing the extremely high aerothermal loads that occur in localized regions on the cylinder surface.

A two-dimensional 12.5° wedge/cylinder shock-wave interference model was modified to sweep at angles of 15° and 30°. The swept model was tested in the Calspan Corporation 48-Inch Hypersonic Shock Tunnel at Mach 8, unit Reynolds number per foot of 1.4×10^6, dynamic pressure of 800 lb/ft^2, and total temperature of 2800°R. The 3-in.-diameter cylinder of the swept model was located at various positions relative to the wedge to produce the different shock-wave interference patterns, and detailed surface loads on the cylinder were measured.

The peak pressure P_p and heating rate q_p for each test condition are normalized by the undisturbed stagnation point value P_o or q_o and plotted as functions of their location Θ for each sweep angle ($\Lambda = 0°$, $15°$, and $30°$). The undisturbed distributions are also shown for comparison purposes. The peak pressure and heat transfer rate amplification decreases with increasing sweep angle demonstrating that the extremely high localized aerothermal loads produced shock-wave interference patterns that can be reduced by sweeping.

(Christopher E. Glass, 4441)

Reduction of Leading-Edge Temperatures, Gradients, and Stresses by Thermal Superconducting Materials and Fins

Leading edges on hypersonic vehicles experience intense stagnation point pressures and heating rates. Engine cowl leading edges can have these loads greatly amplified when an impinging shock interacts with the cowl bow-shock. These amplified heating rates cause severe temperature levels and thermal gradients in the structural material. Hydrogen-impingement-cooled leading edges are candidate concepts if the structural material temperature levels and thermal gradients can be reduced to an acceptable level.

In this example, an 0.25-in.-diameter leading edge is subjected

to transient shock wave interference heating typical of acceleration of the National Aero-Space Plane through Mach 16 with the vehicle nose-bow-shock sweeping across the engine cowl leading edge from an outboard to an inboard position. The sweeping shock wave produces a family of shock-on-lip interference patterns represented by the worst-case situation, a Type IV supersonic jet interaction. The interference heating rate reaches a peak value of 30,000 Btu/ft^2/sec at about 22° above the horizontal centerline of the leading edge. The inner surface is convectively cooled by the direct impingement of the sonic hydrogen jet stream with an inlet temperature of 50°R and pressure of 1000 psia. Internal tapered fins around the circumference of the leading edge increase the physical area for heat transfer by a factor of 5; however, because nonisothermal effects reduce the fin efficiency factor to 50 percent, the effective convection area is increased by a factor of 2.5. This example considers a nickel structure without internal fins as the baseline design and copper and beryllium as alternate superthermal conductivity materials coupled with the internal fin design. The peaks of the thermal conductivity for copper and beryllium, which occur at 20°R and 70°R, are approximately 300 and 80 times higher than nickel, respectively, as shown in the figure.

The alternate materials and fin design reduced the peak material temperature predicted by analysis from 2500°R for the nickel to 1000°R for the beryllium and 766°R for the copper, as shown in the figure. The circumferential temperature gradients, and therefore the circumferential thermal stresses, were also reduced significantly by the combination of improved heat transfer to the hydrogen and higher circumferential conductivity of the materials.

(Pramote Dechaumphai, 3423)

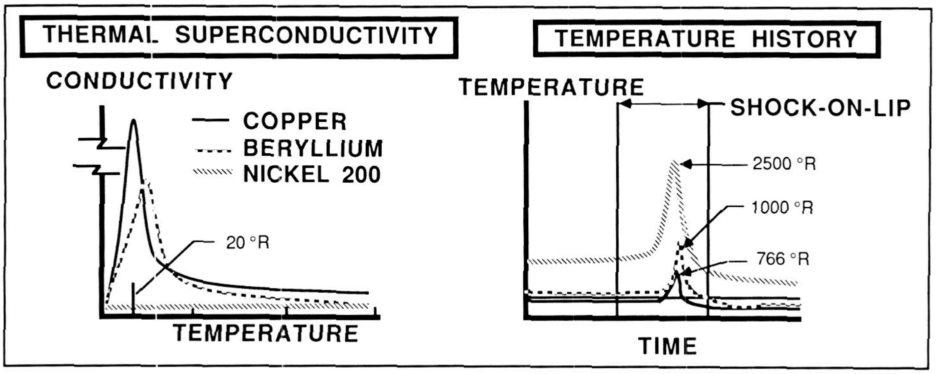

Thermal conductivity and temperature history of leading edge subjected to shock interference heating.

Efficient Space Station Construction With Mobile Transporter

The Mobile Transporter (MT) is a utility vehicle that will reside on the space station to enhance the effectiveness of the astronauts extravehicular activities (EVAs). This vehicle will enable efficient EVA construction and maintenance of the truss structure and integration of subsystems and payloads, while providing the operational versatility needed for unplanned contingency operations. The functional features of the Mobile Transporter have been derived from EVA truss construction experiments conducted by Langley Research Center over the past 10 years. The first figure depicts the MT concept for EVA truss construction. A primary feature of the MT is the use of astronaut positioning devices.

A program was established to evaluate the utility of the MT for EVA construction of the space station. This program included development of a full-scale, functioning engineering model of the MT, and evaluation of the system through one-*g* and simulated zero-*g* truss construction and utility tray integration tests. One-*g* tests were conducted in a "shirt sleeve" environment to develop construction procedures, train personnel, and determine one-*g* construction times. The average time to construct three bays (44 struts) of truss without utility tray integration was 15 min in one-*g*, which results in a unit assembly time of 20 sec per strut.

Simulated zero-*g* tests were conducted in the Marshall Space Flight Center Neutral Buoyancy Simulator (shown in the second figure) using test subjects in both scuba and Space Shuttle extravehicular mobility units (EMU). Scuba construction times were approximately the same as those from the one-*g* tests, indicating that the effects of gravity on the one-*g* tests were essentially the same as the effects of water drag on the scuba tests. Tests with subjects in the EMUs resulted in an average time of 20 min to construct three bays of the truss and to integrate utility trays, which

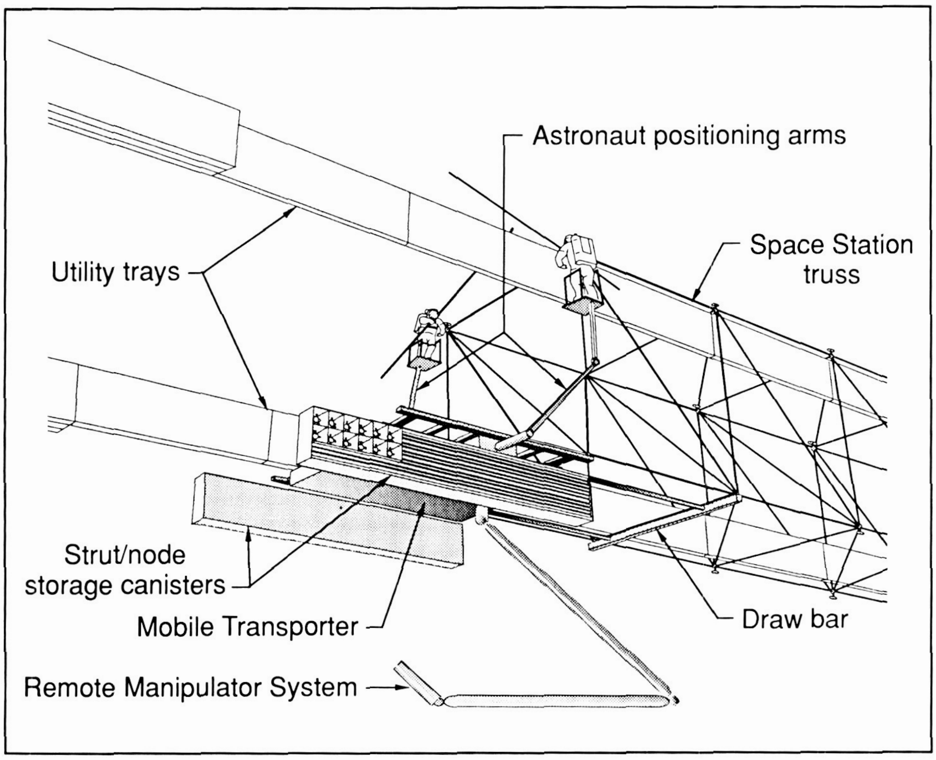

Mobile Transporter configuration for space station truss construction.

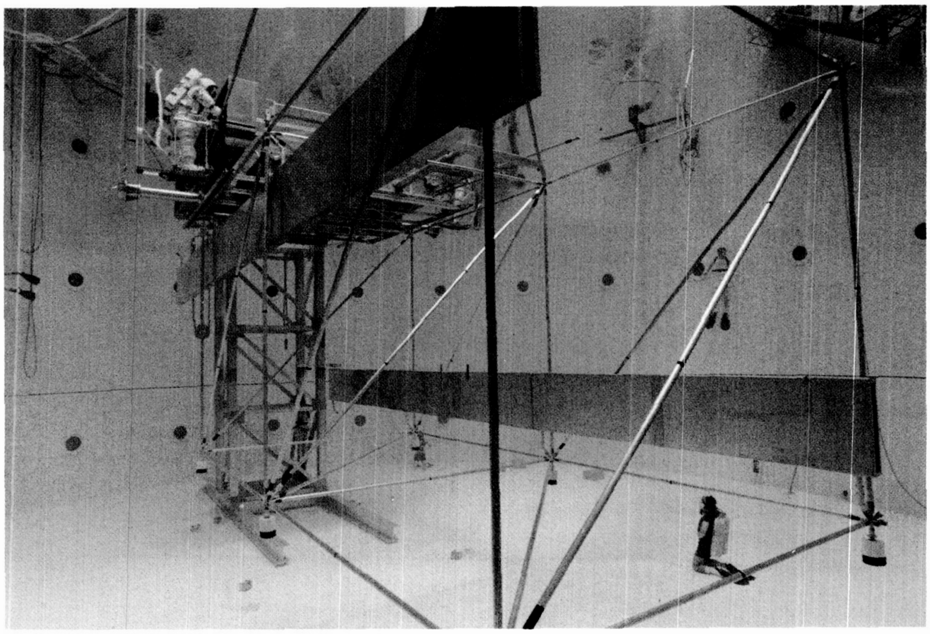

Simulated zero-g space station truss construction with Mobile Transporter.

ORIGINAL PAGE
COLOR PHOTOGRAPH

indicates a unit construction time of 27 sec per strut. This unit construction time is faster than the times measured from all other construction tests conducted to date using a space station-sized structure. This unit construction time is also considerably lower than the benchmark time of 60 sec per strut currently being used for prediction of on-orbit construction times. The main reason for the low construction time is the use of the remotely operated positioning devices that enable rapid and accurate positioning of the astronauts throughout all phases of the construction process. The results of this study indicate that EVA construction of the space station truss and integration of utility trays can be efficiently and reliably performed using the Mobile Transporter.
(Walter L. Heard, Jr., 2608, Judith J. Watson, Harold G. Bush, and Mark S. Lake)

Noise Control Using Active Vibrational Actuators

Recent flight-testing of advanced turboprop aircraft has proved the concept viable for commercial applications. Although the gain in fuel efficiency is significant, passenger acceptance dictates that interior noise levels should be no higher than present turbofan-powered aircraft. Traditional low-frequency noise treatments impose additional weight penalties that threaten to eliminate the gain in fuel efficiency. To attain the required 50 to 70 dB of noise suppression through the sidewall, conventional treatments must be augmented with innovative sound isolation techniques of

low weight and cost. Active control techniques using vibrational inputs to the fuselage structure are currently under investigation to determine their applicability for effective control of the cabin acoustic environment.

To demonstrate the use of active control technology, a finite-length, thin-wall aluminum cylinder 0.508 m in diameter, 1.245 m in length, and 1.6 mm in thickness was used. This structure was excited into vibration by an exterior acoustic source representing a propeller. The resulting acoustic field inside the cavity is shown in the figure at the source plane $x = 0$ as the primary noise field. This field is represented as a pressure contour map of the sound pressure level (SPL) and ranges from 105 to 65 dB. The pressure field is dominated by a single $\cos(2\theta)$ mode as evidenced by the four-lobed color pattern. By attaching a single electrodynamic shaker to the cylinder as indicated by the arrow in the lower left picture, a composite internal acoustic field is generated with an overall 15-dB noise reduction. This reduction is achieved by effectively suppressing the $\cos(2\theta)$ mode, leaving a strong $\sin(2\theta)$ mode again characterized by a four-lobed pattern but turned 90° By attaching a second shaker at a position 45° around the cylinder as shown in the lower right contour, both the $\cos(2\theta)$ and the $\sin(2\theta)$ modes are effectively controlled, and an additional 10 dB of noise reduction is attained.
(Richard J. Silcox, 3561)

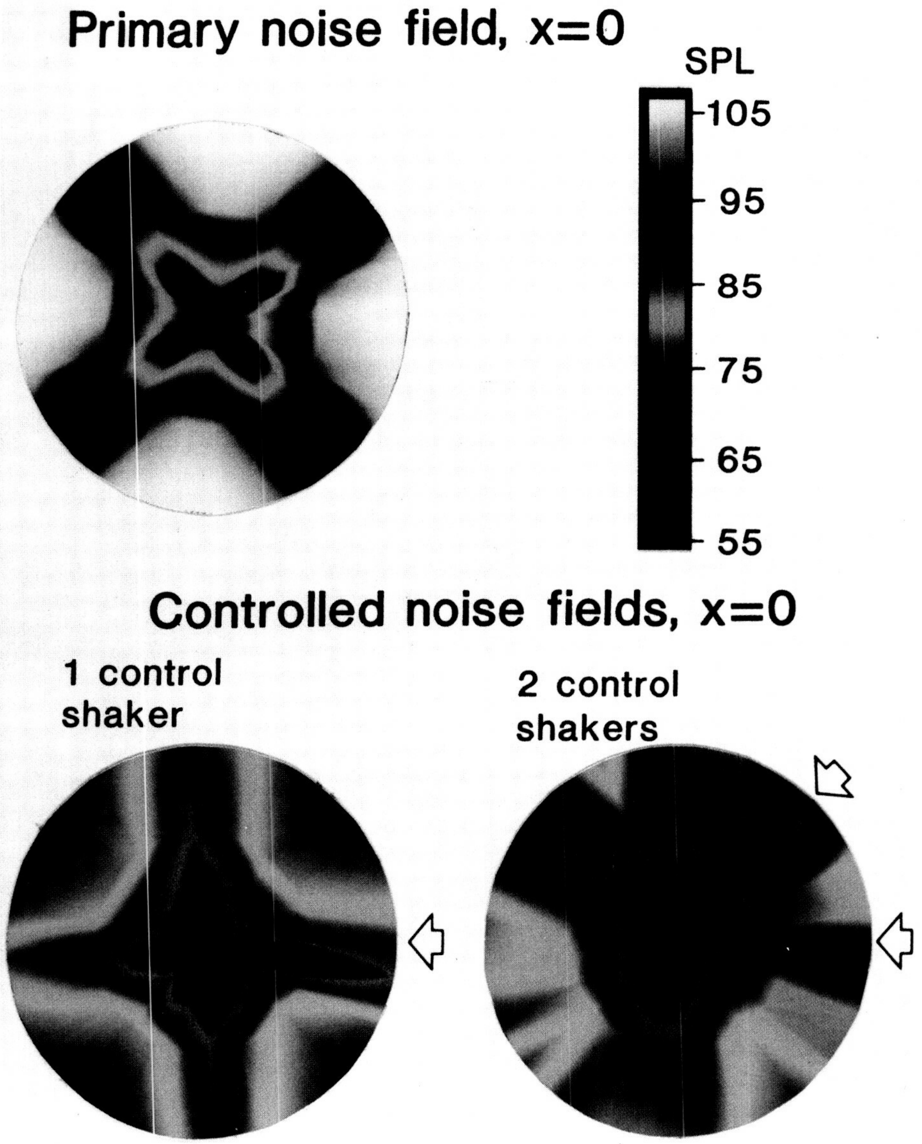

L-88-7174

Comparison of primary and controlled acoustic fields for two control configurations.

Interior Noise Reduction of Advanced Turboprop Aircraft

A NASA-sponsored experimental and analytical effort has shown that the use of advanced turboprop (ATP) technology instead of conventional turbofans can result in a substantial reduction in fuel consumption. The full realization of these economic benefits requires that acceptable interior noise levels within ATP aircraft be achieved with minimal additional weight.

An ongoing NASA/industry program is aimed at the measurement, prediction, and control of interior noise in ATP aircraft. In recent flight tests, McDonnell Douglas Aircraft achieved a cabin environment that was as quiet or quieter than their existing MD80 aircraft series.

ORIGINAL PAGE
COLOR PHOTOGRAPH

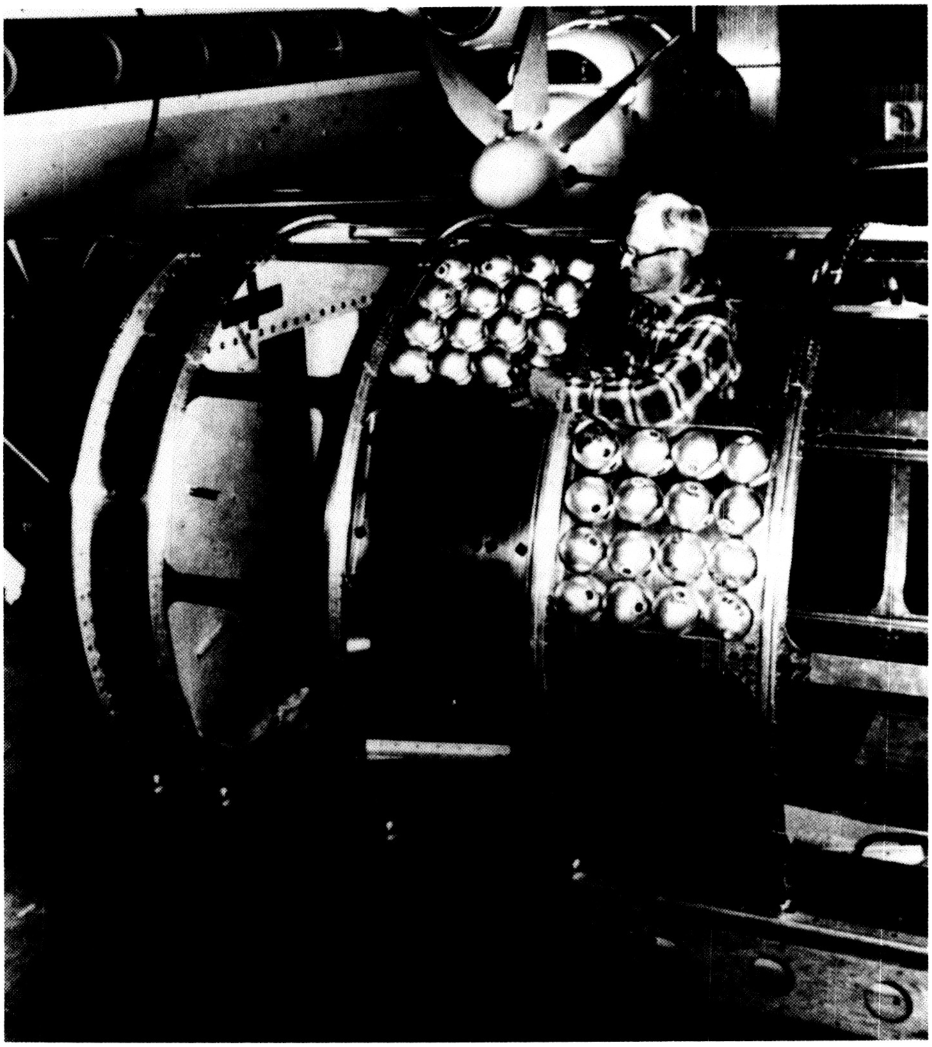

Helmholtz resonator acoustic treatment. L-88-7623

The Lockheed Corporation recently completed flight tests to evaluate an advanced cabin wall acoustic treatment. The treatment consists of a sealed, vibration-isolated chamber within the bare cabin equipped with approximately 600 Helmholtz resonators on its sidewalls and under its floor. The figure shows the assembly of the acoustic treatment prior to installation in the aircraft. Each hemispherical resonator was tuned to 225 Hz, the fundamental propeller frequency for cruise conditions. This frequency dominates the noise within the cabin. Preliminary test results indicate that the acoustic treatment reduced sound levels at the fundamental propeller frequency by 25 to 30 dB relative to the untreated case.

(Kevin P. Shepherd, 3561)

Nonlinear Shell Response of SRB/ETA Ring Interface

The Space Shuttle system is comprised of an orbiter, an external tank (ET), and two solid rocket boosters (SRBs). Each SRB is attached to the ET at the forward and aft ends. The aft end attachment is provided by an ET attachment (ETA) ring and three struts. This region, shown in the first figure, is referred to as the SRB/ETA ring interface region.

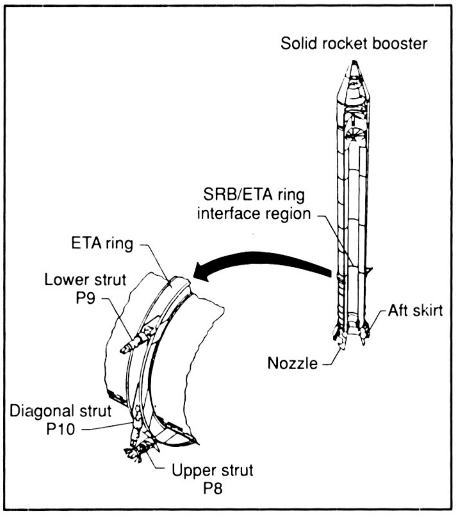

SRB/ETA ring interface region.

The SRB/ETA ring interface models were developed using the STAGSC-1 finite-element computer code and executed on the Numerical Aerodynamic Simulation (NAS) computer system. These models are based on the original Space Transportation System (STS) 51-L geometry configuration. The SRB/ETA ring interface consists of the complete ETA ring, a portion of the SRM aft attachment segment including a factory joint, and a portion of the aft center segment including a field joint. The total length of the model is 136 in. The field and factory joints are modeled by using equivalent stiffness joints instead of detailed models of the joint. With that idealization, the global shell behavior of the SRB/ETA ring interface was calculated (including nonlinear effects) to determine the

relative influence of the ET strut loads and the internal pressure loading. These analyses included the asymmetric loads resulting from the aft ET strut loads and the equivalent shell loads derived from the reconstructed flight loads for STS 51-L.

The nonlinear analyses of the SRB/ETA ring interface model were performed using the reconstructed loads for time $t = 5.3$ and 7.2 sec after the Space Shuttle main engine (SSME) ignition. The nonlinear radial deflections at the ETA ring, normalized by the nominal SRB case thickness (0.479 in.), are shown in the second figure as a function of circumferential location around the SRB. Time $t = 5.3$ sec corresponds to the time at which maximum bending occurs and has been referred to as "max twang." At that time, the SRM is unpressurized since it has not yet been ignited. The ET strut loads at maximum bending result in an asymmetric radial deflection pattern; however, the amplitudes of these deflections are small compared to either the nominal shell thickness or the radial deflections caused by internal pressure loading only. Time $t = 7.2$ sec corresponds to the time at which the SRM reaches full pressure and liftoff occurs. At SRM pressurization, the overall shell response is dominated by the effects of the internal pressure, and the effect of the ET strut loads is secondary.

(N. F. Knight, Jr., 4892)

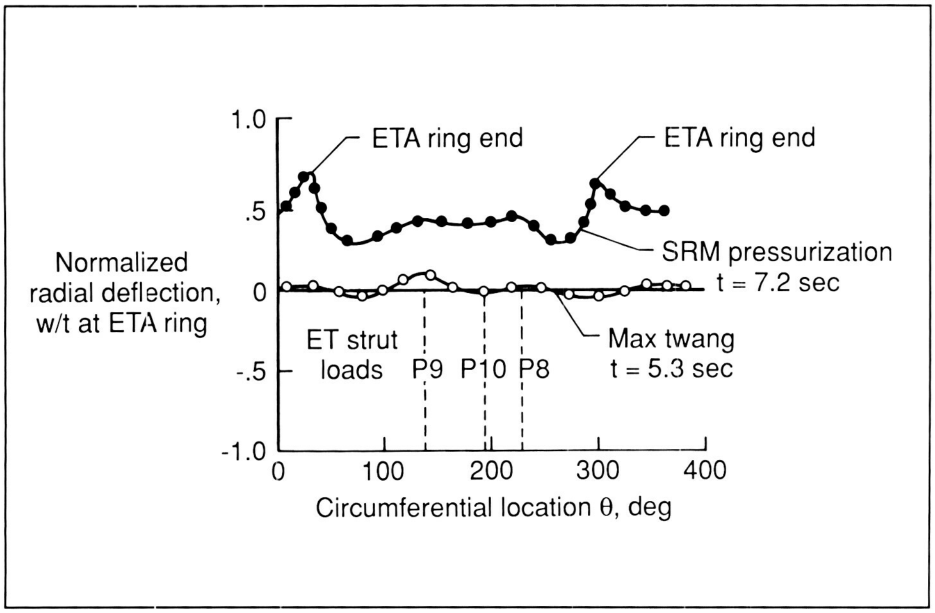

Correction of Conventional Slewing Predictions by Nonlinear Analysis

Because of the importance of nonlinear effects in the dynamic analysis of slewing flexible booms, a research study has been initiated to investigate the effects of various nonlinear terms arising from different analysis assumptions. As spacecraft components become more flexible or on-orbit operations are performed faster, accurate modeling procedures become more critical to performance, stability, and active control. Thus, the accurate analysis of slewing of flexible booms is critical to on-orbit construction (robotics), payload pointing, and deployment.

The conventional approach to dynamic slewing analysis has been to use a precise nonlinear kinematics model in conjunction with an imprecise linear deformation model, usually given by a summation of linear modes. As shown on the left in the figure, this imbalance of nonlinear and linear modeling can lead to predictions of erroneous behavior. The imprecise deformation (linear) model forces the boom tip to move normal to the undeformed boom shape, which is then interpreted by the precise kinematics as constituting an increase in the boom's radial arm distance from the center of rotation. In turn, the increased arm results in a Coriolis force acting in the direction of motion (nonrestoring); thus, the ingredients for predicting a destabilized condition are set in place. The right-hand figure illustrates correct and incorrect predictions in lockup time as the flexible deploying booms are simultaneously slewed until the boom root rotates through 90°. The linear deformation model erroneously predicts a dramatic increase in lockup time at a certain value of a nondimensional flexibility parameter. However, a converged balanced analysis reveals the physically expected decrease in lockup time as the boom is made more flexible or the stiffness of the driving root rotational springs is in-

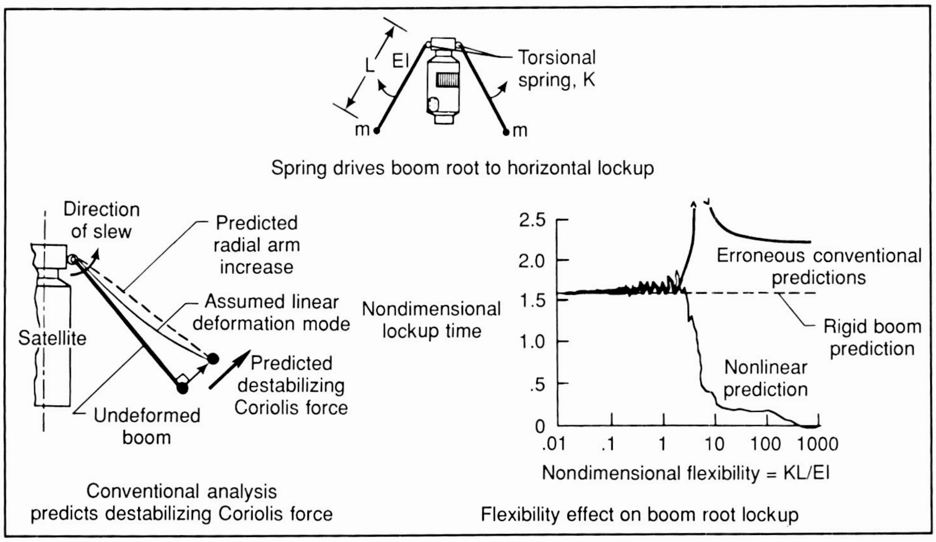

Nonlinear effects in dynamic analysis of slewing flexible booms.

creased. A rigid boom solution is also shown for comparison purposes. **(Paul E. McGowan and Jerrold M. Housner, 3054)**

Demonstration of Three-Dimensional Active-Truss Concept for Vibration Attenuation

Because the concept of using a variable geometry truss actuator for controlling structural vibrations shows much promise for future space applications, a study has been undertaken to determine if vibration attenuation of a truss-type structure can be realized using a spatial active truss, that is, a truss comprised of extensible links.

A mathematical model of the spatial truss (shown schematically in the figure) with an attached generic beam continuum was developed. The beam continuum was discretized using a three-mode Ritz expansion. The truss was modeled as a kinematic input to the beam because the beam has no dynamic effect on the truss. Using a specific beam continuum (0.25 in. brass rod) a computer simulation was run to determine the system response to initial conditions. Experimental digital control was performed on a spatial truss test article with an attached 0.25 in. brass rod to verify the analytical model. The system nonlinearities were linearized for this initial study. Control laws were generated for this multi-input system using a full-state linear quadratic regulator (LQR) optimal approach; however, partial state feedback (position only) was used in both simulations and experiments. Digital control consisted of measuring the states (beam strain and link position) with strain gauges and potentiometers, computing the control law, and sending the control voltages to the truss motors. The control objective was to drive the beam strain to zero without modifying the truss final position.

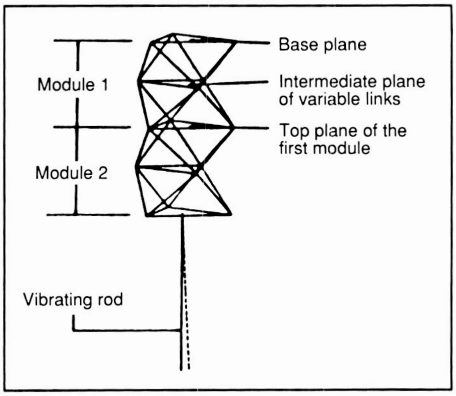

Schematic representations of active spatial truss arrangement.

The analytical simulation and experimental results agreed with each other and showed excellent potential for vibration control of the attached structure. The effective damping ratio of the beam for a first-mode vibration was improved from 0.002 to 0.06. **(Garnett C. Horner, 3699)**

Improved Deployment Characteristics for Doubly-Curved Reflector Support Truss

A concept for reliably deployable and high-precision support truss structures has been developed for application to doubly-curved reflectors. This concept utilizes a PACTRUSS-type structure (a deployable truss with efficient packaging characteristics) and is a proposed design for the primary support structure of space-based precision segmented reflectors (PSR) such as the Large Deployable Reflector (LDR). PACTRUSS was first conceived as a synchronously deployable flat truss beam, and it has the significant advantages of ease of deployment and compact stowage volume. Recent efforts have concentrated on extending the PACTRUSS concept to doubly-curved reflector support structures.

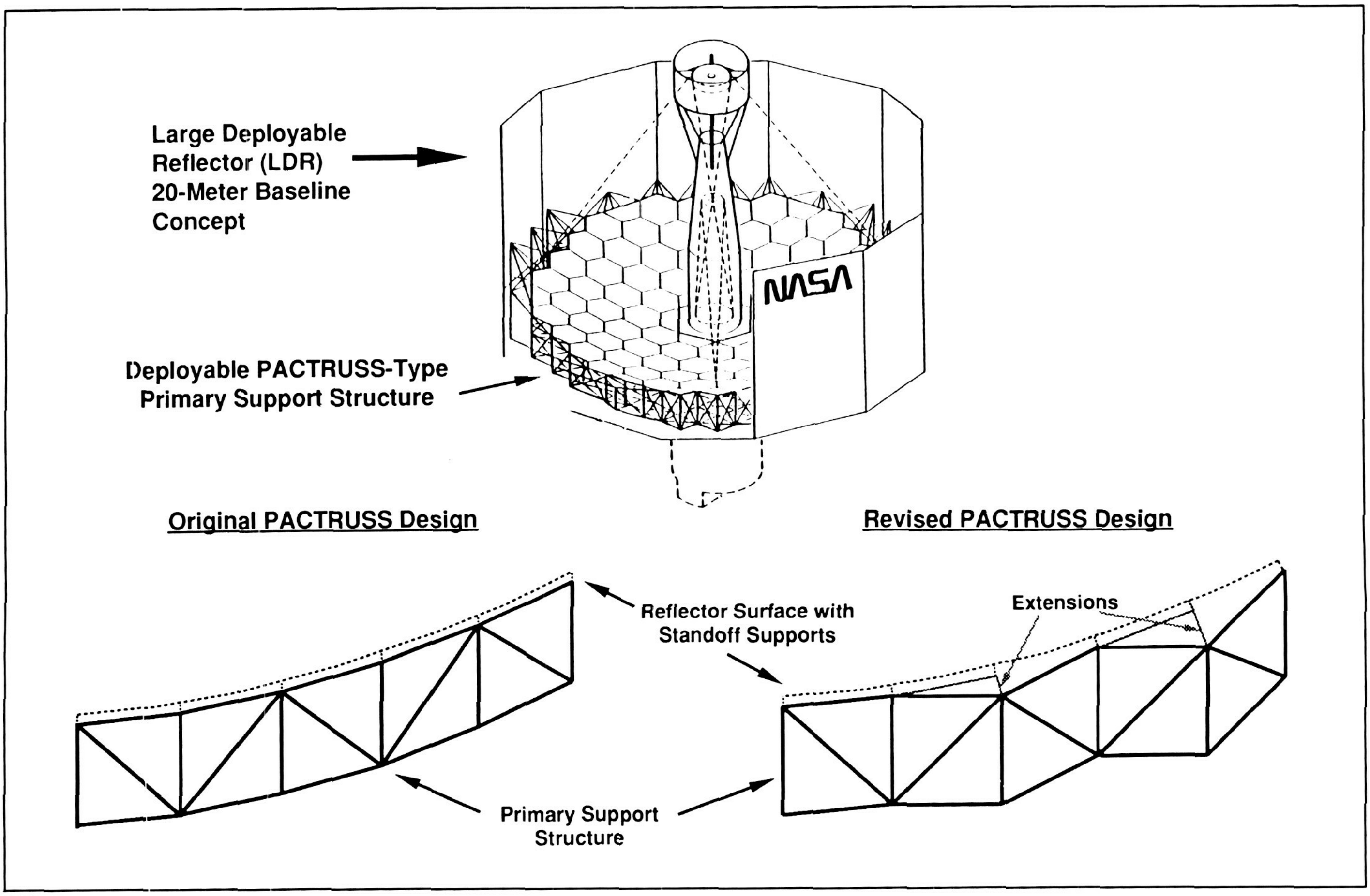

Revised PACTRUSS design that eliminates deployment hard points for doubly-curved reflector truss.

Through in-house conceptual design studies and a contract with Astro Aerospace Corporation, deployment analyses were conducted for several different doubly-curved PACTRUSS concepts. Computer programs were developed for generating various truss designs and for handling the deployment analysis of each structure.

The original concept for a PACTRUSS-type reflector support structure consisted of a doubly-curved truss structure with a surface that matched the contour of a parabolic reflector (as shown in the figure). The uppermost truss nodes were constrained to lie on a parabolic curve that was offset from the reflective surface by a constant standoff distance. Extensive analysis of this design showed that intolerable lockup conditions or hard points occur during deployment. To overcome the lockup problem, a revised PACTRUSS design was formulated. In this design, alternate bays of the PACTRUSS are not allowed to deploy past the horizontal position. This results in a structure that has a step-like profile. For this revised PACTRUSS, a doubly-curved parabolic surface is achieved by adding extensions to the basic truss at those nodes that do not naturally lie on the desired parabola. Deployment analyses for the new PACTRUSS concept exhibited no tendency for lockup and no significant member straining. Analysis of the new PACTRUSS design indicates that a doubly-curved support structure can be reliably deployed.

(Timothy J. Collins, 2414 and Martin M. Mikulas, Jr.)

Enhanced Diffusion Bonded Ti_xAl-Ti Honeycomb Core Sandwich Panels

The National Aero-Space Plane program requires the development of advanced titanium aluminide

(Ti_xAl) intermetallic alloys having improved specific properties at elevated temperatures as well as joining processes capable of incorporating these materials into efficient structural components. To support this need, a joining process termed Enhanced Diffusion Bonding (EDB) was developed for fabricating lightweight, high-temperature Ti_xAl-Ti honeycomb core (H/C) sandwich panels. The process relies on a combination of brazing and solid-state diffusion to promote bonding.

The EDB panel shown in the figure consists of two Ti-14Al-21Nb (Ti_3Al) face sheets joined to a Ti-3Al-2.5V H/C. Using a selective maskant and electroplating technique, only the very edges of the H/C were electroplated with the EDB filler material prior to bonding. By limiting the placement of EDB filler material to only the areas where it is needed, the structural weight and potential deleterious metallurgical interaction effects are minimized. The assembled panel components were then heated to 1700°F for a period of 30 min to promote bonding. Panels as light as 0.5 lb/ft^2 of panel area have been produced using this technique.

Structural element test results of EDB joints produced in Ti-14Al-21Nb alloy have demonstrated load-carrying capability at temperatures higher than the 1700°F bonding temperature. Consequently, EDB offers the potential of fabricating lightweight structural panels with high service temperatures relative to their bonding temperature.

(E. K. Hoffman, 3372)

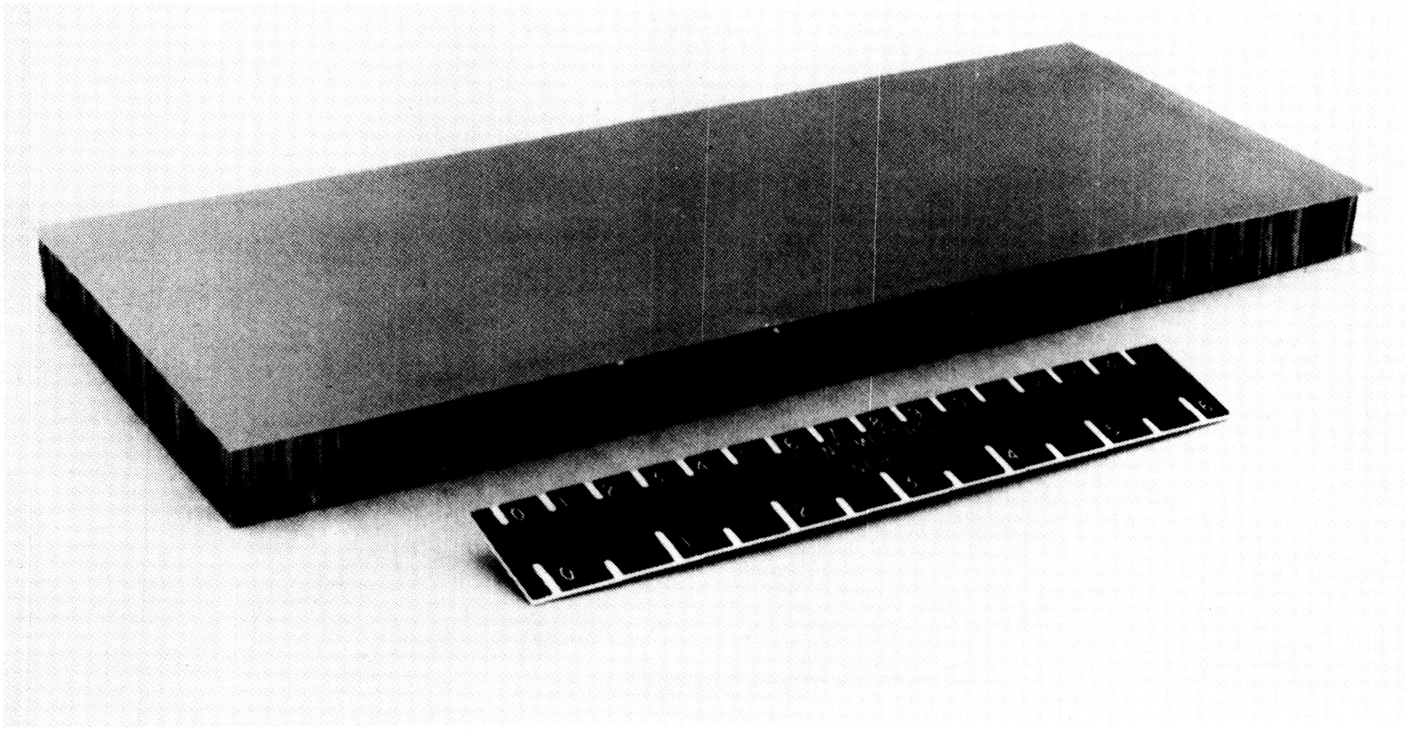

Enhanced diffusion bonded Ti_3Al-Ti honeycomb core sandwich panel. L-88-1165

ORIGINAL PAGE
BLACK AND WHITE PHOTOGRAPH

Systems Engineering and Operations Directorate

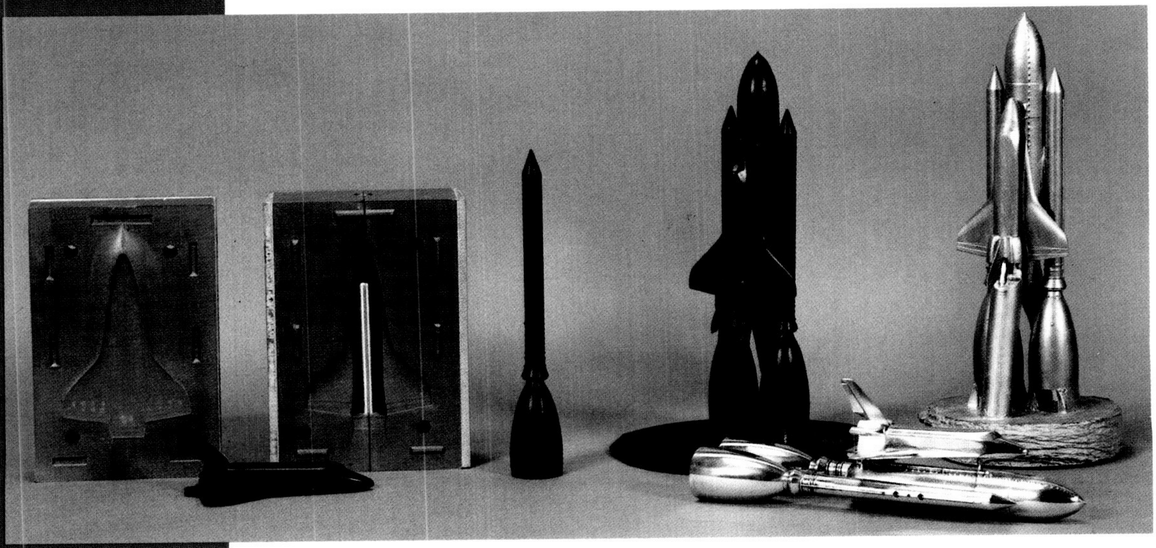

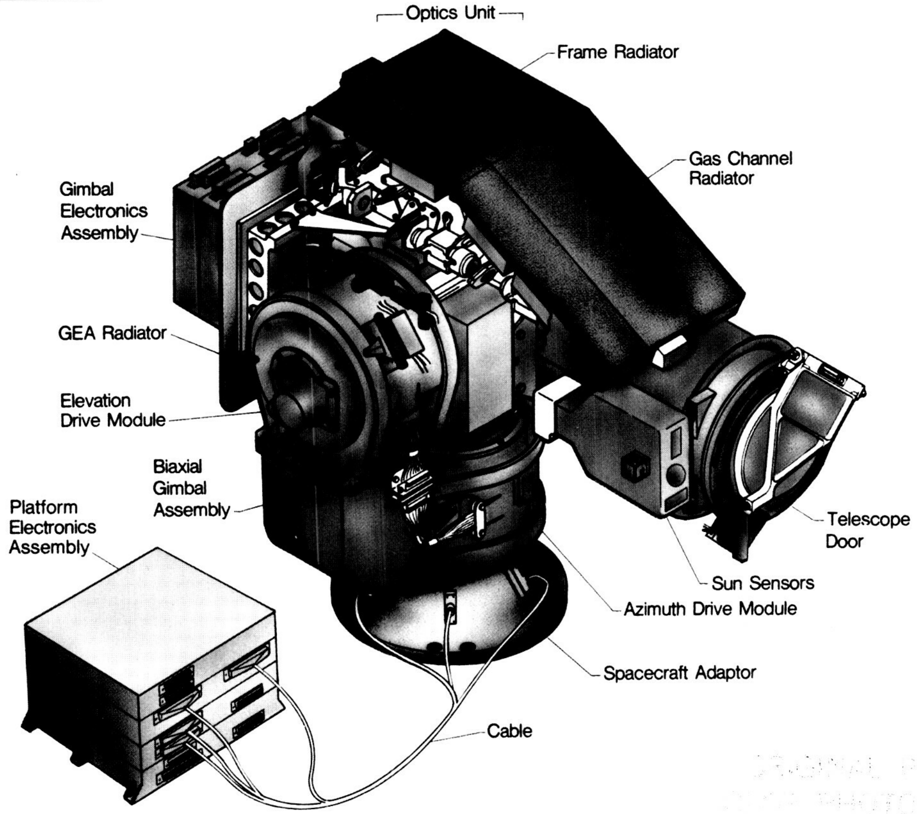

The function of the Systems Engineering and Operations Directorate is to support ongoing aeronautical and space research at Langley Research Center. This work force is divided into five divisions with specific support functions. The Systems Engineering Division is responsible for structural, mechanical, thermal, electrical, and aeronautical systems engineering functions required to provide flight hardware and research models for aerospace research applications and technology. The Facilities Engineering Division is responsible for engineering and design of aerospace research and development equipment and institutional facilities for aeronautical and space research, such as special handling equipment, model supports, and special test equipment. The Fabrication Division is responsible for developing and fabricating aeronautical and aerospace research hardware related to ground support equipment as well as research facilities test equipment. This division provides developmental manufacturing, technology and electronics technical support, including communications systems and instrumental hardware. The Operations Support Division is responsible for providing the technical, mechanical, electrical, and maintenance services for research and institutional facilities. This division operates laboratory equipment and wind tunnels and collects, records, and interprets test data. The Systems Safety, Quality, and Reliability Division has overall responsibility to ensure the safety of operation of all aerospace and ground facilities as well as to ensure that the aerospace hardware and ground research equipment meet all quality and reliability standards. This division also manages the environmental health program for the Center and inspects the construction of major modifications to the many unique research facilities. In addition to the five divisions, the Facilities Program Development Office is responsible to the directorate.

The Systems Engineering and Operations Directorate made significant contributions to numerous space, aeronautical, and facility programs during the past year. Major accomplishments in support of space programs include the development of a radiator fluid transfer coupling for the rotary joints of Space Station Freedom, *the design of a 270° external tank attachment ring for the Space Shuttle, the assembly and critical alignment of the Halogen Occultation Experiment (HALOE), and the development of two different designs of a crew escape system for the Space Shuttle. In support of the Center's aeronautical programs, an important achievement was the design, fabrication, and installation of an experimental leading edge for the F-106 Vortex Flap Project. Also, approximately 90 wind tunnel and free-flight models were designed and fabricated. In addition to the operation and maintenance provided by the directorate for the Center's research facilities, the facilities were upgraded by the addition of a rain simulation system for the Aircraft Landing Dynamics Facility, the reassembly of the 20-Inch Supersonic Wind Tunnel, which was transferred from the Jet Propulsion Laboratory to Langley Research Center, modifications to the Refused-Fired Steam Generating Facility, which resulted in significant emission reductions, and new model support and turntable systems for the Langley 30- by 60-Foot Tunnel.*

Because of the unique requirements of some of the aerospace research performed at the Center, both engineers and technicians are involved in applied research in solving engineering and fabrication problems. These problems relate to the support hardware and software necessary to provide the experimental systems requested by research. The following contributions represent typical engineering fabrication research and technology development highlights in the Systems Engineering and Operations Directorate.

Space Station Rotary Coupling

A permanent, manned space station, as currently envisioned, will be gravity gradient stabilized and will incorporate rotating solar arrays and thermal radiator panels. The rotation of the solar arrays and radiators will provide much more efficient thermal and power systems, thereby reducing overall size, weight, and cost of the systems.

As part of an advanced development effort for the space station, a rotary fluid coupling has been

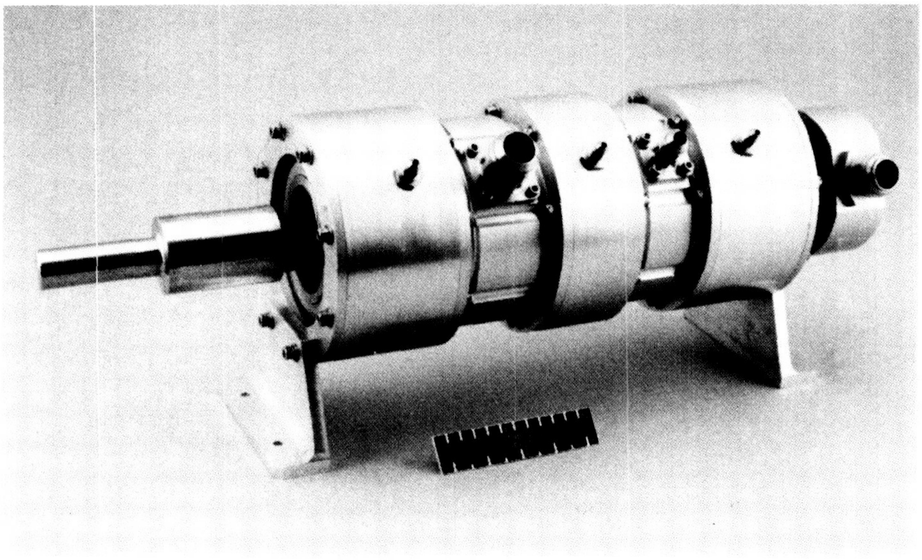

Rotary fluid coupling for space station application. L-86-9631

designed, built, and tested. The coupling has met all of the design requirements that would allow the transfer of coolant fluid (anhydrous ammonia) across the rotating joints that connect the radiator panels to the space station. Included in these requirements is a 20-year lifetime of continuous rotation with little or no maintenance while maintaining a very low leakage rate. The design rotation rate is about 0.01 r/min (1 revolution per orbit). The ammonia flow rate through the coupling would provide 150 kW of cooling with a maximum pressure drop of 1.0 lb/in^2.

The unit shown was fabricated of 6061-T6 aluminum. The shaft was coated with a commercial proprietary Teflon® coating to enhance its wear characteristics. A combination of mechanical face seals and rotary shaft seals was used.

Testing was accomplished in the Ammonia-Flow Test Facility at Langley Research Center. The unit completed the equivalent of 22.6 years of rotation before the test was terminated. The measured leakage rate from the unit ranged between 1.9×10^{-6} and 2.0×10^{-5} standard cc/sec NH_3 over the entire test. **(Obie H. Bradley, Jr., 4508)**

Increasing Aeroelastic Divergence Pressure of Wind Tunnel Models by Varying Balance Flexibility

Interest has recently developed in modifying model support systems in the National Transonic Facility in order to increase their aeroelastic divergence dynamic pressures, thereby permitting higher tunnel operating speeds. A study has been conducted to investigate the effect of increased flexibility of the forward portion of the balances on the divergence pressures of wind tunnel models. Wind tunnel models are usually designed such that the attachment to the balance is forward of the center of pressure of the aerodynamic lift forces. At the attachment, the moment induced by the lift force tends to rotate the forward end of the balance in a direction opposite to that due to the lift force. Therefore, the

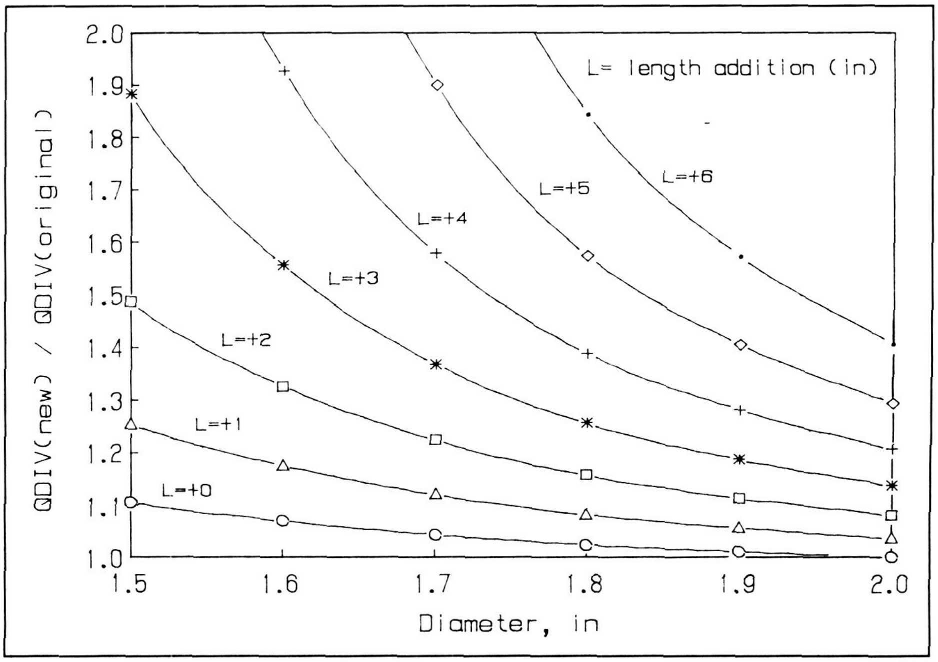

Divergence pressure results for Pathfinder I model.

increase in flexibility of the forward portion tends to pitch the nose down, resulting in an increase in divergence pressure.

Several existing model support systems have been studied to determine the feasibility of increasing the divergence dynamic pressure by increasing the flexibility of the forward portion of the balances. The divergence pressures of the model support systems were determined by means of a computer program that utilizes a transfer-matrix method for solving the homogeneous two-point boundary value problem. A transfer-matrix method, which is based on fourth-order Runge-Kutta integration, was used to solve a set of governing first-order differential equations. In the math model of the support system, two design parameters of the balance's forward portion, the diameter and the length between the balance moment center and model attachment point, were varied.

The analytical results show that a significant increase in divergence pressure can be obtained from the increased flexibility of the balance's forward portion for many models and their support systems. The figure shows, for the *Pathfinder I* model, the ratio of the modified divergence pressure to the original divergence pressure for variations in the balance's forward portion diameter and the additional length between the balance moment center and the model attachment point.

This study has demonstrated the benefit of balance flexibility changes in achieving increases in divergence pressure for various models and their support systems.
(Robin W. Edwards, 4508)

Rotating Light System for In-Flight Flow Visualization of Leading-Edge Vortex Systems on F-106B Aircraft

A vapor screen technique, which uses three basic systems (seeding, light-sheet generation, and visual recording of events), was developed and applied to the F-106B aircraft to obtain research data about near-field vortex flows above the highly swept wings of high-performance fighter aircraft. The light-sheet system previously flight-tested was fixed to observe one particular location above the wing. A new light-sheet system has been designed which rotates to study the leading-edge vortex over the region of interest on the upper wing surface.

The source of light for the rotating light system is a high-intensity mercury-arc vapor lamp. The light passes through an 0.012-in.-wide slit and is focused onto two optical lenses that are used to produce the 0.75-in.-wide sheet of light. A mirror is used to direct the light toward the wing surface. The point at which the light sheet strikes the

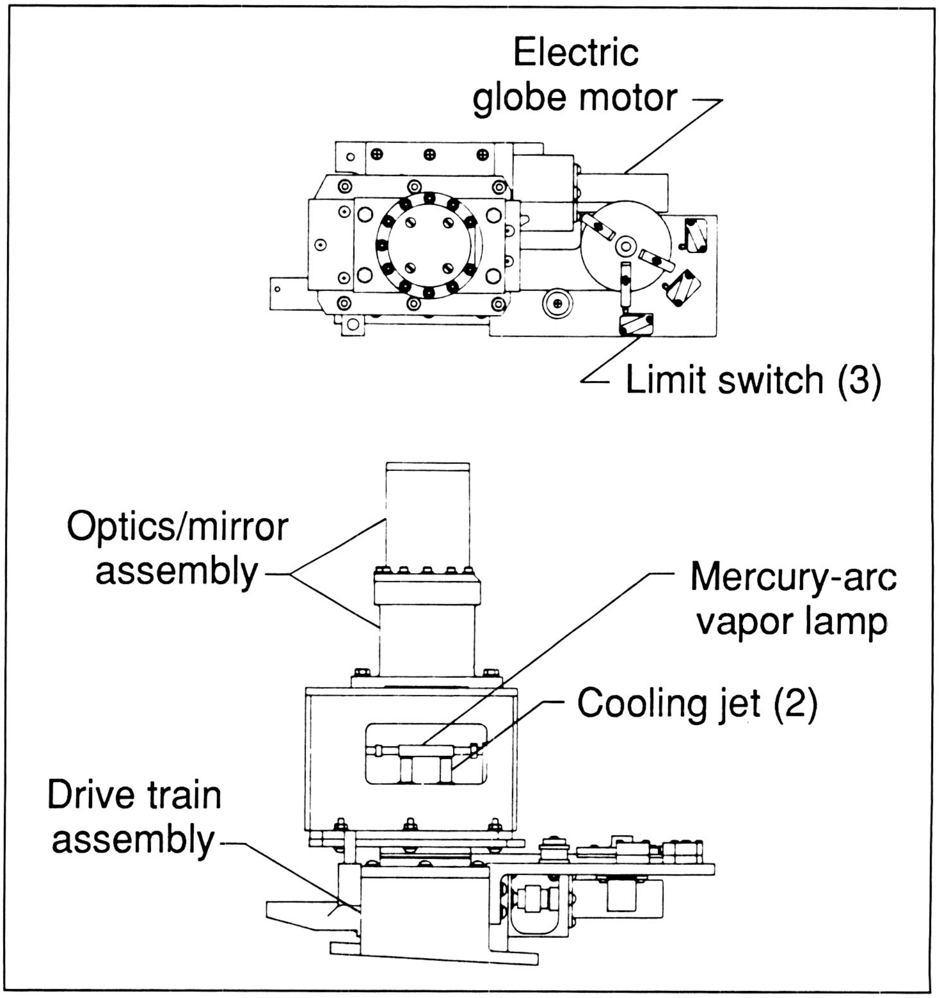

Rotating light system.

wing can be varied by changing the angle of the mirror. Rotation of the light source and the optics assembly is accomplished by an electric globe motor that powers a drive train assembly. The rotational rate of the light-sheet sweep is fixed at 10°/sec, and the included angle of sweep is 30° to 160° from the forward fuselage centerline, for a total angle of 130°. Limit switches are used to stop or reverse rotation at the sweep limits. Active cooling for the lamp is provided by a small air compressor and is supplemented by ram air.

The rotating light and cooling systems are packaged vertically above the center fuselage in a thin airfoil-shaped aerodynamic fairing to reduce aerodynamic disturbances. The fairing is made from fiberglass/epoxy and is 0.10 in. thick. The design static and dynamic loads are well within the load-carrying capability of the integrated structural assemblies.
(K. W. Davis and G. S. Ng, 4666)

Cessna 172X Stall/Spin Ventral Fin Design/ Integration

Flight tests of a Cessna 172X high-wing aircraft have been conducted at Langley Research Center as a part of the Stall/Spin Resistance Program. The wing surface was modified by attaching leading-edge droop sections of various lengths and configurations. These flight tests and scale-model tunnel tests showed that the leading-edge droop sections in combination with a fuselage-mounted ventral fin increased stall/spin resistance. Also, the ventral fin provides an added benefit of enhanced lateral stability at high angles of attack.

Cessna 172X ventral fin.

The location and the size of the ventral fin were determined during tunnel testing. The fin is a rearward-swept assembly constructed of an aluminum sheet with a maple wood stiffener bonded internally to the leading edge. Attachment of the fin to the structure required integration into the existing internal aircraft structure and spin recovery parachute truss assembly. Particular attention was given to the ventral fin design/integration procedure to assure proper clearances were maintained for safe operation of the spin-recovery parachute system.

Data from ongoing in-flight tests at Wallops Flight Facility, utilizing candidate leading-edge droops and the ventral fin, are being evaluated using established stall/spin criteria. Initial results show that the ventral fin offers significant aircraft stall/spin resistance during the test flight envelope.
(Michael Tyree, 4666)

Facility for Full-Scale Testing of Airfoil Performance in Simulated Rain

The performance of airfoils has traditionally been studied in wind tunnels without environmental effects such as rain. The potential hazards to aircraft operation imposed by wind shears, which can be accompanied by heavy rain, have prompted studies of the effects on the performance of airfoils in a rain

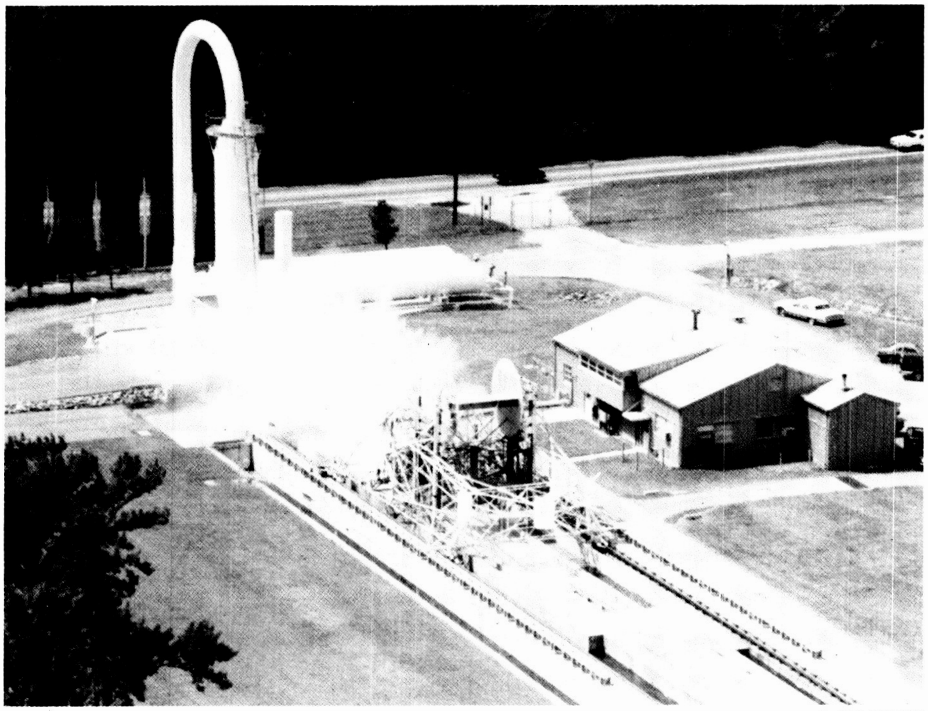

L-88-09589

ALDF carriage with end plates and wing during propulsion phase.

environment. However, concern exists over the full-scale effects of rain on aerodynamics and how to scale parameters associated with simulated rain in wind tunnel testing. To confirm and establish the proper scaling laws, NASA plans to "fly" a full-scale wing section in a simulated rain environment. These tests will be conducted at the Langley Research Center Aircraft Landing Dynamics Facility (ALDF).

The ALDF was designed to test full-size aircraft landing gear systems at operational velocities (up to 220 knots) under closely controlled conditions. Although the facility was not designed to test airfoils, it does possess many of the features required for these tests (such as a maximum test velocity of 220 knots, sufficient track length to provide adequate test time, and a test carriage large enough to support a full-scale wing section).

Major additions to the ALDF consisted of the rain simulation system and a wing model mounted on the carriage. To conduct a test, the carriage with the wing model is propelled to the required test velocity and allowed to coast down the track, thus "flying" the wing through the simulated rain.

The rain system is located approximately 800 ft downtrack from the start position of the propulsion stroke. This system provides uniform simulated rain over an area 15 ft wide, centered over the track, by 500 ft long. The duration of the rain is 20 sec, which is sufficient time for the wing to "fly" through the simulated rain field. The rain environment duplicates natural rain as closely as practical. The rain system produces rain rates of approximately 2, 10, 30, and 40 in./hr with a uniform rain intensity within ±10 percent.

ALDF rain simulation system.

L-88-9867

The drops produced have mean volumetric drop diameters (MVD) of 0.5 to 2.0 mm and velocities within ±10 percent of terminal velocities.

The two-dimensional (2-D) wing model for the ALDF tests is developed from the NACA 64-210 airfoil section. This airfoil is representative of a typical commercial transport wing section. The airfoil chord length is 10 ft and the wing span is 13 ft. The model spans between two 15-ft-diameter end plates to provide 2-D aerodynamics.
(J. T. Taylor, 4551 and C. T. Moore III)

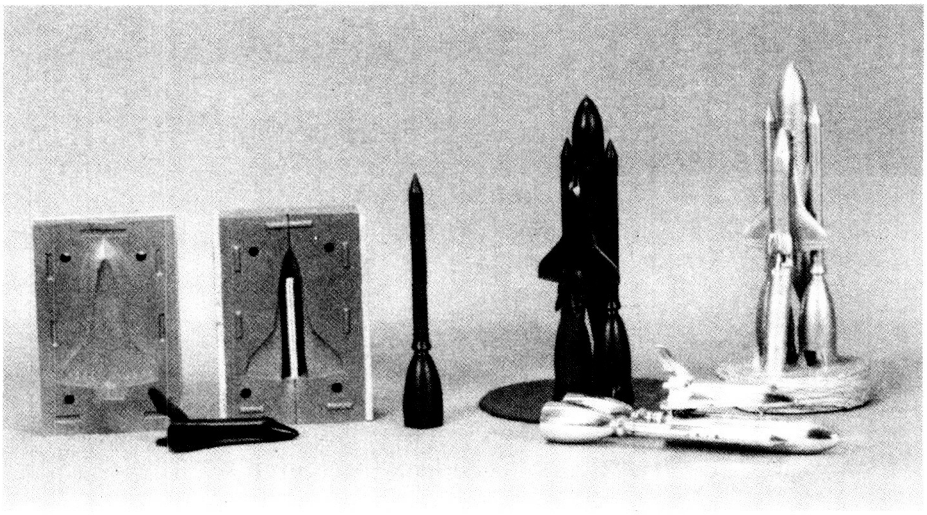

Near-net-shape metal model castings. L-87-1060

Near-Net-Shape Metal Model Castings

High-strength stainless-steel models have been tested and evaluated in Langley Research Center wind tunnels for many years. Many of these precision models are expensive and time consuming to produce. Near-net-shape models can be manufactured by investment casting techniques using a minimal amount of material, thus saving both machining costs and schedule time. Technician skill and attention to details are critical in this process, as well as the employment of precision measuring equipment at every stage of the model fabrication.

Basically, the process includes fabrication of a wooden pattern and casting a wax mold from this pattern. The hollow wax pattern is produced by injecting wax into a mold consisting of the model, gates, and risers. A ceramic shell mold reinforced with silica sand is fabricated by dipping the wax mold into a slurry containing the solid ingredients and then curing the ceramic at room temperature. The wax pattern is then melted and leaves the cavity. The mold is now ready to receive molten metal. The sand-reinforced ceramic mold must then be heated to 1800°F before the 2700°F molten stainless steel is introduced. This process can produce metal models within ±0.006 in. of symmetry and ±0.012 in. of nominal values.
(John S. Powell, Jr., 2651)

Helicopter Tail Rotor Torque Measurement System Integration

The NASA/Army Boom Strake Project involved the attachment of strakes to the tail boom of the Langley Resesarch Center Bell 204B helicopter in order to disrupt the airflow produced by main rotor downwash over the boom. The research objective was to demonstrate increased performance by reduction of the tail rotor power. An Acurex Universal Data Coupler integrated with the tail rotor shaft and gear box produced a noncontact transmission system to record shaft strain data. The primary system components included an inductive power supply unit, a high-speed fiberglass collar, a shaft sleeve, and shaft clamp.

System integration involved both component redesign to withstand flight load conditions and hardware fabrication to properly align and secure the instruments. The induction power supply unit required design and fabrication of a housing for the printed circuit board which provided environmental protection of the electronic components. Support hardware affixed to the gear box prevents excessive antenna vibration and allows translational positioning of the power supply unit-antenna assembly relative to the high-speed collar for optimum signal response. Constraints for the high-speed collar mounting included no modification of the tapered tail rotor shaft, no slippage of the collar relative to the shaft, and the ability to reassemble the system without affecting the strain-gauge calibration. The interfacing hardware was fabricated in two halves

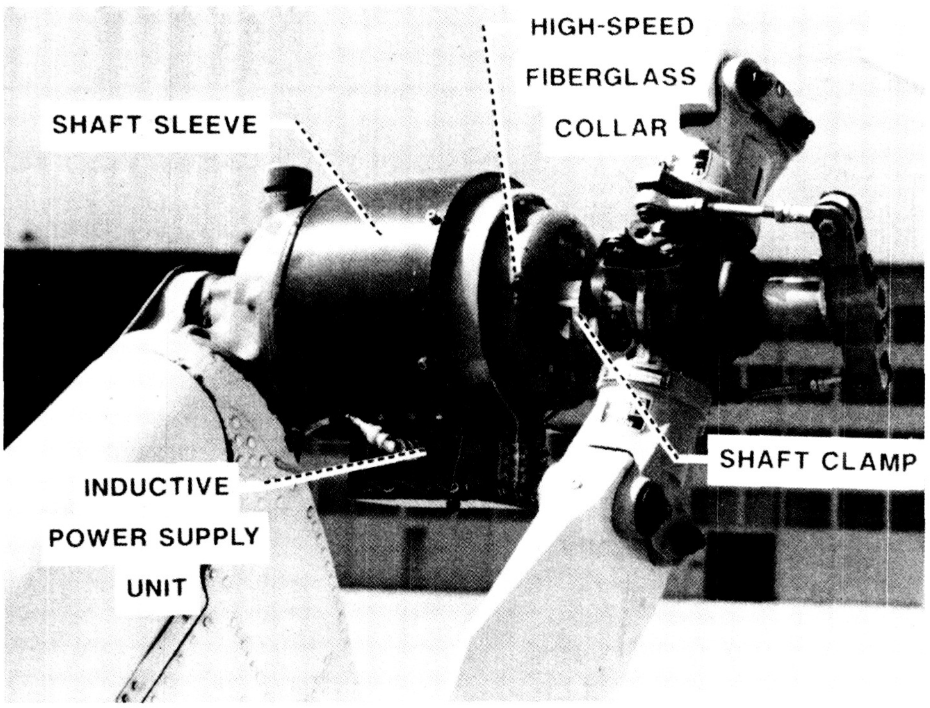

Torque measurement system. L-88-03653

to allow installation without requiring the tail rotor blade removal. A rubber lining isolates the sleeve from the shaft, thus preventing interferring load transmission in the vicinity of the strain gauges. The fiberglass collar is keyed to the sleeve, and this entire assembly is keyed to a shaft clamp. The clamp halves, which bolt together around the shaft, develop friction between the clamp and the shaft and thus prevent slippage.

The system successfully withstood the vibration test spectrum for equipment mounted on helicopters outlined in Military Standard 810D. Strain-gauge calibrations by Bell Helicopter Textron verified that system disassembly and reassembly had no effect on the strain-gauge signal output. Angular acceleration testing and spin balancing of the rotating hardware further qualified the system for flight operations. The Acurex Universal Data Coupler and integration hardware have been successfully flown at Langley Research Center and Wallops Flight Facility.

(Mark T. Lord, 4666)

Dual-Crystal Harmonic Generator for Lasers

A dual-crystal harmonic generator has been developed which incorporates both frequency doubling and tripling crystals in a single oven. This device enables a neodymium-YAG laser oscillator to produce three widely separated output wavelengths simultaneously. The dual-crystal design improves optical and thermal efficiency by eliminating optical surfaces and by reducing the required oven heater power.

Previous designs of harmonic generators accommodated only one crystal per oven. If frequency doubling and tripling were required, the laser beam had to be directed through two harmonic generators, one containing the doubling crystal and another containing the tripling crystal. This approach increased complexity and introduced additional losses into the system due to the greater number of optical surfaces.

The main feature of the dual-crystal harmonic generator is the use of two crystals within one unit. The CD*A doubler crystal partially converts the 1064-nm fundamental wavelength to 532 nm. The KD*P tripler crystal converts an additional portion of the 1064-nm wavelength to 355 nm. All three wavelengths are emitted simultaneously. The conversion efficiency of the crystals is extremely sensitive to temperature and humidity, and consequently they must be maintained in a controlled environment.

A two-piece copper heat sink holds the crystals in place. The pieces of the heat sink can be rotated so that the optical axes of the crystals are oriented perpendicular to each other. This arrangement allows the crystals to be individually angle-tuned by tilting the entire oven about two orthogonal axes. Optical windows at each end seal the oven while allowing the laser beam to enter and exit. The crystals, the heat sink, and the windows are enclosed in a stainless-steel pressure cell that is purged with dry nitrogen. The operating temperature of the crystals is maintained within 0.05°C by a proportionally controlled Kapton heater. Thermistors are located in the heat sink to measure crystal temperature. The pressure cell is insulated from the

ORIGINAL PAGE
BLACK AND WHITE PHOTOGRAPH

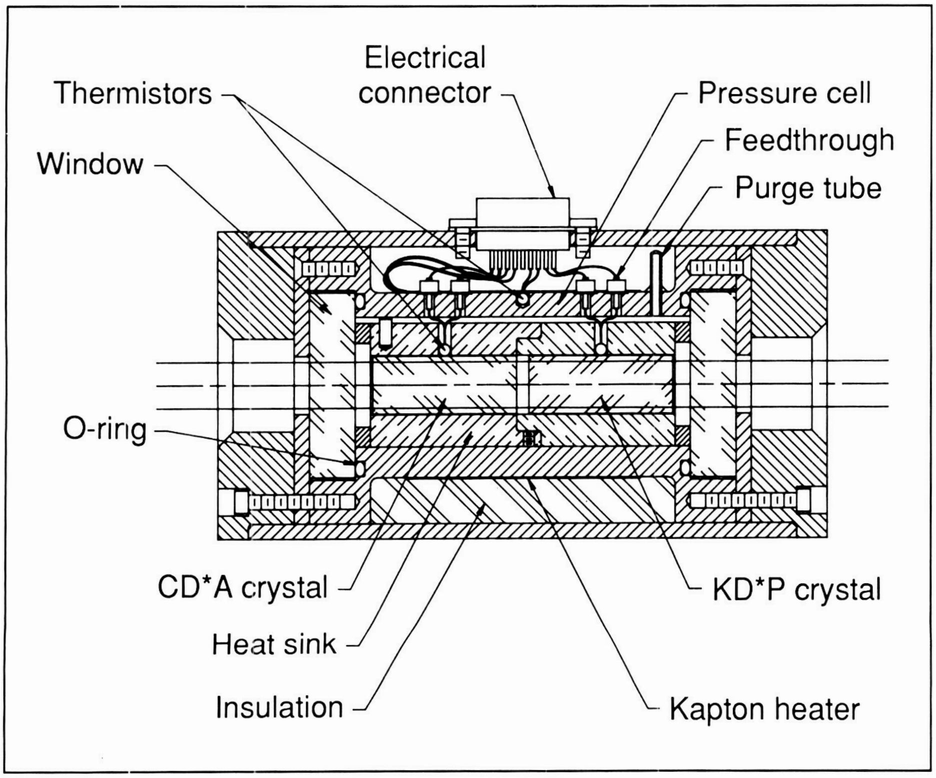

Dual-crystal harmonic generator.

surrounding environment by fibrous insulation and a G-10 laminated tube, which forms the outer surface of the oven. Delrin plugs close the ends of the oven.

The dual-crystal harmonic generator is 5.00 in. long and 2.50 in. in diameter. This generator requires approximately 17 W of heater power, and operates at a nominal temperature of 60°C. **(Christopher L. Moore, 4571)**

Spiral Platen Robotic End Effector

The purpose of the double-lead spiral platen parallel-jaw end effector is to provide the means to securely grasp a wide variety of objects for robotic manipulation. The parallel jaw refers to the action by which the gripping members (fingers) remain parallel while moving transversely along a rail/carriage. The unique drive system, the double-lead spiral platen, is designed to provide an increase in gripping force over conventional units while maintaining a high degree of control over the gripping members. The spiral platen converts the rotary motion of the motor to linear motion in a simple and effective manner.

Commonly available end effectors are limited by a number of factors. There is a tradeoff between physical size, weight, and the gripping force available in most devices. Many end effectors use a worm/rack gear arrangement and a four-bar mechanism to obtain the desired motions. These arrangements can bind and jam in a self-locking mode, which results in the ability to grasp an object without being able to release it. Four bar arrangements move the fingers upward while these fingers move inward. This is a complex motion for which the operator must compensate. Worm and rack gear arrangements also suffer from gear wear and transmission losses, which results in excessive backlash and poor mechanical efficiency.

The double-lead spiral platen end effector addresses these problems. An electric motor turns a shaft that drives a harmonic gear reducer, which in turn decreases the turning rate and greatly increases the output torque. The gear reducer is attached to the double-lead spiral platen, which is a rotating plate into which two mirror-image spiral grooves have been cut. Rolling pins ride in the grooves and are attached to the carriage. The carriage is constrained by rails to only move in the transverse direction. As the platen rotates, the pins are guided by the inclined plane of the spirals to move the carriage, and each rotation of the platen results in one transverse pitch increase for each finger. This motion provides a mechanical advantage that further increases the gripping force. Backlash is minimal due to the tight tolerances between the grooves and the pins. Wear is kept to a minimum by the rolling action of the pins in the hardened grooves, and the rolling action also prevents jamming. The finger positions are predictable and repeatable due to the mirrored spirals, which assure that the fingers are always a known distance from the center for any given platen angle. The harmonic drive is not "backdrivable," which allows the fingers to maintain their force and position even when the power is off.

c - 3

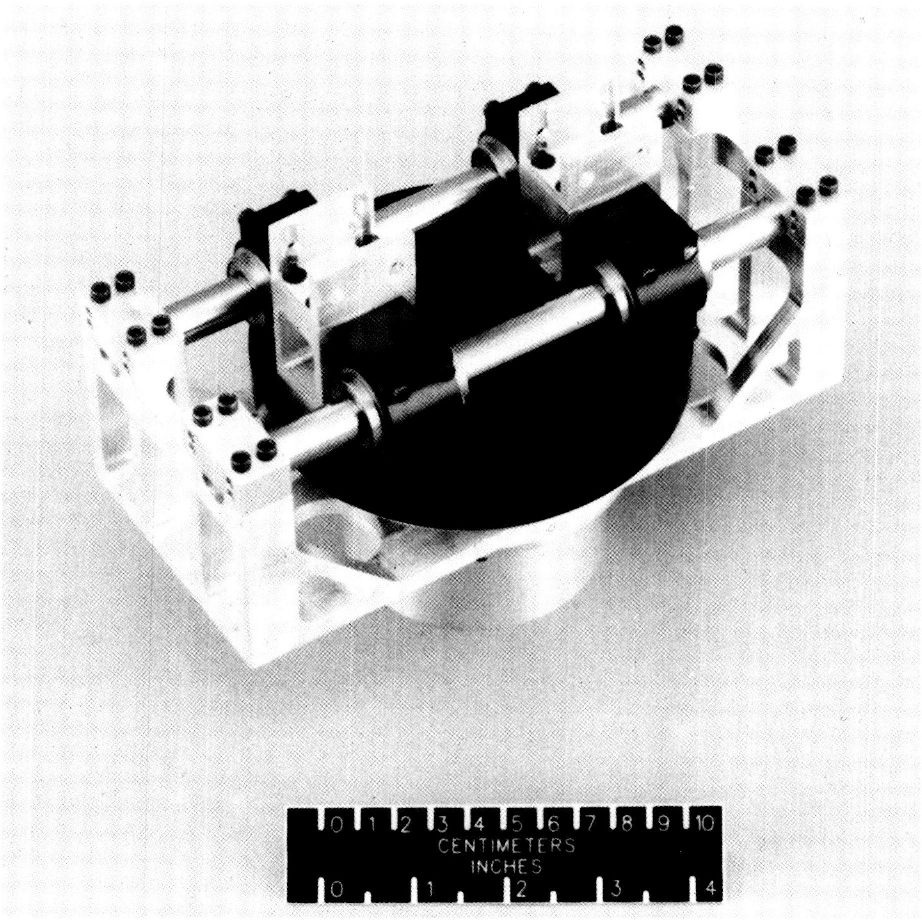

Double-lead spiral platen end effector. L-88-8074

The result is a compact, simple, highly controllable and very strong end effector.

(David C. Beals, 4571)

Development of Composite Equipment Mounting Deck for LASE Instrument

The Equipment Mounting Deck (EMD) is designed to provide a precision mounting surface for the Lidar Atmospheric Sensing Experiment (LASE) modules. Requirements of low weight, high strength, and very low thermal expansion lead to a choice of graphite/epoxy elements to form the deck.

The EMD consists of 19 molded, closed-end channel elements with flat plate doublers at critical joints. The 42 layers of graphite/epoxy prepreg material were hand fitted into an aluminum exterior mold, thus maintaining the designed fiber orientation. A special molded rubber picture frame shaped element was placed in the mold between the graphite/epoxy layup and the vacuum bag material to maintain pressure in the corners of the layup during the cure operation. Each element was cured under vacuum and 100 psig, at 350°F in an autoclave.

After curing, each channel element was ground to the desired thickness. The element was then inspected to ensure acceptable layup quality, and ground to a precise length. Low-cost hardened steel drill fixtures were used to locate the more than 600 close fitting holes required for assembly of the EMD. Use of these fixtures enabled drilling the holes with carbide tipped drills in a hand-held drill motor. Following this approach instead of setting up the elements in a jig boring machine resulted in a large reduction in fabrication time. Care to prevent unraveling of

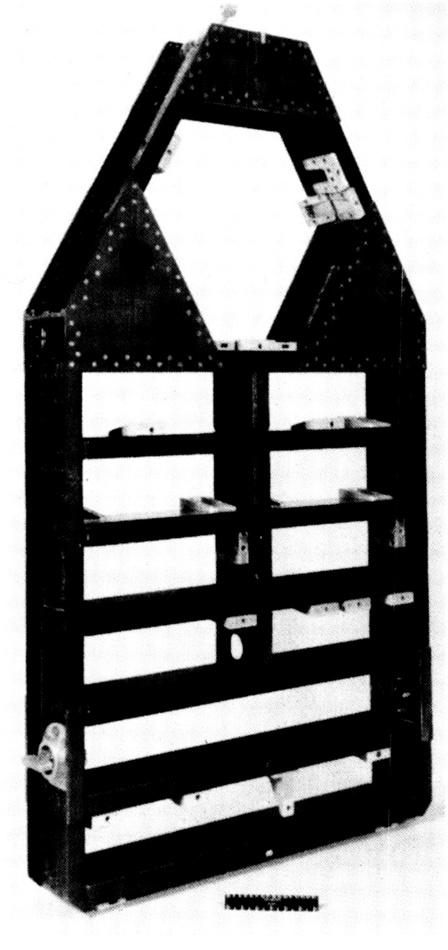

L-88-6408

LASE graphite/epoxy Equipment Mounting Deck.

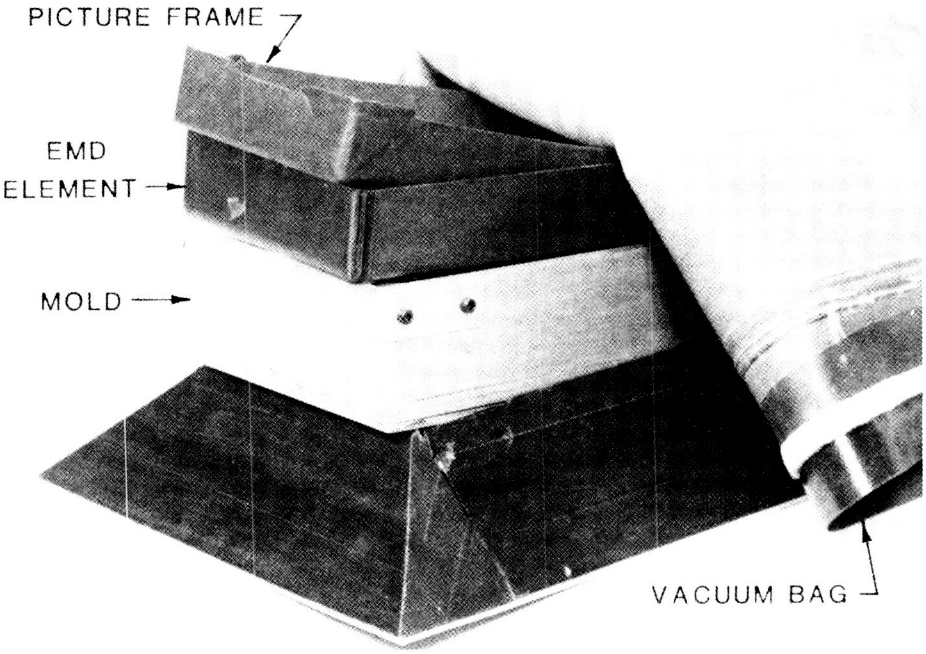

Exploded view of molding components. L-86-3589

the graphite fibers at drill breakthrough was accomplished by sandwiching plastic tape, body putty, and a wooden strip to the back of the element being drilled. Module mounting brackets were fastened onto the individual elements using titanium lock bolts and an epoxy bond with glass beads to ensure a constant bondline thickness. All 19 elements were then fastened together in the same manner to form the completed EMD structure. The final operation involved machining the module mounting brackets on the top and bottom of the deck to the desired height, and installing the mounting holes in the brackets using dimensional tolerances and drill fixtures as required.

This fabrication technology will play an important part in the overall development of composite structural elements for optical platforms on future research programs.
(Leland Bryant, 2781 and David Coombs)

Performance Tests of LASE Heat Exchanger

Tests were performed in the Langley Low-Velocity Aerodynamic Research Tunnel (LVART) to determine the performance of the uniquely designed external heat exchanger for the Lidar Atmospheric Sensing Experiment (LASE). The heat exchanger is designed to cool the electronics and the laser system housed in the Q-bay of the ER-2 aircraft and is attached externally underneath the fuselage. Estimates of cooling the Q-bay with a conventional staggered design indicated marginal results. Thus, a design was developed which increased the frontal tube area exposed to the ram air. Reliable estimates of performance could not be made from correlations for conventional staggered designs. Hence, wind tunnel tests were carried out in which the performance of the design configuration was compared to the performance of a conventional staggered configuration.

The design configuration consisted of 28 circular, finned, aluminum tubes of equal lengths (0.413-in. inner diameter) arranged in two parallel banks. The tubes were housed in a rectangular en-

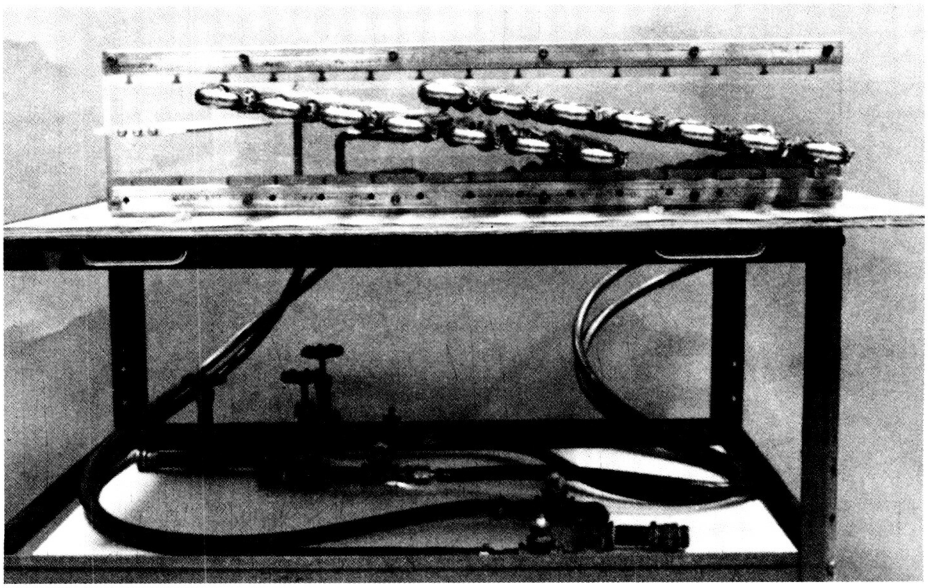

L-87-04732
Full-scale performance test model of LASE external heat exchanger.

closure 3.75 in. by 22 in. by 36 in. The test model was full-scale of the design configuration and is shown in the figure. Water was circulated through the tubes at velocities simulating the flight Reynolds number of the flight coolant, ethylene glycol mixed with water. Wind tunnel tests were carried out at an airflow Reynolds number simulating flight conditions of about 8×10^5. This resulted in a tunnel velocity of approximately 55 ft/sec. Results of the tests indicate that, at the flight coolant Reynolds number of about 3500, the design configuration outperforms a conventional staggered configuration by approximately 6 to 7 percent. This improved performance was then applied to empirical analyses for conventional configurations in the calculation of predicted performance of the design configuration over the LASE flight envelope.
(William S. Lassiter, 4508)

Assembly of Halogen Occultation Experiment (HALOE) Into Flight Configuration

HALOE is a satellite solar occultation experiment designed to monitor the vertical distributions of a number of key upper atmosphere trace gases. The experiment includes the development of the HALOE instrument, the development of the necessary software packages and data reduction procedures, and the analysis of data for science investigations by members of the HALOE Science Team. The science investigations will include studies of trace gas sources and sinks, validation of photochemical models, studies of upper atmosphere transport, and validation of atmospheric dynamic models.

The HALOE objectives are to improve understanding of ozone depletion due to the oxides of chlorine, nitrogen, and hydrogen by collecting and analyzing global vertical profile data on key chemical species (O_3, HCl, CH_4, H_2O, NO, and NO_2) and to study the chlorofluoromethane impact on ozone including interactions among the oxides of chlorine, nitrogen, and hydrogen by measuring HCl and HF in addition to the other key chemical species and by using data on CF_2CL_2, $CFCL_3$, CLO, and $CLONO_2$ obtained from other experiments.

The instrument has undergone a series of electrical and optical characterization tests. Modifications were made in the electronics and optical components based on these test results. Flight thermistor bolometers and photovoltaic detectors have been installed, and final optical alignments have been performed. The instrument has been assembled into the flight configuration, and environmental testing has begun. The HALOE instrument is scheduled to be delivered for integration onto the Upper Atmosphere Research Satellite (UARS) in September 1989.
(James L. Raper, 2668)

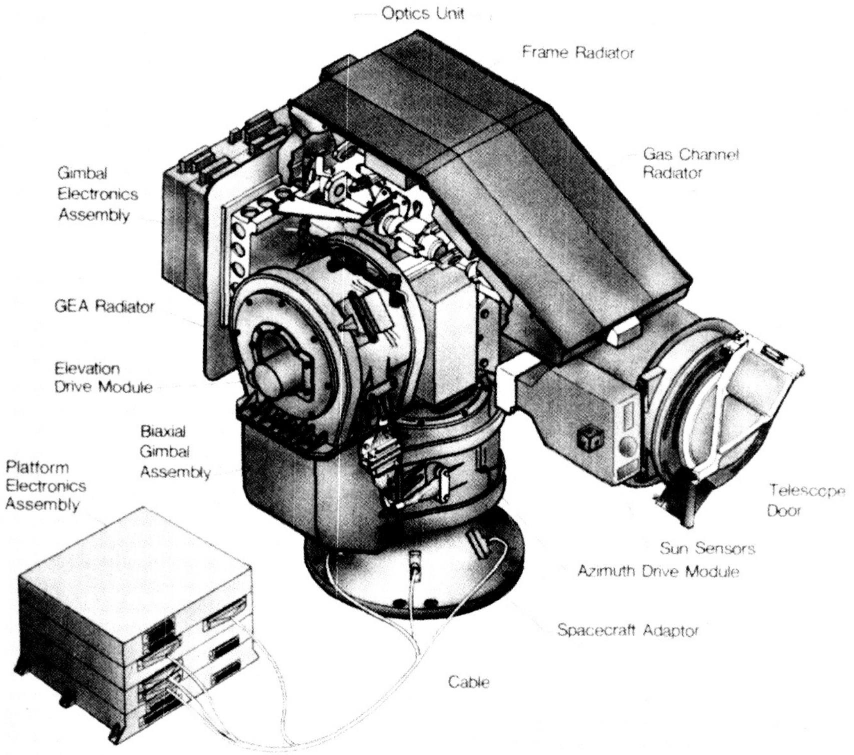

HALOE instrument.

L-86-3584

Technology Utilization

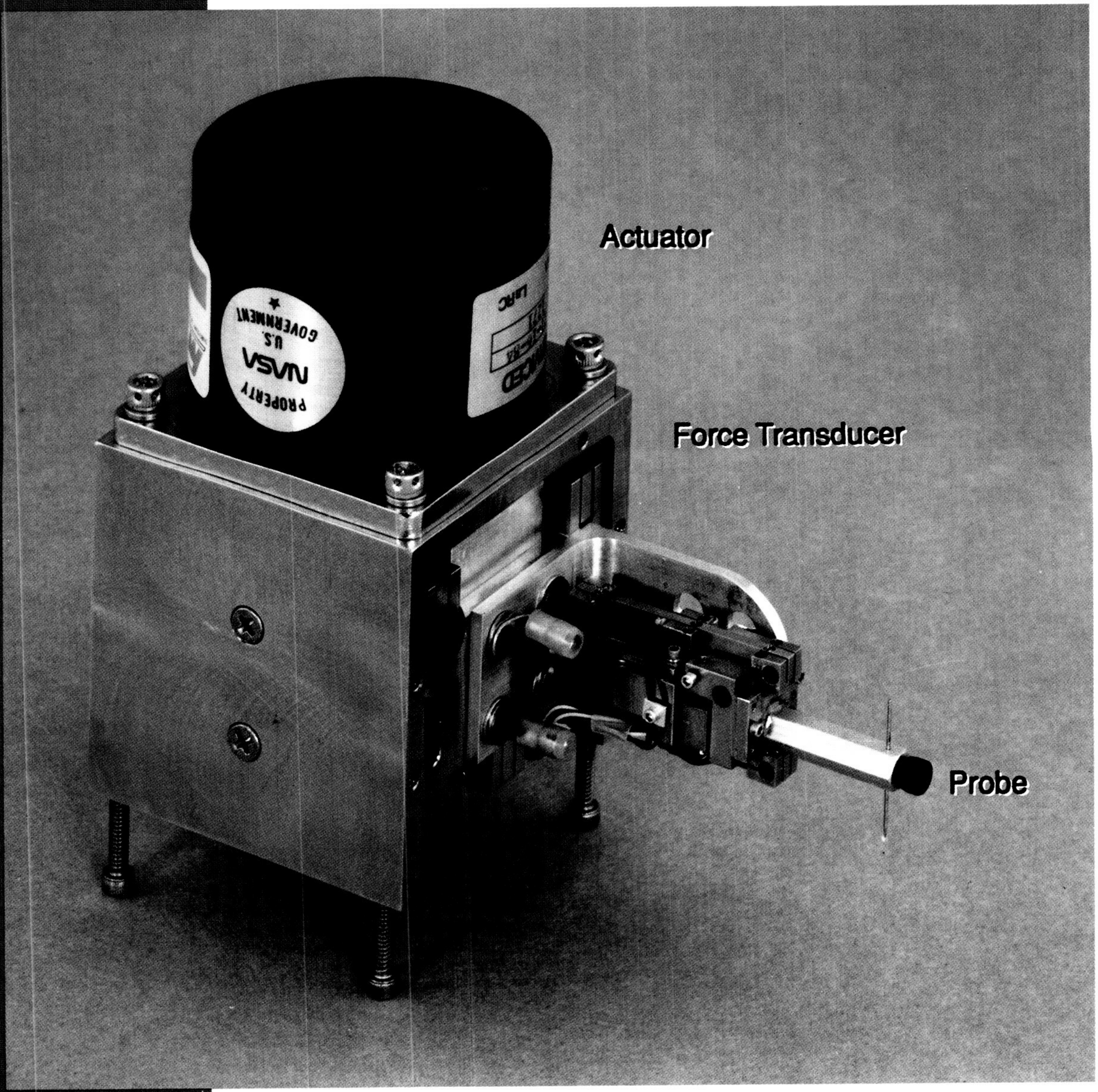

ORIGINAL PAGE
COLOR PHOTOGRAPH

One of the Congressionally mandated responsibilities of NASA is to promote economic and productivity benefits to the Nation by facilitating the transfer of aerospace-generated technology to the public domain. NASA's means of meeting this objective is its Technology Utilization Program, which provides a link between the developers of aerospace technology and those in either the public or private sectors who might be able to employ the technology productively.

One important facet of the NASA Technology Utilization Program is its applications engineering projects, which involve the use of NASA expertise to redesign and re-engineer extant aerospace technology to solve problems delineated by federal agencies or other public-sector institutions. Applications engineering projects originate in various ways; some stem from requests for NASA assistance from other government agencies and some are generated by NASA engineers and scientists who perceive possible solutions to public-sector problems through the adaptation of NASA technology. Additionally, NASA employs a multidisciplinary applications team that maintains liaison with public-sector agencies, medical and public-health institutions, professional organizations, and academia to uncover significant problems in diverse fields such as health care, public safety, transportation, and industrial processes which might be amenable to solution by the application of NASA technology.

This year marks the 25th anniversary of the Technology Utilization Program. During this quarter century, the efforts of NASA to reapply the technology, coupled with those of imaginative entrepreneurs, have generated thousands of secondary applications (or spinoffs). The projects reported here are typical of the latest applications projects.

Aviation Fuel Quality

An expressed need exists to improve the performance of Fuel Quantity Gauging (FQG) systems used aboard commercial and military aircraft. Prior studies have identified acoustic pulse-echo and torsional waveguide probes as suitable sensing technologies to meet the FQG requirements for next-generation aircraft. As a necessary corollary of advanced FQG system development activities, an industry-wide cooperative study of jet fuel properties that affect fuel gauging has been initiated. Parameters of interest are density, permittivity, viscosity, refractive index, freeze point, conductivity, water content, and nuclear absorption characteristics. These parameters will be measured in fuel samples obtained from various world-wide sources, through seasonal variations. Langley Research Center will measure the mass attenuation coefficients of the fuel samples using americium-241 (Am-241) gamma rays.

Nuclear attenuation monitoring system. L-88-8042

To accomplish this task, a new mass attenuation monitoring system (shown in the figure) has been developed. This system is based on a highly collimated Am-241 source and a sodium iodide counter; the source and counter are separated by a geometrically well-defined test fuel cell. A computer program for determining the mass attenuation coefficient of the test fuel sample, based on data acquired for a preset counting period, has been generated and tested for several types of aviation fuel. The values of mass attenuation coefficients derived, using the described system and procedures, agree with previously reported values to within ±1 percent.

Fuel samples, which are being furnished by participating airlines, began arriving at Langley Research Center in August 1988 and will continue through the spring season of 1989.
(Jag J. Singh, 3907)

Catalytic Monoliths for Carbon Dioxide Lasers

Pulsed CO_2 lasers have several potential remote-sensing applications, including operation on satellites and other space vehicles. However, the electrical discharges generally used to excite such lasers decompose some of the CO_2 to CO and O_2. Because of weight and volume constraints, space-based lasers must operate in a closed-cycle mode with no addition of makeup gas or removal of decomposition products. Thus, to maintain laser power, the CO and O_2 formed must be catalytically recombined to regenerate CO_2. Volume and power constraints require that the catalyst used be situated in the laser itself and that it be highly porous. To prevent contamination of the laser optics, the catalyst must not be in the form of a powder but must be in a form to survive the forces associated with space launch. Ideally, the catalyst should be coated on a highly porous, structurally robust, monolithic support.

High-efficiency CO and O_2 recombination catalysts have been and are currently being developed and tested at Langley Research Center. The design of suitable monolithic catalyst supports for CO_2 lasers is both time-consuming and expensive, however. This problem has been addressed in a collaborative technology applications project between Langley and the University of California, San Diego, resulting in development of a laser/catalyst model and computer program. The fully functional monolithic-design computer program accepts laser operating parameters and catalyst properties as inputs, and the required monolithic dimensions are outputs. The program, which accounts for all important mass and heat transfer phenomena as well as first-order catalyst kinetics, has been used to design high-efficiency, high-priority prototype catalyst monoliths with parallel square channels for various laser parameters using current Langley catalyst technology. This program can be readily modified to other monolithic configurations as required.
(David R. Schryer, 2818)

Laser Velocimeter (Autocovariance) Buffer Interface

The acquisition of data from a laser velocimeter presents a unique instrumentation problem. Normally, data acquisition instrumentation samples the continuous analog output from classical sensors at regular intervals as determined by the acquisition clock. Since all sensors are sampled simultaneously, calculations of time-dependent statistics and cross correlations are straightforward using classic processing algorithms. However, the laser velocimeter provides measurements of velocity only when a particle passes through the sample volume. These particles arrive randomly in time according to Poisson statistics, and they may or may not yield a measurement in any or all measurement components. Therefore, the data acquisition instrumentation must be able to acquire data every time each signal processor has made a measurement. Under these conditions, time-dependent statistics and cross correlations can be made only if the data acquisition instrumentation provides internal measurement timing and ensures coincidence between measurement components.

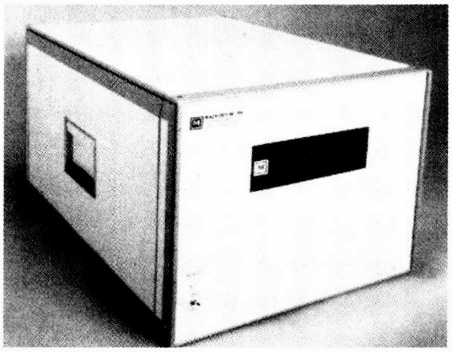
L-86-799

LVABI data acquisition system.

The Laser Velocimeter (Autocovariance) Buffer Interface (LVABI) was designed at Langley Research Center to provide the data acquisition capabilities and controls required to maximize the information obtainable from laser velocimeter measurements. The LVABI can

acquire data from up to six signal processors at an acquisition rate of up to 650 kHz per channel. Each channel can acquire data independently of the remaining channels, or channels may be placed in coincidence with a user-determined data acceptance time window. All channels have companion interarrival timing acquisition channels. These channels measure the time between successive particle velocity measurements acquired by their companion channels. The interarrival time measurements provide the capabilities to remove statistical sampling bias and calculate the flow turbulence power spectra. Applying the coincidence requirement between velocity components allows the direct calculation of statistical cross correlations (such as Reynolds stress and velocity vector analysis of the flow) since the velocity vector of each particle can be determined directly. While coincidence between the velocity components is important, it is also necessary to simultaneously acquire data from other sensors to obtain correlations between velocity and other phenomena.

The LVABI provides this capability with auxiliary data acquisition channels. These channels will acquire either 16-bit digital data or analog data digitized with an integral 12-bit analog-to-digital converter (500 kHz maximum sampling rate). Each auxiliary channel is triggered by a user-selected laser velocimeter data acquisition channel or coincidence control line. Up to 20 auxiliary channels may be included in the LVABI to provide conditional sampling of shaft encoders, microphones, hot wires, or other high-response sensors. Once the user selected number of data points (up to 64,000 acquisitions per each channel) has been acquired, the host computer is signaled to receive the acquired data. The acquired data from all channels are passed to the host via direct memory access through a single 16-bit parallel interface. The use of the LVABI provides the necessary control and timing capabilities for the laser velocimeter to yield similar data as obtained from standard flow diagnostic instrumentation.

The LVABI data instrumentation system (shown in the figure) has been licensed to and is being manufactured by Macrodyne, Incorporated, Schenectady, New York. **(James F. Meyers, 2791)**

Bladder Monitor for the Handicapped

More than five million individuals in the United States are estimated to suffer from the problem of urinary incontinence. In an effort to address this problem, a prototype, portable, ultrasound-based bladder monitor system has been developed as depicted in the figure.

The device uses a small 500 kHz transducer to launch a low-power tone burst of sound into the abdomen and then receive the returning echo. Each returning echo is digitized into 128 time blocks, which represent a depth of several inches into the abdomen. The returning echo is evaluated by an onboard microprocessor for the location of the back wall of the bladder. The depth of field of the device is adjustable to compensate for individual differences in the distance of the back wall of the bladder from the surface of the abdomen. Special transducer systems have been developed to permit the transducer to look into the abdomen at an angle.

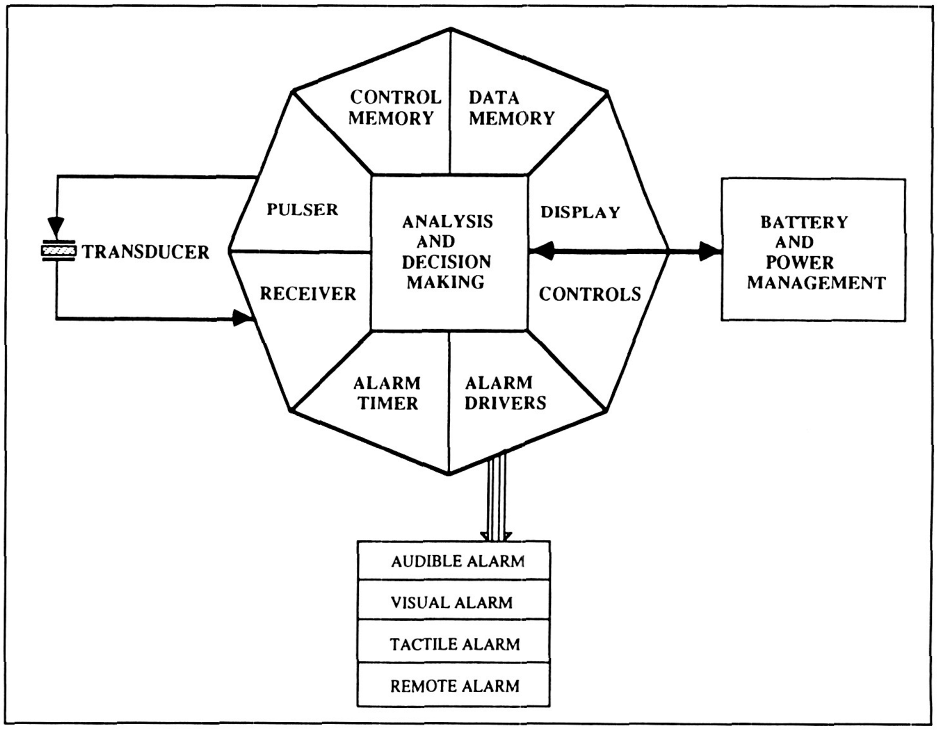

Bladder monitor system schematic.

In this manner the device accommodates the wide variability in both abdominal contour and the location of the bladder relative to the pelvis.

The echoes returning from the back wall of the bladder are tracked and characterized over time. Each signal is digitally processed to extract and evaluate the degree of relative distension of the bladder. The trend is tracked through time, and the result is compared to preselected levels stored in memory. When the desired degree of distension is reached, the system activates the alarm circuit to alert the wearer that it is an appropriate time to void. A number of different alarms (audible, visual, tactile, and remote) are available to suit the circumstances. The device is battery operated and amenable to miniaturization. Patents have been applied for on both the device itself and the transducer systems, and a license has been granted by NASA to the Association for Retarded Citizens of the United States (ARCUS).
(Eric Madaras and Joseph S. Heyman, 3036)

Urodynamic Catheter System

Langley Research Center engineers, working in collaboration with the Medical College of Virginia (MCV), have completed development of a pressure catheter system to measure sphincteral action by passively and dynamically providing simultaneous and circumferential pressure information from a series of discrete points along the urethral length. The catheter consists of five strain-gauge transducers within the 4.0-cm-long urethral measurement section plus a bladder pressure transducer near the catheter tip. Each sensor element consists of a C-shaped cross section to minimize the effect of circumferential orientation. Additionally, one lumen is provided for infusion. These characteristics have been accomplished while maintaining the overall diameter of the catheter, including a sheath, below 3.5 mm.

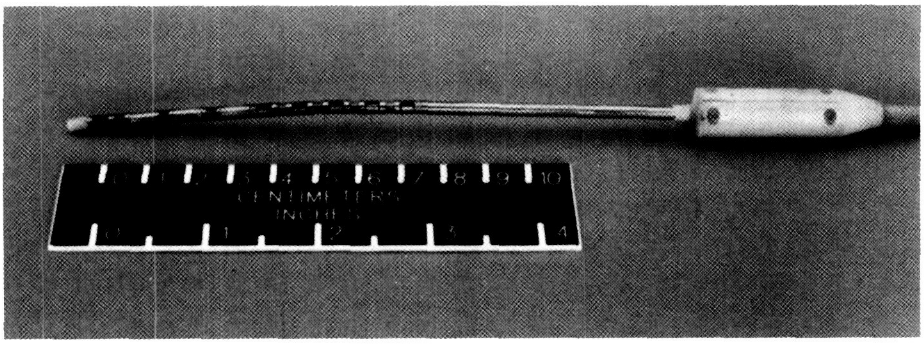

Multisensor catheter assembly. L-87-6278

By constructing each strain element in a C-shaped cross section, the bending element is made sensitive to mechanical forces tending to squeeze it from all directions. Four-arm strain-gauge bridges bonded to each element provide an electrical signal proportional to these forces. Custom designed strain gauges were obtained for this application in order to minimize temperature effects and to optimize the signal output. Individual sensors are separated by 9 mm and connected by coupling bellows to provide controlled flexibility in the catheter.

In addition to the multisensor catheter assembly (shown in the figure), the system consists of a strain-gauge excitation power supply and signal conditioning electronics for amplification and electrical isolation, an analog-to-digital converter, and a microcomputer and associated software to control the experiment and process, display, and data recording. Significant advantages of this technology over current systems include the ability to measure an integrated pressure around the circumference, obtain measurements at several (currently six) discrete locations along the length of the device, simultaneously sense dynamic or rapid transient pressure fluctuations at these locations, and process and display the results in real time.

Initial tests were conducted at MCV in December 1987, and the results exceeded expectations; the sensors demonstrated excellent dynamic response and stability. Development of the software for control and data acquisition has been completed, and clinical trials were initiated at MCV in November 1988.

In an alternate embodiment of this system, the transducer assembly may be connected to a battery-powered conditioning module, which in turn is integrated into a multiplexed telemetry system. The respective transducer signals are digitized and transmitted from the subject over an optical, radio frequency, or ultrasonic beam. This serially transmitted information stream can be received at a remote location and subsequently processed in the microcomputer. These features

would provide fully remote data receiving, computation, and display and thus allow complete subject mobility.
(Harlan K. Holmes, 3483)

Nerve Stimulator

In an investigation into nerve injury during surgery, medical researchers at the Eastern Virginia Medical School (EVMS) Department of Otolaryngology reported a need for a device that could be used to mechanically stimulate nerves. Furthermore, the applied stimulation force needed to be quantified. Such a device, intended for use in animal studies, would improve researcher ability to quantify initiation of injury to the nerve. A request for assistance by EVMS to the Langley Research Center Technology Utilization Office resulted in an in-house project that was initiated in December 1987.

This project has resulted in the development of an electromechanical precision Nerve Stimulator that can apply and monitor stimulating pulses to a nerve fiber. Two existing force-measuring units, one a flight skin-friction transducer and the other a miniaturized skin-friction transducer (both normally utilized for measuring aerodynamic drag), were modified and combined to form this precision instrument. The device (shown in the figure) consists of three units that include a miniature probe with a spherical tip that serves as a force applicator; an actuator that positions the probe to contact a nerve fiber; and a transducer that measures the force being exerted on the nerve fiber by the probe.

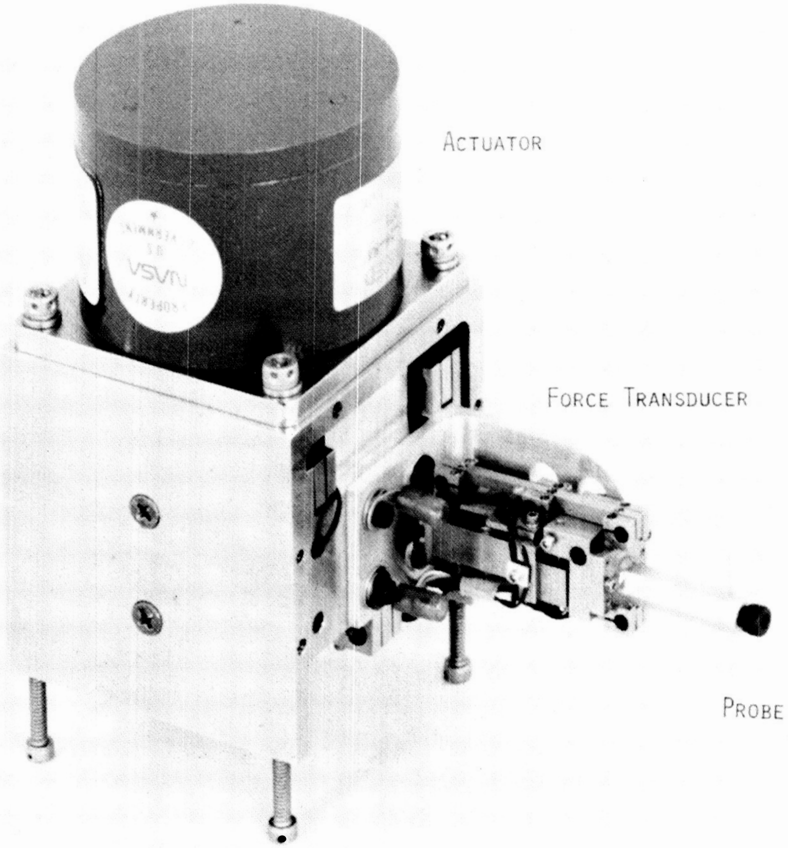

Electro-mechanical Nerve Stimulator. L-88-4450

The Nerve Stimulator is a repositioning servomechanism capable of applying and monitoring pulses of 0 to 10 grams force with a precision of better than 0.05 grams. The device can also be used independently to apply stimulating pulses by displacing a nerve fiber from 0 to 0.25 mm with a precision of 0.01 mm while simultaneously measuring the level of the applied load. Excluding the electronic controller, the Nerve Stimulator weighs about 2 kg and is approximately 80 cm × 80 cm × 130 cm in size.

A prototype device was delivered to the EVMS in 1988.
(Ping Tcheng and Frank H. Supplee, Jr., 3483)

ORIGINAL PAGE
BLACK AND WHITE PHOTOGRAPH

National Aeronautics and Space Administration

Report Documentation Page

1. Report No. NASA TM-4078	2. Government Accession No.	3. Recipient's Catalog No.

4. Title and Subtitle
Research and Technology 1988
Annual Report of the Langley Research Center

5. Report Date
December 1988

6. Performing Organization Code

7. Author(s)

8. Performing Organization Report No.
L-16518

9. Performing Organization Name and Address
NASA Langley Research Center
Hampton, VA 23665-5225

10. Work Unit No.

11. Contract or Grant No.

12. Sponsoring Agency Name and Address
National Aeronautics and Space Administration
Washington, DC 20546-0001

13. Type of Report and Period Covered
Technical Memorandum

14. Sponsoring Agency Code

15. Supplementary Notes

16. Abstract

The mission of the NASA Langley Research Center is to increase the knowledge and capability of the United States in a full range of aeronautics disciplines and in selected space disciplines. This mission will be accomplished by performing innovative research relevant to national needs and Agency goals, transferring technology to users in a timely manner, and providing development support to other United States Government agencies, industry, and other NASA centers. This report contains highlights of the major accomplishments and applications that have been made during the past year. The highlights illustrate both the broad range of the research and technology activities at NASA Langley Research Center and the contributions of this work toward maintaining United States leadership in aeronautics and space research. For further information about the report, contact Dr. Richard W. Barnwell, Chief Scientist, Mail Stop 105-A, NASA Langley Research Center, Hampton, Virginia 23665, (804) 864-6062.

17. Key Words (Suggested by Authors(s))

Research and technology
Aeronautics
Space
Structures
Materials
Aerodynamics
Electronics
Flight systems
Technology utilization
Engineering

18. Distribution Statement
Unclassified—Unlimited

Subject Category 99

19. Security Classif.(of this report) Unclassified	20. Security Classif.(of this page) Unclassified	21. No. of Pages 214	22. Price A10

NASA FORM 1626 OCT 86 NASA-Langley, 1988
For sale by the National Technical Information Service, Springfield, Virginia 22161-2171